IOP Conference Series:
Earth and Environmental Science

2019 3rd International Conference on Power and Energy Engineering (ICPEE 2019)

October 25-27, 2019
Shandong University, Shandong, China

ISSN: 17551307
E-ISSN: 17551315

IOP Conf. Series: Earth and Environmental Science **431** (2020) 011001 doi:10.1088/1755-1315/431/1/011001

PREFACE

It is our great pleasure to thank all of you for your participations to 2019 3rd International Conference on Power and Energy Engineering (ICPEE 2019) which was held during October 25-27, 2019, in Shandong University, Qingdao, China.

ICPEE 2019 is organized by Shandong University, assisted by Xiamen University of Technology, via their South-South Collaborative and Sustainable Development Center and International Society for Environmental Information Sciences (ISEIS). ICPEE 2019 is dedicated to issues related to Power and Energy Engineering. It was a golden opportunity for students, researchers and engineers to interact with the experts and specialists to get their advices and consultations on technical matters, dissemination and marketing strategies.

ICPEE 2019 is highlighted by several senior academic and professional speakers, including Prof. Gordon Huang from University of Regina, Canada, Prof. Edward McBean from University of Guelph, Canada, Prof. Yongping Li from Beijing Normal University, China, Prof. Zhijun Peng from University of Bedfordshire, UK, Prof. Christophe Guimbaud from National University of Orlean, France and Dr. Pengfei Xia from Center for Applied Geosciences, University of Tübingen, Germany who have attended the conference as keynote speakers. There were ten sub-sessions with various topics: Modeling of energy management systems, Energy and environmental Studies, Technologies of power and energy engineering, etc.

These proceedings present a selection from papers submitted to the conference by universities, research institutes and industries. All papers were subjected to peer-review by conference committee members and international reviewers.

This volume is presenting recent advances in the field of Environment and Renewable Energy and various related areas, such as High voltage transmission and insulation technology, Smart Grid Operations and Management, Mechatronics, Power system and performance assessment, Electrical engineering and automation, Electricity and energy, Electronic information engineering.

We would also like to express our sincere gratitude to organizing committee and the volunteers who had dedicated their times and efforts in planning, promoting, organizing and helping the conference.

Prof. Zhijun Peng
University of Bedfordshire, UK
2019-11-18

Conference Committee

Conference Chairs

Gordon Huang, International Society for Environmental Information Sciences

Yongping Li, Beijing Normal University, China

Wang Shuguang, Shandong University, China

Program Chair

Satya Harpalani, Southern Illinois University Carbondale, USA

International Program Committee

International Program Committee Co-Chair: Shuguang Wang, Shandong University, China

Co-Chair: Mohamed El-Din, University of Alberta, Canada

Yanfeng Li, South-South Cooperation Center for Sustainable Development, China

Yongtae Ahn, Gyeongnam National University of Science and Technology, Korea

Bandar Alqahtani, Duke University, USA

Hasan Aydogan, Mechanical Engineering Department, Selcuklu, Konya, TURKEY

Ipek Barut, Istanbul University, Turkey

Serdar Celik, Southern Illinois University Edwardsville, USA

Ali Cheshmehzangi, University of Nottingham Ningbo, China

Bal Deshwal, A. I. Jat H. M. College, India

Saad El-Syaed, Mechanical power engineering-Zagazig university, Egypt

Ahmed Hossam-Eldin, Alexandria University, Alexandria, Egypt

Jinliang Liu, Ontario Ministry of Environment and Climate Change

Lei Liu, Dalhousie University, Canada

Rodrigo Muñoz, Bataan Peninsula State University, Philippines

Hui Kwun Nam, University of Macau, China

Hedayat Omidvar, National Iranian Gas Company, Iran

Nugroho Pambudi, Sebelas Maret University, Indonesia

Wei Peng, University of Regina, Canada

Xiaosheng Qin, Nanyang Technological University, Singapore

Jagdish Sharma, JK Lakshmipat University, India

Sunil Singal, Indian Institute of Technology, India

Eric Strauss, Michigan State University, USA

Wei Sun, Zhongshan University, China

Qian Tan, China Agricultural University, China

Mohd Teridi, National University of Malaysia, Malaysia

Tsung-Mou Huang, Taiwan Power Company, Taiwan

Dimiter Velev, University of National and World Economy, Bulgaria

Shuo Wang, Hongkong Polytechnical University, Hong Kong

Xiuquan Wang, University of Louisiana, USA

Jia Wei, Beijing Polytechnical University, China

Bin Yan, Xiamen University of Technology, China

IOP Conf. Series: Earth and Environmental Science **431** (2020) 011003 doi:10.1088/1755-1315/431/1/011003

Peer review statement

All papers published in this volume of *IOP Conference Series: Earth and Environmental Science* have been peer reviewed through processes administered by the proceedings Editors. Reviews were conducted by expert referees to the professional and scientific standards expected of a proceedings journal published by IOP Publishing.

Table of Contents

Chapter 1: High Voltage Transmission and Insulation Technology

Chapter 2: Smart Grid Operations and Management

Chapter 3: Mechatronics

Chapter 4: Power System and Performance Assessment

Chapter 5: Electrical Engineering and Automation

Chapter 6: Electronic Information Engineering

Chapter 7: Electricity and energy

Chapter 1:
High Voltage Transmission and Insulation Technology

IOP Conf. Series: Earth and Environmental Science **431** (2020) 012001 doi:10.1088/1755-1315/431/1/012001

Simulation study on ±320kV DC power cable steady-state temperature field distribution and its influencing factors

Zhihan Shi[1], Youxiang Yan[2], Weiwei Zhang[3], Zhipeng Yang[1], Pengpeng Wu[4], Weilin Lin[5] and Wenzhang Zhu[6]

1 School of Electrical Engineering and Automation, Xiamen University of Technology, No.600, Ligong Road, Jimei District, Xiamen, P.R.China
2 State Grid Xiamen Electric Power Supply Company, No.21, Hubinnan Road, Siming District, Xiamen, P.R.China
3 State Grid Zhejiang Shaoxing Shangyu Electric Power Supply Company Limited, No.500, Fuxingdong Road, Shangyu District, Shaoxing, P.R.China
4 School of Information Science and Engineering, Fujian University of Technology, No.3, Xueyuan Road, Minhou District, Fuzhou, P.R.China
5 State Grid Jinjiang Electric Power Supply Company, Jinjiang, P.R.China
6 School of OPTO-Electronic and Communication Engineering，Xiamen University of Technology, No.600, Ligong Road, Jimei District, Xiamen, P.R.China
E-mail: 54253025@qq.com

Abstract. Temperature distribution is an important parameter in the operation of DC cables, while there are few studies at present. In this paper, the steady-state temperature field distribution of DC cable was calculated by simulation, and the factors including conductor current and outer surface temperature were discussed and analyzed. The results showed that there is a temperature gradient in the radial direction of the cable; Both the conductor current and the outer surface temperature have a significant effect on the overall temperature of the cable; The increase in the conductor current and the outer surface temperature will significantly increase the conductor temperature. However, the insulation temperature difference changes little.

1. Introduction

High Voltage Direct Current (HVDC) transmission plays an increasingly important role in the power system with the advantages of long transmission distance, large transmission capacity and flexible operation style [1]. In recent years, with the Nan’ao ±160kV multi-terminal flexible DC transmission project, Zhoushan ±200kV five-terminal flexible DC transmission project and Xiamen ±320kV flexible DC transmission project been put into operation, HVDC crosslinked polyethylene (XLPE) cable has been rapidly developed and application [2-5].

A large number of studies have shown that the AC cable temperature distribution is an important parameter reflecting its operating state and an important basis for determining the current carrying capacity [6-8]. Although the DC cable is similar in structure to the AC cable, some scholars have proposed that the DC cable current carrying capacity calculation should consider the temperature distribution of the insulation in addition to the maximum allowable operating temperature of the conductor, even if the specific constraints have not been determined [9].

At present, Yan Youxiang, Yang Yuexi, et al have studied the cable selection and laying, control mode and operation performance, switching method and system control strategy of Xiamen ±320kV flexible DC transmission project [10]. However, the steady-state temperature field distribution and current carrying capacity of the cable have not been specifically studied. Therefore, it is necessary to study ±320kV power cable steady-state temperature field distribution and its influencing factors.

This paper took Xiamen ±320kV DC cable as an example, used COMSOL Multiphysics finite element simulation software to establish a two-dimensional axisymmetric model and calculated its steady-state temperature field distribution. On this basis, the effects of different conductor currents and different outer surface temperatures on the temperature of the cable conductor and the temperature difference of the insulation were studied.

2. Simulation model

2.1. Finite element method and governing equation

The finite element method is an approximate mathematical simulation for real physical systems and is a commonly used numerical calculation tool for solving practical engineering problems. The basic idea is to divide a continuously solved region into a finite number of interconnected elements, and then combine the relations of each unit into a system of equations, and finally obtain an approximate solution of the entire solution domain.

COMSOL Multiphysics is a simulation calculation software based on finite element method. The software integrates various physical modules such as AC/DC and heat transfer in advance, and has strong computing performance. This article uses the solid heat transfer module in COMSOL Multiphysics to study the steady-state temperature field distribution of the DC cable.

The governing equation for solid heat transfer is[2]

$$\rho C v \nabla T = \nabla (\lambda \nabla T) + Q \qquad (1)$$

where: ρ is the density of the solid material, kg/m^3; C is the constant pressure heat capacity of the solid material, J/(kg·K); v is the velocity vector, m/s; ∇ is the vector differential operator; T is the temperature of the solid material, K; λ is the thermal conductivity of the solid material, W/(m·K); Q is the heat source in the solid material, W/m^3.

2.2. Geometrical model and material parameters

The structure of ±320kV DC cable is mainly composed of conductor, conductor screen, XLPE insulation, insulation screen, water-blocking tape, aluminum sheath and outer sheath, as shown in Figure 2. The structural parameters and material parameters of the cable were given in table 1.

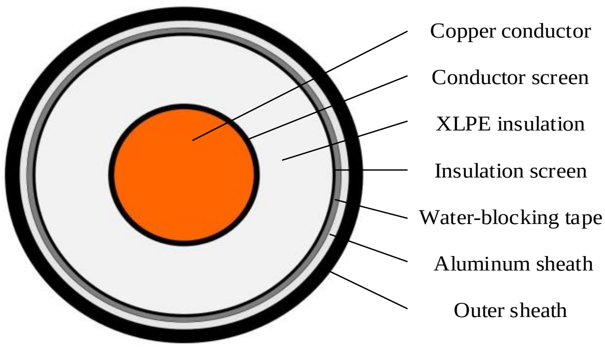

Figure 1. The structure of ±320kV DC cable.

Table 1. The structural parameters and material parameters of ±320kV DC cable.

NO.	Structures	Outside radius / mm	Thermal Conductivity / [W/(m·k)]	Constant pressure heat capacity / [J/kg·K]	Density / [kg/m³]
1	Copper conductor	25	400	385	8700
2	Conductor screen	27	0.2857	2603	922
3	XLPE insulation	53	0.2857	2603	922
4	Insulation screen	54	0.2857	2603	922
5	Water-blocking tape	56	0.4	2182	1100
6	Aluminum sheath	58.8	238	900	2700
7	Outer sheath	63.8	0.2857	2532	948

When studying the temperature distribution of a cable, the cable structure is usually simplified to a two-dimensional radial plane or a two-dimensional axisymmetric model, as shown in Figure 1. Studies have shown that the two-dimensional axisymmetric model can reflect the change of the DC resistance of the conductor with temperature, which is more in line with the actual situation. Therefore, a two-dimensional axisymmetric model of ±320kV DC cable was established.

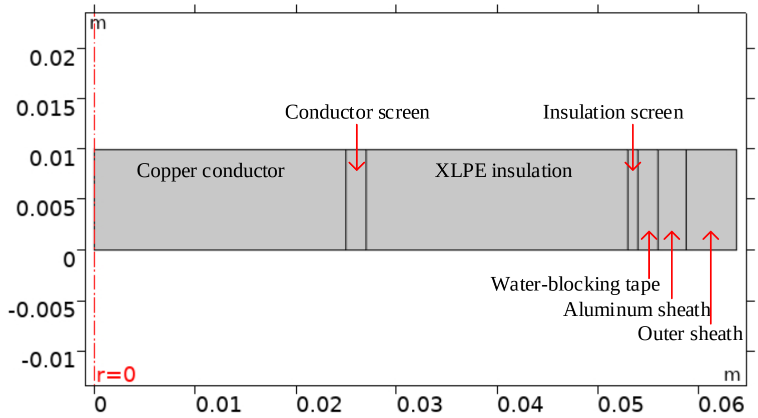

Figure 2. Two-dimensional axisymmetric model of ±320kV DC cable.

In addition, the calculations are properly assumed from an engineering perspective:

- The thermal conductivity of each layer of the cable is constant;
- The thermal conductivity of the cable is the same in all directions;
- The outer surface of the cable is an isothermal surface.

2.3. Boundary conditions and meshing

The temperature of the outer surface of the cable is set to 30 ℃, the heat flux density at the upper and lower ends of the cable model is set to 0, and the Joule heat generated by the current in the conductor is equivalent to a heat source[11]. They are used as the first, second and third types of boundary conditions in heat transfer calculation. The triangle mesh adaptive segmentation of the model effectively avoids the shortage of manual processing, greatly improves the calculation efficiency, and ensures that the minimum mesh is smaller than the thinnest layer.

3. Simulation results

3.1. Steady-state temperature field distribution

At present, the current carrying capacity of the DC cable is mainly determined according to the constraint that the maximum operating temperature of the conductor does not exceed the maximum allowable temperature of the insulation. In this paper, the maximum operating temperature of the conductor is 70 ℃ as a constraint to determine the current carrying capacity. In the case where the outer surface temperature of the cable is 30 ℃, the conductor temperature reaches 70 ℃ when the current flowing through the conductor is equal to 1479A.

Figure 3 shows the steady-state temperature field distribution of the cable in this case. As can be seen from the figure, there is a temperature gradient in the radial direction of the cable--a downward trend from the inside out. The conductor temperature is the highest and the outer surface temperature is the lowest; The temperature is mainly borne by the insulation layer, and the temperature difference of the layer reaches 30.74 ℃.

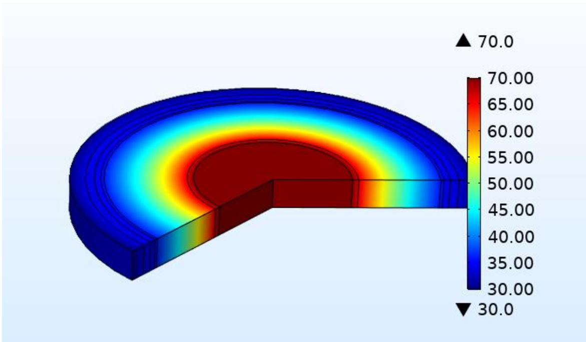

Figure 3. Steady-state temperature field distribution of ±320kV DC cable.

3.2. Conductor current

Different Joule heats produced by different currents will cause differences in the radial temperature distribution of the cable, especially the insulation temperature distribution. Set the temperature of the outer surface of the cable to 30 ℃. The temperature field distribution under low load (conductor current IC=600A/800A/1000A), normal load (IC=1200A/1400A/1479A) and excessive load (IC=1600A/1800A/2000A) was studied. As can be seen from figure 4:

- Under the same current, the temperature of the copper conductor and the aluminum sheath remain unchanged in the radial direction, while the temperature of the other structures shows a downward trend and the insulation temperature drops the fastest.
- As the conductor current I_C increases, the overall temperature T of the cable increases. The larger I_C is, the more significant the temperature increase trend is. When the current I_C=600A, the curve changes gently; when the current I_C=2000A, the curve becomes very steep.The thermal conductivity of the cable is the same in all directions;

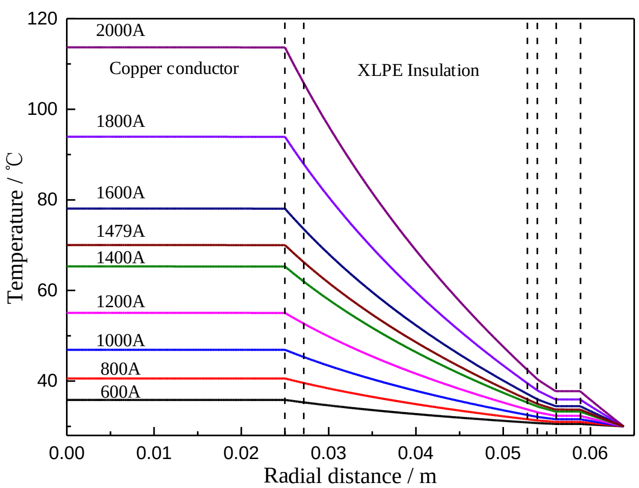

Figure 4. The relationship between temperature and radial distance.

The conductor temperature and insulation temperature difference are the influencing factors of the two constraints on the current carrying capacity. Further analysis is carried out to obtain the results as shown in figure 5. As the conductor current I_C increases, the conductor temperature T_C and insulation temperature difference ΔT both increase exponentially. When I_C=600 A, T_C=35.85°C, ΔT=4.49°C; When I_C=2000 A, T_C =113.68°C, ΔT=64.27°C.

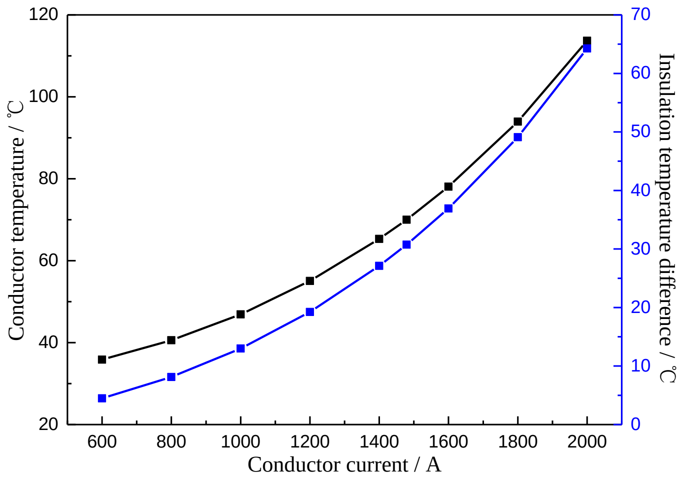

Figure 5. The relationship between conductor temperature/insulation temperature difference and conductor current.

3.3. Outer surface temperature

The cable laying environment will cause the temperature of the outer surface of the cable to be different. Different outer surface temperatures can affect the heat dissipation of the cable, which in turn affects the cable temperature distribution. Set the cable conductor current I_C=1479A, study the temperature distribution of the outer surface temperature of the cable T_S=10 ℃/20 ℃/30 ℃/40 ℃/50 ℃, and get the results as shown in figure6. When the temperature of the outer surface of the cable increases, the overall temperature T curve of the cable is basically upwardly inclined.

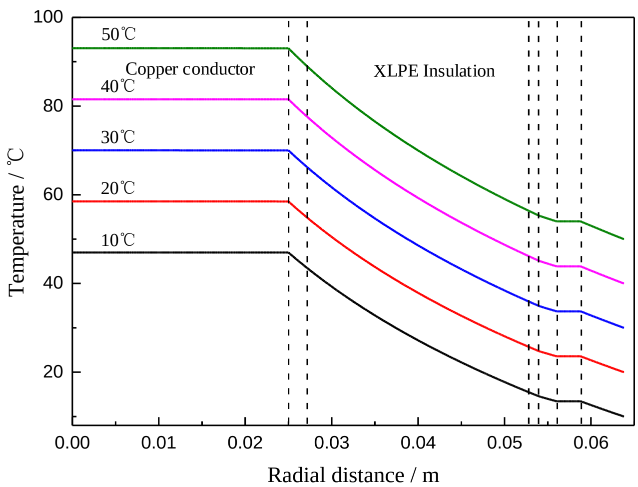

Figure 6. The relationship between temperature and radial distance.

It can be seen from figure7 that as the outer surface temperature increases, both the conductor temperature and the insulation temperature difference increase in a positive proportion. When the temperature of the outer surface increases, the temperature of the conductor rises more obviously while the temperature difference of the insulation changes less. When T_S=10 ℃, T_C=47.00 ℃,

ΔT=28.42°C; When T_S=50 ℃, T_C =93.05°C, ΔT=33.07°C. It can be considered that the influence of the outer surface temperature on the overall temperature distribution of the cable is small compared to the conductor current.

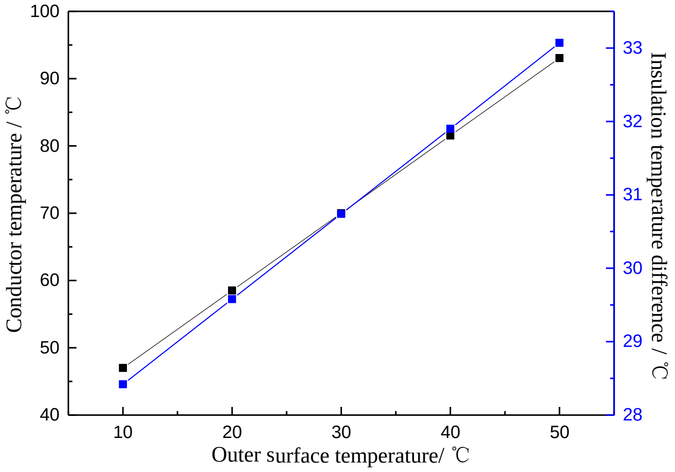

Figure 7. The relationship between conductor temperature/insulation temperature difference and outer surface temperature.

4. Conclusions

In this paper, ±320kV DC cable steady-state temperature field distribution and its influencing factors were simulated and the following conclusions were drawn:
In addition, the calculations are properly assumed from an engineering perspective:

- There is a temperature gradient in the radial direction, that is the temperature gradually decreases from the conductor to the outer sheath.
- The conductor current has a significant influence on the conductor temperature. As the conductor current increases, the insulation temperature difference increases.
- The external surface temperature also has a significant effect on the conductor temperature, but the effect on the insulation temperature difference is negligible.
- The influence of the conductor current on the overall temperature distribution of the cable is greater than the influence of the external surface temperature.

5. References

[1] Zhao J K, Zhao P and Chen Z Z *et al* 2017 Review on Progress of HVDC Cables Insulation Materials *High Voltage Engineering* **43** 3490-503
[2] Hao Y P, Chen Y and Yang L *et al* 2017 Coupled Simulation on Electro-thermal-fluid Multiple Physical Fields of HVDC Submarine Cable *High Voltage Engineering* **43** 3534-42
[3] Lin W J, Sun W Z and Zhang J *et al* 2016 Analysis of Typical Operating Modes of Zhoushan Multi-Terminal VSC-HVDC Pilot Project *Power System Technology* **40** 1571-8
[4] Yan Y X, Fang X L and Zhang W G *et al* 2014 Cable Section and Laying of Xiamen ±320 kV Flexible DC Cable Transmission Project *High Voltage Engineering* **41** 1147-53
[5] Xie S H, Fu M L and Yin Y *et al* 2015 Triple Jumps of XLPE Insulated HVDC Cable Development in China: from 160 kV to 200 kV and then to 320 kV *Southern Power System Technology* **9** 5-12
[6] Liu G, Wang P Y and Mao J K *et al* Simulation Calculation of Temperature Field Distribution in High Voltage Cable Joints *High Voltage Engineering* **44** 3688-98
[7] Liu G, Wang Z H and Xu T *et al* Current Capacity Calculation and Experimental Analysis of 110 kV Cable Joint *High Voltage Engineering* **43** 1670-76
[8] Liu G, Lei M and Ruan B Y *et al* Model Research of Real-time Calculation for Single-core Cable Temperature Considering Axial Heat Transfer *High Voltage Engineering* **38** 1877-83

IOP Conf. Series: Earth and Environmental Science **431** (2020) 012001 doi:10.1088/1755-1315/431/1/012001

[9] Hao Y P, Huang J C and Yang L *et al* Analytical Calculation Method of Steady-State Current Capacity of HVDC Cables *Power System Technology* **40** 1283-8
[10] Yang Y X, He Z Y and Zhou *et al* Control Mode and Operating Performance of Xiamen ±320 kV VSC-HVDC Project *Smart Grid* **4** 229-34
[11] Li Z H, Yang L and Tian Y *et al* Steady-State Temperature Field of HVDC Cable Joint and Its Influencing Factors *Electric Power* **49** 48-53

Acknowledgements
This work was supported by the Science and Technology Research Foundation of State Grid Corporation of China (2019202).

IOP Conf. Series: Earth and Environmental Science **431** (2020) 012002 doi:10.1088/1755-1315/431/1/012002

Single-phase ground fault location technology research and application based on transient recording wave

YIN Hui[1], SHI Changkai[1], LI Baikui[1], GUAN Shilei[1] and Liu Yue[2]

1China Electric Power Research Institute, Beijing, China
2Tianjin Haoyuan Huineng Technology Co., Ltd., Tianjin, China
E-mail: 2034946676@qq.com

Abstract. Fault location is an important part of distribution automation. Aiming at the problem of single-phase grounding fault detection, a fault location system based on transient recording technology is proposed. Compared with the advantages and disadvantages of the traditional single-phase ground fault detection method, the single-phase ground fault location application based on transient recording is proposed. The proposed method is not only theoretically verified in the simulation of the distribution network system, but also applied to the operation of fault location network in the true test field, which verifies the effectiveness of the proposed method.

1. Introduction
The distribution network is at the end of power system, which plays an important role in the transmission of electric energy. Whether the whole power system can run stably and safely depends on its operation condition. Most of the 6 ~ 35 kV distribution systems in China are small current grounding systems, and the neutral point is grounded by arc suppression coil or ungrounded. About 80% of the total faults are single-phase grounding faults [1]. When grounding occurs, because the system still maintains the three-phase symmetrical characteristic and can continuously supply power to users, so the power grid is allowed to continue to operate within 2 hours even if single-phase grounding occurs. However, if the power grid runs for a long time after the fault, it will lead to the damage of substation equipment, and may result in personal and property losses. In addition, the non-fault voltage rises after the fault, which may break through the insulation protection layer and even cause short circuit fault [2], seriously affecting the safe operation of the distribution network.
The types of single-phase ground fault are complex and varied, because the steady-state current of the fault is very small, the arc is unstable, and the noise interference in the field, the detection is very difficult [3].Therefore, the accurate and fast location of fault points, shortening the outage time, affects the power supply quality of users and affects the reliability of distribution network operation. The demand of social development must be to improve the reliability of single-phase grounding fault detection.
Therefore, combined with signal processing, wireless information communication and artificial intelligence technology, this paper proposes a single-phase ground fault location system based on transient wave recording technology. The method can accurately reflect the current amplitude of the line and the transient changes of current and voltage, provide rich operation data for ground fault analysis, and can also provide early warning for abnormal state of the line, carry out inversion for complex fault process, and effectively improve the automation level of the distribution network.

2. Traditional detection method of grounding fault

Fault indicator technology (abbreviated as indicator) is widely used in fault location system, bringing revolutionary changes. At present, there are mainly three types of single-phase grounding detection methods for fault indicators: transient method, steady-state method and signal injection method [4].

2.1. Steady state method

The indicator of zero sequence current method locates the faulty line by collecting the zero sequence current of the line current signal to be greater than the set value, and the direction of the current flowing through the indicator is opposite to the direction of other lines [5], thereby locating the faulty line. This method is commonly used in neutral point ungrounded systems, but in actual operation, when the three-phase asymmetry of the line brings a large zero-sequence current, the method will also cause misjudgment.

Different from the zero sequence method, the principle of the fifth harmonic method indicator is mainly based on the same characteristics as the fundamental waves of power frequency in the ungrounded system [6]. The method reduces the compensation effect of arc suppression coil to a minimum, but it is affected by uncertain factors in actual operation, such as the position of nonlinear load, the line impedance, etc.

2.2. Transient method

The indicator of first half wave method uses the fault transient information to judge the ground fault. Find out the line where the transient current and the transient voltage are opposite in the direction of the first half of the wave when single-phase grounding occurs, and locate the line as the fault line for alarm indication.

The method can detect a single fault point and a relatively simple ground fault process. However, the criterion is based on the assumption that the fault occurs at a phase voltage of 90 degrees. The current and voltage characteristics are very short and affected by the line parameters [7]. In practical application, this method is not suitable for locating the fault point.

2.3. Signal injection method

The indicator of the signal injection method mainly detects the line characteristic coded signal according to the change of the induced electric field. The signal source judge the ground fault and inputs a specific coded signal to the bus after the ground fault occurs [8]. For the small current grounding system, the method is relatively stable and is a common grounding detection scheme. However, in practical applications, the injected signal strength is limited by the capacity of the voltage transformer. When the operation mode of the distribution network changes, it is also possible for multiple signal sources to input signals at the same time, resulting in long voltage fluctuation at the neutral point and even causing phase-to-phase short circuit fault [9].

3. Transient recording fault location system

3.1. Transient wave recording technology

Transient wave recording technology is a combination of fault indicator technology, signal processing, wireless information communication and artificial intelligence technology. Through indicator, it carries out high-precision sampling of line current and ground electric field, tracks load current trend and ground electric field change, and monitors the running state of line in real-time. When the line state changes abnormally, the high-frequency sampling and recording is automatically triggered, which is not less than 4kHz. With the help of high-precision wireless synchronization technology, the synchronization time of three-phase recorded data is guaranteed to be less than 100μs, providing rich and accurate transient information for ground fault detection. The intelligent analysis will be carried out by three-phase waveform data of the line or the change of the synthesized zero sequence current. The ground fault line is positioned such that the induced electric field of the line drops obviously while the zero sequence current has obvious mutation and is larger than a certain value.

3.2. Transient recording fault locating system

The transient wave recording fault location system consists of indicator and power distribution master station. The indicator includes acquisition unit equipment and collection unit equipment. The positioning schematic diagram is shown in figure 1.The acquisition unit is the core sensing part of the system. According to the distribution network wiring diagram, the acquisition unit is installed on the branch line of the distribution line and coded address, which is used for labeling in the geographic information system (GIS) of distribution master station. The collection unit serving as a bridge between the collection unit and the distribution master station is correspondingly installed on the telegraph pole at the branch, and receives the state information, fault, recorded wave data and other information from collection through a short-distance wireless communication mode. The use of the general packet radio service (GPRS) technology facilitates the communication between the collection unit and the distribution master station, and uploads recorded wave files including synthesized transient zero sequence current, electric field waveform and other information. The master station constructs a network model according to the coded information of the installed monitoring points, and detects the state information array of each node. In case of fault or abnormal state, each monitoring point will actively send a recording file. The master station will firstly analyze the characteristics of zero sequence current of each monitoring point according to the zero sequence current method, and select the network nodes with large zero sequence current to locate the fault lines. According to the network model comparison table, the entire network topology is simplified to the network model of the fault line, and then the nodes in the simplified model are analyzed in detail for single-phase current waveform, and the fault phase is determined according to the characteristics of the electric field waveform that the electric field of the fault phase drops and the electric field of the normal phase rises. Because the zero sequence current increment at the position before the fault point is larger than that after the fault point, the zero sequence current change critical point is finally screened out from the indicator of the fault phase, and the precise location of the fault point is displayed on the geographic background of GIS. According to this information, the maintenance personnel can quickly get to the fault area for troubleshooting.

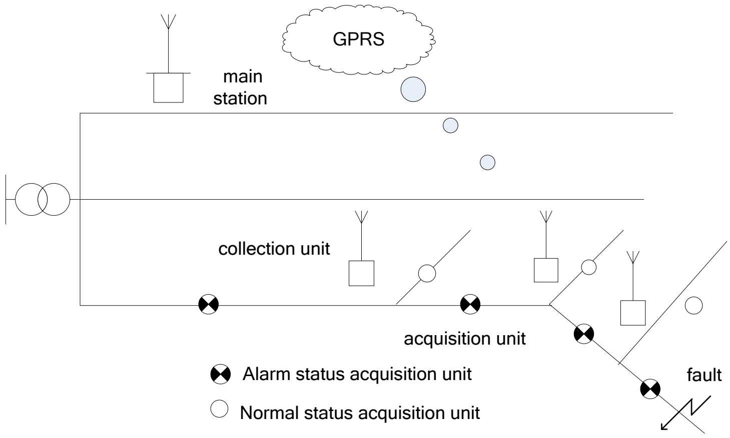

Figure 1. Schematic diagram of fault location system.

4. System verification

In order to verify the effectiveness of the proposed fault location system in single-phase grounding fault detection, the power system simulation software platform and the actual field line operation are respectively used for verification.

With the help of electromagnetic transient simulation software (PSCAD), several distribution network models with different neutral grounding modes are built to simulate and monitor the transient waveforms before/after the ground fault line, normal line and fault point. By modifying the grounding resistance parameters, the simulation of metallic, small resistance and high resistance ground fault is realized. Taking a single radiation grid structure as an example, the simulation model is shown in figure2, and a 10kV neutral point ungrounded system model with three outgoing lines L1-L3 is designed. Among them, the transmission line coupling model (PI) is used for short line simulation, and the model at the end of the line is used for load simulation. Ground fault simulation test of 800 ohm grounding resistance is carried out for phase A of L3 line. As shown in figure 3, it can be seen from the L3 electric field waveform diagram in part (a) that the fault occurs at the moment when the phase A voltage is 45 degrees, the phase A electric field U_a decreases, and the electric fields of the normal phases U_b and U_c increase. In part (b), the zero sequence current I_0 of the normal line L2 and the fault line L3 both have abrupt changes at the time of fault, and the zero sequence current of L3 is greater than L2's, while the abrupt changes of I_0 are in opposite directions. The waveform directions of L3's zero sequence voltage U_0 and zero sequence current I_0 are also opposite. Similarly, comparing and analyzing the transient output results of simulation waveforms of other grounding resistances and angles, it is found that the current and voltage of the fault phase have the above obvious transient characteristics in the ground fault is different from the non-fault line. Therefore, it is theoretically feasible to detect ground detection by wave recording.

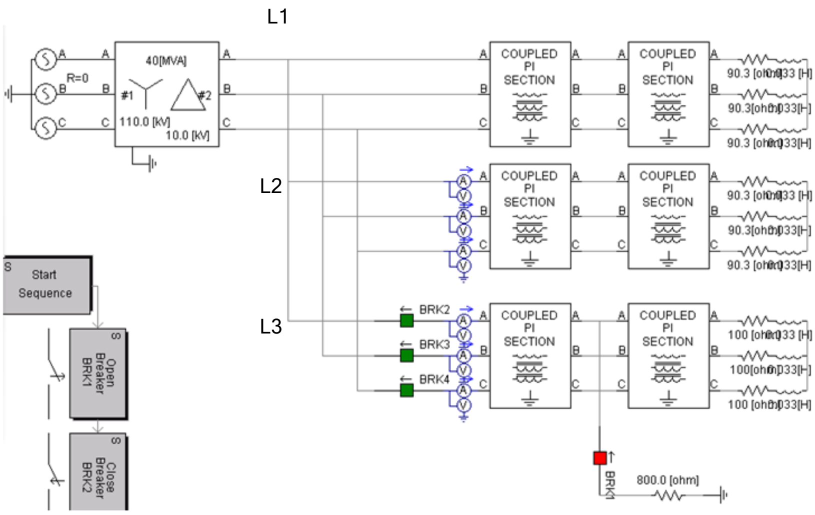

Figure 2. PSCAD simulation model.

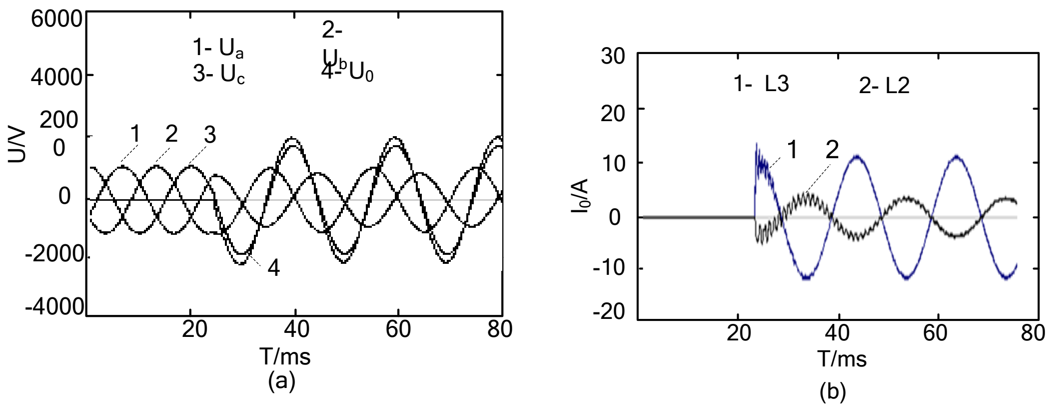

Figure 3. Waveform of line.

The system is also used in the real test field of the small current grounding system to verify the fault location system. As shown in figure 4, indicators are respectively installed on the three lines of 10kV ungrounded system, i.e. No.43 indicator is installed on No.1 pole of zhenpei line I, No.42 indicator is installed on No.1 pole of zhenpei line II, No.45 indicator is installed on No.5 pole, and No.40 indicator is installed on zhenpei line III. After the line is running normally, a ground fault experiment with a grounding resistance of 3kΩ is carried out on phase A of the line through switch control at the experimental grounding point of Zhenpei II line. When a ground fault occurs, the indicator starts recording according to the sudden change of the induced electric field, synthesizes the three-phase current data into a zero sequence waveform, and uploads it to the distribution master station. The distribution master station receives the waveform files uploaded by all line indicators and analysis the waveforms. The waveforms of zero sequence current I_0 and zero sequence voltage U_0 are shown in figure 5. It can be seen that the zero sequence currents waveforms of No.42indicators in part (a),No. 45'sin part (b), No. 43'sin part (c) and No. 40'sin part (d). The waveforms of No.42 and No.45 have obvious abrupt changes compared with the waveforms of other indicators, and the directions are opposite. In addition, the zero sequence current of No.42 is greater than No.45's. The master station gives an alarm prompt for ground fault through complex network topology analysis, and locates the fault area between No.42 and No.45 indicators of Zhenpei II line. It can be seen that the position result of the operation test is consistent with the theoretical verification of the simulation software platform, and the fault zone can be determined by comparing the direction and magnitude of zero sequence current of each line through various algorithms and combining the change of electric field.

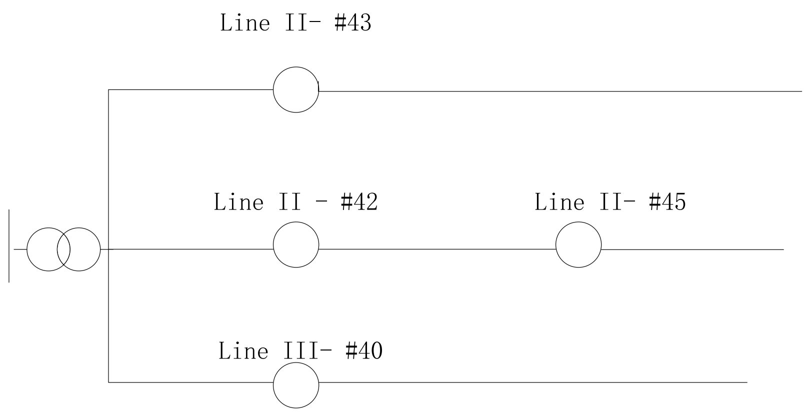

Figure 4. Installation diagram.

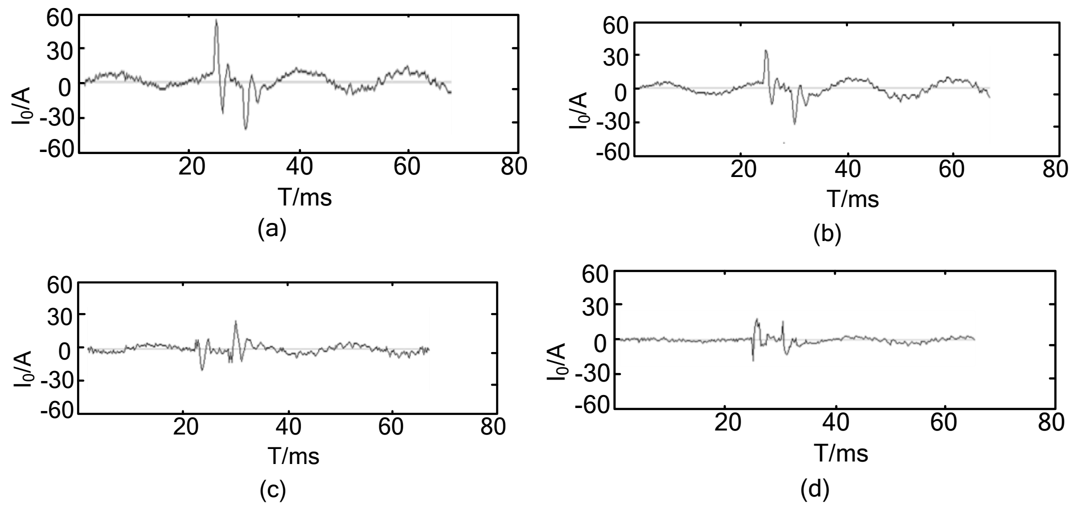

Figure 5. Zero sequence waveform of each line.

5. The end

The requirement of high reliability of power supply will surely bring users' attention to single-phase grounding fault location technology. According to the characteristics of the grid structure in our country, after analyzing various ground fault detection principles and comparing their respective advantages and disadvantages, this paper proposes a single-phase ground fault location method based on transient wave recording technology. This method can obtain accurate line operation parameters and fault transient informations, restore the change process of current and electric field, not only realize ground fault judgment and rapid fault location, but also can carry out early warning for abnormal states. As a new method of ground fault detection, the relation criterion of current and voltage transient waveforms under different grounding conditions still needs to be improved and optimized by on-site measured.

6. References

[1] Wang chen2014Single-phase Grounding Fault Location System for Distribution Network Based on Wireless Communication and Its Dynamic Model Experiment [J] *Power Grid Technology* vol 38 p2280
[2] Sun qidong, Zhang kairu, Liu jian, Yi lifeng, Song xiangmin and Li yayun 2016 Research of single-phase fault earth fault line selection method for the distribution network based on fifth harmonics and wavelet reconstruction [J] *Electrical Measurement and Instumentation* vol 53 p1-4
[3] Tang jinrui, Yin xianggen, Zhang zhe, Yang chen, Ye lei, Qi xuanwei and Lin jin 2013 Survey of fault location technology for distribution networks [J] *Electric Power Automation Equipment* vol 33 p7-13
[4] Yin maolinand Zhai hanbing 2014 Analysis of Single-phase Ground Fault in Distribution System [J] *Shandong Electric Power Technology* vol 41 p18-23
[5] Cui Demin, Liu jian and Li xiaobo 2013 Research on Single-phase Ground Fault in Distribution Network [J] *China Electric Power Education* p196-207
[6] Zhang caiyou2007 Analysis of Current Situation of Single-phase Earth Fault Indicator Technology [J] *Power Grid Technology* vol 31 p280-282
[7] Yang fan and Guan huanxin 2017 Design automation of distribution system of single-phase earth fault detection model [J] *Science Technology and Engineering* vol 17 p219-222
[8] Yuan Qincheng 2007 *Automatic Fault Handling Technology for Distribution System* (China: Power Equipment Press) p74
[9] Yang haisheng 2018 Research on the coordinated control strategy of single phase to ground injection signal source in small current grounding system [J] *Electrical Measurement and Instumentation* vol 55 p66-69

Acknowledgments

Thesis was funded by State Grid science and technology project (Research and Development of Key Technologies for Distribution Network Fault Simulation and Test Detection Platform), Project No.PDB17201700211.
I would like to thank everyone who helped me during the writing of this article. I am very grateful for the help of the technical staff and the remaining authors who provided me with valuable advice in academic research. Without their patient guidance, profound criticism and expert guidance, the completion of this paper will not be possible.

IOP Conf. Series: Earth and Environmental Science **431** (2020) 012003 doi:10.1088/1755-1315/431/1/012003

Study on insulation performance of EPR cable terminal containing metal particles

Huang Jisheng[1], Xiang Enxin[2], Li Lini[3]

1 Senior Engineer, Lincang Power Supply Bureau, Yunnan Power Co., Ltd. Lincang, Yunnan, China.
2 Senior Engineer, Yunnan Elecric Power Research Institute, Yunnan Power Co., Ltd., Kunming，Yunnan, China.
3 Master's degree, College of Electrical Engineering Southwest Jiaotong University Chengdu, Sichuan China’
E-mail: 419722987@qq.com/47585275@qq.com/ huangxusheng@yn.csg.cn

Abstract. The 35kV EPR cable terminal is widely used in the distribution network. During the production process, metal particles are easily introduced due to environmental and technological reasons, resulting in frequent breakdown of the terminal breakdown accident. In order to study the influence of metal particles on the insulation performance of EPR cable terminals, a model of metal particles defect in cable terminals on the extension line of the main insulation and the control tube is built. The electric field distribution of cable terminals under power frequency voltage is calculated by COMSOL simulation software. At the same time, a sample of cable terminals containing metal particles is made, and local discharge is used. The partial discharge information of the cable terminal sample is tested by the electric test platform. The results show that the introduction of metal particles will increase the electric field distortion inside the cable terminal, strengthen the discharge activity of the cable terminal, and increase the discharge amount significantly, which seriously affects the insulation performance of the EPDM cable terminal.

1. Introduction

As an important part of the distribution network, the 35kV ethylene-propylene rubber(EPR) cable bears the key role of transmitting electrical energy. As the weakest part of its insulation, the cable terminal has its electrical insulation performance, which directly affects the transmission system and electricity. The effective operation of the equipment [1] is related to the reliability of the distribution network. According to the fault data of the cable line, in the 35kV EPR cable, the terminal operation failure accounted for about 70% of the total number of cable line operation failures [2]. When the cable terminal is installed in the field, the external semiconductor shielding layer, conductive shielding layer and sheath of the cable need to be cut off, and the interception is prone to electric field distortion during operation [3], which affects the insulation performance of the cable termination; In the process of environmental and manufacturing processes, it is easy to introduce conductive impurities, which change the electric field distribution at the end of the cable, and affect its electrical insulation performance.

At present, domestic and foreign scholars have carried out various researches on various types of cable defects, and have achieved fruitful results. The Liu Gang team of South China University of Technology studied the breakdown characteristics of the main insulation of the cable joint with impurities. The results show that the impurity-containing defects will cause partial electric field

IOP Conf. Series: Earth and Environmental Science **431** (2020) 012003 doi:10.1088/1755-1315/431/1/012003

distortion inside the cable joint, and will break down the insulation material in severe cases [4]; Rittmam GW and other scholars have provided some directions for fault diagnosis of cable joints by studying the partial discharge information of cable joints containing impurities [5]; North China Electric Power University scholars are currently studying the effective electric materials and structures to make the internal electric field of cable accessories effective. Optimization [6]. However, after the metal particles are mixed, how the electric field of the 35kV cable terminal is distorted in the presence of defects, how the metal particles with different parameters affect the highest electric field value, how the discharge at the metal particles develops, and how the discharge performance of the terminal changes. There are fewer reports and there is an urgent need for relevant research.
Based on there, this paper studies the influence of the internal electric field distribution when the metal particles in the cable terminal are located at different positions, and finds the position with the greatest impact, so as to focus on the pre-fabrication and normal operation; and through the partial discharge test, the key is extracted. Information to explore the local discharge characteristics of particles inside, providing a basis for fault diagnosis.

2. Electric field analysis

2.1. Modeling of cable terminal

According to the on-site anatomical results and the ex-factory data, the cable termination is to cut off the outer semi-conductor layer, the metal shielding layer and the sheath of the cable body [7], and the control tube and the heat-shrinkable tube which can uniformly distribute electric field are pre-formed by layer-by-layer heat shrinking. Finally, the shed is used to isolate the waterproof, so the cable end is a multi-layer structure, and its model is shown in Figure 1.

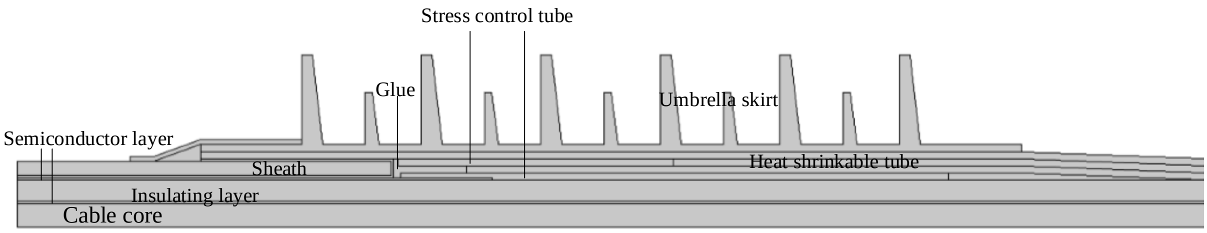

Figure.1 Cable terminal model diagram.

In this study, the electric field analysis of the 35kV cable termination is required. The required material parameters are conductivity and relative dielectric constant. By understanding the factory parameters and field test, the relevant material parameters are shown in Table 1.

Table 1. Material parameter table.

Material name	Relative dielectric constant	Reference conductivity(S/m)
Cable core	1	5.71e7
Semiconductor layer	100	2
Stress control tube	30	1e-8
Insulating layer	3.5	1e-15
Heat shrinkable tube	2.3	1e-12
Sheath	6	5e-12
Umbrella skirt	7.7	5e-12
Glue	7	5e-9

2.2. Theoretical analysis of electric field

The cable terminal runs at 35kV power frequency. The power frequency changes slowly in time. It can be solved by electrostatic field. The electrostatic field belongs to the scattered and non-rotating field. It needs to meet several basic equations [8]:

$$\nabla \times E = 0 \tag{1}$$

$$\nabla \times D = \rho \tag{2}$$

Among them, E in formula (1) is the electric field strength, which indicates that the loop characteristic of the electrostatic field is an irrotational field; D in formula (2) is the electric current density and p is the charge density, this formula is a differential equation of Gauss law, which shows that the electrostatic field is a divergent field, and the divergence of the electric flux density at any point in the electrostatic field is equal to the free charge volume density at that point.

The cable terminal is a multi-layer structure, and the layers are inconsistent with the materials of the layers. They belong to different media. The interfaces on different media need to meet the connection relationship, as shown in equation (3), where D1 and D2 are shown in Figure 2, D1 is the normal component of the electric flux density of the first layer of material, D2 is the normal component of the electric flux density of the second layer of material, and σ is the free charge surface density, equation (3) indicates that the normal component of the electric flux density on both sides of the interface is not Continuously, the amount of discontinuity is equal to the free charge areal density at the interface. At the same time, this study uses finite element simulation analysis, for each layer of material, meshing is required. For the grids in the same layer of material, the electrical flux density needs to be changed without meshing.

$$D_2 - D_1 = \sigma \tag{3}$$

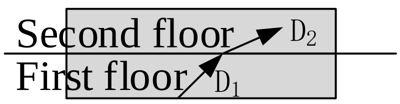

Figure.2 Dielectric interface diagram

2.3. Analysis of simulation results

2.3.1. Electric field simulation without metal particles .

According to the actual operating conditions, the cable terminal runs at a power frequency of 35kV, and the metal shield layer is grounded. The electric field distribution is shown in Figure 3.

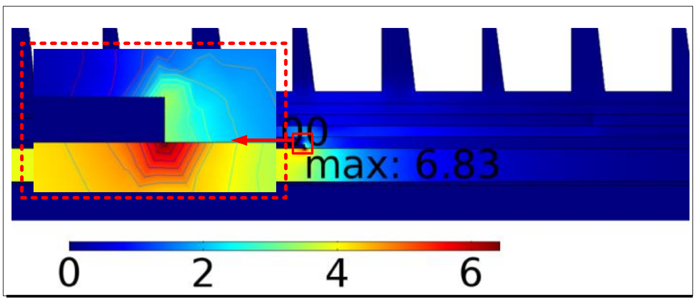

Figure.3 Electric field distribution at cable terminal without conductive impurities

As can be seen from Figure 3, when no metal particles appear at the cable terminal, the maximum electric field intensity appears at the truncation point of the external semiconductor layer, and the maximum value is 6.83MV/m. It can be seen from the enlarged picture that the larger electric field intensity is distributed in the insulating layer area, and the distortion of the electric field distribution is obvious near the maximum value.

2.3.2. Electric field simulation of metal particles.

The cable terminal is a multi-layer structure. During the installation process, due to the environment and manufacturing process, metal particles are easily introduced during the heat shrinking process. In order to better analyze the influence of the introduction of metal particles on the insulation performance of the cable terminal, this paper builds A cable termination model of metal particles at different positions, respectively, a triangular metal particle with a bottom edge of 1 mm and a height of 1 mm placed at a position 0 mm, 65 mm, 130 mm, 193 mm, 193.5 mm, 194 mm, 258 mm from the outer semiconductor layer cut-off. The electric field distribution of the cable terminal at 35 kV power frequency is obtained, wherein the junction of the outer semiconductor layer is 194 mm, which is the connection between the control tube and the tail glue. Figure 4(a)-(g) correspond to the electric field distribution of the metal particles introduced at seven different positions.

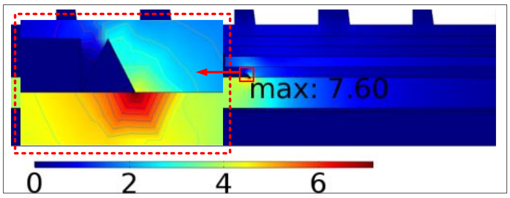

(a) Electric field distribution of metal particles at a distance of 0 mm from the cutoff

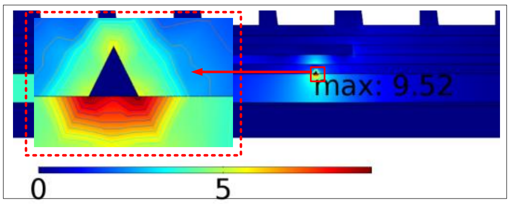

(b) Electric field distribution of metal particles at a distance of 65 mm from the cutoff

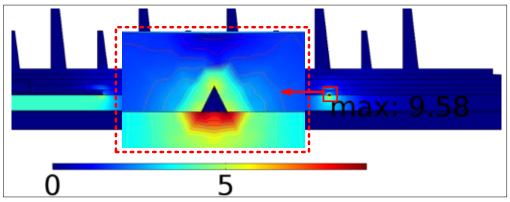

(c) Electric field distribution of metal particles at a distance of 130 mm from the cutoff

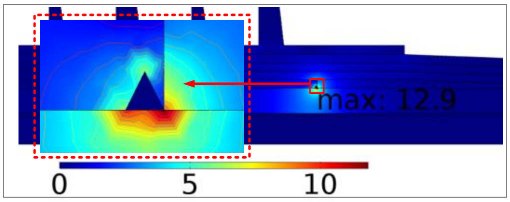

(d) Electric field distribution of metal particles at a distance of 193 mm from the cutoff

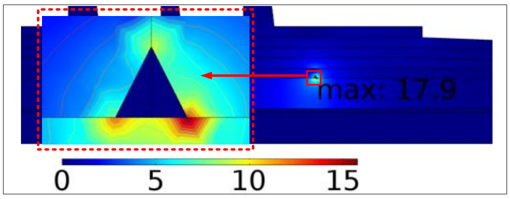

(e) Electric field distribution of metal particles at a distance of 193.5 mm from the cutoff

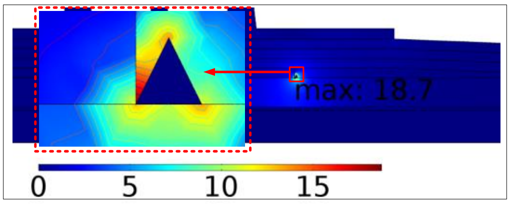

(f) Electric field distribution of metal particles at a distance of 194 mm from the cutoff

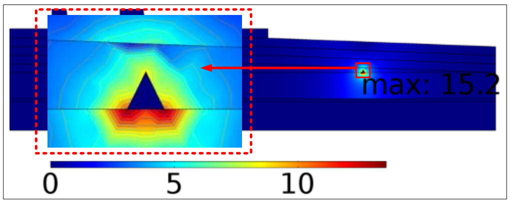

(g) Electric field distribution of metal particles at a distance of 258 mm from the cutoff

Figure. 4 Electric field distribution map of cable terminal containing conductive impurities

It can be seen from Figure. 4 that when the metal particles are introduced into the cable terminal, the electric field distribution distortion is intensified; as shown in Figure 4(a), the metal particles are located at the cutoff of the outer conductor layer, and the electric field strength is 7.6 MV/m at the maximum. The maximum electric field strength of the particles increases by 11.7%. This position is also the position where the maximum electric field strength is minimized when the metal particles are introduced. As shown in Figure 4(b) and 4(c), the metal particles are located in the control tube and the insulating layer. When the time is between, the electric field strength increases, but by comparing the two positions, the introduction position of the metal particles has a small influence on the distribution of the electric field strength within a certain range of the two positions; Figure 4(d)- 4(f) is the introduction of metal particles near the junction of the control tube and the tail glue. It can be seen from the Figure that the introduction of metal particles near the position has a great influence on the electric field distribution, especially the positional distance at which the metal particles are introduced. The outer semiconductor layer is 194mm, which is the position where the electric field distribution is the most affected at all positions where the metal particles are introduced. The maximum electric field strength is 18.7 MV/m, which is three times the maximum electric field strength when no metal particles are introduced. The position is the (356, 20) position corresponding to the cable termination model, and the breakdown field strength of the ethylene-propylene rubber is 20 to 45 MV/m [9]. The maximum electric field strength is close to the breakdown field strength. In this case, the insulation loss will be accelerated continuously, and the insulation breakdown accident is likely to occur; Figure 4(g) shows that the metal particles are introduced to the junction of the tail rubber and the insulation layer, and the electric field distortion is very serious near the junction of the metal particles and the insulation layer. The maximum electric field strength is 15.2 MV/m, which is 123.5% higher than the maximum electric field strength when no metal particles are introduced. Therefore, the introduction of metal particles in the tail rubber portion has a great influence on the insulation performance of the cable termination, and needs to be emphasized in the installation prefabrication.

In order to better analyze the influence of the introduction of metal particles on the electric field distribution at the end of the cable, the distribution of the electric field strength along the extension of the radial length of the extension line at the interface between the insulating layer and the outer semiconducting layer is introduced when the metal particles are not introduced and the metal particles are drawed at 7 positions, as shown in Figure 5.

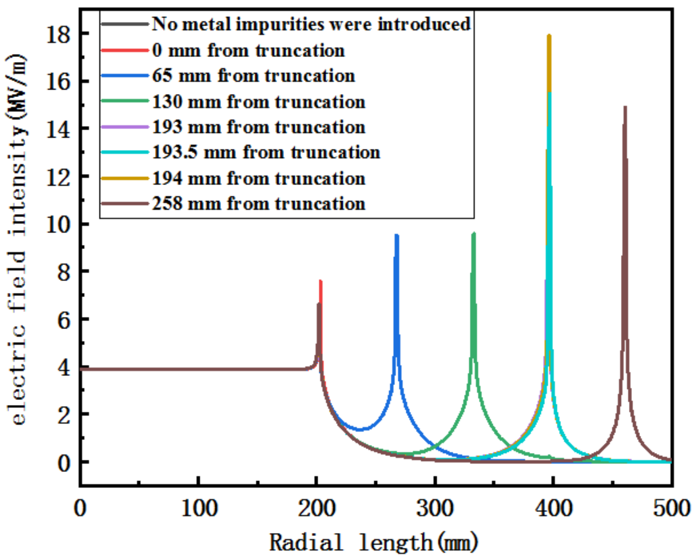

Figure. 5 Electric field intensity distribution curve

As can be seen from Figure 5, when metal particles are not introduced, electric field distortion occurs at the intersection of the outer semiconductor layer; when metal particles are introduced, two electric field distortions appear on the extension line of the boundary between the semiconductor layer and the insulating layer. The position is located at the interception of the outer semiconducting layer, and the other position is at the position where the metal particles are introduced, in the vicinity of the position, the electric field distortion is very serious, and the electric field intensity change can be rapidly increased from 0.5 MV/m to 18.7 MV/m, then rapidly drops, the rapidly distorted electric field is more likely to accelerate the insulation aging near the location and reduce the insulation performance.

3. Experimental verification

In order to more intuitively explore the influence of the introduction of metal particles on the insulation performance of cable terminations, two metal particles were introduced in this study, which are the most easily introduced particles into the outer semiconductor layer and the location where the electric field distribution distortion is the most serious, which is at the cut-off point of 194 mm, the defects produced are as shown in Figure 6. The triangular metal particle having a width of 1 mm and a height of 1 mm is placed in the designated position, and the control tube, the insulating tube, and the shed are sequentially mounted in the specified order.

(a) Metal particle distance 0 mm from truncation

(b) Metal particle distance 194 mm from truncation

Figure.6 Drawing of conductive impurity defects

Due to its structural characteristics and micro-defects introduced during the prefabrication process, the cable terminal is severely deformed in some special parts during normal operation, some areas will have a slight discharge, accelerate the insulation aging for long-term operation, and further increase the partial discharge. The effect will cause insulation breakdown accident [10,11], so the detection of partial discharge signal is of great significance for diagnosing cable terminal defect failure.

Referring to the relevant standard [12,13], a partial discharge test circuit as shown in Figure 7 was constructed. The test circuit was shown in Figure 8. The cable terminal sample with no metal particles introduced was sample No. 1. The cable termination sample where the metal particle is introduced at the junction of the semiconductor layer is sample No. 2, and the metal particle introduction position is a cable termination sample at a distance of 194 mm from the outer semiconductor layer cut-off. No. 3 sample, and three cable termination samples are subjected to partial discharge test.

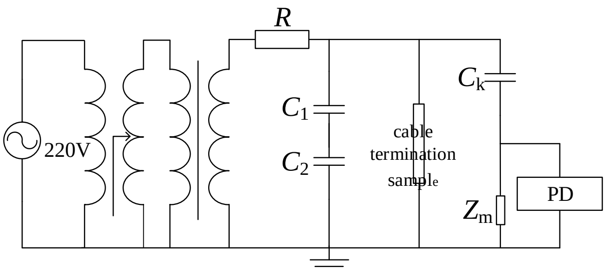

Figure.7 Partial discharge test circuit

Figure.8 Partial discharge circuit diagram

Three kinds of cable termination samples were tested by this partial discharge test platform. The step of each pressurization was 0.5kV [14]. After each pressurization, it was stabilized for 1 min, and the discharge was observed. When partial discharge occurred, The step length is gradually reduced by 0.1kV, and the stabilization time is 1min, so that the voltage is gradually reduced until the discharge phenomenon disappears, and then gradually increases in steps of 0.1kV, and stabilizes for 1 minute until the discharge phenomenon occurs again, and the current voltage value is recorded. It is recorded as the initial discharge voltage. The initial discharge voltage of the cable samples No.1 to No.3 is 18.3kV, 13.5kV, and 3.7kV, respectively. The results show that Low initial discharge voltage of cable terminal with slight electric field distortion. Then, by gradually increasing the voltage to 35 kV, the discharge spectra of three cable samples in five cycles are tested, as shown in Figure 9.

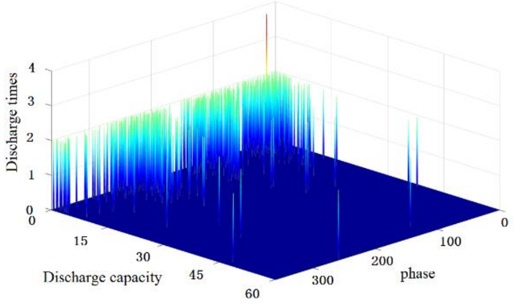

(a) Spectrum of No.1 Cable Terminal Sample

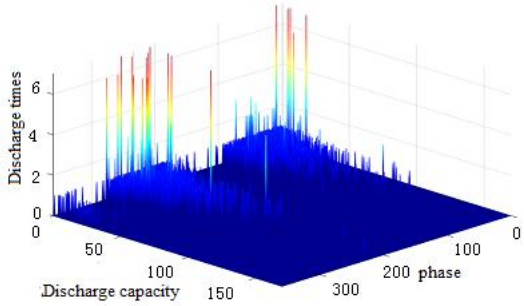

(b) Spectrum of No.2 Cable Terminal Sample

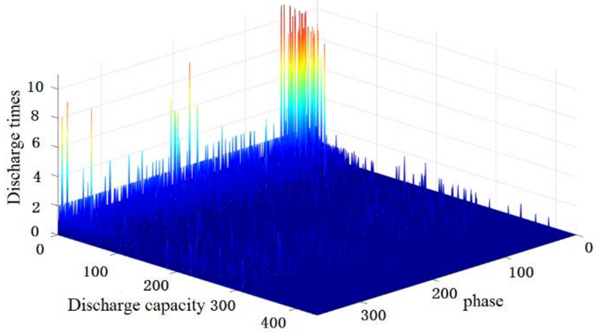

(c) Spectrum of No.3 Cable Terminal Sample

Figure.9 $\varphi - q - n$ of Spectrum of cable terminal samples

It can be seen from Figure. 9 that when the metal terminal is not introduced into the cable terminal, the discharge is concentrated in three regions, respectively, 45° to 100°, 200° to 220°, and the discharge amount of 270° to 300° is generally distributed at about 10pC, the maximum, and the number of discharges is 4 times; when the cable terminal introduces metal particles at the cut of the outer semi-metal layer, the discharge activity is active, mainly concentrated between 80°-100° and 245°-300°, and the discharge amount reaches 150pC at the maximum; It can be seen from Figure 9(c) than, when the position of the metal particles introduced into the cable terminal is 194 mm away from the outer semiconductor layer, the discharge activity is very active, the maximum discharge capacity can reach 350 pC, and the discharge activity is not limited to the peak value of the operating voltage. There is obvious discharge phenomenon in the whole cycle. That can be seen that when the metal particles are introduced, the electric field distortion inside the cable terminal is severe, which will increase the internal discharge activity. The more active the discharge activity is, the larger the discharge is, and the cable interior is easily accelerated. The insulation aging, long-term operation will eventually lead to breakdown of the cable terminal, causing serious economic losses.

4. Conclusion

In this paper, by using the finite element simulation software to simulate the electric field distribution of the cable terminal when introducing metal particles at different positions, and testing the partial discharge information of the cable terminal through the partial discharge test platform, the following conclusions are obtained:

(1) When the cable terminal introduces metal particles at a distance of 194 mm from the cutoff of the semiconductor layer, that is, the connection between the control tube and the tail glue, the electric field distortion is the most serious, and the electric field strength is 18.7 MV/m at the maximum;

IOP Conf. Series: Earth and Environmental Science **431** (2020) 012003 doi:10.1088/1755-1315/431/1/012003

(2) The results of partial discharge detection show that the introduction of metal particle makes the internal discharge activity of the cable terminal more active. When the metal particle is introduced at 194 mm from the cutoff of the semiconductor layer, the maximum discharge can reach 350 pC.

(3) The electric field distribution and partial discharge activity of the cable terminal with metal particles introduced at different positions have different characteristics, which provides a good foundation for the fault diagnosis work to be carried out next.

5. References

[1] Wan Hang，Zhou Kai，Zeng Qin，Zhang Chunshuo，Gong Jun，Huang Yonglu. Research on the location method of medium voltage cable terminal operating voltage based on phase location device [J]. *Electrical Measurement & Instrumentation*, 2019, 56(7): 30-34.

[2] CHENG Zihua. *Faults and Prevention Measures of 35kV Power Cable in Tianjin CX Power Supply Company* [D]. Tianjin: Tianjin University, 2015.

[3] Wu Ke, Ma Chunliang, Zhou Kai, et al.Partial discharge and surface ablation characteristics of air gap defects in 10 kV cable termination [J]. *Insulating Material*, 2015(7): 38–43.

[4] LIU Gang,CHEN, et al . Analysis on breakdowm attribute of 110kV XLPE cable joint main insulation with impurities [J]. *High Voltage Engineering*, 2010, 36(10):2450-2453.

[5] Rittmam G W, Heyer S V. Water contamination in a crosslinked polyethylene cable joint [J]. *IEEE Transactions on Power Aparatus and Systems*, 1976, 95(1):302-306.

[6] SHANG Kangliang, CAO Junzheng, ZHAO Zhibin, et al. Simulation Analysis and Design Optimization of 320 kV HVDC Cable Joint [J]. *Proceedings of the CSEE*, 2016: 2019-2024.

[7] Zhao Qingjie, Zhou Kai, et al. The analysis of high frequency harmonic and the research of the problem for cable termination during passing natural section of traction locomotive [J]. *Electrical Measurement & Instrumentation*, 2017, 54(6): 17-22.

[8] Feng Cizhang, Ma Xikui. *Introduction to Engineering Electromagnetic Field* [M]. Beijing: Higher Education Press, 2000, 20.

[9] Lin Kongyong, Jin Chenjuan, Liang Xingyu. *Rubber Industry Manual, Volume 6* [M]. Beijing: Chemical Industry Press, 1993:1-13.

[10] Zhang Ji Pei. *The Study on Extraction and Processing Technology of High Frequency Signal of Partial Discharge in Cable*[D]. Si Chuang : Southwest Jiaotong University, 2018.

[11] Tian Y, Lewin P L, Davies A E, et al. Partial discharge detection in cables using VHF capacitive couplers [J]. *Dielectrics & Electrical Insulation IEEE Transactions on*, 2003, 10(2): 343-353.

[12] National Electrical Appliance Industry Association. GB 18889-2002. Test method for power cable accessories with rated voltage of 6 kV (Um=7.2 kV) to 35 kV (Um=40.5 kV). Shanghai: Shanghai Cable Research Institute, 2002.

[13] National Electrical Industry Association. GB-T 7354-2003. Partial discharge measurement. Xi'an: Xi'an Institute of High Voltage Electrical Appliances, Wuhan: Wuhan Institute of High Voltage, 2003.

[14] Zhu Lin. *Electric field simulation and structural optiomization of cable termination and line side cubicle for locomotive in alpine region* [D]. Si Chuang: Southwest Jiaotong University, 2018.

Acknowledgments

Thank you for the support of the project YNKJXM20180719 of China Southern Power Grid Corporation.

IOP Conf. Series: Earth and Environmental Science **431** (2020) 012004 doi:10.1088/1755-1315/431/1/012004

The research to reduce the transient grounding resistance of communication protection system with resistance matching method

Zheng Wan[1], Dongliang Tian[2], Lei Li[3], Jianping Chen[4], Wangrong Wang[5], Xinbo Qu[6], Bin Hu[7]

1 Lecturer, Army Academy of Border and Coastal Defense, Xi'an, China
2 Associate Professor, Army Academy of Border and Coastal Defense, Xi'an, China
3Lecturer, College of Information and Communicaiton, National University of Defense Technology, Xi'an, China
4 Professor, Army Academy of Border and Coastal Defense, Xi'an, China
5 Chief Editor, Army Academy of Border and Coastal Defense, Xi'an, China
6 Research Associate, The Sixty-third Institute, National University of Defense Technology, Nanjing, China
7 Associate Professor, PLA Army Engineering University, Nanjing, China
E-mail: 513781105@qq.com, 1439569555@qq.com, hubsx@163.com, quxbo@163.com, 34235116@qq.com, 250556595@qq.com

Abstract. In this paper, we study reducing the transient grounding resistance (TGR) of communication protection system with resistance matching method. We set single or double matching layers surround the grounding rod and change their sizes and conductivity to get the laws about reducing the TGR peak and stable value. The finite-difference time-domain (FDTD) method is adopted for calculating. For the single matching layer, both of the peak and stable value of the vertical grounding rod TGR reduce, compared with normal case, as matching layer exists when the conductivity of matching layer is larger than that of ground. For the double matching layers, the TGR value will reduce even more than single matching layer case when the conductivity of outer matching layer is larger than that of ground.

1. Introduction

For communication protection system, the grounding is one of the methods to reduce the lightning electromagnetic pulse coupling and provide a discharge path for coupling and lightning current to the ground. Hence, the grounding is an important measure to enhance the protection ability of electric and electrical equipment and has been studied for many years. The transient characterization [1-3] and reduction of the grounding resistance [4-5] are two important aspects of the grounding problem research. Moreover, the FDTD method is a common way to analyze the grounding problems and often adopted for numerical calculation [2-3]. K. Yamamoto et al use the FDTD method to research the effectiveness and problems of deeply buried grounding electrodes [6]. R. Xiong et al study the TGR of angle iron, flat and square electrode by algorithm improvement with less computational memory and time [7-10].

In this paper, we comprehensively research the issue of reducing the TGR of grounding system from a new point of view. We take the vertical grounding rod for an example and adopt resistance matching way to reduce its TGR value. The FDTD method is adopted for numerical calculation. To our best knowledge, this content has not been discussed in the published literature.

The paper is organized as follows. In Section II, the matching method is briefly described. Section III introduces the FDTD calculation model. The numerical analysis of single and double matching are discussed in Section IV, Finally, some general conclusions are given in Section V.

2. The matching method discussion

We research the issue of reducing the grounding system TGR from the view of resistance matching. The single port net, which is shown in Fig.1, is a kind of transmission line net in the microwave net theory and single dipole antenna is the representative one. As is shown in Fig.2, the coaxial line can be the input end of single dipole antenna and the antenna with free space constitute the passive component of single port net. The voltage between the inner and outer conductor of coaxial line can supply power for the single dipole antenna. Then, we can change the structure of the antenna to realize resistance matching and radiate more energy. If the lifting line and grounding rod can be regarded as microwave component, the grounding rod and ground can be treat as single port net when lightning current discharge into ground through grounding rod, that is, lifting line is input end, grounding rod and ground constitute the passive component of single port net.

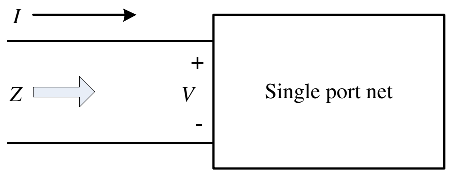

Fig.1: The single port net block diagram

We adopt vertical grounding rod for analyzing in this paper. The vertical grounding rod and its lifting line are shown in Fig.3. The vertical grounding rod can be regarded as single dipole antenna, the lifting line is the coaxial line which supply power, and the ground is equal to free space. Compare single dipole antenna with vertical grounding rod, we can learn that the antenna radiate electromagnetic wave to the free space while grounding rod discharge current into the ground. Just as the single dipole antenna can radiate more energy with resistance matching, the current that discharge into the ground through grounding rod will increase if the resistance matching between ground and grounding rod realize. Then, the purpose of reducing the grounding rod TGR will also achieve.

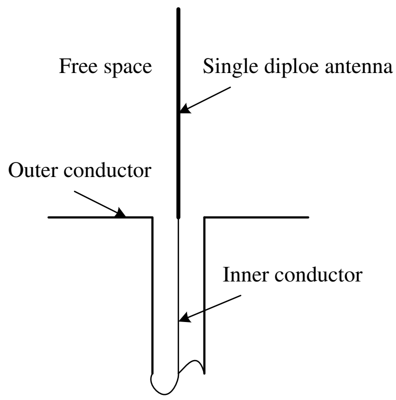

Fig.2: The single dipole antenna

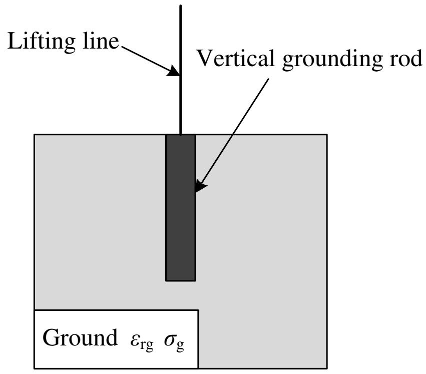

Fig.3: The vertical grounding rod and its lifting line

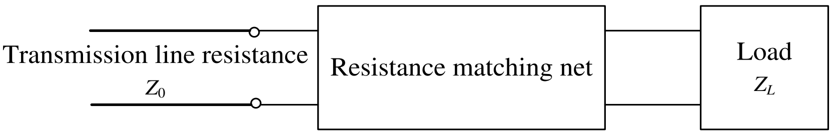

Fig.4: The resistance matching net

Fig.4 shows the schematic diagram of resistance matching net, Z0 is the transmission resistance, ZL is load resistance, and the matching net is set between transmission line and load. When add matching net, the energy that have not transmitted out will reflect between matching net and load repeatedly and transmit out entirely at last. However, for the transmission line at the left side of matching net, all the energy have transmitted out equivalently and no energy reflection exists. Thus, the TGR of grounding rod reduce.

According to the analysis above, we take vertical grounding rod for an example and achieve resistance matching by changing the soil situation around the grounding rod. Then, some laws about reducing the grounding rod TGR by resistance matching are studied.

3. The FDTD calculation model

In this part, we adopt the FDTD method to analyze the resistance-reducing method of resistance matching. The computational model is shown in Fig.5. Fig.5 (a) shows the side view of the model and Fig.5 (b) is the platform. The reference electrode, connecting line, lifting line, grounding rod and ground constitute a discharge circuit. In Fig.5 (a), L = 20m is connecting line length, Li = 10m is the transient voltage integrating path length, ha = 0.5m is the connecting height above the ground and the lifting line height, and hr =1.0m is the reference electrode length.

We select homogenous ground which has constant electrical parameter in our simulations. The ground conductivity is σ1 = 0.001 S/m, and the relative permittivity is εr1 = 9.

Two layers of matching medium are set around the grounding rod. The vertical metal grounding rod is adopted and has square cross section. l1 = 2m is the ground rod vertical length and d1 = 0.2m is the length of a section side. l2 and d2 are the inner layer matching medium vertical length and its section side length, respectively. σ2 is the inner layer medium conductivity, εr2 is the inner layer medium relative permittivity. l3 and d3 are the outer layer matching medium vertical length and its section side length, respectively. σ3 is the outer layer medium conductivity, εr3 is the outer layer medium relative permittivity. And εr1 =εr2 =εr3 = 9. The space step is Δs = 0.1m and the time step Δt = Δs / 2c, where c is the lightning speed in the vacuum.

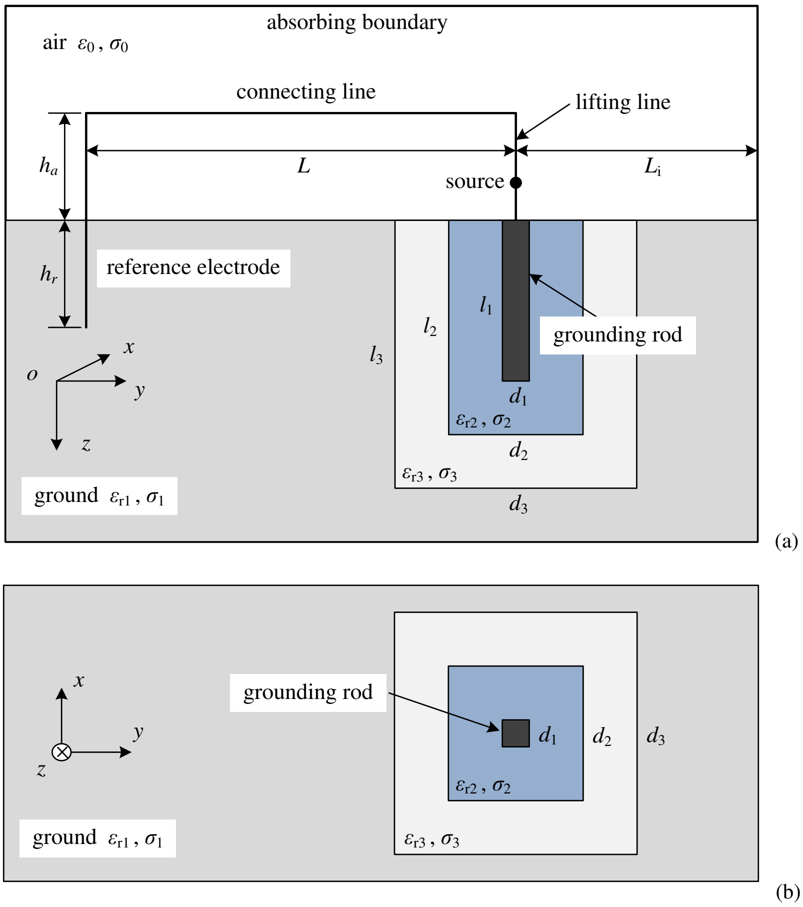

Fig.5: The TGR computational model, (a) side view, (b) platform

The double exponential function I(t) of 1.2/50μs with inner resistance 50Ω is selected as the excitation resource, which can be modeled by

$$I(t) = kI_0(\mathbf{e}^{-\alpha t} - \mathbf{e}^{-\beta t}) \tag{1}$$

Where k =1.043, I0 = 5.4 kA, α = 14730 s-1, β = 2.08×106s-1 and the normalized waveform of resource is shown in Fig.6.

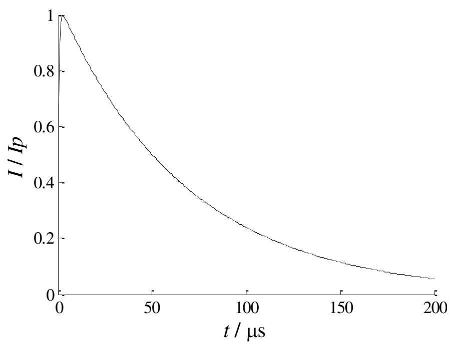

Fig.6: The normalized waveform of resource

The point resource and forced excitation resource join technology are adopted in the calculation, as shown in Fig.7. The excitation resource can join as voltage or current resource and we select the latter one in this paper. The joining way of current resource is following equation (2) to amend the magnetic fields around the point resource.

$$H_x^{n+1/2}(i, j+\frac{1}{2},k) = H_x^{n-1/2}(i, j+\frac{1}{2},k) + I^n/(4\Delta s) \quad \text{(2a)}$$

$$H_y^{n+1/2}(i+\frac{1}{2}, j,k) = H_y^{n-1/2}(i+\frac{1}{2}, j,k) - I^n/(4\Delta s) \quad \text{(2b)}$$

$$H_x^{n+1/2}(i, j-\frac{1}{2},k) = H_x^{n-1/2}(i, j-\frac{1}{2},k) - I^n/(4\Delta s) \quad \text{(2c)}$$

$$H_y^{n+1/2}(i-\frac{1}{2}, j,k) = H_y^{n-1/2}(i-\frac{1}{2}, j,k) + I^n/(4\Delta s) \quad \text{(2d)}$$

Where I n is the value of current resource at time n, Δs is space step.

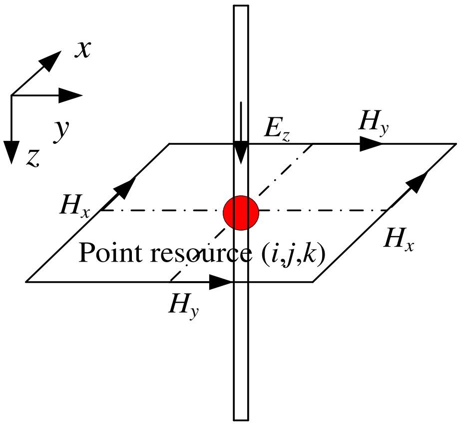

Fig.7: The joining of point resource

The computational domain should be terminated for the limited internal storage of computer. The excitation resource we adopted is a single pulse with low frequency band and have low request to the absorbing boundary condition, so we select interpolation absorbing boundary condition which can be realized easily and occupy very few internal storage, as shown in Fig.8 and equation (3).

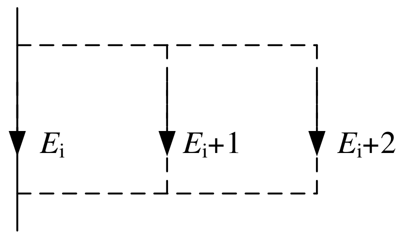

Fig.8: The electric field distribution of interpolation absorbing boundary condition

$$E_i = 2E_{i+1} - E_{i+2} \quad (3)$$

The TGR is the ratio of transient voltage Vt and transient current It , and can be defined as

$$R_t = V_t / I_t \quad (4)$$

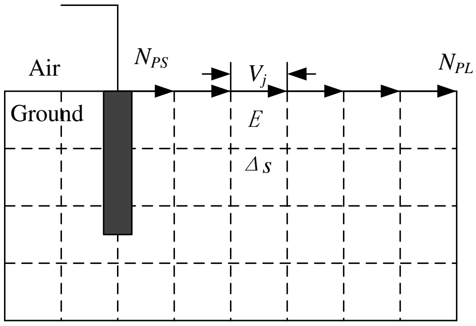

Fig.9: The calculation of transient voltage

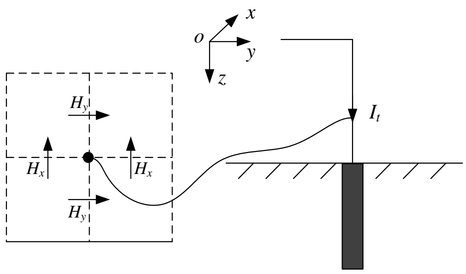

Fig.10: The calculation of transient current

As is shown in Fig.9, the electric field of every cell can be regard as homogeneous and the voltage Vj between the two sides of a cell can be defined as[11]

$$V_j = -E_j \cdot \Delta s \quad (5)$$

The transient voltage Vt can be obtained by integrating the voltage along the air-ground interface from the lifting line to the absorbing boundary and the integrating direction is parallel to the y-direction in Fig.5.

$$V_t = \sum_{j=N_{PS}}^{N_{PL}} V_j \quad (6)$$

Where Vj is the voltage in the air-ground interface, NPS is the mesh index of lifting line projection point on the ground, NPL is mesh index of absorbing boundary point.

As shown in Fig.10, according to Ampere circuital theorem, the transient current of any point of lifting line can be defined as

$$I_t = [H_x(i, j-\frac{1}{2}, k+\frac{1}{2}) - H_x(i, j+\frac{1}{2}, k+\frac{1}{2})]\Delta x +$$

$$[H_y(i+\frac{1}{2}, j, k+\frac{1}{2}) - H_y(i-\frac{1}{2}, j, k+\frac{1}{2})]\Delta y \quad (7)$$

4. Numerical analyze and discussion

In this section, we discuss the effect of matching layer on the TGR value of the vertical grounding rod. The number, conductivity, size of matching layer are considered.

4.1. The influence of single matching layer

4.1.1 The matching layer conductivity

Set single matching layer surround the vertical grounding rod and keep medium vertical length l2 = 2.2m, section side length d2 = 0.4m. The result is shown in Fig.11 and compared with the normal case without matching layer.

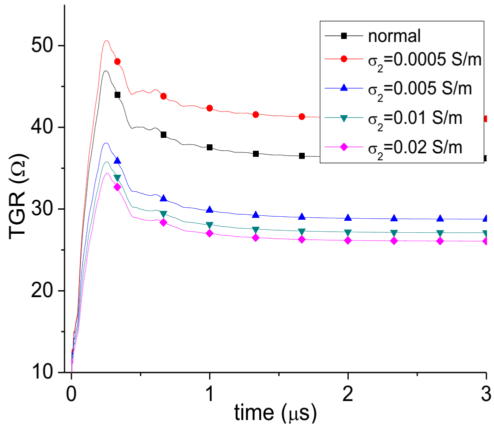

Fig.11: The TGR of vertical grounding rod with different matching layer conductivity

It can be seen from the Fig.11 that the matching layer can affect both of the peak and stable value of the vertical grounding rod TGR. The peak and stable value of TGR reduce as the matching layer conductivity increase. The peak value of TGR reduces for adding matching layer and the effect of reducing resistance is very obvious.

4.1.2 The effect contrast of medium vertical length and section side length on TGR

In this part, we keep the single matching layer conductivity σ 2 = 0.01S/m and invariable. Then we contrast the result of d2 = 0.6m, l2 = 2.2m and d2 = 0.4m, l2 = 2.4m with d2 = 0.4m, l2 = 2.2m, respectively, which is shown in Fig.12.

We can learn from Fig.12 that both of the peak and stable value of TGR reduce as the matching layer vertical length l2 and section side length d2 increase, but the extent is different. The adding of d2 can reduce more TGR value than that of l2.

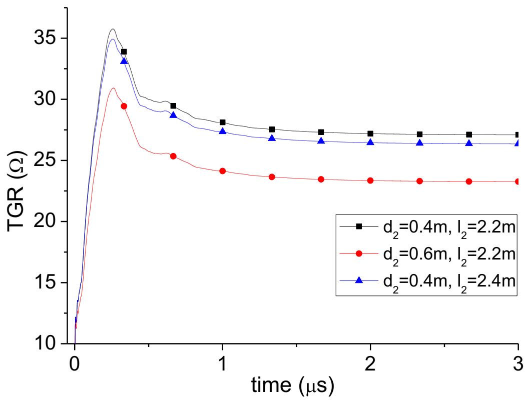

Fig.12: The TGR contrast of vertical grounding rod with different matching layer length and section side length

4.1.3 The matching layer section side length d2

Keep the single matching layer conductivity σ 2 = 0.01S/m and l2 = 2.2m and set d2 = 0.4m, 0.6m, 0.8m, 1.0 m respectively. The calculated result is shown in Fig.13.

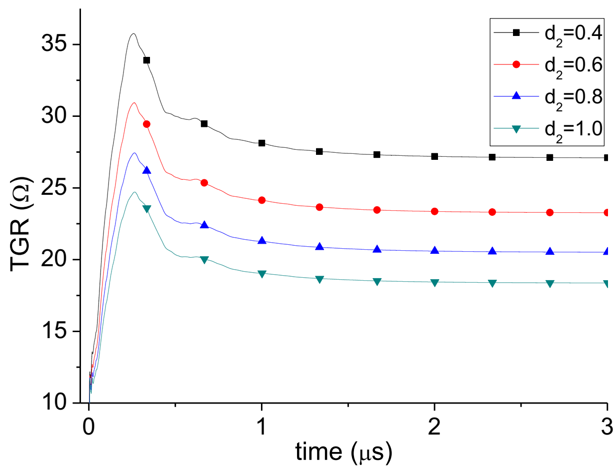

Fig.13: The TGR of vertical grounding rod with different matching layer section side length d2

The Fig.13 shows that both of the peak and stable value of the vertical grounding rod TGR reduce as the matching layer section side length d2 increase and the decrement is decrease. We can see that the TGR value is relative to the contact area between matching layer and ground and the effect of section side length d2 is nonlinear.

4.1.4 The matching layer vertical length l_2

Keep the single matching layer conductivity σ 2 = 0.01S/m and d2 = 0.4m and set l2 = 2.2m, 2.4m, 2.6m, 2.8 m respectively. The calculated result is shown in Fig.14.

The Fig.14 shows that both of the peak and stable value of the vertical grounding rod TGR reduce as the matching layer vertical length l2 increase and the effect is not obvious. The contact area between matching layer and ground is 3.68 m2 when l2 = 2.2m, 4 m2 when l2 = 2.4m, 4.32 m2 when l2 = 2.6m and 4.64 m2 when l2 = 2.8m. We can see that the contact area between matching layer and ground increase slowly as vertical length l2 increases.

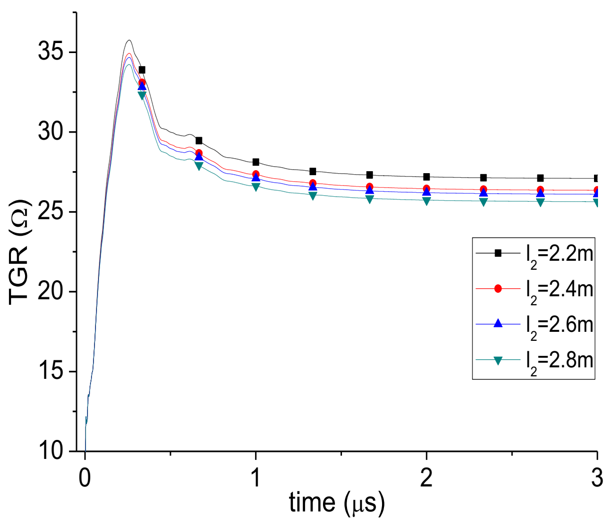

Fig.14: The TGR of vertical grounding rod with different matching layer vertical length l2

The peak and stable value of the vertical grounding rod TGR with single matching layer existing is shown in Tab.1.

Tab.1: The peak and stable value of the vertical grounding rod TGR with single matching layer

Parameter setting			TGR	TGR
d_2(m)	l_2(m)	σ_2(S/m)	peak value (Ω)	stable value (Ω)
normal			46.89	36.45
0.4	2.2	0.0005	50.59	41.25
		0.005	38.06	28.82
		0.01	35.76	27.13
		0.02	34.27	26.09
0.6	2.2	0.01	30.92	23.27
0.8			27.41	20.51
1.0			24.71	18.37
0.4	2.4	0.01	34.68	26.37
	2.6		34.63	26.13
	2.8		34.23	25.67

4.2. The influence of double matching layer

In this part, we talk about the effect of double matching layer on the TGR of the vertical grounding rod and mainly focus on the matching layer conductivity. The size of matching layer is inner layer d2 = 0.4m, l2 = 2.2m and outer layer d3 = 0.6m, l3 = 2.4m. We calculate two kinds of situation, one is keeping σ 2 = 0.01S/m and setting σ 3 = 0.0005S/m, 0.005S/m, 0.02S/m, the other is keeping σ 3 = 0.01S/m and setting σ 2 = 0.0005S/m, 0.005S/m, 0.02S/m. The results are shown in Fig.15 and Fig.16.

We can learn from Fig.15 that both of the peak and stable value of the vertical grounding rod TGR reduce, compare with normal case, as single matching layer exists. The TGR value will reduce even more than single matching layer case, and the conductivity of outer matching layer must be larger than that of ground. Moreover, the TGR value will reduce with the σ 3 increasing when σ 1 and σ 2are invariants.

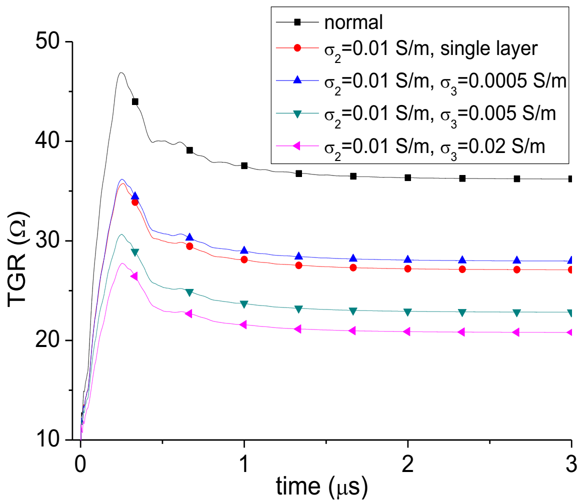

Fig.15: The TGR of vertical grounding rod with no, single and double matching layers

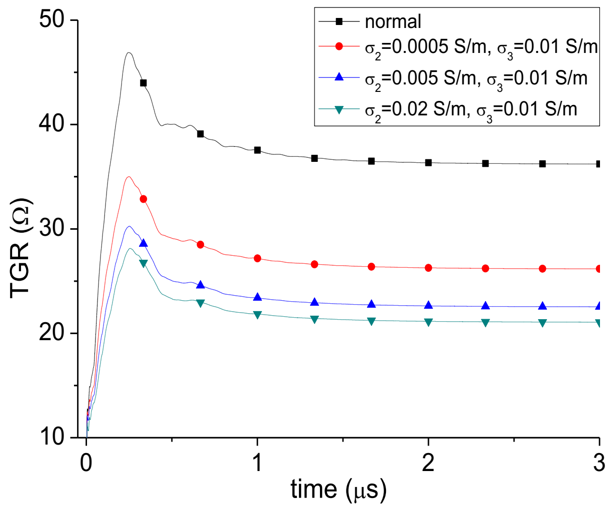

Fig.16: The TGR of vertical grounding rod with no and double matching layers

Fig.16 shows that both of the peak and stable value of the vertical grounding rod TGR reduce greatly, compare with normal case, as double matching layer exists. The TGR value will reduce with σ 2 increasing when σ 1 and σ 3 are invariants.

The peak and stable value of the vertical grounding rod TGR with double matching layer in Fig.15 and Fig.16 are shown in Tab.2.

Tab.2: The peak and stable value of the vertical grounding rod TGR with double matching layer

Parameter setting		TGR peak value (Ω)	TGR stable value (Ω)
σ_2 (S/m)	σ_3(S/m)		
normal		46.89	36.45
single matching layer σ_2=0.01S/m		35.76	27.13
0.01	0.0005	36.05	28.0
	0.005	30.66	22.84
	0.02	27.74	20.83
0.0005	0.01	34.97	26.18
0.005		30.26	22.54
0.02		28.11	21.07

5. Conclusions

In this paper, the single and double matching layer cases are discussed and we can draw the following conclusions.

For single matching layer:

1) The matching layer can affect both of the peak and stable value of TGR. The peak and stable value of TGR reduce as the matching layer conductivity increase.

2) All the TGR waveforms are similar and the rise edge of waveforms become gentle. In addition, the conductivity of matching layer must larger than that of ground, otherwise the value of TGR will become larger.

3) Both of the peak and stable value of TGR reduce as the matching layer vertical length and section side length increase, but the extent is different. The adding of section side length can reduce more TGR value than that of vertical length. The effect of vertical length is not obvious and the effect of section side length is nonlinear.
4) The increasing of contact area between matching layer and ground can reduce the TGR value of ground rod effectively.
5) The most effective way of reducing the TGR is increasing the matching layer section side length; secondly, the matching layer conductivity; finally, the matching layer vertical length.
For double matching layer:
1) Both of the peak and stable value of the vertical grounding rod TGR reduce greatly, compare with normal case, as double matching layer exists.
2) The TGR value reduce even more than single matching layer case when the conductivity of outer matching layer is larger than that of ground.
3) The TGR value will reduce with the conductivity of outer matching layer increasing when inner layer and ground conductivity are invariants.
4) The TGR value will reduce with the conductivity of inner matching layer increasing when outer layer and ground conductivity are invariants.
5) We can get smaller TGR peak and stable value when inner matching layer conductivity is less than outer layer one for the same set of matching layer conductivity, but the difference is not obvious.

Competing Interests
The authors declare that there is no conflict of interests regarding the publication of this paper.
[The paper is on the phasic achievement of Research on Informationized Border Management and Control System(project code:L020211) ,which is part of the 13th Five-year Plan]

6. References

[1] M. I. Lorentzou, N. D. Hatziargyriou, and B. C. Papadias, “Time Domain Analysis of Grounding Electrodes Impulse Response,” IEEE Trans. Power. Del., vol. 18, no. 2, pp. 517–524, Apr. 2003.
[2] R. Xiong, B. Chen, B. H. Zhou, and C. Gao, “Optimized Programs for Shaped Conductive Backfill Material of Grounding Systems Based on the FDTD Simulations,” IEEE Trans. Power. Del., vol. 29, no. 4, pp. 1744–1751, Aug. 2014.
[3] R. Xiong, B. Chen, C. Gao, Y. Yi, and W. Yang, “FDTD Calculation Model for the Transient Analyses of Grounding Systems,” IEEE Trans. Electromagn. Compat., vol. 56, no. 5, pp. 1155–1162, Oct. 2014.
[4] H. E. Martínez, E. L. Fuentealba, L. A. Cisternas, H. R. Galleguillos, J. F. Kasaneva, and O. A. de la Fuente, “A New Artificial Treatment for the Reduction of Resistance in Ground Electrode,” IEEE Trans. Power. Del., vol. 19, no. 2, pp. 601–608, Apr. 2004.
[5] J. L. He, G. Yu, J. P. Yuan, R. Zeng, B. Zhang, J. Zou, and Z. C. Guan, “Decreasing Grounding Resistance of Substation by Deep-Ground-Well Method,” IEEE Trans. Power. Del., vol. 20, no. 2, pp. 738–744, Apr. 2005.
[6] K. Yamamoto, K. Yoshioka, S. Sumi, S. Yanagawa, and S. Sekioka, “Mutual Influence of a Deeply Buried Grounding Electrode and the Surrounding Grounding Mesh,” IEEE Trans. Industry. Applications., vol. 51, no. 6, pp. 4900–4906, Nov/Dec. 2015.
[7] R. Xiong, B. Chen, Y. F. Mao, W. Deng, Q. Wu, and Y. Y. Qiu, “FDTD Modeling of the Earthing Conductor in the Transient Grounding Resistance Analysis,” IEEE Antennas Wireless Propag. Lett., vol. 35, pp. 1248–1257, Aug. 2012.

[8] R. Xiong, B. Chen, and D. Fang, "An algorithm for the FDTD modeling of flat electrodes," IEEE Trans. Antennas Propag., vol. 62, no. 1, pp. 345–353, Jan. 2014.
[9] R. Xiong, B. Chen, and D. Fang, "Square Electrode Representation in FDTD Method," IEEE Trans. Antennas Propag., vol. 62, no. 10, pp. 5425–5428, Oct. 2014.
[10] R. Xiong. "Study on FDTD Method and Its Application in the Electromagnetic Protection," A Thesis for the Doctor Degree of PLA university of Science and Technology, 2014.
[11] H. H. Bing, B. H. Zhou, and J. Q. Chen. "Influence of the Soil on Transient Grounding Resistance under Pulsed Dischargeing Current," High Power Laser and Particle Beams, vol. 16, no. 10, pp. 1295–1298, Oct. 2004.

IOP Conf. Series: Earth and Environmental Science **431** (2020) 012005 doi:10.1088/1755-1315/431/1/012005

Research on blackout simulation model considering hidden failures and reclosing

Qingqing HAO[1], Qun YU[1]

1 College of Electrical Engineer and Automation, Shandong University of Science and Technology, Qingdao 266590, China.
Email:553423552@qq.com

Abstract. In this paper, a blackout simulation model considering hidden failures and reclosing is proposed, which is more realistic than the previous model. The operation of reclosing devices, the synchronization control for reclosing in two-ended sources transmission lines and the interaction between reclosing and relay protection are simplified. Simulation results of IEEE39-bus test system are obtained to confirm the validity of the model. Compared with the blackout simulation model considering only the hidden failures of relay protection, it shows that the trip caused by the transient faults and hidden failures induced by transient faults can be corrected in this large-scale blackout simulation model. It also shows that with the increase of the probability of hidden failure, the failure rate of reclosing becomes an important factor affecting the system recovery.

1. Introduction

In recent years, there have been many large-scale blackouts at home and abroad. In order to analyze the mechanism of their generation and propagation, a large number of theories and models have been proposed by domestic and overseas scholars. Self-organized criticality theory has become an effective tool to investigate large-scale blackouts. Many blackout simulation models based on this theory have also been recognized by scholars, such as OPA model, Hidden Failure model, Cascade model, SOC-Power Failure model, etc.[1-4]. In the process of exploring the above mechanisms and models, the hidden failures of relay protection have become a hot issue that scholars pay more and more attention to. Reference [5] analyzed the causes of hidden failures in protection devices and applied risk theory to evaluate the impact of hidden failure probability on cascading trip during power outages. Reference [6] considered the hidden failures of relay protection and proposed a risk assessment model associated with a capacity of transmission lines. Reference [7] proposed a blackout simulation model considering the hidden failures of relay protection and studied the effect of hidden failures on the self-organized criticality of the power grid.

Reclosing is an automatic device used in power systems, which can quickly correct the malfunction of relay protection [8]. At present, scholars' research on reclosing mainly focuses on how to reduce the failure rate of reclosing, such as the method of identifying accurately the permanent faults [9] and the control strategy of reclosing [10-11]. But how does reclosing hinder power outages? What is the relationship between reclosing and hidden failures during the blackout? These are important problems worth of study.

In order to solve the above problems, this paper proposes a more realistic blackout simulation model than the previous, which can be used to study hidden failures and reclosing during large-scale power blackouts. Taking the IEEE39-bus system as the research object, this paper verifies the validity of the model and compares it with the model without considering reclosing.

2. Description of model factor

2.1 Model of hidden failure

At present, when quantitatively describing the impact of hidden failures on the protected lines, scholars usually use a variable to measure the probability of line outage. In this paper, the hidden failure probability model considered over-flow [5] is used and is shown in figure 1. F is the active power flow, F_L is the active power flow limit, P_H is the probability of hidden failure, P is the probability of line outage.

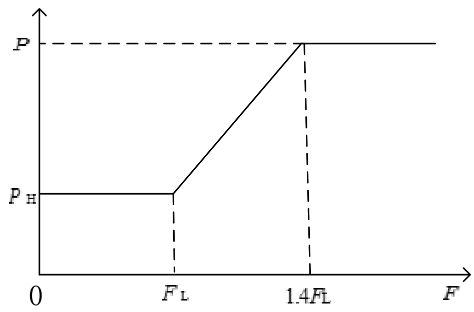

Figure 1. Hidden failure probability model.

The probability of hidden failure is affected by external environment, worn circuit and human error. According to figure 1, the concrete expression of the probability of line outage due to hidden failures is as follows:

$$P_i = \begin{cases} P_{\mathrm{H}} & F_i < F_{\mathrm{L}} \\ (F_i - F_{\mathrm{L}}) \times \dfrac{P - P_{\mathrm{H}}}{1.4F_{\mathrm{L}} - F_{\mathrm{L}}} + P_{\mathrm{H}} & F_{\mathrm{L}} \le F_i \le 1.4F_{\mathrm{L}} \\ P & F_i > 1.4F_{\mathrm{L}} \end{cases} \tag{1}$$

2.2 Simplification of reclosing

2.2.1 Operation of reclosing devices. By analyzing GB/T14285-2006 "Technical Regulations for Relay Protection and Safety Automatic Devices", it can be seen that the operation of reclosing devices is different when the different type of faults happen. However, the success of reclosing always depends on whether the fault is a transient fault. Therefore, the mechanism of reclosing can be simplified as follow: if the fault is a transient fault, reclosing will success and the system will resume normal operation; if the fault is a permanent fault, the relay circuit breaker will trip again.

2.2.2 Synchronization control for reclosing. In high-voltage power systems, reclosing of two-ended sources transmission lines need to consider the optimal reclosing time and synchronization of circuit breakers. When ignoring switching onto faulted lines in the asynchronous, whether the system resume normal operation depends on whether the circuit breaker closes successfully on the detecting voltage-free side [12]. In other words, it also depends on whether the fault is a transient fault.

2.2.3 Interaction between reclosing and relay protection. In order to improve the power supply reliability of the transmission lines, reclosing controls switch and circuit breaker to realize the front acceleration and rear acceleration protection of the whole power net. 220kV and above systems adopts post-acceleration protection, that is, the circuit breaker is first closed and then the fault type is identified.

3. Blackout simulation model

Imitating the fast dynamic process of the OPA model and the Hidden Failure model [13-14], a blackout simulation model considering hidden failures and reclosing is proposed. The procedure of simulation can be described as follow (figure 2).

Step1 Reading parameter of power grid.
Step2 Generating initial faults randomly.
Step3 Tripping and cutting off the faulted lines.
Step4 Calculating power flow and tripping according to the hidden failure probability model.
Step5 Judging whether reclosing is successfully. If yes, turn to step 6. If not, turn to step 8.
Step6 Judging whether the fault is a transient fault. If yes, return to step 2. If not, turn to step 7.
Step7 Tripping again of faulted lines.
Step8 Judging whether the power system generate lost load or islands. If yes, turn to step 9. If not, turn to step 2.
Step9 Calculating lost load and outputting the result.

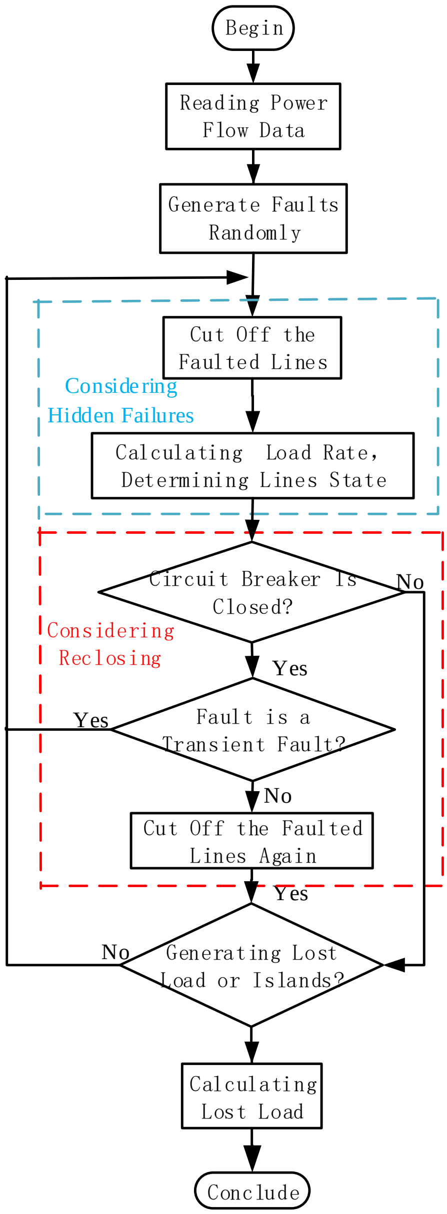

Figure 2. Model calculation flow chart.

4. Blackout simulation model

In this paper, IEEE39-bus system is taken as an example (figure 3), whose reference voltage is 345kV.

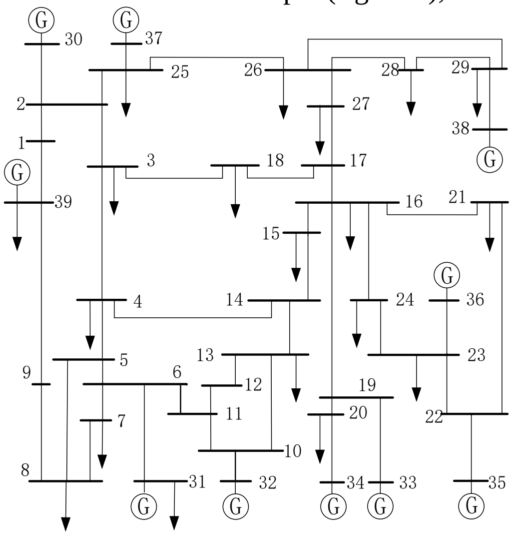

Figure 3. IEEE39-bus system.

4.1 Parameter setting

According to reference [15], setting the probability of hidden failure P_H is 0.0013. Statistics show that the success rate of reclosing depends mainly on the proportion of transient faults caused by external environment to the total faults. In this paper, let the ratio of transient faults to permanent faults in the initial faults caused by the external environment is 3:1. In addition, reclosing itself has a certain failure rate, such as equipment failure or misjudgment, which may lead to reclosing failure. Refer to [16], this paper sets the failure rate of reclosing is 0.0015.

4.2 Model verification

The research shows that there are self-organized criticality characteristics of power outage at home and abroad. According to the theory, the validity of the model can be verified by simulating the large-scale blackouts based on this model. Repeatedly run the model 200 times and the time series of the power outages are shown in figure 4. The corresponding loss load is counted in a scale-frequency double logarithmic graph with a base of 10, as shown in figure 5.

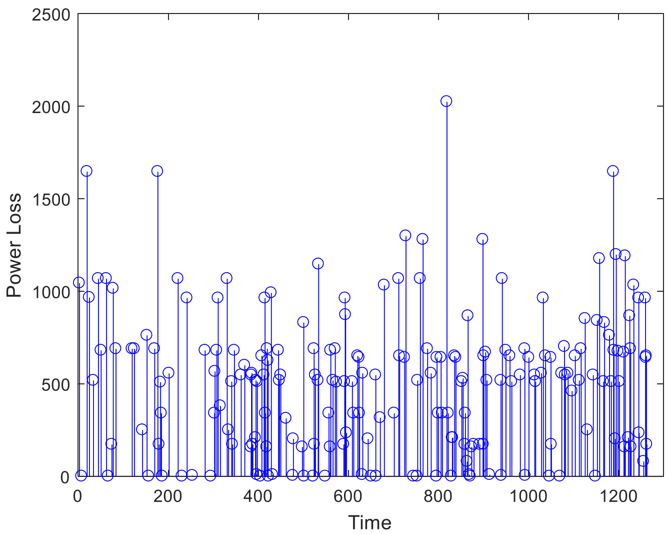

Figure 4. Time series of the power outage.

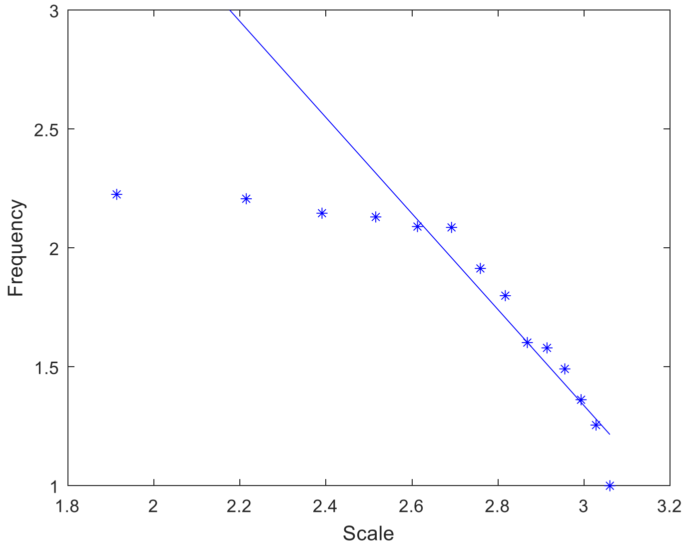

Figure 5. Scale-frequency double logarithmic graph.

Least-square curve fitting method is used to fit 10 discrete points in the tail of figure 5. The fitted line and its correlation coefficient are obtained:

$$\lg N = 7.4625 - 2.1069 \lg r \tag{2}$$

$$R = -0.9348 \tag{3}$$

By checking the corresponding standard in the correlation coefficient test table, $R_{0.01}$ is 0.765. Due to $|R| > R_{0.01}$, it can be seen that the fitting equation is effective. Thus, the double logarithmic distribution of the scale-frequency of blackouts loss load using this model obeys the basic mathematical representation of self-organized criticality--power law distribution, which proves the feasibility of the model.

4.3 Comparison and analysis

Assuming that branch 17-18 has an initial fault, the impact of the fault on the system is analyzed as follows.

(1) Only considing the hidden failures of relay protection.

After cutting off branch 17-18, the power flow is shifted and redistributed. According to the hidden failure probability model, the load rate and outage probability of adjacent lines can be obtained, as shown in table 1.

Table 1. Load rate and outage probability of adjacent lines.

Branch	Load rate	Outage probability
3-18	1.8508	1.0000
17-27	1.3404	0.8512
16-17	0.3499	0.0013

(2) Considing the hidden failures and reclosing.

When the initial fault is a permanent fault, reclosing will not successful. The outage of the lines is the same as in case (1).

When the initial fault is a transient fault, the fault source will disappear after the branch 17-18 is cut off once. All the circuit breaker can be switched on and the system can reach stability again. At this time, whether the relevant electric transmission lines resume power supply in time depends on whether reclosing devices have working ability, that is, reclosing's failure rate.

Compared case (1) and case (2), it can be known that when faults happen, hidden failure of relay protection in power system plays the role of expanding the outage range and reclosing can avoide cascading trip through correctting the transient faults. That is, reclosing can reduce effectively the probability of large-scale blackouts in the power grid. Establishing a blackout simulation model based on the case 1 and running it 200 times, a time series diagram of the blackouts can be obtained, as shown in figure 6.

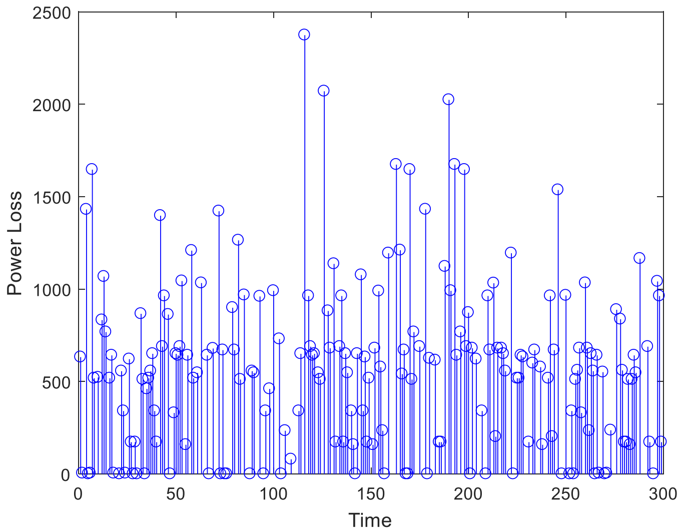

Figure 6. Time series diagram of power outage based on model built in case (1).

In the case of 200 power outages, the simulation model considering reclosing (figure 4) takes more than 1200 days, which is about four times as long as the model without consindering reclosing (figure 6). The ratio is basically consistent with the setting of the success rate of reclosing. It can be further analyzed that reclosing plays an important role in delaying blackouts. If ignoring reclosing in the simulation and early warning of blackouts, the stability of the system will be underestimated and the accuracy of the assessment will be affected.

According to the above mentioned analysis, the success rate of reclosing is mainly determined by the proportion of the transient faults caused by the external environment, which is a factor with less controllability. The probability of hidden failure of relay protection depends on the reliability of relay protection equipment in the power system, which is a factor with greater controllability. In order to further study the interaction between hidden failures and reclosing during the blackouts, the ratio of the transient faults to the permanent faults 3:1 is maintained and the probability of hidden failure of relay protection is changed. The value of the hidden failure probability is shown in table 2.

Table 2. The value of the hidden failure probability.

Situation	P_H	Situation	P_H	Situation	P_H
1	0.0003	3	0.0023	5	0.0043
2	0.0013	4	0.0033	6	0.0053

The histogram in figure 7 shows the time required for 1000 power outages in systems which considering reclosing or not under different hidden failure probabilities. The broken line indicates the ratio of the time required by the two models.

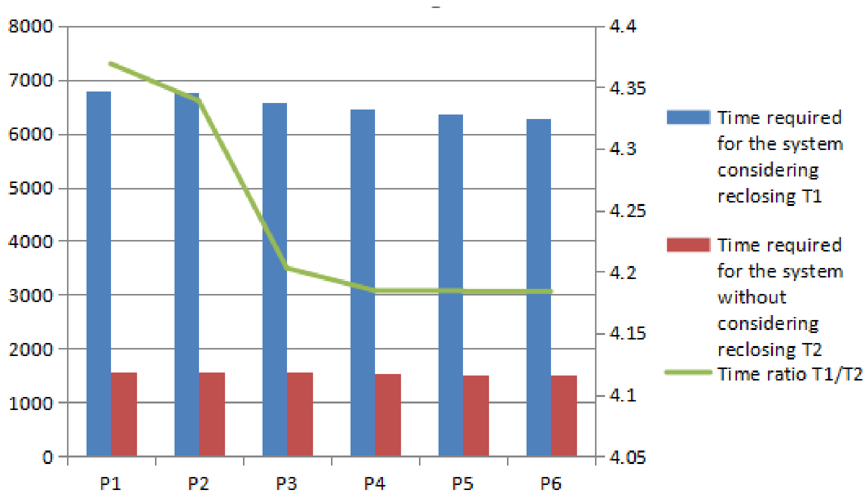

Figure 7. The combined effect of reclosing and hidden failture with different probabilities.

It can be seen from figure 7, as the hidden failture probability increases, the time required for both models decreases and the time ratio also decreases. That is, the effect of reclosing on reducing the risk of power system blackouts is gradually weakened. When there are more hidden failures in relay protection equipment, there will be more broken lines need to be re-closed. The factors of reclosing failure caused by self-fault is magnified and the failure rate of reclosing plays an increasingly important role in system recovery. Therefore, in the case where the external environment cannot be changed, in order to ensure the stability of the system, it is necessary to improve the operating conditions of reclosing to reduce the failure rate of reclosing.

5. Conclusion

Considering that reclosing can quickly correct instantaneous faults, a blackout simulation model considering hidden failtures and reclosing is proposed in this paper by reasonable simplifing reclosing. Taking IEEE39-bus system as an example, the validity of the model is proved by using the self-organizing criticality theory of blackouts. Based on the proposed model, the role of reclosing during the blackout and the relationship between reclosing and hidden failures are analyzed.

1. In the process of power outage, reasonable consideration of the role of reclosing is in line with the actual operation of the system. By correcting transient faults in the system, reclosing can eliminate most of the power outages caused by transient faults and reduce the frequency and scale of blackouts. Therefore, it is necessary to consider the role of reclosing in the blackout simulation modeling and accurate risk assessment.

2. Reclosing can correct trips caused by instantaneous faults and further correct false trips caused by hidden failure of relay protection induced by instantaneous faults, so as to avoid the expansion of the scope of the fault caused by hidden failure of relay protection. The success rate of reclosing mainly depends on whether the fault is a transient fault. However, when too many hidden failures happen in the system, the failure rate of the reclosing will gradually become an important factor affecting the success of the reclosing.

6.References

[1] YU Qun, ZHANG Min, CAO Na, et al. Grid cascading failure control based on fuzzy CA[J]. *Electric Power Automation Equipment*, 2016, 36(8): 90-95, 102.

[2] LI Hui, JIA Xiaofeng, LI Lijuan, et al. Key Line Identification Method for Grid Implicit Fault Propagation Model Based on Cellular Automata[J]. *Power System Protection and Control*, 2018(6): 16-23.

[3] LI Baojie, LI Jinbo, LI Hongjie, et al. Analysis of the "3.31" blackout in Turkey and its implications for the safe operation of China's power grid[J]. *Proceedings of the CSEE*, 2016, 36(21): 5788-5795.

[4] ZHONG Qing, ZHANG Zhe, XU Zhong,, et al. SOC characteristics of power-supply failure of Guangzhou distribution network[J]. *Electric Power Automation Equipment*, 2017, 37(4): 109-113, 121.
[5] YANG Mingyu, TIAN Hao, YAO Wanye. Analysis of Cascading Failure of Power System Based on Recessive Faults of Relay Protection[J]. *Power System Protection and Control*, 2010, 38(9): 1-5.
[6] LI Zhongqing, GAO Xiang, LI Yongli, et al. Research on Risk Assessment Technology Considering Recessive Faults in Relay Protection[J]. *Proceedings of the CSEE*, 2016(s1):29-35.
[7] YANG Yali. Influence of relay protection considering multiple factors on the self-organization criticality of power grid and application[D]. *Shandong University of Science and Technology*, 2017.
[8] WANG Tikui, GUO Jianqiang, GAO Xiaorong, et al. Combination of adaptive auto-reclosing and relay protection[J]. *Modern Electronic Technology*, 2011, 34(16): 126-130.
[9] LIANG Zhenfeng, SUONAN Jiale, KANG Xiaoning, et al. Permanent Fault Identification of Three-Phase Reclosure Using Free Oscillation Frequency Identification[J]. *Proceedings of the CSEE*, 2013, 33(7): 124-130.
[10] WANG Yi, LIU Jianzheng. New Topology and Reclosing Control Strategy for MMC-HVDC DC Fault Protection[J]. *Power System Technology*, 2015, 39(8): 2312-2319.
[11] YANG Mingfa, XIE Zhide. DC Fault Protection Based on Hybrid Bypass and System Recovery Strategy in MMC-HVDC[J]. *High Voltage Engineering*, 2019, 45(2): 564-570.
[12] ZHU Yueling, WU Junhong, ZHOU Zhuojun. On the Application of Automatic Reclosing in Substation[J]. *Information and Computer (Theoretical Edition)*, 2014(4): 166-169.
[13] DOBSON I, CARRERAS B, LYNCH V, et al. An Initial Model for Complex Dynamics in Electric Power System Blackouts. *Hawaii International Conference on System Sciences*, Maui, Hawaii, January 2001.
[14] CHEN J, THORP J S, DOBSON I. Cascading dynamics and mitigation assessment in power system disturbances via a hidden failure model[J]. *International Journal of Electrical Power & Energy Systems*, 2005, 27(4): 318-326.
[15] SHEN Xiaofan, SHU Zhihuai, LU Pengfei, et al. Operation of Relay Protection Devices of State Grid Corporation of China in 2006[J]. *Power System Technology*, 2008, 32(3): 18-21.
[16] QIU Yutao, LING Guang, WANG Yi, et al. Analysis on Relaying Protection and Its Operation Conditions in 220 kV and Above AC System of Zhejiang Power Grid in the Last Ten Years[J]. *ZHEJIANG ELECTRIC POWER*, 2017, 36(9): 1-7.

Acknowledgments

This work is supported by the Science and Technology Project of SGCC in 2018(Multi-sand Pile Theory of Interconnection Power Grid Blackouts Early Warning Technology and System Development, No.XTB17201800166).

IOP Conf. Series: Earth and Environmental Science **431** (2020) 012006 doi:10.1088/1755-1315/431/1/012006

A novel single-ended fault location method for long-distance HVDC transmission lines based on cross-correlation analysis

Lei Shi[1], Ningming Guo[2 4], Jincheng Qi[3], Ruopeng Liu[1] and Chunxiang Mao[1]

1 State Grid NingXia Power Maintenance Company, Yinchuan city, NingXia Autonomous Region, China
2 C-EPRI Electrical Power Engineering Co,.ltd, ChangPing district, BeiJing city, China
3 Xi'an Jiaotong University， BeiLin District, Xi'an, Shaanxi, China
4 North China Electric Power University, ChangPing District, BeiJing city, China
E-mail: guoningming@sgepri.sgcc.com.cn

Abstract. The transmission line, as the faultiest device in power system, cross many complex areas which will cause worse work condition. This is, both the rate of faulty and the difficulty of the manual fault location are raised. While accurate fault location method could reduce the workload and outage cost, increase the speed of repairing and improve both the reliability and economics of power system. Therefore, it is essential for HVDC systems which have much longer transmission lines. The existing fault location device of HVDC transmission lines are based on the principle of transient travelling-wave. However, due to the interference caused by on-off of power electronic devices and signal resonances, the single-ended travelling-wave method can not be applied in HVDC. The characteristics of clutter interferences of HVDC system and the coupling between double pole lines are analyzed in paper. A novel single-ended travelling-wave fault location method for HVDC transmission lines based on the correlation between two pole lines is proposed. The signal of the non-fault pole line is applied as reference signal; the method suppresses interference through the cross-correlation calculation between the fault and the no-fault pole line. So the reflected wave is enhanced and the identification reliability of the reflected wave is improved. The validity of the method is verified by simulation and on-site data analysis.

1. Introduction

For HVDC transmission lines which length is long, accurate fault location is of great significance for post-processing of HVDC line failures [1]. At present, the two-ended travelling-wave fault location is mainstream fault location method in the HVDC transmission projects. From the operational experience, the accuracy of two-ended travelling wave method has satisfied the on-site requirement, but it needs both ended data, and the fault location may fail if one side device is abnormal. However, the length of HVDC transmission line is long in general, the abnormity probability of one side device is relatively higher suffered from severe signal attenuation. In the backup measures research of the two-ended travelling-wave method, due to the influences of the signal transformer, the line parameters, and other factors the methods based on the principle of frequency-domain analysis or voltage distribution analysis cannot replace the travelling wave method.

In AC transmission system, single-ended travelling-wave fault location method can locate faults based on one side data. It has been widely used as the backup method in fault analysis. But the research on single-ended fault location of HVDC line is relatively few. In [2], the identification of reflected wave

based on waveform correlation analysis is proposed. A method using auxiliary time window to solve the problem of reflected wave identification is presented in [3]. [4] proposes improving the identification method of reflected wave through neural network technology; and the paper [5] proposes the method of single-ended fault location of HVDC line. Overall, the existing research focuses on the waveform and polarity analysis of reflected wave and similarity comparison [6,7], the influence of system clutter interference and signal resonance is seldom considered. However, the background noise caused by the on-off of power electronic equipment in HVDC system is much stronger than that of the AC system, which makes the identification of reflected waves more difficult.
In this paper, a single-ended travelling-wave fault location method for HVDC transmission based on cross-correlation analysis of bipolar signal is proposed. The signal of non-fault pole line is used as reference quantity. The influence of interference and resonance are suppressed through the cross-correlation calculation of the two poles, so the identification success rate of reflected wave is improved. It ensures the reliability of single-ended fault location.

2. Principle and Influencing Factors of Single-ended Travelling-Wave Method for DC Lines

2.1. Principle of Single-ended Travelling-Wave Location

$$d_1 = (t_1 - t_0) \times v/2 \tag{1}$$

$$d_1 = L - (t_2 - t_0) \times v/2 \tag{2}$$

The basic principle of single-ended travelling-wave fault location for the transmission line is shown in formula 1 [8~10]. The location is completed by using the arrival time difference between initial travelling wave and the reflected wave of the fault point, or the reflected wave of the opposite side. Among them, d_1 is the distance between the fault point and the measuring device, t_0 is the arrival time of the initial travelling wave, t_1 is the arrival time of the fault point reflected wave, t_2 is the arrival time of the reflected wave at the opposite end of the line, L is the full length of the line, and v is the propagation speed of the travelling wave. The main difficulties of single-ended travelling wave fault location of HVDC lines as following:
The reflected wave is relatively weaker. Because the length of HVDC line is generally long, the transient travelling wave attenuates seriously in the process of long-distance propagation.
The background noise is serious. The noise intensity of HVDC system is obviously higher than that of AC system due to the system clutter interference caused by the on-off of power electronic equipment. When the background noise and reflected wave are superimposed, the identification of reflected wave is greatly affected.

2.2. Characteristics of Background Noise in HVDC System

For HVDC transmission projects, the influence background noise includes:
System clutter interference
The clutter interference in HVDC system includes: 1) the interferences caused by the on-off process of converter valves; (2) the interferences caused by load fluctuation, LLC-HVDC is equivalent to current source, and the load fluctuation can lead to voltage fluctuation, which is more obvious in the inverter side. In addition, the smoothing reactor will shield the interferences from the converter side in theory, but the [11,12] shows that the shielding effect of the separately installed smoothing reactor is relatively reduced. The interference from the AC side can still enter the line.

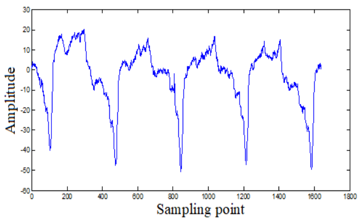

(a)

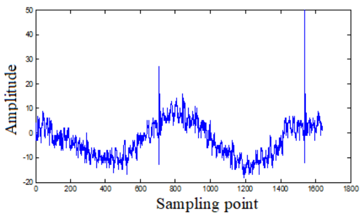

(b)

Figure 1. Typical interference signal in HVDC

Figure1. is the typical HVDC system interference which is collected in field. As is shown in figure 1(a), the influence of the interferences caused by the on-off process of power electronic equipment is more serious. Its frequency-band is wider, and its high frequency component exceeds 10 kHz, which crosses the frequency-band commonly used in fault location. Thus, these interferences cannot be removed thoroughly by using the traditional frequency-band filtering. But these interferences have one characteristic that it is mainly related to the working-condition of the convert valves. As shown in figure 2, the interference signals of two poles is not synchronous, and their frequency-spectrum also have some differences.

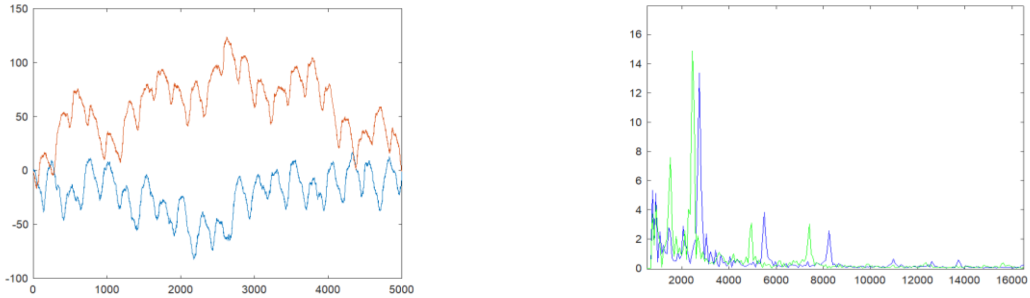

(a) (b)

Figure 2. Frequency spectrum and waveform of interference signal in HVDC

Signal Resonance

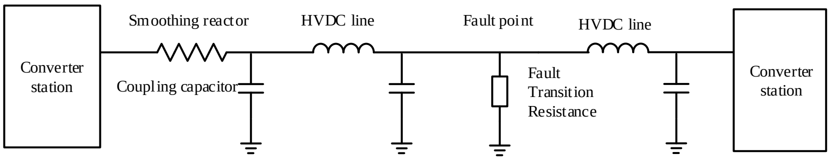

Figure3. Equivalent circuit of the faulty HVDC line

The equivalent circuit of the faulty HVDC lines is shown in figure 3; the transient travelling-wave will reflect between the converter station and the fault point after failure, it produces a series of resonance signals in the process. At the same time, the inductance/capacitance of the transmission line and reactor/coupling capacitor at the convert station will produce a specific frequency resonance signal, especially when the fault point is close to the converter station. The above resonance signal is another important factor for identification of reflected wave. But the resonance signals of the non-fault pole line is quite different from that of the fault pole because there is no fault point in circuit.

Overall, the on-off process of power electronic equipment and signal resonance cause a lot of clutter interferences in HVDC transmission project. The frequency-band of these interferences and the fault signals is overlap. So, the weaker reflected wave may be affected by the noise in the pass-band even after filtering, and the filter process may reduce the signal characteristics in part. Therefore, the existing fault location methods based on frequency-band filtering is affected in HVDC projects.

3. Signal coupling process of two pole lines

3.1. Signal Coupling Process

When HVDC transmission lines failure, it can be considered as a transient voltage/current source is superimposed on the fault point. Because there is mutual inductance and coupling capacitance between positive and negative pole lines, the transient voltage will be emerged on the non-fault pole line.

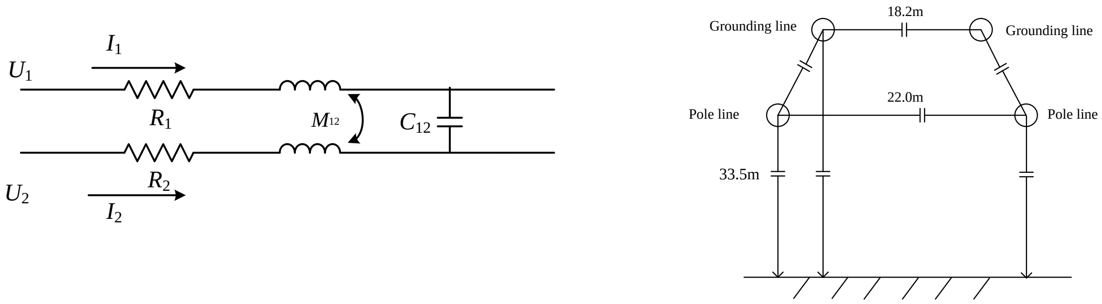

Figure 4. Equivalent circuit of two pole lines

As shown in figure 4, the coupling process between the two pole lines includes: electromagnetic coupling and electrostatic coupling. The coupling quantity is shown in equation 3/4 [13~16].

$$-\frac{d}{dx}\begin{bmatrix}U_1\\U_2\end{bmatrix}=\begin{bmatrix}R_1\\R_2\end{bmatrix}\begin{bmatrix}I_1\\I_2\end{bmatrix}+\begin{bmatrix}L_{11}&M_{12}\\M_{21}&L_{22}\end{bmatrix}\frac{d}{dt}\begin{bmatrix}I_1\\I_2\end{bmatrix}=\begin{bmatrix}Z_s&Z_m\\Z_m&Z_s\end{bmatrix}\begin{bmatrix}I_1\\I_2\end{bmatrix} \tag{3}$$

$$-\frac{d}{dx}\begin{bmatrix}I_1\\I_2\end{bmatrix}=\begin{bmatrix}G_1\\G_2\end{bmatrix}\begin{bmatrix}U_1\\U_2\end{bmatrix}+\begin{bmatrix}C_{11}+C_{21}&-C_{12}\\-C_{21}&C_{12}+C_{22}\end{bmatrix}\frac{d}{dt}\begin{bmatrix}U_1\\U_2\end{bmatrix}=\begin{bmatrix}Y_s&Y_m\\Y_m&Z_s\end{bmatrix}\begin{bmatrix}U_1\\U_2\end{bmatrix} \tag{4}$$

Since the direction of the electrostatic coupling and electromagnetic coupling is opposite. Formulas 3 and 4 can be simplified as follows:

$$\frac{d^2}{dx^2}\begin{bmatrix}U_1\\U_2\end{bmatrix}=\begin{bmatrix}Z_sY_s+Z_mY_m&Z_sY_m+Z_mY_s\\Z_sY_m+Z_mY_s&Z_sY_s+Z_mY_m\end{bmatrix}\begin{bmatrix}U_1\\U_2\end{bmatrix} \tag{5}$$

Among them, Zs is self-impedance and Zm is mutual impedance. Both of them are frequency-dependent, so it means that the coupling signal on two pole lines is frequency-dependent too.

3.2. Characteristics of Bipolar Coupled Signals

Based on the parameters of 800 kV Yunnan-Guangzhou HVDC transmission project, the EMTDC simulation model is established in figure 5. The coupling process between positive and negative poles is analyzed by injecting fixed frequency signals. If the signal which frequency is 5kHz is injected, the transient voltage waveforms on the two pole lines are shown in figure 6. It demonstrates that the waveform of the coupling signal in is basically the same as that of the original signal, but amplitude and phase is different.

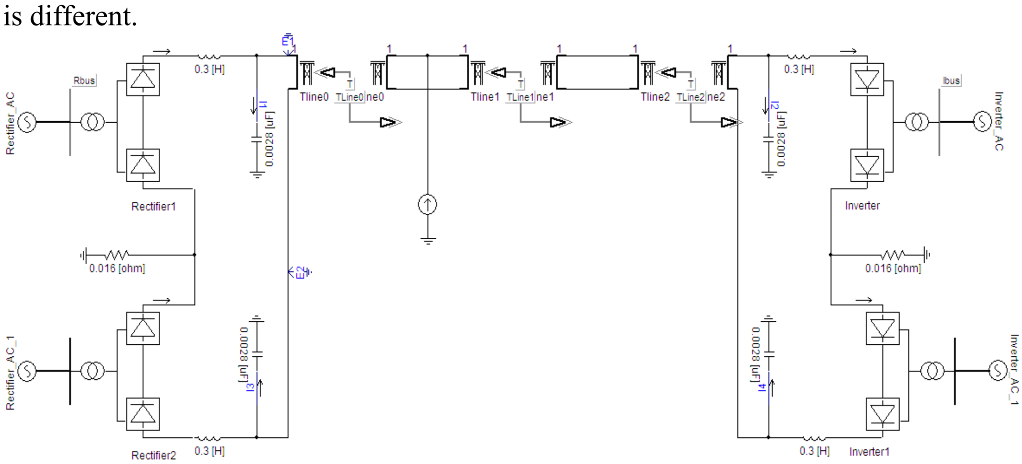

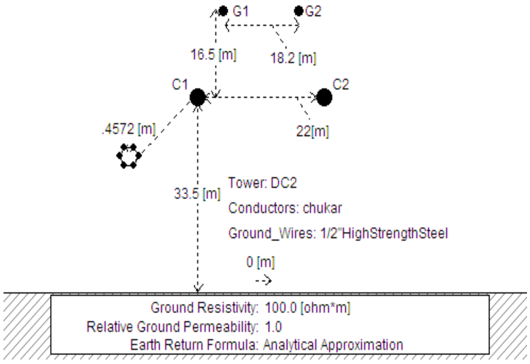

Figure 5. EMTDC simulation model

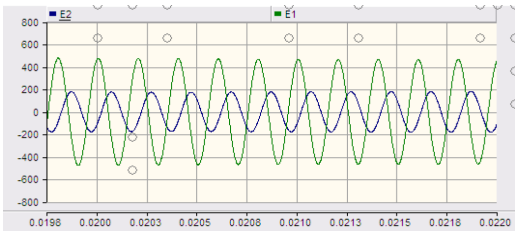

Figure 6. Transient voltage waveform of two pole lines

Note: The unit of ordinate is V, the unit of abscissa is S, the larger amplitude is the injected signal.

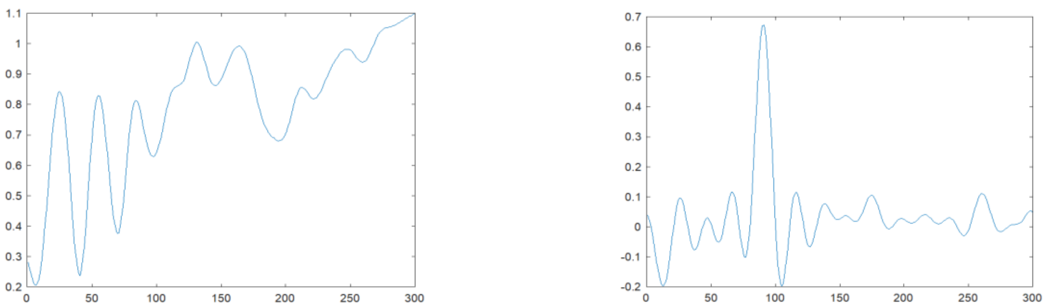

(a) (b)

Figure7 The character of coupling signal in two pole lines

Note: The unit of ordinate in figure7(a) is kHz, The unit of ordinate in figure7(b) is rad.

The coupling coefficient and phase-shift of the signal in two pole lines is shown in figure 6/7, which is calculated through sweeping frequency. The higher the frequency is, the stronger the signal on the non-fault pole line is. In signal phase aspect, there is a phase-shift (it can be considered as time-delay) between the two-pole signals, but it is relatively stable as a whole.

4. Single-terminal fault location method for HVDC transmission based on cross-correlation analysis

4.1. Basic Principles

From the analysis of section 1 and section 2, it can be concluded that the interference signals of the two pole lines are different in time and frequency domain, while the coupling signals of the two pole lines are highly similar. Therefore, using non-fault pole transient voltage as reference signal and enhancing the common part of signal in two pole lines through cross-correlation calculation can reduce the influence of interference and resonance signal in theory. Assuming that the fault pole signal is x (t), the non-fault pole signal y (t) is used as the reference quantity, and the principle of cross-correlation calculation is shown in figure 8. There are two key-points in calculation.

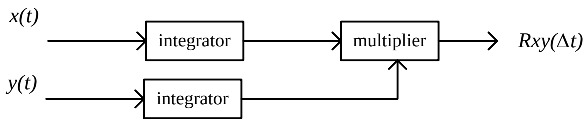

Figure 8. The principle of cross-correlation calculation

There is a time-delay between the signal of the non-fault pole line and the original signal of the fault pole. Therefore, the time-delay correction should be carried out in the cross-correlation calculation.

Although the coupling coefficient is positive correlated with frequency, and the higher components is suit for fault location in theory. However, in actual fault analysis, because the frequency component of the signal is uncertain and related to the fault point and the fault condition, multi-scale analysis should be adopted.

Take the artificial short-circuit test of the 1100kV Changji-Guquan UHV transmission project as example, the cross-correlation calculation process is analyzed in paper. The current of neutral point that flows through coupling capacitor is shown in figure 9 (a)/(b). It is difficult to figure out the reflected wave from background noise if only filtering is performed. Figure 9(c)/(d) is the transient voltage after the waveform restoration based on time-domain integral calculation, the low-frequency signal has been restored in part. Figure10 (a)/ (b) are the frequency-spectrum of the fault pole and the non-fault pole signal which are extracted through the Morlet wavelet transformer. It can be found that the similarity parts of the two poles signal after cross-correlation operation are enhanced in figure10(c). The waveform of the main analysis scale after cross-correlation calculation is shown in figure11; the identification difficulty of reflected wave is significantly reduced.

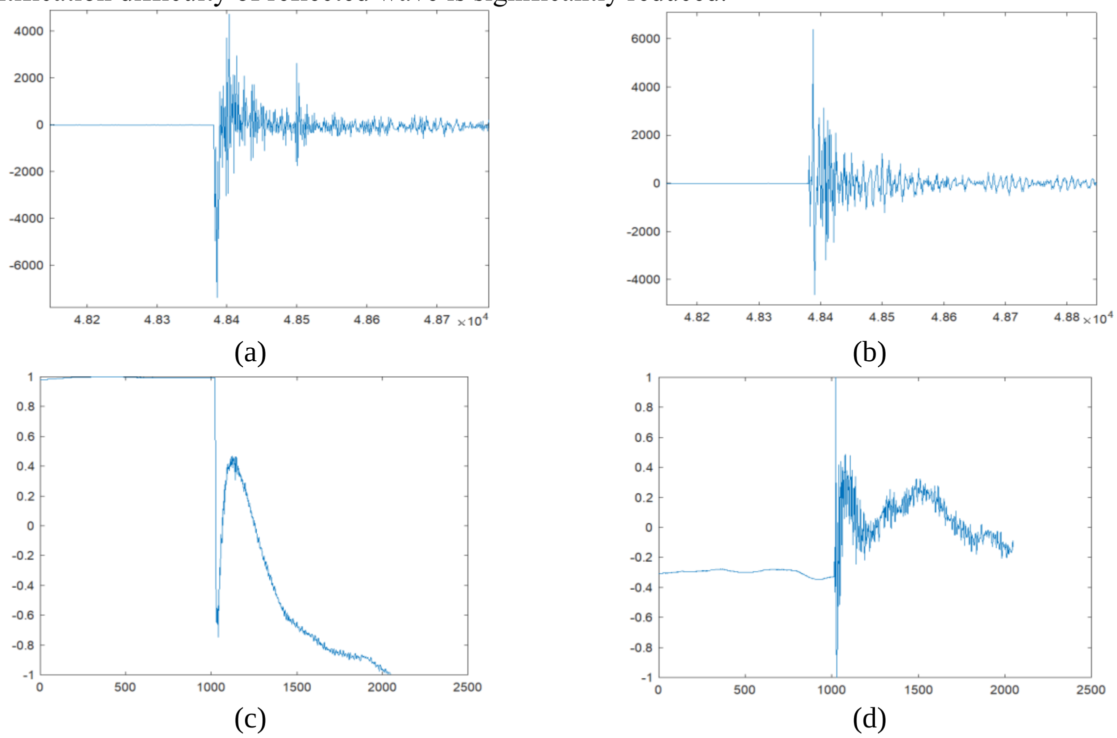

(a) (b) (c) (d)

Figure 9. Transient voltage and neutral point current of the two pole lines

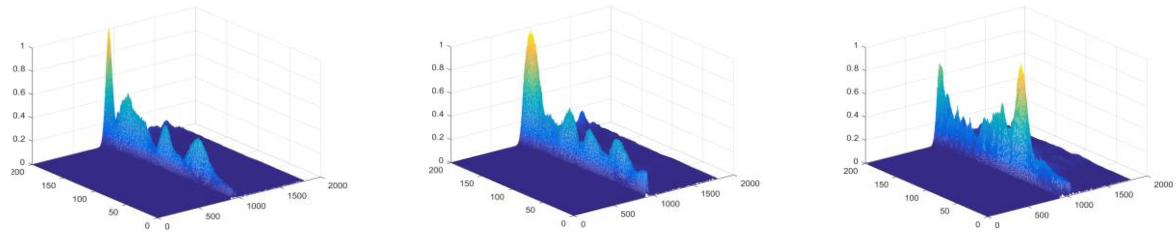

(a) (b) (c)

Figure 10. Frequency spectrum

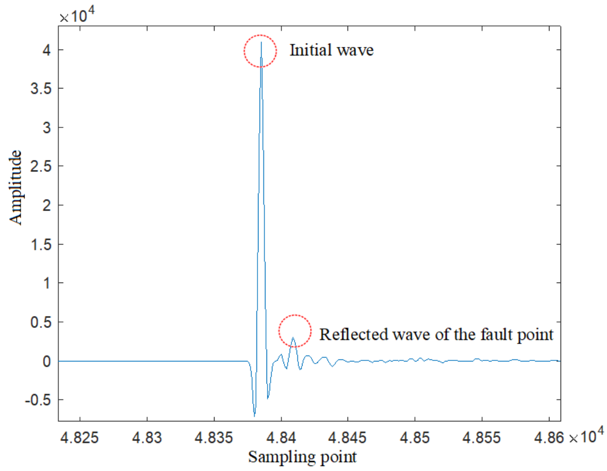

Figure 11. Wavelet transformer coefficient of transient under main analysis scale

4.2. Algorithmic Flow
The flow chart of single-ended fault location method for HVDC transmission line based on cross-correlation analysis is as follows:

(1) Time-domain integration: Generally, the existing fault location device collects the neutral point current of the coupling capacitor, which corresponds to the difference value of voltage. The voltage difference restrains the lower frequency components and the signal waveform is changed. Therefore, the transient voltage is restored by the time-domain integral calculation as follows:

$$u(t)=u(t_0)+\int_{t_0}^{t}(\frac{1}{C})i(t)dt \tag{6}$$

In the above formula, C is the capacitance value of the coupling capacitor and the neutral point current sampling signal is $i\,(t)$.

(2) Time-shift compensation and correlation calculation: the arrival time of non-fault pole and fault pole can be figured out by the modulus maximum method based on wavelet transform [8]. Assuming that arrival time is t_1 and t_2, then the time-shift of the two pole lines is $\Delta t = t_2 - t_1$. The wavelet cross-correlation of $x\,(t)$ and $y(t)$ at given scales and time-shift Δt is defined as:

$$WC_{XY}(a,t)=E\left[W_{XX}\left(a,t\right)W_{YY}\left(a,t+\Delta t\right)\right] \tag{7}$$

In formula 7, $W_{xx}(a,t)$ corresponding to the wavelet transform detail coefficient of the fault pole signal $x\,(t)$, and $W_{yy}(a,t+\Delta t)$ corresponding to the non-fault pole signal $y(t)$, a is the wavelet transform scale, and using the forward shift of the non-fault pole wavelet coefficients Δt to compensate the time delay. So, the wavelet correlation sequence of the two poles signal can be obtained.

(3) Identification of reflected wave: the catadioptric characteristics of the two polar lines are consistent, the reflected of the fault point is positive, and the reflected wave from the opposite end of the HVDC line is negative. But compared with the fault pole line, the reflected wave of the non-fault

pole line has two characteristics: 1) the reflected wave of the opposite end is relatively high; 2) the reflected wave for the fault point is only generated by the coupling between the two poles, thus, the amplitude is lower. The above characters can be used as another auxiliary criterion for the identification of the reflected wave.
(4) Single-ended fault location: After the identification of reflected wave, the traditional single-ended travelling wave can be used to complete the final fault location.
In actual fault analysis, compared to the two-ended travelling wave method. For the reason that it is not affected by the timing error, and the distance and velocity errors are relatively small, the accuracy of single-terminal travelling wave method is superior to the two-ended travelling-wave method.

5. Simulation and verification of actual fault data

5.1. Simulation Verification
Based on the section 3.2 model, the proposed method is verified through EMTDC simulation. In the calculation, different fault location points are set: the head of the line, the end of the line and the 3/4 position of the line. Metallic and high-resistance grounding faults are simulated respectively. The fault transition resistance is 1 ohm for metal grounding fault and 150 ohm for high resistance fault. Under typical fault conditions, the waveform of non-fault pole and fault pole line are collected by 2.8nF coupling capacitor. In the simulation, Gauss noise is added which to simulate the actual noise interference. After simulation, the current of neutral point that flows through coupling capacitor is shown in figure 12 and the signal after cross-correlation calculation is shown in figure13. After cross-correlation calculation, the interference is suppressed and the identification difficulty of reflected wave is reduced.

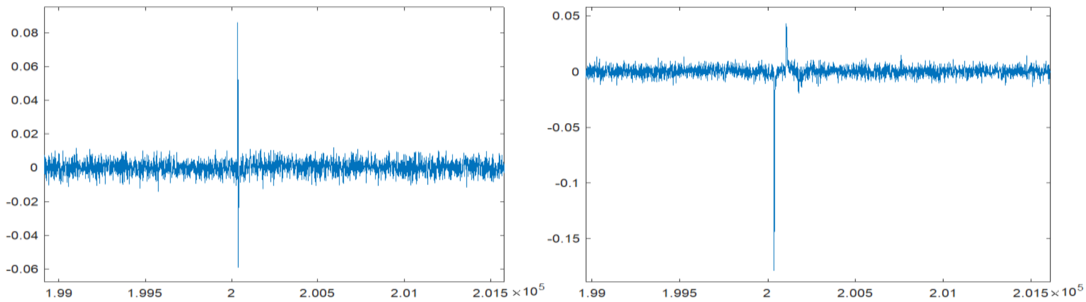

Figure 12. Simulated neutral point current of two pole lines

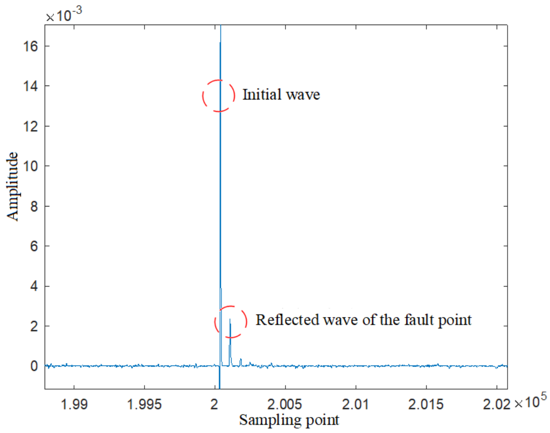

Figure 13. Transient voltage after cross-correlation calculation

Under different fault conditions, the simulation results are shown in the table1. In case that the identifying the reflected wave is precise; the single-ended travelling wave method has higher accuracy. Even in the case of 150 ohm fault transition resistance, its errors are basically within 500 m.

Table1. Simulation result

Fault distance	Fault transition resistance=1Ω		Fault transition resistance=150Ω	
	Fault location(km)	Error(km)	Fault location(km)	Error (km)
10km	10.098	0.098	10.19	0.19
1350km	1350.22	0.22	1350.33	0.33
1020km	1020.36	0.36	1020.47	0.47

5.2. Verification of Actual Fault Data

The following is the analysis of the artificial short circuit test data, the test data is collected during the test of 800 kV QiShan-ShaoXing HVDC transmission project in May,2017. The total length of the HVDC transmission line is 1095.6 km. The artificial short circuit test point is 13.8km away from to Qilian converter station. The test is nearly a metal-grounding fault. The sampling frequency of the equipment is 1.25 MHz. Figure14(a) is the neutral point current waveform of the non-fault pole line, figure 14(b) is the waveform of the fault pole line. The amplitude of the non-fault pole line is about 90% of the fault pole line; figure 14(c)/(d) is the transient voltage waveform after integral transformation.

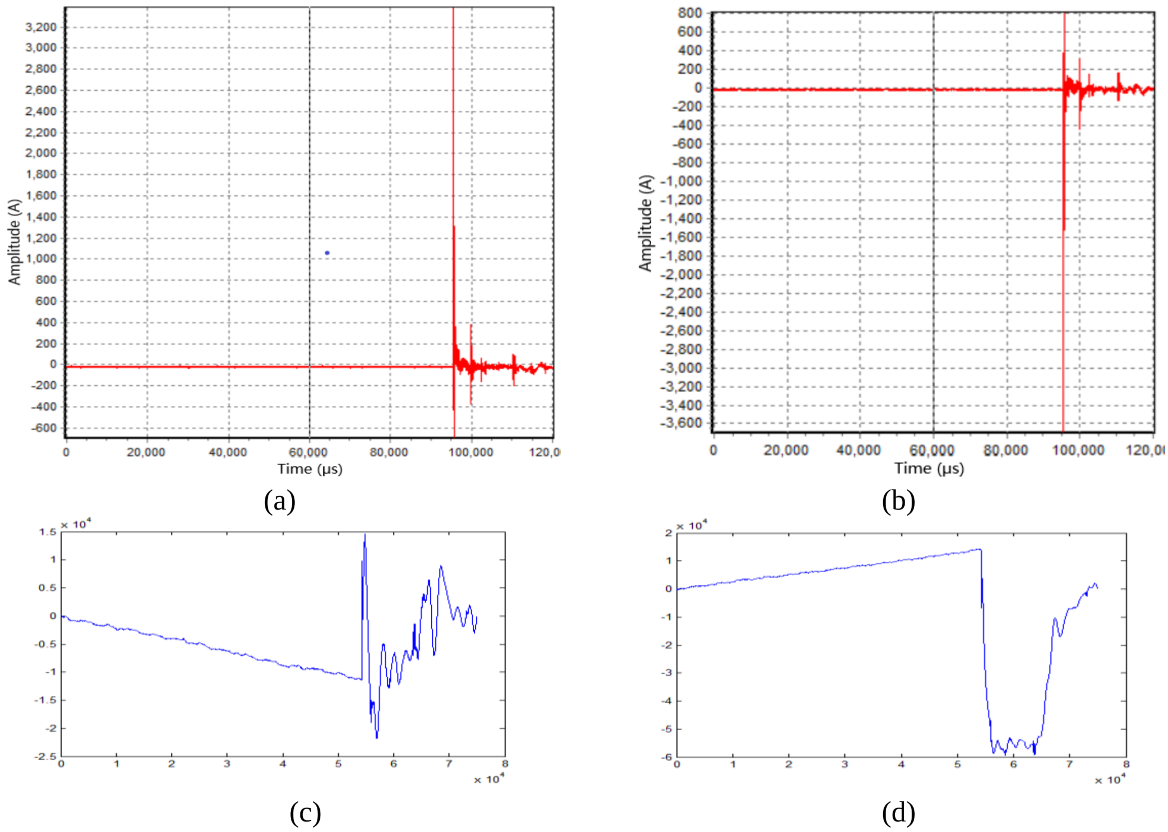

Figure 14. Actual failure data

As shown in figure15(a)/(b), the wavelet coefficients are obtained by decomposing the positive and negative pole signals through wavelet transform. After the time-delay compensation of the non-fault pole and the fault pole line, the cross-correlation sequence is calculated as shown in the figure15(c). The interference is effectively suppressed after the cross-correlation calculation.

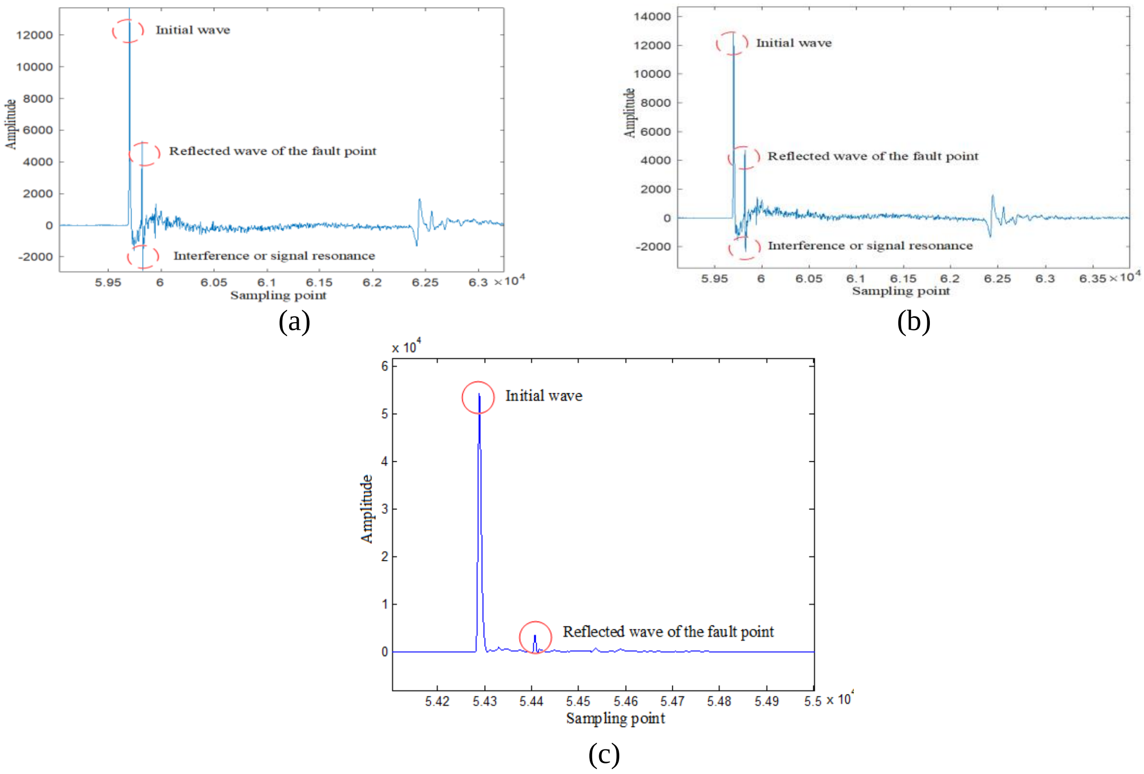

Figure 15. Actual failure data

After recognizing of the reflected wave, the traditional single-ended fault location method can be adopted to complete the location calculation. As shown in figure15, there are 119 sampling points between the reflected wave of the fault point and the initial travelling-wave, corresponding time difference is 95.2us. Assuming that the velocity of travelling wave is 296.2m/us, the distance between the fault point and the converter station is 14.099km. The error is about 300 meters. In this test, because the fault point is close to the converter station, the accuracy of single-ended fault location is even higher than the traditional two-ended travelling wave method.

6. Conclusion

In HVDC, the existing single-ended travelling-wave method based on the identification of waveform similarity is influenced by interference caused by the power electric equipment. The success rate of reflected wave identification is relatively low, the reliability of fault location is affected greatly. To solve the above problems, the following research work has been carried out:

(1) In HVDC, the interference caused by power electric equipment and signal resonances have wide frequency band, they are main influence factors for the single-ended fault location. However, the interference of the two pole lines is basically independent, and there are differences in frequency band and time domain. Thus, it is feasible to suppress interference by cross-correlation analysis.

(2) The signal coupling process of the non-fault pole and the fault pole in HVDC system is analyzed in paper. The EMTDC simulation reveals that the coupling coefficient of the two poles is positive correlated with frequency, and there is a time-shift in the coupling signal of two poles.

(3) A novel single-ended travelling-wave fault location method for HVDC lines is proposed in paper. Using the signal of non-fault pole lines as reference quantity, it suppresses interference by cross-correlation calculation of two polar signals and improves the reliability of reflected wave identification. The validity of the method is verified by simulation and on-site data analysis in paper.

7. References

[1] M. Ando, E.O. Shweitzer, R.A. Baker, *Development and field-data evaluation of single-end fault locator for two-terminal HVDC transmission lines*. Part I: data collection system and field data, IEEE Trans. Power App. Syst. PAS-104 (12)(1985) pp3524–3530.

[2] Hanif Livani, Cansin Yaman Evrenosoglu etc, *A single-ended fault location method for segmented HVDC transmission line [J]*. Electric Power Systems Research ,2014,107 pp190–198

[3] Mohammad Farshad, Javad Sadeh, *A Novel Fault-Location Method for HVDC Transmission Lines Based on Similarity Measure of Voltage Signals [J].* IEEE transactions on power delivery, 2013, vol28 (4) pp123-132.

[4] J. Sadeh, H. Afradi, *A new and accurate fault location algorithm for combined transmission lines using adaptive network-based fuzzy inference system [J]*, Electrical power System.2009,vol79 (11) pp1538–1545.

[5] I. Niazy, J. Sadeh, *A new single ended fault location algorithm for combined transmission line considering fault clearing transients without using line parameters [J]*, Electrical power System,2013,vol44 (1) pp616–623.

[6] SHU Hong-chun, WU Qian-jin, ZHANG Guang-bin, et al. *Single terminal travelling wave fault location method based on ANN[J].* Proceedings of the CSEE, 2011, 31(4) pp85-92.

[7] R. Salat, S. Osowski, *Accurate fault location in the power transmission line using support vector machine approach,* IEEE Trans. Power Syst. 29 (2) (2004) pp979–986.

[8] QIN Jian, GE Wei-chun, QIU Jin-hui, et al. *Study on single terminal method and double terminal method of travelling wave fault location in transmission line[J].* Automation of Electric Power Systems, 2006, 30(6) pp92-95.

[9] O.M.K.K. Nanayakkara, A.D. Rajapakse, R. Wachal, *Fault location in extra long HVDC transmission lines using continuous wavelet transform,* in: International Conference on Power Systems Transients, Delft, The Netherlands, 2011, pp14–17.

[10] WANG Kui-xin, ZHU Cheng, SUN Jia-jia, et al. *Research of combined travelling wave fault location method on transmission lines[J].* Power System Protection and Control, 2012, 40(15) pp82-86.

[11] Mo Fu-jiang, Chen Yun-ping, Ruan Jiang-jun, *Analysis of coupling mechanism and calculation of lightning induced over-voltage for overhead transmission lines[J],* Power Systems Technology, 2005, 29(6) pp72-96.

[12] Sun Ban-xin *Configuration scheme of smoothing reactor in UHVDC system [J], Electrical engineering technology,* 2009, 13(5) pp2-7.

[13] Xiao Yao, Deng Jun, Xia Gu lin, *A New Method for Measuring Distribution Parameters of HVDC Transmission Lines[J].* Proceedings of the CSEE, 2015, 35(20) pp5375-5382.

[14] Wang De-ling, Lv Peng-fei，Ruan Si-Ye etc *Mutual inductance effect of UHVDC bipolar transmission lines and Its Countermeasures[J].* Proceedings of the CSEE, 2015, 35(18) pp4210-4216.

[15] Zhang Fu-xuan, Zhou qiang etc, *Mutual Inductance Effect and Control Strategy Improvement of UHVDC Bipolar Lines[J],* Power Systems Technology, 2017, 41(11) pp3547-3542.

[16] Chu xu, Wang Liang, Wang Hua-wei, *Effect of inter-pole coupling on HVDC transmission line and fault pole selection scheme[J]* , Power Systems Technology, 2017, 37(4) pp140-145.

Current pole inner distribution method for measuring tower grounding resistance

Jun Guang Zhao[1], Yu Ying Luo[1], Jun Zhang[1], Xin Gan[1], Zhao Liu[1], Zhan Long Zhang[2] and Zi Jian Dong[2]

1 State Grid Chongqing Electric Power Company Jiangjin Power Supply Branch, Jiangjin, Chongqing, China
2 State Key Laboratory of Power Transmission Equipment & System Security and New Technology, Chongqing University, Shapingba, Chongqing, China
E-mail: dongzj@cqu.edu.cn

Abstract. Three electrode method is a common method in measuring tower grounding resistance. However, its wiring distance is too long to complete accurate measurement in some terrain narrow areas, which is also an application problem to be solved urgently in the field of tower grounding resistance measurement. The traditional three electrode method is to find the compensation point between the grounding pole and the current pole. After calculation, there are also compensation points near the current pole besides the grounding pole and the current pole by using the traditional three electrode method. Based on this principle, the current pole is arranged between the grounding pole and the voltage pole by the current pole inner distribution method, which can greatly shorten the distance of the distribution pole. Through simulation analysis and test verification, the pole inner distribution method can control the pole distribution distance around 50m on the basis of ensuring the accuracy of the measurement results. Compared with the three-pole method, the pole distribution distance is shortened to 60%.

1. Introduction

Tower grounding, as an important factor affecting trip rate of transmission lines, has attracted more and more attention. The status of tower grounding body directly affects the performance of tower grounding. Frank Wenner put forward the method of measuring soil resistivity in 1915 for measuring power frequency grounding resistance [1]-[3]. Up to now, scholars at home and abroad have explored many different measuring methods and devices based on the relationship between basic physical quantities such as voltage, current and power. They mainly include potential drop method, three electrode method, high-frequency parallel method, clamp meter method, etc. [4] - [6]. Among them, three electrode method is the most widely used method for measuring tower grounding resistance.

At present, the traditional grounding resistance measurement methods used by power companies generally have the problems of long wiring distance and limited pole distribution area [7]. In order to ensure the measurement accuracy of the three electrode method, the current pole must be arranged more than 100m from the grounding lead in accordance with the pole distribution rule of 1:0.618. It is difficult to meet the requirement of wiring distance when the distance between poles is limited in complex terrain, which leads to inaccurate measurement of grounding resistance. The current pole inner distribution method proposed in this paper is an improved method based on the principle of three electrode method. The new compensation point position is deduced theoretically and verified by simulation. The biggest advantage of this new method is that it can greatly shorten the wiring distance of three-pole method. The voltage pole is arranged on the outside and the distribution distance is controlled at about 50m. This method not only reduces the workload of pole distribution and improves the detection efficiency, but also has very high practical value in mountainous and hilly areas where the terrain is narrow and the pole distribution is not easy for long distance.

2. Current pole inner distribution method

Three electrode method is the most commonly used method for measuring grounding resistance at present. Current pole inner distribution method is a new method based on three electrode method. This chapter will introduce the basic principle of current pole inner distribution method combined with the principle of three electrode method.

2.1. Three electrode method

Based on the principle of voltage and current, the three electrode method is a measurement system consisting of grounding body G, current pole C and voltage pole P. When measuring, the voltage pole and current pole are arranged first, then the current I is injected into the grounding body to be measured, and the voltage U on the voltage pole is measured. Through the formula: $R = U / I$, the grounding resistance can be obtained [8]-[10].

In the measurement of tower grounding resistance, the equivalent model of grounding resistance of single independent hemispherical grounding body is often used. Assuming that the grounding body buried in the soil is hemispherical, its radius is a, uniform soil resistivity is ρ, and the current injected into the grounding body is I, the grounding resistance of the hemispherical grounding body can be obtained as follows:

$$R_0 = \frac{V}{I} = \frac{\rho}{2\pi a} \tag{1}$$

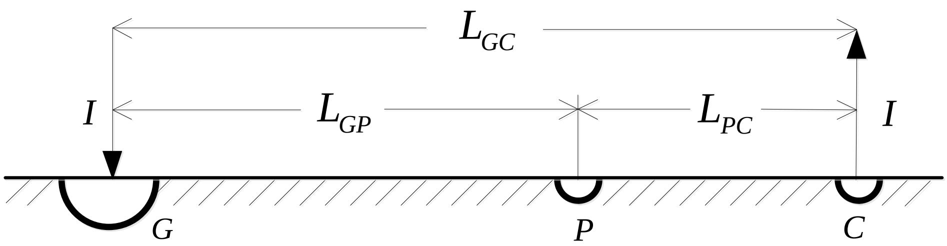

Figure 1. Electrode arrangement of three electrode method.

As shown in Figure1,In the three-pole method, G, P and C are used to represent the grounding body, voltage electrode and current electrode respectively. L is the distance between the electrodes. By calculating, the potential difference between the grounding body G and the current pole C can be obtained. The voltage between GP can be obtained by applying the superposition theorem, and the grounding resistance can be obtained. At the same time, combining with the grounding resistance of the hemispherical grounding body in (1), the measurement error of the grounding resistance can be obtained as follows:

$$R - R_0 = \frac{\rho}{2\pi}\left(-\frac{1}{L_{GP}} - \frac{1}{L_{GC}} + \frac{1}{L_{PC}}\right) \tag{2}$$

In order to make the measured grounding resistance equal to the accurate value, it is necessary to make the measurement error 0. The final result of the three electrode method is as follows:

$$L_{GP} = 0.618 L_{GC} \tag{3}$$

2.2. Current pole inner distribution method

If the voltage poles in the triode method are arranged outside the current poles, the arrangement of the electrodes will become the form shown in Figure 2.

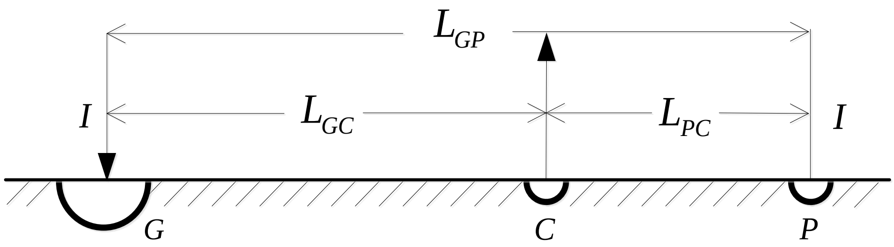

Figure 2. Electrode arrangement of current pole inner distribution method.

The potential difference between GP generated by grounding body G current and the potential difference between GP generated by current pole C are as follow:

$$U_1 = \frac{I\rho}{2\pi a} - \frac{I\rho}{2\pi L_{GP}} \quad \text{and} \quad U_2 = -\frac{I\rho}{2\pi L_{GC}} + \frac{I\rho}{2\pi L_{PC}} \tag{4}$$

According to the superposition theorem, the measured value of grounding resistance can be obtained as follows:

$$R = \frac{U_1 + U_2}{I} = \frac{\rho}{2\pi}\left(\frac{1}{a} - \frac{1}{L_{GP}} - \frac{1}{L_{GC}} + \frac{1}{L_{PC}}\right) \tag{5}$$

Similarly, the error of grounding resistance measurement can be obtained by using the three electrode method. Its form is the same as (2). In order to make the measured grounding resistance equal to the accurate value, it is necessary to make the measurement error of grounding resistance zero. So we can get the following equation.

$$\frac{1}{L_{PC}} - \frac{1}{L_{GP}} - \frac{1}{L_{GC}} = 0 \tag{6}$$

Suppose that the relationship between the distance between G and C and the distance between G and P is k:1. From equation (6), we can get k = 0.618.

Because the accuracy of measurement can only be guaranteed by the hemispherical grounding body model in soil with infinite radius, it is generally considered that the hemispherical equivalent model can be applied only when the radius is greater than 2.5 times the length of grounding body. So the distribution distance of the voltage poles must be greater than 2.5 times the length of the grounding body. In the current pole inner distribution method, the current pole is arranged between the grounding body and the voltage pole, and the farthest voltage pole is 2.5 times the length of grounding body. In the three electrode method, the farthest electrode is the current electrode and the shortest distribution distance is 4.04 times the length of the grounding body. Therefore, compared with the three-pole method, the distribution distance of the current pole is reduced by 0.618 times.

3. Simulation and data analysis

A 200 m radius hemispherical earth model is simulated by Comsol finite element simulation software. The length of grounding body is 20m and the current pole position is 50m. The potential distribution of XY plane and XZ plane is obtained as shown in Figure 3 and Figure 4.

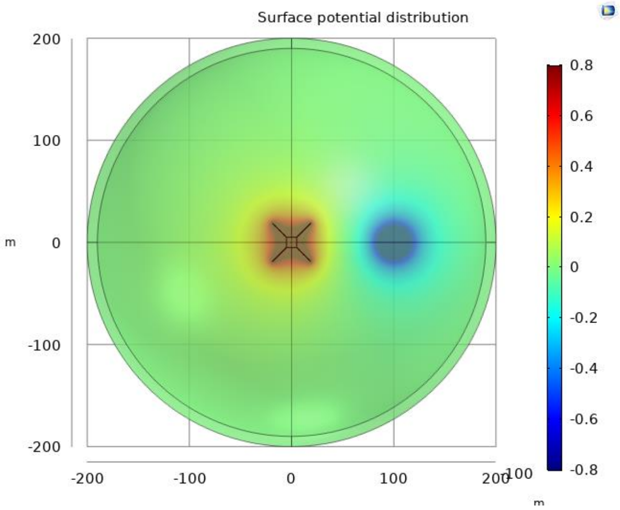

Figure 3. XY plane potential distribution.

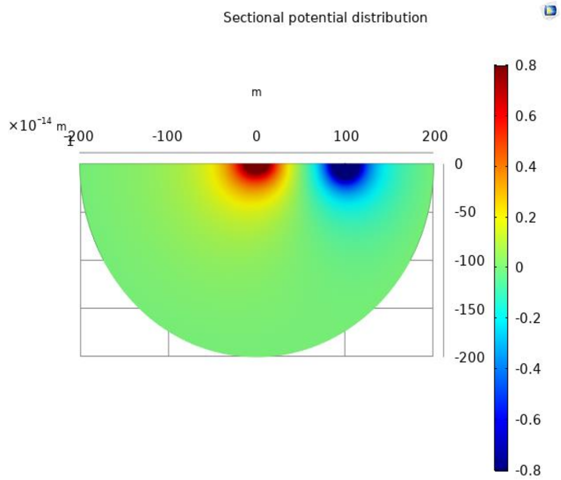

Figure 4. XZ plane potential distribution.

The simulation results show that the current pole internal distribution principle is scientific. There are zero compensation points on both sides of the current pole on the X-ray axis. After removing the current pole, the simulation results are obtained again, and the ground potential distribution without the influence of the current pole is obtained. The grounding resistance value(2.053Ω) at this time is taken as the standard value. At the same time, we take the distribution distance as a variable parameter to study the grounding resistance measurement results of two methods under different distribution distances, and the results are shown in Table 1.

Table 1. Comparison of measurement results by two methods.

Current pole inner distribution method				Three electrode method			
Current pole distance	Voltage pole distance	Grounding resistance	measurement error	Current pole distance	Voltage pole distance	Grounding resistance	measurement error
30.9	50	2.106388	0.026005				
37.08	60	2.110064	0.027796				
43.26	70	2.112582	0.029022				
49.44	80	2.114285	0.029852	80	49.44	2.114279	0.029848
55.62	90	2.113608	0.029522	90	55.62	2.113927	0.029677
61.8	100	2.112494	0.028979	100	61.8	2.112505	0.028984

It can be seen that the measurement errors of the current pole inner distribution method and the three pole method are very similar, so there is not much difference in the measurement performance between the two methods. However, the current pole should be arranged at least 80m under the three-pole method, and the current pole inner distribution method breaks through this limit. When the farthest electrode (voltage pole) is arranged between 50m and 80m, the measurement accuracy can still be guaranteed.

4. Conclusion

IOP Conf. Series: Earth and Environmental Science **431** (2020) 012007 doi:10.1088/1755-1315/431/1/012007

Based on the measurement of tower grounding resistance by three-pole method, an improved current pole inner distribution method is proposed in this paper. Through theoretical deduction, the potential compensation points on the outer side of the current pole are found, and the current pole is innovatively arranged between the voltage pole and the earth body, which greatly shortens the distribution distance and improves the applicability of tower grounding resistance measurement in complex terrain where the distribution distance is limited. Through simulation analysis and field measurement, the accuracy of this method is comparable to that of the three electrode method, and the measurement error is less than 3%. But it can effectively shorten the distribution distance by 60%, so it has high application value.

5. References

[1] Frank Wenner 1915 *A method of measuring earth resistivity.bulletin, Washington-60-DC:National Bureau of Standards.* 16(11):12-58.

[2] Hans R Seedher,J K 1992 *Arora.Estimation of Two Layer Soil Parameters Using Finite Wenner Resistivity Expressions. IEEE Transaction on Power Delivery.*7(3):1213-1217.

[3] Huina Yang,Jiansheng Yuan,Wei Zong 2001 *Determination of Three layer Earth Model from Wenner Four-prode Test Data. IEEE Transactions on Magnetics.*37(5):3684-3687.

[4] *ASIC/IEEE Std.80-1983.IEEE guide for measuring earth resistivity,ground impedanee,and earth surface potentials of a ground system.*

[5] Sun Pengyan，Meng Suimin 2011 *Study on Grounding Resistance Measurement of Ground Grid by Multi-auxiliary Current Pole Method. Journal of Electric Power(in Chinese).* 03:186-191.

[6] Zhang Qihua 2007 *Technology and Device for Measuring Tower Grounding Resistance by High Frequency Parallel Method. High Voltage Technology(in Chinese).* 01: 194-195.

[7] Jian Jiehua, Liao Xuejing 2006 *Analysis of factors affecting tower grounding resistance and Countermeasures . Sichuan Electric Power Technology(in Chinese).* 04:36-38.

[8] Ying Shunchao 1992 *Determination of the Position of Test Pole in Grounding Resistance Measurement. High Voltage Technology(in Chinese).* 01: 80-83.

[9] Chen Jianzhi，Shi Xiugang 2006 *Research on Testing Technology of Tower Grounding Resistance. Power grid technology(in Chinese).* S2: 495-498.

[10] Li Maotang 1996 *The measurement of grounding resistance based on third-order cumulant measuring method.1996.3rd International Conference on Signal Processing.* 1(3):572-575.

IOP Conf. Series: Earth and Environmental Science **431** (2020) 012008 doi:10.1088/1755-1315/431/1/012008

Distribution terminal automatic test system based on portable solution

Liang Weichen[1], Liu Bo[1], Liu Junna[1], Li Xuan[1] and Xiao Lin[2]

1 North China Electric Power Research Institute Co., Ltd, Beijing, China
2 CYG Sunri Co., Ltd, Guangdong, China
E-mail: liangweichenheng@163.com

Abstract. Distribution terminals have been widely and maturely applied in China currently. However, due to the large number of manufacturers, the differences in production technology, research and development technology lead to inevitable differences in the quality stability of distribution terminals. At the same time, it is also necessary to locate the faults of distribution terminals that are operating online and have faults. The traditional manual test method is difficult to meet the requirements of test specifications. It is also necessary to consider the requirements for testing batch operations and multi-scene applications. Based on the background, this paper proposes a distribution terminal automatic test system based on portable solution, which can complete the automatic test for distribution terminal in multiple scenarios.

1. Introduction

The distribution automation system is the core of distribution automation. It realizes the monitoring and control of distribution network system by comprehensively utilizing multiple communication methods [1]. Distribution automation helps improve the reliability of power supply and power quality, and reduce operation costs. A typical distribution automation system usually consists of a distribution master station, distribution terminals, distribution stations and communication channels.

Distribution terminal is an important part of the distribution automation system, as the basis of the whole system, the integrity and reliability of its function is the prerequisite and guarantee for the normal operation of the system [2] [3]. At present, the State Grid requires that the distribution terminals pass the full or sampling inspection at each provincial electric power institute before they are put into use on the site, and they should strictly meet the requirements of the inspection specifications [4] is necessary to confirm the function and performance of the distribution terminals provided by different suppliers to ensure the same the consistency and quality reliability. At the same time, stable and reliable test tool is also required for the maintenance of the distribution terminals in the field operation and the problem location of the distribution terminals with the existing failure.

According to the specific requirements of the test, in the normal manual test mode, the tester needs a series of instruments and equipment, and it is difficult to match the test specification requirement, and the test operation process of many items is cumbersome and difficult to implement [5] [6] For example, the basic error test of telemetry needs to provide a wide output range and high-precision source, and because the distribution terminal has no display screen, so the actual collected AC volume needs to be established after it is connected by the remote desktop. This method has too much impact on test efficiency. And for tests similar to telecommunicating anti-shaking, it is hard to control the time delay of the ms level, so the test items are hard to be tested accurately.

Research and develop a portable distribution terminal automation test system for practical application needs. It can be applied to batch testing by integrating multiple sets of portable power distribution terminal automatic test systems with the cooperation of load simulation devices, wave recording devices, switches and other equipment. It can simultaneously support automated testing of multiple power distribution terminals and simultaneously output test reports. In the application scenario of maintenance and small batch fault location, it can also realize the automatic test of most functions.

2. Overall system design

According to the requirements of the State Grid for the test of distribution terminals, the inspection is refined to the appearance and structure inspection, interface inspection, main function test, wave recording function test, basic performance test, wave recording performance test, telecommunicating anti-shaking test, timing test, insulation performance test, power supply test, communication test, etc [7]. In order to realize all the test functions, it is necessary to integrate a high-precision, wide-range output range of program-controlled AC standard source module, input-output module, timing module, program-controlled AC and DC source module, fault recording module, external interface module and other functional components and QR code scanner.

In order to balance the application in laboratory and on-site application environment, the test system is designed based on portability solution which is in control of volume and weigh. Because of such considerations, the system integrates the industrial computer, the display module, the AC standard source module, the input-output function module, the timing module and the program-controlled AC and DC source module.

The distribution terminal is usually divided into two specifications: 1A and 5A. The accuracy level of the voltage and current is 0.5, and the current impact test of 10 times and 20 times is required, and it corresponds to 4U, 4I input test requirements. So design the AC standard source module to achieve 0-450V voltage, 0-100A current output, while the output voltage accuracy level is 0.1, when the current does not exceed 20A, its preparation level is 0.1, and the preparation level is 0.2 when the output range is 20-100A, and it can output 4U, 4I at the same time. The input-output module adopts a passive design, which establishes a connection with the hard contacts of the distribution terminal, and then implements automatic testing of the switching quantities through software matching. As the time acquisition requirements for the switching quantity are strict during the test, it is necessary to achieve extremely low opening delay. The timing module can accept GPS and Beidou satellite signal to ensure the synchronization of the various functional components of the test system, at the same time, it can output accurate timing signal through IRIG-B code, 1 PPM/1PPS/1PPH(TTL) and other pulses. The program-controlled power module can output the set AC and DC voltages in time series under the control of the host computer to match the objective test conditions of the power switching test.

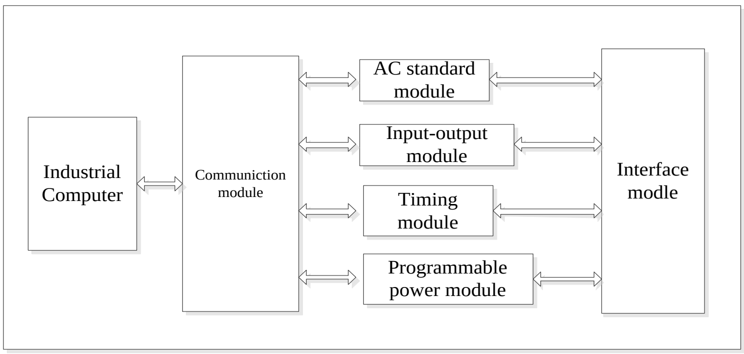

Figure 1. Portable distribution terminal test system block diagram.

The test system integrates the main functional modules, and its industrial computer installs and runs the test software. The software establishes a connection with the distribution terminal through the function of the main station, and it can control the distribution terminal and exchange information with it. The specific output and collection functions are completed by controlling the integrated function modules, and the distribution terminal can be tested in turn. Depending on the configuration of the test system, each test system can correspond to an automated test of distribution terminal. Its system structure block diagram can be as shown in Figure 1.

As shown in the above figure, the test system can be directly applied to the basic test of a single distribution terminal. However, due to the portability requirements, the system does not integrate the load simulation function component and the wave recording function component, so that the actual reference recording in the power performance test and the wave recording performance test has consistency in consistency with the expected waveform, therefore, in the laboratory scenario, load simulation device and wave recording device need to be added to make up for the defects here. In the laboratory scenario, due to the demand for batch testing, multiple sets of portable distribution terminal test systems can be networked, and the test system software runs from the server of the laboratory. The terminal, under the condition of correct wiring, completes the automated test of batching according to the setting of the existing test cases of the system.

Due to the high performance requirements, the above components and functions need to be developed and implemented. And the simulation of the fault scene waveform is difficult to achieve through the timing addition method, so the fault waveform playback is also the focus of research.

3. Implementation of automatic test function components

Analysis from the principle, the test procedure can be summarized as applying basic external conditions required for a certain type of test to the distribution terminal, and then analysing information such as telemetry, remote signal, SOE, and wave recording files generated by the terminal in response to the condition, this is a criterion for compliance with the requirements of the specification.

Considering the needs of the State Grid for the test and the existing mature solutions in the market, some functional modules such as timing module, programmable power module can use mature solutions already on the market, and the specific function can be achieved by structurally designed and installed and control matching of the software. The AC standard source module design achieves 0.1% high precision under normal working conditions of the distribution terminal, so as to meet the requirement that the test standard source is at least 5 times higher than the tested equipment, and for the 10 times and 20 times current impact test scenarios, its accuracy can be relaxed to 0.2%. Due to power consumption considerations, 10 times and 20 times currents are only allowed for short-time loading, and the system will be protected from exiting when timeout.

The program-controlled input-output module is based on a mature and stable CPU+FPGA+CPLD architecture and runs the VxWorks real-time operating system to ensure excellent industrial-grade real-time performance. The output signal needs to maintain the delay accuracy of less than 200us, the operation time of the traditional mechanical relay cannot meet the test of the distribution terminal. Therefore, the method of driving optical coupling relays by CPLD is realized. Its architecture is shown in Figure2 below.

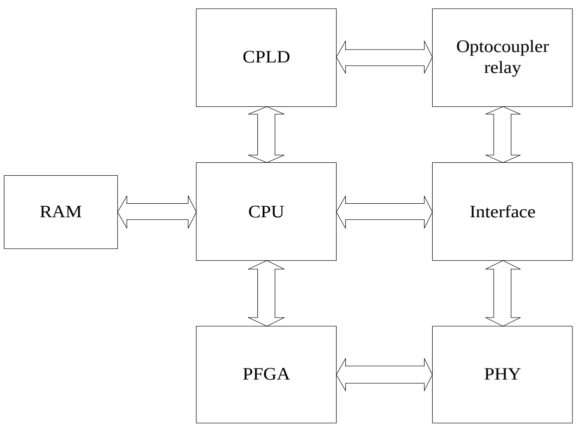

Figure 2. Program-control input-output module hardware architecture block diagram.

4. Waveform playback function implementation

The distribution terminal stores the recorded wave files in a format defined by the Comtrade 1999 standard. The recorded wave file usually records not less than 4 cycles before the occurrence of the fault and not less than 8 peripheral waveform data after the occurrence of the fault. Recording files are stored in CFG configuration files in ASCII text and DAT data files in binary format. The configuration files contains channel information such as sampling speed and number of channels, and the data file contains each sampling channel and its corresponding sampling value.

In the application of the system, the programmable AC standard source module reconstructs and outputs the fault waveform characterized by the data analysed from the waveform file data, and then the system acquires and compares the waveform recorded by the fault recorder under the condition of the recording starting condition. The system collects the actual action information of the distribution terminal, and compares it with the expected state, thereby completing the evaluation of the function and performance.

In essence, the waveform file records a series of discrete points in the time domain. Waveform playback is to reduce the discrete points into continuous waveform by fitting and modelling. Generally, when the sampling rate standing for discrete time-domain interval is higher, the waveform that is directly point is closer to the continuous analog signal recorded by the waveform files. In practical applications, waveform files usually record data at a sampling rate up to 10ksps, but in order to maximize the representation of the continuous signal represented, the system uses the interpolation algorithm to establish a mathematical simulation, simulates the sampling rate of 100ksps and above, and uses it as the basis of the inversion waveform to maximize the approximation of the actual recorded waveform.

For the interpolation of consecutive discrete sampling points in the time domain, if the sampling interval is small, an interpolation algorithm with equal three-point interpolation can be used. Let N be the sampling interval, A(T0) be the sampling value at time T0, A(T1) be the sampling value at time T1, A(T2) be the sampling value at time T2, and A(Ts) be the sampling value at time Ts, the interpolation time Ts is within the effective latching range of the three time points T0, T1, T2, then A(Ts) can be calculated by the following formula 1.

$$A(Ts)=A(T0)+\left(A(T1)\text{-}A(T0)*\frac{Ts\text{-}T0}{N}\right)+\left(A(T2)\text{-}2*\left(Ts\text{-}T0\right)*\frac{Ts\text{-}T1}{2N*N}\right) \tag{1}$$

If the sampling interval of the sampling points is large, it can be realized by a line one-time interpolation algorithm. That is: when A(T1) is the sampling value corresponding to T1, A(T2) is the sampling value corresponding to T2, and Ts is the sampling time within the range of T1 and T2, then the sampling value corresponding to Ts can be obtained by formula 2 shown below:

$$A(Ts)=A(T1)+\left(Ts\text{-}T1\right)*(A(T2)\text{-}A(T1))/(T2\text{-}T1) \tag{2}$$

After the waveform is reconstructed by the interpolation algorithm, the programmable AC standard source module outputs the reconstructed waveform according to a strict definition to complete the subsequent test.

The waveform library pre-stores the operational status of the various types of faults that characterize the actual distribution terminal or the operational status required to characterize a steady-state test item. The waveform inventory is located under a specific path folder, the software reads the specific waveform file under the path, and parses the waveform file, establishes a mathematical simulation by the application of the interpolation algorithm, restores the analog signal recorded by the waveform file, and then controls the waveform the AC standard source module output matching the waveform file. According to this, the transient characteristics of the operating state such as the fault state of the simulated distribution network can be realized, and the mode can also test the characteristics of the distribution terminal in other working states.

The high precision of the wave recorder makes it a property of the comparison benchmark. By reading the fault recording recorded by the distribution terminal and automatically comparing it with the waveform recorded by the wave recorder, the recording function and the recording performance of the distribution terminal to be tested can be judged.

The control flow of waveform playback is shown in Figure 3 below.

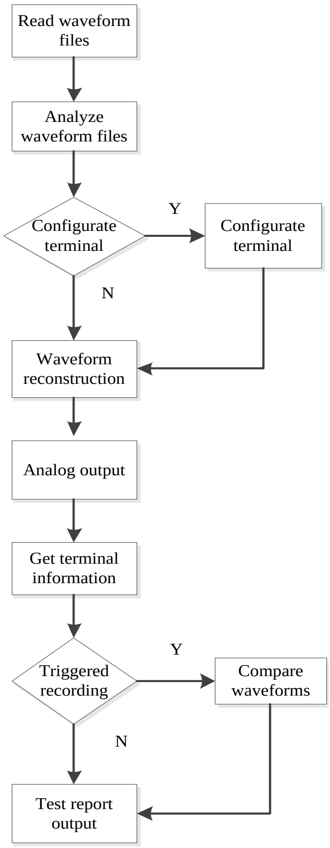

Figure 3. Summary flow of waveform playback.

5. System software function

The design of system software follows the principles of scalable, traceable and easy-using, the basic architectural block diagram is shown in Figure 4 below.

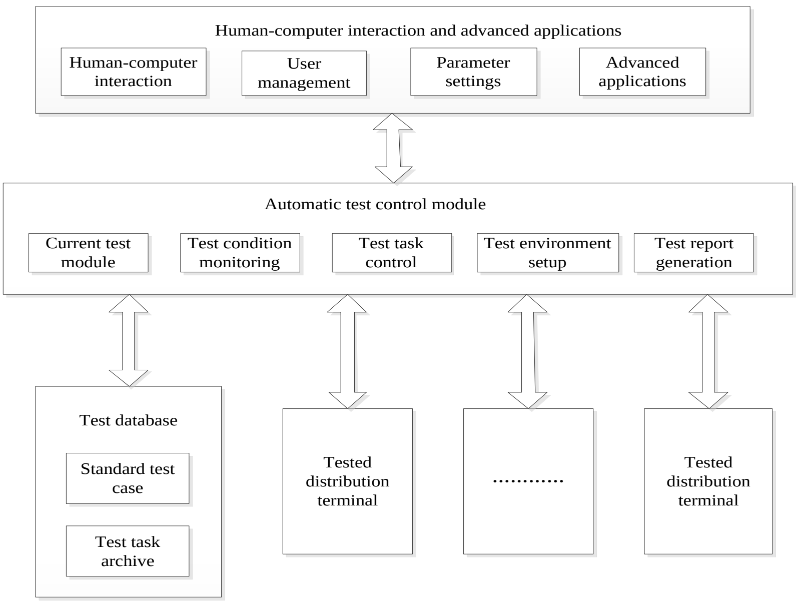

Figure 4. System software function block diagram.

The test case contains the required test sequence of the sequence of AC volume, the sequence of switches, and so on. It shows a particular test item, and the expected response of the distribution terminal under this condition. The software completes the test of the item by comparing the signal of the remote signal, telemetry, SOE and other signal outputted by the distribution terminal in response to the actual excitation condition with the expected response. For the actual operator, the test case is the most basic tool and means of the testing. Standard test cases and test tasks are stored in the database, so that standard test cases and modified test cases can be saved, and it can be transplanted.
In the human-computer interaction interface and the advanced application function module, the user management can set the specified test system user and perform the necessary authority management. The advanced functions include functions such as reading and setting parameters of the distribution terminal, reading of the recorded files, and reading and judging the two-dimensional code information.
The automatic test control module is the core control centre of the test system software, its function is including test environment construction, test task control, test status monitoring and test report generation. The test report takes the test results saved for each test item and outputs the test report according to the specific format requirements [8].
The principle and execution process of the test cases of different test items are similar, taking the terminal current and voltage acquisition accuracy test as an example: the test case sets the addition sequence of the AC standard source, and sets the amount of remote communication and the allowable error range that the terminal will send in the expected time. After the test is started, the software controls the AC standard source to output the current and voltage according to the time, amplitude and phase set by the sequence. At the same time, the software monitors and acquires the action of the telemetry information sent up by distribution terminal. The expected results are compared to make an automatic judgment. The test results and test procedures are stored in the database and displayed in the test report.

6. Practical application effect

The portable power distribution terminal detection system studied in this paper is suitable for on-site and small-scale maintenance. And it is suitable for large-scale testing in the laboratory environment. The system has the advantages of simple configuration and operation, which can reduce the requirements for actual operators. At the same time, the rigorous testing principle and testing process ensure the reliability of the test. The detection system has full automatic test function which could effectively improve the testing efficiency. It has great significance for the full inspection, sampling inspection, on-site maintenance and fault location of the distribution terminal, and has broad promotion space and application prospects.

7. References

[1] XIE Baojiang, ZHANG Junda, CHEN Xin, XU Cong.2019 *Design and Application of Automatic Verfication System for Dsitribution Terminal* (Low Voltage Apparatus) p 33-38
[2] Chen Bin.2019 *Research on Network Detection Technology of Intensifield Distribution Automation Terminals* (Electrical Automation) p 108-111,118
[3] Lu Renjun, Wang Li, Sun Xinghua.2018 *Hidden Fault Detection System for Automatic Telemetry Terminal in Distribution Network* (Computer Measurement & Control) p 34-38
[4] Bai Xuefeng, Liang Ying, Fan Wenbo, Guan Shilei, Han Shaigen, Li Baikui, Wang Pengxiang, Cao Jinyuan.2016 *Design of distribution terminal auto-test system* (Electrical Measurement & Instrumentation) p 191-198
[5] Han Xiaojun. 2014, Design and implementation of a test system for the smart substation auxiliary platform based on the IEC 104 telecontrol protocol (Electrical Measurement & Instrumentation) vol. 51
[6] Chen Qianyi, Li Kewen, Kuang Chengzhong, Ou Shifeng, Huang Kaiwen. 2018, An Automatic Testing Method for Voltage-time Type Distribution Terminal (GuangXi Electric Power) p 14-18

IOP Conf. Series: Earth and Environmental Science **431** (2020) 012008 doi:10.1088/1755-1315/431/1/012008

[7] Zhang Zhihua, Zhou Jie, Cai Yueming, Zhou Jun, Liu Runmiao, Zhou Liangjun. 2017, Distribution Automation Terminal Based on Modular Configuration Design (Automation of Electric Power Systems) p 106-110

[8] LIU Bo, LIANG Weichen, WANG Changrui, LIU Junna, LI Xuan, XIE Jingchi, XIAO Lin.2019 *Design of Closed-loop Automatic Test Platform for full-type Fault Indicator* (Electric Engineering) p 35-37

IOP Conf. Series: Earth and Environmental Science **431** (2020) 012009 doi:10.1088/1755-1315/431/1/012009

Optimizing the distribution of transmission line tower and foundation

ZHU He-yan[1], LIU Jing-bo[1], LI Yi-ran[2] and XU Ao-ran[3]

1 State Grid Liaoning Electric Power Company Limited Economic Research Institute, No.183-1 Wenxue Road , Shenhe District, Shenyang,110000, China
2 Audit Center of State Grid Liaoning Electric Power Co., Ltd, No. 18 Ningbo Road, Shenyang City, 110004, China
3 School of Electric Power, Shenyang Institute of Engineering, Shenyang 110136, China
E-mail: 51036214@qq.com

Abstract. In the mountainous transmission lines, in order to respond to the national and national grid requirements for environmental protection, the design institute needs to design the towers for the long and short legs and the foundation of the tower. To this end, the paper gives the design scheme of the long and short leg iron tower in Liaoning area, and analyzes the design conditions of the iron tower, the base surface measurement of the iron tower, the insulation coordination and the optimization design of the tower. The purpose of this paper is to find the mutual configuration of the long and short leg towers and the high and low foundations that can be used to optimize the transmission line in mountainous projects, and use finite element software to verify that the minimum amount of base materials is the same when the tower position is constant. The basic base surface has the least amount of shovel excavation, which can better protect the geographical environment of the area where the tower is located, and can also control the amount of basic materials to a certain extent and reduce the total investment of the project.

1. Introduction

In the general design of the national grid, the 06B1-B8 iron tower universal design chess block has been used in the design and application of the 66 kV transmission line tower. The data has been checked and 38 problems have been found. Among them, the tower type problem: the design condition table and the part of the foundation root opening bolt spacing in the structure diagram are different, the base foot bolt spacing in the tower front structure diagram is different from the tower iron foot board size, the tower type foot bolt There are 32 problems such as small specification value, unsatisfactory strength check, and the difference between the base foot bolt spacing and the size of the iron foot plate. The problem of the metal fittings: the ground hanging string, the use of the fittings is wrong, and it is impossible to install the construction. The size of the structure can not meet the installation requirements of the windshield insulator jumper string. The ground string is connected to the tower with the front and rear strings, and the series jump is not used. The ground line is not conducive to six problems such as diversion.

In the general design of the national network, 04GG1-GG5 steel pipe universal design module double-back overhead ground type is double lightning line hanging line and the universal design 06B tower universal design module double-back overhead ground type single lightning line hanging line Correspondingly, some of the 06GG steel pipe universal design modules can not be used in actual

work, and the general design of the tower weight selection plan is too large, no drawings and other specific indicators, the guidance is not strong. In addition, when the designer provides the design to the winning bidder according to the electrical layout and application conditions, the winning bidder often artificially increases the root diameter and wall thickness of the steel pipe, and intentionally increases the weight of the tower, resulting in the amount of foundation concrete. And the increase in the amount of reinforcement, resulting in an increase in the floor area of the tower, wasting steel and valuable land resources, resulting in a substantial increase in project cost.
The emergence of all-round long and short iron towers [1-2] is a great leap in the design of mountainous routes, which greatly reduces the amount of opening caused by the excessive opening of the roots and effectively reduces the height of the upper slope after the opening. The application of the long and short legs of the 500kV tower was earlier. It was applied from the 1980s. At that time, the application of the 220kV tower was short. After the design of the long and short leg tower of the State Grid in 2005, the long and short legs of the 220 kV tower were pushed to the factory application. The practice over the years has proved that the all-round long-legged iron tower has the superiority of the flat-legged iron tower in the construction and operation of the mountain environment, which is conducive to saving the cost of the engineering body. The average direct savings per base tower is 30,000 RMB ; Safe operation, reduced or no basic slope protection, greatly reduces the maintenance work and costs of the foundation slope protection; is conducive to environmental protection, conforms to the modern environmental protection concept, and maximizes the use of the natural structure of the mountain body, minimizing The destruction of mountains and vegetation.

2. Design and measurement conditions

2.1. Design conditions for transmission line towers
According to the meteorological parameters under various operating conditions, the requirements of the new technical specifications regarding the meteorological return period and the height of the wind speed sample from the ground are met. For the maximum ice-covered value, because the long and short-legged iron tower lines are in the mountainous area, the 66kV transmission line adopts JL/G1A-300/25 steel-cored aluminum stranded wire; the ground wire adopts two JLB20A-100 aluminum-clad steel stranded wires. The arrangement of the wires of the double-circuit tower is mainly divided into vertical arrangement and triangular arrangement. In the domestic double-circuit pole tower of the same pole, in addition to the large spanning tower, in order to reduce the tower height, the three-phase conductors are arranged in a triangle, and the general lines are mostly arranged in a vertical arrangement of three-phase wires. Vertically arranged lines, due to the small line corridor, clear circuit, simple structure, clear transmission force, convenient construction and maintenance, are widely used in China, and also accumulated rich operational experience; Fine, the triangular arrangement has a greater impact on the tower body, the economy is not high, and the line corridor is wider. Therefore, the engineering wires are arranged in a vertical arrangement.
The two-circuit pole tower wire vertically arranged tower type mainly has a drum type and an umbrella type. According to the regulations, the horizontal deviation between adjacent wires in the upper and lower layers of the ice-covered area is considered, and the tower adopts a drum type. The meteorological conditions used in the design are shown in **Table.1**.

2.2. Method for measuring the base surface of an iron tower
The basic base surface measurement of the iron tower is mainly to measure the terrain trend around the foundation in order to meet the requirements of the tower foundation for uplifting, that is, to indirectly consider the volume of the uplifting soil. The foundation pull stability is the ability to calculate the tower foundation against the uplift load. Two methods are used in engineering: shearing method and soil weight method. The shearing method is in line with the failure mechanism of the uplifting soil. It not only considers the self-weight of the soil and foundation, but also makes full use of the soil's own pullout resistance, but it is difficult to determine the physical and mechanical properties of the backfilled soil. The shearing method is only used for the original anti-soil body. The soil weight method is an empirical method that has been used for many years. It relies mainly on the

self-weight of the foundation and the soil above the foundation floor to resist the pull-up force. The principle is simple, the calculation is simple, and it has been widely used in the design. Therefore, before the configuration of the tower's long and short legs and high and low foundations, we must first accurately measure the tower base surface (relative elevation). At present, the major design institutes in China mainly use GPS to measure the basic surface of the transmission tower. It is characterized by high accuracy, high speed, automatic recording of all information (coordinates and elevations) of the sampling points, and automatic mapping by post-software, when the designer is positioned in the final survey.

Table.1 Design weather conditions list

Terms / Conditions	Air temperature T (℃)	Wind speed v (m/s)	Ice thickness b (mm)
Maximum temperature	40	0	0
Minimum temperature	-40	0	0
Icing	-5	10	0
Basic wind speed	-5	29	0
Installation condition	-15	10	0
Mean temperature	-5	0	0
Lightning Overvoltage	15	10	0
Operating Overvoltage	-5	15	0

3. Insulator coordination design

3.1 Insulator selection for transmission line towers

According to the investigation of the transmission line projects that have been put into operation, synthetic insulators, suspended glass insulators and stain-resistant ceramic insulators are the main types of insulators in 110 kV transmission lines. Therefore, the design of insulators [3-6] in this paper is based on composite insulators, suspended glass insulators and stain-proof porcelain insulators. The selection of insulator types is as follows: 1) conductor suspended insulator strings: composite insulators; 2) conductor jumper insulator strings: fixed wind-proof composite insulators; 3) conductor tension-proof insulators. String: Composite insulators are used in the feeding gear, and suspended glass insulators or stain-resistant ceramic insulators are used in the rest.

According to the requirements of relevant documents: the external insulation of transmission lines should be arranged according to the requirements of pollution grade, ordinary porcelain or glass insulators can be used in pollution areas of grade B and below, and anti-pollution insulators or composite insulators can be used when approaching the upper limit value; composite insulators or anti-pollution insulators with good self-cleaning property should be used in pollution areas of grade c; Composite insulators should be used in the area. If the use of ceramic or glass insulators does not meet the requirements, measures such as coating anti-pollution flashover coatings or composite insulators of porcelain and glass can be taken in the design and construction stages.

3.2 Determination of insulator technical parameters

The mechanical strength of double and multiple insulator strings should be checked after one connection is broken, and the load and safety factor should be considered according to the situation of disconnection. Insulators should also meet the normal operating conditions under perennial load condition, the safety factor is not less than 4.0. The safety factor of mechanical strength of insulators K_I shall be calculated according to the following formula:

$$K_I = \frac{T_R}{T} \tag{1}$$

In formula (1) ,T_R denotes the rated mechanical failure load of insulators, in terms of kN; T denotes the maximum service load, broken line, broken connection, checked load or perennial load that insulators bear, respectively, in terms of kN.

Perennial load refers to the load that insulators bear under the condition of annual average temperature. The checking load is the load that the insulator bears under the checking condition. The meteorological conditions of disconnection are windless, ice-free, -5oC、10 mm and below ice conduction. In order to ensure the safety of the suspension insulator, the maximum load of the suspension insulator should be calculated. In order to ensure the safety of the tension insulator, it is necessary to check the strength of the tension insulator string. The allowable load should be equal to or greater than the maximum suspension point tension of the conductor, and the tension of the suspension point of the conductor should be calculated by formula. The insulator creeping distance should be selected and the insulating level of the conductor should meet the requirement of leakage ratio distance [7-8].

The first fittings of V-type suspension string of steel tube towers are U-type hanging rings, and the first fittings of I-type, L-type and long I-type suspension string are UB-type hanging plates. UB hanging plate is the first fittings of the suspension string of steel tube towers.

The tension strings of steel tube towers are designed with single hanging point, with hanging plate as hanging point and U-shaped hanging ring as the first fittings. The ground tension strings of steel tubular towers are designed with single hanging point, hanging point is hanging plate, and the first fittings are U-shaped hanging rings. The jumper string adopts "I" type windproof bias fixed jumper string, and UB hanging plate is used to connect with steel pipe tower.

Compared with other types of electrical fittings, the pre-stranded fittings have the following characteristics: (1) outstanding fatigue resistance. Pre-stranded fittings have no bolts acting on the conductor to reduce the static compressive stress of the fittings on the conductor. At the same time, pre-stranded fittings have relatively long pre-formed spiral lines. Some pre-stranded fittings, such as suspension clamps, split conductor spacers, also have rubber pads, which can further reduce the static compressive stress of the fittings on the conductor. Or distribute it evenly in a larger area. In addition, the bending stiffness of the contact area between the wire and the fittings is enhanced and the dynamic bending stress caused by the breeze vibration in these areas is weakened after the pre-stranded fittings are wound on the wires. Under the same conditions, the static and dynamic stresses on the conductor are obviously reduced by using the pre-stranded metal fittings compared with the traditional bolt-compacted metal fittings, which improves the harsh stress environment in the contact area between the conductor and the metal fittings, and protects the conductor from destructive vibration and fatigue. Practice has proved that it has excellent fatigue resistance and prolongs the service life of the fittings; (2) It is easy to install and has strong consistency. The utility model has the advantages of simple and fast installation, no need for installation tools for bare-handed installation, light weight, convenient carrying and transportation. These improves the installation speed, reduces the labor intensity of workers, and improves labor efficiency. Generally, skilled workers only need a few minutes to install a pre-twisted metal tool. Because of the unarmed installation, visual inspection can check the installation quality and eliminate the installation inconsistency caused by the use of tools by the installation workers. These characteristics make it more economical; (3) high efficiency and energy saving; (4) strong adaptability. Pre-stranded metal fittings can be used not only in galvanized steel strand, aluminium-clad steel strand, copper-clad steel strand, aluminium strand, aluminium alloy strand, steel-cored aluminium strand and steel-cored aluminium alloy strand, but also in high temperature conductor, insulated conductor, all-dielectric self-supporting optical cable and ground composite optical cable. It can be applied to almost all overhead lines.

According to the above analysis, considering the pollution area of grade IV, the wire suspension insulator adopts 100kN FXBW-220/100 composite insulator, and the jumper adopts 70kN LXHP5-70 tempered glass insulator. A piece of LXAP1-70 tempered glass insulator is added to the suspension point of the conductor near the suspension point of the suspension string of suspension insulator and jumper insulator string. The tension resistance of conductor is 120 kN grade LXHP4-120 tempered glass insulator, and the intake gear is 100 kN grade FXBW-220/100 composite insulator.

4. Tower optimization design

4.1 Overview of the basic situation

It can be known from the "I" type string in China for many years of operation that this type of insulator string has a large swing angle, which is the main factor causing the width of the line corridor. According to the comparison and practical experience, for the 110kV line, the following comparison is made: 1) The cross-arm of the "V" string needs to be lengthened, the weight of the tower is increased, and the cost is increased; the width of the corridor is not reduced, and since the line is located in the middle of the road, The advantage of controlling the wind bias is not obvious; 2) The "L" string can reduce the length of the crossbar of the tower without changing the conventional tower type, but the lateral supporting insulator and the fitting are not standardized, and special customization is required; The support affects the strength of the tower body, the stability of the tower body becomes higher, the tower body needs to be strengthened, the cost increases; the width of the corridor is not much reduced, and the advantage of controlling the wind bias is not obvious because the line is located in the middle of the road. 3) Although the long "I" type insulator string can be used to control the wind deflection to reduce the length of the cross arm, it needs to be fixed by the cross arm on the upper and lower sides; if the lower phase conductor is used, the cross arm should be added, and the middle phase needs to consider the horizontal spacing of the upper and lower wires. The length of the cross arm of the long "I" type string is not much reduced compared with the length of the middle phase cross arm of the ordinary "I" type string, and affects the length of the cross arm of the lower phase conductor and Force, economic applicability is not good; and the insulator structure is more complicated, there is a requirement for the distance between the upper and lower wires, and it is not universal. Therefore, only the upper phase wire is partially applied in the following tower section, and a special tower type is designed, but has its limitations.

The vertical span has the maximum vertical span and the minimum vertical span. As the vertical span for determining the head gap is generally the minimum vertical span. The minimum vertical span is generally determined by the coefficient method. For different terrains, the coefficient selection is Different, the coefficient of the coefficient of the tower head is about 0.75 when drawn. The maximum vertical span selection is also related to the terrain, generally taking 1.2 to 1.3. The horizontal distance between the center line of the gear is mainly determined by the condition that the wire is not synchronized (or galloping) caused by the wind, so that the air gap should not be broken under normal working voltage. As for the operation overvoltage and the lightning overvoltage, since it has a small probability of simultaneous occurrence of a large wind and causing the wires to be asynchronously oscillated (or galloping), it is not a control condition for determining the horizontal distance between the center conductors of the gear pitch.

4.2 Finite element analysis of dynamic characteristics and stability of long and short leg iron towers

In the current engineering design calculations, the calculation of the displacement of the steel tube tower head adopts the industry standard, the empirical formula combined with the chart and various correction factors. The empirical formula generally has low calculation accuracy and poor theoretical theory. The finite element method [9-10] is a numerical calculation method for structural analysis, and it is the application and development of the matrix method in the fields of structural mechanics and elastic mechanics. The finite element method relies on mathematical tools such as matrices. Although the computational workload is large, the whole analysis is consistent and has strong regularity, so it is especially suitable for programming computer programs. This time, the long and short towers were analyzed by dynamic and static analysis using the finite element general program software Midas Gen to verify the correctness of the design and the accuracy of the design software.

The basic idea of the finite element method is to regard the complex structure as a whole connected by a finite number of elements only at the node. The elastic continuous structure to be studied is divided into finite units, which are connected to each other on a finite number of nodes. . Firstly, each unit is analyzed for its characteristics. Under certain precision requirements, each unit is described with a finite number of parameters to describe its mechanical characteristics, and the correlation between related physical quantities is established. Then, according to the association combines the various units into a whole, thus establishing a balance equation of the continuum, and applying the corresponding solution of the equation, the analysis of the whole problem can be completed.
Due to the structural characteristics of the tower, it is sensitive to wind vibration and earthquake. The vibration response of the tower structure is related to the dynamic characteristics of the structure itself and the lateral load, and the vibration mode and frequency affecting the dynamic characteristics of the structure. It is related to many factors such as the form of the iron tower, the nature of the material, the size of the section of the rod, the mass distribution, and the weight of the wire.
Firstly, the basic cost in the design of power transmission lines accounts for about 14 to 24% of the cost of the project. The ratio fluctuates greatly, which is related to the terrain, geological conditions and tower type of the line, indicating the basic selection.
The importance of the basic selection will directly affect the indicators of the cost of transmission line engineering. With the continuous development of economic construction, the auxiliary construction cost of transmission lines has an increasing impact on the overall cost of the project, mainly reflected in the awareness of the whole society on environmental protection and the awareness and requirements for sustainable development. Therefore, the basic selection and planning as well as the application of high and low foundations should not only consider safe and stable operation and economic benefits, but also consider social benefits. Choose a reasonable basic type and optimize the configuration to reduce the amount of excavation of the construction earth and reduce damage to the environment. Achieve a win-win goal of safety, environmental protection and economy.
Secondly, the mountain towers that are usually used are often set with high and low legs with a height difference of -1 or -1.5 depending on the length of the main material of the leg and the actual engineering needs (such as leg lengths of 0, -1, -2...-6, or -1.5, -3...-6, etc.). Then configure different high and low legs according to the actual terrain to meet the terrain needs. In addition, the use of high and low foundations as a way of coordinating the terrain, which relatively reduces the use of the tower's high and low legs, makes construction measurement convenient, but relatively increases the amount of concrete. The material of the tower is Q345 and Q235. Bolts are rated 4.8 and 6.8, and all components of the tower are hot-dip galvanized. In order to ensure the safe operation of the line, anti-theft bolts are used within 8m of the tower (from the ground), and other bolts are used [11-12].
In the design of the tower, the static internal force of the iron tower and the static force (basic force) of the tower to the foundation are usually used as the design basis. The basic force of the whole tower under various dangerous conditions, the distribution of the internal force of the rod and the deformation of the tower are obtained by software Midas Gen.
Due to the structural characteristics of the tower, it is sensitive to wind vibration and earthquake. The vibration response of the tower structure is related to the dynamic characteristics of the structure itself and the lateral load, and the vibration mode and frequency affecting the dynamic characteristics of the structure. It is related to many factors such as the form of the iron tower, the nature of the material, the size of the section of the rod, the mass distribution, and the weight of the wire.

5. Conclusions

The core content of this paper is the optimal configuration of the long and short legs and the high and low base of the transmission line tower. The main determinants are three. The first is the accurate measurement of the base surface of the tower; the second is to determine the variables that need to be optimized during the optimization configuration process, and to build a complete, detailed and accurate configuration calculation model that conforms to the actual engineering practices to achieve qualitative and quantitative analysis and optimization; The final screening of the configuration results is based on the actual engineering conditions. Through the research and analysis, summarization and summary of this paper, the optimal configuration of the long and short legs and the high and low foundations of the tower is proposed. The optimal configuration scheme is verified by the actual mountain line engineering. The dynamic characteristics and stability analysis of the long and short towers are carried out by using the finite element method simulation software.

6. References

[1] C. Rebelo, A. Moura, H. Gervásio, et al. Comparative life cycle assessment of tubular wind towers and foundations [J] *Engineering Structures*.2014,(02):40.
[2] Dongxue Hao, Rong Chen, Guangsen Fan. Ultimate Uplift Capacity of Transmission Tower Foundation in Undisturbed Excavated Soil[J] *Energy Procedia*.2012,(17):1209-1216.
[3] Jiang B, Zhang C F, Wang X Y, et al . Development of Electric Field Stress Control Devices for a 132 kV Insulating Cross-arm using Finite Element Analysis[J] *IEEE Transactions on Power Delivery*,2016,31 (5) : 2105-2113.
[4] Miller M F. Fiberglass distribution poles a case study[J]. *IEEE Transactions on Power Delivery*, 1995, 10(1): 497-503.
[5] Zhao Wei , Zhang Huazhao , Wu Yongcong , et al. Structural optimization design of lightning protection for 220 kV composite material tower [J]. *Engineering Journal of Wuhan* University,2015,48(2): 225-229.
[6] Shin J, Kim I, Biju K P, et al. TiO2-based metal-insulator-metal selection device for bipolar resistive random access memory cross-point application[J]. *Journal of Applied Physics*, 2011, 109(3):033715-4.
[7] Baker A C, Farzaneh M, Gorur R S, et al. Insulator Selection for AC Overhead Lines With Respect to Contamination[J]. *IEEE Transactions on Power Delivery*, 2009, 24(3):1633-1641.
[8] Liu M, Hwang H Y, Tao H, et al. Terahertz-field-induced insulator-to-metal transition in vanadium dioxide metamaterial.[J]. *Nature*, 2012, 487(7407):345.
[9] Dexter R J. The Finite Element Method: Linear Static and Dynamic Finite Element Analysis by Thomas J. R. Hughes[J]. *Religion*, 2003, 6(2):222.
[10] Geng J P, Tan K B, Liu G R. Application of finite element analysis in implant dentistry: a review of the literature.[J]. *Journal of Prosthetic Dentistry*, 2001, 85(6):585-598.
[11] Gao P, Luo Y, Wang X, et al. Research on Application of Angle Steel Q420 for Power Transmission Iron Tower in Cold Region[C]// *International Conference on Smart City & Systems Engineering*. 2017.
[12] Tang C, Hua Z. The Iron-Tower Manufacture Enterprise Oriented PDM System Design[C]// *International Forum on Information Technology & Applications*. 2009.

Acknowledgments

The authors gratefully acknowledge the support from the State Grid Liaoning Electric Power Company Limited Economic Research Institute Foundation of China through its grant no. SGLNJY00SJJS1700014.

Chapter 2:
Smart Grid Operations and Management

IOP Conf. Series: Earth and Environmental Science **431** (2020) 012010 doi:10.1088/1755-1315/431/1/012010

Energy management for isolated microgrid to mitigate "demand & abandon" phenomenon with two types of subsidy policies

Li Liming[1], Chen Weidong[1] and Shi Xueqi [2]

1 College of Management and Economics, Tianjin University, Tianjin, China
2 School of Electrical and Information Engineering, Tianjin University, Tianjin, China
E-mail: shixueqi@tju.edu.cn

Abstract. This paper presents a game model about the microgrids energy management problem and its implementation in the centralized energy management system for isolated microgrids. The model mainly provides power management strategies based on the problem that power is imbalance, and analyses the impact of two types of subsidy policies on "Demand & Abandon" in the operation of microgrid. By analysing the experiment results, we conclude that: 1) energy storage device improves the flexibility of power usage strategy; 2) the implement of infrastructure subsidy policies can solve "Demand & Abandon" in a better way while the electricity subsidy policies are invalid.

1. Introduction

The excessive emissions of CO2 have incurred worldwide environment and energy problems such as globe warming. To reduce the emissions of CO2 and conserve energy, many major countries are trying to develop new technologies to utilize environment friendly energies (e.g. solar energy) without emitting much pollution [1]. Microgrid (MG) is such a promising approach. In MG, new power generation techniques, such as wind turbines (WTs), photovoltaics (PVs), fuel cells (FCs) and microturbines (MTs), utilize renewable and clean energies to produce power; new energy storage systems (EES) and energy conversion devices can improve the comprehensive efficiency of energy utilization [2, 3]. Therefore, the study of MG has obtained attentions from some major countries and they have put forward a series of encouragement policies [4]. For example, in USA, 30% initial investment subsidies were designed for renewable energy projects; in China, the government mandated utility companies to purchase electricity generated by renewable energy [5].

Generally speaking, the subsidy policies on MG can be divided into two categories: electricity subsidy policy and infrastructure subsidy policy, in which electricity subsidy policies include feed-in-tariff, investment tax credits, renewable energy portfolio, financing facilitation, net metering and government mandates and regulatory provisions, and infrastructure subsidy policies includes investment tax credits, public investment and government mandates and regulatory provisions [6, 7]. These policies have attracted a lot of attentions from researchers and they made a lot of contributions in analysis of policy utility, analysis and optimization of policy model, comparison of different policies, and policy market review [8-10].

Most of previous works have studied the influences of policies for development of MG, however, the study about impact of different polices for the operation of MG has been largely ignored [11, 12]. This motivated us to study how to choose polices to solve operation problems of MG. Specifically, one of the most serious operation problems is "Demand & Abandon", which refers to the phenomenon that

distributed energy resources (DERs) will still abandon some of power when the power demands of users are unsatisfied [13]. “Demand & Abandon” is mainly resulted from the peak period discordance between DERs’ power generation and agents’ power usage. Besides, the distribution of power produced from environment-friendly energies within a day is uneven, which further aggravates the “Demand & Abandon”. These characteristics lead to the unbalance of power supply and usage, and thus MG is not efficiently utilized [14]. To this end, we discuss the impact of existing policies on reducing the peak periods discordance between DERs and users to mitigate the “Demand & Abandon” of MG by using an energy management system (EMS) with an energy storage device.
Generally, according to a series of literatures, EMS methods can be divided into centralized optimization (CEMS) and distributed optimization (DEMS) [15,16]. For the DEMS, it mainly focuses on methods which include game theory-based distributed optimization, distributed convex optimization, alternating direction method of multipliers. For the CEMS, based on one operator, the framework for the development of CEMS is studied, such as a CEMS for a MG composed of hydrogen storage and wind power with a dynamic linear programming (LP) formulation, and a CEMS for a PV-storage in MG with an LP solution technique together with heuristics. Meanwhile, different algorithms and models are designed to make the centralized approach the most suitable for application of optimization techniques, such as a three-phase unbalanced system with presence of both dispatchable and non-dispatchable distributed generation for testing EMS in an isolated MG [17,18].

2. Model

In this paper, the trading problem within the MG can be modelled as a Stackelberg game, where the EMS is the leader, and buyers and sellers (defined as follows) are the followers, to capture the interaction.

2.1. Model of MG

Generally, in MG, agents are composed of different loads, PVs and WTs, named users and DERs respectively. Before participating in an energy sharing zone, define daily power generation of agent i as:

$$E_i = [E_i^1, E_i^2, \cdots, E_i^{24}], i \in \{1, 2, \cdots, n\} \tag{1}$$

where n is the total number of agents in MG, and the operation time is grouped into 24 hours.
Define daily power consumption of agent I as

$$D_i = [D_i^1, D_i^2, \cdots, D_i^{24}], i \in \{1, 2, \cdots, n\} \tag{2}$$

Therefore, daily net power of agent i is shown as:

$$Q_i = \sum_{h=1}^{24} \left(E_i^h - D_i^h \right), i \in \{1, 2, \cdots, n\} \tag{3}$$

when Qi > 0, the power of agent i is surplus; when Qi < 0, the power of agent i is insufficient.
In a trade, we define agents as: $\mathbf{B} = \{i | Q_i < 0\}$ and $\mathbf{S} = \{i | Q_i < 0\}$. Obviously, $\mathbf{B}$ is the set of buyers, $\mathbf{S}$ is the set of sellers, and the role of agents is variable but confirmed at time.
The total demand in MG is

$$Q_D = \sum_{i \in B} Q_i \tag{4}$$

The total supply in MG is

$$Q_T = \sum_{i \in S} Q_i \tag{5}$$

where $Q_D \le Q_T$. Generally, Q_T is 8% higher than Q_D with high quality of power, but the characteristics, including fluctuation and intermittent, of DERs could increase the margin between Q_T and Q_D .

The fixed load set of user i in the special period is defined as:

$$FL_i \triangleq \left\{FL_i^1, FL_i^2, \cdots, FL_i^{24}\right\},\ i \in \{1, 2, \cdots, n\} \tag{6}$$

For the shiftable load, it means that users can choose the time to use the electrical appliances or equipment according to their preference. In this paper, each user is assumed to have dozens or hundreds of appliances or equipment with shiftable loads. Such appliances or equipment may include PHEVs, washers, dryers, dishwashers, etc. The shiftable load set of user i is defined as:

$$SL_i \triangleq \left\{SL_i^1, SL_i^2, \cdots, SL_i^{24}\right\},\ i \in \{1, 2, \cdots, n\} \tag{7}$$

where k is the number of appliances or equipment with shiftable loads for user i, and SL_{ik}^h, shiftable loads for user i in the specified period h is transferable power caused by k appliances or equipment. For example, user i often wash cloth at night and the washer consumes 0.225kW for working in 1h generally. In order to avoid the peak hours of power consumption, it would regulate the time to use washer. Therefore, 0.225kW is the shiftable load of washer for user i.

For EMS, we assume that there is only one storage devise in EES, and its charging (CE) and discharging (DCE) strategies are

$$\begin{aligned} CE &= \left\{CE^1, CE^2, \cdots, CE^{24}\right\}, \\ DCE &= \left\{DCE^1, DCE^2, \cdots, DCE^{24}\right\}, \end{aligned} \tag{8}$$

Meanwhile, exist

$$E(t+1) = E(t) + CE^h - DCE^h - \delta E \tag{9}$$

where E(t) is remaining capacity of energy storage devise at time t, CE^h is charging strategy in period h, DCE^h is discharging strategy in period h, E is the capacity of energy storage devise, and δE is self-discharging of EES.

Then we consider discharging strategy at time t as:

$$DCE^t = E(t) - \eta E \tag{10}$$

where ηE is the security capacity of energy storage devise with ηE .

2.2. Regulation strategy

$Q^h < 0$ means that the power generation could not satisfy the demand of agents in period h. In this case, agents are required to transfer shiftable loads which are approximately equal to the margin between power generation and the demand of agents, Q^h, from this period h.

$$min\left|\sum SL_{ik}^h + Q^h\right| \tag{11}$$

When all shiftable loads are transferred from this period h, the power generation is still far less ($\left|\sum SL_{ik}^h + Q^h\right| \le 0.5Q^h$) than the demand of agents in period h. There exists supplement from the energy storage device, hence, eq. (11) can be rewritten as:

$$min\left|\sum SL_{ik}^h + DCE^h + Q^h\right| \tag{12}$$

where $SL_{ik}^h \in SL_i^h$

$Q^h > 0$ means that the power generation is more than the demand of users in period h so that, after satisfying the self-power consumption first, agents would supply EES with surplus power. In this case, agents could transfer shiftable loads which are transferred from other periods into this period h. When there exists the surplus power, agents could supply to EES. The transfer-in loads is set of all transfer-out loads. However, the real transfer-in loads (TL_i^h) are selected by(12) and form into

$$\mathbf{TL} = \begin{bmatrix} TL_{i1}^1 & TL_{i1}^2 & \cdots & TL_{i1}^{24} \\ TL_{i2}^1 & TL_{i2}^2 & \cdots & TL_{i2}^{24} \\ \vdots & \vdots & \ddots & \vdots \\ TL_{in}^1 & TL_{in}^2 & \cdots & TL_{in}^{24} \end{bmatrix} \tag{13}$$

where if SL_{ik}^h is selected in the period h, $TL_{ik}^h = SL_{ik}^h$; if SL_{ik}^h is not selected in the period h $TL_{ik}^h == 0$. Then agents are required to transfer shiftable loads which are approximately equal to the margin between power generation and the demand of agents, Q^h, in this period h.

$$min\left| \sum_{TL_{ik}^h \in TL} TL_{ik}^h - Q^h \right| \tag{14}$$

when all shiftable loads are transferred in this period h, the power generation is still far more $\left|\sum TL_{ik}^h - Q^h\right| \geq 0.5Q^h$) than the demand of agents in period h. There exists supplement to the energy storage device, hence, (14) can be rewritten as:

$$min\left| \sum_{TL_{ik}^h \in TL} TL_{ik}^h + CE^h - Q^h \right| \tag{15}$$

2.3. Cost structure

In a trade, for sellers, the generation cost is:

$$COS_i = aPV_i^2 + bPV_i \tag{16}$$

where PV_i is the capacity of generation of DER_i.
Therefore, the profit generic function is:

$$\pi_p = \max \sum \left[P_2 Q_s - \left(aQ_s^2 + bQ_s \right) \right] \tag{17}$$

where power generation of DERs is not only traded in MG, but could use by themselves. For the cost caused by the part of power generation used by DERs themselves, we do not consider. After considering electricity subsidy, the profit generic function is:

$$\pi_p = \max \sum \left[\left(P_2 + \lambda_1 \right) Q_s - \left(aQ_s^2 + bQ_s \right) \right] \tag{18}$$

where λ_1 is unit electricity subsidy.

For EMS, its cost is divided into initial investment cost βE^2 and operation cost γCE, where βE^2 means that, with increasing capacity of energy storage device, the investment increases and marginal cost decreases.

$$COE = \beta E^2 + \gamma CE. \tag{19}$$

Therefore, the profit generic function is:

$$\pi_p = \max \sum_{t=1}^{24} \left[\left(P_1 - P_2 \right) Q_D - \beta E^2 - \gamma CE^t \right] \tag{20}$$

where P_1 is the unit price to buy power, and P_2 is the unit price to sell power.
After considering infrastructure subsidies, the profit generic function is:

$$\pi_p = \max\sum_{t=1}^{24}\left[\left(P_1 - P_2\right)Q_D - \beta E^2 - \gamma CE^t\right] + \lambda_2 E \tag{21}$$

where λ_2 is the unit infrastructure subsidy.

3. Implementation

In this section, we will build an optimal model based on the discussion above and give an optimal solution of the model.

3.1. Optimal solution

Now consider the case that the government provides electricity subsidies. Suppose that the unit price to sell power is P_2 which is a constant, and the unit electricity subsidy from the government is λ_2. Then the total profit for sellers in a trade can be formulated as following(18)
Proposition 1. For sellers in a trade, the optimal trading strategy:

$$Q_S^* = \left(P_2 + \lambda_1 - b\right)/2a \tag{22}$$

Then consider the case that the government provides infrastructure subsidies. Suppose that the unit price to by power is P_1 which is a constant, and the unit infrastructure subsidy from the government is λ_2. Then the total profit for EMS in a trade can express as(21)
In the isolated MG, there exists the power balance equation, which can be formulated as:

$$Q_S = CE + Q_D \tag{23}$$

where Q_S is power trading between DERs and EES, and $Q_S \le Q_D$.
Then the optimal operation strategy problem of EMS can be formulated as following:

$$\begin{cases} \max\sum_{t=1}^{24}\left[\left(P_1 - P_2\right)Q_D - \beta E^2 - \gamma CE^t\right] + \lambda_2 E \\ \text{subject to.} \\ Q_S = CE + Q_D \\ DCE^t = E\left(t\right) - \eta E \\ E\left(t+1\right) = E\left(t\right) + CE^h - DCE^h - \delta E \end{cases} \tag{24}$$

Proposition 2. Consider the optimal strategy model (12) for EES to keep stable operation of EMS:
the optimal discharging strategy is:

$$DCE^{t*} = E\left(h\right) - \eta\frac{24\gamma\left(\eta-\delta\right)+\lambda_2}{2\beta} \tag{25}$$

The optimal charging strategy is:

$$CE^{t*} = E\left(h+1\right) - \left(\eta-\delta\right)\frac{24\gamma\left(\eta-\delta\right)+\lambda_2}{2\beta} \tag{26}$$

The optimal capacity of the energy storage device is:

$$E^* = \frac{24\gamma\left(\eta-\delta\right)+\lambda_2}{2\beta} \tag{27}$$

The implementation process of the Stackelberg game model is a problem of linear programing. It is difficult to directly obtain the optimal solution with conventional mathematical methods. Therefore, an

IOP Conf. Series: Earth and Environmental Science **431** (2020) 012010 doi:10.1088/1755-1315/431/1/012010

algorithm will be adapted to solve this problem. The general implementation process of the model executed by users is shown in Figure 1.

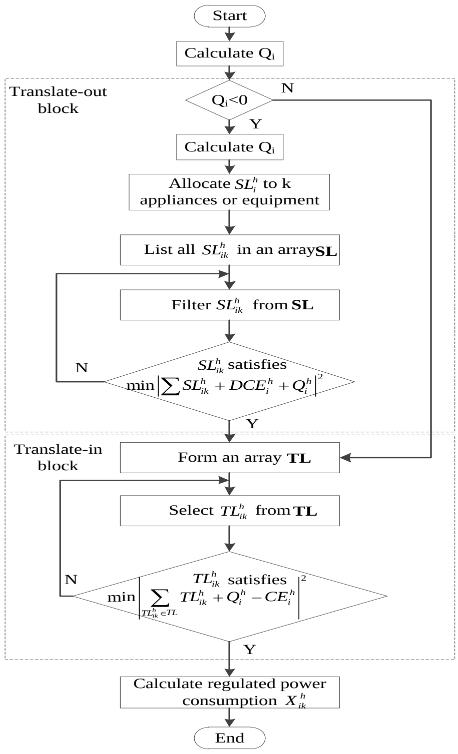

Figure 1. The flow chart of Algorithm.

4. Case study

4.1. Basic data

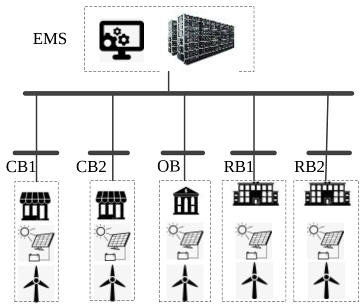

Figure 2. Study case network of the insolated microgrid.

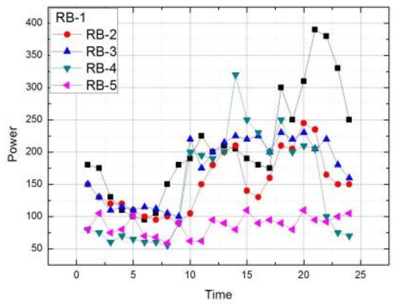

Figure 3. Load curves of the typical day.

Actual data of a demonstration project of China Midland Grid, Zhumadian Wenquan power station, is used for the case study. In the system, there are Residential Buildings (RB), Commercial Buildings (CB) and Office Building (OB), as shown in Figure 2. All of the buildings have installed PVs with capacity ranging from 100 to 300 kW, and WTs with capacity ranging from 200 to 300 kW. The output curves of PV and microturbine of a typical day are shown in Figure 3. The daily consumption curves of these agents are shown in Figure 4.

Agents have different load characters and power outputs. These mainly lie in the following two aspects: (1) the numbers and the times of peaks of power generation and consumption are not same. For example, as shown in Figure 5, the peak of power consumption is at approximate 20:00, and there is a large quantity of power generated by agents around 13:00. (2) the numbers of power generation and consumption in the rest periods do not match. For example, in the period from 0:00 to 5:00, the power consumption exists while the power generation of this period is 0.

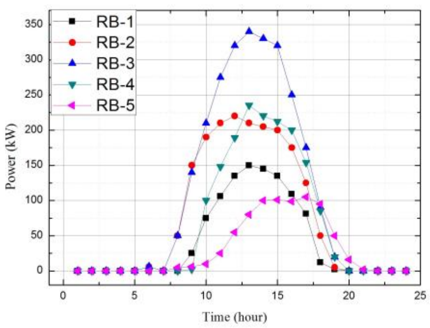

Figure 4. Power curves of the typical day.

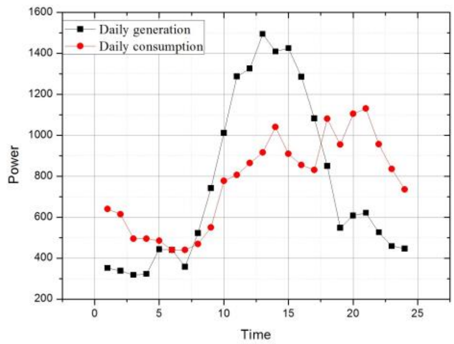

Figure 5. Total power consumption and generation curves of the typical day.

4.2. Power regulation strategy

In this section, we will show how to regulate shiftable loads between agents and EMS by using the model and algorithm. According to Figure 3 and Figure 4, total net power of each period (Q^h) could be formulated by EMS

Then EMS could judge the condition of each period to regulate power. When $Q^h > 0$, shiftable loads could be transferred in this period, and when $Q^h < 0$, shiftable loads should be transferred from this period. For example, the shiftable load should be transferred from the periods 0:00-7:00 and 18:00-24:00 respectively, and the shiftable load could be transferred in the period 8:00-17:00.

In the periods 0:00-7:00 and 18:00-24:00, EMS requires to transfer a certain shiftable loads out, and agents could fulfill this requirement as possible according to their actual situation. Previous studies show that shiftable loads account for 35%–55% of the total loads. In this section, we assume that shiftable loads account for 55% of the total loads and shiftable loads of each agent are allocated to 5 appliances or equipment randomly. Then, for all agents, their shiftable loads are allocated to 5 appliances reasonably. Then agents provide information about shiftable loads to EMS. By using the algorithm, the EMS could obtain the optimal power regulation strategy and the power charging and discharging strategy.

4.3. Results of power regulation strategy with different shiftable loads rates

Considering electricity subsidy policies, EMS adopts the optimal power regulation strategy to transfer power from the periods 0:00-7:00 and 18:00-24:00 respectively to the period 8:00-17:00. Then the power consumption can be changed as shown in Figure 6.

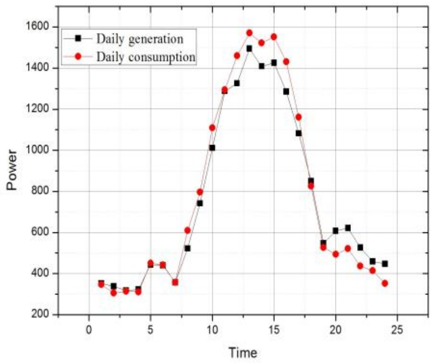

Figure 6. Regulated total power consumption and generation curves of a day (45% shiftable loads).

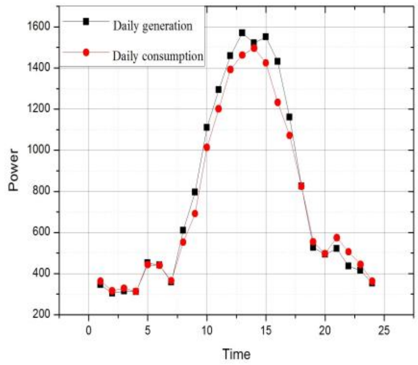

Figure 7. Regulated total power consumption and generation curves of a day (55% shiftable loads).

Figure 6 show that daily generation curve will better fit daily consumption curve after adopting the optimal regulation strategy than before (simply adopting electricity subsidy policies), which means that the discordance between the power consumption composed of shiftable loads and net power and power generated by WTs and PVs decreases, and the effect of fluctuation and intermittent of distributed generation on agents' demand decreases as well. However, there still exists a gap between regulated total power generation and consumption. This means that power curtailment condition exists in the period 5:00-17:00 while the power demand could not be satisfied in the period 0:00-4:00 and 18:00-24:00. Therefore, there still exists “Demand & Abandon”.

5. Conclusion

In this paper, we study the problem of the operation in isolated MG. Our proposed methods address following major challenges: (1) the management strategy of EMS with energy storage device and without energy storage device respectively, (2) how to solve the operation problem (“Demand & Abandon”) in MG with different subsidy policies.

To cope with these challenges, we propose a game model about the MG's energy management problem with a CEMS in isolated MGs. The model shows that, without energy storage device, agents could not effectively relieve power curtailment condition by regulating shiftable loads to reduce the discordance between their generation and consumption.

However, after this regulation, “Demand & Abandon” cannot be solved. When the percentage of shiftable loads increases to 55%, the power demand can be satisfied but power curtailment still exists, as shown in Figure 7. This means that “Demand & Abandon” can be better improved. But, for general agents, the shiftable loads which account for 55% of total loads are difficult to achieve, because agents are forced to shift loads and freedom of power usage is limited, after which use of comfort would be affected or damaged.

With energy storage device, our model shows that, with 45% shiftable loads, “Demand & Abandon” can be solved, because the surplus power could be charged into energy storage device to solve power curtailment condition, and power in energy storage device could be discharged to satisfy agents' demand when the generation is not enough. Meanwhile, the regulation strategy of power is more flexible for agents.

6. References

[1] Arcos-Aviles D, Pascual J, Marroyo L, et al. *Fuzzy Logic-Based Energy Management System Design for Residential Grid-Connected Microgrids*[J]. Ieee Transactions on Smart Grid, 2018, 9(2): 530-543.

IOP Conf. Series: Earth and Environmental Science **431** (2020) 012010 doi:10.1088/1755-1315/431/1/012010

[2] Cintuglu M H, Martin H, Mohammed O A. *Real-Time Implementation of Multiagent-Based Game Theory Reverse Auction Model for Microgrid Market Operation*[J]. Ieee Transactions on Smart Grid, 2015, 6(2): 1064-1072.

[3] Du Y, Wang Z, Liu G, et al. *A cooperative game approach for coordinating multi-microgrid operation within distribution systems*[J]. Applied Energy, 2018, 222: 383-395.

[4] Jin M, Feng W, Marnay C, et al. *Microgrid to enable optimal distributed energy retail and end-user demand response*[J]. Applied Energy, 2018, 210: 1321-1335.

[5] Khan M R B, Jidin R, Pasupuleti J. *Multi-agent based distributed control architecture for microgrid energy management and optimization*[J]. Energy Conversion and Management, 2016, 112: 288-307.

[6] Marzband M, Azarinejadian F, Savaghebi M, et al. *Smart transactive energy framework in grid-connected multiple home microgrids under independent and coalition operations*[J]. Renewable Energy, 2018, 126: 95-106.

[7] Ma L, Liu N, Zhang J, et al. *Energy Management for Joint Operation of CHP and PV Prosumers Inside a Grid-Connected Microgrid: A Game Theoretic Approach*[J]. Ieee Transactions on Industrial Informatics, 2016, 12(5): 1930-1942.

[8] Marzband M, Javadi M, Pourmousavi S A, et al. *An advanced retail electricity market for active distribution systems and home microgrid interoperability based on game theory*[J]. Electric Power Systems Research, 2018, 157: 187-199.

[9] Nemati M, Braun M, Tenbohlen S. *Optimization of unit commitment and economic dispatch in microgrids based on genetic algorithm and mixed integer linear programming*[J]. Applied Energy, 2018, 210: 944-963.

[10] Noor S, Yang W, Guo M, et al. *Energy Demand Side Management within micro-grid networks enhanced by blockchain*[J]. Applied Energy, 2018, 228: 1385-1398.

[11] Olivares D E, Canizares C A, Kazerani M. *A Centralized Energy Management System for Isolated Microgrids*[J]. Ieee Transactions on Smart Grid, 2014, 5(4): 1864-1875.

[12] Saad W, Han Z, Poor H V, et al. *Game-Theoretic Methods for the Smart Grid*[J]. Ieee Signal Processing Magazine, 2012, 29(5): 86-105.

[13] Taha A F, Hachem N A, Panchal J H. *A Quasi-Feed-In-Tariff policy formulation in micro-grids: A bi-level multi-period approach*[J]. Energy Policy, 2014, 71: 63-75.

[14] Wustenhagen R, Menichetti E. *Strategic choices for renewable energy investment: Conceptual framework and opportunities for further research*[J]. Energy Policy, 2012, 40: 1-10.

[15] Zeng Z, Yang H, Tang S, et al. *Objective-Oriented Power Quality Compensation of Multifunctional Grid-Tied Inverters and Its Application in Microgrids*[J]. Ieee Transactions on Power Electronics, 2015, 30(3): 1255-1265.

[16] Zeng Z, Zhao R, Yang H, et al. *Policies and demonstrations of micro-grids in China: A review*[J]. Renewable & Sustainable Energy Reviews, 2014, 29: 701-718.

[17] Zhang C, Wu J, Zhou Y, et al. *Peer-to-Peer energy trading in a Microgrid*[J]. Applied Energy, 2018, 220: 1-12.

[18] Zhao Z Y, Zuo J A, Fan L L, et al. *Impacts of renewable energy regulations on the structure of power generation in China - A critical analysis*[J]. Renewable Energy, 2011, 36(1): 24-30.

Acknowledgments
This work was supported in part by National Natural Science Foundation of China under Grant. 71373173, National Social Foundation of China under Grant. 12&ZD208, Doctoral Foundation of Ministry of Education under Grant. 20130032110072.

IOP Conf. Series: Earth and Environmental Science **431** (2020) 012011 doi:10.1088/1755-1315/431/1/012011

Stability analysis of DC microgrid considering the action characteristics of relay protection

Lu HUANG[1], Qun YU[1]

1 College of Electrical Engineer and Automation, Shandong University of Science and Technology, Qingdao266590, Shandong Province, China.
Email: hl930713@163.com

Abstract. The stability of microgrid is the key issue of microgrid operation control. This paper focuses on the transient stability after the correct operation of relay protection. In this paper, 400V DC microgrid with photovoltaic and energy storage system is taken as the research object. Research on the fault characteristics of voltage and current after the system is subjected to short-circuit, it is proposed to introduce current differential protection. With bus voltage as the only indicator, whether the transient stability is improved after the protection system operates correctly. The DC microgrid is modeled and simulated based on MATLAB/Simulink to confirm the validity of the proposed statement. The simulation results show that the fault can be correctly located, accurately isolated and timely removed by the protection system after the short-circuit fault occurs, bus voltage is restored to maintain stable operation of the system.

1. Introduction

With the international energy crisis and the increasingly intensified environment, DG (Distribution Generation) based on renewable energy, can greatly alleviate the pressure of environment and energy, which has attracted attention at home and abroad, and has made rapid progress. However, due to the randomness and uncontrollability of distributed generation, microgrid technology has emerged. It is a small power generation, distribution and utilization system which is composed of distributed generation, energy storage system, energy conversion device, monitoring and protection device, load and so on [1]. It can be divided into DC microgrid, AC microgrid and AC/DC hybrid microgrid. The existing research mainly focuses on the AC microgrids. In the current era, DC loads such as electric vehicles and information equipment in urban distribution networks are increasing rapidly. Compared with the AC microgrid, the DC microgrid has the characteristics of high conversion efficiency, small line loss. Therefore, as a way of networking with higher operation efficiency, lower comprehensive cost and less space, DC microgrid has been paid more and more attention.

Since there is no reactive power flow in the DC microgrid, the DC bus voltage is the only indicator to measure the safe and stable operation of the DC microgrid [2]. By controlling the voltage stability in the DC microgrid, the stable operation of microgrid can be controlled. If the dc bus voltage is unstable, the steady operation of load will be threatened, even lead to the false tripping of protection system, and even affect the normal operation of power network in serious cases [3]. The stability of DC microgrid includes static stability and transient stability. In recent years, the static stability problem of microgrid has been extensively studied [4]. However, in contrast with static stability of the microgrid, the research on transient stability of the microgrid is still limited. Static stability analysis methods include eigenvalue analysis based on state space equation and impedance analysis based on impedance model. In [5], based on the stability problem of DC microgrid, the average model of various converter and their control systems in DC microgrid is established by state space method, which is linearized at the equilibrium point, and static stability analysis of the DC microgrid is performed on this basis. By establishing small signal model, the stability of DC microgrid is analysed using Middlebrook impedance ratio criterion [6] in [7]. Transient stability analysis methods are mainly divided into the time domain simulation and Lyapunov direct method. Based on the Popov absolute stability criterion [8-9], the dissipative system theory [10] and other methods based on Lyapunov energy function, it has been studied in the transient stability analysis of microgrid.

At present, there is no research on whether the correct action of the protection strategy can improve the transient stability of the microgrid when internal faults occur in the system. In this paper, the DC microgrid is taken as the research object. The DC microgrid shown in figure 1 is built in MATLAB/Simulink to analyse the fault characteristics of the system when a short- circuit fault occurs. When the protection is correct, the influence of the system transient stability is analysed, and the correctness of the conclusion is verified by MATLAB/Simulink simulation.

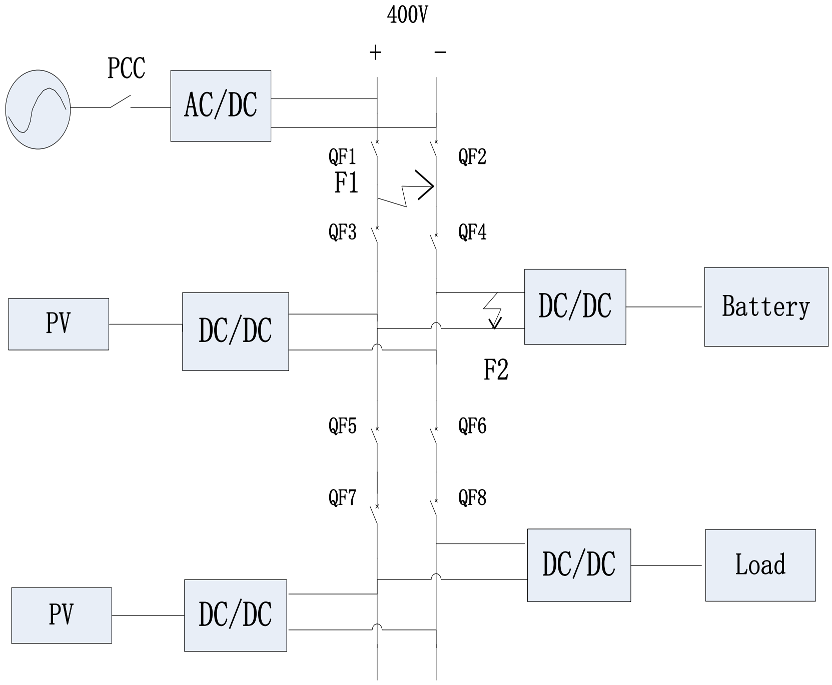

Figure 1. DC microgrid with PV and battery

2. Characteristics of short-circuit fault

2.1 Fault types of DC microgrid

According to the faults location, the faults of the DC microgrid can be divided into two types: bus faults and feeder faults; according to the type, it is divided into pole to pole faults(mainly short -circuit) and single pole to ground faults, among them, the bus pole to pole faults are the most harmful. Therefore, the busbar protection should be the highest level of the protection scheme [11]. In the event of a feeder fault, it is only necessary to disconnect the faulty line from the microgrid. This paper mainly studies the case of pole to pole short-circuit faults.

2.2 Pole to pole faults characteristics analysis

2.2.1 Bus faults. As shown in figure 1, photovoltaic is used as the main distributed generation, which is connected to the bus through DC/DC line. There are two types of bus fault F1 and feeder fault F2. Fault F1 will affect all sources and loads connected to the bus. Since the sources are connected in parallel, they can be treated separately. Taking the energy storage system as an example, the battery can be connected to the DC bus through a cable. When a bus bipolar short-circuit fault occurs, the equivalent fault diagram is shown in figure 2:

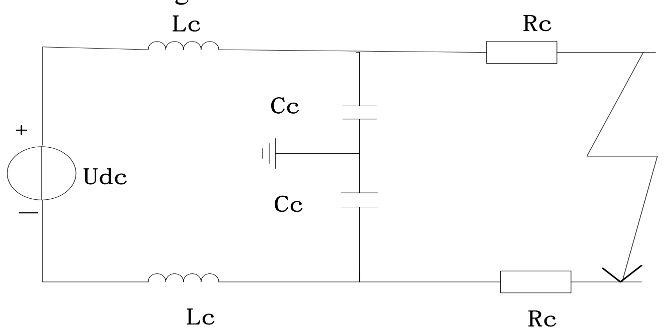

Figure 2. Equivalent circuit for bus fault

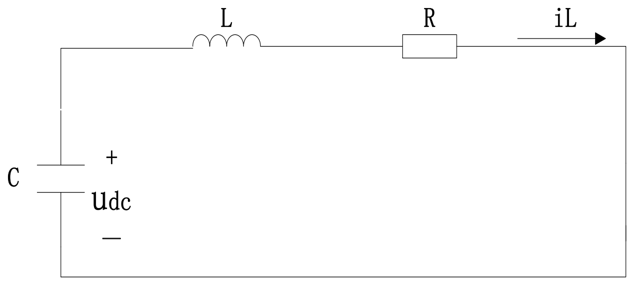

Figure 3. Equivalent circuit RLC second-order

Part of the fault current is provided by the battery u_{batt}, and part of it comes from the rapid discharge of the capacitor. The total impedance of the energy storage system is the sum of the internal battery impedance (R_{batt} and L_{batt}) and the cable impedance (R_L and L_L) (the cable capacitance can be ignored during pole to pole short-circuit fault) [12], so the fault current provided by the battery can be calculated as:

$$i_{batt}(t) = \frac{u_{batt}}{R_{batt}+R_L}[1 - \exp(-\frac{t}{\tau_{batt}})] \tag{1}$$

Where $\tau_{batt} = \frac{L_{batt}+L_L}{R_{batt}+R_L}$, the design of the battery determines how long it can supply a short-circuit current without causing internal damage [13]. The DC/DC converter is directly connected to the bus and, hence, has a low impedance, mainly consisting of the series impedance of the capacitors $R_c$and L_c, where the latter can be neglected.Fault F1 will cause the capacitors to discharge, which results in a current with high amplitude and low rise time, but with limited duration. The capacitor fault current can be calculated as:

$$i_c(t) = \frac{u_{dc}}{R_{eq}}\exp(-\frac{t}{\tau_c}) \tag{2}$$

Where $R_{eq} = 2R_c$,$C_{eq} = 2C_c$,$\tau_c = R_{eq}C_{eq}$,$u_{dc}$is the DC bus voltage. When the bus has a bipolar short-circuit fault, the fault current $i_f(t)$comes from the above two parts:

$$i_f(t) = K_A i_{batt}(t) + i_c(t) \tag{3}$$

Because of the current limiting effect of the circuit control module in the energy storage system, the current limiting coefficient K_A[14] is introduced. $K_A$depends on the voltage level of the DC microgrid and the equivalent resistance of the fault feeder, with a value of 0.01 ~ 0.02. Therefore, the short-circuit current provided by the battery can be ignored. So $i_f(t)$ can be calculated as:

$$i_f(t) \approx i_c(t) = \frac{u_{dc}}{R_{eq}}\exp\left(-\frac{t}{\tau_c}\right) \tag{4}$$

2.2.2 Feeder faults. When a bipolar short-circuit fault occurs on the DC microgrid feeder, the fault F2 and distributed generation form a new low impedance circuit. Taking AC/DC converter in

grid-connected power supply for example, the system will go through three stages in a short time after the fault occurs.
The first stage is the capacitor discharge phase, at which time the system is equivalent to an RLC second-order circuit, the equivalent circuit diagram is shown in figure 3.The converter is blocked at the moment of short-circuit fault, the DC capacitor is discharged to the fault point quickly, the fault current rises rapidly, and the fault voltage drops to 0 quickly. The discharge current of the DC capacitor is much larger than the AC side of the large power network, so the AC current is ignored at this time. Available from Kirchhoff's law：

$$\begin{cases} u_c = L\frac{i_L}{dt} + Ri_L \\ \frac{du_{dc}}{dt} = -\frac{1}{C}i_L \end{cases} \tag{5}$$

Finishing is available:

$$\mathrm{LC}\frac{d^2u_{dc}}{dt^2} + RC\frac{du_{dc}}{dt} + u_{dc} = 0 \tag{6}$$

Where u_{dc} is the DC capacitor voltage, considering that the short-circuit in the system is mostly metallic short-circuit fault and the transition resistance is small. So the capacitor discharge process is an underdamped oscillation process, that is, $\mathrm{R} < \sqrt{\frac{L}{C}}$. It is assumed that the pole to pole short-circuit fault occurs at the time of t_0, the initial condition is $u_{dc}(t_0) = U_0$,$i_L(t_0) = I_0$. Because the circuit oscillates and discharges, the second-order RLC circuit will have an oscillating fault current with the following values:

$$i_L(t) = \frac{U_0}{\omega L}e^{-\delta t}\sin(\omega t) \tag{7}$$

The second stage is the diode freewheeling phase. When the DC capacitor voltage is reduced to 0, the inductor is discharged, and the fault current continuously flows through the inverse parallel diode, the circuit is equivalent to the first-order circuit.
The third stage is the uncontrolled rectification phase. Due to the conduction of the freewheeling diode, the fault current exhibits an uncontrolled rectification characteristic, so that the short-circuit current cannot be naturally attenuated.

3. Protection system design

The traditional protection methods mainly include: three-stage overcurrent protection, distance protection and differential protection. Due to the small capacity of the DC microgrid and the short transmission line, the three-stage overcurrent protection is based on overcurrent protection, however, in instantaneous overcurrent protection, the short line below 25km may have no protection range. Therefore, the choice of three-stage overcurrent protection does not meet the selectivity and fastness of protection; distributed generation in microgrid will increase the uncertainty of internal power flow in microgrid due to its uncertain output. Therefore, the use of directional components may lead to protection false or failure to trip. Based on the above aspects and fault characteristics, the current differential protection is selected as the main protection of the DC microgrid. Its selectivity is guaranteed according to Kirchhoff's current law, that is, the sum of the currents leading to the fault point is equal to zero. It is suitable for DC microgrid with small capacity and short line.
The principle of line current differential protection of DC microgrid system is as follows: the direction from the bus to the protected line is positive. When the system is running normally or an external fault occurs, the current input to the DC bus is equal to the output current, and the differential current is equal to zero; when a DC bus internal short-circuit fault occurs, the input current and the output current are not equal, and can reach tens or even dozens of the setting value of the differential protection. The magnitude of the input current and the output current are detected, the absolute value of the sum is compared with the protection setting current. If it is greater than the current setting value, it can be determined that an internal short-circuit fault occurs, and the protection at both ends sends the permission signal to the opposite. So that the protection device is tripped and the fault line is cut off.
Define the differential current I_{diff} as:

$$I_{diff} = -\sum_{i=1}^{n} I_i \tag{8}$$

IOP Conf. Series: Earth and Environmental Science **431** (2020) 012011 doi:10.1088/1755-1315/431/1/012011

Where $n$is the number of lines connected to the bus, and I_i is the current flowing through the article iline.
The current differential protection criterion is:

$$I_{diff} = |-\sum_{i=1}^{n} I_i| > I_{set} \tag{9}$$

The setting principle is to avoid the sum of the absolute values of the maximum measurement errors of the measuring components in normal and external faults.
As mentioned above, current differential protection is a fast protection principle with absolute selectivity, and the short-circuit current of the bus short-circuit fault is generally much larger than the differential current setting value, so the sensitivity is higher.
Another characteristic of the short-circuit fault is that the bus voltage is reduced, and under-voltage protection can be used. However, since the voltage drops sharply of short-circuit, even drops to 0, if the under-voltage protection is used as the main protection, there may be an action dead zone. So under voltage protection can be used as backup protection. When the current differential protection is failure to trip, the under voltage protection can be operated to ensure the damage of the peak current to the power electronic components.

4. Stability and simulation analysis

4.1 DC bus voltage stability

It is unlikely to traditional AC systems, traditional AC power is mainly generated by synchronous generators, and its stability is a problem in which synchronized synchronous generators are kept in sync. For DC systems, the power balance of the system is guaranteed, and the DC microgrid is kept stable. So the voltage becomes the only indicator reflecting the power balance of the system. The voltage stability of a DC microgrid can be defined as the ability to maintain the DC bus voltage within a certain range (voltage fluctuations do not exceed ±5% of the rated value) when the system is disturbed [15]. When the DC microgrid is suffered to large disturbances, if the DC microgrid is oscillated to transition to a new steady state operation, the microgrid system is considered to be transiently stable; if the difference between the DC bus voltage and the original rated value or the steady-state value increases and diverges, the microgrid system is considered to be transient unstable.
In this paper, the fault characteristics of the voltage and current when the system is subjected to the bipolar short-circuit faults are analysed. After the current differential protection, if the protection is correctly operated, the voltage is restored to a stable state. Then it can be considered that the addition of the protection system can restore the unstable DC microgrid to a stable state, and the indicator of restoring stability is that the bus voltage is restored to its original value after being disturbed.

4.2 Analysis of bipolar short-circuit faults in different positions

It is constructed the simulation model of DC microgrid with photovoltaic and battery that based on the MATLAB/Simulink simulation software as shown in figure1. Where the line resistance is 0.1Ω/km, the line capacitance is 0.2mH/km, the line inductance is 0.23μF/km, the filter capacitance is 30mF, the bus voltage is 400V and the bus length is 0.6km.
The following simulation is made for the pole to pole short-circuit fault of bus and feeder. The simulation time is 3s, and figure4 is the bus voltage and current in normal operation.

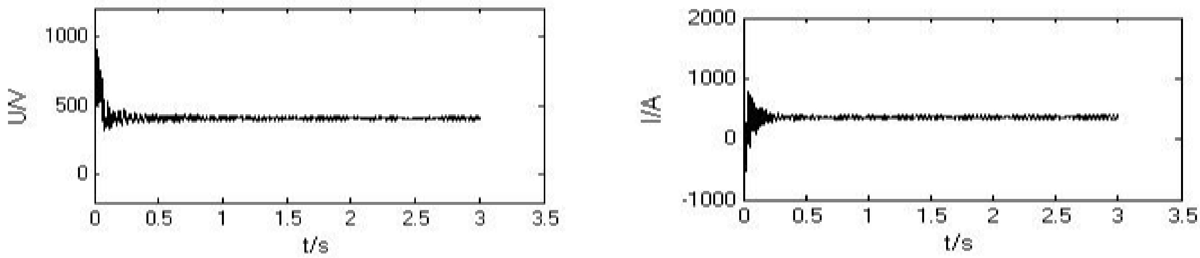

(a) Bus voltage during normal operation (b)Current during normal operation

Figure 4. Bus voltage and current during normal operation

IOP Conf. Series: Earth and Environmental Science **431** (2020) 012011 doi:10.1088/1755-1315/431/1/012011

The bipolar short-circuit fault is set when the simulation time is 1s, and the bus and feeder voltage and current are as shown in the following figure 5:

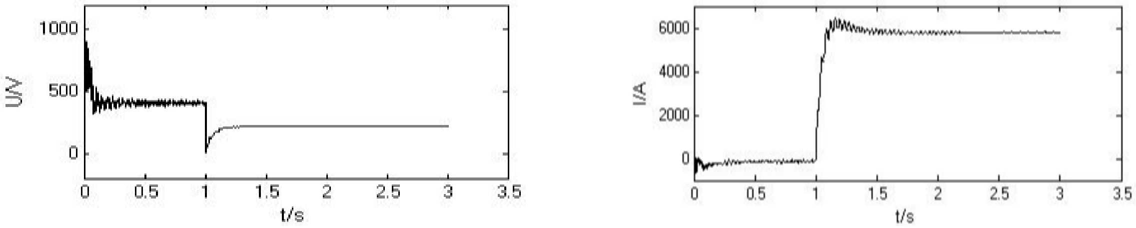

(a) Bus voltage during bus fault (b) Current during bus fault

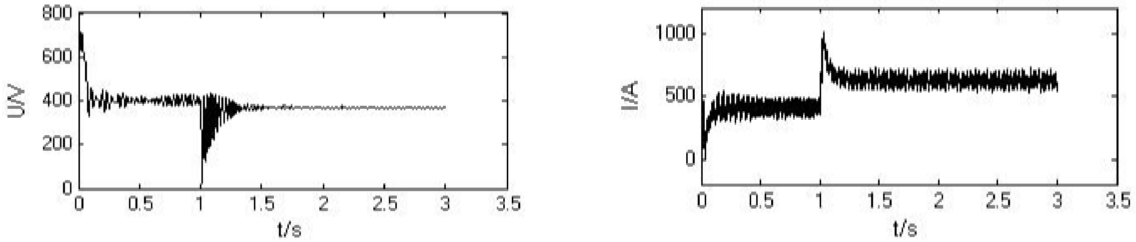

(c) Voltage during feeder fault (d) Current during feeder fault

Figure 5. Voltage and current during bus and feeder faults

It can be seen from the above waveform diagram that the amount of change in the fault voltage and current is different when the fault is at different positions, and the change of voltage and current is greater when the bus fault. When the fault occurs on the bus, the bus fault voltage drops rapidly to 0, and then stabilizes at 200V, the current rises sharply, reaching tens or even dozens of times before the fault; the feeder fault will be recovered after 0.5s, and the fault current is several times the current before the fault. It can be seen that the bipolar short-circuit occurring on the bus has a greater influence on the system, which verifies that the protection of the bus mentioned above is the highest level of the protection scheme.

4.3 System operating characteristics when adding current differential protection

Figure 6 shows the current at both ends of the DC line before and after the external fault and the internal fault. It can be seen from the figure that before and after the external fault, the current values at both ends of the line are equivalent reversed, which satisfies the above-mentioned: In the specified positive direction, when the DC line has an external fault, the differential current is 0. When the internal fault occurs, the current is in the same direction in the specified positive direction.

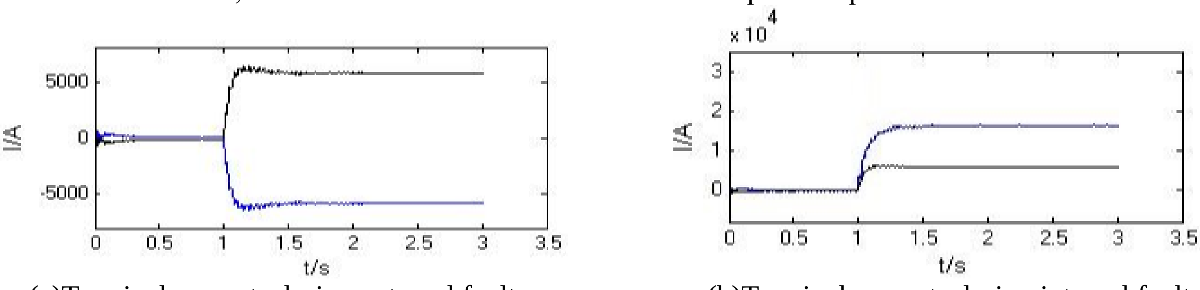

(a)Terminal currents during external fault (b)Terminal currents during internal fault

Figure 6. currents across the line during short-circuit fault

Figure 7 shows the differential current internal fault. The differential current setting I_{set} in the protection control module can be set to 1200A. It can be seen from the simulation diagram that the differential current can reach the set value when the fault occurs for 6ms. The DC breaker in the simulation has a 2ms error in the action delay. Therefore, after 8ms of the fault occurs, the circuit breakers at both ends act and the fault circuit is cut off.

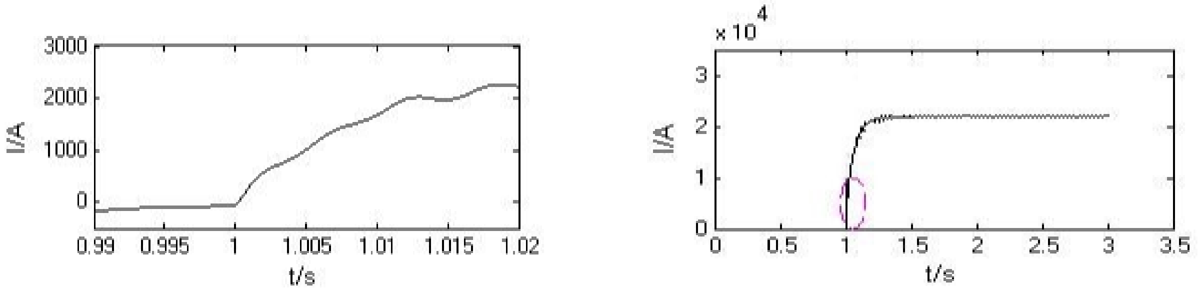

Figure 7. Differential current during internal short-circuit fault

Figure 8 shows that after the protection system is operating correctly, the circuit breaker cuts off the line at 8ms. Compared with the waveform diagram of the short-circuit fault voltage of the bus in figure 5(a), it can be seen that the low voltage phenomenon disappears, and the bus voltage is restored to the original 400V after a period of fluctuation. It meets the requirements of voltage stability and ensures the stable operation of the system. The correctness of the conclusion is verified.

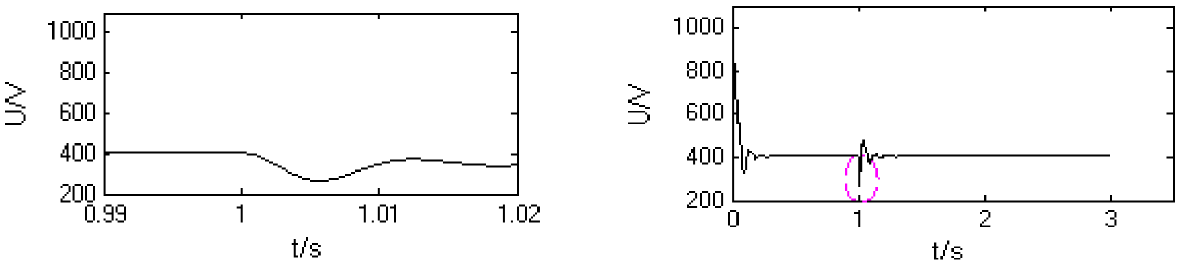

Figure 8. Bus voltage with protection

5. Conclusion

In this paper, research on the fault characteristics of the DC microgrid voltage and current after bipolar short-circuit fault. On this basis, current differential protection is added as main protection and under voltage protection as backup protection. In the DC microgrid, since the flow of reactive power is not considered in the system, the voltage becomes the only indicator reflecting the power balance of the system. By controlling the voltage stability of the DC microgrid, it is possible to control the stable operation of the microgrid. Therefore, the correct action of the relay protection is used to judge the stability of the system, and the bus voltage is used as an indicator to determine whether the system can recover after the internal short-circuit fault. The simulation verification and analysis are carried out in MATLAB/Simulink. It is concluded that the correct action of relay protection can restore the system in a short time and has important application value for the stable operation of DC microgrid.

6. References

[1] WANG Chengshan， WANG Shouxiang. Research on Several Problems of Distributed Generation Energy Supply System[J]. *Automation of Electric Power System,* 2008，33(30):1-4.
[2] ZHANG Guorong, WANG Xinbing, QIAO Longyang. Influence of Bus Voltage on DC Load in DC Microgrid[J].*Electrical Automation,*2013，35(2):65-67.
[3] WANG Chengshan, LI Wei.DC Bus Voltage Fluctuation Classification and Restraint Methods Review for DC Microgrid[J].*Proceedings of the CSEE,*2017，37(1):84-97.
[4] MA Tianyi, JIN Xinmin, HUANG Xing. Modeling and Stability Analysis of Microgrid with Multi-converter[J].*Automation of Electric Power System,*2013，37(6):12-17.
[5] SHI Jie, ZHENG Zhanghua, AI Qian. Modeling and Stability Analysis of DC Microgrid[J].*Electric Power Automation Equipment,*2012，30(2)：86-9.
[6] Middlebrook R，Cuk S．Input Filter Considerations in Design and Application of Switching Regulators[C].*IEEE Industrial Applications Society Annual Meeting*．Chicago，USA，1976：366-382.

[7] Amr Ahmed A Radwan，Yasser Abdel-Rady I Mohamed. Linear Active Stabilization of Converter- dominated DC microgrids[J].*IEEE Trans. on Smart Grid*,2012, 3(1):203-216.

[8] Karimipour D，Salmasi F R．Stability Analysis of AC Microgrids with Constant Power Loads Based on Popov's Absolute Stability Criterion[J]．*IEEE Transactions on Circuits and Systems II: Express Briefs*，2015，62(7)：696-700.

[9] Andrade F, Kampouropoulos K. Study of Large-signal Stability of an Inverter-based Generator Using a Lyapunov Function[C].*IECON 2014-40th Annual Conference of the IEEE Industrial Electronics Society*．Dallas，USA：IEEE，2014：1840-1846．

[10] ZHANG Y，XIE L,DING Q．Interactive control of coupled microgrids for guaranteed system-wide small signal stability[J]．*IEEE Transactions on Smart Grid*，2016，7(2)：1088-1096．

[11] Robert M. Cuzner, Giri Venkataramanan. The Status of DC Micro-Grid Protection[C] *IEEE Industry Applications Society Annual Meeting*, 2008:1-8.

[12] Daniel Salomonsson, Lennart Söder. Protection of Low-Voltage DC Microgrids[J].*IEEE Transactions on Power Dilivery,*2009,24(3):1045-1052.

[13] IEEE Guide for the Protection of Stationary Battery Systems, IEEE Std. 1375-1998, 1998.

[14] LIU Xinrui, XIE Zhiyuan, SUN Qiuye. Fault Analysis and Protection for LV Bipolar DC Microgrid[J]. *Power System Technology,* 2016, 40(3):749-755.

[15] SHI Jie.Networking Mechanism of Distributed Generation andResearch on Stability of Microgrid[D].*Shanghai Jiao Tong University*.Shanghai,China.

Acknowledgments
This work was supported by the2018 National Grid Corporation of Science and Technology Project" Interconnected power grid blackout early warning technology and system development based on multi-sand-pile theory ".

IOP Conf. Series: Earth and Environmental Science **431** (2020) 012012 doi:10.1088/1755-1315/431/1/012012

Optimal design of energy sstorage capacity of distributed photovoltaic microgrid based on random error model

Longfei Jin[1], Zhenhe Ju[1], Desheng Duan[2] and Fanju Kong[1]

1 Shenyang Institute of Engineering Shenyang, China
2 Liaoning Solar Research and Application Co., Ltd. Shenyang, China
E-mail: 1512595111@qq. com

Abstract. The allocation of capacity of distributed photovoltaic energy storage System has always been an urgent problem to be solved, and reasonable capacity allocation plays an important role in stabilizing the power fluctuation of PCC node and smoothing the load output. In order to reasonably configure energy storage, this paper establishes an energy storage model based on the analysis of random error, which combines load prediction error and the randomness of photovoltaic output prediction error to meet the characteristics of normal distribution, and estimates the random error not considered by the original model, so that the results calculated by the model are more accurate. Combining with the example of the Liaoning branch of China Tower, and the capacity configuration of the photovoltaic energy storage system is verified by combining its load power and photovoltaic power curve.

1. Introduction

China has the largest number of thermal power plants in the world, which poses a huge challenge to air quality [1]. New energy power generation came into being, photovoltaic power generation, hydropower generation, tidal energy, nuclear energy has developed rapidly in recent years, photovoltaic power generation due to its own clean, environmentally friendly renewable, flexible and other advantages quickly became the main force in new energy power generation [2], Distributed photovoltaics are generally built in the load center [3], and the generated electric energy are directly absorbed by the load, saving huge costs such as long-distance transmission lines and towers, and reducing energy loss during transmission lines [4-5]. Since distributed photovoltaic power generation is suitable for combination with buildings and can save a lot of land resources, in recent years, the installed capacity of distributed photovoltaics has been greatly improved. The rational allocation of the capacity of the energy storage system is the key to establish a distributed photovoltaic microgrid.

The traditional energy storage model only considers photovoltaic power generation output (P_{GE}) and system load power consumption (P_{CO}) to configure the capacity of the photovoltaic energy storage system. Neglecting the photovoltaic output and load consumption capacity is susceptible to weather, temperature, and even policy, so it is difficult to accurately predict, which will lead to a large deviation between the capacity configuration and the theoretical value.

The on-site field survey of the roof of Liaoning Tower office building is about 1215 square meters, which is suitable for building truss structure photovoltaic power generation system. And the energy storage system model was established according to the literature [6], because both photovoltaic output and load power have randomness and volatility. [7-8]

Since the photovoltaic output and load power are affected by various meteorological and uncertain factors, considering the photovoltaic output and load consumption capacity error both conform to the

normal distribution, the central limit theorem is used to analyze the error of the established model and accurately calculate the result.
Combining the load power curve and photovoltaic power curve of China Tower Liaoning Branch [9-10], analyze various off-grid modes, [11] determine the capacity design of energy storage system. Combined with its load power curve, the correctness of the capacity allocation of the PV energy storage system is verified.

2. Photovoltaic energy storage capacity configuration scheme

2.1. Analysis of photovoltaic energy storage system

To configure the capacity of the PV energy storage system, the energy storage mode should be selected first. The appropriate energy storage mode plays a key role in smoothing the load output, maintaining the power grid power stability and reducing the energy storage cost.
According to the way of energy storage, it is mainly divided into: physical energy storage, chemical energy storage, and electromagnetic energy storage. According to the energy storage performance, it is mainly divided into: energy density type and power density type.
The advantage of the energy density type is that the capacity of the energy storage system is large, and there is still a long battery life when working in the off-grid mode. The power density type energy storage system is charged and discharged very quickly, and can quickly adjust the PCC of the power grid.
Through the comparison of several energy storage methods in the above table, it can be seen that: flywheel energy storage, superconducting energy storage, lithium ion battery energy storage power density is high, can suppress power fluctuations in a short time, suitable for maintaining the stability of power system.
Lithium-ion battery energy storage, sodium-sulfur battery energy storage has good off-grid working ability, comprehensive analysis can be concluded that lithium-ion battery energy storage can ensure high power density, maintain the stability of the power system.
Good energy density ensures that the energy storage system can operate stably in off-grid mode. Therefore, the energy storage system was selected as the lithium ion battery for energy storage.

3. Energy storage capacity configuration based on contingent error model

3.1. Photovoltaic energy storage system modeling

The distributed PV energy storage system consists of distributed photovoltaic array, DC-DC conversion system, inverter control system and energy storage system. The energy storage system has three modes of operation: the grid-connected mode, the energy storage mode and the off-grid mode.As shown in Figure 1 below：

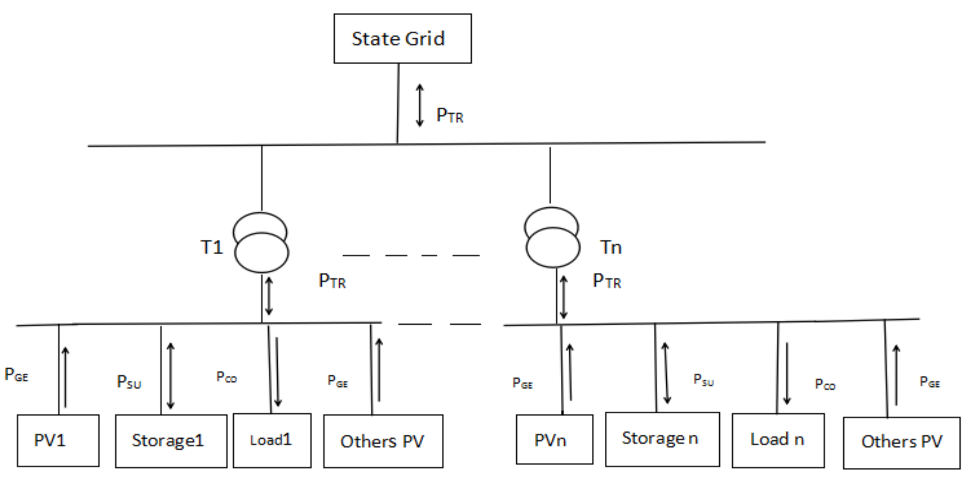

Figure 1. Scheme of distributed arrangement of energy storage.

When the photovoltaic power generation output (P_{GE}) is greater than the system load power consumption (P_{CO}), $P_{SU}=P_{GE}-P_{CO}$, The control system sends the remaining energy (P_{SU}) into the energy storage system in an energy storage mode. When the photovoltaic power generation (P_{GE}) is insufficient to provide the power consumed by the system load (P_{CO}), the additional power required by the load will be transferred from the grid to the load by the grid, called the delivery power (P_{TR}).

$$P_{TR}=P_{CO}-P_{GE} \tag{1}$$

The system is now in the grid mode. The photovoltaic energy storage system will be affected by various factors, such as temperature, weather and wind speed in actual operation. The above mentioned P_{TR} can be called calculating the transmission power. When the load fluctuates greatly or the PV output is greatly affected by the climate, the actual delivery power P_{TR}' and the P_{TR} value also differ greatly, and cannot be ignored. If $P_{TR}'>P_{TR}$, It indicates that the main grid provides insufficient power, and the surplus power will be provided by the energy storage system: when $P_{TR}'<P_{TR}$. It can be concluded that the power provided by the main grid is too high, and the surplus power will be absorbed by the energy storage system.

The modified power equation is:

$$P_{TR}' = \delta P_{CO}-\delta P_{GE} \tag{2}$$

δP_{CO} for load output error and δP_{GE} is a short-term prediction error for photovoltaics.

3.2. The error analysis of photovoltaic energy storage system

When the theoretical value symbytes of PV output forecast and load power forecast are the same as actual values, the traditional PV energy storage capacity configuration model can be used. However, photovoltaic power generation is vulnerable to weather and other factors, load and PV output will produce fluctuations and thus have a greater impact on the energy storage system, so we based on the random error model of energy storage system capacity to improve accuracy, avoid the negative impact due to error.

Table 1. PV actual power and predicted power error analysis.

Times	Actual photovoltaic power /MW	PV power forecast/MW	Power error value/MW	Relative error/MW
06. 00	1. 3265	1. 5998	-0. 3352	-0. 2510
07. 00	4. 1023	5. 102	-1. 0223	-0. 2499
08. 00	14. 0235	12. 3654	1. 2584	0. 09874
09. 00	15. 412	16. 289	-1. 6588	-0. 1111
10. 00	19. 5562	18. 0221	1. 6251	0. 08654
11. 00	28. 0215	25. 3654	1. 6854	0. 0598
12. 00	27. 3965	29. 0584	-1. 679	-0. 0692
13. 00	30. 0258	30. 0125	-0. 3584	-0. 01524
14. 00	24. 369	26. 324	-1. 6954	-0. 0694
15. 00	19. 9845	21. 9845	-1. 9547	-0. 09812
16. 00	19. 6842	18. 3021	1. 0521	0. 04987
17. 00	12. 0684	13. 2587	-1. 3571	-0. 1422
18. 00	6. 3199	6. 8488	-0. 3332	-0. 0215
19. 00	2. 6324	2. 2324	0. 3332	0. 21
Mean (expected value)			-0. 3432	-0. 04987

The analysis data shows that as the measurement time interval becomes shorter, the expectation of the PV output prediction error value gradually decreases. According to the Bernoulli limit theorem, when the time interval approaches 0, the PV predicted power approaches the actual PV power.

By central limit theorem. The law shows that the random variables X1, X2, . . . Xn exist independently of each other, the expected value is μ, the variance is σ^2, (σ not 0), K = 1, 2, 3. . . The calculation of any normal distribution is easily converted to the standard normal distribution is N (0, 1). Easy to prove: $Y = (X - \mu)/\sigma \approx N(0,1)$.
Then random variable:

$$Y_n = \frac{\sum_{k=1}^{n} X_k - E(\sum_{k=1}^{n} X_k)}{\sqrt{D(\sum_{k=1}^{n} X_k)}} = \frac{\sum_{k=1}^{n} X_k - n\mu}{\sqrt{n}\sigma} \tag{3}$$

Actually:

$$P(Y \le x) = P((X-\mu)/\sigma \le x) = (\sqrt{2\pi}^{-1} \int_{-\infty}^{x} e^{-\frac{v^2}{2}dv} \tag{4}$$

The expected error of PV output prediction in a certain region within the micro-grid is μ_{Ge}, variance is $\sigma_{Ge}{}^2$, So its normal distribution can be expressed as:

$$f(\Delta P_{Ge}) \approx N\left(\mu_{Ge}, \sigma_{Ge}{}^2\right), \tag{5}$$

According to the density function formula of the normal distribution, the probability density function of the normal distribution can be obtained as follows:

$$f(\Delta P_{Ge}) = \frac{1}{\sqrt{2\pi}\sigma_{Ge}} e^{\frac{(\Delta P_{Ge} - \mu_{Ge})^2}{2\sigma^2{}_{Ge}}} \tag{6}$$

The load forecasting error is mainly affected by the load power situation, weather, geographical location, etc. The impact factor of each influencing factor is less than 0. 5, so the load forecasting error is in line with the normal distribution.
The PV output prediction error is mainly affected by temperature, humidity, wind speed, etc.and each impact factor has only a low weight. Similarly, the PV output prediction error is also in line with the normal distribution.As shown in Figure 2 below：

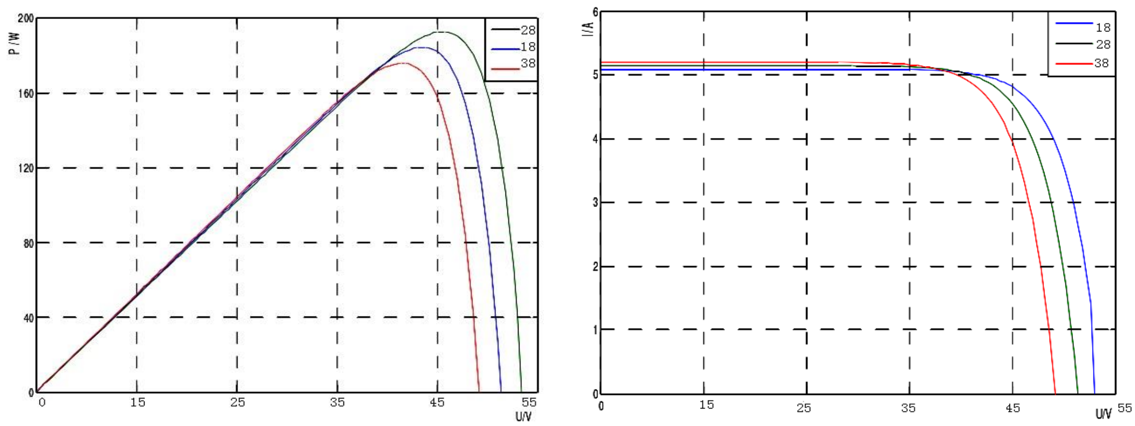

Figure 2. Output curves corresponding to different light intensities.

The figure below shows the effects of power and current on different temperatures and light intensities. The expected value of the load power prediction error in a certain area of the microgrid is μ_{load} , and the variance is $\sigma_{load}{}^{2}$, so its normal distribution can be expressed as:

$$f(\Delta P_{loadi}) = \frac{1}{\sqrt{2\pi}\sigma_{loadi}} e^{\frac{(\Delta P_{loadi}-\mu_{loadi})^2}{2\sigma^2{}_{loadi}}} \tag{7}$$

Let M and N respectively represent the PV output prediction error and load prediction error of a microgrid. When the capacity of the energy storage system is configured, the total error is W=M+N, and the total error W directly determines the capacity of the energy storage system. The density function is:

$$\begin{aligned} f_{w_i}(w_i) &= \int_{-\infty}^{+\infty} f_{m_i}(m_i) f_{n_i}(w_i - n_i) dm_i \\ f_{w_i}(w_i) &= \frac{1}{2\pi * \sigma_{Ge} * \sigma_{load}} * \int_{-\infty}^{+\infty} e^{\frac{-(\Delta P_{Ge}-\mu_{Ge})^2}{2\sigma^2{}_{Ge}}} * e^{\frac{-(-\Delta P_{Ge}-\mu_{load})^2}{2\sigma^2{}_{load}}} d(\Delta P_{Ge}) \end{aligned} \tag{8}$$

The above equation can be simplified to:

$$f_{w_i}(w_i) = \frac{1}{\sqrt{2\pi} * \sqrt{\sigma_{Ge}{}^2 * \sigma_{load}{}^2}} e^{-\frac{(-\mu_{Ge}-\mu_{load})^2}{2(\sigma^2{}_{load}+\sigma_{Ge}{}^2)}} \tag{9}$$

The influence factors of photovoltaic output prediction error and load prediction error are different, so they are independent of each other and do not interfere with each other. The sum of two independent normal distributions is also normal distribution.

$$\Delta P_{TR} = \Delta P_{Ge} + \Delta P_{load} \tag{10}$$

$$Y = \frac{\overline{X} - \mu}{\sigma_0 / \sqrt{n}} \sim \mathrm{N}(0, 1) \tag{11}$$

Combined with the standard normal distribution definition. The maximum power of the energy storage system is:

$$P_{TR} = \frac{\sigma_{TR}}{\sqrt{n}} Y_{\alpha/2} \tag{12}$$

4. Application analysis

In order to give full play to the flexible and controllable characteristics of distributed PV energy storage systems, reasonable capacity configuration is essential.

Excessive capacity configuration will cause the energy storage system to be discharged for a long time, greatly reducing the service life and increasing the cost of the energy storage system.

If the selected capacity is too small, the energy storage capacity will be weak, and the ability to cut the peak and fill the valley will be poor, which will greatly affect the effect of suppressing the PPC power countercurrent and adjusting the voltage fluctuation. The available area of the roof of Liaoning Tower office building is about 1215 square meters. However, because the elevator company and the owner's corporate logo are too high, the installed capacity of the truss structure photovoltaic power generation system is 200KW.

Through the field test to draw the user office building load curve, the maximum load of the user is not more than 150KW. Therefore, according to the normal operation requirements of the user and the installed capacity of the photovoltaic system, the capacity of the energy storage system is 387KWh, and the photovoltaic power station is installed in the roof area provided by the owner.As shown in Figure 3 below：

Figure 3. Load power curve.

The scale of the photovoltaic power station that can be constructed through survey and design is about 234KWp. According to the load power curve of the office building, the maximum load does not exceed 150KW. The power generation curve of the photovoltaic power generation system is approximately parabolic, and the system efficiency is about 80%-85%, and the photovoltaic installed capacity that meets the stable power generation capacity is 200 KWp.

The 325W double-sided photovoltaic module is installed horizontally in the roof of the available area. It is estimated that the number of PV modules that can be paved is 624. The installed capacity of the photovoltaic power station is 202KWp. The grid connection point selects the nearest TV from the roof of the PV module.

During the peak season of photovoltaic power generation, 400KWh is depleted during the peak period of photovoltaic power generation. The energy storage system is needed for peak clipping and valley filling. The energy supply during the non-working day of the solar energy season can meet the load demand during the peak period, without the energy storage system working, non-power supply. Seasonal PV generation will be greater than the load demand, with a 252 KWh surplus.

According to the above analysis, it can be determined that the installed capacity of the photovoltaic tower of China Railway Tower Liaoning Branch is 400KW.

5. In conclusion

Firstly, through the comparison of several energy storage methods, the lithium ion battery with the main energy density is the main energy storage method.

The structure of distributed photovoltaic dispatching energy storage system is analyzed, and the basic mathematical model is established. Since both PV output and load power prediction have randomness and volatility, in order to calculate the accuracy of the result, both errors are obeyed in a normal state.

According to the characteristics of the distribution, the error model is integrated and the capacity configuration of the energy storage system is estimated.

Based on the characteristics of China Railway Tower Liaoning Branch, a distributed photovoltaic power station was built on the roof. To ensure reasonable capacity allocation, the capacity of the energy storage system was estimated by the model.

6. References

[1] Li Binggang. On China's Energy Crisis and Economic Development[J]. Modernization of Shopping Malls, 2016, 40(19): 17-23
[2] Xu Hongxing. Status quo and countermeasures of energy utilization in China [J]. Sino-foreign Energy, 2018, 31(9): 19-20
[3] Li Dadong, Li Jiadong. Efficient use of petroleum resources [J]. World Petroleum Industry, 2017, 15 (9): 11-20
[4] Zhou Dadi. A turn to the new energy era [J]. Energy, 2018, 1 (9): 39-50
[5] Li Bihui, Shen Hong, Tang Yong et al. The effect of energy storage capacity of wind and light storage combined power generation system on active power and Evaluation Indicators Grid Technology: 2012, 40(19): 17-23
[6] Li Jiannan, Qiao Ying, Lu Zongge. Research on statistical modeling of large-scale wind power multi-scale output volatility [J]. solar energy, 2013, 08:8-19.
[7] Power System Protection and Control, 2012, 40(19): 17-23
[8] Hou Youhua, Fang Dazhong, Qi Jun et al. Analysis of active power fluctuation characteristics and power generation of large-scale wind power grid access, 2018, 5(2): 21-32
[9] Plan Simulation [J]. Power Grid Technology, 2016, 34(5): 68-78
[10] Cui Yang, Mu Gang, Liu Yu, et al. Temporal and spatial distribution characteristics of wind power fluctuations [J]. Power System Technology 2011, 35(2): 121-132
[11] Guo Kang, Xu Yuqin, Zhang Li et al. Reactive power optimization of distribution network taking into account the random output of photovoltaic power plants [J]. 2012, 32 (3): 99-105

IOP Conf. Series: Earth and Environmental Science **431** (2020) 012013 doi:10.1088/1755-1315/431/1/012013

Research on fault location of distribution network based on Radar principle

Yu Jia[1], Wei Linhuan[1], Leng Xuemin[1] and Gao Yang[1]

1 Shenyang Institute of Engineering, Shenyang, China
E-mail: 916472935@qq.com

Abstract. When the distribution network fails, the operation and maintenance personnel need to quickly determine the fault location and minimize the scope of the inspection line so that the fault repair personnel can accurately reach the vicinity of the fault point to carry out work. Whether the fault location method is advanced and reliable directly affects the power failure time of the power supply user, and further affects the social, economic, and life aspects. Therefore, the fault location of the distribution network needs to satisfy both reliability and accuracy. It is the basis and premise for troubleshooting, isolating and restoring the power supply. The automation level of China's distribution network is relatively backward, and the reliability of power supply equipment is relatively low, making it difficult to find fault points. If we find out the intelligent algorithms that can meet the requirements of rapid positioning, accuracy and fault tolerance through theoretical research, we can Improve the fault location efficiency very well.

1. Introduction

Whether the fault location of the distribution network can satisfy the rapidity, accuracy and fault tolerance directly affects the reliability, continuity, and security of the user's power supply [1-3]. The existing distribution network fault location methods mainly include the following three categories: one is to use the 95598 complaint telephone dialed by the user when a power failure occurs to determine the fault point; the other is to use the action signals of the recloser and the segmenter to perform fault location; The Supervisory Control And Data Acquisition (SCADA) system is used to analyze and process the overcurrent information uploaded by the Feeder Terminal Unit (FTU) to locate faults [4-7].

2. Fault location of non-measurement control area in distribution network based on fuzzy information fusion

In the non-measurement control area, a small number of demarcation switches or fault indicators are often installed at the load switch in the distribution network main line and some important branch lines. When the fault occurs, the switch can be automatically opened and the alarm information is uploaded to the main station system. Based on this, this chapter first introduces the basic principle of fuzzy set theory. For the non-measurement and control area of the distribution network where the user's electricity data has been collected, the fuzzy integrated telephone complaint information and the alarm information uploaded by a small number of devices in the actual running line (including the demarcation switch information) are proposed. And fault indicator information, etc.) to locate the fault, use the alarm information to improve the fault weight of the branch line where the alarm device is located, to reduce the uncertainty of the telephone complaint information, and then modify the fault location result by defining the evaluation parameters, thereby reducing the multi-node The misjudgment problem under the fault improves the fault tolerance of fault location..

2.1. Fuzzy set geometric description

There is a certain difference between the fuzzy set and the concept definition of the ordinary set. Here, the fuzzy set is A, and the feature function which takes one in the [0,1] interval is the membership function, which is recorded as $\mu_A(x)$The fuzzy set is specifically defined as follows:

$$\mu_A: U \to [0,1] \tag{1}$$

$$\mu_A:\ x \to \mu_A(x) \tag{2}$$

In equations (1) and (2), the fuzzy set A is represented by a real-valued function on the universe U. For x∈U, the function A is called the membership function of the fuzzy set A, and the function value $\mu_A(x)$ is the membership degree of the variable x for the fuzzy set A. The value range of $A(x)$ is [0,1]. When $\mu_A(x)$ approaches 1, it means that the membership of variable x is higher for set A; otherwise, the more representative of variable x for set A low. A value of $\mu_A(x)$ of 0.5 indicates that the variable x has the most ambiguity for the membership of the set A, or the variable x is called the fuzzy transition point of the set A. The essence of a fuzzy set is a generalized subset of a classical set. Since there is no precise boundary, it is necessary to use a membership function to represent the smoothing process from affiliation to non-dependent.

2.2. Fault location algorithm

Aiming at the telephone complaint information in the non-measurement and control area of the distribution network and the small amount of equipment alarm information existing in the actual operation line, the fuzzy information fusion algorithm can make full use of the collectible information in the line for fault location. For the determined distribution network topology, the power supply path between each power supply station area and the bus line is first represented by an array. Based on the power flow direction, the array equipment is hierarchically classified according to the number of alarm information in different power supply links. Different alarm information in the power supply link defines the membership function to determine the fault membership degree of the equipment and then fuses the fault complaint telephone information to calculate the fault membership degree of the power supply link. Finally, the fault location result is obtained through fuzzy fault evaluation, thereby improving the fault location. Fault tolerance and shortened fault location time.

Through the above classification method, the fuzzy information of the fusion device and the fault complaint telephone information are blurred, and the fault weight of the complaint telephone in the power supply link is adjusted according to the maximum number of alarm information of different equipment sections in the power supply link, and the maximum number of alarm information is increased. More, the less the weight of the fault complaint call, the shorter the time required for fault location. Therefore, the method can adopt different strategies to determine the fault weights of different branch lines of the non-measurement control area of the distribution network that cannot collect user meter information and has wide applicability in the continuous popularization of smart meters and further upgrading of the collection equipment. In the background, in some non-measurement and control areas of the distribution network, relying on the two-way communication system, the power enterprise can also obtain various power values of the user through the smart meter in time or in real time. Based on this, for a given distribution network topology, in the non-measurement and control area of the distribution network where the user meter information has been collected, the user's smart meter information, user telephone complaint information and equipment alarm information are used as the condition attributes of the fault classification to establish a fault. Make a decision table and find the minimum reduction. Then, according to the three types of information, attribute matching is performed on the reduced fault decision table to determine the fault section. Since the user meter collection information and the device alarm information are used as the fault information source, the number of complaint telephones required for fault location is greatly reduced, and the fault location time is shortened.

3. Fault location of non-measurement and control area in distribution network based on rough set theory and data fusion

Under the background of the continuous popularization of smart meters and the further upgrade of collection equipment, in the non-measurement and control area of the distribution network, relying on the two-way communication system, the power enterprise can also obtain the user's various power values through the smart meter in time or in real time. . Based on this, this chapter first introduces the basic principle of rough set theory. For a given distribution network topology, in the non-measurement and control area of the distribution network where the user meter information has been collected, the user's smart meter information, user telephone complaint information and The device alarm information is used as a condition attribute of the fault classification to establish a fault decision table and find a minimum reduction. Then, according to the three types of information, attribute matching is performed on the reduced fault decision table to determine the fault section. Since the user meter collection information and the device alarm information are used as the fault information source, the number of complaint telephones required for fault location is greatly reduced, and the fault location time is shortened.

3.1. Fault location step

The implementation of fault location includes the following two steps:

Step 1: Determine the maximum power outage range When the distribution network fails, the power supply department receives the complaint call from a power outage user, determines the user's station area, and then selectively calls the user's power level data of the station area. According to different call results, the fault range can be preliminarily determined: if the power data of the user's smart meter in the same floor of the user is normal, it can be determined that only the user's internal power supply fault occurs, and the maximum power outage range is a single user; The smart meter data of the floor of the user, and the recall data of other floors is normal, it can be determined that the power failure occurs on the floor, the maximum power outage range is a single floor; if the smart meter data of the building where the user is located cannot be recalled, and other buildings If the recall data of the building is normal, it can be determined that there is a power failure in the building. The maximum power outage is a single building; if all the smart meter data in the station cannot be recalled, it means that all power supply abnormalities in the station need to be combined with other The user's electricity data and user complaint information in the station area, and the fault alarm and the device alarm information uploaded by the demarcation switch are integrated for comprehensive analysis. If the smart meter and smart interactive terminal are not installed in the station, the user's power data of other stations will be directly called.

Step 2: Fault location based on rough set theory and camping data fusion

If the maximum power outage range is obtained by calling the user's power data to a single user, floor, building or internal area, the fault range of the low voltage side can be directly determined. Otherwise, the smart meter of the entire distribution line will be collected and matched with the fault decision table after reduction. If the corresponding decision rule can be found in the decision table according to the power data of the user of the station, the fault occurs in the section where the faulty device is located. If the corresponding decision rule cannot be found in the decision table by the user power data, it is necessary to continue to wait for the user complaint calls of other stations until the corresponding decision rule is found. This chapter combines device alarm information, user power recall information and telephone complaint information. Based on the rough set theory, the fault location decision table is generated according to the situation of all possible faulty devices in the line, and the user power consumption is eliminated by reducing the decision table. The redundancy of the measurement information and the telephone complaint information enables the fault section to be judged based on less user power information and telephone complaint information, which effectively shortens the fault location time and lays a good foundation for fault elimination and power restoration.

4. Fault location based on universal gravitation search algorithm for measurement and control area

The Gravitational Search Algorithm (GSA) is a group intelligence optimization method developed by Professor Esmat Rashedi and based on the gravitational law of gravity and mass interaction between different particles in the physics discipline. The algorithm first calculates its own mass according to the fitness value of the population particles and then generates the interaction force of the population particles based on the law of universal gravitation. Each particle is attracted by other particles, and each attracted particle moves under the gravitational force of other particles. The best position to get the best results. Because the fault location problem of distribution network is an optimization problem with 0 and 1 constraints, this paper applies the improved universal gravitation search algorithm to the problem of fault location in distribution network, avoiding the traditional continuous optimization algorithm. Various problems that arise during discrete data processing to shorten the positioning time and improve the efficiency of positioning.

The attribute characteristics of the universal gravitation search algorithm are partially similar to the particle swarm optimization algorithm. Each individual in the gravitational search algorithm has its corresponding spatial position and movement speed. The quality of different individuals can be obtained by the degree of fitness value corresponding to the spatial position of the individual. The corresponding fitness of the individual with higher individual quality. The value is better, and the individual's quality is smaller, and the corresponding fitness value is worse. The gravitational search algorithm is significantly different from the particle swarm optimization algorithm and the bee colony algorithm. It is mainly reflected in the fact that the particles in the gravitational search algorithm do not need to perceive the situation in the environment through external factors but through the gravitational interaction between individuals. To pass optimization information. Suppose there are N particles in a D-dimensional search space, and the position of the i-th particle is:

$$\mathrm{X_n} = (\mathrm{x_n^1}, \mathrm{x_n^2}, \ldots, \mathrm{x_n^i}, \ldots, \mathrm{x_n^d}); \qquad \mathrm{n} = 1,2,\ldots,\mathrm{N} \tag{3}$$

where x_n^i represents the position of the n-th particle in the i-th dimension.

A. Fault Location Algorithm

The universal gravitation search algorithm is applied to the fault location of the distribution network. Firstly, the fault segment vector is regarded as the solution to the optimization function. By establishing a uniform function model, the model is sampled and calculated in turn, and the optimal fault segment vector is gradually improved. The probability in space, and finally the solution that obtains the optimal value of the objective function is the fault segment.

In principle, the fault location problem of distribution network is an optimization problem with 0 and 1 constraints. In the process of searching for faulty segments, it is necessary to find the fault section that best meets the given conditions of the algorithm. Therefore, after establishing the switching function and the evaluation function according to the network topology, the final result is that a reliable algorithm is needed to find the optimal fault section. When the circuit breaker fault information sequence is uploaded, the fault section can be located. In the early stage, the universal gravitation search algorithm optimizes the

gravitational effect of the population by multiple action particles in the global scope. With the passage of time (the number of iterations), the gravitational constant G index decreases, and the population's gravitational effect due to the decreasing effect of the particles Aggregate into the neighborhood space of the optimal solution and search within the local scope to find the optimal solution. Therefore, applying the universal gravitation search algorithm to the fault location of the distribution network can ensure the accuracy and rapidity of the positioning results.
In order to further test the effect of the universal gravitation search algorithm in the fault location process of distribution network, the same fault of IEEE-33 node distribution network is repeatedly run 60 times by genetic algorithm, bee colony algorithm and universal gravitation search algorithm respectively. For example, as shown in Table 1.

Table 1. Comparison of three algorithms for fault location simulation results.

Algorithm type	genetic algorithm	bee colony algorithm	universal gravitation search algorithm
Average number of iterations	53.6	41.8	23.9
Result number of false positives	42	26	8

Figure 1 shows the convergence curve of the gravitational search algorithm and the genetic algorithm and the bee colony algorithm under the same fault condition. The abscissa is the number of iterations and the ordinate is the optimal evaluation value of the corresponding iterations.

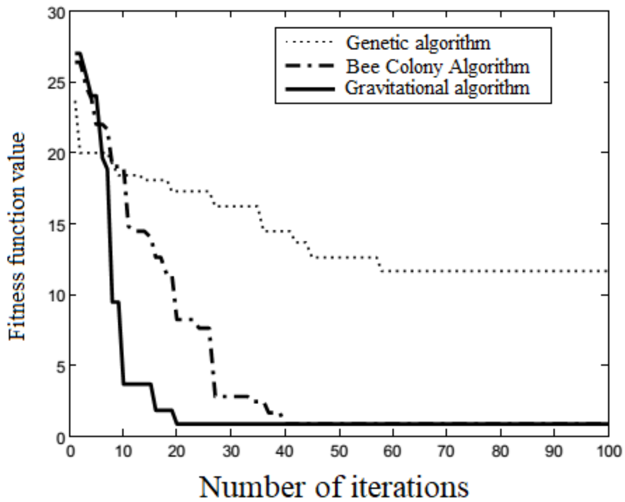

Figure 1. Algorithm convergence comparison.

5. Conclusion

With the large investment of the grid company in the construction of the cooperative management and control platform and the improvement of the electricity information collection system, the urban area (including the county) in the non-measurement and control area of the distribution network and some power supply areas in the township will be able to collect the user's electricity information. . The method of fuzzy fusion fault complaint telephone information and a smalld amount of equipment alarm information is used to locate the fault. First, the power supply link is hierarchically based on the maximum number of alarm information, and the membership function based on the hierarchical model of the power distribution network is defined by combining two different fault information. The device alarm information is used to improve the fault weight of the branch line where the alarm device is located, and then the evaluation parameter is defined according to the source of the complaint, and the fault location result is corrected, thereby reducing the uncertainty of the telephone complaint information and improving the rapidity of the fault location. Fault tolerance. In the non-measurement and control area of the distribution network that has collected the user's electricity information, based on the rough set theory and the data fusion method, the user's electricity information is taken as one of the fault information, supplemented by the user's telephone complaint information and equipment alarm information for fault location, and the minimum is found. Degenerate fault matching. Priority is given to the user's power information, supplemented by telephone complaint information, which greatly reduces the number of complaint calls required for fault location, further shortens the fault location time, and reduces the subjective factors of fault information. The universal gravitation search algorithm is applied to the reliability and accuracy of fault location in the distribution network and overcomes the shortcomings of common optimization algorithms such as genetic algorithm and bee colony algorithm which are easy to fall into local extremum and slow convergence.

6. References

[1] Jia Guangjun, Analysis of the Problems Existing in the Overhead Lines of Power Engineering Distribution Network and Their Solutions [J]. Mechanical and Electrical Information 2019.17.055.
[2] Liang Weibing, Dangerous points and preventive measures for overhead line construction of electric power engineering [J]. Science and Technology Innovation Herald, 2014-04-082.
[3] Lang Ming, Overhead line faults and preventive measures [J]. Xinjiang Nonferrous Metals, 2019-01-050
[4] Luo Guohong, Research on Fault Identification and Finding Method of Distribution Lines [J]. Science and Technology & Innovation,2018-21-035
[5] Chen Liangbin, Fault Detection Technology For Distribution Line Operation In Power System [J].Electronic Technology & Software Engineering,2017-22-193
[6] Zeng Xianlin, Inspection and Repair of Distribution Line Operation Faults in Power System [J]. Electronic Test, 2017.08.044
[7] Wang Yang, Overhaul of distribution line operation faults in power system [J]. 2015-12-198.

IOP Conf. Series: Earth and Environmental Science **431** (2020) 012014 doi:10.1088/1755-1315/431/1/012014

Research on restraining low voltage of distribution power network using STATCOM

Jin Qingren[1], Zhou Ke[1], Guo Mei[1] and Zhou Yangjun[1]

1 Electric power research institute of guangxi power grid Co.,Ltd., Nanning, Guangxi, 530023, China
E-mail: tianbu081247121@163.com

Abstract. In order to solve the problem of low voltage in distribution power network, this paper proposes a novel static synchronous compensator (STATCOM) based on modular multilevel converter. When the bus voltage of distribution power network changes rapidly, The MMC-STATCOM can quickly provide reactive voltage support and maintain the stability of bus voltage. Firstly, this paper introduces the operating principle of the MMC-STATCOM, and then propose three-level control strategies including device-level-, converter-level- and system level-control. Finally, based on the data of a power station in the distribution network, Simulation is carried out in the power system analysis and synthesis program (PSASP). The simulation results show that the MMC-STATCOM control function is reasonable and can respond quickly to the system reactive power change. It can effectively realize the voltage support and ensure the safe and stable operation of the power network.

1. Introduction

In recent years, with the application of electric power devices in distribution power network more and more widely, the power load has a large number of equipment with frequent changes of reactive power, such as welding machine, rolling mill and rectifier equipment [1-3]. Once, the distribution power network lacks the support of dynamic reactive voltage, the power grid voltage will fluctuate violently, and even cause the large area collapse of the power grid voltage [4]. In particular, a large number of impact loads will cause typical power quality problems such as voltage fluctuation, flicker, harmonic and three-phase imbalance, which may pose a serious threat to the safety and stability of the power system. A new generation of dynamic reactive power compensation equipment of static reactive power compensator (STATCOM) is constructed using power electronic devices [5-6]. It has the following advantages: fast dynamic response, strong compensation ability, and small power consumption. The STATCOM is considered as the most effective way to solve the voltage fluctuation and flicker.

The basic principle of STATCOM is that the self- commutating circuit is comprised by high power electronic devices and it is connected in parallel with power grid [7]. Then, the STATCOM can absorb or provide dynamic reactive power by appropriate adjustment ac output voltage amplitude and phase, or direct control of the ac current. Doing so, compensating reactive power dynamically into power grid is achieved. However, with the increasing of reactive power which needs to be compensated, the traditional topology of two-level or three-level converter can't not meet the requirements. Therefore, this paper suggests the modular multilevel converter (MMC) is as the topology of STATCOM. MMC is a new multilevel topology proposed by German scholars in 2002 [8]. This topology can realize high-voltage output by using low-voltage power devices, and has the advantages of low harmonic output and easy expansion.

2. Application of MMC-STATCOM

As shown in Figure 1, the 220kV substation is one of the important voltage points in the local area. There is a main transformer in the station, and there are four feed-in and outlet lines, of which #1 and #2 provide power for the traction substation high-speed railway. Influenced by the intensive operation of electrified railway, 220kV bus line has obvious voltage fluctuation and flicker and needs large capacity reactive power compensation. However, the traditional manual switching of capacitors cannot solve the above-mentioned problem. Therefore, the MMC-STATCOM as a new generation of dynamic reactive power compensator is used in this substation.

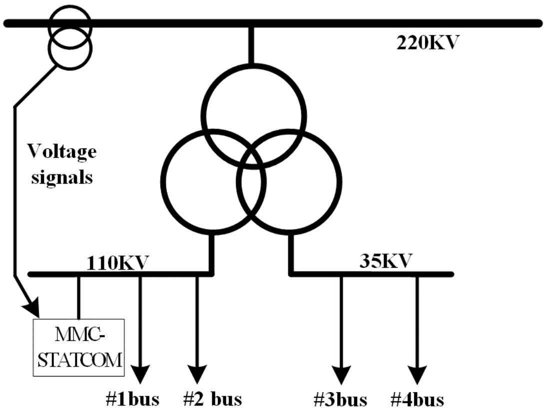

Figure 1. Wiring diagram of MMC-STATCOM in distribution power network.

Figure 2 gives the topology of MMC-STATCOM. It can be seen that MMC is composed of six bridge arms, and each bridge arm is composed of several interconnected sub-modules with the same structure in series. The upper and lower bridge arms form a phase unit. The six arms are symmetrical, and the electrical parameters and reactance of each submodule are the same. A sub-module of MMC is shown in the upper right part of Figure 2. Each sub-module is composed of two IGBTs, D1 and D2 are anti-parallel diodes. UC is the capacitive voltage of the submodule, USM and i_{SM} are the output voltage and current of the submodule respectively.

At any time, the dc side voltage U_{dc} is shared by the sub-modules in the output state of each phase upper and lower bridge arm and the two reactors LS. Namely to satisfy the following equation [9-10]:

$$U_{dc} = L_s \frac{d}{dt}\left(i_{px} + i_{nx}\right) + \sum_{i=1}^{n}\left(u_{px} + u_{nx}\right) \quad \text{(x=a, b, c)} \tag{1}$$

Where, Udc is the bus voltage of the dc side, i_{px} and i_{nx} are the upper and lower bridge arm current of phase x (x=a, b, c) respectively.

Theoretically, the number of submodules in the output state of each phase in MMC is constant and is half of all submodules in the phase, namely, n. If M_x is set as the number of submodules in the output state in the upper bridge arm of phase x, and P_x is the number of submodules in the output state in the lower bridge arm of phase x, then

$$M_x + P_x = n \tag{2}$$

During normal operation, uneven energy distribution between three phases of MMC will generate phase circulation. Let the circulation flowing through phase x be i_{zx}, as shown in Figure 2. Due to the strict symmetry of MMC structure, it can be regarded as energy sharing equally in upper and lower bridge arms. Thus the following equation can be obtained:

$$\begin{cases} i_{px} = \frac{1}{2} i_x + i_{zx} \\ i_{nx} = -\frac{1}{2} i_x + i_{zx} \\ i_{zx} = \frac{1}{2}\left(i_{px} + i_{zx}\right) \end{cases} \tag{3}$$

The following expression can be obtained based on KVL equation:

$$\begin{cases} \frac{U_{dc}}{2} - \sum_{i=1}^{n} u_{px} - L_S \frac{di_{px}}{dt} = u_{xo} \\ -\frac{U_{dc}}{2} - \sum_{i=1}^{n} u_{nx} - L_S \frac{di_{nx}}{dt} = u_{xo} \end{cases} \tag{4}$$

$$u_{xo} = \frac{1}{2}\left(\sum_{i=1}^{n} u_{nx} - \sum_{i=1}^{n} u_{px}\right) - \frac{L_S}{2}\frac{di_{zx}}{dt} \quad \text{(x=a, b, c)} \tag{5}$$

The above equation is the dynamic mathematical model of output voltage of MMC. The required three-phase ac voltage is output by controlling the input state of sub-modules of upper and lower bridge arms. When the converter operates at steady-state, the fluctuation of dc voltage and the voltage drop of inductance are ignored. The errors caused by them are corrected through the closed loop of the control system.

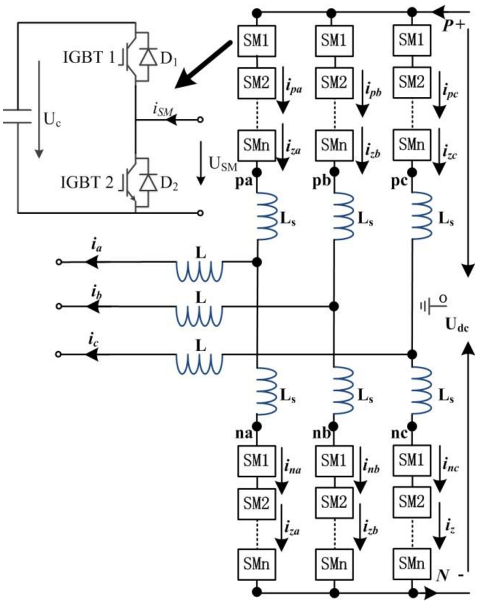

Figure 2. Main circuit of MMC-STATCOM

3. Control strategy of MMC-STATCOM

There are three operating modes of MMC-STATCOM, namely open-loop commissioning operation, constant-reactive power operation and voltage stable operation. The operation mode can be selected according to the operation requirements. Among them, open-loop commissioning mode is only used for pre-operation debugging, so it will not be considered in this paper.

(1) Constant reactive power operation mode: the STATCOM can output constant reactive power under this operation mode. And the reference value of output reactive power can be set arbitrarily from rated capacitive reactive power to rated inductive reactive power.

(2) Voltage stable operation mode: due to the variation of daily load and the influence of other power grid factors, the system voltage will fluctuate to some extent. The regulation of system voltage fluctuation and maintenance of voltage level can be realized within a certain range depend on the automatic control and quick response function of STATCOM.

In order to achieve better control of MMC-STATCOM, the control strategy is divided into three levels: system-level control, converter-level control and device-level control, as shown in Figure.3.

3.1. System-level control
System-level control layer is in the highest level of the MMC -STATCOM control system. It is the dispatching center responsible for receiving the amount of active and reactive power in setting value and scheduling control instruction. The reactive quantity reference value is produced by regulating control in dispatching center and then is sent to converter-level layer by control bus. At the same time, running information of system is feedback to the dispatch center.
When STATCOM is in voltage stable operation mode, system voltage is as the control target and make the system voltage stable within the allowable error range by changing its output reactive power. When STATCOM is running in constant reactive power mode, the remote communication interface is adopted to receive the reactive power instruction from the dispatching center or AVC master control unit.

3.2. Converter-level control
The converter-level control layer is the core control layer of MMC-STATCOM control system. It is the bridge between the system-level control layer and the device-level control layer. The converter-level control layer is mainly responsible for receiving the reference values of active and reactive power commands from the system-level control layer. The modulation ratio M and the phase shift Angle are transmitted to the device level control layer through the control of the device level control layer. The control strategy mainly includes direct current control and indirect current control.

3.3. Device-level control
Device-level control layer is the lowest control layer in MMC-STATCOM control system, which is also called executive control layer. It mainly controls the switching devices of MMC, and realizes the specific execution and operation of various instructions. The control instructions including modulation ratio M and phase-shifting Angle are received from the converter-level control layer. And then generate the bridge arm voltage reference. The switching devices turn on or off by PWM modulation trigger pulse. The control strategies includes: generation of reference voltage of bridge arm, selection of modulation strategy, capacitor voltage balance control, phase circulation suppression, fault protection control, etc.

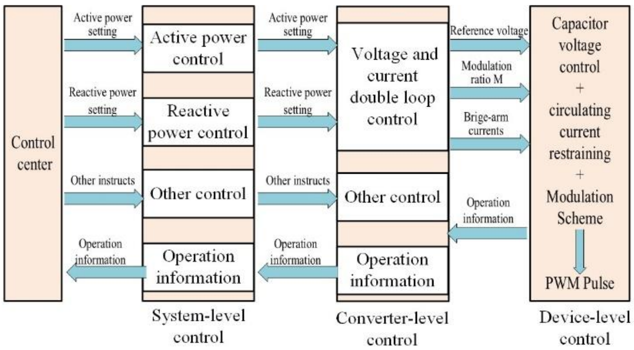

Figure 3. Control diagram of MMC-STATCOM

4. Simulation
Based on the data model of a substation mentioned above, the simulation model of MMC-STATCOM is established in the power system analysis and synthesis program (CPSASP). The control protection device consists of system-control layer, converter-control layer, device-control layer and monitoring layer. The system-control layer is mainly responsible for the system-level control strategy of MMC-STATCOM, which generates the reference reactive power signal. The converter-level control layer is mainly responsible for receiving the instructions from the system-level layer and obtaining the

IOP Conf. Series: Earth and Environmental Science **431** (2020) 012014 doi:10.1088/1755-1315/431/1/012014

required modulation waveform. The device-control layer is mainly responsible for generating PWM modulation signal, capacitor voltage balancing and phase current instruction.

4.1. Voltage stable operation control

In order to verify the dynamic response characteristics of STATCOM in the voltage stability control mode, the 220kV side bus voltage is set as the main voltage control target. Referring to the field test of substation, simulation results of the voltage fluctuation by switching reactor and capacitor in the substation, the output reactive power is set within the range of (-80, +80) MVA in CPSASP test. In the initial state, the 220kV bus voltage is the rated voltage, namely 220kV. After 0.2s, the reactive power of 60Mvar is injected into power grid. The bus voltage variation and output characteristic of MMC-STATCOM were observed.

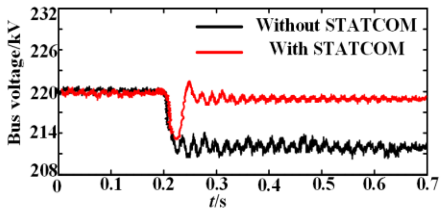

(a) Simulation results of 220kV bus voltage

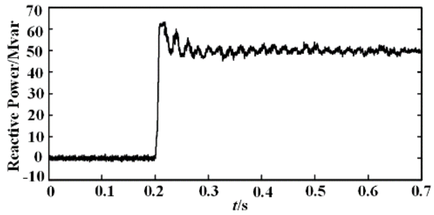

(b) Simulation results of output reactive power of MMC-STATCOM.

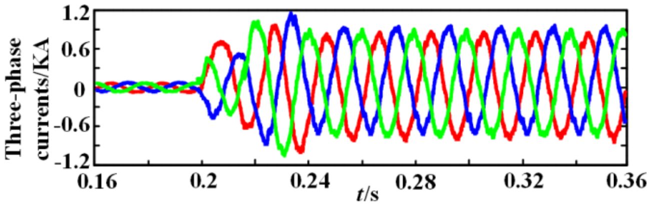

(c) Simulation results of output reactive current of MMC-STATCOM

Figure 4. Simulation results when the reactor is put into system.

Figure 4(a) gives simulation waveforms of 220KV bus voltage before and after MMC-STATCOM are connected into grid. It can be seen that the 220 kV bus voltage drops by about 10% without MMC-STATCOM. However, once the MMC-STATCOM is connected to power grid, the 220kV bus voltage keep at 219kV due to the capacitive reactive power is injected to grid instantaneously. It indicates the MMC-STATCOM has the good ability to restrain voltage fluctuation. Figure 4(b) and (c) show the output reactive power and three-phase output current waveform of MMC-STATCOM. According to Figure 4(b), the reactive power stabilizes rapidly after a small overshoot through a very short response time. Figure 4(c) shows that the output current waveform is good quality and low THD, and the harmonic can be effectively filtered by using a small filtering device.

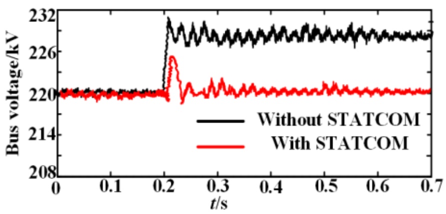

(a) Simulation results of 220kV bus voltage

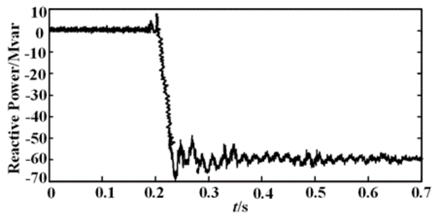

(b) Simulation results of reactive power.

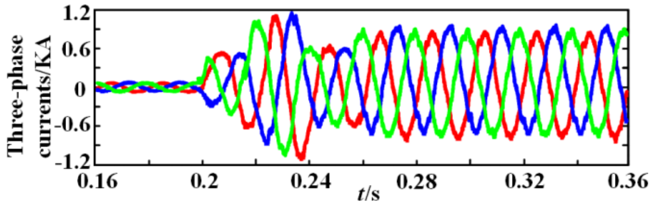

(c) Simulation results of output currents

Figure 5. Simulation results when the capacitor is put into power grid.

At 0.2s, replacing the 60Mvar reactor with the 60Mvar capacitor, the simulated waveform is shown in Figure 5. the 220kV bus voltage increases by 10% due to the input of capacitors when the MMC-STATCOM is not used. Once the MMC-STATCOM is used, the inductive reactive power is quickly injected into grid to suppress the rise of voltage. Therefore, the bus voltage eventually stabilizes around 222kV. Figure 5(a) and (b) respectively show the output reactive power and three-phase current waveform of STATCOM. It can be seen that the overshoot is slightly larger than the overshoot that inhibits the switching of inductive load. This is because the transient process voltage changes greatly due to the large rate of current change in the switching of capacitor.

4.2. Constant reactive power operation control

The purpose of this mode is to change the reactive reference value of STATCOM, and observe the accuracy and corresponding characteristics of the output reactive power. The simulation condition is as follows: the rated voltage is 220kV and the reactive power of STATCOM is limited to (-80, 80) Mvar. At 0.2s, the reference value of reactive power changes from +30Mvar to -30Mvar.

Figure 6(a) shows the active and reactive power waveform of MMC-STATCOM. It can be seen that the MMC-STATCOM can quickly track the reactive power changing, accurately output the corresponding reactive power, and has good dynamic response characteristics. Figure 6(b) shows the three-phase output current waveform of the MMC-STATCOM. It can be seen that the three-phase output current is rapidly in a stable state after a short fluctuation. Figure 6(c) shows that the rapid change of output reactive power has a small impact on bus voltage, which can be ignored.

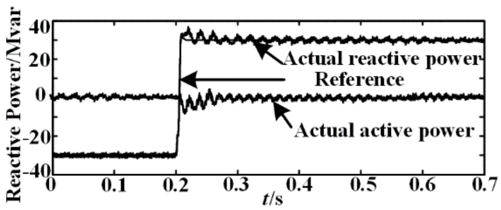

(a) Simulation results of active and reactive power

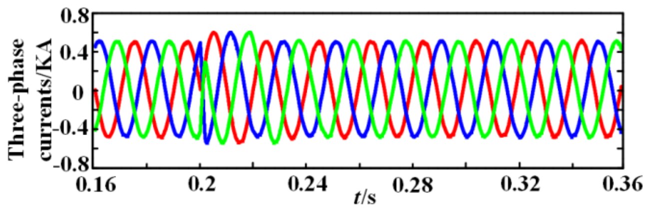

(b) Simulation results of three-phase output current.

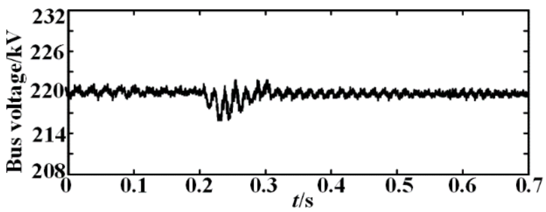

(c) Simulation result of 220kV bus voltage.

Figure 6. Simulation results when it is constant reactive power operation control.

5. Conclusion

Based on the actual operation of a substation, this paper studies the operation control strategy of the MMC-STATCOM. According to the actual parameters of the substation, the control model of

STATCOM is built in PSASP software. Simulation results verify the dynamic response characteristics of the MMC-STATCOM under constant voltage control and constant reactive power control respectively. Simulation results show that the MMC-STATCOM can not only effectively solve the problems of the bus voltage fluctuation, but also can automatically track the system's reactive power changing, dynamically and adjust the reactive power output rapidly.

6. References

[1] L. G. Narain G. Hingoranl, *FACTS Concept and General System Considerations*, Chapter 1 in Understanding FACTS, *Concepts and Technology of Flexible AC Transmission Systems*, New York, John Wiley & Sons, Hoboken, NJ, 2000, pp. 1-64.

[2] FACTS Terms & Definitions Task Force, *Proposed terms and definitions for flexible AC transmission system (FACTS)*, IEEE Trans. on Pow. Del., vol. 12, no. 4, pp. 1848–1853, 1997.

[3] E. Hassan, S. Khan, M. Habaebi, T. Gunawan, B. Hamida, & M. Yaacob, *Effect of modulation index of pulse width modulation inverter on Total Harmonic Distortion*, in Proc. ICISE, International Conference on Intelligent Systems Engineering, Jan 2016, pp.192-196.

[4] F. Shahnia, S. Rajakaruna, and A. Ghosh *Static compensators (STATCOMs) in Power Systems, Springer*, Singapore, 2015.

[5] A. Yazdani and R. Iravani, *Voltage-Sourced Converters in Power Systems: Modeling, Control, and Applications*, John Wiley & Sons, Hoboken, New Jersey, 2010.

[6] Transmission & Distribution Committee of the IEEE PES Society, *Recommended Practice and Requirements for Harmonic Control in Electric Power System*s, IEEE Standard 519-2014, New York, 2014.

[7] H. Akagi, S. Inoue, and T. Yoshii, *Control and performance of a trans former less cascade PWM STATCOM with star configuration*, IEEE Trans. Ind. Appl., vol. 43, no. 4, pp. 1041–1049, Jul./Aug. 2007.

[8] A. Lesnicar and R.Marquardt, *An innovative modular multilevel converter topology suitable for a wide power range,* presented at the IEEE Power Tech Conf., Bologna, Italy, 2003.

[9] A. Dekka, W. Bin, N.R. Zargari, R. L. Fuentes, *Dynamic voltage balancing algorithm for modular multilevel converter: A unique solution*, IEEE Transactions on Power Electronics, vol. 31, no.2, pp.952-963, Feb. 2016.

[10] S. Cui, S. Kim, J. Jung, and S. Sul, *Principle, control and comparison of modular multilevel converters (MMCs) with DC short circuit fault ride-through capability*, in *Proc. IEEE 29th Appl. Power Electron. Conf. Expo.*, Mar. 2014, pp. 610–616.

IOP Conf. Series: Earth and Environmental Science **431** (2020) 012015 doi:10.1088/1755-1315/431/1/012015

Energy storage locating and sizing method in grid-connected micro-grid

Guo Furan[1], Song Wenzhuo[1], Meng Fanbin[1], Zhang Qingfeng[1] and Gao Yao[2]

1 Economics & Technology Institute of State Grid Henan Electric Power Co., Ltd., Henan 450000, China
2 School of Electrical Engineering, Dalian University of Technology, Dalian 116024, China
E-mail: 1602048882@qq.com

Abstract. In micro grid, the distributed generations have a large proportion and the energy storage system is the fundamental structure of the micro grid. Wind and photovoltaic power generation contain intermittent and uncertain characteristics. Energy storage system in micro grid can smooth the volatility of distributed power and supply power to important loads in case of the insufficiency of distributed power generation. In this paper, a location and capacity planning method of energy storage system is proposed. The energy storage installation points are the key points of the system, which are identified based on the electrical distance. Further, the capacity is optimized and solved on these basics. Finally, the effectiveness of the proposed method is verified through case studies.

1. Introduction

With the large consumption of fossil energy and the warming of the climate caused by greenhouse gases, the development of renewable energy power generation is the focus of energy transformation. Research and practice show that the most effective way to develop distributed power supply is to connect the distributed power supply into the grid in the form of micro-grid[1]. However, large-scale grid integration of distributed power supply will bring problems of grid safety and economic operation.

The energy storage system is characterized by its fast power absorption and supply capability, which can provide active and reactive power, stabilize voltage fluctuation and improve power supply reliability. It is a significant means to deal with the uncertainty of distributed generation.

Reference [2] summarized the research status of large-capacity energy storage technology applied to power grid peak regulation and the energy storage system planning methods for centralized and distributed access mode. Reference [3] built a cost-benefit calculation model for the whole life cycle of battery energy storage. Further it built a capacity configuration model of secondary frequency modulation with battery energy storage participation. . Reference [4] analyzed different scheduling modes of photovoltaic energy storage power station and built an energy storage optimization model with the objective of net earnings, which can provide reference information for the selection of energy storage capacity under different scheduling modes and different market environments. According to the different wind power stabilize strategies, reference [5-6] built different capacity optimization models, in which the locations of energy storage are selected at the wind power connection points. . In reference [7], considering the correlations among wind speed, light intensity and load, the opportunity constrained planning method was used to establish the distributed generation location and capacity planning model aiming at the minimum annual comprehensive cost.. reference [8-10] established a two-layer decision model, and the outer optimization model was responsible for solving the planning problem of energy storage system, including the location selection and capacity allocation of energy storage. The inner optimization model is responsible for solving the operation problems of the energy storage system, including generator control and energy storage charge and discharge strategy. .Most of the above researches are on the energy storage locating and sizing optimization models in distribution grid, but rarely of them are applied in micro grid. Moreover, the synchronous energy storage location and capacity optimization will cause the installation location is scattered and the capacity is small at each point. In this paper, an energy storage location and capacity optimization model in the micro grid is proposed. A location determination method of energy storage based on the electrical distance connection coupling degree is provided, which is the first step and followed by capacity optimization. Through the comparison of network loss and voltage fluctuation under different planning schemes different planning schemes, the validity of the proposed method is verified.

2. Planning of the single point

2.1. Energy storage locating

In this paper, the energy storage locating and sizing are determined separately due to the mixed integer nonlinear functions are difficult to solve. Furthermore, the characteristic identification model of complex power network based on electrical coupling connection degree can reflect the heterogeneous structural characteristics of power grid [11].

In power system the electrical distance between node i and node j can be defined as equivalent impedance $Z_{ij,equ}$ between the two points, which is equal to the voltage U_{ij} between node i and node j under unit current from node i shown in Equation (1).

$$\mathrm{Z_{ij,equ}} = \frac{\mathrm{U_{ij}}}{\mathrm{I_i}} = \mathrm{U_{ij}} \tag{1}$$

where, $Z_{ij,equ}$ can be expressed as Equation (1) and Z_{ij} is the element in row i and column j of the node impedance matrix.

$$\mathrm{Z_{ij,equ}} = (\mathrm{Z_{ii}} - \mathrm{Z_{ij}}) - (\mathrm{Z_{ji}} - \mathrm{Z_{jj}}) \tag{2}$$

In an N-node power network, the electrical coupling connection degree of node i is:

$$\mathrm{D_{e,i}} = \sum_{\mathrm{j=1,j\neq i}}^{\mathrm{N}} |\mathrm{Z_{ij,equ}}| \tag{3}$$

where the importance of node i in the power network is represented by the sum of the electrical distance between node i and other nodes in the system. This index can quantitatively describe the strength of the electrical coupling connection between a node and other nodes in the system. The smaller the value of $D_{e,i}$ is, the stronger the electrical coupling effect between node i and other nodes is, and the failure at this node is more likely to cause the overall accident of the system.

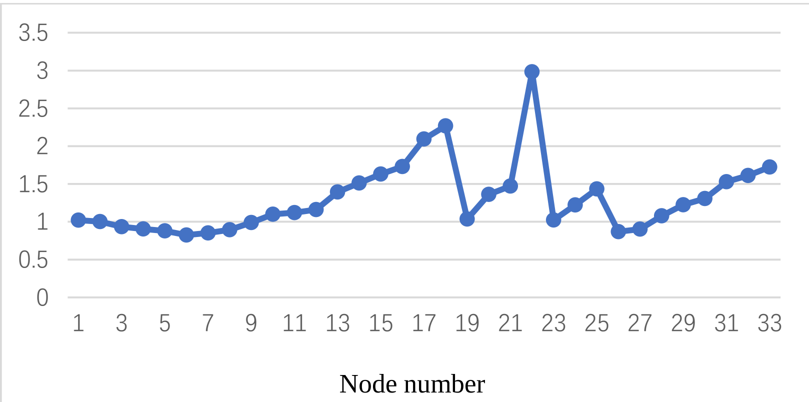

Figure 1. Electrical coupling connectivity index.

IOP Conf. Series: Earth and Environmental Science **431** (2020) 012015 doi:10.1088/1755-1315/431/1/012015

The electrical coupling connectivity index of each node in IEEE 33-node network is shown in Figure 1. The index of $D_{e,i}$ of each node is distributed as follows. The value of $D_{e,i}$ of node 6 is the smallest, that is, the coupling degree of node 6 and other nodes is the strongest. The battery energy storage should be installed at node 6.

2.2. Operation strategy of energy storage

During the peak period of electricity consumption, if the renewable power is larger than load, the excess power will be sent to the higher power grid priority, and the remaining power will be used to the energy storage system charging. If the renewable power is less than load, the energy storage discharge priority to supply power, and the insufficient part is provided by the grid.

During the period of electricity throughs, when the renewable energy power is larger than load, the excess power will be provided to the energy storage charging. If the energy storage is not fully charged, the superior power grid will continue to provide power to the energy storage system. If the power of renewable energy is less than the load, it purchases power from the superior power grid priority and the insufficient part is provided by the energy storage system.

2.3. Optimization of energy storage capacity

Under the premise that the energy storage installation location is known, the optimization of the energy storage capacity is conducted, shown as follows.

$$C = C_{bess} + C_{pline} + C_{pb} \tag{4}$$

$$C_{bess} = \frac{1}{365} * \frac{d(1+d)^{y0}}{(1+d)^{y0}-1} k * S * E_b \tag{5}$$

$$C_{pb} = \sum_{t}^{N_t} cp_t * Pb_t \tag{6}$$

$$C_{pline} = \sum_{t}^{N_t} cp_t * Pline_t \tag{7}$$

where, $C_{bess}$is the installation cost of energy storage; k is the installation cost of per unit capacity; S represents the number of energy storage batteries installed at node 6；E_b is the rated capacity of a single battery; C_{pb} is the arbitrage benefit of energy storage peak and valley; $N_t$is the number of time periods in a day; cp_t is the electricity price; $Pb_{j,t}$ is the charging and discharging power of the battery, where, discharging is positive and charging is negative; C_{pline} is the revenue from buying and selling electricity to the bulk power system; $Pline_t$ is the power exchanged with the bulk power system, where buying electricity from the grid is positive and selling is negative.

The constraints include the power balance of network nodes, voltage amplitude and phase angle constraint, tie line power constraint, charging and discharging constraints and SOC constraint of energy storage.

(1) Node voltage constraint:

$$u_j^{min} \le u_{j,t} \le u_j^{max} \quad j \in 1..n, t \in 1..N_t \tag{8}$$

where, $u_j^{min}$and u_j^{max} is the upper and lower limit of node voltage amplitude, respectively.

(2) Phase Angle constraint:

$$\theta_j^{min} \le \theta_{j,t} \le \theta_j^{max} \quad j \in 1..n, t \in 1..N_t \tag{9}$$

where, θ_j^{min}andθ_j^{max} is the upper and lower limit of node phase Angle, respectively.

(3) Node power balance equation:

$$P_{i,t} = U_{i,t} \sum_{j \in n} U_{j,t}\left(G_{i,j} * \cos\theta_{ij,t} + B_{i,j} * \sin\theta_{ij,t}\right) \tag{10}$$

$$Q_{i,t} = U_{i,t} \sum_{j \in n} U_{j,t}\left(G_{i,j} * \sin\theta_{ij,t} - B_{i,j} * \cos\theta_{ij,t}\right) \tag{11}$$

where, $P_{i,t}$、$Q_{i,t}$ is the active and reactive power injected into node i at time t, respectively. ; $U_{i,t}$、$U_{j,t}$ is the voltage of node i and j ; $G_{i,j}$、$B_{i,j}$ are the real and imaginary parts of row i and column j of node admittance matrix, respectively.
(4) Battery charging and discharging constraints:

$$-S * p_n \leq p_t \leq S * p_n \tag{12}$$

where, p_n is the rated power of a single battery and S is the number of installations to be optimized.
(5) Battery capacity constraint:

$$0.3 * S * E_b \leq E_t \leq 0.95 * S * E_b \tag{13}$$

$$E_{t-1} - p_t = E_t \quad t \in 1..N_t \tag{14}$$

$$E_{24} - p_1 = E_1 \tag{15}$$

where, E_t is the capacity of the battery at time t; E_b is the rated capacity of a single battery; In addition, to ensure the continuous working capacity of the energy storage battery, it is necessary to ensure the consistency of the initial SOC during a day.
(6) Tie line constraint:

$$0 \leq |P_{line,t}| \leq P_{line}^{max} \tag{16}$$

where, P_{line}^{max} is the upper limit of power exchange with large power grid.
(7) Branch constraint:

$$P_{ij} = |V_i V_j (G_{ij}\cos\theta_{ij} + B_{ij}\sin\theta_{ij}) - V_i^2 G_{ij}| \leq P_{ij}^{max} \tag{17}$$

where, P_{ij}^{max} is the upper limit of branch capacity.
(8) Reserve constraint:
According to the trial measures for promoting the construction of grid-connected micro-grid, the micro-grid should guarantee the continuous power supply of important loads longer than 2 hours under the independent operation, shown in Equation (18).

$$(Soc_t - 0.1) * S * E_b \geq P_{cl} * T \tag{18}$$

where, the limit of SOC during charging in independent operation is 0.1; P_{cl} represents the important load and T represents the continuous operating time.

2.4. Experiment analysis
The improved IEEE 33-node system was used for example analysis. In the system, the rated voltage of the system is 10 kV and the allowable voltage offset is plus or minus 7%. The maximum interactive power of the tie line is 1MW, critical load is 15% of the base load and the island operation time is 2 hours. The service life is 15 years and the discount rate is 8%. Battery related parameters are shown in table 1, the peak valley price information is shown in table 2.

Table 1. Battery related parameters.

Rated capacity	$40\mathrm{kW \cdot h}$
Rated charging-discharging power	5kW
Installation cost of per unit capacity	$3000\mathrm{RNB}/(\mathrm{kW \cdot h})$
soc operating range	$0.3 - 0.95$

Taking wind power, photovoltaic power and load power of a typical day as examples, the wind power, photovoltaic power and load power curves of a typical day are shown in figure 2.

IOP Conf. Series: Earth and Environmental Science **431** (2020) 012015 doi:10.1088/1755-1315/431/1/012015

Table 2. The peak valley price.

Period of time	The unit price [RNB/$(KW \cdot h)^{-1}$]
06:00-08:00	0.744
08:00-12:00	1.197
12:00-15:00	0.744
15:00-21:00	1.197
21:00-22:00	0.744
22:00- next day06:00	0.356

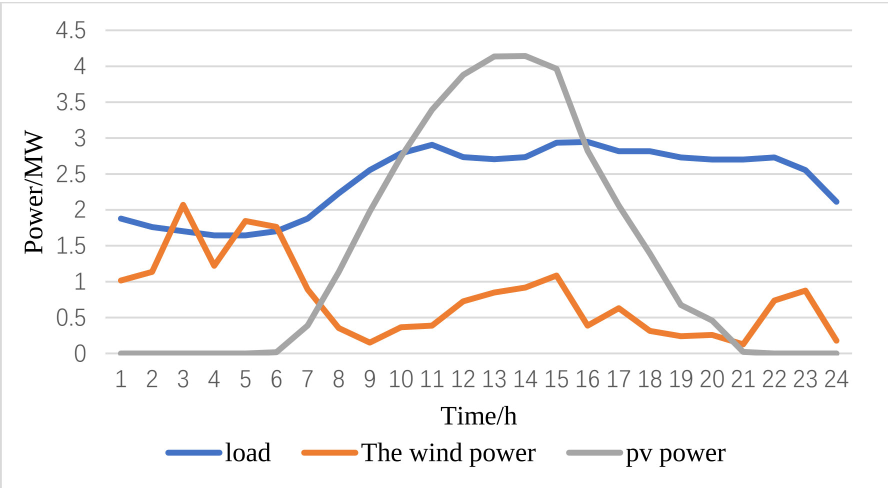

Figure 2. Typical data curve of wind power PV and load.

The result of optimization is that the number of installations is 317, equal to 1.585MW, which met the design specification for access of distributed energy storage system to distribution network and the grade table recommended in technical regulations for access of electrochemical energy storage system to power network.

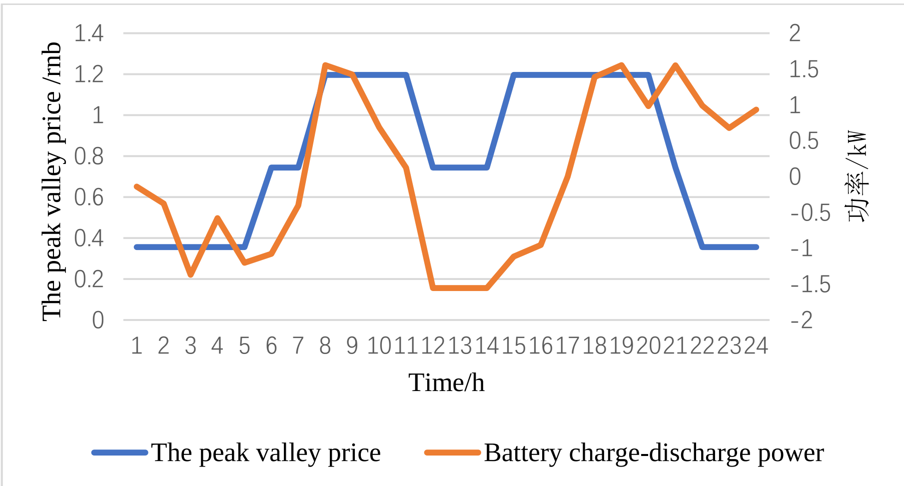

Figure 3. Charging and discharging curve of battery.

Figure 3 shows that the photovoltaic output is larger than the load demand at 12:00-15:00, during which the energy storage battery is charged, and the energy storage battery is discharged at other peak

IOP Conf. Series: Earth and Environmental Science **431** (2020) 012015 doi:10.1088/1755-1315/431/1/012015

periods. Although it is in the load trough period from 2:00 to 6:00, the energy storage battery is charged due to the large wind power. Wind power and tie line power are less than load power at 22:00-24:00, during which the energy storage battery is discharged, which conforms to the operation strategy of energy storage system.

If there is no additional constraints on the installation location of energy storage, the optimization results are shown in Figure 4.

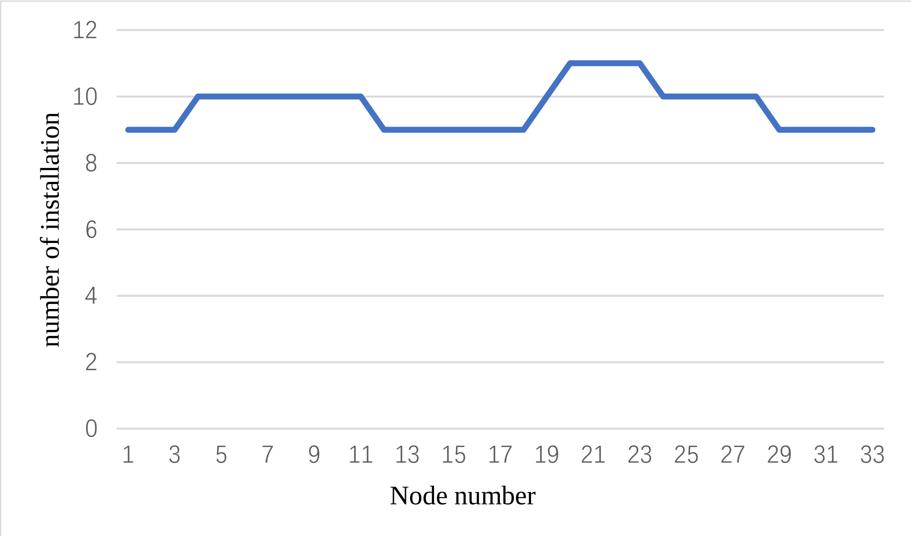

Figure 4. Optimization results of energy storage location without constraint scheme.

The energy storage installation optimization results of each node is not much different and the energy storage installation locations are scattered, and the installation capacity is small at each point,. According to the design specification for access of distributed energy storage system to distribution network, the access power of a single point energy storage is between [400kW, 6MW] at the voltage level of 10kV. In Figure 4, the energy storage power of a single point in this scheme is far less than 400kW, thus this scheme is not feasible.

3. Comparison of different planning schemes

On the premise of meeting the design specification for access of distributed energy storage system to distribution network, the network loss and voltage fluctuation are compared under the three schemes of single-point planning, three-point planning and five-point planning, shown in Figure 5.

Under the three planning schemes, the installation positions of energy storage batteries are all located on the feeder line at the node with high electrical connection degree. Under the three schemes, the network loss are all small and the tendency of the three curves are very close. Only in a few time periods, the result of single-point planning is slightly larger than that of the other two schemes.

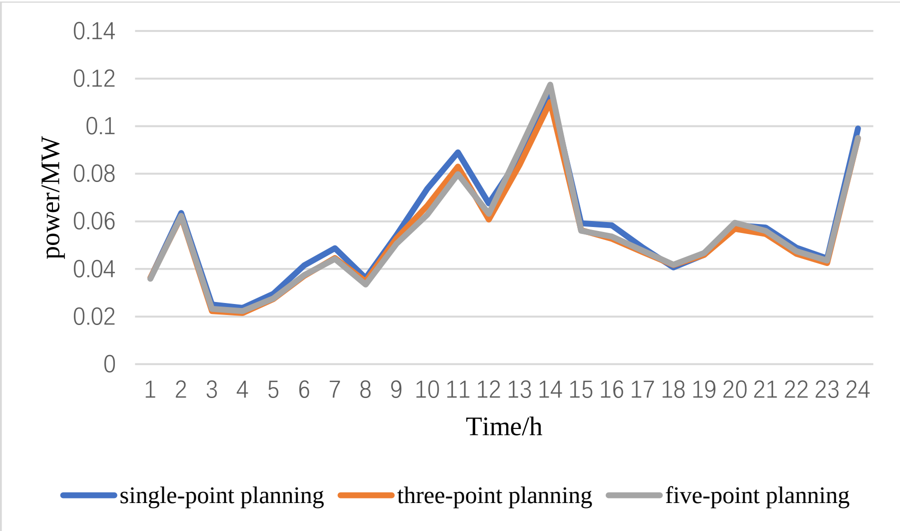

Figure 5. Network loss comparison curve.

The voltage fluctuation curve of node 9 and node 20 are shown in Figure 6 and Figure 7, respectively.

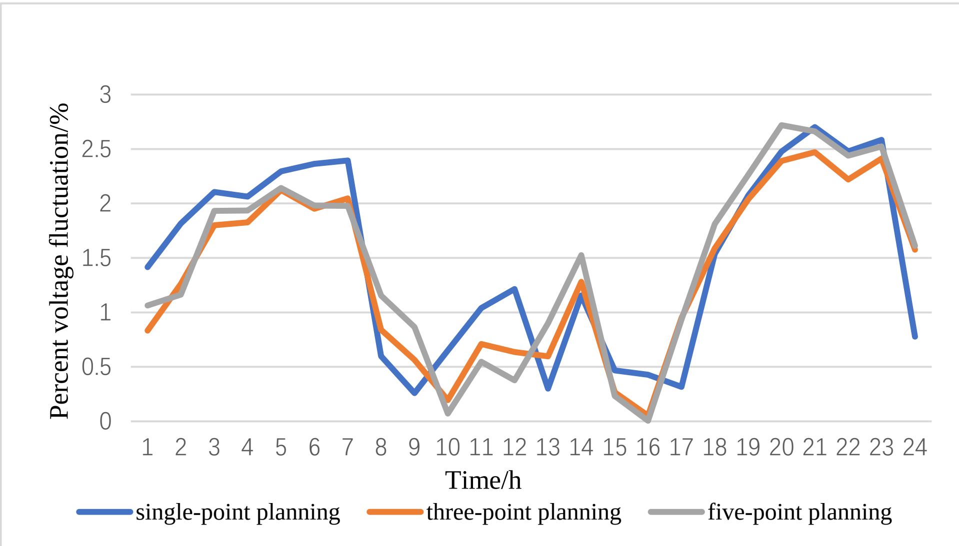

Figure 6. Voltage fluctuation curve of the node9.

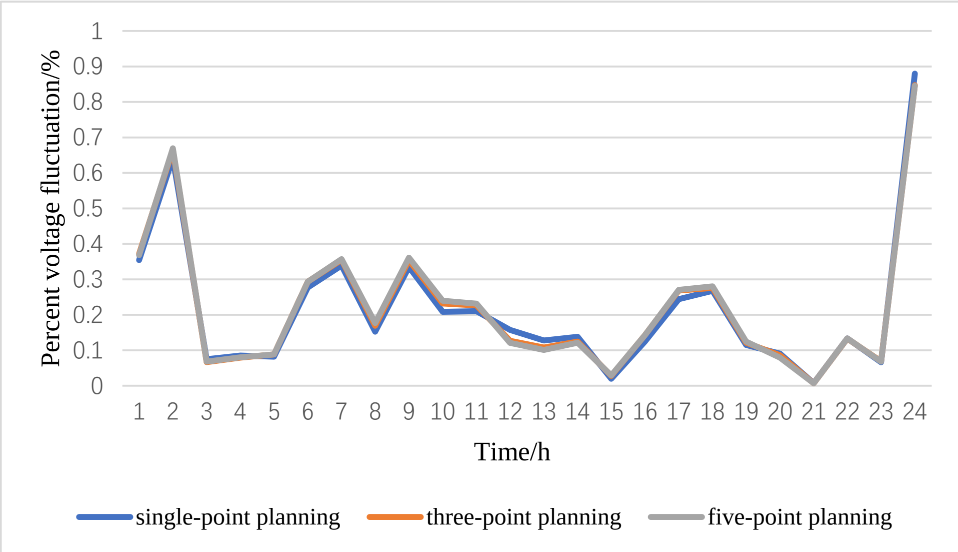

Figure 7. Voltage fluctuation curve of the node20.

In the comparison of voltage fluctuation, it can be seen that under the three planning schemes, the voltage fluctuation is less than the 7% upper limit. In the node near the energy storage installation location, such as node 9 in Figure 6, the voltage fluctuation range is large. During the period of large power charging and discharging of energy storage, the voltage fluctuation under the single-point planning scheme is slightly larger than the other two schemes. At the node far away from the energy storage access point, such as node 20 in Figure 7, the voltage fluctuation almost coincides in the three schemes.

4. Conclusion

Due to the characteristics of short transmission distance and low voltage level of micro grid, the energy storage installed capacity is small. The energy storage equipment configured on a node can not only meet the requirements of national standards, but also reduces the installation workload of the corresponding plant lines. In addition, the investment cost of the energy storage inverter required is also decreased correspondingly. According to the comparison of different schemes, the network loss and voltage fluctuation are far less than the upper limit under the single-point planning scheme. This scheme provides a reference for energy storage planning of micro grid.

5. References

[1] Wang chengshan and li peng. 2010 Development and challenges of distributed generation, micro grid and smart distribution network. *Automation of Electric Power System*, 34 (2) p 10-15.

[2] Xu guodong, Cheng haozhong and Ma zifeng. 2017 Summary of energy storage system planning methods for relieving peak load regulation. *Electric Power Automation Equipment*, 37(8) p 3-11.

[3] Tang jie, Li Xinran and Huang jiyuan. 2019 The energy storage battery with the goal of maximizing net benefit participates in the capacity allocation method of secondary frequency modulation. *Transactions of China Electrotechnical Society*, 34(5) p 963-972.

[4] Xu yan, He Chen and Fu chao. 2019 Analysis on the optimal energy storage capacity configuration of optical storage power station under various scheduling modes. Acta *Energiae Solaris Sinica*, 40(6) p 1632-40.

[5] Ding Ming, Wu jie and Zhang jingjing. 2019Capacity allocation method of hybrid energy storage system oriented to wind power leveling. *Acta Energiae Solaris Sinica*, 40(3):593-599.

[6] Sun yushu, Tang xisheng and Sun xiaozhe. 2017 Research on the energy storage capacity allocation method of wind power fluctuation flattening. *Proceedings of the CSEE*, 37(Supplement) p 88-97.
[7] Zhang shenxi, Li ke and Cheng haozhong. 2015Siting and capacity determination planning of intermittent distributed power supply considering relevance. *Automation of Electric Power System*, 39(8) p 53-59.
[8] Wang yanhong, tei neng ling and ji kang. 2019 Location and capacity optimization scheme of energy storage battery in distribution network with large-scale wind-solar power. *Journal of electric power science and technology*, 2017, 32(2)p 23-30.
[9] Cheng tingli, Chen minu and luo huan. 2017 Multi-objective optimal allocation method for energy storage in distribution network containing renewable energy generation . *Power System Technology,* 41 (9) : 2808-2815.
[10] Chen houhe, liu lina and jiang tao. 2018Optimal allocation method of distributed energy storage economy to improve the voltage quality of distribution network . *Power System Technology*, 42(7)p 2127-35.
[11] Tan yudong, Li xinran, and Cai ye.2014 Key node identification of complex power grid based on electrical distance. *Proceedings of the CSEE*, 34(1)p 146-52.

IOP Conf. Series: Earth and Environmental Science **431** (2020) 012016 doi:10.1088/1755-1315/431/1/012016

Research on protection configuration of AC/DC hybrid distribution network in industrial park

Wenjing XIE[1], Kangheng FENG[1], Jianzong HE[1], Fenglei ZHENG[1] and Rongfu ZHONG[1]

1 Dongguan Power Supply Bureau of Guangdong Power Grid Corporation, Dongguan, Guangdong, China
E-mail: 477611966@qq.com

Abstract. Under the rapid development of power electronics technology, AC/DC hybrid power supply can be used to comprehensively solve the demand for source and supply.The article takes the first comprehensive demonstration project of the dual-stage AC-DC hybrid system based on multi-function power electronic transformer cluster in China as the research object.A distributed renewable energy system simulation platform with AC/DC hybrid is established in the hardware RTDS to simulate and analyze the fault characteristics under different conditions.Based on the fault characteristics and the principle of protection division, in order to ensure that the ranges between the protection zones overlap each other and cover the entire AC-DC distribution network,This paper studies the specific protection zones and configurations for the industrial park system, and has developed a comprehensive protection configuration plan.

1. Background introduction

The traditional AC distribution network has been unable to meet the demand for efficient access load of AC and DC power supplies [1, 2].The problem of high AC/DC energy conversion loss, poor flexibility of power distribution, and low matching between power distribution and power consumption is becoming increasingly serious.Driven by the rapid development of power electronics technology, AC/DC hybrid power supply can comprehensively solve the source and load requirements. The use of AC/DC power technology can reduce the intermediate link of AC and DC conversion in the process of power supply, and improve the economy, reliability and flexibility of the power distribution. It is an important development direction in the field of international power distribution research [3, 4, 5, 6, 7,8].

However, the distributed renewable energy system with AC/DC hybrid has a series of new complex problems such as decentralization, complicated power flow direction, unstable renewable energy intermittent, and AC/DC network cooperative operation[9, 10, 11, 12].

In order to solve these problems, it is necessary to consider the energy usage requirements of different scenarios, such as data centers, office and living parks, and industrial parks. Design and analysis of AC/DC distribution network structure under typical energy scenarios, multi-source optimization configuration in the system, selection and integration design of system primary and secondary equipment, data communication system architecture design, and finally form AC/DC hybrid distributed Renewable energy system demonstration program.

The protection of AC/DC distribution network is still not mature in China. At present, the main protection is based on high-voltage AC-DC protection, and the characteristics of low-voltage AC-DC are not considered.The article takes industrial park as the research object, and establishes a distributed

IOP Conf. Series: Earth and Environmental Science **431** (2020) 012016 doi:10.1088/1755-1315/431/1/012016

renewable energy system simulation platform based on AC/DC hybrid distributed renewable energy system demonstration scheme. Complete the feasibility verification of the demonstration program.
The article discusses the fault characteristics, protection zones and the protection configuration scheme of the industrial park system.It has pointed out the direction for the development of AC and DC hybrid distribution network protection.

2. Introduction of industrial park scene

As the first comprehensive demonstration project of dual-stage AC/DC hybrid system based on multi-function power electronic transformer cluster in China, this project covers three typical energy use scenarios: data center, office and living park and industrial park.Among the three, the industrial park mode uses two transformers to connect back and forth through the voltage level busbars to form a cluster system, which realizes the free bidirectional flow of power between the ports of different voltage grade busbars. It contains four ports, including 10kV AC, 380V AC, 10kV DC and ±375V DC, as shown in Fig 1.

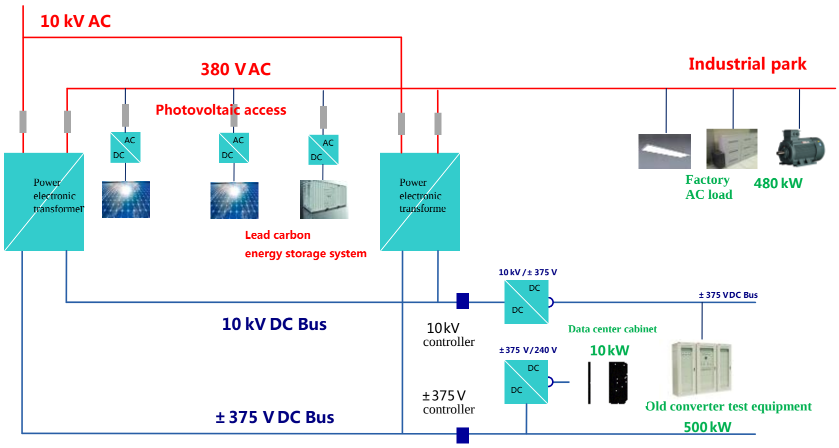

Figure 1. Connection diagram of industrial park demonstration site.

3. Fault test and protection analysis

Models including power electronic transformers, fault current controllers, photovoltaic systems, energy storage systems, etc. are built in RTDS real-time digital simulation software. The RTDS simulation platform is used to connect the tested devices and all the control and protection system devices involved in the test into a complete Simulation test system.
Based on the topology of the industrial park, the RTDS test was used to simulate the failure test of two power electronic transformers under the full load of DC.The simulation is carried out according to the different voltage levels and AC/DC characteristics of the four ports, including the outlet side, the bus side and the load side of the two power electronic transformers, and the fault categories are comprehensive.

3.1. Analysis of fault characteristics in 10kV DC region

The 10kV DC system uses a monopole line operation, the zero pole is grounded through a high resistance (1000 Ω).The positive output voltage is U_{dc} and the zero-pole output voltage is zero.Figure 2 shows the 10kV DC positive pole grounded through R_k .
When a ground fault occurs in which the positive pole generates a resistance, the positive current is as shown in Fig. 3. Due to the presence of the zero-grounding resistance, the positive voltage drops to near zero and the pole voltage remains almost unchanged.

At this time, the positive current is the superposition of the rated current and the grounding short-circuit current. Since the rated current is much larger than the amplitude of the grounding current, the peak value of the fault current is only 1.1 times the load current (from 0.1A to 0.11A).
The short-time discharge of the DC capacitor installed at the corresponding port of the power electronic transformer causes a voltage drop,as shown in Fig. 4.

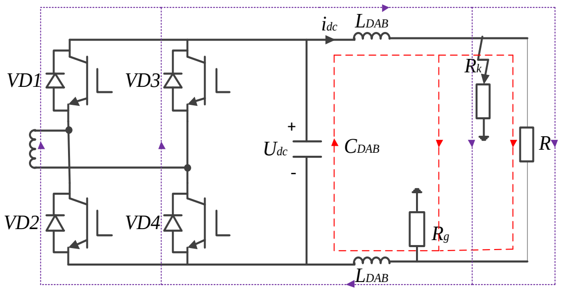

Figure 2. Fault Model of 10kV DC single-pole grounding

As can be seen from the above two figures, the amount of change in current does not have sufficient sensitivity, so overcurrent protection is not applicable to DC positive faults.
The positive voltage will drop and the zero voltage will become a negative voltage, so the low voltage protection can operate correctly.

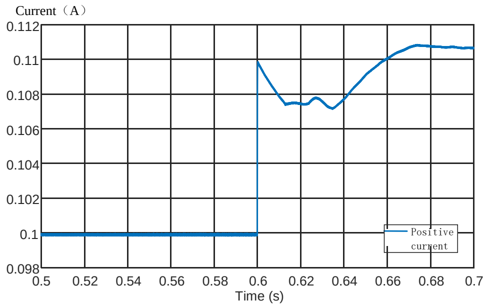

Figure 3. Positive current of 10kV port positive ground fault.

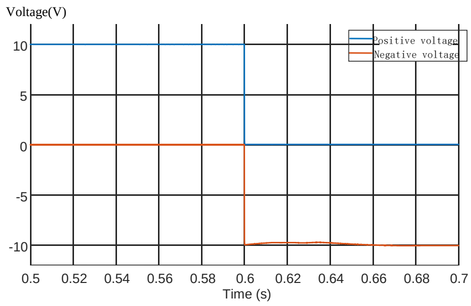

Figure 4. Positive and negative voltages of 10kV port in case of positive ground fault.

When a pole fault occurs in the 10kV DC region, the DC capacitor installed at the corresponding port of the power electronic transformer will discharge to the external circuit. During this process, the short circuit current increases sharply and decays to zero within tens of milliseconds.
Figure 5 reflects the positive and negative current waveforms of the 10kV port in the event of an inter-pole short circuit fault. In the above process, overcurrent protection can effectively protect the faults between the poles.

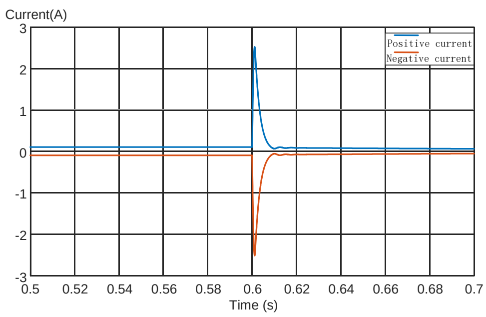

Figure 5. Positive and negative current of 10kV port short circuit between poles.

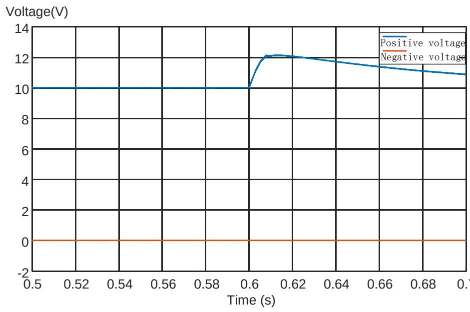

Figure 6. Positive and negative voltages of 10kV port DC open circuit fault.

IOP Conf. Series: Earth and Environmental Science **431** (2020) 012016 doi:10.1088/1755-1315/431/1/012016

Figure 6 reflects the positive and negative poles and the inter-electrode voltage waveform of the 10kV port when the DC-line occurs open-circuit fault. The positive and inter-electrode voltages rise. It can be seen that the overvoltage protection can operate correctly.

3.2. Analysis of fault characteristics in ±375V DC region

The ±375V DC system is operated in bipolar mode with the midpoint grounded through a 10 ohm resistor.

When a unipolar ground fault occurs in the zone, the unbalanced current of the two poles will flow from the midpoint grounding resistance to the ground. Fig.7 reflects the ground current of the ±375V port positive ground fault. Since the value is much smaller than the load current, the overcurrent protection is not applicable to the DC ground fault.

When the system is in normal operation, the positive and negative poles operate symmetrically in the low-voltage DC distribution network system. When a unipolar ground fault occurs in the network, it can be considered that a transient fault power supply is superimposed at the fault location. At this time, the positive and negative lines will no longer operate symmetrically, and an unbalanced voltage will appear between the two poles. There are two reasons for the existence of the unbalanced voltage between the poles: the voltage drop caused by the capacitor discharge of the fault pole; and the offset of the reference potential caused by the ground fault voltage drop. As shown in Figure 8, the unbalanced voltage that occurs after the positive ground fault is negative. The phenomenon is similar when the negative pole is grounded. Therefore, unbalanced voltage protection can be used to protect single pole ground faults.

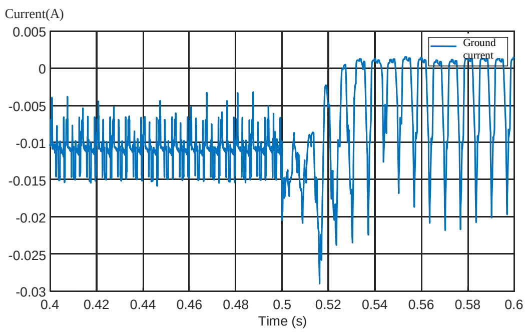

Figure 7. Ground short-circuit current of ±375V DC port positive ground fault.

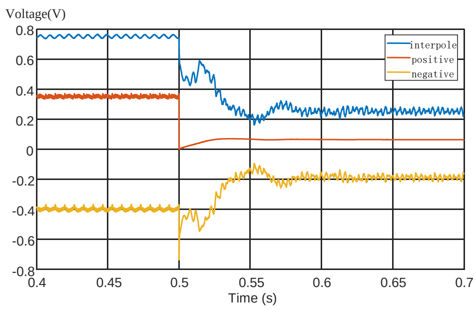

Figure 8. Bus voltageof ±375V DC port positive ground fault.

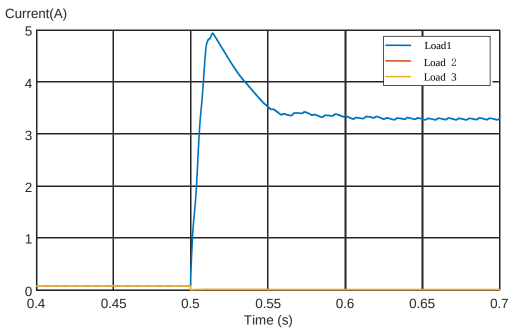

Figure 9. Branch current of ±375V DC port interpole short circuit fault.

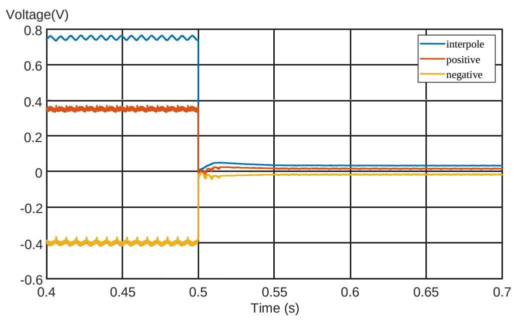

Figure 10. Bus voltageof ±375V DC port interpole short circuit fault.

When an inter-pole short circuit fault occurs, the short-circuit current in the DC line rises rapidly.The short-circuit current mainly flows through the load branch which the fault is located, while the non-fault line current is close to zero.Figure 9 shows the ±375V port load branch current waveform for a short-circuit fault between poles.When the fault occurs, the current of the fault branch rapidly increases, and the non-faulty branch current decreases to zero.So fault isolation can be achieved by overcurrent protection.

Figure 10 shows the voltage waveform of the ±375V port between the inter-pole short-circuit faults. When the fault occurs, the short-time discharge of the DC capacitor, the voltage between the poles drops significantly in a short time. Low voltage protection works correctly.

3.3. Analysis of fault characteristics in 10kV AC region

The 10kV AC bus adopts an ungrounded connection. The fault is the same as the conventional 10kV side action. In the case of single-phase or phase-to-phase faults, large short-circuit currents are generated, so overcurrent protection can be used for fault identification and isolation. So there is nothing special about the protection configuration. No further analysis is done here.

3.4. Analysis of fault characteristics in 380V AC region

In the AC/DC hybrid power grid of this demonstration project, due to the special characteristics of the power electronic transformer, the 380V port is the output of the inverter, and the characteristics of the fault current are different from the short-circuit current of the traditional power grid, mainly in the amplitude and duration.Analysis takes the most severe three-phase short circuit as an example

Figure 11 and 12 shows the short-circuit current waveforms of the inverter bridge arm and the 380V AC port in the 380V AC area. The inverter bridge arm current is over current. In order to protect the converter device and limit the over current peak, the 3ms inverter is blocked. After 5ms, the AC breaker in the fault area moves, and the fault is removed and isolated.

It can be seen that increasing the response speed of the inverter to the fault, the fast blocking inverter can significantly suppress the fault current flowing on the bridge arm.

Under various fault types, the 380V port current fault phase current suddenly increases, while the non-fault phase current does not change much. The above is in accordance with the operating conditions of conventional over current protection.

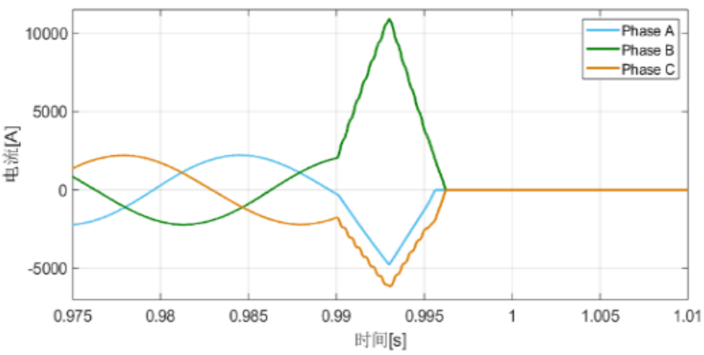

Figure 11. Inverter bridge arm current of three-phase ground fault.

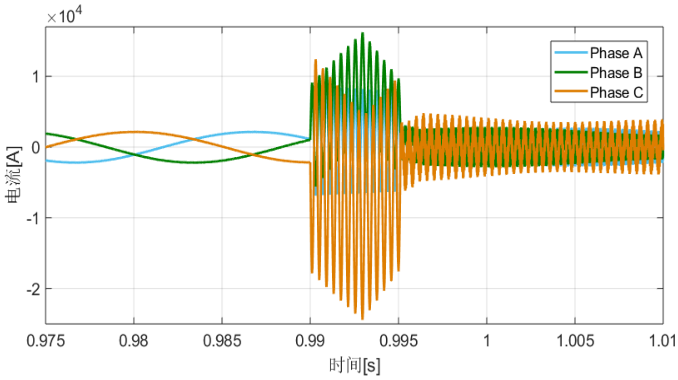

Figure 12.380V port current of three-phase ground fault.

4. Industrial Park Protection Configuration

The power electronic transformer and fault current controller developed by this project have been configured with self protection, which can quickly isolate (cut) the abnormal working conditions that affect the safety of the main equipment. The protection configured by the system discussed in this paper is considered as its backup.
In order to ensure that the protection scopes of the protection zones overlap each other and cover the entire AC-DC distribution network, the industrial park system is mainly divided into several protection zones: 10kV AC protection zone, 10kV DC protection zone, low-voltage AC protection zone, low-voltage DC protection zone and power electronic transformer protection zone, as shown in Figure 13.
1.10kV DC protection zone: The protection range is DC bus and DC outlet switch, and it can also be used as backup for the protection of the equipment connected to the outlet. The main protection functions are DC bus differential protection, overcurrent protection, overvoltage/undervoltage protection.
2. ±375V DC protection zone: The protection range is the part between all DC measurement points, and can be used as a backup for the protection of the equipment connected to the DC outlet. The main protection functions are bus differential protection, overcurrent protection, overvoltage/undervoltage protection, and unbalanced voltage protection.
3. 10kV AC protection zone: The main protection functions include quick-break protection, over-current protection, and zero-sequence protection. The upper level protection of the power inlet switch is used as backup protection for this switch.
4. 380V AC protection zone: It realizes the protection of 380V station power outlet and 380V AC load outlet. The main protection functions are overcurrent protection and overload protection.
5. Power electronic transformer protection zone: The protection range is the four voltage level switches of the power electronic transformer. The protection devices in this zone are arranged according to the transformer, and each transformer is equipped with a transformer protection.

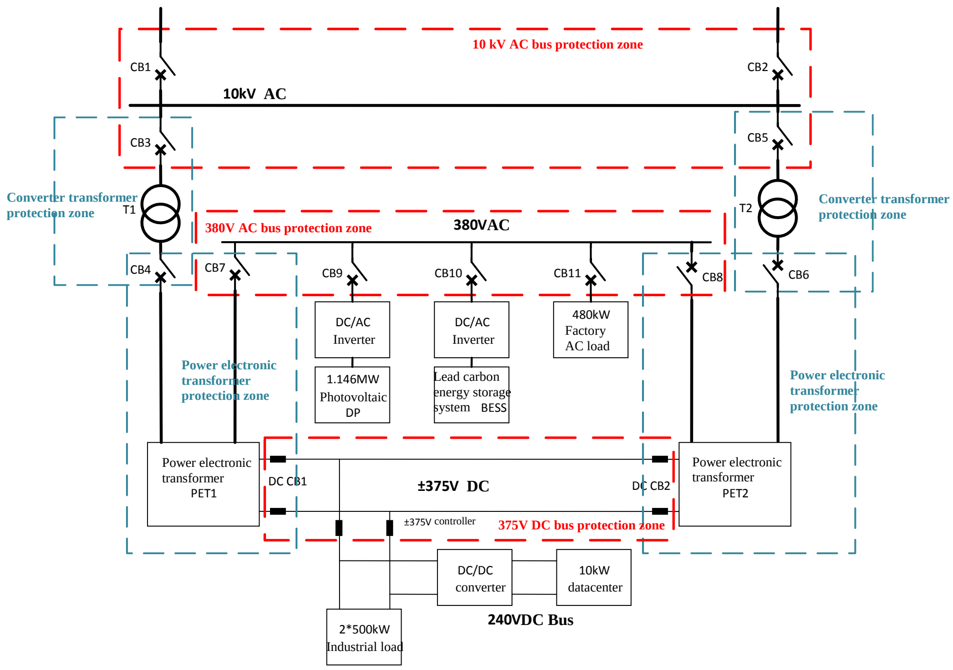

Figure 13. Protection configuration.

5. Summary

In the RTDS real-time digital simulation software, the tested device and all the control and protection system devices involved in the test are connected into a complete simulation test system. Based on the system, a real-time simulation test project is carried out to verify the fault protection test. For the fault characteristics analysis of 10kV AC, 380V AC, 10kV DC, ±375V DC region, this paper proposes a protection configuration scheme for AC/DC hybrid system, which can quickly and reliably remove all kinds of typical faults and ensure the safe and stable operation of the system. This paper provides a reference for the protection scheme of AC/DC hybrid systems with high proportion of distributed renewable energy in China. It has strong reproducibility and scalability.

6. References

[1] Guerrero J M, Loh P C, Lee T L, et al, Advanced Control Architectures for Intelligent Microgrids—Part II:PowerQuality,EnergyStorage,and AC/DC Microgrids[J]. IEEE Transactions on Industrial Electronics,2013,60(4):1263-70.

[2] Kojima,Y,Koshio,M.,Nakamura,S.,Maejima,H.,Fujioka,Y.,Goda,T.. A Demonstration Project in Hachinohe:Microgrid with Private Distribution Line[P]. System of Systems Engineering,2007. SoSE'07.IEEE International Conference on,2007.

[3] Navigant Research. More Than 400 Microgrid Projects are Under Development Worldwide [EB/OL]. http://www.navigantresearch.com/newsroom/more-than-400-microgrid-projects-are-under-development-worldwide,2013-4-2.

[4] Kazuyuki Takada. The 2011 Earthquake & Tsunami and Microgrid Research[C]. Evora 2012 Symposium on Microgrid,2012.

[5] Majumder R. Control of Parallec Converters for Load Sharing with Seamless Transfer between Grid Connected and Islanded Modes[C]// IEEE Pes General Meeting. 2008.

[6] Zhao B,ZhangX,Chen J. Integrated Microgrid Laboratory System[J]. IEEE Transactions on Power Systems,2012,27(4):2175-2185.

[7] ZhengZeng,Rongxiang Zhao,Huan Yang,et al. Policies and demonstrations of micro-grids in China: A review[J]. Renewable and Sustainable Energy Reviews,2014,29:701-718.

[8] Guillermo Jimenez Estevez. Survey of Microgrid R&D in Latin America[C].Tianjin 2014 Symposium on Microgrid,2014.

[9] Anderson,G.W.J.,Watson,N.R.,Arnold,N.P.,Arrillaga,J.A new hybrid algorithm for analysis of HVDC and FACTS systems[P].Energy Management and Power Delivery,1995.Proceedings of EMPD '95.,1995 International Conference on,1995.

[10] Turner K S,Heffernan M D,Arnold C P. Computation of AC-DC System Disturbances. Part II - Derivation of Power Frequency Variables from Convertor Transient Response[J]. IEEE Power Engineering Review,1981,PER-1(11):16-16.

[11] Xuegong Wang,Wilson,P.,Woodford,D..Interfacing transient stability program to EMTDC program[P]. Power System Technology,2002.Proceedings.PowerCon 2002.International Conference on,2002.

[12] Hongtian Su,Ka Wing Chan,Snider,L.A.,TakShing Chung. A parallel implementation of electromagnetic electromechanical hybrid simulation protocol[P].Electric Utility Deregulation,Restructuring and Power Technologies,2004,(DRPT 2004). Proceedings of the 2004 IEEE International Conference on,2004.

Acknowledgments

Funding organisation: Supported by National Key Research and Development Program 2017YFB0903205.

Research on key technologies of highly reliable flexible distribution facing tidal load

Qiang LIU[1], Peifeng SHEN[1], Di WU[2], Zhuofei YU[2], Jian LUO[2], Chen ZHAO[2]

1 State Grid Nanjing Power Supply Company, Nanjing, Jiangsu Province, China
2 NARI Group Corporation, Nanjing, Jiangsu Province, China
E-mail: zchen1016@126.com

Abstract. Under the background of steady development of DC transmission and distribution technology, a series of pilot projects and demonstrations have been carried out gradually in the Engineering application of DC distribution network. In this paper, the typical mode of low voltage DC distribution network- flexible distribution system，is taken as the main research object. The interface between low voltage DC distribution and AC distribution, the distributed energy resource and electric vehicle, and the characteristics of electrical load is considered synthetically. The DC voltage level, power supply radius and capacity, the mode of grounding and connection, and topology structure are analyzed and studied. The typical DC distribution structure is analyzed by simulation. And the DC network load mutual supply experiment system suitable for different scenarios is constructed.

1. Introduction

In recent years, new energy, DC load and conventional AC load developed rapidly [1]. On the one hand, the controllable and adjustable demand of new energy and DC load is Growing continually, on the other hand, the uneconomic operation is common in conventional load [2]. DC distribution is based on flexible DC technology and communication technology, which can effectively solve the above problems of traditional AC distribution, flexible distribution is one type of DC distribution technology [3]. When multiple electric vehicle loads are connected to different platforms, there is the characteristic of tidal power, which requires the distribution network to reasonably control the charging power [4].

Flexible distribution is a composite technology, which is based on voltage source converter based high voltage direct current (VSC-HVDC) and Distribution network operation control [5]. Flexible distribution is equipped with AC/DC converters (PCS) in the distribution station area, the converters in multiple stations are connected by the DC bus, photovoltaic and energy storage are connected directly to the nearby DC bus through the DC/DC converters. Flexible distribution operation control system collects the operation data of each station and optimizes the power flow [6]. The converter (PCS) of Flexible platform area converter does not need H-bridge cascade or modular multilevel, but only needs two/three level technology to realize the transformation from low-voltage distribution voltage to DC supply voltage. Flexible distribution could solve the "two-way" problem caused by the new energy access to the distribution network, realize the efficient absorption of new energy, and improve the convenient access and orderly regulation of new loads such as electric vehicles [7].

State Grid Jiangsu Electric Power Company Science and Technology Project:
Key technology research and engineering demonstration of cooperative operation
and control for flexible platforms facinglarge scale electric vehicles(J2019066)

IOP Conf. Series: Earth and Environmental Science **431** (2020) 012017 doi:10.1088/1755-1315/431/1/012017

2. System architecture of flexible distribution

Flexible distribution is based on AC distribution network, AC/DC converters are installed on the side of the AC feeder in each distribution station to form several independent AC/DC distribution networks. DC distribution systems are connected by the DC bus to form a multi-terminal AC/DC distribution network system, DC loads such as charging piles and distributed power supply are connected to the DC bus. The typical system architecture of flexible distribution is shown in figure1, the DC bus voltage usually choose 750~900V.

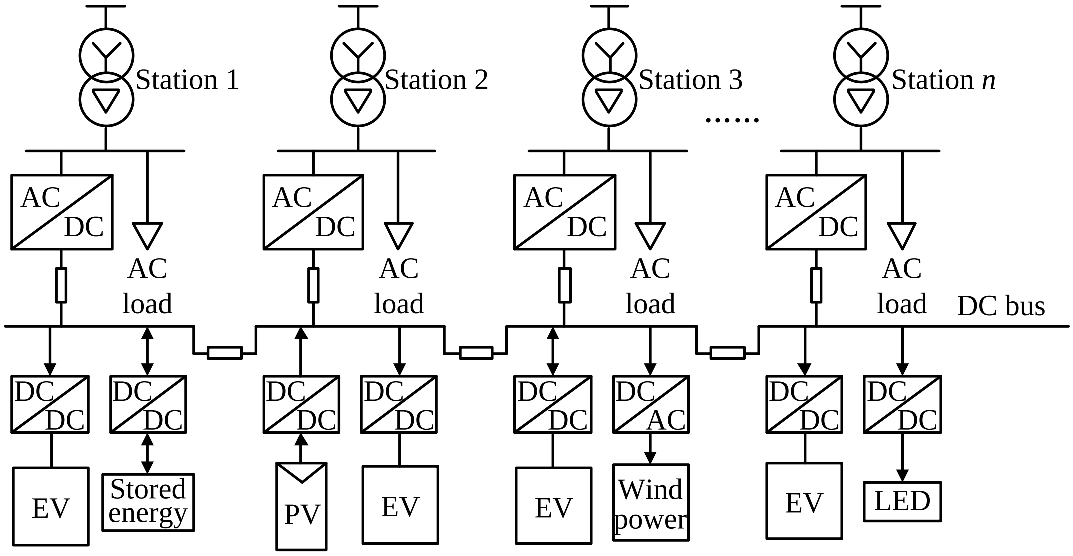

Figure 1. The typical system architecture of flexible distribution.

The main operating modes of flexible distribution include multi-terminal power supply, single-terminal power supply and fault isolation, as shown in figure 2. When the grid operating boundary or load condition changes, the multi-terminal AC/DC system can automatically switch to the operating mode suitable for the new operating conditions, forming the switching relationship between the operating modes and corresponding specific conditions. Each VSC works in single-end power supply mode when there is no sudden large capacity load and the distribution transformer load rate is in economic interval. When sudden large-capacity load is connected, power flow can be transferred to the sudden load through the dc interconnection system, and the power flow can be withdrawn when the capacity demand is small. The converter at the fault end would be removed for fault isolation when fault occurred in multi-terminal AC-DC system, and reconnect the DC grid after fault recovery.

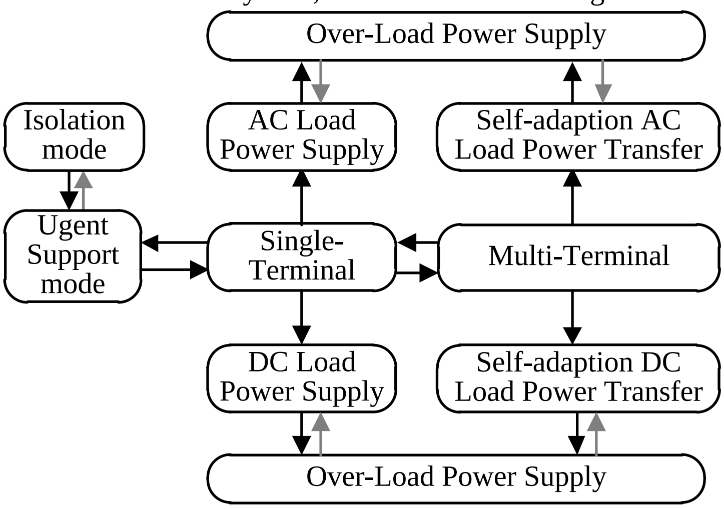

Figure 2. The main operating modes of flexible distribution

3. System analysis of flexible distribution

The design of flexible distribution topology need according to the data of grid and load. The optimal interconnection of nearby zone node is obtained by using the genetic optimization algorithm. The capacity of flexible station system for electric vehicles could be fully increased by capacity complementation. In this way, the voltage of overload area could be improved and the network loss could be decrease. Specific optimization steps are as follows:

3.1. Objective function

The optimal object of this project considers three aspects: 1) Largest active capacity during the whole time of the day when the network is added; 2) Minimum overall voltage deviation of the network; 3) Minimum network loss.As follows:

(1) Maximum active capacity during the whole time of the day.

$$\max \sum_{t=1}^{T}\sum_{i=1}^{N}\Delta P_{t,i} \tag{1}$$

Where: $\Delta P_{t,i}$ is the capacity increased of node i in time period$t$ after optimization of interconnected, N is the number of network nodes, T is the number of study periods. Considering the timing sequence characteristics of distribution transformer load at different nodes, it is assumed that the time period when the load rate of heavy and overload distribution transformer is less than 70% can be independently undertaken, otherwise the interconnection node output is required, in this way, the active capacity of the network increased by interconnection is calculated.

(2) Minimum overall voltage deviation of the network

$$\min \sum_{t=1}^{T}\sum_{i=1}^{N}\left|\frac{U_{t,i}-U_n}{U_n}\right| \tag{2}$$

Where: U_n is nodal standard voltage, generally selected as 1; $U_{t,i}$is voltage amplitude of node$i$ in time period t.

(3) Minimum network loss

$$\min \sum_{t=1}^{T}\sum_{j\in B}P_{loss,t,j} \tag{3}$$

Where: B is the collection of network branches, $P_{loss,t,j}$is the loss of network in branch j.

3.2. Constraint condition

(1) Constraints of distribution transformer capacity

$$\sqrt{P_{i,t}{}^2+Q_{i,t}{}^2}\le S_i \tag{4}$$

Where: S_i is distribution transformer capacity of node i, $P_{i,t}$ and $Q_{i,t}$ is distribution transformer active and reactive load of node i in time period t.

Further, for interconnected nodes, the load rate of both nodes after binding interconnection is lower than 70% to ensure the load balance. As follows:

$$\sqrt{P_{j,t}{}^2+Q_{j,t}{}^2}\le 0.7\cdot S_i \tag{5}$$

Where: j is the collection of interconnection nodes.

(2) Constraints of power flow voltage and current

$$\underline{U}\le U_{i,t}\le \overline{U} \tag{6}$$

$$\underline{I}\le I_{ij,t}\le \overline{I} \tag{7}$$

Where: $U_{i,t}$ is the voltage amplitude of node *i* in time period *t*, $\underline{U}$ and $\bar{U}$ is lower bound and upper bound of voltage, $I_{ij,t}$ is the current amplitude of branch *i-j* n time period *t*, $\underline{I}$ and $\bar{I}$ lower bound and upper bound of current.

3.3. Solution algorithm

Genetic optimization algorithm is used to solve the optimal interconnection of this scheme. The solution steps are as follows:

(1) Input basic network parameters, including node parameter matrix, line parameter matrix, 24 time period load matrix of distribution transfoemer.
(2) Generating the initial population randomly with the size of 50.
(3) Calculating the fitness value of each individual, Fitness value is obtained by weighting the three objective function values.
(4) New individuals are generated by selection, crossover and mutation operations, and calculating the fitness value of new individuals. Compared with the fitness value of original individuals, the new population is gradually generated by retaining the larger one.
(5) Setting the maximum number of iterations to 100, finally decode and output the result.

4. Key technologies of flexible distribution

4.1. Planning and design

4.1.1. Design of voltage. The basic requirements of selecting DC supply voltage are to meet the relationship of load supply demand, capacity and operation economy. (1) Power supply capacity and radius. The higher the DC distribution voltage level, the stronger the power supply capacity, the larger the power supply radius. (2) Compatibility with AC grid. The DC voltage level should match the AC distribution network voltage level, such as 35kV, 10kV and 380V. (3) Power supply efficiency and operating loss. The overall efficiency of energy conversion should be the highest. (4) Compatibility with converters. The DC voltage level is closely related to the efficiency and stability of converters.

4.1.2. Design of capacity. The capacity design of PCS in the flexible distribution system should fully consider the large-scale access requirements of renewable energy and electric vehicles, especially the access demands of large-capacity distributed power sources such as light and storage and charging stations. The capacity design methods are as follow: Firstly, the DC load of each station area is calculated and analyzed, and a certain DC mutual supply capacity is considered. And then, the transfer capacity of AC load is calculated and analyzed, the system capacity is designed based on DC load, DC transfer capacity and AC transfer capacity. Lastly, the PCS capacity of each station is configured according to Historical average available capacity.

4.1.3. Network architecture. The basic requirements of selecting DC supply voltage are to meet the relationship of load supply demand, capacity and operation economy. The Architecture of flexible distribution system includes star power supply structure, ring power supply structure, bus power supply structure and tree power supply structure. The design principles are as follows: the interconnection selection results of the station area, the power supply reliability demand, power supply radius and system design cost. Grounding mode needs to consider grounding mode of AC side filter and DC side, the design principles are as follows: (1) Provide reference potential for DC distribution system. (2) Restrain the zero-sequence current by designing zero sequence circuit. (3)Improve the transient characteristics of DC system in case of AC/DC fault.

4.2. Operational control

The operation control system of the flexible distribution is composed of three levels: system level, operation level and equipment level. The flexible distribution system can ensure the economic operation and stable operation of the region through the regulation of PCS, energy storage and DC load, and realize the coordination and interaction between regions through inter-region scheduling.

4.2.1. System management layer. Including energy management and operation control, operation mode switch, flow scheduling between different platform, source-grid-load and storage coordination control, start-stop control, grid tied/off control, single/multiple terminal control. The main task of the system management is to realize the system level functions of larger spatial scale and time scale, and to provide auxiliary decision-making for the coordination and scheduling between regions.

4.2.2. Centralized coordination control layer. Including every operation mode, such as control and distribution of flow in the platform, multi-terminal coordinated control(slope control or droop control), AC/DC load transfer, fault isolation, fault operation(emergency power support), fault recovery, stable control. The main task of centralized coordination control layer is to determine and issue the control instructions of local device according to the operating objectives of the system management layer, adjust the operation mode, working mode and power instructions of each local device, and summarize and analyze the status of each local device and upload it to the system layer.

4.3. Key equipment
The key equipment of DC distribution includes AC/DC converter, coordinating controller.

4.3.1. AC/DC converter(PCS). PCS usually use VSC(Voltage Source Converter). In DC distribution network, low voltage PCS mainly have the following applications: (1) As the supply power of the low-voltage dc bus, it is commonly seen in the low-voltage dc distribution network. (2) As the backup power supply circuit, it is often seen in multilevel dc distribution network. (3) As the reverse power loop from DC to AC. The controller of converters could adopt master-slave control or independent control, and the independent control adopts bi-directional active power (P)-DC voltage (Udc) slope control. The P-Udc droop strategy proposed in this paper is aimed at the active bi-directional flow VSC, as shown in figure 3 Slope independent variable is Udc and dependent variable is active power flow P, When the active power flow control target is adjusted, the DC bus voltage level is changed to achieve instantaneous active power and DC voltage rebalancing.

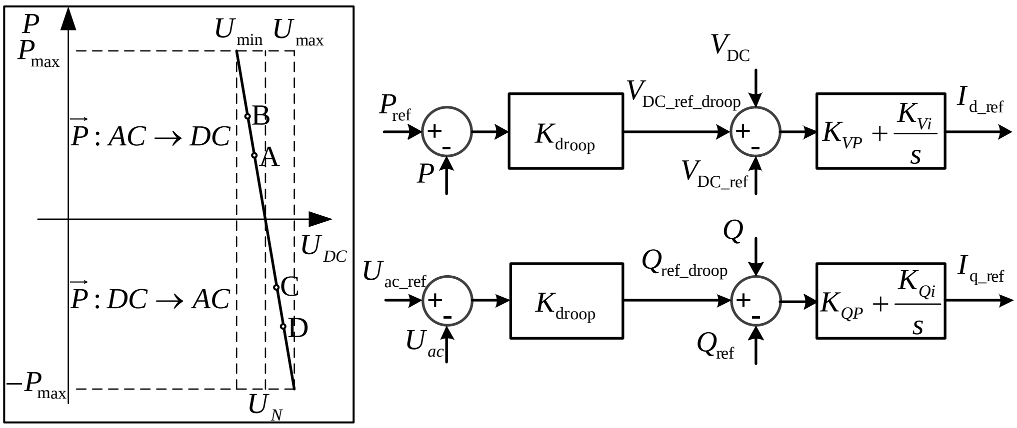

Figure 3. Diagram of droop control strategy

4.3.2. Coordinating controller of flexible distribution. Flexible station coordinate controller can detect the information of the distribution network, such as running data, power grid status, the information would be summarized and analyzed by communication system. In this way, the working state of the current distribution network and the most suitable system operation mode are obtained. The flexible distribution coordination controller can also realize the distribution network control objectives, including: (1) Load concentration method for low load state of system. (2) Recovery mechanism for temporary failure states.

IOP Conf. Series: Earth and Environmental Science **431** (2020) 012017 doi:10.1088/1755-1315/431/1/012017

5. Simulation experiment system

In this paper, a flexible distribution simulation experiment system based on DC network technology is built to conduct load mutual supply experiment of distribution network. The scheme of operation control and safety protection is verified on the experiment platform. In this experiment system, the capacity simulation ratio is 80:1, the AC voltage simulation ratio is 10:1, the DC voltage simulation ratio is 1:1. The wiring layout of the experiment system is shown in figure 4. The experiment platform consists of one dynamic mode booster transformer, four sets of analog transformer stands, six panel cabinets, three V2G AC load cabinets and battery cabinets. The six panel cabinets consists of an incoming line cabinet, four converters and one DC feedback load cabinet, among them, four converter cabinets have the same structure, and each AC/DC converter cabinet contains one AC/DC converter.

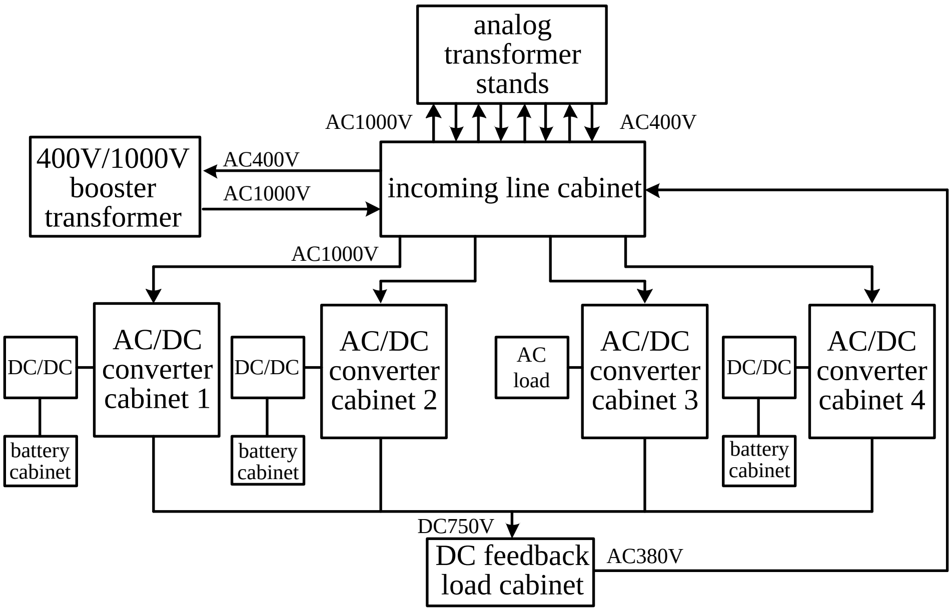

Figure 4. Structure chart of experiment platform

The DC load of the flexible distribution platform system is set to be low, the PCS in the two areas will be used to conduct the DC load transfer experiment to meet the DC load power supply. The experimental waveformis shown in figure 5. The experiment results show that the DC voltage is stable at 750V, the active power flow in the station is controlled according to the set target, and the deviation from the active power target value in the respective stations is less than 3%, and a good dynamic response process is indicated.

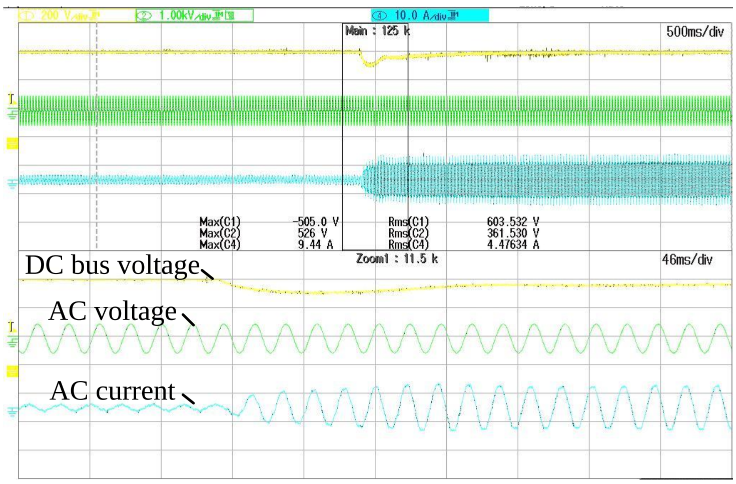

Figure 5. Experimental waveform of DC load transfer

IOP Conf. Series: Earth and Environmental Science **431** (2020) 012017 doi:10.1088/1755-1315/431/1/012017

6. Conclusion

The application of DC distribution technology can promote the adjustable and controllable in distribution network, and realize the transfer of distribution network load and inter-regional power flow. In this paper, the typical mode of low voltage DC distribution network-flexible distribution system is taken as the main research object. The method of selecting points and capacity is studied, and key technologies such as topology architecture, voltage, operation control and key equipments are studied. The simulation experiment platform is set up for experimental verification, the experimental results verify the feasibility of the flexible distribution and the control strategy.

7. References

[1] XIONG Xiong, JI Yu, LI Rui, et al. An Overview of Key Technology and Demonstration Application of DC Distribution and Consumption System[J]. Proceedings of the CSEE, 2018, 38(23): 6802-6813.

[2] ZENG Rong, ZHAO Mingyu, ZHAO Biao, et al. A Prospective Look on Research and Application of DC Power Distribution Technology[J]. Proceedings of the CSEE, 2018, 38(23): 6791-6801.

[3] ZHANG Jinlong, SHI Shuqing, YANG Haisen, et al. Overview of Development of DC Power Distribution Network[J]. SOUTHERN ENERGY CONSTRUCTION, 2016, 3(S1): 93-98.

[4] Giel V D B, Jeroen S, Johan D . A critical review of power quality standards and definitions applied to DC microgrids[J]. Applied Energy, 2018, 229: 281-288.

[5] MA Zhao, JIAO Zaibin, LI Rui. Network Structures and Key Technologies of DC Distribution Systems[J]. Power System Technology, 2017, 41(10): 3348-3357.

[6] HUANG Jingye, LI Hui, CHEN Xueqin, et al. Review of Domestic and International Standardization of Low Voltage Direct Current[J]. Electrical & Energy Management Technology, 2018(22): 6-11.

[7] WU Jun, WU Di, ZHU Jinda, et al. Grounding Method Design of Multi-terminal Flexible DC Distribution[J]. Proceedings of the CSEE, 2017, 37(9): 2551-2560.

Acknowledgments

This work was supported by State Grid Jiangsu Electric Power Company Science and Technology Project: Key technology research and engineering demonstration of cooperative operation and control for flexible platforms facing large scale electric vehicles (J2019066).

Chapter 3:
Mechatronics

IOP Conf. Series: Earth and Environmental Science **431** (2020) 012018 doi:10.1088/1755-1315/431/1/012018

Research on virtual synchronous generator grid-connection based on phase-locked loop

Shun Wang[1], Xuemei Zhu[1], Yijie Fan[1], Shuai Shao[1] and Changyan Lei[1]

1 Nanjing Normal University, Nanjing, China
E-mail: wangshunnjnu@foxmail.com

Abstract. When a single Virtual Synchronous Generator (VSG) is connected to the grid, the output voltage amplitude and frequency are significantly different from the grid voltage, which will impact the power grid. In order to solve this problem, the paper proposes a grid-connected pre-synchronization control method. By controlling the virtual synchronous generator based on the Phase Locked Loop (PLL) pre-synchronization unit, the voltage amplitude, frequency and phase of the VSG output before the grid connection can be consistent with the grid side, reducing the instantaneous impact of the grid. At the same time of the current, the output voltage of the virtual synchronous generator is stabilized. The single-machine VSG grid-connected model was built on the MATLAB/Simulink simulation platform and the effectiveness of the method was verified.

1. Introduction

When the VSG control system operated by the island is merged into the large power grid, in order to prevent the grid-connected impact from the difference between the VSG output voltage amplitude and the frequency and the grid voltage, a certain technology is needed to make the VSG output voltage before the grid-connected switch is closed. This technology is called pre-synchronization technology [1-3]. Literatures [4-6] proposed a variety of distributed energy quasi-synchronous grid connection methods by using the idea of quasi-synchronous parallel devices to achieve single pre-synchronous grid connection. In literatures [7-9], a pre-synchronization technique using droop control is proposed to regulate the voltage output of the inverter through indirect control of voltage, phase Angle and frequency. Literature [10] studies the micro-grid system composed of different power sources, and the regulation instructions in the power control system with low inertia, and then proposes the pre-synchronous control method suitable for the micro-grid with multiple power sources. The grid connection method controlled by detecting the phase Angle difference of VSG is simple to operate, but slow to respond, requiring several seconds [11]. Based on the Phase Locked Loop (PLL) grid-connected method, the Phase Angle difference between the output voltage of the power grid and the system is detected, and the closed-loop control of Phase Angle difference is realized through the PI regulator [12-15].

2. VSG control strategy

2.1. Basic principle of control system

As shown in figure 1, the voltage source three-phase full bridge topology is selected as the carrier of VSG in this paper, and the energy storage is replaced by an ideal DC source. From left to right are DC voltage source, DC support capacitor, inverter, LC filter, switch and power grid at PCC parallel point. The inverter inverts the DC voltage and the LC filter can filter out the high harmonics near the switching frequency. PCC is the public connection point between micro grid and large power grid. By closing the switch at the PCC point, the inverter can achieve grid-connected operation mode. While the switch is turned on, the inverter is self-contained, forming island operation mode.

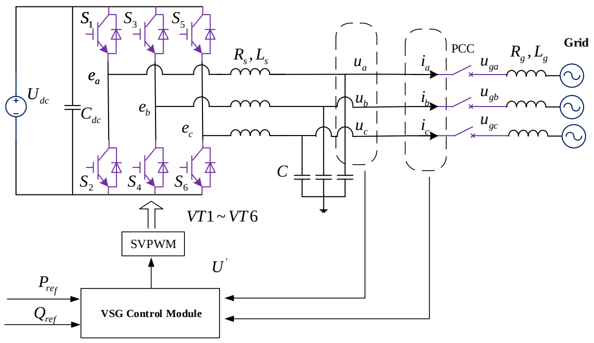

Figure 1. Virtual synchronization control system.

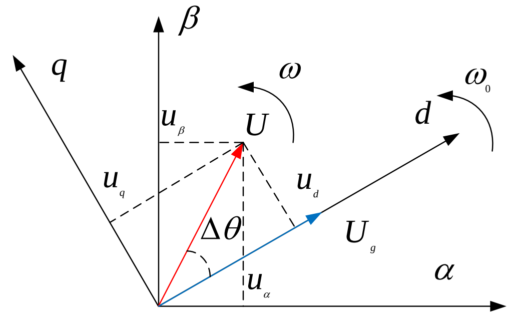

Figure 2. Grid synchronous voltage vector.

2.2. Phase-locked loop control

To achieve the purpose of VSG and grid voltage synchronization, PLL control technology first obtains the frequency, amplitude and phase of VSG and grid voltage, and then controls them.

Vector diagram model is shown in FIG. 2. Constant power Park variation is adopted for coordinate change, as shown in equation (1).

$$C_{abc/dq}=\sqrt{\frac{2}{3}}\begin{bmatrix}\cos(\omega t) & \cos\left(\omega t-\frac{2\pi}{3}\right) & \cos\left(\omega t-\frac{2\pi}{3}\right)\\ -\sin(\omega t) & -\sin\left(\omega t-\frac{2\pi}{3}\right) & -\sin\left(\omega t-\frac{2\pi}{3}\right)\end{bmatrix} \tag{1}$$

When the VSG is connected to the grid, the controller detects the voltage difference between the two sides of the PCC in real time. When the effective value of Δu is less than the threshold value 311×10% ≈30V, it indicates that the voltage difference between the two sides of the PCC is small enough to realize the synchronization of the voltage of the VSG and the voltage of the power grid, and the VSG can be connected to the grid.

The schematic diagram of PLL-based VSG synchronization control is shown in figure 3. In the figure, U_s is the voltage amplitude setting value of VSG control system, U_m is the voltage amplitude of the machine terminal, U'_{ref} is the voltage amplitude instruction value of the machine terminal, ΔU_s is the voltage amplitude synchronization quantity of the power grid, and $\Delta\omega_s$ is the phase synchronization quantity. The three-phase PLL is used to obtain the phase, amplitude and frequency of the grid, and ΔU_s and $\Delta\omega_s$ are controlled to 0 to achieve synchronization with the grid.

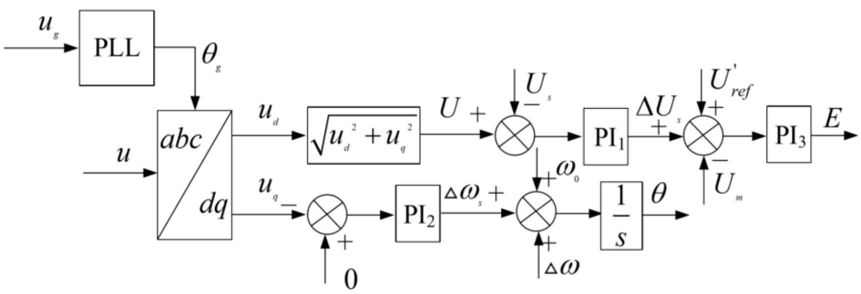

Figure 3. VSG grid-connected synchronization control.

Figure 4 shows the simulation waveform of synchronous grid connection. In the figure(a), ωt_1 is the phase of the grid, ωt_2 is the phase of VSG. In the figure(b), u_{ga} is the *a*-phase waveform of power grid voltage, and u_a is the *a*-phase waveform of VSG voltage. Add the pre-synchronization control strategy on the VSG model to realize the smooth grid connection of VSG. Take the output voltage of VSG and the phase of the grid and control it through the phase-locked loop, so that the *q*-axis component is 0 and the *d*-axis component is the amplitude of the grid (the *q*-axis component of the grid is 0 and the *d*-axis component is its amplitude), so as to realize pre-synchronization.

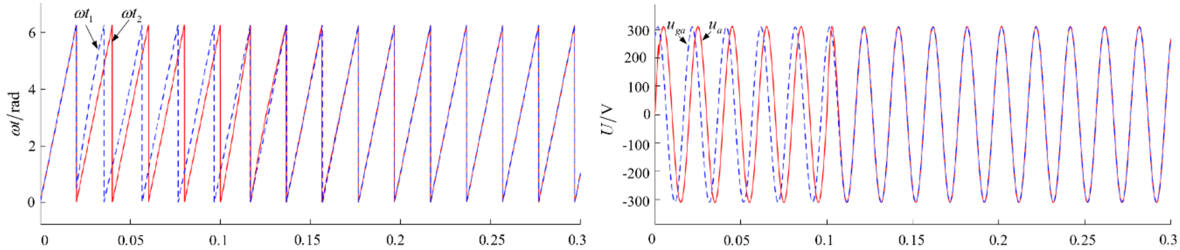

(a) Phase tracking (b) Voltage tracking

Figure 4. Synchronous grid connection waveform.

3. Experimental simulation verification

As shown in figure 5, the VSG control model was built.

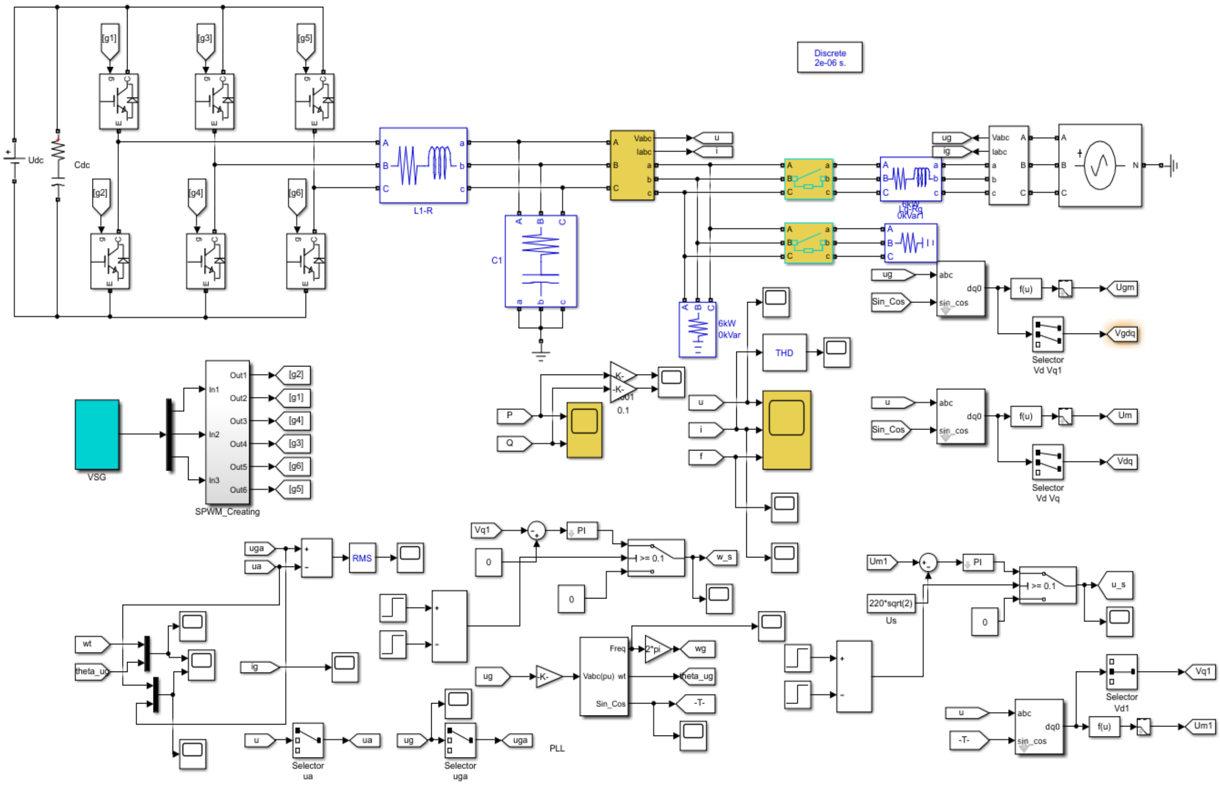

Figure 5. VSG simulation model.

System parameters are selected as shown in table 1 below:

Table 1. Simulation parameters.

Parameter	Value	Parameter	Value
U_{dc} (V)	800	Q_{ref} (Var)	0
U_g (V)	220	L_i (mH)	8
f_0 (Hz)	50	P_{ref} (W)	6000
f_c (KHz)	20	C (μF)	3

The inverter under the control of VSG is connected with 6kW load when it is off-grid and connected with 5kW load in parallel at 0.1s. The inverter adopts LC filter, and the output reference active/reactive power instruction of the inverter is 6kW/0kVar.After parameter setting, the system is simulated and analyzed.

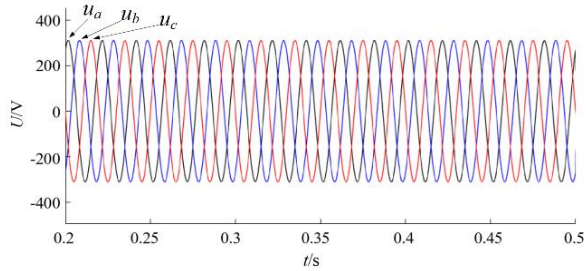

Figure 6. VSG voltage waveform.

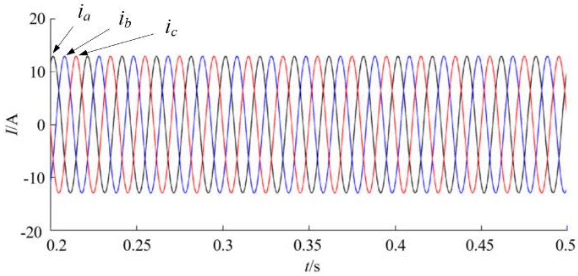

Figure 7. VSG current waveform.

VSG closes the grid-connected switch PCC to realize the grid-connected operation of the system. When the power grid runs normally, its three-phase voltage is balanced, but the sudden change of load will lead to the fluctuation of the amplitude and frequency of the power grid voltage. When VSG is connected to the grid, its voltage is clamped by the grid, and the amplitude and phase can be synchronized, as shown in FIG. 6 and 7. The voltage and current connected to the grid have high sinusoids and low harmonic distortion rate.

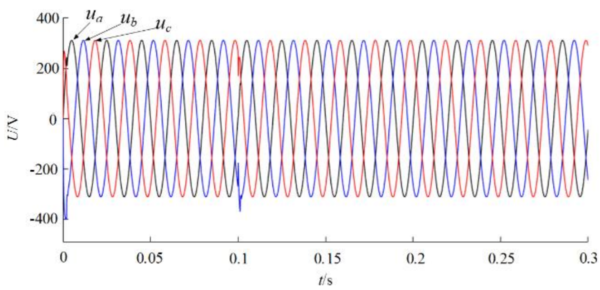

Figure 8. Voltage waveform with sudden load.

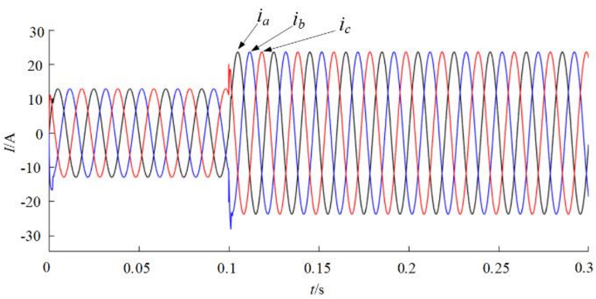

Figure 9. Current waveform with sudden load.

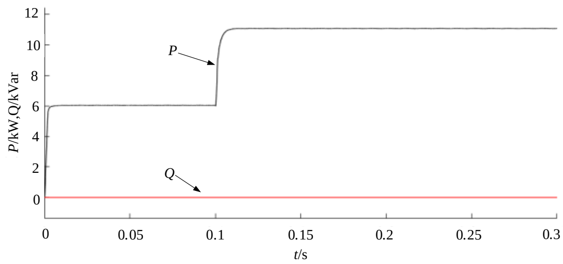

Figure 10. Power waveform with sudden load.

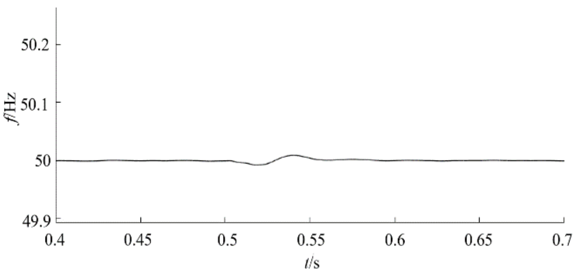

Figure 11. Frequency waveform with sudden load.

The switch KM is closed and the load (P_2=5kW) is integrated at 0.5s. As shown in FIG. 8 and 9, the output voltage is always constant, not affected by load mutation, the stability of the system is good. As can be seen from FIG. 10 and 11, the grid-connected power can effectively track the command power, and the frequency of the system only fluctuates slightly, but quickly tends to be stable.

4. Conclusions

Based on the introduction of the basic principles of VSG, this paper builds a grid-connected inverter system model based on VSG control strategy on MATLAB/Simulink. The pre-synchronization unit based on phase-locked loop controls the voltage amplitude, frequency and phase of VSG and make them consistent with the grid side, thereby reducing the instantaneous inrush current of the grid, and realizing the output voltage and frequency stability of the virtual synchronous generator. This paper only studies a VSG grid connection. When multiple VSGs are combined into a microgrid, they will also face the problem of active power allocation between VSGs. How to make each VSG output a suitable and stable active power is worthy of further study.

5. References

[1] Wang K. Research on Interface Characteristics of Wind Power Generation System Based on Virtual Synchronous Generator[D]. North China Electric Power University,2015.
[2] Li D, Zhu Q, Lin S, et al. A Self-Adaptive Inertia and Damping Combination Control of VSG to Support Frequency Stability [J]. IEEE Transactions on Energy Conversion, 2017, 32(1):397-398.
[3] Zhang C, Chen M Y, Wang Z C, et al. Study on control scheme for smooth transition of micro-grid operation modes [J]. Power System Protection and Control, 2011, 39(20).
[4] Balaguer I J, Lei Q L Q, Yang S Y S, et al. Control for Grid-Connected and Intentional Islanding Operations of Distributed Power Generation [J]. IEEE Transactions on Industrial Electronics, 2010, 58(1): 147-157.
[5] Gaztanaga H, Etxeberria-Otadui I, Bacha S, et al. Real-Time Analysis of the Control Structure and Management Functions of a Hybrid Microgrid System[C]. IEEE Industrial Electronics, IECON 2006 - 32nd Annual Conference on. IEEE, 2006.
[6] Yang X Z. Research on Microgrid Inverter and Coordinated Control Strategies of Multi-inverters[D]. Hefei University of Technology,2011.
[7] Vasquez J C, Guerrero J M, Savaghebi M, et al. Modeling, Analysis, and Design of Stationary Reference Frame Droop Controlled Parallel Three-Phase Voltage Source Inverters[J]. IEEE Transactions on Industrial Electronics, 2013, 60(4): 1271-1280.
[8] Savaghebi M, Jalilian A, Vasquez J C, et al. Secondary Control Scheme for Voltage Unbalance Compensation in an Islanded Droop-Controlled Microgrid [J]. IEEE Transactions on Smart Grid, 2012, 3(2): 797-807.
[9] Du W, Jiang Q R, Chen J R. Frequency Control Strategy of Distributed Generations Based on Virtual Inertia in a Microgrid [J]. Automation of Electric Power System, 2011, 35(23): 26-31+36.
[10] Cho C, Jeon J H, Kim J Y, et al. Active Synchronizing Control of a Microgrid[J]. IEEE Transactions on Power Electronics, 2011, 26(12): 3707-3719.
[11] Wang K, Wang Z Z, Chai J Y, et al. Analysis of Grid -connection Pre-synchronized Process for Synchronously Controlled Inverter Power Source [J]. Automation of Electric Power System, 2015, 39(12): 152-158.
[12] Liang J G, Jin X M, Jing L, et al. An Improved Control Strategy for Quasi-Synchronous Grid-Connection of Microgrid [J]. Power System Technology, 2014, 38(11): 3071-3078.
[13] Yang L, Wang C, Lu Z P, et al. The Method of Pre-Synchronized Grid-Connection of Synchronverter [J]. Power System Technology, 2014(11): 3103-3108.
[14] Wu H. Control Strategy for Three-Phase-Four-Wire Virtual Synchronous Generator [D]. Nanjing University of Aeronautics and Astronautics.2015
[15] Guerrero J M, Vasquez J C, Matas J, et al. Hierarchical Control of Droop Controlled AC and DC Microgrids—A General Approach Toward Standardization [J]. IEEE Transactions on Industrial Electronics, 2011, 58(1): 158-172.

Acknowledgements

This work was supported by The National High Technology Research and Development Program of China, Project 2013AA050201 and by National Natural Science Foundation of China, Project 612731000.

IOP Conf. Series: Earth and Environmental Science **431** (2020) 012019 doi:10.1088/1755-1315/431/1/012019

Research on improvement of ambient temperature of wind turbine engine room

Gao Yang[1], Fu Shiming[1], Liu Baoliang[1], Leng Xuemin[1]

1 Shenyang Institute of Engineering, Shenyang, China
E-mail: gaoyangsie@163.com

Abstract. A good cabin environment and reasonable cabin temperature are a powerful guarantee for the safe operation of wind turbines. By installing the cabin intelligent intelligent filtering and cooling system in the wind turbine, the cabin environment can be effectively improved, the cabin temperature can be reduced, the downtime of the wind turbine can be reduced, the grid-connected operation time of the wind turbine can be improved, the safe operation of the wind farm can be guaranteed, and the wind farm can be improved. Operational efficiency and economic benefits.

1. Introduction

With the increasing shortage of energy in the world, the global warming of the climate, and the increasing awareness of environmental protection, the low-carbon economy has become the focus of global attention [1]. Wind power generation has a low-carbon, low-pollution, low-carbon power development model, and has become one of the important strategic choices for sustainable energy development. In recent years, China's demand for energy and environmental protection have been continuously strengthened. The advantages, advantages, economics and practicality of wind power generation have been prominent, making the installed capacity of wind turbines the first place in the installed capacity of renewable energy power generation.

The wind turbine is a large and complex mechanical device that is unattended for high-altitude operation. The installation location is in a harsh environment, and the work will continue to generate heat in the form of friction, collision, and electromagnetic loss. Although the wind turbine is equipped with a heat sink, there are still serious problems such as an increase in the cabin ambient temperature, a decrease in the lubrication level of the lubricating oil, an acceleration of the cabin pipeline aging, and even a deflagration of the cabin. To this end, the temperature rise threshold of the main heat-generating components bearings, gearboxes, generators, etc. in the engine room is set. After the over-temperature, the wind turbine group actively implements shutdown and risk avoidance. According to the statistics of Datang (Chifeng) wind farm, the number of unit shutdowns caused by over-temperature of components exceeds 40% of the total number of abnormal shutdowns. It can be seen that the problem of heat dissipation in the cabin has not been effectively solved, which seriously inhibits the availability of wind turbines and Cost recovery. The study of the ambient temperature over temperature problem in the wind turbine nacelle focuses on three aspects. (1) Internal study of component heating. Many scholars analyze the distribution of temperature fields by simulating wind turbines [2-3]. (2) Research on heat dissipation of wind turbine cabin structure. Ma Tieqiang et al. studied the layout of the wind turbine nacelle and its different heat dissipation airflow

IOP Conf. Series: Earth and Environmental Science **431** (2020) 012019 doi:10.1088/1755-1315/431/1/012019

configuration, the heat dissipation efficiency of the unit is different, and the thermal coupling between the airflow and the components becomes a key factor affecting heat dissipation [4]. (3) Research on the influence of working environment of wind turbines on heat generation. SMAILI and others provide power matching for the cabin cooling system by studying the thermal performance of the wind turbine nacelle at extreme temperatures [5].

The above research laid the foundation for controlling the heating and cooling of the wind turbine engine room. However, for the actual operation of the wind power system, it is still very important to improve the cabin environment to reduce the cabin temperature, avoid the limited power operation of the unit, and even be forced to stop the research.

2. Cabin temperature over temperature causes

2.1. Cooling system itself problem

Problems with the cooling system itself can cause the cabin temperature to be too high. (1) Cooler failure, such as short circuit of the internal wiring of the cooler, open circuit, burned out of the motor, etc., can cause the fan to not operate and affect heat dissipation. (2) The large amount of dust on the cooler fins affects the heat dissipation of the cooler, resulting in insufficient cooling. (3) The relief valve is a pressure relief element and should function when the oil temperature of the gearbox is low and the pressure is high. At present, when the oil temperature is high, the overflow valve still has oil flow, so that the amount of oil that has been cooled is reduced, and some of the oil is directly returned to the gear box without cooling, resulting in insufficient overall cooling and high oil temperature. (4) Insufficient cooling causes the oil temperature to be too high, so that the high-speed bearing temperature cannot be effectively removed, resulting in an excessively high bearing temperature and an increase in the cabin ambient temperature.

2.2. Lubrication system does not function fully

The lubrication system does not function effectively and the cabin temperature is too high. (1) Open the rear box observation cover to check the bearing oil condition, and find that the oil is small, indicating that the bearing oil quantity is insufficient. The main reasons for this situation are: the oil inlet hole design is too small, resulting in insufficient oil intake; the tank oil inlet hole and the oil inlet ring oil tank are misplaced; the oil hole is blocked by impurities, resulting in a decrease in oil volume; the oil inlet hole is not drilled. through. (2) The pressure valve or temperature control valve of the lubrication system is wrong. When the oil connection between the filter and the gearbox is correct, when the oil temperature exceeds 55 ℃, the filter to the oil distributor tube still has oil flowing, indicating that there is a problem with the temperature control valve of the filter and affecting heat dissipation. (3) If the gear is insufficiently injected or the oil hole is not aligned with the gear, the gear temperature will be too high, and the bearing temperature will be high[6].

3. Traditional treatment methods for the cabin environment

3.1. Manual dust removal

Traditional dust removal methods in the cabin environment are usually carried out by the operation and maintenance personnel on the top of the wind turbine. Generally, manpower is used to clean the cabin equipment and the heat exchanger of the gear box. If the cabin environment temperature is high, the operation and maintenance personnel open the cabin sunroof and rely on the natural wind to reduce the cabin temperature. This requires both manpower and material resources, long downtime, and limited dust removal and heat dissipation. At the same time, due to repeated flushing of the surface of the gearbox cooler, the service life of the gearbox oil cooling fan oil circuit board is seriously affected[7].

3.2. Using a high power cooler
In order to avoid overheating of the gearbox, the equivalent cooling power of the “wind/oil cooler” in the system can be increased by increasing the heat exchange capacity of the lubrication system, ie, the design is larger without changing the original oil circuit and the fan structure. The power cooler replaces the original cooler.

3.3. Add a cooler
In order to improve the heat exchange capacity of the lubrication system, a separate air-cooled oil cooler is added to the original cooling system to work with the original cooler, and the oil circuit is connected in series with the original cooler.

4. Intelligent control of the cabin ambient temperature
In order to solve the shortcomings of the traditional treatment methods in the cabin environment, this paper installs the cabin environment intelligent filtration and cooling system in the wind turbine to improve the cabin environment and reduce the cabin temperature.

The cabin environment intelligent filtering and cooling system has 6 temperature sensor access control systems, which are arranged in the front and rear ends of the gearbox radiator, the circulation and outer circulation in the gearbox radiator oil pipe, the outside of the engine room cabinet and the outside of the engine room. When the temperature difference between the front end and the rear end of the heat sink is less than 10 ℃, it proves that the heat dissipation effect of the heat sink is not good, and the heat sink is clogged with dust, and the control system automatically sends a start command to the cabin dust removal filter device. The frame of the cabin dust removal filter device adopts German standard 50*50 aluminum profile, the structure is fastened, shockproof and tensile; the filter mesh adopts 304 stainless steel with good air permeability, which does not affect the heat dissipation effect of the radiator. When the control system sends a servo motor start signal to the dust filter device, the servo motor automatically drives the filter through the synchronous toothed belt to drive the screen guide shaft. In order to ensure that the filter is always stretched, it will not slant and run out of the track. The filter device is equipped with a damping device to work with the servo motor.

When the temperature of the gearbox tubing outer circulation and internal circulation monitors that the temperature reaches 60 ℃, and the internal circulation temperature is greater than the external circulation temperature, it proves that the temperature control valve fails. When the control system monitors that the cabin temperature exceeds 45 ℃, the cabin temperature is high, and the control system sends a start command to the axial fan of the ventilation device. When the cabin temperature drops below 45 ℃, the axial fan stops working. The axial flow fan adopts integrated thick cast iron fan blade design, which has high strength and is not easy to deform and fall off. The impeller has a good aerodynamic performance after strict dynamic balance calibration, large air volume, thick cast iron casing, high temperature spray paint treatment, and wear resistance. Loss, corrosion resistance, light weight, high hardness, anti-shock and anti-drop. At the same time, the motor is fixed by triangular mechanics, which can effectively reduce the vibration generated by the motor during operation and ensure the continuous and safe operation of the motor. The motor is powered by 220V, the power is 0.12kW, the speed can reach 1450r/min, and the air volume is 2000m3/h. It achieves low energy consumption, low noise and high air volume, and the cooling effect has been tested to 7.6℃.

5. Economic Benefit Analysis
The wind turbines of the wind farm each have a capacity of 1.5 MW. Each year, due to the high temperature and windy weather, the wind turbines are shut down about 10 times, and the average time for each downtime recovery is 8 hours. Each wind turbine is polluted by the fan environment and the heat dissipation of the gear box is not good. The resulting oil temperature is overheated and the power loss can

reach 1.2 million kWh. A wind farm with 33 units of 49.5 MW capacity will lose 39.6 million kWh per year. According to the standard of wind power on-grid 0.6 yuan/kWh, the annual loss will be 2.376 million yuan. It can be seen that after the wind turbine is installed in the cabin environment intelligent filtering and cooling system, the cabin environment is improved, the cabin temperature is reduced, the number of shutdowns of the unit is reduced, the grid-connected operation time of the wind turbine is effectively improved, and the power generation of the wind farm is increased, thereby improving The economic benefits of wind farms.

6. Conclusion

After installing the cabin intelligent environment filtering and cooling system, the wind turbine greatly improved the cabin environment of the wind turbine, reduced the cabin temperature, ensured the safe operation of the wind farm, reduced the downtime of the wind turbine, ensured the utilization of the wind turbine, and improved the operating efficiency of the wind farm. Economic profitability.

7. References

[1] Liu Bo, He Zhijia, Jin Wei. Current Status and Development Trend of Wind Power Generation[J]. Journal of Northeast Electric Power University, 2016, 36(2): 7-13.
[2] Hu Tian, Tang Renyuan, Li Yan, et al. Calculation and analysis of three-position temperature field of permanent magnet wind turbine[J]. Transactions of China Electrotechnical Society, 2013, 28(3): 122-126.
[3] SHAFAIE R, KALANTAR M, GHOLAMI A. Thermal analysis of 10-MW-class wind turbine HTS synchronous generator [J]. IEEE Transactions on Applied Superconductivity, 2014, 24(2): 1-9.
[4] Ma Tieqiang, Sun Debin, Su Yangyang, et al. Analysis Method of Thermal Performance of Wind Turbine Engine Room Structure[J]. Computer Aided Engineering, 2016, 25(3): 63-68, 73.
[5] SMAILI A, ATAHI, MASSON C. Thermal analysis of wind turbine nacelle operating in Algerian Saharan climate [J]. Energy Procedia, 2012, 18(2): 187-196.
[6] Thermal Analysis of Wind Turbine Nacelle Operating in Algerian Saharan Climate[J] . Arezki Smaili,Ali Tahi,Christian Massfon. Energy Procedia . 2012
[7] Cost-effective condition monitoring for wind turbines. Yang, Wenxian,Tavner, Peter J.,Crabtree, Christopher J.,Wilkinson, Michael. IEEE Transactions on Industrial Electronics . 2010

The development of a high efficiency microturbine generator for a vehicle

R Iakunin[1], A Kostyukov[1], A Kozlov[1], G Nadareyshvili[1] and A Terenchenko[1]

1 NAMI Russian State Scientific Research Center, Moscow, Russia
E-mail: r.yakunin@nami.ru

Abstract. Currently, microturbines are becoming increasingly common in power generation. There is a desire to use them as an energy source for the hybrid cars with the wheels driven by an electric motor. However, stationary microturbines are not well adapted for use on the automobiles. The main differences are frequent engine stops and lack of space for large heat exchangers. These differences lead to a decrease in the engine efficiency. The article discusses the technical solutions for the design of microturbines with high efficiency, small size of the heat exchanger and the bearings with reduced friction losses. The calculation studies have shown a possibility of achieving high efficiency for microturbines in a car. Currently, tests of real engine components to confirm the calculations have ended. Based on the test data, a microturbine is being designed. This microturbine will have been made by the end of this year.

Nomenclature
Latin alphabet
T temperature, K
N power, kW
Greek alphabet
σ efficiency of the heat exchange
η efficiency
π pressure ratio
Abbreviations
CNG Compressed Natural Gas
ICE internal combustion engine

1. Introduction

Currently, microturbines are becoming increasingly common in power generation. A promising trend is the application of a microturbine as a component of an electric hybrid vehicle [1, 2, 3, 4].

In this work, the development of a prototype model of a 40-60 kW multi-purpose gas turbine engine for power plants of various purposes, including those for vehicles, is shown.

A Gas turbine engine have several problems, which are especially important on vehicles:

- engine cost;
- high fuel consumption (low efficiency), especially at partial load;
- large volume of hot exhaust gases to be removed;
- noise level.

The solution of these problems has been made possible by using a heat exchanger (regenerator). The heat exchanger uses the lost energy of the exhaust gases to preheat the air entering the combustion chamber.

It solves these problems as follows:

IOP Conf. Series: Earth and Environmental Science **431** (2020) 012020 doi:10.1088/1755-1315/431/1/012020

- the cost of the engine is reduced, because to ensure the high efficiency, you can use only one radial compressor and turbine stage instead of several axial stages with a high degree of the pressure increase;
- the fuel consumption is reduced, especially at partial loads;
- the exhaust gases are not so hot;
- a side effect of the heat exchanger is noise damping.

A disadvantage of a heat exchanger – an increase in the engine size.

Several vehicles obtaining serial microturbines as range extenders are shown in Figure 1.

Figure 1. Vehicles with serial microturbines. On the top: Kenworth hybrid electric truck with Capstone C65 microturbine; Mack hybrid electric truck with Wrightspeed microturbine. Below: Russian hybrid electric bus "Trolza-5250 Ecobus" with Capstone C65 microturbine.

In Russia, in 2010, a pilot batch of environmentally friendly Trolza-5250 “Ecobus” buses, equipped with Capstone C65 microturbines, was manufactured. In 2011, these buses were successfully tested in Moscow and Sochi, and are currently operated in the Krasnodar region.

However, serial microturbines have poorly adapted bearings for frequent starts, and their heat exchangers take up a lot of space. Thus, it has become necessary to develop a microturbine, which can be successfully used both in transport and in a stationary application.

The engine being under development is multi-fueled and of high efficiency. It can also use CNG, which allows low environmental pollution. A car with such a power plant meets the environmental requirements of the state of California (the toughest in the world) without the use of a catalytic converter, diesel particulate filter and the use of AdBlue [5].

IOP Conf. Series: Earth and Environmental Science **431** (2020) 012020 doi:10.1088/1755-1315/431/1/012020

2. Calculations

The engine must be developed with a high efficiency. Currently, it is not possible to significantly improve the efficiency of the compressor and turbine. Given the efficiency of the compressor and the turbine, the effective specific fuel consumption improves when the temperature at the turbine inlet rises. We can achieve this by increasing the degree of pressure increase, but this requires the use of expensive multistage axial compressors and turbines. At small sizes, their efficiency considerably worsens. Therefore, for microturbines it is advisable to use a heat exchanger with a radial compressor and a turbine.

The heat exchanger (regenerator) provides the Brighton cycle with regeneration.

The temperature at the turbine outlet (T_{out}) is higher than that of the air leaving the compressor. Ideally, with the infinite heat transfer area, the air from the compressor can be heated to the temperature T_{out} before it is supplied to the combustion chamber. This allows burning less fuel to heat up to the required temperature. In a real heat exchanger, the heat cannot be transferred completely; moreover, some of the energy is required for the air passage through the heat exchanger. Therefore, the heat exchanger must be carefully designed. A poorly designed heat exchanger may not only be useless, but also decrease the efficiency.

The effectiveness of the heat exchanger may be expressed as

$$\sigma = \frac{T_{cc} - T_{com}}{T_{out} - T_{com}}$$

Where:

T_{out} – the temperature at the turbine outlet;

T_{com} – the temperature after the compressor;

T_{cc} – the temperature before the combustion chamber.

The efficiency of the heat exchangers in the modern microturbines is within the range of 80-86%. These indicators are essentially the limits for the fixed plate heat exchangers. Attempts to increase their efficiency above these limits lead to an unacceptable increase in their size. Nevertheless, a further increase in the efficiency of the heat exchanger is highly desirable. Increasing the degree of regeneration of the heat exchanger from 86% to 95% provides an increase in the efficiency of the microturbine 50 kW from 32% to 38% (Figure 2).

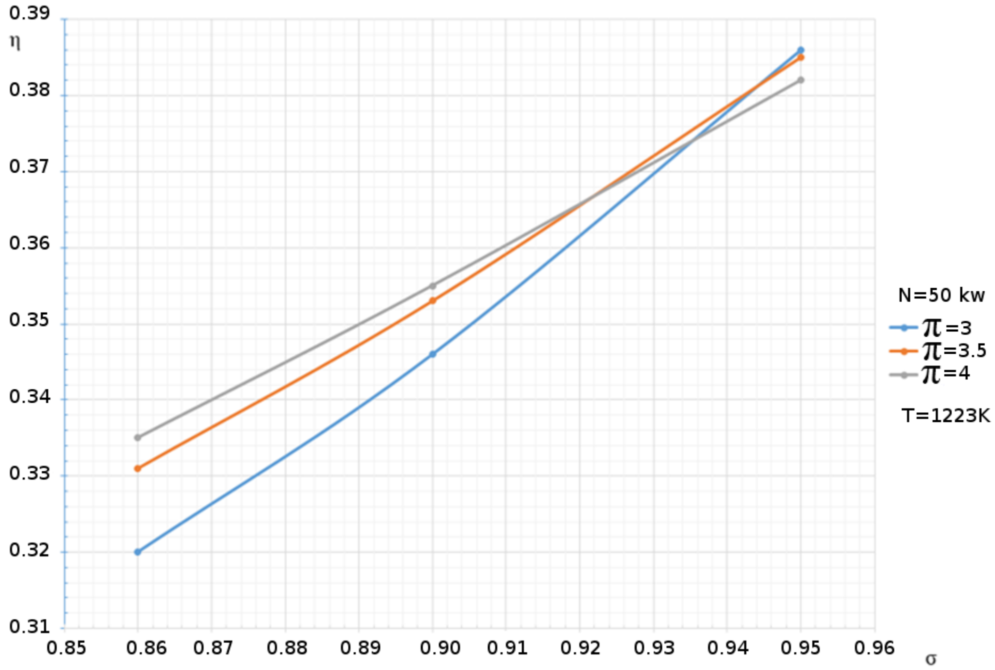

Figure 2. Effect of recuperation degree on the 50 kW microturbine efficiency (gas temperature after the combustion chamber 12230K)

IOP Conf. Series: Earth and Environmental Science **431** (2020) 012020 doi:10.1088/1755-1315/431/1/012020

High regeneration rate is achievable in a rotary regenerator. For example, in a ceramic rotary heat exchanger, a regeneration rate of 95–97% was achieved [6].
By using a less exotic material, it is also possible to achieve the regeneration rate up to 95%, which provides competitiveness of microturbines in terms of the fuel efficiency comparable with a reciprocating ICE [7].
The developed microturbine with a power of 50 kW should have an efficiency of 37.8%.
According to the results of the calculations, to ensure the obtained calculated efficiency of the microturbine, parts of the microturbine must meet the following requirements:

The compressor
- air flow at the compressor inlet – 0.41 kg/s
- pressure increase degree in the compressor – 3,5.
- adiabatic efficiency – not less than 0.8;
-

The turbine
- gas temperature before the turbine – 1223K: modern alloys used in gas turbine technologies can operate at temperatures up to 1223 K without cooling and at the same time provide a resource of up to 60 thousand hours.
- adiabatic efficiency – not less than 0.86
- gas temperature at turbine outlet – 967.5 K
- gas pressure at the turbine inlet – 327200 Pa;
- gas flow through the turbine – 0.40 kg / s
-

The heat exchanger
- recovery rate σ – not less than 0.95;
- total pressure loss from the compressor outlet to the combustion chamber inlet must not exceed 2%;
- total pressure loss from the turbine outlet to the gas exhaust device inlet must not exceed 8%;
- gas temperature at the regenerator inlet – 967.5 K;
- air temperature at the regenerator inlet – 442.9 K;
- regenerator inlet air flow - 0.41 kg / s
- regenerator inlet air pressure - 347800 Pa

The combustion chamber
- the combustion chamber must ensure the fuel combustion with minimal formation of harmful substances (no more than 10 ppm);
- air flow rate at the combustion chamber inlet – 0.41 kg / s;
- air temperature at the combustion chamber inlet – 941.3 K;
- gas temperature at the combustion chamber outlet – 1223K;
- air pressure at the combustion chamber inlet – 340800 Pa;
- total pressure losses from the combustion chamber inlet to the turbine inlet must not exceed 2%.
-

Other
- air loss from the compressor to the turbine is not more than 3%;
- total pressure loss in the flow part of the microturbine is not more than 15%;

3. Design development

The rotary heat exchanger

The main problem of the rotary regenerators is their seals. The disc frame regenerators have minimum leakage in seals. In them, the seals do not work on a porous heat transfer matrix, but on flat surfaces. To reduce the frame thermal deformations and, accordingly, to reduce leaks, as well as to enable using of graphite seals (maximum temperature 450-4700C) the frame is cooled. The cooling system of the frame has been patented. The most promising heat transfer element, as shown by a computational analysis, are slotted elements (Figure 3). They have been successfully tested.

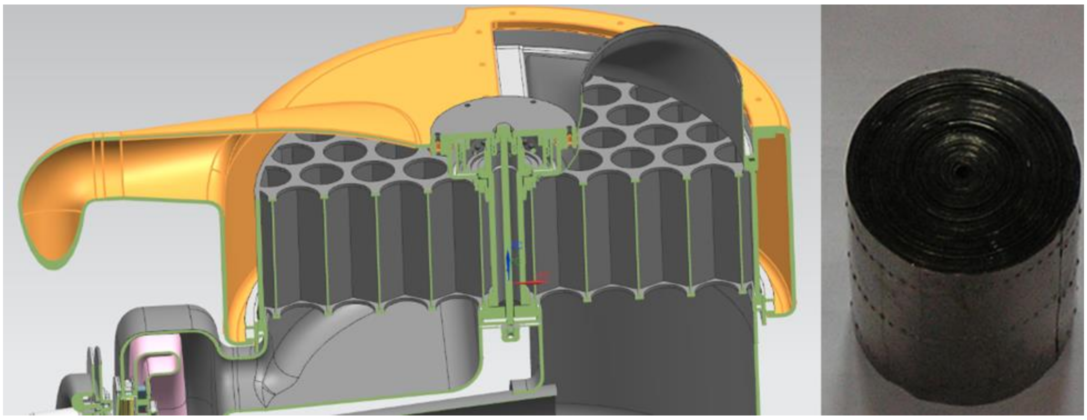

Figure 3. The frame of the heat exchanger and the cylindrical slotted heat transfer element.

The combustion chamber. For a microturbine with a rotary disc heat exchanger, a tube-type combustion chamber is preferable for the layout reasons. In addition, the tube-type combustion chamber has only one nozzle, and, therefore, has no problem with uneven fuel supply in the different injectors. To reduce emissions, computational studies have been carried out. Based on their results, a combustion chamber with calculated NOx emissions [ppm] 10 has been developed.

The turbine.

A computational analysis of the diffuser efficiency after the turbine has shown a significant advantage (in terms of the microturbine efficiency) of the elongated diffuser. The overall layout of the microturbine with an elongated diffuser and a rotating heat exchanger is shown in Figure 4.

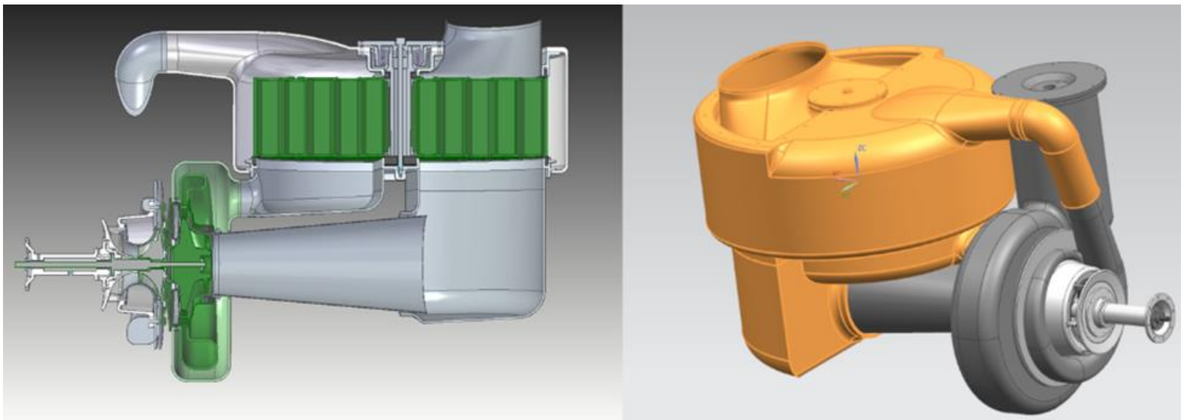

Figure 4. The overall layout.

This layout has the following advantages:
- low length of the heat exchanger seal;
- design simplicity;
- efficiency of the diffuser;
- modularity design.

Bearings.

The most problematic issue for a turbocharger is the high-temperature heat flow to the bearings, especially after the microturbine has stopped. The removal of this heat is very energy-intensive and complicates the operation of the microturbine power plant. To isolate the bearings from the turbine, the layout with a console mounting of the turbine wheel has been adopted.

It was decided to move away from the air bearings, despite their low friction losses. During the launch of the microturbine, the rotor of the turbocharger rests on elastic petal elements, which leads to a significant reduction in the life of the bearings. The developed turbine is to be used in road transport and, therefore, it will often be launched during operation. In addition, when operating in vehicles, shock loads may occur. Obviously, in these cases, the use of air bearings is hardly advisable.

Currently, liquid bearings are also used in microturbines. The rotor in these microturbines is mounted on one hybrid ball bearing and on one radial liquid bearing. The installation of the oil system does not lead to any significant increase in the cost of the microturbine, because the oil system is useful in any case. In our layout, bearing has been moved to the cold zone, and the oil is not coxed during operation.

The disadvantage of the fluid bearings is large friction losses. Friction in fluid bearings depends on the surface area of the bearings. At high rotary speed, which is a characteristic of the gas turbine engines, it would be a quite small bearing area. However, before achieving the required speed of rotary in the bearing, there is a mode of boundary friction. In this mode, we must provide a small pressure on the bearing material to avoid material wear. For this reason, the area of fluid bearings in turbo compressors is excessively large, which means that the friction losses are large. To reduce wear during boundary friction, the bearing is made of a silicon carbide-based composite. This has made it possible to make the area of the bearing as minimum as necessary to create an oil wedge at operating speed. For this reason, the friction losses in the liquid bearing at the operating speed have been significantly reduced. The exact value of the possible reduction in bearing area will be obtained from the test results on the bench.

4. Conclusion

1) The selection and justification of the main target parameters of the microturbine has been carried out:

- fuel consumption – 10.95 kg / hour;
- microturbine power – 50 kW;
- microturbine efficiency – 37.8%;
- degree of pressure increase – 3.5;
- heat exchanger efficiency 95%.

2) The selection and justification of the optimal layout of the microturbine has been carried out:

- liquid composite bearings;
- with a rotary regenerator;
- with a tube-type low-toxic combustion chamber;
- with an extended diffuser.

3) 3D microturbine model has been developed

4) Mathematical modeling has been carried out:

- flows in the gas-air pipes of the heat exchanger with an ultra-high degree of regeneration;
- gas-air flows in the pipe connecting the combustion chamber and the microturbine,
- gas-air flows in the diffuser;
- thermal state of the microturbine composite bearings;
- thermal stress state of the microturbine body elements;
- gas-air flows in the compressor and the turbine.

The optimization calculations of the efficiency and service life of the compressor and turbine for the heat-stressed state: the efficiency values have been obtained for the full parameters 0.801 and 0.901 for the compressor turbine stages. The impeller meets the requirements of the static strength (safety factor $n > 2.5$), and durability when operating at the nominal conditions for 40,000 hours.

5) Individual engine parts have been manufactured and tested:

- bearings;

- heat transfer element.

5. References

[1] Kulikov I A, Shorin A A, Bakhmutov S V, Terenchenko A S, Karpukhin K E 2016 A Method of Powertrain's Components Sizing for a Range Extended Electric Vehicle. SAE Technical Papers 2016-01-8096

[2] Bakhmutov S V, Karpukhin K E, Terenchenko A S, Kurmaev R Kh, Kondrashov V N, Sklyarinskiy S F 2015 Production of the electric vehicle experimental prototype with the range extender. Biosciences Biotechnology Research Asia, Vol. 12 (spl. Edn. 2)

[3] Asgharian P, Noroozian R, 2019 Modeling and Efficient Control of Microturbine Generation System With Battery Energy Storage for Sensitive Loads. Iranian Journal of Electrical and Electronic Engineering, Volume 01

[4] Moore M J, 2002 Micro-turbine generators. Professional Engineering Publishing, UK

[5] Cobb J 2014 «Wrightspeed's microturbine REV Promises Huge Fuel Savings» https://gm-volt.com/2014/02/18/wrightspeeds-microturbine-rev-promises-huge-fuel-savings/

[6] Wilson, David Gordon and Korakianitis T P 1998 "The design of high-efficiency turbomachinery and gas turbines" second edition, Prentice-Hall, Upper Saddle River, NJ.– T.1. – №4. – C. 6-15

[7] Kostyukov A V, Kosach L A, Gornovskii A A, Ni Weidou, Valeev A G, Kovalchuk E V 2016 Multi-purpose highly efficient microturbine with a power of 50 kW – «European Science and Technology». Materials of the XIV international research and practice conference – Munich, «Vela Verlag Waldkraiburg», # 14

Acknowledgements
This work has been supported by the Ministry of Education and Science of the Russian Federation: Agreement # 075-11-2018-233. Unique project identifier: RFMEFI62518X0045.

IOP Conf. Series: Earth and Environmental Science **431** (2020) 012021 doi:10.1088/1755-1315/431/1/012021

Advanced design and optimization of wind turbines based on turbine theories

Zh Zhang

Zurch University of Applied Science, Zurich, Switzerland
E-mail: zhengji.zhang@zhaw.ch

Abstract. A review of wind turbine technology showed that many flaws in both the flow models and computations are involved in the traditional fundamentals. While traditional methods for design and computation are all based on the airfoil theory, a new method based on turbine theories has been developed and is shown to be ideally applicable. Against the traditional method, the new method also considers non-uniform pressure distribution in flows downstream of the rotor plane and is thus highly accurate. The blade efficiency or tip swirl number has been introduced. It enables computation of the power coefficient to be very reasonable. Its optimum can be directly applied to the geometrical design of turbine blades. Between the tip speed ratio λ, blade efficiency ε, and power coefficient c_p, a closed solution of both the optimum design and the operation of wind turbines exists. It is demonstrated that the maximum achievable power coefficient can be 10% larger than that predicted by all previous theories.

1. Introduction

In times of increased use of renewable energies, wind energy is gaining increased attention. More and more wind turbines are installed both on-shore and off-shore. Modern manufacture technology enables large wind turbines with a power output up to 8 MW to be built and installed.

Wind power technology basically comprises flow-dynamic design, manufactures and operations of wind turbines. The fundamental technology of wind turbines is thus fluid mechanics and aerodynamics. First, Betz's law, based on flow dynamics, limits the maximum achievable power at 59% (power coefficient c_p=0.59). Second, aerodynamic designs of wind turbines are uniquely based on airfoil theory, to which apply the Schmitz theory and the blade element momentum method (BEM) [1, 2].

A review of these fundamentals demonstrates that, first, all these basics are insufficient if compared with those in water turbines. Second, as indicated in this paper, they are to some extent imperfect or inaccurate and could lead to significant design errors. Third, the reachable efficiencies of wind turbines (<75% of Betz's maximum) are generally much lower than those in water turbines (>90%). For the most fundamental Betz law, for instance, only the flow through the "actuator disc" is considered for balancing the pressure forces and the resistance force based on the momentum equation. A detailed study by the author of this paper showed that the used actuator-disc model is not exact. The Schmitz theory and the BEM suppose that the flow through the turbine wheel is comparable to the flow passing through a single blade as treated by the airfoil theory. Because it is in reality not the same and the non-uniform pressure distribution in the flow has been ignored, one has to make corrections in the aerodynamic design of the blade profiles. In other words, both the Schmitz theory and the BEM have followed considerable detours with unreasonable assumptions in computing and designing the blade profiles.

Some defects in fundamentals of wind turbines will be indicated below in Sect. 2. They are found in both Betz's law and Schmitz's theory including the BEM for turbine design.
Primarily, this paper aims to introduce a new design method of turbine wheels based on much effective turbine theories (instead of the airfoil theory). At its center is the application of the Euler equation for specific work in fluid machinery. For this reason, it is indispensible to reveal the most significant flow dynamic fundamentals of wind turbines and to present conditions for applying the Euler equation.

2. Defects in fundamentals of wind turbine technology

The fundamental background of wind turbine technology is the Betz law which is derived based on the Froude-Rankine theorem. The flow through an "actuator disc" is considered according to figure 1. There, in a 2D-view, the control volume for mass and momentum conservations is bounded by two streamlines which pass through die edge of the disc. At section 3, the flow velocity has the value c_3 and the pressure reaches the ambient pressure p_0. The flow resistance (thrust) caused by the disc is denoted by T. It is computed for steady flow by applying the momentum law to the volume flow Q from section 0 to section 3:

$$T = \rho \dot{Q}(c_0 - c_3) \tag{1}$$

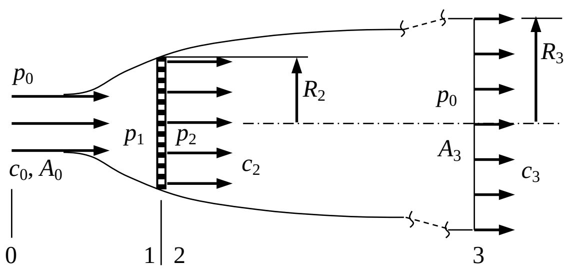

Figure 1. Actuator disc and flows.

Based on the mechanical principle, use of the momentum law to determine the flow resistance requires that a control volume around a disc must be given by real streamlines. This condition is obviously not fulfilled in figure 1. Because of the singularity at the edge of the disc and thus the flow separation there, the streamlines shown in figure 1 will no longer maintain after the disc. The flow model shown in figure 1 must be considered as the first flaw or defect in the fundamentals of wind power technology. As will be shown below, many disagreements and faults found in analyses are connected to this flaw.
On the other hand, the thrust is computed with the resistance coefficient c_D as

$$T = c_D A_D \frac{1}{2} \rho c_0^2 \tag{2}$$

with A_D as the physical area of the disc.
Equalizing Eq. (1) and (2) with $\dot{Q} = c_0 A_0$ and $c_3 A_3 = c_0 A_0$ yields

$$c_D = 2 \frac{A_0}{A_D} \left(1 - \frac{A_0}{A_3}\right) \tag{3}$$

The power which is related to the thrust on the disc is computed as $P = c_2 T$. Because of Eq. (1), this is written as

$$P = \rho \dot{Q} c_2 (c_0 - c_3) \tag{4}$$

Moreover, with $p_3 = p_0$ at section 3, the power extracted from the air flow between section 0 and 3 can be expressed as

$$P=\frac{1}{2}\rho\dot{Q}\left(c_0^2-c_3^2\right) \tag{5}$$

Equalizing Eq. (4) and (5) yields

$$c_2=\frac{1}{2}\left(c_0+c_3\right) \tag{6}$$

This relation is known as the Froude-Rankine theorem. Because the mean velocity c_2 is used in association with $P=c_2T$, it is in fact not proved to be applicable to computations of the volume flow rate by multiplying the area of the actuator disc. In all previous applications, the difference has been simply ignored. This must be considered as the second flaw or defect in the fundamentals of wind power technology.

By assuming the velocity c_2 to be equal to that for volume flow, the volume flow rate through the actuator disc is given as $\dot{Q}=c_2A_\mathrm{D}$. Then, it follows from Eq. (6) with $c_0A_0=c_2A_\mathrm{D}=c_3A_3$

$$\frac{A_0}{A_\mathrm{D}}=\frac{1}{2}\left(1+\frac{A_0}{A_3}\right) \tag{7}$$

Combining this equation with Eq. (3) yields

$$\frac{A_0}{A_3}=\sqrt{1-c_\mathrm{D}} \tag{8}$$

For a closed disc (A_0=0), it follows c_D=1. This resistance coefficient does not exactly agree with measurements leading to c_D=1.1 to 1.17. The reason for this disagreement lies obviously in both the first and the second flaws mentioned above.

The power coefficient of the actuator disc is defined by relating the extracted power to the total power of air flow through a flow area equal to the disc area. With $\dot{Q}=c_0A_0$ one obtains

$$c_\mathrm{p}=\frac{P}{\frac{1}{2}\rho c_0^2A_\mathrm{D}c_0}=\frac{A_0}{A_\mathrm{D}}\left(1-\frac{c_3^2}{c_0^2}\right)=\frac{A_0}{A_\mathrm{D}}\left(1-\frac{A_0^2}{A_3^2}\right) \tag{9}$$

Because of Eq. (7), this is further written as

$$c_\mathrm{p}=\frac{1}{2}\left(1+\frac{A_0}{A_3}\right)\left(1-\frac{A_0^2}{A_3^2}\right) \tag{10}$$

This is the Betz law. The power coefficient is expressed as a function of the area ratio A_0/A_3. It is easy to show that the maximum power coefficient is given at A_0/A_3=1/3, at which one obtains

$$c_\mathrm{p,max}=\frac{16}{27}=0.593 \tag{11}$$

This is the Betz limit of maximum extractable energy from the air flow.

At the closed disc (A_0=0), the power coefficient does not vanish but takes c_p=0.5. This value is obviously incorrect. The reasons are again the first and the second flaws in the fundamentals of wind power technology, as mentioned above.

Physically, the meaning of the area ratio A_0/A_3=1/3 is unclear. Especially, it is not clear, how it is related to flow dynamic property of the used actuator disc. For this reason, A_0/A_3 from Eq. (8) is further concerned and inserted into Eq. (10). One obtains

$$c_\mathrm{p}=\frac{1}{2}c_\mathrm{D}\left(1+\sqrt{1-c_\mathrm{D}}\right) \tag{12}$$

This novel equation with independent variable c_D is obviously much more meaningful than Eq. (10) with independent variable A_0/A_3, which appears to be incomprehensible because of the flow area A_3.

The corresponding maximum of the power coefficient is found at an actuator disc with $c_{D,m}$=8/9. Figure 2 shows the graph of Eq. (12).
As indicated above, two flaws in the fundamentals of wind power technology have been confirmed. Extended studies with corresponding improvements have been conducted by the author of this paper. One of them is based on a new flow model with streamlines away from the actuator disc, different from that in figure 1. For comparison, the first approach of new computations has also been shown in figure 2. The Betz limit has been exceeded by a new limit $c_{p,max}$=0.61, which is predicted at an actuator disc with $c_{D,m}$=1.10 in the closed position. The details of computations will be published soon.

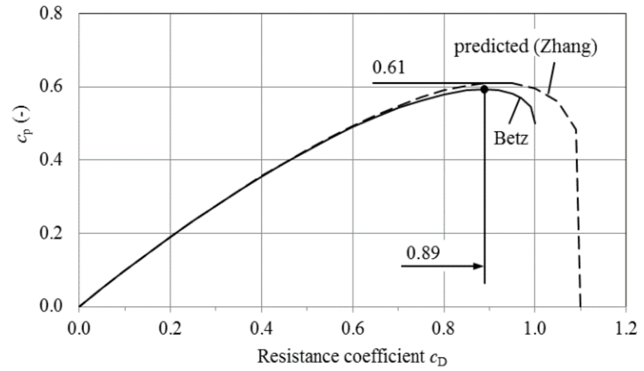

Figure 2. Recalculated Betz law for the power coefficient c_p as a function of the resistance coefficient c_D of an actuator disc.

3. Turbine theory and applications

3.1. Potential flow and flow distribution

The most significant difference between air flows at a wind turbine and a single blade is that the flow after the wind turbine maintains its rotation. This rotation is basically an indication of the extracted power from the air flow. That is to say that it is tightly related to the specific work based on the Euler equation.
The flow before entering the wind turbine is a sort of potential flow. Because viscous friction only has a negligible influence on the flow distributions both in the rotor plane and after the turbine wheel, the flows can be assumed to satisfactorily fulfill the condition of potential flows.

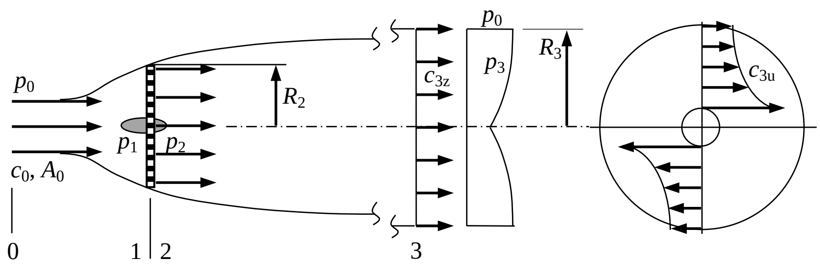

Figure 3. Flow and the flow rotations both at and downstream of a wind turbine wheel.

A new flow model with rotation after the wind turbine is shown in figure 3. For simplicity of the analysis, the control volume of the flow is again assumed to be bounded by axial-flow streamlines which pass through the perimeter of the turbine wheel. The axial velocity component at each flow section is uniform. Because of the rotation, however, both the distribution of the circumferential velocity component and the pressure distribution are non-uniform. In section 2, the rotation of fluid (velocity component c_{2u}) must fulfill the condition of potential flows and is thus characterized as

$$c_{2u} r_2 = c_{2u,R} R_2 = \text{const} \tag{13}$$

or because of $u_2=r_2\omega$, with ω as the angular rotational speed,

$$u_2 c_{2\mathrm{u}} = u_{2,\mathrm{R}} c_{2\mathrm{u,R}} = \mathrm{const} \tag{14}$$

On the other hand, the pressure distribution in section 2 is determined, from Euler equations (fluid dynamics), by

$$\frac{\partial p_2}{\partial r_2} = \rho \frac{c_{2\mathrm{u}}^2}{r_2} \tag{15}$$

With respect to Eq. (13) satisfying the potential flow condition as given by $c_{2\mathrm{u}} = (R_2/r_2)c_{2\mathrm{u,R}}$, one obtains by integrating the above equation the pressure distribution

$$p_2 + \frac{1}{2}\rho c_{2\mathrm{u}}^2 = p_{2,\mathrm{R}} + \frac{1}{2}\rho c_{2\mathrm{u,R}}^2 \tag{16}$$

This is a type of energy equation. It states that along the radial coordinate in section 2 the energy is constant and equal to that on the boundary at the radius R_2. In fact, such a flow distribution exactly agrees with the condition for assumed potential flow, i.e., the total pressure is constant.

Both $p_{2,\mathrm{R}}$ and $c_{2\mathrm{u,R}}$ in the above equation need to be determined. The flow from section 2 towards section 3 must fulfill the condition of potential flow and the law of conservation of angular momentum. This means, for instance, that along the boundary streamlines there must be $c_{3\mathrm{u,R}} R_3 = c_{2\mathrm{u,R}} R_2$ for the velocity component c_u. In section 3, the rotation of the flow is characterized in a similar way as

$$u_3 c_{3\mathrm{u}} = u_{3,\mathrm{R}} c_{3\mathrm{u,R}} = \mathrm{const} \tag{17}$$

Correspondingly, like Eq. (16), there is (with $p_{3,\mathrm{R}}=p_0$)

$$p_3 + \frac{1}{2}\rho c_{3\mathrm{u}}^2 = p_0 + \frac{1}{2}\rho c_{3\mathrm{u,R}}^2 \tag{18}$$

To determine the parameter $p_{2,\mathrm{R}}$ of Eq. (16), the energy balance between section 2 and 3 is considered. According to the Bernoulli equation, it follows

$$p_{2,\mathrm{R}} + \frac{1}{2}\rho\left(c_{2\mathrm{u,R}}^2 + c_{2\mathrm{x}}^2\right) = p_0 + \frac{1}{2}\rho\left(c_{3\mathrm{u,R}}^2 + c_{3\mathrm{x}}^2\right) \tag{19}$$

In explicit form, this is also written as

$$p_{2,\mathrm{R}} = p_0 - \frac{1}{2}\rho c_{2\mathrm{u,R}}^2\left(1 - \frac{c_{3\mathrm{u,R}}^2}{c_{2\mathrm{u,R}}^2}\right) - \frac{1}{2}\rho c_{2\mathrm{x}}^2\left(1 - \frac{c_{3\mathrm{x}}^2}{c_{2\mathrm{x}}^2}\right) \tag{20}$$

Then, employing $c_{3\mathrm{u,R}} R_3 = c_{2\mathrm{u,R}} R_2$ and $c_{3\mathrm{x}} A_3 = c_{2\mathrm{x}} A_2$, one further obtains

$$p_{2,\mathrm{R}} = p_0 - \frac{1}{2}\rho\left[c_{2\mathrm{u,R}}^2 + c_{2\mathrm{x}}^2\left(1 + \frac{A_2}{A_3}\right)\right]\left(1 - \frac{A_2}{A_3}\right) \tag{21}$$

The parameter $c_{2\mathrm{u,R}}$ will be determined in the next section in connection with the Euler equation for specific work.

3.2. Euler equation and specific work with uniform distribution

To determine the power exchange between the wind flow and the turbine wheel, the flow in section 2, i.e., after the rotor plane is considered. According to the Euler equation and in view of Eq. (14), the specific work exchanged between the flow and the wind turbine is given by

$$Y = u_2 c_{2\mathrm{u}} = u_{2,\mathrm{R}} c_{2\mathrm{u,R}} = \mathrm{const} \tag{22}$$

This is a very pleasing fact. Along the radial coordinate, constant specific work is obtained. This uniform energy extraction just represents an ideal case which should be approached for each blade design. With the total volume flow rate, the total power exchange between the flow and the wind turbine is then given as

$$P=\rho\dot{Q}u_{2,\mathrm{R}}c_{2\mathrm{u,R}} \tag{23}$$

On the other hand, the power extracted from the wind flow is obtained from the energy balance between section 0 and 3. To this end, first, the total pressure in the flow at section 3 is given by

$$p_{3,\mathrm{tot}}=p_3+\frac{1}{2}\rho\left(c_{3\mathrm{x}}^2+c_{3\mathrm{u}}^2\right) \tag{24}$$

Because of Eq. (18), this is further written as

$$p_{3,\mathrm{tot}}=p_0+\frac{1}{2}\rho\left(c_{3\mathrm{u,R}}^2+c_{3\mathrm{x}}^2\right) \tag{25}$$

Then, the power extracted from the air flow is obtained as $P=\dot{Q}\left(p_{0,\mathrm{tot}}-p_{3,\mathrm{tot}}\right)$, which alternatively can also be written as

$$P=\frac{1}{2}\rho\dot{Q}\left(c_0^2-c_{3\mathrm{x}}^2-c_{3\mathrm{u,R}}^2\right) \tag{26}$$

Equalizing Eqs. (23) and (26) and using $c_{3\mathrm{u,R}}R_3=c_{2\mathrm{u,R}}R_2$ yields

$$\frac{R_2^2}{R_3^2}c_{2\mathrm{u,R}}^2+2u_{2,\mathrm{R}}c_{2\mathrm{u,R}}-\left(c_0^2-c_{3\mathrm{x}}^2\right)=0 \tag{27}$$

This is a quadratic equation for $c_{2\mathrm{u,R}}$. Its solution is given as

$$\frac{c_{2\mathrm{u,R}}}{c_0}=-\frac{R_3^2}{R_2^2}\frac{u_{2,\mathrm{R}}}{c_0}+\frac{R_3^2}{R_2^2}\sqrt{\frac{u_{2,\mathrm{R}}^2}{c_0^2}+\frac{R_2^2}{R_3^2}\left(1-\frac{c_{3\mathrm{x}}^2}{c_0^2}\right)} \tag{28}$$

In this equation, the velocity ratio $c_{3\mathrm{x}}/c_0$ can be replaced by A_0/A_3; furthermore, $R_2^2/R_3^2=A_2/A_3$. When, additionally, using the tip speed ratio $\lambda=u_{2,\mathrm{R}}/c_0$ of the turbine wheel, then one obtains

$$\frac{c_{2\mathrm{u,R}}}{c_0}=\frac{A_3}{A_2}\sqrt{\lambda^2+\frac{A_2}{A_3}\left(1-\frac{A_0^2}{A_3^2}\right)}-\lambda\frac{A_3}{A_2} \tag{29}$$

In a first approximation, Eq. (7), arising from the Froude-Rankine theorem, can be applied (here A_D=A_2). This is an approximation, because the fluid rotation has not been considered in the Froude-Rankine theorem. It follows then

$$\frac{c_{2\mathrm{u,R}}}{c_0}=\frac{1}{2}\lambda\left(1+\frac{A_3}{A_0}\right)\left[\sqrt{1+\frac{2}{\lambda^2}\frac{A_0}{A_3}\left(1-\frac{A_0}{A_3}\right)}-1\right] \tag{30}$$

It appears here as a function of both the tip speed ratio λ and the flow area ratio A_0/A_3. For A_0=0, one obtains $c_{2\mathrm{u,R,0}}/c_0=0.5/\lambda$. This is mathematically correct. But physically, it cannot be true. The reason is again the first and the second flaws in the used simplified flow model in figures 1 and 3.

3.3. Blade efficiency and power coefficient

The specific work is determined by Eq. (22). Because it is uniformly distributed in section 2, it can be used as a system parameter. Its ratio to the specific kinetic energy of the air flow is therefore defined as the blade efficiency:

IOP Conf. Series: Earth and Environmental Science **431** (2020) 012021 doi:10.1088/1755-1315/431/1/012021

$$\varepsilon = \frac{Y}{c_0^2/2} = \frac{2u_{2,\mathrm{R}}c_{2\mathrm{u,R}}}{c_0^2} \tag{31}$$

Substituting the tip speed ratio $\lambda = u_{2,\mathrm{R}}/c_0$ and Eq. (30) into this expression yields

$$\varepsilon = 2\lambda\frac{c_{2\mathrm{u,R}}}{c_0} = \lambda^2\left(1+\frac{A_3}{A_0}\right)\left[\sqrt{1+\frac{2}{\lambda^2}\frac{A_0}{A_3}\left(1-\frac{A_0}{A_3}\right)}-1\right] \tag{32}$$

For A_0=0 there is ε=1. This incorrectness, just as in Eq. (30), arises from the first and the second flaws in the used simplified flow model. For A_0/A_3=1 there is ε=0, as expected.
With the definition of the blade efficiency, the power extracted from the wind flow can be recalculated from Eq. (23), leading to

$$P = \varepsilon\rho\dot{Q}\frac{c_0^2}{2} \tag{33}$$

Obviously, the blade efficiency ε is a significant parameter which exactly represents the "turbine efficiency" of converting the kinetic energy of the total collected flow into the mechanical energy. However, it is not denoted as "turbine efficiency", because it is only an intermediate parameter and does not include the maximum of the collected air flow and so does not behave as significant as the power coefficient c_p. It, therefore, does not deserve the denotation "turbine efficiency" which sounds even more pompously than "power coefficient". For this reason, it is denoted by ε rather than η. Furthermore, because of Eq. (32) and the proportionality to $c_{2\mathrm{u,R}}/c_0$, the blade efficiency is also called here "tip swirl number". It behaves, like the tip speed ratio, as a design parameter. As shown below in Sect. 4, the blade efficiency ε is actually of geometrical character.
Analogously to Eq. (9) and in view of Eq. (33), the power coefficient is further obtained as

$$c_\mathrm{p} = \frac{2P}{\rho c_0^2 A_2 c_0} = \frac{\dot{Q}}{c_0 A_2}\varepsilon \tag{34}$$

With $\dot{Q} = c_0 A_0$ and $A_2 = A_\mathrm{D}$ from Eq. (7), this last equation takes the form

$$c_\mathrm{p} = \frac{A_0}{A_2}\varepsilon = \frac{1}{2}\left(1+\frac{A_0}{A_3}\right)\varepsilon \tag{35}$$

It represents a function in form c_p=f(ε,λ), because the area ratio A_0/A_3 is, according to Eq. (32), simply a function of same variables.
Against the Betz law in Eq. (10), the power coefficient shown in Eq. (35) is additionally a function of the rotational speed (n) of the wind turbine, which is involved in both parameters (λ and ε). This exactly represents the objective of the present studies.
Figure 4 displays computational results from Eq. (35). The use of the blade efficiency ε as a design parameter is evidently of great significance. It is possible to directly specify ε_m at which the maximum power coefficient is obtained. As shown in Sect. 4 below, the use of ε_m helps to directly design the turbine blade.
For large value of λ, all computations can be simplified. With respect to the expression under the square root in Eq. (32), it follows first

$$\varepsilon \approx 1-\frac{A_0^2}{A_3^2} \tag{36}$$

Then, Eq. (35) becomes

$$c_\mathrm{p} \approx \frac{1}{2}\left(1+\frac{A_0}{A_3}\right)\left(1-\frac{A_0^2}{A_3^2}\right) \tag{37}$$

It is equal to Eq. (10) of the Betz law.

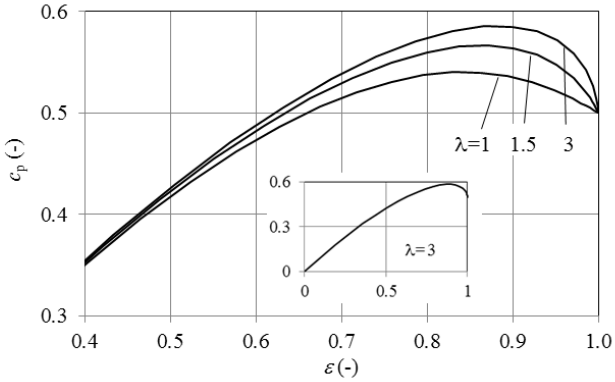

Figure 4. Power coefficient of a wind turbine in dependence on the tip swirl number (ε) for different tip speed ratios (λ).

3.4. Maximum power coefficient and flows

Figure 4 is further considered. Obviously, for each given tip speed ratio λ a tip swirl number ε_m exits, for which the power coefficient assumes its maximum. The function ε_m=f(λ) can be found basically from Eq. (35) together with Eq. (32). An explicit function of ε_m=f(λ), however, cannot be obtained. Based on the analysis, the following two equations can be used for performing iterative computations (with $x=A_0/A_3$):

$$\varepsilon_{\mathrm{m}}=\frac{4x^3}{1-x}+(1-x) \quad \text{and} \quad \frac{\varepsilon_{\mathrm{m}}}{\lambda^2}\frac{x}{1+x}=\sqrt{1+\frac{2}{\lambda^2}x(1-x)}-1 \tag{38}$$

Computational results are shown in figure 5 by the solid line. It is obtained without any assumption.

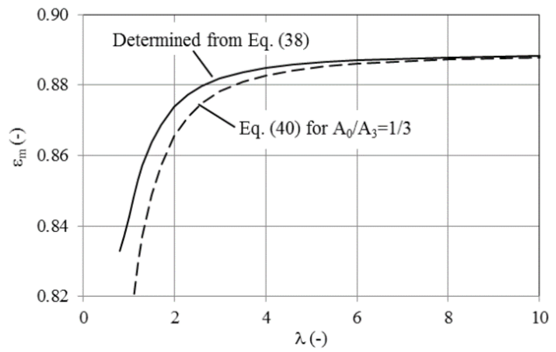

Figure 5. Tip swirl number plotted against the tip speed ratio of the wind turbine under the condition of the maximum power coefficient.

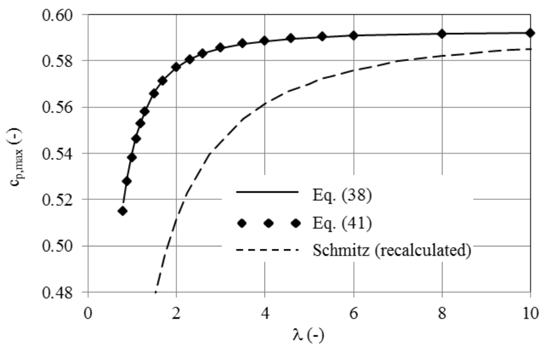

Figure 6. Maximum reachable power coefficient plotted against the tip speed ratio and comparison with computations based on Schmitz's theory.

Once the relation ε_m=f(λ) is obtained, the maximum power coefficient $c_{p,max}$=f(λ) can be computed from Eq. (35) together with Eq. (38), as shown in figure 6 (solid line).

For the case of a large tip speed ratio, one obtains from Eq. (38) the area ratio $(A_0/A_3)_m=1/3$ and further $\varepsilon_m=8/9$. This is comparable with $c_{D,m}=8/9$ in figure 2. The corresponding maximum of the power coefficient is obtained from Eq. (35) as

$$c_{\mathrm{p,max}}=\frac{16}{27} \tag{39}$$

It exactly agrees with the Betz limit.

While performing computations for the maximum power coefficient $c_{\mathrm{p,max}}$ from Eq. (35), both the area ratio $(A_0/A_3)_{\mathrm{m}}=\mathrm{f}(\lambda)$ and the area ratio $(A_0/A_2)_{\mathrm{m}}=\mathrm{f}(\lambda)$ have also been found. The former is from Eq. (38) and the latter from Eq. (35), as shown in figure 7. Obviously, only at large tip speed ratios, respective area ratios tend to reach 1/3 and 2/3, which correspond to the condition of Betz's limit for $c_{\mathrm{p,max}}$.

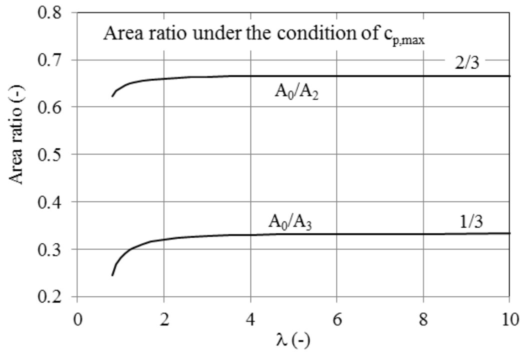

Figure 7. Flow area ratios plotted against the tip speed ratio λ under the condition of maximum reachable power coefficient.

All the above computations have been conducted without any assumptions. They provide a closed solution of ε_{m}, $c_{\mathrm{p,max}}$ and the area ratio A_0/A_2 and A_0/A_3 as a function of only the tip speed ratio λ under the condition of maximum power coefficient. They are therefore applicable for optimum design of the wind turbine.

3.5. Approximations relying on A_0/A_3=1/3

It is known that in Betz's law of using the "actuator disc" model the condition $A_0/A_3=1/3$ for the maximum power coefficient is applied. If this condition is generally applied in the current case as an approximation, then, one obtains from Eq. (32) and further from Eq. (35), respectively

$$\varepsilon_{\mathrm{m}} \approx 4\lambda^2\left(\sqrt{1+\frac{4}{9\lambda^2}}-1\right) \tag{40}$$

$$c_{\mathrm{p,max}} \approx \frac{8}{3}\lambda^2\left(\sqrt{1+\frac{4}{9\lambda^2}}-1\right) \tag{41}$$

For comparison, computations performed with both of these equations have also been shown in figure 5 (dashed line) and figure 6 (symbol), respectively. While in figure 5 good agreement between the two curves is evidenced only at large tip speed ratios, almost exact agreement between Eq. (35), i.e., Eq. (38) and (41) is documented in Figure 6. Thus, Eq. (41) can be considered to be well applicable. Especially, the maximum $c_{\mathrm{p,max}}$=16/27 in Eq. (39) can also be directly obtained from Eq. (41) for large tip speed ratio.

The ratio of $c_{\mathrm{p,max}}$ to ε_{m} is 2/3. It also corresponds to the area ratio A_0/A_2 according to Eq. (35).

3.6. About Schmitz's theory and BEM

For the reason of comparison, computations of power coefficients based on Schmitz's theory [1] have also been conducted by the author, as shown in figure 6 (dashed curve). From the literature, curves of computations based on Schmitz's theory are even somewhat lower than those computed here. The Schmitz theory applies in fact also to ideal fluids and was established under all optimum conditions for power exchange, including the Betz condition $A_3=3A_0$. It, however, ignored the non-uniform pressure distribution in the flow. It is, furthermore, based on some assumptions which, unfortunately, even do not fulfill the law of conservation of angular momentum like $c_{3u,\mathrm{R}}R_3=c_{2u,\mathrm{R}}R_2$ used in the current paper with Eq. (17). This can be considered as the third flaw or defect in the fundamentals of wind turbine technology.

Against the prediction by Schmitz's theory, the current computations, both Eq. (35) and Eq. (41) based on turbine theories, clearly demonstrate that the maximum reachable power coefficient is significantly higher than believed till now. There is a great reserve and thus possibility to further enhance the power coefficients of wind turbines. At a tip speed ratio λ=2, for instance, the maximum reachable power coefficient can be reset from $c_{p,max}$=0.51 (Schmitz) to $c_{p,max}$=0.57, a difference of more than 10%. For information of readers, in the field of water turbines (Pelton, Francis and Kaplan turbines), engineers have been trying hard since decades to enhance the hydraulic efficiencies of machines only for 1%.

The BEM is actually a computational tool to compute all aerodynamic forces exerted on a given blade and further to compute the aerodynamic performance including the power coefficient of a given wind turbine. It has thus been considered to be only applicable to case studies. Unlike the turbine theories and the Schmitz theory, the BEM is unable to predict the maximum reachable power coefficient in a wind turbine. In addition, the aerodynamic flow at a single airfoil blade fundamentally differs from the aerodynamic flow at a rotating blade, even if it is about a wind wheel with only one blade.

4. Turbine design and operations

The analyses made above can be directly applied to optimize the geometrical design of wind turbines. To this end, the tip swirl number plays a key role. According to figure 5, the tip swirl number is simply a function of tip speed ratio λ. For accurate computations, ε_m and further $c_{2u,R}$ should be computed from Eq. (38) or directly from figure 5. For approximation, however, Eq. (40) can be applied. Together with Eq. (32), it follows

$$\frac{c_{2u,R}}{c_0} = 2\lambda\left(\sqrt{1+\frac{4}{9\lambda^2}}-1\right) \tag{42}$$

It is for the tip radius (R_2) of the blade.

The angular velocity component along the blade in the radial direction is obtained with respect to $c_{2u}r = c_{2u,R}R = \text{const}$ as

$$c_{2u} = 2\lambda c_0\left(\sqrt{1+\frac{4}{9\lambda^2}}-1\right)\frac{R_2}{r} \tag{43}$$

This velocity component represents the flow rotation which must be generated at the turbine wheel.

In the geometrical design of blades, the blade angle (β_b) along the trailing edge of the blade is the most significant parameter. First of all, it must be consistent with the flow angle at the trailing edge of the blade (figure 8) and thus must be designed with respect to the desired velocity component c_{2u}.

According to figure 8 with u_2=$r\omega$ as the circumferential speed of the blade, the following geometrical relation between three velocity vectors can be obtained:

$$c_{2u} + r\omega = w_2\cos\beta_2 \tag{44}$$

With $w_2 = c_{2x}/\sin\beta_2$ this implies

$$\tan\beta_2 = \frac{c_{2x}}{c_{2u}+r\omega} \tag{45}$$

Inserting Eq. (43) and with $\lambda = R_2\omega/c_0$ and $A_0/A_2 = 2/3$, one finally obtains

$$\tan\beta_2 = \frac{2}{3}\frac{1}{\lambda}\frac{1}{2\left(\sqrt{1+\frac{4}{9\lambda^2}}-1\right)\frac{R_2}{r}+\frac{r}{R_2}} \tag{46}$$

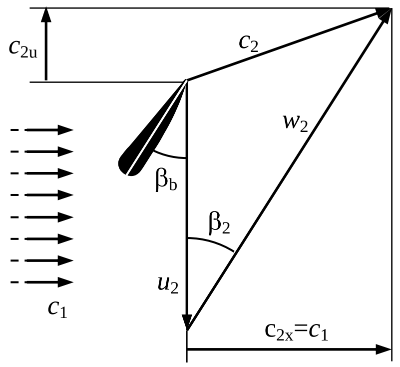

Figure 8. Velocity triangle at the trailing edge of the blade.

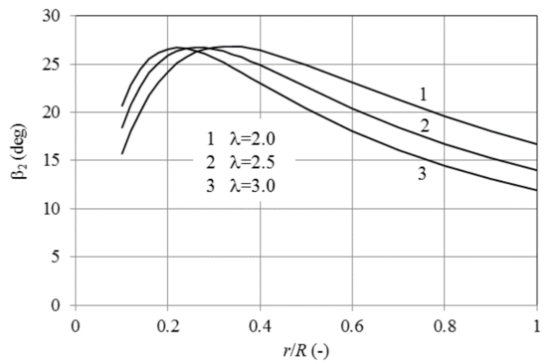

Figure 9. Relative flow angles along the trailing edge of blade for optimum operations at given λ.

Figure 9 shows computation results for three different tip speed ratios. Such flow angles can be basically used as reference to design the blade angles $\beta_b \approx \beta_2$. This, however, relies on the assumption that the flow at the trailing edge of a blade would completely follow the blade angle. This is only the case, if the blade number is sufficiently high. By only using three blades, for instance, the flow angle will deviate from the blade angle. The meaning of all above computations is that corresponding corrections can be made at this final stage of the blade design.

The operation of the wind turbine is specified by the tip speed ratio λ. According to figure 6, the tip speed ratio λ directly determine the power coefficient. On the one hand, a large tip speed ratio should be used. On the other hand, a high tip speed ratio will cause diverse mechanical problems inclusive increased friction losses and operation safety of all related mechanical components. It can be certainly expected that the c_p-curve shown in figure 6 will drop with increased tip speed ratio λ, if viscous friction losses, for instance, are also accounted for. A large tip speed ratio λ always means a large relative velocity (w in figure 8) which, in turn, causes large friction losses on blade surfaces. Because a sufficiently high power coefficient, say 0.57 for a maximum, could be reached already at a tip speed ratio λ=2, there is no need to run the turbine at other high tip speed ratios. This is the reason why wind turbines usually all operate at relatively low rotational speeds.

5. Summary

Diverse flaws or defects in the fundamentals of the wind turbine technology have been pointed out, as they are included in Betz’s law and Schmitz’s theory. They are considered to be the main cause of contradictions in all previous theoretical analyses.

Against the use of airfoil theory in both flow computations and geometrical designs of turbine blades, the turbine theory of using the Euler equation has been introduced into the wind turbine techniques. Because of the accurate consideration of non-uniform pressure distribution in the flow, the turbine theory and all related computations are accurate. The introduction of the blade efficiency, which is also called the tip swirl number, considerably contributes to the simplification and the completeness of the theoretical analysis. Based on such accurate performance analyses, the reachable maximum power coefficient can be considerably enhanced against the prediction in all previous analyses. With the help of the blade efficiency as a design parameter, the geometrical design of turbine blades has received a significant reference and thus can be well performed.

6. References

[1] Gasch R and Twele J 2012 Wind Power Plants. Second Edition, Springer Verlag.
[2] Sørensen J 2016 General Momentum Theory for Horizontal Axis Wind Turbines, Springer Verlag.

IOP Conf. Series: Earth and Environmental Science **431** (2020) 012022 doi:10.1088/1755-1315/431/1/012022

Speed control of brushless dc motor using Ant Colony Optimization

B A Kouassi[1,3], Yiming Zhang[1,3], M J Mbyamm Kiki[2,3] and S Ouattara[1,3]

1 College of Electronic Information and Control Engineering;
2 College of Computer Science and Technology
3 Beijing University of Technology, 100124, Beijing, China
E-mail: kabonzad@yahoo.fr

Abstract. DC motor has as a key aspect of industrial applications. Thus, due to their high performance, BLDC motors are preferred as a small horsepower motor. However, it is hard to acquire the good controlling performance with traditional tuning approaches in order to solve the speed control. This paper provides an approach of determining the optimum control parameters of PID for the BLDC speed control using the Ant Colony Optimization (ACO), which is an intelligent algorithm based on feeding behavior of the swarm. The efficiency and validity of the design method based on ACO are shown in the Simulation outcomes.

1. Introduction

There is a lengthy history of using general dc motors. A dc motor offers easy ways of controlling and accurate. It also has high efficiency and a strong starting torque compared to dropping speeds, which helps to avoid a sudden load rise [1]. However, the dc motors with such features have certain deficiencies to deal with that resulted in some other alternate kinds of dc motors being designed [2]. So, developing brushless direct current (BLDC) motors, which are alternatives to the conventional dc motor types, become an interest for researchers. BLDC has a lot of benefits, such as greater velocity versus dynamic response, high effectiveness, high ranges of velocity, low maintenance, etc [3]. In addition, the ratio of torque yielded to the size of the motor is higher, and this abets to its convenience in terms of space and weight perception.

Commonly, BLDC contain sensors to achieve the position of the rotor and the speed measurement. These motors have uncertainty in a discrete time example and have many hardships to design speed regulators. However, to reach the desired performance, the motor requires proper speed controllers. Then, the speed control is usually performed by using the proportional-integral (PI) controller based on traditional approaches such as Ziegler and Nichols [4]. Nevertheless, that approaches required long time and effort for the controller parameters tuning, as well its produce a surge and important overshoot. To overcome these tuning inconveniences, more and more approaches based on clever algorithms are now used in order to optimize PID parameters [5], [6].

The Ant Colony Algorithm (ACO) is a metaheuristic behavior, which based on the swarm intelligence generated by the cooperation in a colony, particularly by pheromone communication between ants on a good path from the colony to a potential food source in an environment [7]. The ACO algorithm is applied to find the good parameters of the PID controller amid a stability area. The PID controller parameters are set with the Ant Colony Optimization algorithm in this research [8].

This paper is arranged as follows: the second section explains briefly the BLDC Motor. The third section explains the PID tuning approach. The fourth section is about the Ant Colony Optimization

(ACO) technique. Section five provides some results of simulations on Matlab/Simulink to show the performance of ACO. Finally, section six gives the conclusion of the research.

2. Mathematical approach of BLDC motor

As shown in fig.1 below, the circuits illustrated a typical dc motor equivalent circuit.

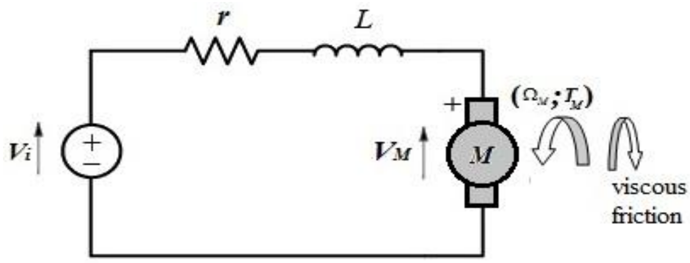

Figure 1. A typical model of DC motor schematic.

Applying Newton and Kirchhoff laws to fig.1, the dc motor is commonly described in the no steady-state, as below in eq.1 and eq.2:

$$L.\frac{di(t)}{dt} = v_i(t) - K_e.\Omega_m(t) - r.i(t) \tag{1}$$

$$J.\frac{d\Omega_m(t)}{dt} = K_t.i(t) - b.\Omega_m(t) - T_L \tag{2}$$

Where $v_i(t)$ is the voltage driven by the source, $i(t)$ is the armature current; L is the armature inductance; r is armature resistance, K_e denotes the back electromotive force constant, K_t denotes the torque constant, J denotes the inertia moment of the rotor, b denotes the mechanical system damping, T_L denotes the load torque and $\Omega_m(t)$ denotes the shaft angular velocity.

By applying the Laplace law to both eq.1 and eq.2 (considering no load $T_L \approx 0$), the motor speed transfer function $G_M(t)$ is given by:

$$G_M(s) = \frac{\Omega_m(s)}{V_i(s)} = \frac{K_t}{L.J.s^2 + (r.J + Lb).s + r.b + K_e K_t} \tag{3}$$

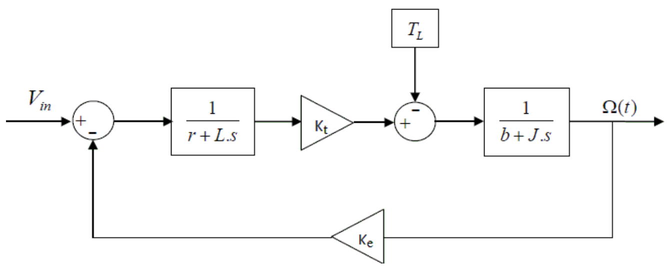

Figure 2. A typical Block diagram of DC motor speed control.

Eq.3 can be rewritten as:

$$G_M(s) = \frac{K_0}{\tau.\tau_e.s^2 + (\tau + \alpha.\tau_e).s + 1} \tag{4}$$

where:

$$\begin{cases} K_0 = \dfrac{K_t}{K_t.K_e + r.b} \\ \alpha = \dfrac{r.J}{K_t.K_e + r.b} \\ \tau = \dfrac{r.J}{K_t.K_e + r.b} \\ \tau_e = \dfrac{L}{r} \end{cases} \tag{5}$$

with τ the time constant and τ_e the electromechanical time constant.

Usually, $K_t.i(t) >> b.\Omega_m(t)$ and $K_e.\Omega_m(t) >> r.i(t)$ then eq.4 can be rewritten as follows with some approximation:

$$G_M(s) = \frac{K_0}{\tau.\tau_e.s^2 + (\tau + \tau_e).s + 1} \tag{6}$$

$$G_M(s) = \frac{K_0}{(1 + \tau.s)(1 + \tau_e.s)} \tag{7}$$

Eq.7 is in accordance with a closed-loop block diagram shown in fig.2. However, for the continuation of the operations, some approximations will be considered ($K_t.K_e >> r.b$ and $\tau >> \tau_e$), so from the transfer function described by eq.6, it yields:

$$G_M(s) = \frac{K_0}{\tau.\tau_e.s^2 + \tau.s + 1} \tag{8}$$

Finally, the transfer function $G_M(t)$ that described the conventional dc motor speed control is given by eq.8. Conventionally, the mathematical model of BLCD motor has some particularities. The phases especially influence the resistive and the inductive of the BLDC setting. So, with symmetrical arrangement, the electromechanical time constant τ_e and the time constant τ are given as follows:

$$\begin{cases} \tau = \dfrac{J}{K_t K_e}.\sum_{i \geq 1} r_i \\ \tau_e = L.\dfrac{1}{\sum_{i \geq 1} r_i} \end{cases} \tag{9}$$

3. Model of PID Controller

PID controller is a device that essentially depends on past and actual error values as well as a premedication of the future control errors. In fact, the integral part acts on the average of past errors; the proportional part takes effect on the present error value; and the derived part acts as a forecast of future errors founded on a linear extrapolation. PID computes continually the error value $err(t)$ as the difference between the needed process variable (output) and the required input (reference) as shown in fig.3 [9].

$$err(t) = reference - output \tag{10}$$

By adjusting the control variable $err(t)$, the control attempts to minimize the failure over time.

Generally, the time description of a PID is given as follows:

$$u(t) = K_p.err(t) + K_I \int_0^t err(t).dt + K_D.\frac{d.err(t)}{dt} \tag{11}$$

With K_p proportional parameter, K_I integral parameter and K_D derivative parameter of the PID controller.

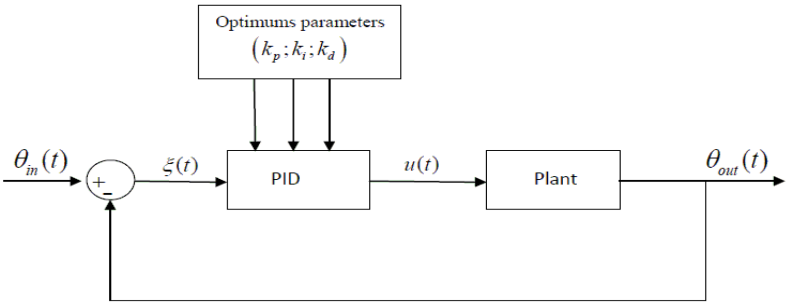

Figure 3. PID parameters optimization based on intelligent algorithms block diagram.

The tuning parameters are usually based on the performance of the controller described by the objective function [10]. That typical criteria for PID tuning, can be such as the absolute error, the time-weighted absolute error, the time-weighted square error and the square error. These different evaluated errors have distinct judgments on the system great performance, but this has no essential repercussion on the designing of robust PID [11], [12].

4. The Ant Colony Optimization algorithm

Intelligent swarm is a paradigm that sees collective cleverness as a behavior that emerges through the interaction and cooperation of large numbers of lesser clever agents. The paradigm is inspired by the swarms foraging and flocking behavior. These algorithms are probabilistic investigations [13].
The Ant Colony Optimization (ACO) is a new population-based technology for problem solving optimization [14]. It is an intelligent swarm based on feeding behavior of ants, particularly pheromone communication between ants on a good path betwixt the colony and an energy source in an environment as seen in fig. 4. That mechanism is called stigmergy.

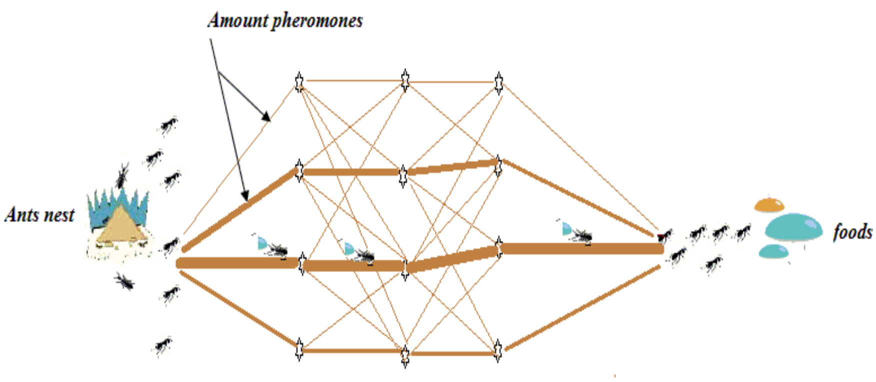

Figure 4. Stignergy between ants nest and food location.

As shown in fig.4, the ants which take the shortest route are those that take the minimum time on the way back and forth between the nest and the food. This path has a higher pheromone concentration and is more attractive for ants, so it is more likely to be borrowed. This path will be further strengthened, and the vast majority of the ants will ultimately choose this path.
The ACO provides the main pseudo-code list to minimize a cost function [15]. The process of updating pheromones is described by a unique equation that combines the contributions of all candidate solutions with a decline coefficient to determine the new pheromone value. Fig.5 shows the flowchart of PID tuning based on Ant Colony Optimization.

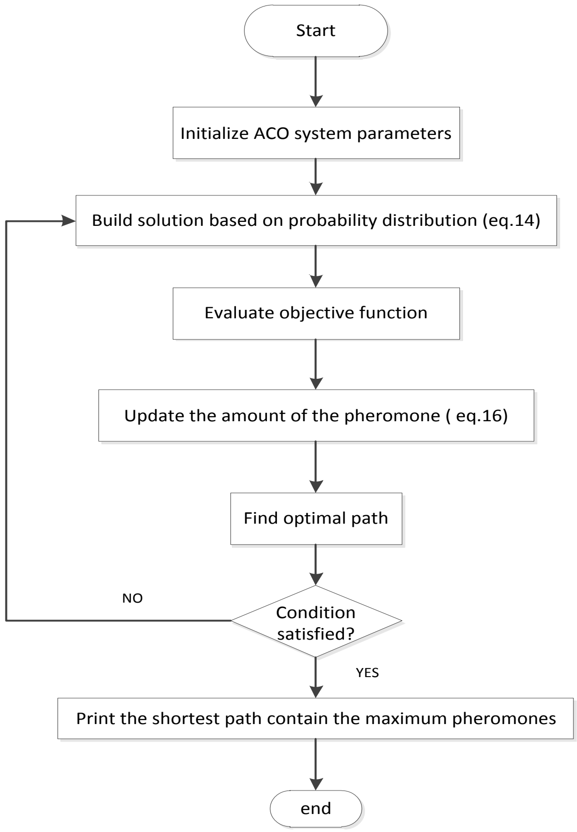

Figure 5. Flowchart of PID tuning based on Ant Colony Optimization.

The fundamental algorithm has three main phases:

- ***Initialization**:* The problem is finding a chart with the shortest cycle and let denote r_{ij} the distance between location *i* and location ***j*.** Each ant crosses the graph and creates a path. The amount of pheromone on the edges is initialized λ_{ij}.
- ***Shaping ant solution:*** In each phase of the solution construction, the ant needs to settle when it is going to move. This decision is taken probabilistic based on pheromone values and statistical information that enables it to find a good solution, in particular. So, the likelihood that an ant *k* will move from i to *j*, which includes some vertices not yet visited by ant denoted by L_i^{α}, is defined as:

$$p_{ij}^{k} = \frac{\lambda_{ij}^{\delta}(t).\eta_{ij}^{\sigma}}{\sum_{l \in L_i^k} \lambda_i^{\delta}(l).\eta_{il}^{\sigma}} \tag{12}$$

δ and σ are two parameters that involve the abundance of the pheromone intensity λ_{ij} and η_{ij} the visibility (statistical information) given by $\eta_{ij} = \frac{1}{r_{ij}}$.

- ***Pheromone updating:*** All the ants have built a solution, when each ant *k* has deposited a certain amount of pheromone $\Delta\lambda_{ij}^{k}$ on its path. For every iteration *t*, the quantities of pheromones deposited on the path *(i ; j)* are in the round of ant *k*, given by:

$$\Delta\lambda_{ij}^{k}(t) = \frac{q}{D^{k}(t)} \tag{13}$$

where $D^k(t)$ is the length of the ant k path, and q is a constant.
The concept of pheromone tracer evaporation is simulated by an evaporation rate φ parameter to avoid the negligence of the worst solutions obtained and therefore, the convergence to low-end local vision:

$$\lambda_{ij}(t+1) \leftarrow (1-\varphi).\lambda_{ij}(t) + \sum_{\alpha=1}^{N} \Delta\lambda_{ij}^{\alpha}(t) \tag{14}$$

where $\varphi \in]0,1[$.

The ACO algorithm is robust and flexible because of its resemblance to natural ant colonies. Many issues that require optimization can be targeted by self-adaptability.

5. Simulation and discussion

In this section, a mathematical model of a DC motor described by fig. 6, is used for simulation. The model is used for building Simulink transfer functions, which makes simulation easier.
In this section, the BLDC motor is a Maxon EC 45 flat Ø42.9 mm, 30 Watt (order number: 200142). The parameters used, are given in table 1. As well, Table 2 gives the ACO algorithm parameters used.

Table 1. DC motor specification.

DC motor parameters	value
Terminal resistance	1.2 Ohms
Terminal inductance	0.56 mH
Torque constant	25.5 rpm/A
Speed constant	374 rmp/V
Speed/torque gradient	17.6 rpm/mNm
Mechanical time constant	17.1 ms
Rotor inertia	92.5 gcm^2
***Number of pole pairs**	8
***Number of phases**	3

Table 2. ACO parameters.

Parameters	Values
Number of ants	20
number of iteration	20
Evaporation rate φ	0.95
Number of parameters	3
Delta δ	0.2
Sigma σ	0.8
Number of nodes	100

From table 1, it follows that:

$$\begin{cases} \tau_e = \dfrac{L}{3.r} = 1.556.10^{-4} \\ K_0 = \dfrac{1}{K_e} = \dfrac{\tau.K_t}{3.r.J} = 13.095 \end{cases} \tag{15}$$

Then eq.8 derives by the BLDC motor parameters becomes:

$$G_M(s) = \frac{13.095}{2.66.10^{-6}.s^2 + 1.71.10^{-2}s + 1} \tag{16}$$

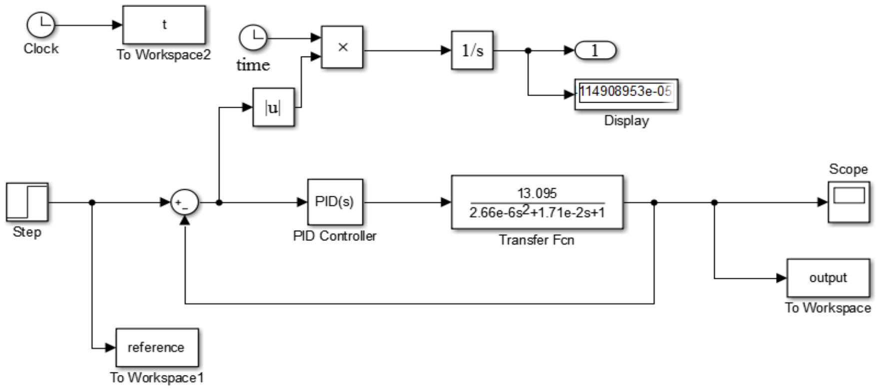

Figure 6. Matlab/Simulink diagram-bloc model of the BLDC motor.

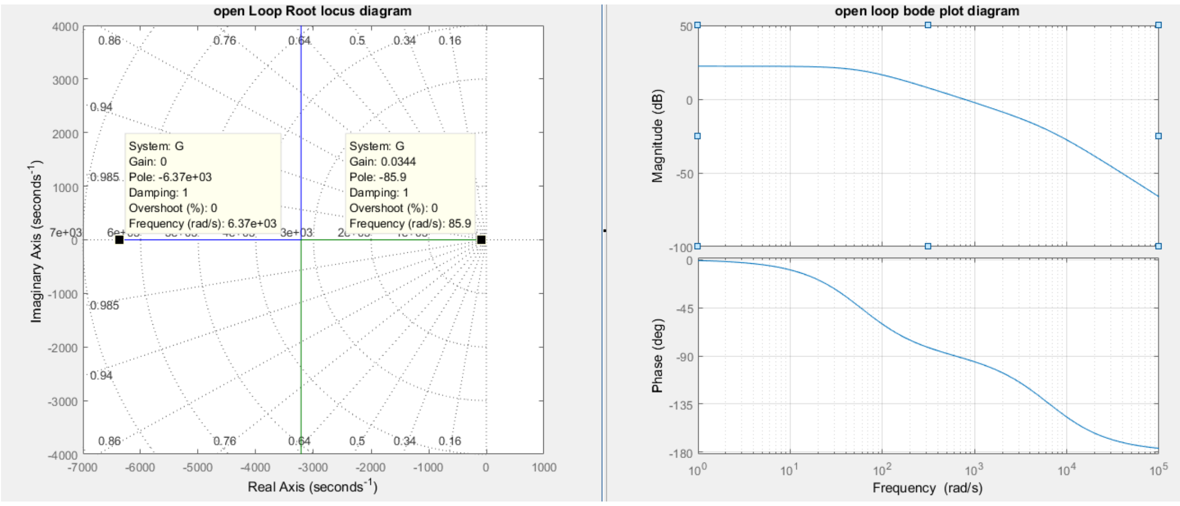

Figure 7. BLDC open loop step Root-Locus and bode diagram.

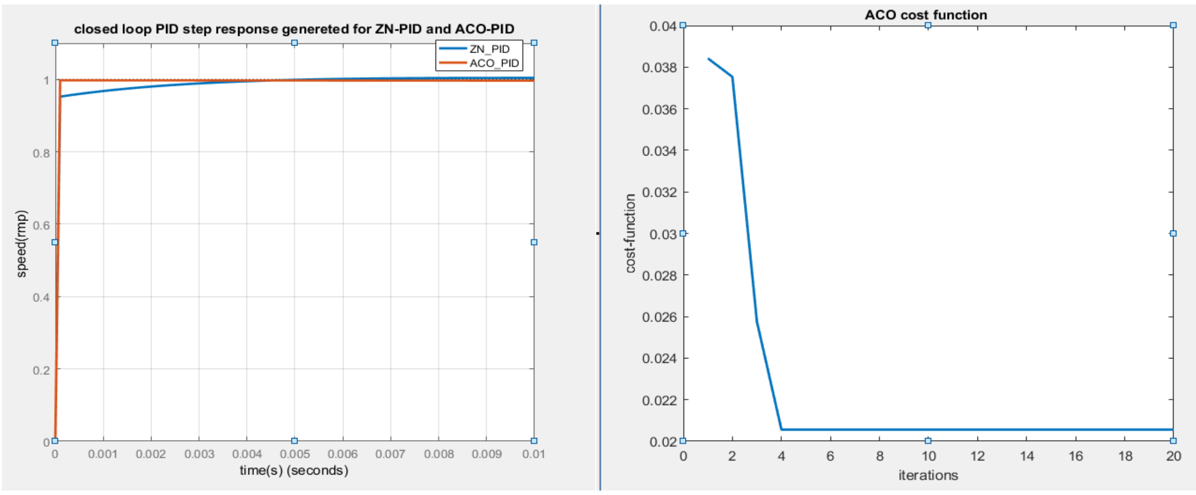

Figure 8. Closed-loop step response and cost function curve.

The open-loop analysis gives the step root-locus and Bode diagram as shown in fig.7. However, the performances of the ACO are shown in fig.8. As seen, the step response from ACO has good setting parameters (zero overshoot and less settling time) than Ziegler-Nichols tuning parameters as given in table 3.

Table 3. ACO and Ziegler-Nichols PID tuning parameters.

PID parameters	K_P	Ki	K_D	O_p(%)	t_s(s)	$t_r(s)$
Ziegler-Nichols	11.327	1381.34	0.0232	0.405	2.10^{-3}	$2.45.10^{-5}$
ACO	6.8718	4.8536	0.5146	0	$9.82.10^{-6}$	$8.02.10^{-6}$

where t_s denotes the settling time, t_r denotes the rise time, and O_p denote the overshoot.

6. Conclusion

The Ant Colony Optimization algorithm is used to adjust the optimal controller for best system performance. It is used to ensure the proper tuning of the PID controller, by eliminating the steady-state error between the BLDC motor speed measured and the reference speed to be tracked. The control goal is to ensure that the speed of the motor follows the input shift by developing a suitable controller.

Simulation results show the achievement and efficiency of using ACO algorithm for the speed control of BLDC motor. This algorithm guarantees the system, its stability and a faster response.

7. References

[1] Jean Pollefliet 2018 *Speed and (or) Torque-Control of a DC-motor* (Editor(s): *Jean Pollefliet, Power Electronics, Academic Press*, Pages 19.1-19.56, ISBN 9780128146415)

[2] Chinmay Kumar Das and Subrat Kumar Swain *2017 International Conference on Power and Embedded Drive Control (ICPEDC).* ,DOI: 10.1109/ICPEDC.2017.8081137.

[3] G.SanthoshKumar, S.Arockia Edwin Xavier 2015 *International Journal Of Current Engineering And Scientific Research (IJCESR), ISSN* volume-2, issue-2.

[4] Praveen Kumar Nambisan, .B.N.Sarkar 2014 *International Journal of Advanced Research in Electrical, Electronics and Instrumentation Engineering (An ISO 3297: 2007 Certified Organization)* Vol. 3, Issue 8.

[5] H.E.A. Ibrahim, F.N. Hassan, Anas O. Shomer 2014 *Ain Shams Engineering Journal*, Volume 5, Issue 2, Pages 391-398, ISSN 2090-4479.

[6] B. Anusha , A.V. Naresh Babu and A. Bala Naga Lingaiah 2017 *International Journal of Electronic and Electrical Engineering.* ISSN 0974-2174 Volume 9, Number 1 , pp. 1-10

[7] J. Kennedy, R. Eberhart and Y. Shi 2001 *Swarm Intelligence* (*Morgan Kaufmann Publishers, 1st Edition*, San Francisco, pp. 80-95).

[8] Hao Feng, Chenbo Yin, Wei Ma, Hongfu Yu and Donghui Cao 2019 *ISA Transactions*; https://doi.org/10.1016/j.isatra.2019.02.022 0019-0578/© 2019 ISA

[9] Karl Johan Åström 2000 *Lund University European Journal of Control* 6:1 (2000) 2-20

[10] J. Fišer, P Zítek, T Vyhlídal 2018 Robust PID controller design for plants with delay using similarity theory, IFAC-Papers OnLine, Volume 51, Issue 14, Pages 236-241, ISSN 2405-8963

[11] Pedro Mercader, Karl Johan Åström, Alfonso Baños and Tore Hägglund 2017 *IEEE transactions on control systems technology*, vol. 25, no. 2.

[12] Yogesh V. Hote and Shivam Jain 2018 *IFAC papers Onlines,* 51-4(2018) 604-609**.**

[13] Dušan Fister, Iztok Fister Jr, Iztok Fister and Riko Šafarič 2016 *Robotics and Autonomous Systems* 84 (2016) 64–75; http://dx.doi.org/10.1016/j.robot.2016.07.005.

[14] Yasser Shekofteh, Sajad Jafari, Karthikeyan Rajagopal and Viet-Thanh Pham 2018 *Circuits, Systems, and Signal Processing ; Springer Science+Business Media*, LLC, part of Springer Nature https://doi.org/10.1007/s00034-018-0967-5

[15] Rabiatuladawiyah Abu Hanifah; Siti Fauziah Toha; Mohd Khair Hassan and Salmiah Ahmad 2016 *Energy 102* (2016) 444e452 http://dx.doi.org/10.1016/j.energy.2016.02.050 0360-5442/© 2016.

Effect of tangential absolute velocity at outlet on open flume turbine performance

Sanjaya BS Nasution[1], Dendy Adanta[1], Warjito and Budiarso[1]

1 Department of Mechanical Engineering, Faculty of Engineering, Universitas Indonesia, Indonesia
E-mail: warjito@eng.ui.ac.id

Abstract. To address the electricity crisis in Indonesia, the use of open flume pico hydro turbines is a potential solution because Indonesia has 19 GW of hydropower resources at mini, medium, and pico scales. There are two concepts for the design of an open flume pico hydro turbine runner: Euler and Nechleba. Euler's concept recommends that the absolute tangential velocity at the outlet of the blade be zero to optimise power absorption. By contrast, Nechleba explains that to reduce flow separation at the outlet of the blade (separation can reduce efficiency), tangential absolute velocity at the outlet of the blade must not be zero. Accordingly, this study compares the performance of blades designed with these two concepts using a computational fluid dynamics method. The results showed that the maximum efficiency of the blade using the Euler concept was 70.08%, while the blade using the Nechleba concept was 74.39%. Based on the results, a runner design concept that assumes a non-zero tangential absolute velocity at the outlet of the blade is recommended for use in designing an open flume pico hydro turbine runner.

1. Introduction

Indonesia has 19 GW of hydropower resources at mini, medium, and pico scales [1][2][3]. However, Indonesia still faces a lack of electricity, especially in rural areas [4]. To overcome this problem, Indonesia is expected to be able to utilise its hydropower resources. One possible option is the use of open flume pico hydro turbines.

An open flume turbine is a pico-scale hydropower turbine which can generate high rotation with stable efficiency [5][6]. An open flume turbine is an axial turbine whose performance depends on the shape of its blade. In designing a blade shape, a velocity triangle is used. A velocity triangle is a triangle that represents absolute, relative, and rotational velocity, and can be represented by a Euler equation [7]. Based on Euler's equation, to generate the highest power, the absolute velocity tangential at the outlet (C_{x2}) of the blade should be zero [7][8].

Contradicting Euler's equation, Hothersall [9] explained that to reduce the separation of flow at the outlet of the blade, where separation could reduce efficiency, the absolute velocity tangential should not be zero. As an example, Singh and Nestmann [10] investigated the exit tip angle effect on runner performance. Their experimental analysis showed that increasing the exit tip blade angle could increase the efficiency of the runner [10]. In addition, Nechleba [9] and Williamson [11] revealed that to receive the highest power, the absolute velocity tangential at the outlet should be the same in magnitude as the relative velocity.

In order to prove the Nechleba explanation and to determine the most appropriate method to calculate the velocity triangle, this study conducts a computational fluid dynamics simulation to compare the performance of two blades, one based on Nechleba's suggestion and the other on a Euler equation.

Furthermore, to describe the comprehensive fluid phenomena at the blade runner, this study conducts a 3D unsteady calculation. The results of the study are expected to act as a future reference for the design of open-flume turbine blades.

2. Methodology

2.1. Geometry of the turbine

This study compares two blades with the same initial parameters. The initial parameters in this case are a discharge (Q) of 0.040 m^3/s, a diameter hub (D_h) of 70 mm, a diameter tip (D_t) of 125 mm, and the number of blades (z), 5. The blades are differentiated only by blade angle. Blade angles are calculated based on the velocity triangle method. The first blade, which we call the Euler blade, is designed with a C_{x2} magnitude of zero ($C_{x2} = 0$). The second, the Nechleba blade, has a (C_{x2}) magnitude of not zero ($C_{x2} \neq 0$) (see Figure 1).

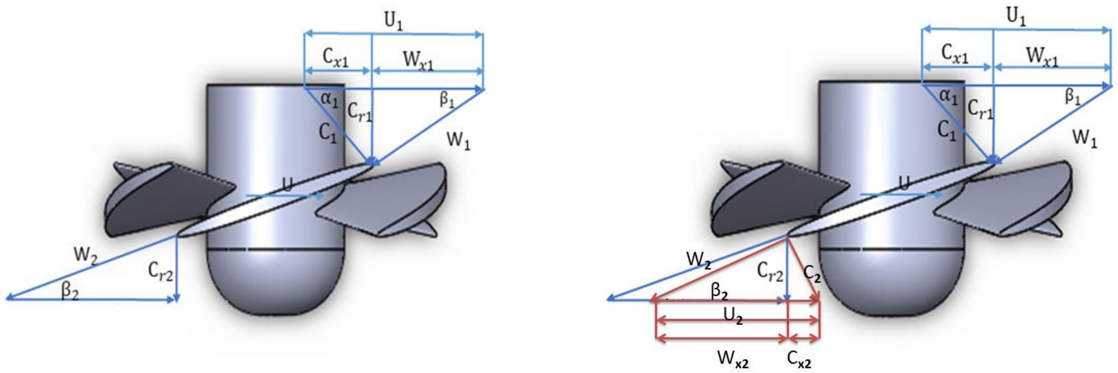

a. Euler blade b. Nechleba blade

Figure 1. Velocity triangle.

The equation below is a power equation based Euler's equation. This equation explains that to receive maximum power, C_{x2} should be zero [7]:

$$\mathrm{P} = \dot{\mathrm{m}}\mathrm{U}(\mathrm{C_{x1}} - \mathrm{C_{x2}}) \tag{1}$$

where ṁ is the mass flowrate, U is the turbine rotational velocity, and C_{x1} is the absolute velocity tangential at inlet. On the other hand, Dixon [12] and Gorla et al. [13] revealed that for axial flow turbo machinery, free vortex theory is used. Free vortex theory explains that the product of tangential flow velocity and radius vector should be constant [14][15]. Therefore, velocity triangles are differentiated from hub to tip [16]. Furthermore, in this case, the blade is divided into seven sections for which the velocity triangle at each section is calculated based on these equations:

$$\mathrm{C} = \mathrm{U} + \mathrm{W} \tag{2}$$

$$\mathrm{C} = \mathrm{C_x} + \mathrm{C_r} \tag{3}$$

$$\mathrm{C_r} = \mathrm{W} + \mathrm{W_x} \tag{4}$$

$$\text{blade angle} = \frac{\beta_1+\beta_2}{2} \tag{5}$$

where C is absolute velocity, W is relative velocity, C_r is absolute velocity radial, W_x is relative velocity tangential, and β_1 is the relative velocity angle at inlet and β_2 at outlet.

Figure 1 shows the geometry of the two blades. Figure 1a is a blade with its blade angle calculated based on Euler and Figure 1b is calculated based on Nechleba's recommendation. Based on the velocity triangle, the blade angle was also obtained.

2.2. Numerical calculation

Numerical calculation is performed with computational fluid dynamics (CFD) software. This study is performed with three-dimensional (3D) analysis. The simulation contains three steps: pre-processing, processing, and post-processing. Pre-processing is performed before running the simulation. It involves defining geometry, boundary condition, and meshing. Processing is the running process of the simulation. In this case, the simulation was run with unsteady calculation. Post-processing displays the results of the simulation.

Figure 2 shows the boundary condition of the study. The inlet is defined as a mass flow inlet with a discharge of 40 l/s, and the outlet is defined as a pressure inlet. In addition, the simulation also contains a stator and rotor interface. This is because the simulation set-up was conducted with a six-degrees of freedom set-up (6-DoF). The 6-DoF is used based on the recommendations of other researchers to define rotational velocity as the output of a simulation [17][18][19]. Therefore, in this study, blade rotation was not defined in the initial parameter. Further, as this is a 6-DoF simulation, it is also necessary to define the moment of inertia of the blade runner. The moment of inertia of the blade in this case is 0.05 N.m. Finally, the k-ε model is used as the turbulent model. Dendy et al. [20] recommend the k-ε model in turbo machinery simulation to reduce time consumption. Simpson et al. [11] also used the k-ε model to predict the performance of a propeller turbine.

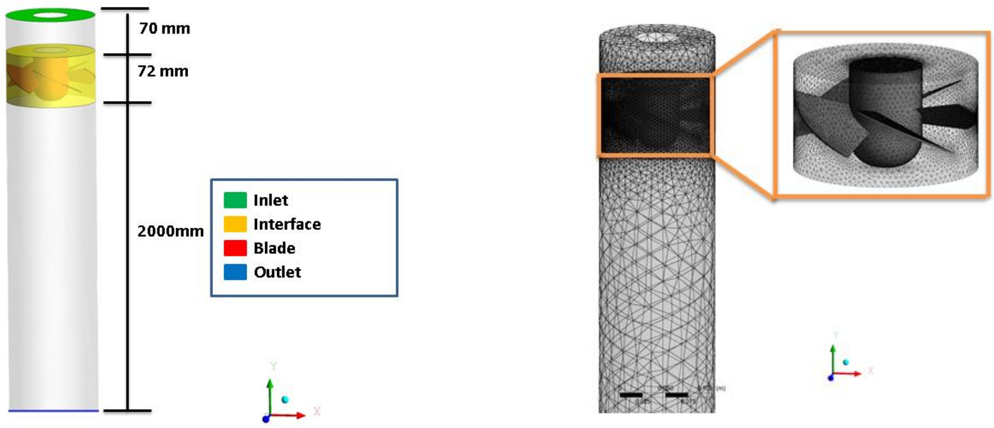

a. Boundary condition b. Mesh of geometry

Figure 2. Boundary condition and mesh of geometry.

2.3. Mesh and time-step independency test

After defining the boundary condition, mesh and time-step independency tests were used. The mesh independency test is a method to determine the appropriate mesh size and number of elements [21]. This study used three different numbers of elements: 1508868, 3062380, and 6006250. To determine the appropriate mesh size, the torque at each mesh number was calculated. Furthermore, the error of simulation was calculated based on the Roache method called the grid convergence index [22]. Figure 2b shows the geometry mesh of all domains; to improve the mesh quality, mesh size near the wall of the blade was refined. The same method was used in the time-step convergence test (TCI). Time step size differs from 0.002 s to 0.001 s and 0.0005 s.

3. Results and discussion

3.1. Runner blade geometry

From hub to tip, the blade was divided into seven sections. This condition induced the angle and chord line at each section to be different. Table 1 below describes the results of calculations according to blade geometry. It shows that the blade angles were different at each section for both blades: the blade angles of the two blades decreased from hub to tip. There was no significant difference at the tip, but at the hub, the blade angle of the Euler runner was lower than that of the Nechleba runner. The chord lines (L) of the two blades in this study were also the same.

Table 1. Comparison of Euler and Nechleba blades.

D_h/D_t	Blade Angle (^{0})		L (m)
	Euler	Nechleba	
1	12.51	28.79	0.022
0.8	24.97	26.41	0.023
0.67	40.77	31.95	0.033
0.57	50.6	45.57	0.045
0.5	57.09	54.11	0.060
0.44	61.68	59.79	0.076
0.4	65.09	63.82	0.094

3.2. Mesh independency test result
Figure 3 shows the results of the calculation of convergence index for mesh and time step. Normalisation of space in Figure 3 relates to the comparison of the independent variable. For CGI, 6006250 elements normalised to 1, 3062380 normalised to 1.96, and 1508868 normalised to 3.98. From Figure 3, it can be seen that increasing the number of elements induces a increasing of blade torque. And in this study, based on CGI analysis, 4402703 elements are used with an error of 0.36 % compared to the exact value.

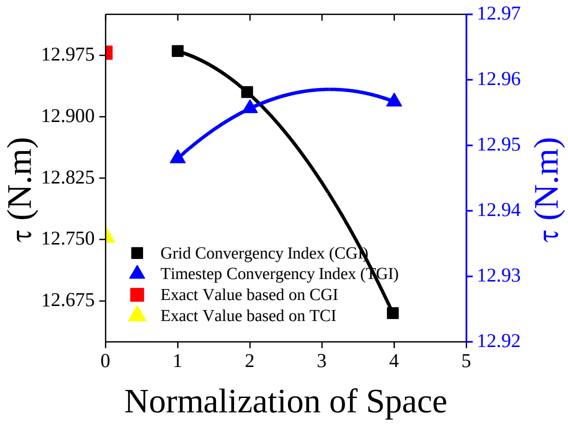

Figure 3. Mesh and time step independency.

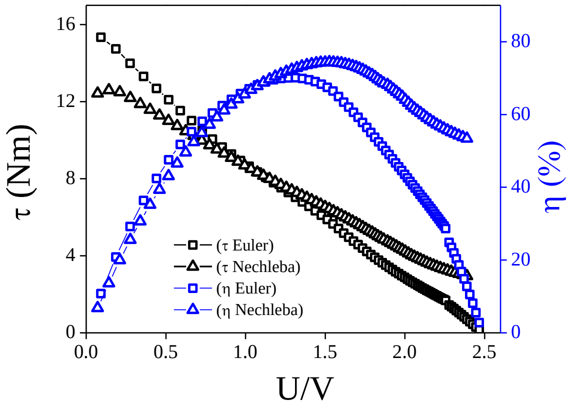

Figure 4. Torque and efficiency of turbine.

Furthermore, the same method is used for the TCI. Time step size 0.0005 normalised as 1, 0.001 normalised as 2, and 0.002 normalised as 4. Based on the TCI calculation, the appropriate time-step size was 0.01 with error of 1.2 % compared to exact value.

3.3. Runner performance
The results of the numerical calculation are shown in Figure 4. Figure 4 is a graph comparison of blade performance between Euler's and Nechleba's blades. The graph compares the torque and efficiency of two turbines to velocity ratio (U/V). The U/V is the comparison between rotational velocity and inlet flow velocity. As shown in Figure 4, increasing rotational velocity (U), in which the inlet flow velocity (V) is constant, decreases the torque of both blades. This is because at constant power, rotational velocity is inversely proportional to torque.
Figure 4 also shows the efficiency of the blades. At low rotational velocity, both blades have similar efficiency; however, there is a significant difference in efficiency at high rotational velocity. The Euler blade has a peak efficiency 70.08 % while the Nechleba blade has a peak efficiency 74.39 %. On the other hand, as seen in Figure 4, to generate maximum efficiency it is necessary to consider the optimum U/V ratio. The optimum U/V ratio for a Euler blade is 1.4 and for a Nechleba blade 1.7.

Thus, based the results shown on Figure 4, it is recommended that an open flume turbine blade be designed using the Nechleba concept where $C_{x2} \neq 0$, because it generates the higher performance.

4. Conclusion

The results of numerical studies using a computational fluid dynamics method show that there are differences in performance between a Euler blade and a Nechleba blade. The study found that the optimum efficiency of a Euler blade is 70.08% at U/W 1.4, while a Nechleba blade has an optimum efficiency of 74.39% at U/W 1.7. Thus, based on this study, the Nechleba concept is recommended for the design of an open flume turbine blade.

5. References

[1] P. Gokhale *et al.*, "A review on micro hydropower in Indonesia," *Energy Procedia*, vol. 110, pp. 316–321, 2017.
[2] N. A. Wibowo, V. Dermawan, and D. Harisuseno, "Studi Perencanaan Pembangkit Listrik Tenaga Mikro Hidro (PLTMH) Wamena di kabupaten Jayawijaya Provinsi Papua," *Malang Tek. Pengair. Fak. Tek. Univ. Brawijaya*, 2013.
[3] R. A. Subekti, "Survey Potensi Pembangkit Listrik Tenaga Mikro Hidro di Kuta Malaka Kabupaten Aceh Besar Propinsi Nanggroe Aceh Darussalam," *J. Mechatronics, Electr. Power, Veh. Technol.*, vol. 1, no. 1, pp. 5–12, 2012.
[4] ESDM, "Statistik Ketenagalistrikan," 2015.
[5] S. B. Nasution, Budiarso, Warjito, and D. Adanta, "A Comparison of Openflume Turbine Designs with Specific Speeds (Ns) Based on Power and Discharge Functions," *J. Adv. Res. Fluid Mech. Therm. Sci.*, vol. 45, pp. 53–60, 2018.
[6] S. J. Williamson, B. H. Stark, and J. D. Booker, "Low head pico hydro turbine selection using a multi-criteria analysis," *Renew. Energy*, vol. 61, pp. 43–50, 2014.
[7] Harinaldi, Budiarso, *Sistem Fluida: Prinsip Dasar dan Penerapan Mesin Fluida, Sistem Hidrolik, dan Sistem Pneumatik*. Jakarta: Erlangga, 2015.
[8] G. F. Round, *Incompressible flow turbomachines: design, selection, applications, and theory*. Elsevier, 2004.
[9] M. Nechleba, "Hydraulic turbines, their design and equipement," 1957.
[10] P. Singh and F. Nestmann, "Exit blade geometry and part-load performance of small axial flow propeller turbines: An experimental investigation," *Exp. Therm. Fluid Sci.*, vol. 34, no. 6, pp. 798–811, 2010.
[11] R. G. Simpson and A. A. Williams, "Application of computational fluid dynamics to the design of pico propeller turbines," in *Proceedings of the international conference on renewable energy for developing countries*, 2006.
[12] C. Hall and S. L. Dixon, *Fluid mechanics and thermodynamics of turbomachinery*. Butterworth-Heinemann, 2013.
[13] R. S. R. Gorla and A. A. Khan, *Turbomachinery: design and theory*. CRC Press, 2003.
[14] K. V Alexander, E. P. Giddens, and A. M. Fuller, "Axial-flow turbines for low head microhydro systems," *Renew. Energy*, vol. 34, no. 1, pp. 35–47, 2009.
[15] P. Singh and F. Nestmann, "Experimental optimization of a free vortex propeller runner for micro hydro application," *Exp. Therm. Fluid Sci.*, vol. 33, no. 6, pp. 991–1002, 2009.
[16] S.-S. Byeon and Y.-J. Kim, "Influence of blade number on the flow characteristics in the vertical axis propeller hydro turbine," *Int. J. Fluid Mach. Syst.*, vol. 6, no. 3, pp. 144–151, 2013.
[17] D. Adanta, S. A. Arifianto, and S. B. S. Nasution, "Effect of Blades Number on Undershot Waterwheel Performance with Variable Inlet Velocity," in *2018 4th International Conference on Science and Technology (ICST)*, 2018, pp. 1–6.
[18] D. Adanta, R. Hindami, Budiarso, Warjito, and A. I. Siswantara, "Blade Depth Investigation on Cross-flow Turbine by Numerical Method," in *2018 4th International Conference on Science and Technology (ICST)*, 2018, pp. 1–6.
[19] D. Adanta, W. Budiarso, A. I. Siswantara, and A. P. Prakoso, "Akademia Baru," *J. Adv. Res. Fluid Mech. Therm. Sci.*, vol. 46, no. 1, pp. 21–31, 2018.

[20] D. Adanta, W. Budiarso, and A. I. Siswantara, "Assessment of turbulence modelling for numerical simulations into pico hydro turbine," *J. Adv. Res. Fluid Mech. Therm. Sci.*, vol. 46, pp. 21–31, 2018.
[21] S. A. RICHARDS, "Completed Richardson extrapolation in space and time," *Commun. Numer. Methods Eng.*, vol. 13, no. 7, pp. 573–582, 1997.
[22] P. J. Roache, "Quantification of uncertainty in computational fluid dynamics," *Annu. Rev. Fluid Mech.*, vol. 29, no. 1, pp. 123–160, 1997.

Acknowledgments
This work support by Directorate of Research and Service Community (DRPM) Universitas Indonesia with grant No: NKB-0050/UN2.R3.1/HKP.05.00/2019.

IOP Conf. Series: Earth and Environmental Science **431** (2020) 012024 doi:10.1088/1755-1315/431/1/012024

Effect of the number of blades on undershot waterwheel performance for straight blades

Dendy Adanta[1], Muhamad Agil Fadhel Kurnianto[1], Warjito, Sanjaya BS Nasution[1] and Budiarso[1]

1 Department of Mechanical Engineering, Faculty of Engineering, Universitas Indonesia, Indonesia
E-mail: agil.fadhel@gmail.com

Abstract. Access to electricity in Indonesia is limited due to the remote area of the community. In the modern era, electricity is a primary necessity and indicator of welfare. To overcome this problem, using renewable energy resources in the remote areas of Indonesia is an appropriate alternative. Based on this condition, the pico hydro-type undershot waterwheel is suitable to be used in Indonesia, because undershot waterwheels are appropriate for low head conditions or low river flow. This study will examine the effect of different blade numbers on the performance of undershot waterwheels for straight blades. There are four blade number variations: 8, 12, 16, and 20. The computational fluid dynamic method was used because it can visualise the flow pattern with more detail than other methods. Activating six degrees of freedom is needed to predict the rotational speed of the turbine's interaction with the water and blade. Based on the results, 20 blades produced higher efficiency than others. However, the 8 blades had a stable performance and produced higher rotational speed than the other. The empirical equation for determining the number of blades of undershot waterwheels adopted by the Pelton turbine is correct.

1. Introduction

In 2018, 2% or 2 million of Indonesians people did not yet have access to electricity. This is due to difficult accessibility to the remote areas of the community. In the modern era, electricity is a primary necessity and indicator of welfare. To overcome this problem, using renewable energy resources in the remote area is an appropriate alternative [1]. Pico hydro (<5 kW) is a possible alternative because the life cycle cost per kW is cheaper than that of a solar PV or wind turbine [2]. Furthermore, Indonesia has 19 GW of water energy sources for small, micro and pico-scale, categorized as low head conditions (< 5m) [3]. Due to this condition, pico hydro-type undershot waterwheel is suitable for use in Indonesia because undershot waterwheels are appropriate for low head conditions or low river flow [4].

Pico hydro type undershot waterwheel is a popular technology in Indonesia called kincir air (water mill) and has been used for a long time (19th century). However, the development of undershot waterwheels continues, especially in the blade characterisation. Sule et al. [5] studied blade shape and the number of undershot waterwheels. The study shows that the performance of 10 blades is higher than 6 and 8 blades [5]. On the other hand, Warjito et al. [4] proposed an empirical equation of the number of blades. The empirical equation is adapted from the Pelton turbine. Based on empirical calculation, the number of blades is 8. Warjito et al. proved the equation by comparing the 8 blades with 6, 7, 9 and 10 blades. This comparison uses the computational fluid dynamics (CFD) method. The results of the study show that the 8 blades have a higher efficiency than other blades [4].

Based on the explanation above, the method to determine the blade number of the undershot waterwheel is still not clear. Using the adopted equation from the Pelton turbine has problems, which for all conditions the calculation will result in 8 blades. Additionally, the results of Warjito et al.'s study showed that there was no significant change in blade efficiency with increasing blade numbers [4]. This is due to the condition of blade number variation being too short. Because of this, we continue the study with more blades. In this study, the variation of blades is 8, 12, 16, and 20 blades. The study was conducted with unsteady CFD simulation.

2. Methodology

2.1. Geometry

In this study, the geometry of the undershot waterwheel turbine has the same main parameter as the previous study [4].The main parameters are: Blade height (h) = 0.164 m, Inner Diameter (D_i) = 0.820 m, Outer diameter (D_o) = 0.984 m and blade angle (0) = 45. However, this study uses a different number of blades: 8, 12, 16, and 20. The representation of main parameters and blade number variation are shown in Figure 1 below.

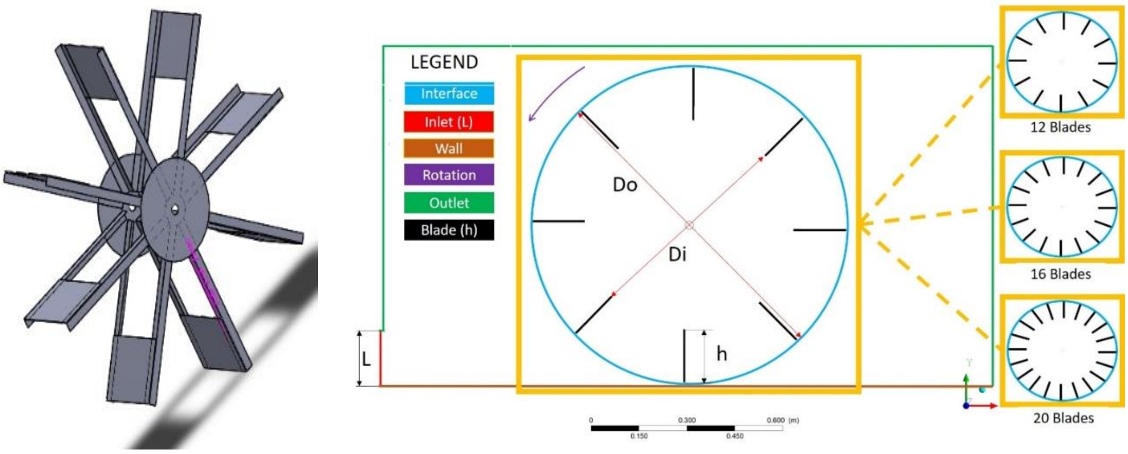

a. Three-dimensional model of wheel

b. Boundary condition of simulation

Figure 1. The model of the undershot waterwheel.

2.2. Simulation setup

This study was conducted with 2-dimensional simulation and was performed with unsteady calculation, which ran in 5 seconds of time step total. On the other hand, the six degrees of freedom (Six-DoF) feature is used. This is due to the recommendation of other researchers that to determine the rotational velocity as a dependent variable, the Six-DoF feature is used to investigate fluid dynamics phenomena by the movement of the domain blades that occur from interactions with fluids [6][7]. According to the Six-DoF feature, it is necessary to perform the simulation with two domains, the rotor domain and the stator domain. Because of this, the interface between the rotor and stator domain is created (see Figure 1b). Additionally, to activate the Six-DoF feature, the blade's moment of inertia and preload must be defined. In this study, we used 24 N.m of preload and various moments of inertia depending on blade geometry (8 blades: 4.2 kg.m^2, 12 blades: 6.2 kg.m^2, 16 blades: 8.3 kg.m^2, and 20 blades: 10 kg.m^2).

The boundary condition of this study is shown in Figure 1b. The inlet of the boundary condition is velocity inlet, which the magnitude is 1 m/s. The outlet is determined as a pressure outlet with 0 Pa of pressure. The numerical calculation was also conducted with a multiphase simulation. In terms of multiphase simulation, volume of fluid option is selected with surface tension between water and air is 0.0728 N/m. Furthermore, standard k-epsilon is used due to this ability to predict a quite representative flow characteristic based on previous study [8][2]. The result of the study shows that the k-epsilon turbulen model is the most suitable turbulent model for this kind of turbine

2.3. Mesh and timestep independency tests

Appropriate mesh and time-step size in unsteady CFD simulation must be determined [8]. Roache explained the grid convergence index (GCI) to calculate the error of mesh number variation [9]. GCI is an extrapolation method to determine the predicted exact value of the dependent variable. In this study, the number of mesh varies at 25,196, 50,969 and 101,117. Figure 2 shows the mesh visualisation with 50,969 elements. Furthermore, to optimize the mesh quality, the mesh size near the wall is refined (Fig. 2).

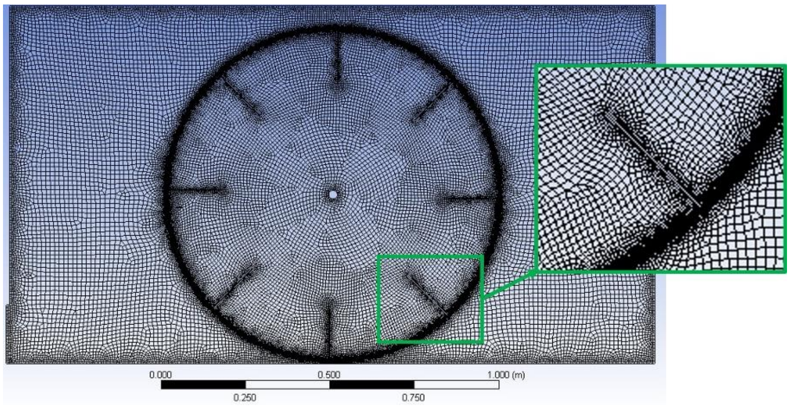

Figure 2. 2D Domain mesh visualization – 50,969 elements.

3. Results and Discussion

3.1. Independency test results

Figure 3 is a complete calculation of GCI; it determines the torque for each normalisation space. Normalisation of space is the comparison between various numbers of elements. In this study, 101,117 elements were normalized as 1, 50969 as 1.4, and 25196 as 2. The calculations show that the appropriate mesh number in this study is 50,969, with an error of 0.55%.

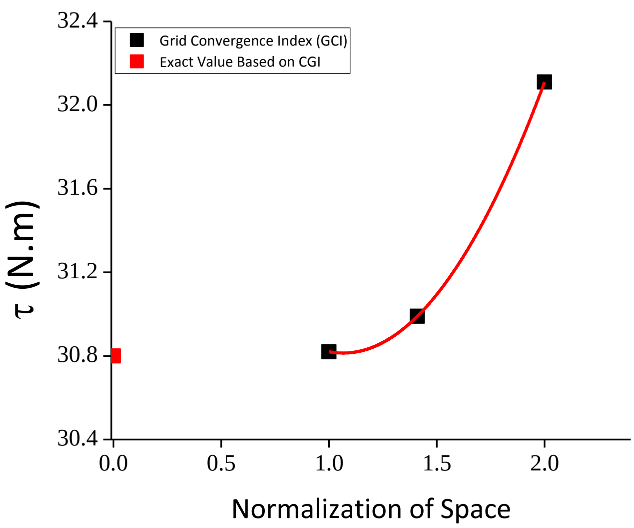

Figure 3. Grid convergence index.

On other hand, for timestep, the same method is conducted. Based on previous study, it is found that the appropriate timestep size is 0.001 s [4].

3.2 Runner Performance

Figure 4 is a comparison graph between blade's tip speed and timestep, showing that the blade's tip speed was increased at the beginning of the simulation until it reached the maximum speed at timestep 1,200. The blade's tip speed then decreased and steadied after timestep 4,000. Figure 4 also shows that the more blades on the undershot waterwheel, the more it will produce lower blade's tip speed. However, anomaly conditions happened with 16 blades, whereas it lowered with 20 blades.

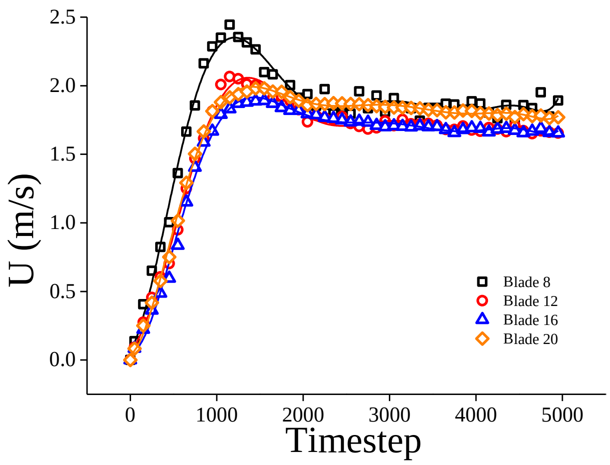

Figure 4. Blades tip speed of undershot waterwheel.

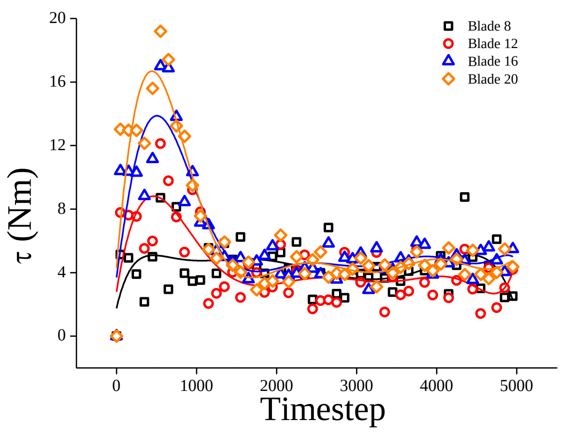

a. Torque

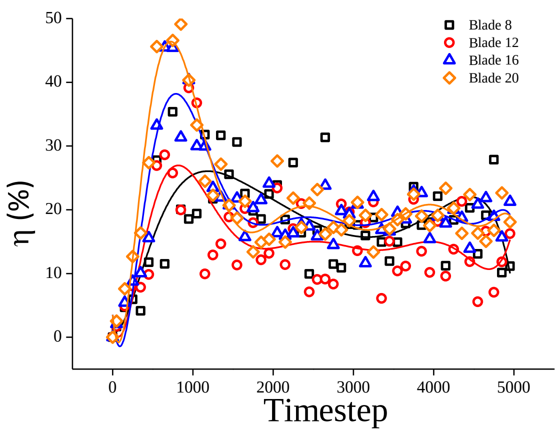

b. Efficiency

Figure 5. Torque and Efficiency of the turbine.

Beside the blade's tip speed (U), the waterwheel's torque is also a variable that expresses the undershot waterwheel performance. Figure 5a is the wheel's torque graph of a various number of blades during the simulation, where they became stable after timestep 2,000. It can be obtained that a higher number of blades produced greater torque. Furthermore, Figure 5b expresses the efficiency of the four testing cases over the simulation process. The highest waterwheel efficiency in this simulation is attained at 46% by 20 blades in the undershot waterwheel with a timestep of about 1,000. Runner-up position is attained by 16 blades, which is about 38% at almost the same timestep. In addition, the undershot waterwheel with 8 blades has the lowest maximum efficiency, which is only about 26%. However, this case has a more stable efficiency graph than others.

IOP Conf. Series: Earth and Environmental Science **431** (2020) 012024 doi:10.1088/1755-1315/431/1/012024

It can be summarized from the above discussion that the undershot waterwheels with 20 blades have better efficiency than other cases. However, the 8-blades undershot waterwheel has more stable efficiency and can attain a higher tip speed, which means that it can produce a higher rotational speed. The higher rotational speed is very important when it is easier to attain the generator's rotational speed requirement. Furthermore, the stable efficiency of the waterwheel is also important due to the fluctuation of input power from the water, which is often faced in micro hydro or pico hydro.

4. Conclusion

Evaluation of the empirical approach of the undershot waterwheel's blade number is important because the result of the approach is almost always the same. The numerical simulation to verify that the chosen number of blades by the mentioned approach is the best choice has already been done by varying the blade number. The simulation resulted in higher blade numbers producing higher waterwheel efficiency. However, the chosen blade number by the empirical approach has still been recommended due to its stable performance and higher rotational speed. This study must also be proven by a comprehensive experimental study.

5. References

[1] B. Ho-Yan, "Design of a low head pico hydro turbine for rural electrification in Cameroon," 2012.

[2] D. Adanta, Budiarso, Warjito, and A. I. Siswantara, "Assessment of Turbulence Modelling for Numerical Simulations into Pico Hydro Turbine," *J. Adv. Res. Fluid Mech. Therm. Sci.*, vol. 45, pp. 21–31, 2018.

[3] "Statistik Ketenagalistrikan T.A 2017," 2018.

[4] Wariito, D. Adanta, S. A. Arifianto, S. B. Nasution, and Budiarso, "Effect of Blades Number on Undershot Waterwheel Performance with Variable Inlet Velocity," *Proc. - 2018 4th Int. Conf. Sci. Technol. ICST 2018*, no. 4749, pp. 1–6, 2018.

[5] L. Sule, "Angled and Curved Bladesof Deep-Water Wheel Efficiency," 2014.

[6] D. Adanta, R. Hindami, and A. I. Siswantara, "Blade Depth Investigation on Cross-flow Turbine by Numerical Method," in *2018 4th International Conference on Science and Technology (ICST)*, 2018, pp. 1–6.

[7] Warjito, D. Adanta, Budiarso, and A. P. Prakoso, "The effect of bucketnumber on breastshot waterwheel performance," in *IOP Conference Series: Earth and Environmental Science*, 2018, vol. 105, no. 1, p. 12031.

[8] A. I. Siswantara and B. Budiarso, "Assessment of Turbulence Model for Cross-Flow Pico Hydro Turbine Numerical Assessment of Turbulence Model for Cross-Flow Pico Hydro Turbine Numerical Simulation," no. December, 2018.

[9] P. J. Roache, *Computational fluid dynamics*, no. BOOK. Hermosa publishers, 1972.

Acknowledgements

This work support by Directorate of Research and Service Community (DRPM) Universitas Indonesia with grant No: NKB-0050/UN2.R3.1/HKP.05.00/2019.

Analysis of large deviation between reheat steam temperature of 200MW unit and main steam temperature of steam turbine side

Ying Le[1]

1 Senior engineer, Huadian Electric Power Research Institute Co., Ltd., Hangzhou,Zhejiang,310010,China
E-mail: ying-le@chder.com

Abstract. With the increasing task of energy conservation and emission reduction, the accuracy of important parameters of the unit is particularly important.In this paper, the main steam temperature on the side of a steam turbine in a thermal power plant is lower than that on the side of a boiler.Through analyzing the possible problems of measuring medium, measuring element, measuring channel and parameter display one by one, the reasons for the deviation of measured parameters are obtained, so as to improve the safe, economic and stable operation of the unit.This article has certain reference value to the similar question.

1. The introduction

A power plant has four 200MW coal-fired generating units. The boiler is a UG-670/13.7-M type boiler manufactured by WuXi boiler factory. The boiler is ultra-high pressure primary intermediate reheat, natural circulation solid slag discharge pulverized coal furnace. Type boiler adopts Π layout. The boiler is designed to be fueled by bituminous coal.

It has been 10 years since the unit was put into operation. With the continuous aggravation of energy saving and emission reduction tasks, it has been exposed that the main steam temperature deviation on the side of the engine and furnace caused by various factors is large, leading to large temperature reduction water volume and economic decline. The steam parameters entering the turbine regulating gate are one of the decisive factors affecting the overall cycle efficiency of thermal power units. Whether the boiler can run stably, safely and reliably is directly related to the social and economic benefits of the power plant.

2. Existing problems

Since the overhaul of the unit, the screen display value of the main steam temperature on the side of the turbine is 13℃ lower than that of the reheat steam temperature of the boiler, which seriously affects the safe, economic and stable operation of the unit. In order to facilitate the analysis of problems, we divided the temperature measurement system into several links: measuring medium, measuring element, measuring channel and parameter display. The thermocouple transmits the signal to the I/O module through compensating wires. The signal arriving at the I/O module is transmitted to the controller through the I/O bus. The controller sends the signal to the operator station through cold end compensation and finally displays in front of the operator on duty. In the measuring medium section, steam temperature, casing temperature, surface temperature of insulation layer and other measuring points are marked[1].as shown in the figure1 below:

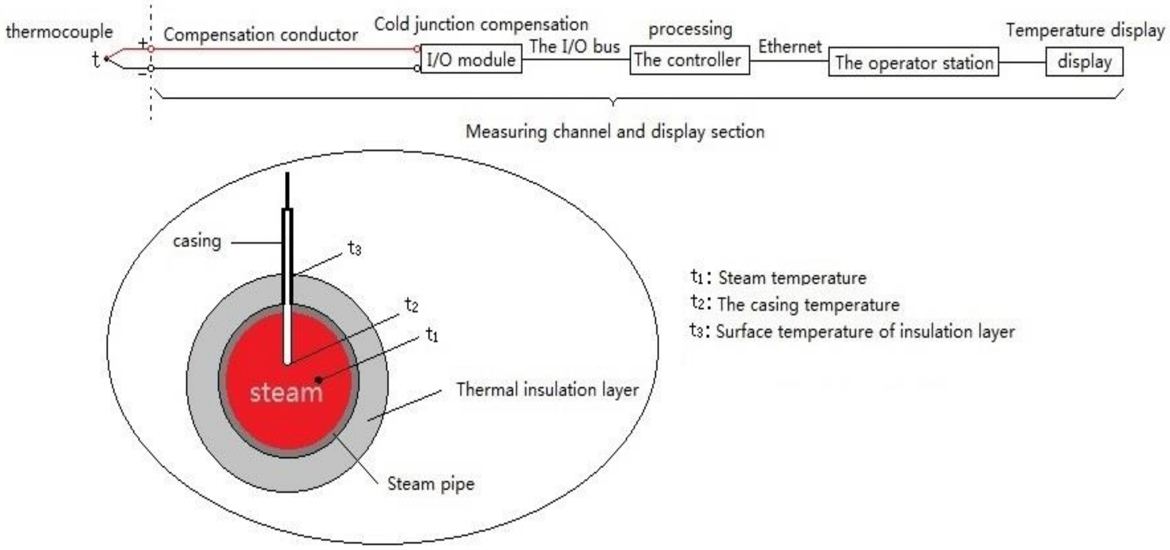

Figure 1. Decomposition diagram of temperature measuring system

The temperature measuring element is thermocouple, thermocouple as one of the most simple, the most common temperature sensor, with its wide temperature measuring range, from -200 ~ +1600℃, even up to 2800℃, can convert the temperature signal into voltage signal, achieve long-distance transmission. However, in the actual work, due to the bad working environment of thermocouple for a long time, if the thermocouple is not paid attention to in the use, or the installation is not correct, it is likely to bring great errors or faults to the measurement, leading to the system working disorder, resulting in product quality and equipment safety accidents.

3. Possible cause of error

Since this phenomenon is of low temperature and the thermoelectric potential output by thermocouple is lower than the actual value, the possible reasons are as follows:

3.1. Local short circuit in thermocouple

3.2. Damp inside thermocouple. There is leakage of air and water inside the protective casing

3.3. The thermocouple electrodes have corroded or deteriorated

3.4. Local short circuit in the internal terminal of the thermocouple junction box

3.5. Local short circuit of compensation conductor, mismatch between compensation conductor and thermocouple, polarity inversion of compensation conductor and thermocouple [2].

The thermocouple temperature measurement principle and the connecting conductor rule decide that the compensating conductor must be used in its connecting line to extend the cold end temperature to the constant instrument room. In the meantime, thermocouple has the cent of positive and negative pole, the compensation wire that matchs with it also has positive and negative pole, compensation wire and thermocouple must have same thermoelectric property, namely the compensation wire model that chooses must match with thermocouple, can produce measurement error likewise otherwise.

3.6. Thermocouple installation location or insert depth is not enough [2].

Regarding the installation environment and location of thermocouple, the representative measuring position of the pipeline should be selected to avoid the high magnetic field area. When the nominal diameter of high-temperature and high-pressure (main) steam pipeline is equal to or less than 250mm, the insertion depth should be 70mm, and when it is larger than 250mm, the insertion depth should be 100mm.

IOP Conf. Series: Earth and Environmental Science **431** (2020) 012025 doi:10.1088/1755-1315/431/1/012025

3.7. Thermocouple reference temperature is too high or two contact temperature is different.

3.8. Too much scaling on the surface of thermocouple protection tube.

4. Troubleshooting

4.1. Thermocouple check
Remove the measuring element and check it with tube furnace. All the test results are qualified. No moisture inside the thermocouple, no leakage of the protective pipe, water leakage and other phenomena. No corrosion or deterioration of hot electrode. There is no local short circuit in the terminal post of the thermocouple terminal box.

4.2. Measurement channel inspection
The display value of the middle pressure reheat steam temperature on the right side of the steam turbine of #1 unit is 15℃ lower than that on the side of the boiler, so the measurement channel is inspected on site. The results are as follows: the temperature measuring element is k-type thermocouple, the polarity connection of compensation cable is correct, and the compensation temperature of cold end in DCS control cabinet is 27℃, which is consistent with the reality. Disconnect the compensation wire of the reheat steam temperature measuring thermocouple on the right side of the #1 steam turbine, and add the voltage signal of 20.7mV there with the signal generator; Meanwhile, the ambient temperature was 31.4℃ measured by infrared thermometer, and the corresponding voltage of K thermocouple indexing meter was 1.28 mV. It's calculated that20.7mV + 1.28 mV= 21.98mV. Check the K thermocouple indexing table, and the corresponding temperature under this voltage is 531.57℃. The temperature curve of DCS screen shows the value of 530℃, and the error is within 1.6℃, which is basically normal. There are no obvious problems in the measurement channel circuit.

4.3. Check the thermocouple protection sleeve
Standard DL 5190.4-2012《The Technical Specification for Electric Power Construction》part 4: requirements for thermal instruments and control devices, "for high and medium pressure pipelines, if the socket is all in the insulation layer, it is appropriate to choose soft insulation material from the end of the socket for insulation, the height of the socket should not be lower than the thickness of the insulation layer.

4.4. Depth check of thermocouple insertion
If the insertion depth of the measuring point protection sleeve is not enough, the thermocouple will not be able to truly feel the actual temperature of the measured steam, affecting the measured value and producing measurement errors. The insertion depth of thermocouple protection sleeve of reheat steam pipe of unit #1 was checked, and the inspection results are shown in table 1:

Table 1. Depth of insertion of thermocouple elements for reheated steam line

Reheater steam outlet pipe		Medium pressure cylinder inlet steam pipe	
Right element insertion depth 1	Right element insertion depth 2	Right element insertion depth 1	Right element insertion depth 2
125mm	120mm	105mm	104mm
Left element insertion depth 1	Left element insertion depth 2	Left element insertion depth 1	Left element insertion depth 2
122mm	121mm	103mm	107mm

Standard DL 5190.4-2012 《The Technical Specification for Electric Power Construction》part 4: thermoelectric instruments and control devices
"When the nominal diameter of high-temperature and high-pressure (main) steam pipeline is no more than 250mm, the insertion depth should be 70mm; When nominal diameter is greater than 250mm, the insertion depth should be 100mm."

"When the outer diameter of general fluid medium pipe is no more than 500mm, the insertion depth shall be 1/2 of the outer diameter of the pipe; When the outer diameter is greater than 500mm, the insertion depth should be 300mm."Therefore, from the perspective of the data of table 1, the steam pipe wall thickness of 20 mm, minus the insertion depth of pipe wall thickness, according to the standard, the side of the furnace components insertion depth basic standard, but the side component insertion depth of less than 100 mm, actually reheat steam pipe nominal diameter greater than 530 mm, and belongs to the medium pressure steam pipeline, therefore, the side temperature measuring element insertion depth did not meet the requirements of the industry standard. This is one of the main reasons for the low measured value of reheat steam on the engine side.

5. Check the measured steam temperature

Since the installation port of thermocouple is welded to the steam pipe at the entrance of the medium pressure cylinder on the side of the steam turbine and the reheater outlet on the side of the boiler respectively, The temperature at the installation port bulge can approximate the surface temperature of steam pipe wall on both sides of the steam turbine and boiler. The temperature difference at the bulge on both sides of the steam pipeline can approximately represent the temperature drop degree of the pipe wall of the pipeline, The temperature difference on the surface of the insulation layer on both sides of the steam turbine and boiler can represent the heat dissipation loss. T1 represents the temperature at the bulge of the thermocouple installation port on the boiler side; T1 'represents the surface temperature of the insulation layer of the steam pipe on the side of the boiler; T2 represents the temperature at the raised installation port of the thermocouple on the turbine side; T2 'represents the surface temperature of the insulation layer in the steam pipeline on the turbine side, as shown in figure 2.

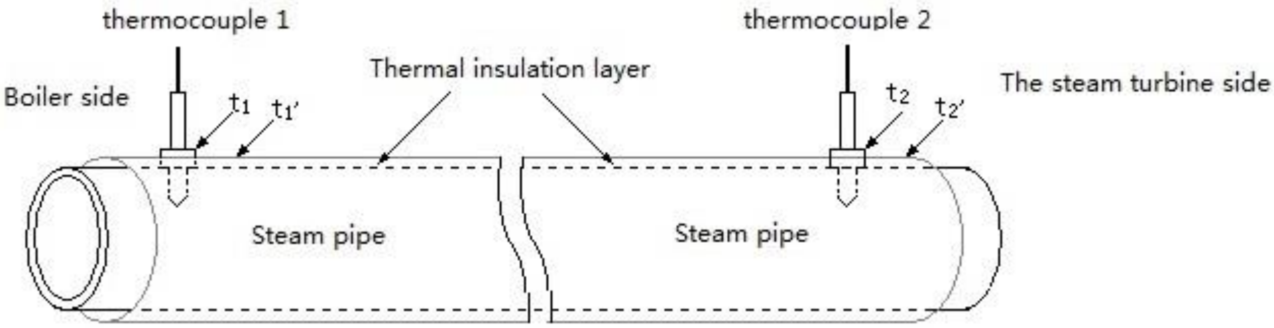

Figure 2. Pipe name and schematic diagram of temperature measuring point

The temperature values of these four points were measured by infrared thermometer, and the temperature values of t1 and t2, t1 'and t2' were compared. Then, the heat dissipation loss of the steam pipeline was judged.Under normal circumstances, the temperature t2 of the thermocouple socket boss on the turbine side should be slightly lower than t1 of the thermocouple socket boss on the boiler side. The surface temperature of the steam pipe insulation layer on the steam engine side t2 'should also be slightly lower than that on the boiler side t1'.If the temperature t2 of the thermocouple socket boss on the side of the steam engine is much lower than the temperature t1 of the thermocouple socket boss on the side of the boiler, it indicates that the temperature loss of the steam pipe is large.

The measurement results of the insulation layer of the reheat steam pipe of unit #1 are shown in table 2.

As can be seen from table 2, the surface temperature of the insulation layer of the inlet pipeline of the medium pressure cylinder is 7℃ higher than that of the outlet pipeline of the reheater, which indicates that the insulation effect of the pipeline is not good, and the heat dissipation loss of the pipeline is large, making the surface temperature of the insulation layer of the pipeline increase.

Table 2. Reheat the surface temperature of the insulation layer of the steam line

Surface temperature of insulation layer at the left exit tube of boiler reheatert1'(℃)	Surface temperature of insulation layer at the left inlet pipe of the steam engine medium pressure cylindert2'(℃)	Steam turbine side contrast boiler side (℃)
62	69	↑7
Surface temperature of insulation layer at the right exit tube of boiler reheatert1'(℃)	Surface temperature of the insulation layer at the inlet pipe on the right side of the steam engine medium pressure cylindert2'(℃)	Steam turbine side contrast boiler side (℃)
53	60	↑7

The measurement results of the reheat steam pipe element socket boss for unit #1 are shown in table 3.

Table 3. Reheat steam pipe temperature measuring element boss temperature

Temperature of thermocouple 1 boss on the right outlet pipe of boiler reheater t1 (℃)	Temperature of thermocouple 2 boss on inlet pipe at right side of steam engine medium pressure cylinder t2 (℃)	Steam turbine side contrast boiler side (℃)
310	250	↓60
Temperature of thermocouple 1 boss on the left outlet pipe of boiler reheater t1(℃)	Temperature of thermocouple 2 boss on inlet pipe at left side of steam engine medium pressure cylinder t2 (℃)	Steam turbine side contrast boiler side (℃)
300	250	↓50

As can be seen from table 3, the poor insulation effect of the reheat steam pipeline of unit #1 results in a large reduction in the surface temperature of the pipeline, indicating a large temperature drop of the pipeline. Therefore, this is a major reason for the low measured value of reheat steam on the turbine side.

6. Conclusion

According to the above investigation results, there are two main reasons for the low inlet temperature of the medium pressure cylinder.

6.1 Thermocouple insertion depth reasons

due to insufficient insertion depth of thermocouple protection sleeve at the inlet of the medium pressure cylinder of machine #1, the thermocouple cannot feel the real steam temperature.

6.2 The insulation layer of main steam pipe does not meet the insulation effect

due to the poor insulation effect of the reheat steam pipe of unit #1, the pipe heat dissipation causes the temperature of the thermocouple protection sleeve to drop, thus reducing the measured value of the thermocouple.

The thermocouple temperature measurement system is complicated and operates in a bad environment.as long as the thermocouple application rules are observed, the error can be effectively reduced by rational selection and correct wiring, and the error of thermocouple temperature measurement system can be controlled within its allowable error range.

7. References

[1] ZHANG Hong. 2010 Error analysis and treatment of thermocouple temperature measuring system .*J. Journal of Anhui University of Technology and Science* **25** 63-66
[2] Wang Rui. 2006 Fault Analysis and Solution for Thermo-couple Temperature Measure System. *J. Metrology & Measurement* **33** 31-32

Acknowledgments

The auther gratefully acknowledge the contributions of the Science and technology project of China Huadian CorporationLtd. (CHDKJ18-01-73)

IOP Conf. Series: Earth and Environmental Science **431** (2020) 012026 doi:10.1088/1755-1315/431/1/012026

Improved method on hydraulic power calculations for conventional sucker rod pumping system

O E Mwangupili[1, 2], P Chunsheng[1], C Bululu[1], S L Nyanswi[1] and S M Muya[2]

1 China University of Petroleum (Huadong), Qingdao, China
2 Mbeya University of Science and Technology, Tanzania
E-mail: Osmund94@gmail.com

Abstract. The annual energy consumption of suck rod pumping units in China is more than 10 billion kWh, but the average efficiency is only about 25-31%. Limited information is known, about the efficiency of various components of the pumping unit. The current methods for calculating the hydraulic power neglect the effect of friction and free gas. This research introduces an improved method for calculating hydraulic power which takes into account the effect of friction and free gas. The model was obtained from the product of two parameters which were, predicted pressure increased by the downhole pump and predicted flow rate. The pressure increased by the pump was obtained by the nodal analysis approach in which the concepts of multiphase flow were included. The Computer program was developed and all calculations in this paper were computed by this program developed from python programming language version 3.5. This model was compared with the previous models and showed that, the previous models underestimated the hydraulic power since the influence of gas and friction were not included.

1. Introduction

When there is inadequate pressure in the reservoir to lift the produced fluid to the surface, artificial lift is inevitable to maintain its production life [1], [2]. Sucker rod pumping system is the oldest of all artificial lift systems, covers approximately 71% of all. It is powered by the electric motor which supplies mechanical energy to the motor shaft then utilizes a subsurface pump to lift reservoir fluid from the bottom of the well to the surface [3], [4].

Beam pumping units have been leading the mechanical oil-production equipment regardless its disadvantages including low efficiency and high energy consumption, but there is a certain degree of difference according to various well conditions. The sucker rod pumping system is limited to severe friction in deviated wells, solids, sensitive problems in gassy wells, deep wells due to rod capacity and offshore operations due to its huge size [5], [6].

According to the related statistics, power consumption makes up about one-third of the total costs in oilfield production. Power consumed by beam pumping unit accounts for nearly 80% of the total. At present, there are more than 100,000 beam pumping units in China, and the total installed capacity is more than 3500 MW, consuming more than 10 billion kWh each year. Therefore, there is a huge potential for energy savings of the beam pumping units [5].

1.1. System efficiency

The ratio of the hydraulic power to the net motor input power is defined as the total system efficiency.
This value accounts for the losses in the motor, belts, pumping unit gearbox, pumping unit bearings, rod string, liquid, viscous losses, tubing back pressure, stuffing box friction, and other losses.

Efficiency measurements are useful in identifying high operating cost components of a beam pumping system. For example, a well may have a relatively high lifting cost due to low average motor efficiency, high mechanical losses in the pumping unit, significant rod/tubing friction, high tubing pressure or many other problems that can be identified by analyzing efficiencies.

System efficiency of the sucker rod pumping systems is contributed by surface and subsurface efficiencies. This research focused on the hydraulic power which is essential for calculating a subsurface efficiency.

As for a conventional sucker-rod pump, the main factors that affect its pumping performance in wells are volumetric efficiency, stroke loss, leakage, and high oil formation volume factor [7].

1.2. Subsurface system efficiency

Subsurface system efficiency of the beam pumping unit is the ratio of the hydraulic power to the polished rod power. Hydraulic Power is the power required to lift the fluid from downhole to the surface, usually regarded as a net lift. Net lift is the height to which the work provided by the pump alone lifts the produced fluid, similarly the depth at which the pump is set is referred to as a net lift.

The following are the components of the subsurface system efficiency; sucker rods, tubing, downhole pump, pump dynamometer card, polished rod and gas separator. Subsurface losses can be grouped into the following categories; frictional losses in the stuffing box, frictional losses between the rods and tubing, hydraulic losses which include fluid friction and pump leakage. The mechanical energy required to operate the polished rod at the surface is defined as the sum of the useful work performed by the pump and all the downhole energy losses detailed previously, i.e., those occurring in the sucker-rod pump, the rod string, and the fluid column.

Energy efficiency of the downhole components of the pumping system is characterized by the relative amount of energy losses in the well.

$$\eta_{sub} = \frac{P_{hyd}}{PRP} \times 100\% \tag{1}$$

where: η_{sub} –Subsurface efficiency, %; P_{hyd} –hydraulic power, kWh; *PRP*-Polished Rod Power, kWh.

The characteristics of the reservoir used in this research were, the reservoir is old, which means, it is the mature reservoir with the high permeability, high water cut and excellent reservoir deliverability. For cost reduction and performance improvement, the integrated analysis and management of the pumping wells are inevitable [8].

Currently, there is no precisely method of studying an oil well system and estimating the hydraulic power of sucker rod pumping system. The current methods of calculating the hydraulic power neglect the effect of friction and the effect of free gas. Therefore this research introduced the improved method for calculating the useful power developed by the subsurface pump.

2. The improved calculation method for predicting hydraulic power

This model was obtained from the product of two parameters which were; the predicted pressure increase by the downhole pump and the predicted flow rate. Basically this model encompassed the effect of friction and the presence of free gas which were not incorporated in the previous models for calculating hydraulic power. The frictional energy losses comprised of hydraulic frictional losses of the fluid as it flows between rods and tubing.

2.1. Predicted pump discharge pressure and pump intake pressure

Pressure gradient prediction requires determination of individual phase velocities, densities, viscosities, and, surface tension at different pressures and temperatures. In dynamic conditions of multiphase flow in pipes, the pressure and temperature of the fluids change continuously, and mass transfer occurs between the liquid and the gas phases.

As pressure decreases below bubble point in the direction of flow, gas evolves from solution in the oil increasing the gas velocity, the oil density and viscosity. Such flow and fluid properties changes are predicted with either compositional or black-oil models.

In this research black oil model was used to determine fluid physical properties. The assumption made in the black oil model was that, at any fixed temperature, pressure, API gravity of the liquid phase and specific gravity of gas, the liquid phase had a fixed gas solubility and formation volume factor.
Most black oil models that relate fluid physical properties can be determined by using Pressure-Volume-Temperature (PVT) cells. McCain Jr presented the fluid physical properties used in this paper. The calculated fluid physical properties were used to predict the pump discharge pressure and the pump intake pressure [9].
Beggs and Brill correlation was used to predict the flow patterns, pressures drops and finally pump intake pressure and discharge pressure. Beggs and Brill model was chosen for this research because, the model considered the inclination angles, the influence of free gas and the friction of the fluid being pumped when predicting pressure.
The total depth of the oil well was divided into segments, each segment being 100m long. The pressure gradient was determined in each of the segment starting from the top (well head) and then added to each successive segment; hence the pump discharge pressure was determined. On the other hand, the pump intake pressure was obtained starting from the fluid level to the pump intake in the annulus between tubing and casing.
The pressure increased by the pump was determined from the difference between the pump discharge pressure and pump intake pressure as shown in the equation (2).

$$P_u = P_d - PIP \tag{2}$$

2.2. Predicted flow rate
Due to effects of stroke loss, pump fillage, leakage and formation oil volume factor, the actual displacement of pump is generally less than the theoretical displacement. Hence pump efficiency was introduced to obtain the actual pump displacement.
Predicted flow rate was determined from the parameters designed by Dong and the pump efficiency [10]. Pump efficiency was found from the pump discharge coefficient simulation model given by Yao [11].

$$Q = 1440 \times \frac{\pi}{4} \times d_p{}^2 sn\eta \tag{3}$$

where: Q –Production rate, m^3/d; d_p –Plunger diameter, m; s –Stroke length, m; n –Pumping speed, min^{-1}; η –Pump efficiency
The volumetric efficiency of the downhole pump depends principally upon the fillage of the barrel. This in turn is related to the presence of gas, the viscosity of the fluid being pumped and the pumping speed. The pump efficiency was calculated by using equation (4). This parameter was introduced in this research to account for the inefficiencies (losses) of the downhole pump.

$$\eta = \eta_S \eta_F \eta_L \eta_V \tag{4}$$

$$\begin{cases} \eta_S = \dfrac{s_P}{s} \\ \eta_f = \dfrac{1 - KR}{1 + KR} \\ \eta_L = \dfrac{f_p s \eta_S \eta_F \eta_V - \Delta Q}{f_p s \eta_S \eta_F \eta_V} \\ \eta_L = \dfrac{1}{(1 - f_w) B_{ops} + f_w B_{wps}} \end{cases} \tag{5}$$

IOP Conf. Series: Earth and Environmental Science **431** (2020) 012026 doi:10.1088/1755-1315/431/1/012026

where: η_s –The effective stroke coefficient of pump, plunger; η_F –The coefficient of fullness; η_L –Pump coefficient of leaking; η_V –The volume ratio of gas dissolution crude oil under bottom pressure; s_p –Pump plunger stroke length, m; R –Pump intake gas fluid ratio, m^3/m^3 ; K –Clearance coefficient; s_o –The clearance length, m ; B_{ops} –The crude oil volume ratio in the pump intake; B_{wps} –The water volume ratio in the pump intake; ΔQ –The fluid leakage between pump plunger and pump barrel in one stroke.

$$K = \frac{s_o}{s} \tag{6}$$

$$R = (1 - f_w)(R_p - \alpha P_s)\frac{P_{st} T_s Z_s}{T_{st} P_s} \tag{7}$$

$$s_p = s - e_t - e_r + e_o \tag{8}$$

where: R_p –Producing gas-oil ratio, m^3/m^3; α –Dissolving coefficient, (m^3/m^3/MPa); P_{st} – Standard pressure, MPa; T_{st} – Standard temperature, K; T_s –Standard temperature, K; Z_s –Gas deviation factor in the pump intake; P_s –Pump intake bottom pressure (absolute), MPa; s_p –Plunger stroke length, m; e_r –rod stretch, m; e_t –tubing stretch, m; e_o -Plunger over travel, m . Predicted hydraulic power was found from equation (2) and (3).

$$P_{hyd} = \frac{Q(P_d - PIP) \times 10^{-3}}{86400} \tag{9}$$

The Subsurface pump of the conventional sucker rod pumping system is powered by the reciprocating rod string, which increases the potential energy of the liquid being pumped. The logic of the model is that, the effective power of the sucker rod pumping system is the power produced by the subsurface pump. When the pressure increased by the downhole pump and the amount of the liquid pumped are given, the hydraulic (effective) power can be determined from the product of these two parameters. In this model the pressure increased by the downhole pump involved the effect of free gas in which the multiphase flow concepts were taken into consideration. The two phases were liquid phase (water and oil) and gas phase. This means the concept of liquid hold up was introduced when the mixture density was calculated. In addition to that, the effect of friction was also included.

3. Computer program

All the calculations used in this research were computed by the computer programming codes. The computer programming language used was python version 3.5. Python is a high-level programming language which was designed for code readability; it uses whitespace indentation to set the limits of code blocks rather than curly brackets. It can express the concept in few lines of codes than C++ or Java.

Figure 1 demonstrates the procedure for computing hydraulic power by the developed program. The calculations began with the inputting data, and then from the data, the average pressure and temperature at the well surface were obtained. The average pressure was obtained by first estimating pressure drop and the estimated pressure drop was divided by two and added to the surface pressure (downhill). The next step involved making PVT calculations to determine the fluid physical properties, from the relevant correlations at the calculated average pressure and temperature. The fluids were oil, gas and water. The calculated physical properties were; specific gravity, gas compressibility, density, viscosity, gas solubility, solution gas, formation volume factor and surface tension. As soon as fluid physical properties were calculated, the slip density of the pumped fluid (multiphase) was determined.

The slip density was found from the superficial velocities, liquid hold up, Froude number, velocity number and flow patterns.
Reynolds number was then calculated to determine type of the flow (laminar or turbulent), followed by determination of the frictional pressure drop. The correlations used for calculating frictional pressured drop were; Drew, Koo and McAdams and Zigrang and Sylvester. The pressure drop in the segment due to elevation was calculated where the depth was equal to the length of the node, 100m. The pressure drop due to acceleration was set equal to zero. The total pressure drop was obtained by summation of the three pressure drops as shown in equation (10).

$$\left\{\left(\frac{dp}{dL}\right)_T = -\left(\frac{dp}{dL}\right)_f - \left(\frac{dp}{dL}\right)_{el} - \left(\frac{dp}{dL}\right)_{acc}\right. \tag{10}$$

Beggs and Brill correlation was an iterative process. When the calculated pressure drop was not equal to the estimated pressure drop, the computed pressure became the new estimated pressure drop. The procedures were repeated to achieve the condition where the estimated pressure drop equalled to the calculated pressure drop. The condition was met and the procedures were repeated to calculate the pressure drop of the next segment. When the pressure drops in each node was calculated, the pump intake pressure and pump discharge pressure were calculated. The pump discharge pressure was calculated by summing the surface pressure and all segments (nodes) pressure drops from the well head to the pump depth. On the other hand, the pump intake pressure was obtained starting from the fluid level to the pump intake in the annulus between tubing and casing. Finally, the hydraulic power was obtained by using equation (9).

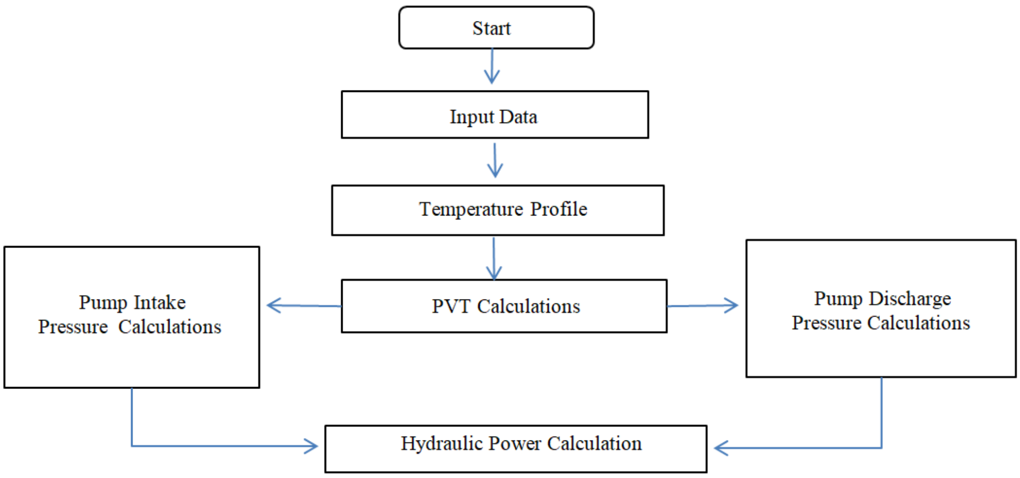

Figure 1. Computer program algorithms for the hydraulic power calculations.

4. Discussion

In this research the improved model considered all concepts that were discussed in the previous models for calculating the subsurface hydraulic power. In addition to that, the improved model included the effect of friction and the free gas. The frictional energy losses were the hydraulic frictional losses of the fluid as it flows between rods and tubing.
The previous hydraulic power models used were; Lea and Minissale, PRC Trade Standard and Takacs model. These models, neglected the effect of friction and the free gas when calculating the useful power developed by the subsurface pump [12], [13], [14]. These models are not suitable for gassy and high friction oil wells. The method for calculating the pressure increased by the pump involved the nodal pressure approach; this means that, the pressures such as pump discharge pressure was calculated starting from the well head to the pump location. Frictions energy losses in all segments were added together, this impacted into higher values of predicted hydraulic power as shown in table 1.

On the other hand, the presence of gas lowers liquid density, which reduces the hydraulic power. In this study the impact of gas was not higher since the data used was from the mature reservoir which had high water cut, less free and dissolved gases.
Table 1 shows the comparisons between the improved model and the previous models. It can be perceived that; the developed model is the advanced model. The model takes into consideration, the factors that were left in the previous models. The model incorporated the actual displacement of the pump instead of using theoretical displacement; in addition to that it also included effect of friction and the effect of gases.
It can be observed that, from figure 2, the Lea and Minassale model predicted values which were almost equal to those of the PRC Trade model. The values were less than those in this proposed model because the latter included the effects of friction and gas. However, they were greater than values in Takacs model, because in Takacs model the well head pressure was excluded in the calculations for the pressure increased by the pump.

Table 1. Hydraulic power (kW) comparison for different models.

Well Name	Hydraulic power calculations model			
	New Predicted	Takács	Lea and Minissale	PRC Trade Standard
A	2.13	1.83	2.02	2.01
B	1.08	0.86	1.03	1.03
C	1.99	1.45	1.72	1.71
D	6.19	5.23	5.99	5.97
E	0.92	0.70	0.83	0.82

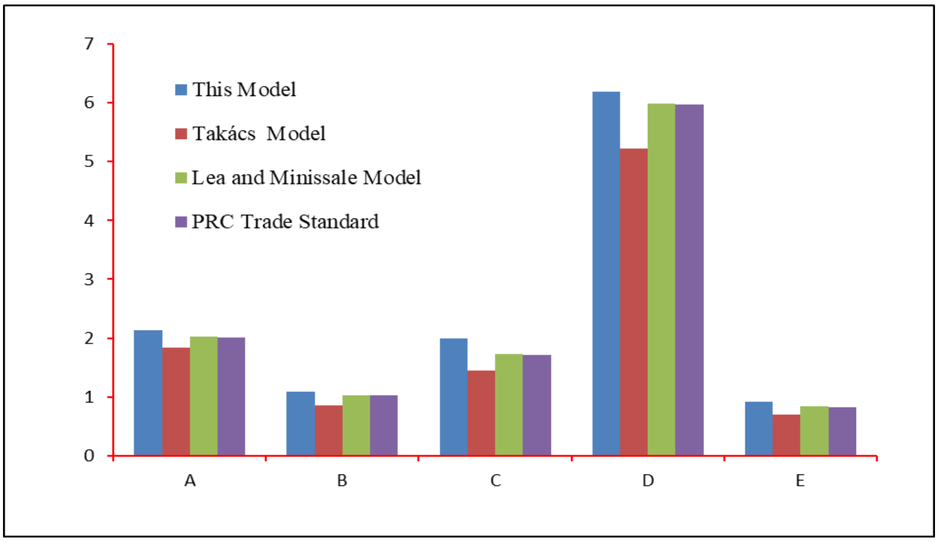

Figure 2. Hydraulic power comparisons between proposed model and previous models.

5. Conclusion

Volumetric efficiency of the pump depends primarily upon the fillage of the barrel. This in turn is related to number of factors such as the presence of gas, the viscosity of the fluid being pumped and the pumping mode. In this model, the effects of stroke loss, pump fillage, leakage and formation oil volume factor, were included for an accurate prediction of the actual pump displacement since, it is generally less than its theoretical displacement.
In this research, the impact of free gas in reducing downhole hydraulic power was considered. However, the presence of gas can contribute to an input energy into the system. Energy is released

during lifting process; the gas expansion power released is the sum of dissolve-gas expansion power and free-gas expansion power. The gas expansion power is the energy that should not be overlooked. The energy plays an important role in the process of lifting, reduces the input power and enhances the system efficiency. In this study the gas expansion power was not considered, nevertheless this parameter is very important, and should not be ignored in the calculation of the total system efficiency. The pump's useful power was obtained as a result of the product of the pressure increase by the downhole pump and production rate. The model used to calculate the pressure increase by the subsurface pump, involved the multiphase flow concepts. This means the concept of liquid hold up was introduced when the mixture density was calculated. In addition to that, the effect of friction was also included in the same model.

Lastly the previous models proved to be less suitable for gassy and high frictions wells since the effect of gas and friction were not included in the models. When this model was compared to the previous models, the proposed model predicted higher values of hydraulic power. Higher values of hydraulic power were because of the effect of frictions.

6. References

[1] Lv H, Liu J, Han J and Jiang A 2016 An energy saving system for a beam pumping unit *Sensors* (Switzerland) vol. **16(5)** 685 http://dx.doi.org/10.3390/s16050685
[2] Goswami, Dr. Tej Singh Chouhan "Artificial Lift to Boost Oil Production", International Journal of Engineering Trends and Technology (IJETT), V26 (1), 1-5 August 2015. ISSN: 2231-5381. www.ijettjournal.org. published by seventh sense research group
[3] Xing, M, and Dong, S 2015 A New Simulation Model for a Beam-Pumping System Applied in Energy Saving and Resource-Consumption Reduction *SPE* doi: 10.2118/173190-PA
[4] Brown K E 1982 Overview of Artificial Lift Systems *SPE* doi: 10.2118/9979-PA
[5] Ziming F, Jindong Z, Huibin G and Yunwei L 2013 Research on Energy-saving Technology of Crank Balanced Pumping Unit *RJASET* 6(**22**): 4152-4157 doi: 10.19026/rjaset.6.3525
[6] Podio A L, McCoy J N and Collier, F 1994 Analysis of Beam Pump System Efficiency from Real-Time Measurement of Motor Power *SPE* doi:10.2118/26969-MS
[7] Wang H, Zheng, S and Yang, D 2015 Designs and Application of Multiphase Sucker-Rod Pumps in Wells with High Gas-Oil Ratios *SPE* doi:10.2118/173963-MS
[8] Podio A L, McCoy J N, Becker D, Rowlan, L and Drake, B 2001 Total Well Management II *SPE* doi:10.2118/67273-MS
[9] McCain Jr, W D 1991 Reservoir-Fluid Property Correlations-State of the Art (includes associated papers 23583 and 23594 *SPE* **6(02)** 266-272 doi:10.2118/18571-PA
[10] Dong, S M 2003 Computer Simulation of Dynamic Parameters of Rod Pumping System Optimization *Petroleum Industry Press*(Beijing) 53–72
[11] Yao, C D 2005 Computer simulation for enhancing system efficiency of rod pumping well ActaPetrol. Sinica, **26(4)**: 106-110.
[12] Lea, J F and Minissale J D 1992 Beam pumps surpass ESP Efficiency *Oil&Gas Journal*
[13] Takacs, G 2015 Sucker-rod pumping handbook: production engineering fundamentals and long-stroke rod pumping Gulf Professional Publishing 247-376 ISBN 9780124172043 https://doi.org/10.1016/B978-0-12-417204-3.00004-2
[14] Zhang X, Wu X, Han G, An Y and Wu D 2013 Research on the Calculation Method of System Efficiency Considering Influence of Free-Gas *RJASET* **5(18)** 4552-4555

Acknowledgments

This research was supported by "Natural Science Foundation of China" (NO.51874339 and N0.51904320).

Chapter 4:
Power System and Performance Assessment

IOP Conf. Series: Earth and Environmental Science **431** (2020) 012027 doi:10.1088/1755-1315/431/1/012027

Research on case management technology of power market simulation

Wang Gaoqin[1], Chen Ailin[1], Lü Jianhu[1], Zhang Hong[1], Zheng Yaxian[1]

1 China Electric Power Research Institute Co., Ltd. Nanjing, Jiangsu 210061
E-mail: wanggaoqin@epri.sgcc.com.cn

Abstract. The construction of electric power spot market in China is gradually advancing. Since the operation of electric power spot market is affected by various factors such as grid structure, supply and demand situation and external environment, and is closely related to grid operation, it is difficult to predict through theoretical analysis and estimate the operational effect of the market, so before the formal operation of the power spot market, it is necessary to verify and analyze the operational process and operational effects of the market. In order to facilitate the recording of market operation process and result data under various simulation scenarios and to carry out data comparison and to analyze the causes and influencing factors of market operation effects, this paper proposes case management and case data comparison of the electricity market operation simulation. The case management is used to manage the process and result data of the market operation simulation, and support the data comparison and analysis of different simulation scenarios, it provides technical support to the verification analysis of the operation effect of the power market and the effective factors.

1. Introduction

The spot market is an important part of the power market system. It plays a fundamental supporting role in the open, competitive and ordered power market, and it is also the key to coordinate the market transactions and grid operation [1]. At present, Guangdong and Zhejiang have successfully started the construction of the power spot market, and other pilot areas are gradually advancing. The operation of power spot market is a long-term dynamic evolution process, it is affected by various factors such as power grid structure, supply and demand situation and external environment, so it is difficult to predict the operation effect of the market only through theoretical analysis.

Power market simulation is an important research method in the field of power market. At present, there are many research institutes in foreign countries that research and develop power market simulation platform to simulate the power market operation processes of various transaction types [2-4]. In order to realize the verification and analysis of the operation effect of the power spot market, it is necessary to simulate the operation process of the power spot market before its practical application. Based on the simulation results of the market operation, we can verify whether the electricity price is reasonable, analysis and verification the trend of market price changes, the security of grid operations and bidding strategies in trends, which is helpful to ensure safely and stably operation of the power spot market [5].

Case management of power market experimental simulation is one of the key technologies to realize simulation data management and market operation effect evaluation and analysis. However, the simulating data's storage and management are rarely mentioned [6-8], and in many information system, case management techniques often identify cases in data during operation, and multiple case data are simultaneously stored in the database at runtime, so that as the number of cases increases, the operating efficiency of the system will gradually decrease.

In view of this drawback, this paper proposes an post case management technology for market operation simulation with which the simulation data is stored and managed after the market operation simulation is completed, and design the case data configuration display tool to realize the configuration display and comparison of the case data, all of that provides technical support for the verification and analysis of power market operation effects and effective factors.

2. Case data management

2.1. Case definition

The case in this paper is used to record the data information involved in the market operation simulation process, including the case information itself and the simulation data corresponding to the case. The case information includes the case ID, name, associated market operation simulation round, creation time, etc. The case simulation data is a data set that can characterize a power market operation simulation process, including physical model, economic model, section data, and bidding data, clearing parameters, clearing results, etc., wherein the physical and economic models refer to the basic model data used for transaction clearing and security constraints, and the cross-sectional data refers to pre-data such as load forecasting, maintenance planning, and tie line planning corresponding to the trading period. The bidding data refers to members' bid of both the power generation and sales side, and the clearing parameters refer to the control parameters of transaction clearing and safety check. The clearing result data refers to the node electricity price, the unit's winning output, the load winning standard power and the corresponding statistical analysis.

According to the business needs of the electricity market operation simulation, the cases can be divided into different types by various uses such as market simulation clearing result records, market operation law analysis, and operation simulation process inversion, the data details corresponding to each type of case may be different.

2.2. Case configuration

The power market operation simulation involves a lot of data. Therefore, in order to improve the adaptability of the case data management to the case data content, before the case data management, the data that needs to be stored and managed in the case should be configured first, and the configuration information includes the storage tables, storage fields, etc. for each type of data. The case data table configuration is shown in figure 1.

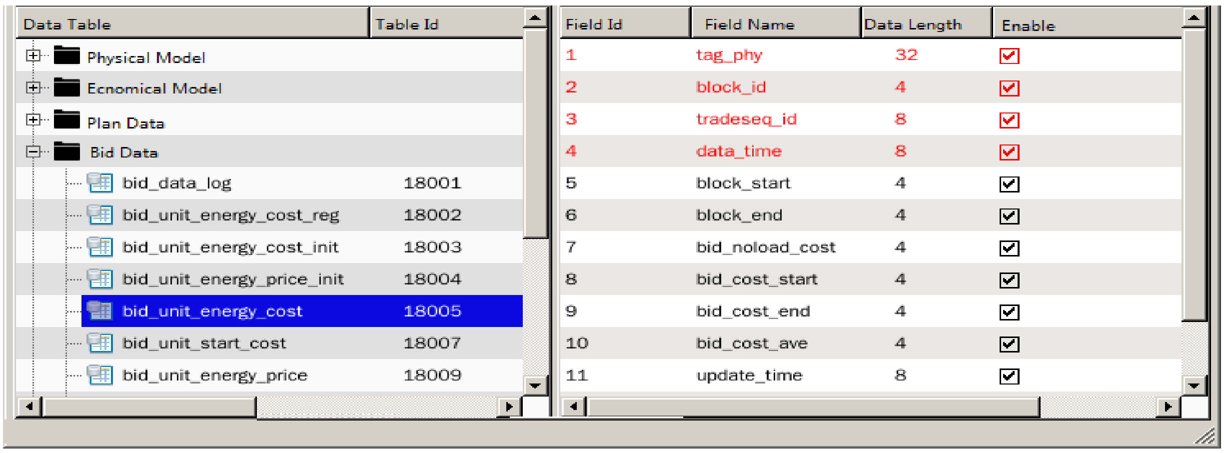

Figure 1. Case configuration diagram.

In fact, due to the difference in the use of the case, the configuration files corresponding to each case are different. Therefore, the system often configures the corresponding data requirements for each type of case to form multiple case data configuration files. When managing, choose one as the case template.

2.3. Case saving

When the market operation simulation is completed, the simulation system's case service can store the data involved in this simulation in the form of a case. According to the definition of the case, the case saving includes two steps, the preservation of the case information data and the preservation of the case data content. When the case information data is saved, the global unique case ID is determined for the case. When the case data content is saved, the data related to the simulation is sequentially retrieved based on the case data configuration file, and wrote into the case database with the case ID as its identifier.

The preservation of case data records the process and result data of market operation simulation for various market scenarios, and provides a data foundation for market operation law analysis and effect verification. Different from the way in which the case data is stored in the running database, the case data management technology in this paper stores the case data in an independent case database, that is, the market operation simulation function runs in the running database, and the increase of case data in the case database does not increase the amount of data in the running workspace, so it does not affect the efficiency of the simulation function.

2.4. Case loading

The market operation simulation case realizes the management of simulation data. The market operation simulation application often needs to analyze and compare the simulation data, for example, inverting the previously saved cases, or adjusting the parameters based on the previous simulation data and simulating once more. Therefore, it is necessary to provide the case loading function on the basis of the case data storage, load the existing case data into the current running workspace, refresh the current system to the state when the case is saved, which is facilitate to observe the case data, and adjust the pre-data to recalculate and compared the case data to seek market operating rules.

From the perspective of data flow, case loading and case saving are the opposite operations. Case loading is to copy case data from the running workspace to the case database, while case saving is to copy the case data from the case database to the running workspace. Therefore, the case loading process also needs to use the previous case data configuration.

2.5. Case import and export

In order to carry out the effect analysis and verification of specific market scenarios, simulation systems often need to access market scenarios or market operations simulation case data from other market simulation systems, and because different simulation systems are often in different network environments, they are difficult to directly interact with each other. Therefore, this paper designs a case-based offline interaction to achieve data interaction between simulation systems. That is, the market operation simulation data is first exported from the source system in the form of a case data file, and then the exported case data file is imported into the destination simulation system.

The import and export of the case is also based on the case data configuration file. When the case is exported, the data configured in the case data configuration file is used as a list, and the data is retrieved from the case database according to the selected case number and written to the case data file. Then, the data in the case data file is read and written into the system’s case database.

In summary, the main functions and processes of case data management can be summarized as shown in figure 2.

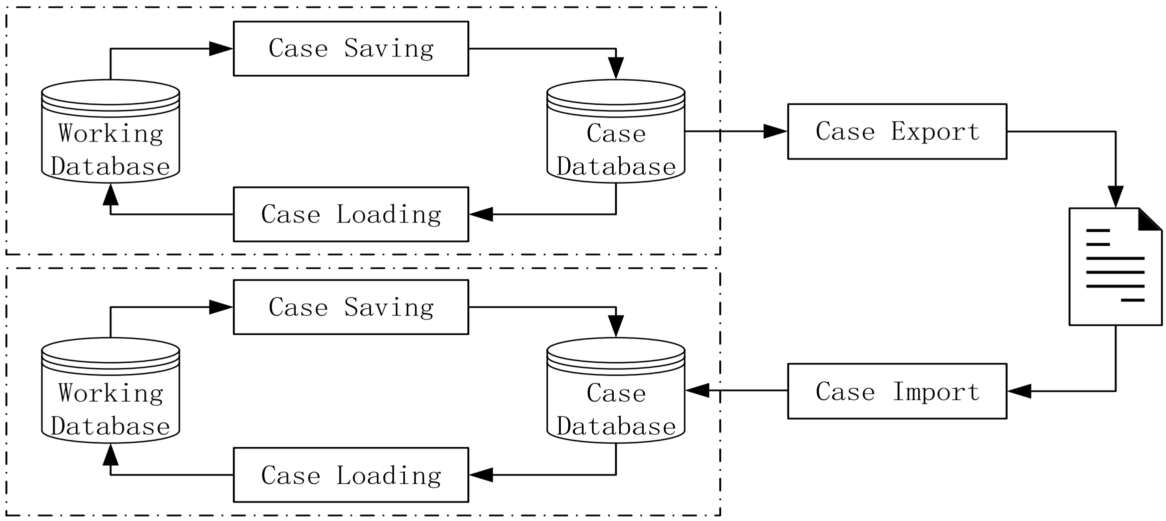

Figure 2. Main functions and processes of case data management

3. Case data comparison analysis

3.1. Case data configuration tool design

In the electricity market operation simulation system, multiple simulation cases can be formed by adjusting the scene data and simulating multiple times. The case comparison refers to selecting several of the saved cases for data difference comparison and development trend analysis. The case comparison process involves statistical processing of large amounts of data and data comparison and data variety trend display. Therefore, in order to adapt to different angles of data comparison analysis, this paper designs the case comparison function into a configuration tool, which can be used to configure the Alignment analysis screen needed.

The content of the case comparison analysis mainly focuses on the analysis and display of the transaction operation simulation process data or result data. Combined with the display requirements of the comparative analysis of the electricity market operation simulation data, the case data configuration tool of this paper designs the following primitives.

- Various input primitives, including text boxes, time selection boxes, drop-down boxes, etc., which are used to define and change the data retrieval conditions.
- Dynamic data, used to display the value of a data field in the data table, supporting the definition of the search condition.
- Pie chart, which can associate the value of a data field of a data table on different pie slices, supporting the definition of search conditions.
- Bar graph / polyline, can display easy data corresponding to different time periods or different body components, display type can flexibly switch bar graph or polyline type.
- The dashboard, can display the value of a data field in the data table and can set different alarm ranges with different colours.
- Data table, support single-table data query function, the table can configure the column name to be retrieved and displayed, supporting to configure the search condition and the data can be sorted.

Through the various types of primitives provided by the case data configuration tool and the associated response between the primitives, the case data can be displayed and the data comparison and trend analysis between the cases can be realized.

3.2. Case data statistics

In effect analysis and case comparison of electricity market operation simulation, it is often necessary to perform statistical comparison based on the original data in the case to form some evaluation indicators before comparison. For this reason, we further design data statistics tool which realizes the customization of the evaluation index calculation by setting the components, the calculation logic, and the multiple configurations of the calculation results. The definition interface of statistics tool is shown in figure 3.

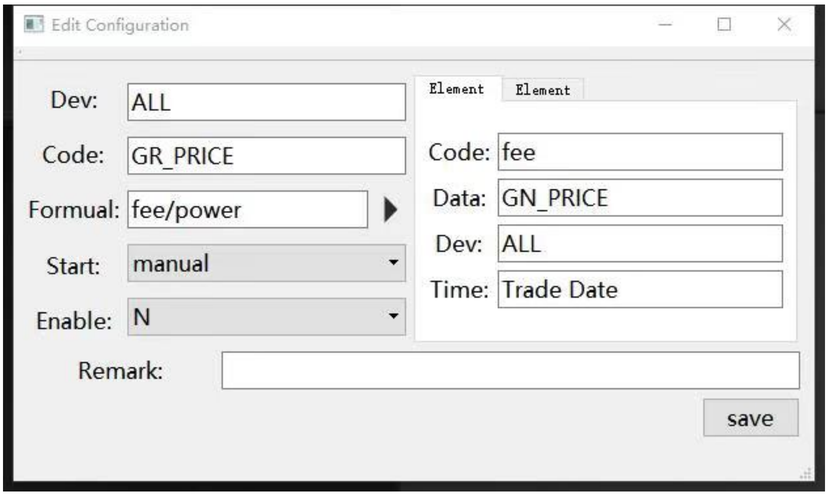

Figure 3. Definition interface of statistics tool

In this way, if we configure the case data display analysis interface with the evaluation index result data, when the case data analysis comparison is performed in the browsing configuration screen, the system performs the calculation component retrieval and the statistical calculation and the result data saving according to the statistical configuration defined by the result data, and according to the retrieval logic configured by the configuration screen, the result data is displayed on the screen.

3.3. Comparison item setting
In the case of multi-case comparison analysis design, in order to ensure the comparability between cases, two or more cases corresponding to the same time period are usually selected for comparison. The indicators for comparison analysis between multiple cases are set as follows.

- Computational condition comparison: refers to the input data of the transaction operation simulation case, including the model data of the unit, load, section, and tie line participating in the market, equipment maintenance plan arrangement, clearing calculation parameter setting, load forecasting, and tie line plan. Data, etc.

- Electricity price index comparison: refers to comparing the electricity price data in the simulation result of the transaction operation simulation case and the corresponding statistical analysis indicators, including the electricity price data of each unit and each node, the average price of each region, and the average price of each group. , the highest daily price of the whole system, the daily minimum price, and the trend of the above price data, etc.

- Cost-benefit comparison: refers to comparing the cost-benefit data of various entities in the simulation results of the transaction operation simulation case, including the single-day purchase and sale cost, revenue, and cost of the main types of units such as units, power plants, power sales companies, and power generation groups. The trend of income, the total power generation cost of the system, the total cost of electricity purchase, the power generation cost of various types of power generation resources, the blocking cost of various statistical calibers, etc.

- Grid operation comparison: refers to the comparison of the operation status of each node in the simulation result simulation data of the transaction operation, including the operation status and output of each unit in each period of the selected comparison time period, and the load of each load node, the transmission power of each section.

4. Conclusion

This paper studies the case management technology of the electricity market operation simulation process, and proposes the design implementation method of case data storage, loading, import and export and case comparison analysis. The case management process is realized through the data configuration of the simulation case which can improve the adaptability of case management to deal with data content and data format changes. The case data comparison is realized through the design of the case data analysis configuration tool and the statistical analysis index calculation tool which support the customization of case data display and comparison analysis. Research results of this paper can provide effective technical support to electricity market operation simulation and market operation effect analysis.

5. References

[1] Zou Peng, Chen Qixin, Xia Qing, He Chang, Ge Rui. Logical Analysis of Foreign Spot Power Market Construction [J]. Automation of Electric Power System. 2016,40 (10):97-102.
[2] Jarrod Moss, Jonathan Cagan, Kenneth Kotovsky. Learning from design experience in an agent-based design system [J], Research in Engineering Design, 2004,15(2):77-92;
[3] Ge Rui, Chen Longxiang, Wang Zhiyu, Liu Dunnan. The Optimum route of Chinese Power Market Construction and Design [J]. Automation of Electric Power System. 2017,41(24):10-15.
[4] Koesrindartoto D, Sun J. An agent-based computational laboratory for testing the economic reliability of wholesale power market designs[C]. IEEE Power Engineering Society General Meeting, 2005, 3:2818-2823.
[5] Yu N, Liu C, Tesfatsion L. Modeling of suppliers learning behaviors in an electricity market environment [J]. IEEE Computational Intelligence Magazine, 3(4):56-72.
[6] Huang Jie, Xue Yusheng, Wen Fushuan, etc. Analysis of Power Market Simulation Platforms [J]. Automation of Electric Power System. 2011, 35 (463), 09 11-18.
[7] Conzelmann G, Boyd G, Koritarov V, et al. Multi-agent power market simulation using EMCAS[C]. Power Engineering Society General Meeting. 2005:2829 - 2834 Vol. 3.
[8] Yang Zhenglin, Cao Shuai, Zheng Yaxian, Yao Jianguo. Designing of Power Market Simulating System [J]. Automation of Electric Power System. 2014, 38(13):18-27.

.

Acknowledgments

This paper is supported by science project of Chinese State Grid Corporation whose name is research and application of global planning decision and core technology of spot market..

IOP Conf. Series: Earth and Environmental Science **431** (2020) 012028 doi:10.1088/1755-1315/431/1/012028

Temperature extraction method for infrared image of high voltage power equipment

HUANG Xueyou[1], ZHANG Yu[1], JIAO Xianan[1], MA Shuheng[1] and XIONG Jun[1]

1 Guangzhou Power Supply Bureau Co. Ltd, Guangzhou, China
E-mail: 1139244964@qq.com

Abstract. An infrared temperature prediction method for power equipment is proposed based on the radial basis function (RBF) network optimized by quantum genetic algorithm (QGA) and orthogonal least squares algorithm (OLSA). The modified compound algorithm was used to optimize parameters of the RBF network. A temperature prediction model was established through the fitting of pixels and temperatures of the infrared image of an equipment. After image matching, the infrared temperature at a position can be directly obtained from the visible image. Meanwhile, we can also directly read temperature values of different positions from the infrared image and identify the corresponding positions in the visible image. Experimental results indicate that the algorithm proposed has a better prediction performance than the RBF network optimized by OLSA alone and by adaptive genetic algorithm (AGA) and OLSA. It improves the generalization capacity of RBF network, resulting a more stable input and a higher prediction accuracy. The algorithm proposed facilitates temperature analysis and condition-based maintenance for substations.

1. Introduction

Infrared thermography has found wide applications in the diagnosis of thermal faults of power equipments due to multiple advantages such as high efficiency, safety, non-contact temperature measurement, large detection range and rapid detection [1-3]. Electric power equipment usually operates under high voltage and high current, which is closely related to heat. Blackouts often occur due to local overheating of equipment, so the operating condition of main power equipments in the monitored substation is considerably useful for the prediction or diagnosis of potential faults and defects in the equipments. However, limited by working principle, external environment and the device itself, infrared images are less clear than normal images and the contrast between target equipment and background is weaker, which are unfavorable for fault analyses.

Online monitoring systems based on infrared and visible images [4-7] have currently been piloted in developed regions and will be further promoted. But the infrared monitor market is almost occupied by foreign large companies, e.g. the US FLIR Systems. Due to industrial monopoly and blockade on new techniques, power companies have no choice but to purchase and use the built-in analytic software of equipments. Personalized requirements cannot be satisfied and the capability of diagnosing faults of power equipments in the substation can hardly be improved, bringing about potential risks for the safe and stable operation of smart grid. The key point of infrared thermography research is to determine the general relationship between temperature and image, namely, temperature fitting and prediction. At present, artificial neural network (ANN) theory has attracted great attention in the research of temperature prediction because of strong self-learning ability and fitting capability for complex nonlinear functions. Therein, radial basis function (RBF) network is able to achieve the global optimal approximation and give a better prediction. In this article, we optimized the RBF network-based infrared temperature prediction method for the substation's equipments by using quantum genetic algorithm (QGA) and orthogonal least squares algorithm (OLSA). The obtained infrared images were processed, and the pixels and temperatures of these images were fitted to establish an infrared temperature prediction model for the equipments. This model was then registered to visible images. Thus, the temperature of a position on an infrared image can be known by directly clicking on the corresponding place of the visible image; meanwhile, the infrared temperature can be directing obtained by clicking on the infrared image, which will also help find the corresponding position in visible image. Using experimental data, we made a comparison on the evolution situation of the fitness of QGA and adaptive genetic algorithm (AGA). Subsequently, the modified RBF algorithm was compared with OLSA-RBF and AGA-RBF algorithms, thus verifying the superiority and effectiveness of the former algorithm.

2. Temperature prediction algorithm based on modified RBF network

2.1. RBF network

RBF network is a traditional technique of multi-dimensional spatial interpolation, overcoming the defects of back propagation neural network such as local minimization and slow convergence. Composed of input layer, hidden layer and output layer, RBF network enjoys a favorable capability of global approximation and a self-adaptive structure. And its output is irrelevant to the initial weight [8]. The structure of RBF network is displayed in figure 1.

The hidden layer of RBF network has various basis functions of which the most common one is Gaussian kernel function

$$R_j(X - c_j) = \exp(-\| X - c_j \|^2 / 2\sigma_j^2),\ j = 1,2,\cdots,p \tag{1}$$

where X is an n-dimensional input vector ($X=[x_1,x_2,...,x_n]$); c_j is the center of the j-th basis function, a vector with the similar dimension as X; σj is a generalized constant of the j-th neuron, i.e., the variance of Gaussian kernel function; n and p denote the number of neurons of input layer and hidden layer, respectively. After determining the function of the hidden layer, the relationship between input and output of the RBF network is expressed as

$$y_i = \sum_{j=1}^{p} w_{j,i} \exp(-\| x - c_j \|^2 / 2\sigma_j^2), i = 1,2,\cdots,m \tag{2}$$

where m denotes the number of neurons in the output layer; y_i is the output value of the i-th neuron of the output layer; $w_{j,i}$ is the weight of connection between the j-th unit of hidden layer and the i-th unit of output layer. To determine the structure of RBF network, three parameters need to be solved: the basis function center c_j, variance j, and the weight from hidden layer to output layer (wj,i).

The construction of a RBF network depends largely on the optional selection of basis function center, unit number in the hidden layer, and network weight [9]. But in traditional RBF network, the algorithm training is prone to local minimization in the adjustment of each parameter.

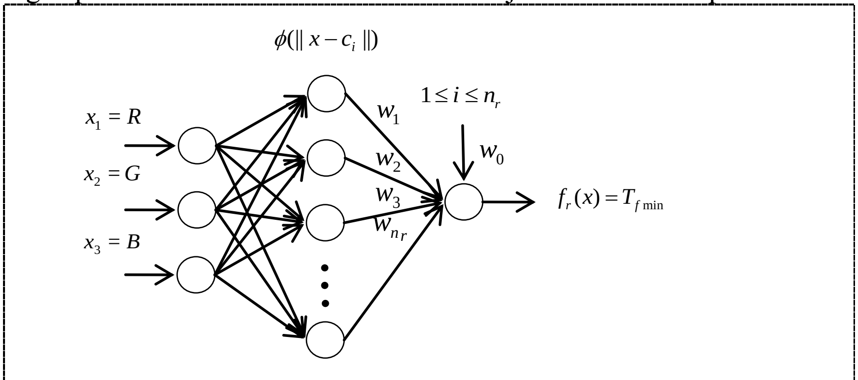

Figure 1. Structure of RBF network.

2.2. OLSA-RBF network

OLSA is a popular algorithm due to small computation amount, less occupation on storage space and rapid convergence [10-11]. OLSA can find the basis function center relatively accurately by introducing an error term:

$$y_i = \sum_{j=1}^{p} w_{j,i} \exp(-\| x - c_j \|^2 / 2\sigma_j^2) + e_k, i = 1,2,\cdots,m \tag{3}$$

It can also be expressed in the form of matrix:

$$Y = BW + E \tag{4}$$

where $Y \in \Re^{m\times 1}$ is the expected output vector of the neural network; $B \in \Re^{m\times q}$ is the regression matrix of each column of vectors; $W \in \Re^{q\times 1}$ is the network weight vector and $E \in \Re^{m\times 1}$ is the vector of errors between actual and predicted values of the network output.

Through Gram-Schmidt orthogonalization, the regression matrix B can be decomposed into a set of orthogonal basis vectors:

$$B = DA = [d_1 \quad d_2 \quad \cdots \quad d_q] \times \begin{bmatrix} 1 & a_{12} & \cdots & a_{1q} \\ 0 & 1 & \cdots & a_{2q} \\ \cdot & \cdot & \cdots & \cdot \\ \cdot & \cdot & \cdots & \cdot \\ 0 & 0 & \cdots & 1 \end{bmatrix} \tag{5}$$

where $A \in \Re^{m\times q}$ is an upper triangular matrix and $D \in \Re^{m\times q}$ is an orthogonal matrix; di can be calculated through equation (6) and (7).

$$D^T D = H = diag(h_1, h_2, \cdots, h_q) \tag{6}$$

$$h_i = d_i^{\,T} d_i = \textstyle\sum_{k=1}^{q} d_{ik}^2 \tag{7}$$

By combining the two equations, the expected network output Y is obtained as follows:

$$Y = DAW + E = DG + E \tag{8}$$

Gram-Schmidt orthogonalization can ensure that matrix E and DG are orthogonal to each other, so

$$Y^T Y = G^T D^T DG + E^T E = \sum_{k=1}^{q} h_k g_k^2 + E^T E \tag{9}$$

Thereby, the equal error rate (EER) of the k-th center is defined as

$$ERR_k = \frac{h_k g_k^2}{Y^T T} \tag{10}$$

During continuous forward regressions of the RBF network, EER provides an effective standard for determining the network center. In each forward regression, when EER reaches the maximum an appropriate network center will be selected, and the regression will terminate at step q1 if the following condition is satisfied:

$$1 - \sum_{k=1}^{q_1} ERR_k < 0 \tag{11}$$

In the construction of a neural network with OLSA, the selection of the initial σ value has great impact on the unit number of the hidden layer [12]. Hence, the parameter selection for OLSA-RBF network should be further optimized.

2.3. Modified OLSA-RBF network

We introduced QGA and optimized the initial σ value and the unit number of the hidden layer, to improve the efficiency of OLSA-RBF network.

QGA, firstly proposed by Ajit Narayanan and MarkMoore [13], is an optimized probabilistic searching algorithm combining quantum computational theory and evolutionary algorithm. It adopts quantum bit (qubit) to encode chromosomes and achieves evolutionary search by using the effect and updating of quantum gate. Compared with normal genetic algorithms, QGA has higher population diversity, faster convergence, and the ability of global optimization [14-15]. The steps of building a modified RBF network are described as follows.

2.3.1. Qubit encoding.

Quantum state is employed to encode information. Besides the two states, 0 and 1, a qubit can also represent any immediate state between 0 and 1. So the state of one qubit can be expressed as

$$|\Psi\rangle = \alpha|0\rangle + \beta|1\rangle \tag{12}$$

where α and β (possibly complex number) represent the probability amplitude of corresponding states and satisfy the following normalization condition:

$$|\alpha|^2+|\beta|^2=1 \tag{13}$$

where |α | represents the probability of $|0\rangle$,and |β | represents the probability of $|1\rangle$. Hence, a chromosome with m qubits can be expressed as

$$q = \begin{bmatrix} \alpha_1 & \alpha_2 & & \alpha_m \\ \beta_1 & \beta_2 & \cdots & \beta_m \end{bmatrix} \tag{14}$$

2.3.2. Population initialization.

Suppose n is the population size (i.e., the number of chromosomes). In the initial population Q(t)={q1^t,q2^t,...,qnt}, the qubits of all chromosomes were assigned the value $2^{-\frac{1}{2}}$. This means that the state of each chromosome is the result of superposition of all possible states at an equal probability.

2.3.3. Adjusting strategy for quantum revolving gate.

Individual adjustment is realized through quantum revolving gate. In other words, the revolving gate in QGA is the final actuator of evolution. The working principle of revolving gate is as follows:

$$\begin{bmatrix} \alpha_i' \\ \beta_i' \end{bmatrix} = \begin{bmatrix} \cos(\theta_i) & -\sin(\theta_i) \\ \sin(\theta_i) & \cos(\theta_i) \end{bmatrix} \begin{bmatrix} \alpha_i \\ \beta_i \end{bmatrix} \tag{15}$$

$$\theta_i = s(\alpha_i \beta_i)\Delta\theta_i \tag{16}$$

Where (αi, βi) is the i-th qubit in chromosome; θ denotes the revolving angle which controls the convergence rate of the algorithm; S(αi, βi) and Dθi denote revolving direction and step size of the revolving angle, respectively. The delta in Table is a coefficient related to the algorithm's convergence rate, to which a reasonable value should be given. By referring to the idea of dynamically adjusting the quantum revolving angle [16], the coefficient can be determined with the following equation.

$$delta = 0.05\pi\left(1 - \frac{k \cdot n}{MAXGEN + 1}\right) \tag{17}$$

Where n denotes the current generation of evolution and MAXGEN is the final generation; k is a constant in the range of [0,1]. The convergence rate of the algorithm is raised in the early operation period because the grid searched is larger. In the late operation period, the searched grid narrows, thus realizing precise searching and facilitating the seeking of optimal solutions.

Table 1. Methods for determining the revolving angle.

x_i	α_i	$f(x)\geq f(b)$	Literature [17] $\Delta\theta_{i'}$	The proposed method $\Delta\theta_i$	$S(\alpha_i, \beta_i)$			
					$\alpha_i\beta_i>0$	$\alpha_i\beta_i<0$	$\alpha_i=0$	$\beta_i=0$
0	0	F	0	0	0	0	0	0
0	0	T	0	0	0	0	0	0
0	1	F	0	0	0	0	0	0
0	1	T	0.05π	*delta*	-1	+1	±1	0
1	0	F	0.01π	*delta*	-1	+1	±1	0
1	0	T	0.025π	*delta*	+1	-1	0	±1
1	1	F	0.005π	*delta*	+1	-1	0	±1
1	1	T	0.025π	*delta*	+1	-1	0	±1

In Table 1, xi and bi represent the binary bit corresponding to the solution x and the i-th qubit of the current optimal individual b, respectively; f(x) is the function of fitness. Guaranteed by the quantum revolving gate, the algorithm will rapidly converge to obtain the chromosome with a higher fitness.
This study conducted a comparison between the evolution of QGA and AGA fitness, as shown figure

IOP Conf. Series: Earth and Environmental Science **431** (2020) 012028 doi:10.1088/1755-1315/431/1/012028

2. The result indicates that QGA has a great improvement in evolutionary efficiency and its best fitness is more ideal (2.3212 vs. 1.5944) compared with the AGA. The average fitness of QGA and AGA is 1.9191 and 1.4369, respectively.

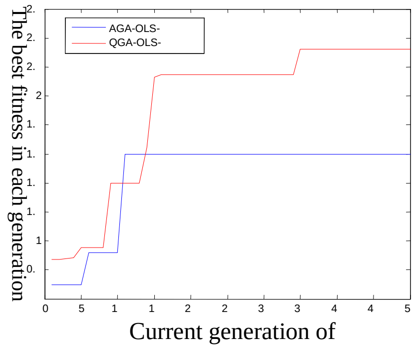

Figure 2. Infrared temperature prediction model.

The model was established for the sake of power equipment analysis by relevant staff. They will be able to know infrared temperature by directing viewing visible images. This progress will reduce the difficulty in positioning thermal anomalies due to vague infrared images, thus improving positioning accuracy. Figure 3 shows the infrared and visible images which reflect thermal anomalies of the transformer in a substation.

It can be found from figure 4 that the upper and lower limits of each temperature bar of infrared images will adjust automatically due to the configuration of bundled software. And infrared images are generally different from each other, e.g. the infrared temperature range in figure 3 is 3℃~28℃ and those in figure 4 are -6℃~7℃ and -13℃~3℃. In this article, the upper and lower limits of temperature bars were manually input tentatively. This step can be improved using digital intelligent recognition in the future.

Preprocessing, registration and fusion were firstly carried out on visible and infrared images of the same scene. It was supposed that the infrared image was smaller than the visible image; if not, the former would be clipped. The image effect after preprocessing is displayed in figure 5.

Then, the pixel matrices of visible and infrared images were matched to realize that the location information can be acquired by directly clicking on the visible image, and the temperature on the infrared image can be known through the prediction of the modified RBF network. Similarly, when clicking on the infrared image, we can know the temperature of a target position immediately and be led to the corresponding area on the visible image. The flow chart of the model is shown in figure 6.

It can be found from figure 4 that the upper and lower limits of each temperature bar of infrared images will adjust automatically due to the configuration of bundled software. And infrared images are generally different from each other, e.g. the infrared temperature range in figure 3 is 3℃~28℃ and those in figure 4 are -6℃~7℃ and -13℃~3℃. In this article, the upper and lower limits of temperature bars were manually input tentatively. This step can be improved using digital intelligent recognition in the future.

Preprocessing, registration and fusion were firstly carried out on visible and infrared images of the same scene. It was supposed that the infrared image was smaller than the visible image; if not, the former would be clipped. The image effect after preprocessing is displayed in figure 5.

Then, the pixel matrices of visible and infrared images were matched to realize that the location information can be acquired by directly clicking on the visible image, and the temperature on the infrared image can be known through the prediction of the modified RBF network. Similarly, when clicking on the infrared image, we can know the temperature of a target position immediately and be led to the corresponding area on the visible image. The flow chart of the model is shown in figure 6.

Figure 3. Images of substation equipments.

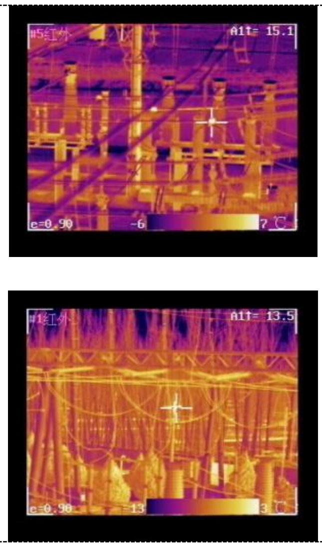

Figure 4. Infrared images of the substation equipment.

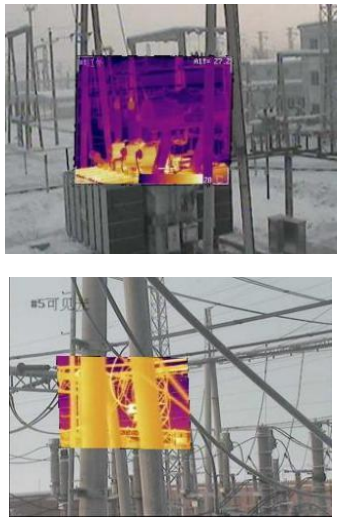

Figure 5. Images fused by visible and infrared images.

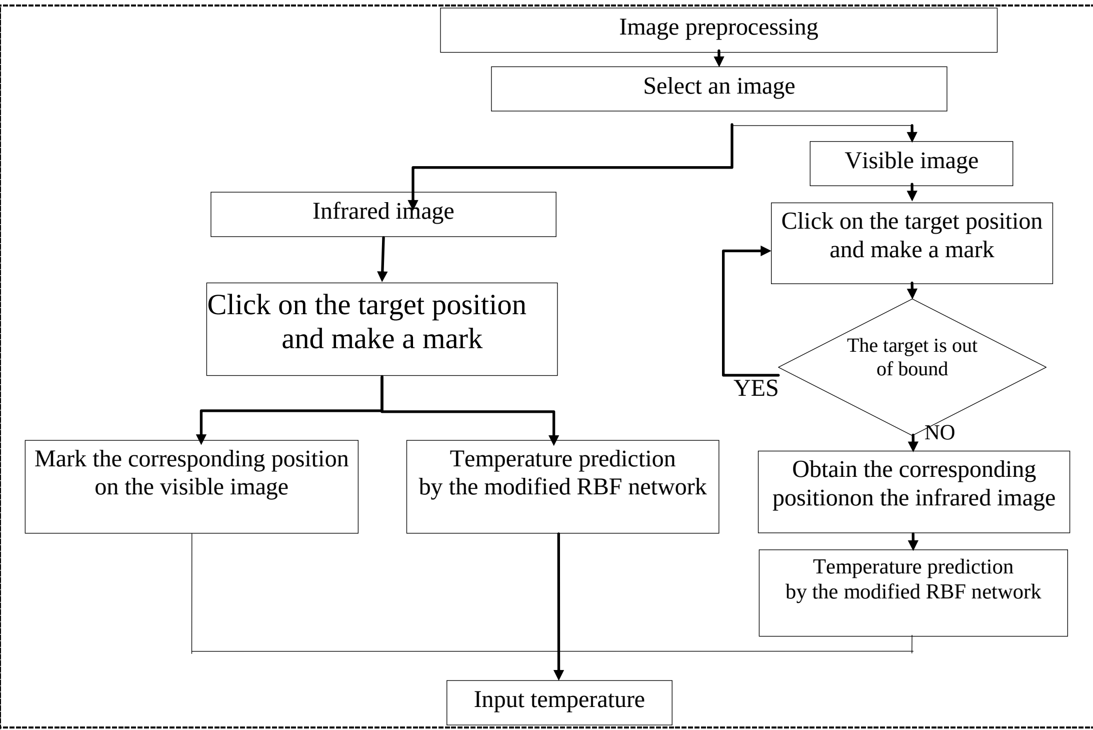

Figure 6. Flow chart of temperature analysis model.

3. Experimental results and analyses

Tests were conducted in the MATLAB environment. By setting points on the visible image, the coordinates of and RGB values at the corresponding positions of these points on the infrared image can be obtained automatically. Fifty sets of data were selected randomly as the input of the modified RBF network while the temperature on infrared image was taken as output. The output value was compared with those of OLSA-RBF network and AGA-OLSA-RBF network. See table 2 for the comparison result.

Table 2. A comparison between evaluation indices of each algorithm.

Algorithm	Average relative error	Maximum relative error
OLS-RBF	0.486425	1.819685
AGA-OLS-RBF	0.141767	0.598378
QGA-OLS-RBF	0.060528	0.240022

Figure 7 shows the predicted temperatures of the modified RBF network almost completely accord with actual temperatures, with little error.

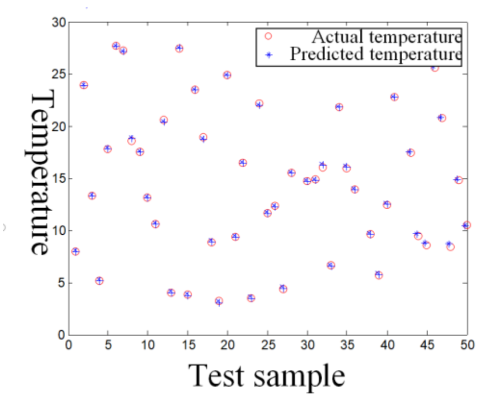

Figure 7. Temperature prediction by the modified algorithm.

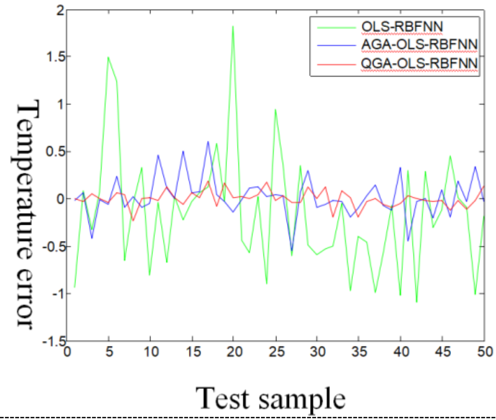

Figure 8. A comparison of prediction errors of each algorithm.

Figure 9. Interface of infrared temperature analysis result.

The distribution of relative errors of each algorithm is exhibited in figure 8, where the green, blue and red curve are the error curve of OLSA-RBF network, AGA-OLSA-RBF network and QGA-OLSA-RBF network, respectively. It clearly reveals that compared with the former two algorithms, our modified algorithm (QGA-OLSA-RBF network) performed better in temperature prediction and enhanced the generalization capacity of RBF network, with a stable input and a high prediction accuracy. The maximum relative error of the OLSA-RBF network was about 1.8, while that of the QGA-OLSA-RBF network was merely 0.24. As for the average relative error, the OLSA-RBF network was eight times that of the QGA-OLSA-RBF network and the AGA-OLSA-RBF network doubled the latter.

We designed a simple operation interface for the temperature analysis program using Matlab GUI. Taking the image of a transformer's thermal anomalies in a substation as an example, the specific interface is shown in figure 9. On the interface, one can separately analyze visible or infrared image, or simultaneously analyze both images. In Figure 9, we randomly selected a point on the visible image and obtained the infrared temperature value of 21.6 ℃ for the target position, which is marked with a red dot. We also selected a point on the infrared image randomly and obtained the infrared temperature value of 8.3 ℃ for the target position, which is marked with a green dot. Its corresponding position on the visible image is marked with a yellow dot, with the coordinate of (123, 100).

4. Conclusion

An infrared temperature prediction method for power equipments in the substation was proposed by optimizing the radial basis function network with quantum genetic algorithm and orthogonal least squares algorithm. It overcomes many shortcomings of original infrared images of those power equipments, such as unclear picture, weak contrast between target equipments and the background, and the resultant inconvenience for fault analysis. The parameters of RBF network were optimized with the modified compound algorithm. Experimental results indicate that the algorithm modified in this article had a better prediction performance than OLSA-RBF network and AGA-OLSA-RBF network, whose maximum relative error was more than 7 times and twice that of our algorithm, respectively. Moreover, the average relative error has also been greatly lowered. These suggest that our algorithm has improved the generalization capacity of RBF network, leading to a stable input and an increased prediction accuracy. The algorithm proposed makes it more convenient to analyze the temperature of power equipments in substations and position the area of thermal anomalies, which is favorable for the condition-based maintenance in substations.

5. References

[1] Hong M, Jiaxue Y and Lei Q 2011 Segmentation of electric equipment infrared image based on CA and OTSU[J]. Electric Power Automation Equipment. 31(9): 92-95

[2] Lihua L, Dongmei W and Jian L et al 2010 Substation infrared early warning system using object segmentation and image registration[J]. High Voltage Engineering. 36(7): 1718-24

[3] Hongwei L 2012 Intelligent vision system of smart substation[J]. Electric Power Automation Equipment. 32(8): 141-147

[4] Ran L 2008 Research and realization of convergence between infrared temperature measurement technology and video surveillance system of substation[J]. Power System Technology. 32(14): 80-84

[5] Zhenbing Z, Qiang G and Jinsha Y et al 2009 An on-line monitoring system for substation power equipment dual-channel image[J]. Automation of Eletric Power Systems. 32(10): 76-79

[6] Lihui L, Yongsheng Z and Yong S et al 2011 Development and application of equipment inspection robot for smart substation[J]. Automation of Eletric Power Systems. 35(19): 85-88

[7] Ming L, Gehao S and Weidong Z et al 2012 A tower and line tracking algorithm for power transmission line inspection based on unmanned aerial vehicles[J]. Automation of Eletric Power Systems. 36(9): 92-97

[8] Cui H, Buying W and Weiming L 2012 Short-term forcasting of wind power output based on improved OLS-RBF ANN model[J]. Electric Power Automation Equipment. 32(9): 40-43

[9] Yan S, Xingliang J and Jihe Y 2009 Flashover voltage forecasting model of iced insulator based on RBF network[J]. High Voltage Engineering. (3): 591-596

[10] Huang C M and Wang F L 2007 An RBF network with OLS and EPSO algorithms for real-time power dispatch[J]. Power Systems. IEEE Transactions on. 22(1): 96-104

[11] Liao C C 2010 Enhanced RBF network for recognizing noise-riding power quality events[J]. Instrumentation and Measurement. IEEE Transactions on. 59(6): 1550-61

[12] Chang W Y 2013 Estimation of the state of charge for a LFP battery using a hybrid method that combines a RBF neural network, an OLS algorithm and AGA[J]. International Journal of Electrical Power & Energy Systems. 53: 603-611

[13] Narayanan A, Moore M 1996 Quantum-inspired genetic algorithms[C]. Evolutionary Computation. Proceedings of IEEE International Conference on. IEEE, 1996: 61-66

[14] Lee J C, Lin W M and Liao G C et al 2011 Quantum genetic algorithm for dynamic economic dispatch with valve-point effects and including wind power system[J]. International Journal of Electrical Power & Energy Systems. 33(2): 189-197

[15] Liao G C 2012 Solve environmental economic dispatch of Smart MicroGrid containing distributed generation system – Using chaotic quantum genetic algorithm[J]. International Journal of Electrical Power & Energy Systems. 43(1): 779-787
[16] Huanlai X, Wei P and Xihua Z 2007 A novel improved quantum genetic algorithm for combinatorial optimization problems[J]. Acta Electronica Sinica. 35(10): 1999-2002
[17] Songming J, Pu H and HUANG Yu et al 2007 Fuzzy quantum genetic algorithm and its application research in thermal process identification[J] . Proceedings of the CSEE. 27(5): 87-92

Acknowledgments

This work is supported by Technological Innovation Project for Employees of China Southern Power Grid Corporation (K-GZZG-2018-215 and K-GZZG-2018-214). We thank Professor Gehao S for valuable discussion.

IOP Conf. Series: Earth and Environmental Science **431** (2020) 012029 doi:10.1088/1755-1315/431/1/012029

Reliability assessment of offshore oil platform power system based on state enumeration method

Che Wei[1], Wei Du[2], Xiuli Wang[2], Xianjue Luo[2] and Qiang Li[1]

1 CNOOC Research Institute, CNOOC, Beijing 100028, China
2 School of Electrical Engineering, Xi'an Jiaotong University, Xi'an 710049, Shaanxi Province, China
E-mail: weidu7048@stu.xjtu.edu.cn

Abstract. Based on the state enumeration method, a reliability evaluation method for offshore platform power system is proposed in this paper. Firstly, the reliability model of land-based components and the modelling method of the system are introduced. In reliability evaluation, all fault states are generated based on state enumeration method, power supply circuit sets are identified based on depth-first algorithm. The effects and losses of multiple faults are calculated based on platform maintenance capability, and fault time and load-loss time are separated and counted. Finally, taking an offshore oil platform as an example, the outage table of the system is generated, and the reliability index of the system is obtained, which verifies the effectiveness and accuracy of the method proposed in this paper.

1. Introduction

Reliability refers to the ability of a component, a device, or a system to perform its prescribed functions in predetermined time and under specified conditions [1]. The reliability of power system is the application of the reliability principle in the power system. The purpose is to obtain the probability of the power system's ability to provide power to the user without interruption [2].
Offshore platform power system, also known as offshore electrical system (OES), refers to the power system designed specifically for offshore engineering, which can meet the special marine environment and is not powered by onshore power supply [3]. It is mainly composed of three parts: power supply, distribution network and load [4], [5]. They are connected in a certain way to form a complete power system which includes generation [6], transmission [7], [8], distribution [9] and used system.
At present, the reliability research of offshore platform power system is relatively scarce. It is necessary for the development of offshore power system to study the reliability of offshore platform power system, which is of great significance to the implementation of China's strategy of ocean power and the safe and stable operation of ocean engineering [10].
To solve the above problems, a method based on state enumeration method is proposed to evaluate the reliability of offshore oil platform power system. Firstly, according to the characteristics of the electrical components at sea, the reliability model of the components on land is introduced. In the state selection, the state enumeration method is used to enumerate all possible fault states. Before state assessment, all the circuit sets of components are identified based on depth-first algorithm. In the condition assessment, according to the actual platform's saturation maintenance capability, the influence and loss of the distribution network under multiple conditions are calculated, and the fault time and load curtailment time are separately counted to facilitate the planning personnel to compare and optimize different structures. Finally, taking an offshore oil platform of a company as an example,

the outage table of the platform is generated, and the reliability indexes are obtained, which verifies the validity and accuracy of the proposed method.

2. Component and system modelling

2.1. Component model

The offshore oil platform power system is mainly composed of power generation equipment, distribution network and load. The main equipment includes generator, transformer set, distribution line, circuit breaker and various loads.

The gas turbine is often used in the generator group, and the system has at least one standby to ensure that the standby generator can be used for continuous power supply under some fault conditions. The transformer is a dry type transformer. Distribution lines are all cables not exceeding tens of meters. The main loads include various medium-voltage or low-voltage motors, electric heating systems, lighting systems, etc. They are connected to medium-voltage buses and 400V distribution panels according to load size and voltage level. The above components are basically closed devices, and the factors leading to failure are basically the same as those on land power grids. Therefore, the reliability models and parameters of land models are also applicable to offshore power systems.

Therefore, transformers, circuit breakers, generators and buses use the three-state model, which corresponds to the normal, maintenance and fault repair state on land. The cable length inside the platform is too short, so the cable components are ignored.

For the reliability parameters of each component, the generator can be summed up according to the fault log and maintenance plan, and the reliability parameters of the other components can be used based on the reliability parameters of the corresponding components of the land distribution network.

2.2. System model

The power system structure of the offshore oil platform is different from that of the onshore distribution network. Its main electrical wiring has a large number of outgoing lines. Some outgoing lines directly supply power to the medium-voltage load, while the others supply power to low-voltage distribution equipment through transformers.

For such a system, the traditional bus-branch model is not applicable, and the main disadvantage is to ignore the influence of circuit breaker and bus, so the reliability of the system cannot be accurately calculated.

The node-component model is used in this paper. Section 1.1 establishes the reliability model of each component according to the actual electrical topological relationship. Circuit breakers, transformers and submarine cables are considered as branch components, while buses, generators, load points and virtual nodes are considered as node components. The two ends of the branch element must be connected with the node element. When all components are connected according to the above requirements, the whole system is modelled.

3. Reliability evaluation based on state enumeration method

3.1. Evaluation process

The evaluation process figure is shown in the figure 1. The reliability evaluation process of this paper is as follows:

1) All road sets are obtained by using depth-first algorithm;

2) The state enumeration method is used in the state selection to obtain the desired state and corresponding probability.

3) Determine the impact and loss of the fault according to the current state s and the system road set.

4) Record the probability of state s, failure time, load curtailment time, *EENS* and other information to the outage table;

5) $s = s + 1$, judging whether all states are computed, if so, turn 6), if not, turn 2);

6) Calculate the overall index of offshore platform according to the outage table.

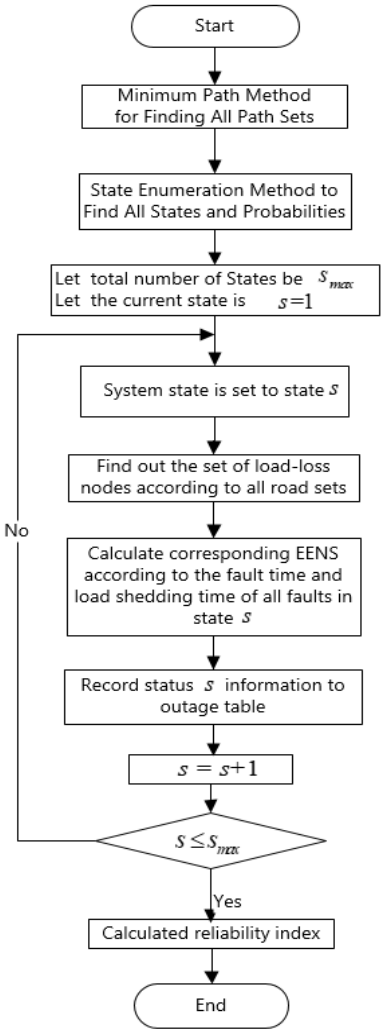

Figure 1. Evaluation Process.

3.2. State enumeration method

The state enumeration method [11], also known as the Boolean truth table method, is the most intuitive method for calculating system reliability. The Principle of State Enumeration Method can be seen in equation (1).

$$(P_1 + Q_1)(P_2 + Q_2)\cdots\cdots(P_N + Q_N) \tag{1}$$

where, P_i and Q_i are the probability of the component i working and failing respectively; N is the number of components in the system.

The state probability of the system is given by equation (2).

$$P(s) = \prod_{i=1}^{N_f} Q_i \prod_{i=1}^{N-N_f} P_i \tag{2}$$

where, N_f and $N - N_f$ are the number of failed and non-failed components in state s, respectively.

In normal condition, when all components are in operation, $N_f = 0$, the equation (2) can become equation (3).

$$P(s) = \prod_{i=1}^{N} P_i \tag{3}$$

All enumerated system states are mutually exclusive, so the cumulative failure probability of the system, which is shown in equation (4), is the direct sum of all failure state probabilities.

$$P_f = \sum_{s \in G} P(s) \tag{4}$$

where, G is a set of all failure states.

Any other reliability index functions corresponding to each system failure state, such as load reduction $C(s)$, can be obtained by state assessment, and then the mathematical expectations of the index functions for all system failure states are given by equation (5).

$$E(C) = \sum_{s \in G} C(s)P(s) \tag{5}$$

Compared with Monte Carlo method, state enumeration method is more effective for systems with fewer components and lower failure probability.

This paper uses state enumeration method to get the outage table. Firstly, enumerate all possible states of all components, then analyses the state of the system, and calculate the output power and various losses in the state, combined with the same impact of the fault, and finally get the simplified shutdown table. The reliability index of the system is obtained according to the outage table.

3.3. Depth-first algorithm for power supply circuit set

There is a transfer of part of the load of offshore platform power grid. In practice, there are more than one feasible power supply path, so the traditional minimum path method is not complete. Considering the above situation, this paper uses depth-first algorithm to search all feasible path sets.

The topological structure formed by 2.2-section system modelling is transformed into an association matrix, and the information of components is stored in the form of branches. Then the correlation matrix is input into the depth-first algorithm.

After calculating the circuit set of each component, the remaining circuit set after component failure is determined. Suppose L is the main connection set.

When the components i fail or overhaul, the remaining roads in the distribution network are set up.

$$X = L \backslash R(i) = \overline{R(i)} \tag{6}$$

According to the X at this time, the unreachable nodes are determined, and the influence range of the fault is obtained.

3.4. Multiple fault

There may be multiple faults in state s. The traditional reliability evaluation directly multiplies the maximum fault time by the maximum fault loss load, so the *EENS* obtained is too large. Moreover, when there is a part of the load that can be transferred under fault conditions, the fault time is not necessarily equal to the load curtailment time. Therefore, this paper simulates the process of system recovery from multiple faults to normal, and improves the accuracy of reliability evaluation.

Consider that the state s is the most serious fault condition, which is N-fault occurs simultaneously. In practice, production workers and maintenance personnel are on duty on offshore platforms. Even if multiple faults occur at the same time, they can be repaired at the same time. Therefore, it is considered that the process of repairing N-fault should be carried out at the same time.

The simulation process of N -fault is as follows:

1) When multiple faults occur in the system, the fault is assumed to be N-fault and the initial time $t = 0$;

2) Set the time of fault duration $time$,and calculate it as follows:

$$time = \min(time_1, \dots, time_N) \tag{7}$$

where, $time_i$ denotes the outage time of component i.

If $time$ is empty set, then turn 5)； otherwise, turn 3)；
3) Check whether the system is load- curtailment in case of failure, record the load curtailment amount as $EDNS$ and calculate $EENS$:

$$EENS = EDNS \times (time - t) \tag{8}$$

4）Record $t = time$.And if $time_i == time$, then $time_i = 0$,delete failure of component i and turn 2);
5) The system restores to its normal state and the simulation process ends.

3.5. Index calculation

In this paper, the loss and time in each state of the system are directly obtained and recorded in the outage table, which is similar to the outage table of generation system reliability evaluation. The form of outage table is shown in table 1.

Table 1. Outage table.

s	$P(s)$	$EDNS_s$	$EENS_s$	EFT_s	$ETLC_s$
-	-	-	-	-	-

where $P(s)$, EFT_s,$ETLC_s$, $EDNS_s$, $EENS_s$,which represent the parameters in state s, can be obtained in the status assessment. The definitions of these parameters can be found in the next paragraph.
In the calculation of index, the reliability indicators of the system, including Probability of system Failure P_f, probability of system load curtailments P_{LC}, probability of system normal P_N, expected time of load curtailments ET , expected fault time EFT, expected demand not supplied $EDNS$ expected energy not supplied $EENS$.These index are obtained directly by using the information contained in the outage table. The calculation methods of the indicators are as follows:

$$P_{LC} = \sum_{i \in C} P_i \tag{9}$$

$$P_N = 1 - P_f \tag{10}$$

$$ETLC = \sum_{s=1}^{s_{max}} ETLC_s \times P(s) \tag{11}$$

$$EFT = \sum_{s=1}^{s_{max}} EFT_s \times P(s) \tag{12}$$

$$EDNS = \sum_{s=1}^{s_{max}} EDNS_s \times P(s) \tag{13}$$

$$EENS = \sum_{s=1}^{s_{max}} EENS_s \times P(s) \tag{14}$$

where C is a set of all failure states include load curtailments; s_{max} is a the number of state.

4. Example analysis

Taking an offshore oil platform as an example, the main electrical wiring of the platform is shown in figure 2. There are two generators in the platform, One in normal use and one in reserve. The main equipment is shown in the table 2.

Table 2. Equipment list.

Device name	Number	Power or load per unit
Turbine generator	2	5.947MW
Gas compressor	3	0.22MW
Associated gas compressor	4	0.415MW

All load information has been labelled in the figure 2.

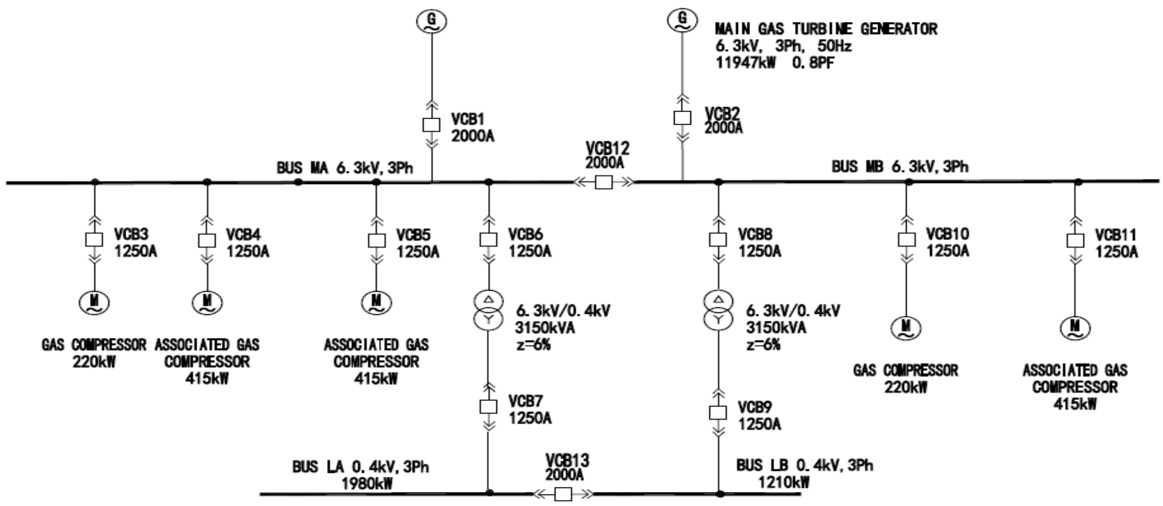

Figure 2. Main electrical wiring diagram of an offshore oil platform.

The system outage table is shown in table 3.

Table 3. System outage table.

s	P(s)	$EDNS_s$	$EENS_s$	EFT_s	$ETLC_s$
1	0.819508255	0	0	0	0
2	0.046926294	0	0	24	0
3	0.030955239	0	0	48	0
4	0.030519582	0	0	120	0
5	0.02167196	4.875	117	24	24
6	0.006087754	0	0	15	0
7	0.005855351	0	0	72	0
8	0.005103631	4.875	351	72	72
9	0.003063345	0.415	19.64	24	24
10	0.003063345	0.415	25.8	24	24
11	0.003063257	0.415	17.22	24	24
12	0.003063257	0.415	21.84	24	24
13	0.00204223	0.22	14.96	24	24
14	0.00204223	0.22	21.12	24	24
15	0.002042171	0.22	12.54	24	24
16	0.002042171	0.22	17.16	24	24

17	0.001988194	0.22	5.28	24	24
18	0.000802153	4.875	117	144	24
19	0.000797904	4.875	117	72	24
20	0.000781993	0	0	144	0
21	0.000682257	4.875	117	48	24
...	…	…	…	…	…

The system reliability index is shown in table 4.

Table 4. System reliability index.

Index	P_N	P_f	P_{LC}	EFT	$ETLC$	$EDNS$	$EENS$
-	0.8195	0.1805	0.0588	10.3624	3.1681	0.1569	5.1023

5. Conclusions

Based on the state enumeration method, this paper presents a reliability evaluation method for offshore oil platform power system, and obtains the system outage table and system reliability index. The proposed method is not only applicable to offshore platforms, but also to independent small power grids with the same characteristics. It has certain practical significance.

6. References

[1] BIE Zhaohong, WANG Xifan. The application of monte carlomethod to reliability evaluation of power systems [J]. Automation of Electric Power Systems, 1997(06): 68-75.
[2] Bie Zhaohong, Wang Xiuli, Wang Xifan. Reliability evaluation of complicated distribution systems [J]. Journal of Xi'An Jiaotong University, 2000(08): 9-13.
[3] Chenglin, hejian. Principle and Application of Power System Reliability [M].Beijing. tsinghua university press, 2015: 320-333.
[4] LI Xue, ZHANG An'an, JING Jiajia, et al. Overview of Offshore Electric Systems[J]. Power System and Clean Energy, 2016, 32(02):1-7.
[5] LI Qiang, LI Xin, WE Che. Power Grid Interlinking Technology for Offshore Oil Fields [J]. SHIPBUILDING OF CHINA. 2011, 52(S1):218-223.
[6] Ehnberg J, Bollen M. Generation Reliability for Small Isolated Power Systems entirely based on Renewable Sources [C]// Power Engineering Society General Meeting. IEEE, 2005.
[7] Xi C, Yixuan X, Anfeng L. Cross Layer Design for Optimizing Transmission Reliability, Energy Efficiency, and Lifetime in Body Sensor Networks [J]. Sensors, 2017, 17(4):900-.
[8] Zhu X, Lu Y, Han J, et al. Transmission Reliability Evaluation for Wireless Sensor Networks [J]. International Journal of Distributed Sensor Networks, 2016, 2016:1-10.
[9] Wei T, Tao Y, Yue W, et al. Reliability Evaluation of Distribution Network Containing Microgrids Based on Multi-State Power Interruption Sequence Model [J]. Power System Technology, 2019.
[10] Zhang Jifen, Hu Peng, Liu Jun. Security and stability control system for offshore platform power grid [J]. Petroleum Exploration And Development, 2009, 36(02):237-241.
[11] Manabe Y, Hara R, Kita H, et al. Two Control Areas Reliability Assessment Method based on the State Enumeration Method Considering Mass Penetration of Intermittent Generation [J]. TRANSACTIONS-INSTITUTE OF ELECTRICAL ENGINEERS OF JAPAN B, 2014, 134(4):328-335.

Acknowledgments

This work is supported by The National Key Research and Development Program of China (2018YFB0904800). The author sincerely thanks the anonymous reviewers and editors for their suggestions on improving the quality of the paper.

IOP Conf. Series: Earth and Environmental Science **431** (2020) 012030 doi:10.1088/1755-1315/431/1/012030

Research on non-intrusive monitoring of large power data industrial users

Wenfeng Li[1], Hongkun Bai[1], Bo Wu[1], Feifei Bu[1], Yuanpeng Hua[1], Hao Lu[2] and Yongchun Yang[3]

1 State Grid Henan Electric Power Company Institute of Economics and Technology, Zhengzhou, 450000, China
2 State Grid Jiaozuo Power Supply Company, Jiaozuo, 454150, China
3 State Key Laboratory of Alternate Electrical Power System with Renewable Energy Sources (North China Electric Power University), Baoding, 071003, China
E-mail: yongchunyang@126.com

Abstract. This paper constructs a non-intrusive monitoring method based on wavelet packet decomposition and fast Fourier decomposition technology to monitor the key production processes of high-energy-consuming and high-pollution industrial enterprises by utilizing the large data of power consumption of key industrial users such as iron and steel. Taking a steel plant in Henan as an example, using the constructed non-intrusive monitoring method, the load curve of the main production process is decomposed to achieve effective monitoring of the main processes of iron making, steel making and steel rolling. At the same time, through the typical link power capacity measurement, the company's steel production capacity is obtained, which can provide technical support for the supervision of key industrial users such as steel.

1. Introduction

With China's economic development entering a new stage, the development environment of various industries has changed, especially in the traditional industries such as iron and steel, non-ferrous metals, such as "capacity removal", "environmental protection management", "energy conservation and emission reduction" and so on. However, at present, there is a lack of effective means to monitor the capacity and output of iron and steel, non-ferrous and other enterprises, and the policy of overcapacity is facing difficulties in supervision. Henan Province is rich in mineral resources, widely distributed and has obvious regional advantages [1]. However, in the face of severe environment such as continuous capacity removal of key industries, increasing efforts to prevent and control air pollution, it is necessary to innovate monitoring methods to accurately grasp the implementation effect of capacity removal, energy saving and emission reduction of key enterprises. Therefore, this paper studies the non-intrusive monitoring method for industrial users based on large power data, which provides key technical support for the effective monitoring of the production situation of key enterprises such as iron and steel and electrolytic aluminium.

At present, the widely used load monitoring system is divided into intrusive monitoring and non-intrusive monitoring. Traditional intrusive monitoring is to install sensors at each load to monitor the operation of each location. Non-intrusive load monitoring (NILM) was originally proposed by Hart in the 1980s, and its core is the efficient decomposition of loads [2]. Non-intrusive load monitoring is to install monitoring equipment at the power entrance. By monitoring the voltage, current and other signals at the entrance, the type and operation of a single load in the overall load can be obtained by using an effective decomposition algorithm.

The American Academy of Electric Power Sciences has developed a non-intrusive load monitoring system. This method is based on the steady-state power change value, which can better detect the input/exit of a single power equipment, but it will fail or misjudge the simultaneous input/exit of multiple power equipment [3-5]. In reference [6], a non-intrusive power load monitoring method based on transient power information is proposed by using abrupt signal detection method. It is proposed that the significant change part of transient power curve can be used as the identification mark of power equipment, and the type of power equipment can be identified to a certain extent. After that, non-intrusive load monitoring has been applied in various fields. Considering voltage disturbance, fuzzy logic pattern recognition and neural network, non-intrusive load monitoring has been further improved [7-9].
This paper studies the non-intrusive monitoring method for industrial users based on large power data, which provides key technical support for the effective monitoring of the production situation of key enterprises such as iron and steel, electrolytic aluminium and so on.

2. Non-intrusive monitoring method for industrial users with large power data

The load curve of industrial users is a non-stationary signal with long power consumption time and heavy load. The signal contains a variety of feature information, and the overall feature is more complex than that of ordinary residential users. However, industrial production generally has typical links, such as iron and steel enterprises, mainly including ironmaking, steelmaking and rolling processes, each process has different load characteristics and cycle characteristics.
Based on the non-stationary characteristics of industrial user load and the periodic characteristics of each production process, this paper uses the combination of wavelet packet decomposition and fast Fourier transform to decompose the signal and transform the spectrum of industrial user load information.

2.1. Data preprocessing method

Before using the data for spectrum analysis, the original data collected need to be preprocessed. Data preprocessing mainly includes data cleaning, data integration and data transformation.

2.1.1. Missing *value completion.* In this study, missing value completion is divided into two steps: calculating the missing data rate in the window by sliding window, deciding whether to complete the missing data according to the missing rate; and completing missing data by mapping the neighboring data sets.
In the process of calculating the missing rate, it is necessary to ensure that the time series at both ends of the sliding window have corresponding measurement values. As shown in Figure 1, the length of sliding window is 13 time series, only window (4) satisfies the calculation conditions, and the data missing rate is 6/13=47%.

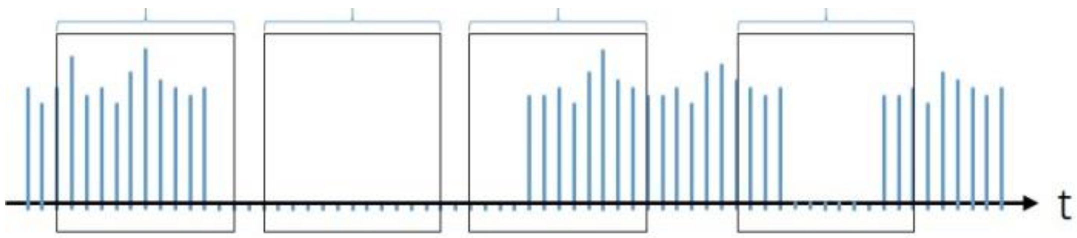

Figure 1. Sketch of sliding window.

2.1.2. Abnormal value processing. The abnormal value of the original data of industrial user load mainly refers to that the value at a certain time point is much larger than the maximum value in the data set nearby.

In this study, outlier processing is divided into two steps: outlier recognition in the selected data set of sliding window using outlier algorithm; outlier modification into the average value of the corresponding data set of sliding window.
The specific flow of outlier algorithm is as follows:
(1) Determining outlier distance

$$S = \frac{Max_t - Min_t}{a}, a = 2, 3, \cdots, 10$$

where a is the outlier constraint value, Max_t is the maximum value in the current sliding window, Min_t is the minimum value in the current sliding window, and S is the outlier distance value.
(2) Calculate the outlier coefficient of each point

$$s_i = n - \sum_{j=1}^{n} \left[\left| m_i - m_j \right| / S \right], j = 1, 2, \cdots, n$$

where n is the number of values contained in the current sliding window, j is the traversal of each value, m_i and m_j represent the values corresponding to the i-th point and the j-th point, respectively, and s_i is the outlier coefficient of the i-th point in the current sliding window. .
(3) Find out one or more points whose outlier coefficient is less than a certain value.
(4) Change the found point value to the average value of other points.

2.2. Wavelet packet decomposition module

Because of the long production cycle of industrial users, the corresponding signal frequency of each process is mainly concentrated in the low frequency band. By decomposing the signal with wavelet packet, the low-frequency information of the signal is obtained, and the spectrum of the low-frequency signal is analyzed.
Wavelet packet decomposition is an improvement and extension of wavelet decomposition [10]. The traditional wavelet decomposition first decomposes the signal into approximation part and detail part, then further decomposes the approximation part into approximation part and detail part, and repeats such decomposition until the decomposition requirements are met. WPD decomposes the details at the same time. The time scale of WPD is arbitrary, and there will be no time-frequency fixing problem. Therefore, it is mostly used in time-frequency analysis, which can better reflect the characteristic information of the signal.
In non-intrusive monitoring of large data industrial users, according to the size of scale factor j, WPD decomposes Hilbert space L_2 (R) into orthogonal sums of multiple wavelet subspaces W_j ($j < Z$), as shown in Figure 2, and subdivides each wavelet subspace according to binary. Where U_j^n is the nth (n = 0, 1, 2,..., 2^{j-1}) wavelet subspace, j is called the scale of wavelet subspace, and its corresponding orthogonal basis is $u_{j,k}^n(t) = 2^{-j/2} u^n (2^{-jt}-k)$, k is the translation factor.

<table>
<tr><td colspan="8">$U_0^0(V_0)$</td></tr>
<tr><td colspan="4">$U_1^0(V_1)$</td><td colspan="4">$U_1^1(W_1)$</td></tr>
<tr><td colspan="2">$U_2^0(V_2)$</td><td colspan="2">$U_2^1(W_2)$</td><td colspan="2">U_2^2</td><td colspan="2">U_2^3</td></tr>
<tr><td>$U_3^0(V_3)$</td><td>$U_3^1(W_3)$</td><td>U_3^2</td><td>U_3^3</td><td>U_3^4</td><td>U_3^5</td><td>U_3^6</td><td>U_3^7</td></tr>
<tr><td colspan="8">...........</td></tr>
</table>

Figure 2. Wavelet packet space decomposition.

In the decomposition process, if the scale is small enough, the sampling sequence $f(k\Delta t)$ of the function $f(t)$ in $L^2(R)$ space is directly used as the coefficient $d_0(k)$ in U space. According to the algorithm principle of orthogonal wavelet transform, the wavelet decomposition coefficients of order j and k can be written as follows:

$$d_j^n(k) = \sum_m h_0(m-2k) d_{j-1}^{n/2}(m), (n \text{ is even})$$

$$d_j^n(k) = \sum_m h_1(m-2k) d_{j-1}^{(n-1)/2}(m), (n \text{ is odd})$$

where, h_0 and h_1 are two orthogonal mirror filters, and the decomposition coefficients of stage j are expressed by the coefficients of stage j-1. According to this recursive relation, the decomposition coefficients of each level corresponding to signal $f(k)$ can be obtained. After j-level decomposition, the corresponding frequency band interval of each subspace is:

$$\{[0, \frac{f_s}{2^{j+1}}];[\frac{f_s}{2^{j+1}}, \frac{2f_s}{2^{j+1}}];[\frac{2f_s}{2^{j+1}}, \frac{3f_s}{2^{j+1}}];...[\frac{(2^j-1)f_s}{2^{j+1}}, \frac{f_s}{2}];\}$$

where f_s is the sampling frequency of the signal $f(t)$.
By calculating the energy spectrum of the load signal in each frequency range, the main information of the industrial user load signal can be determined in which frequency range according to the size of the energy spectrum, so that the corresponding signal of the energy spectrum can be used for spectrum analysis. The formula for calculating the energy spectrum is [11]:

$$E(j,n) = \sum [d_j^n(k)]^2$$

Among them, the recursive algorithm of formula (4) and formula (5) is used to calculate the wavelet packet decomposition coefficient $d_j^n(k)$.

2.3. Fast Fourier transform module
The load signal decomposed by wavelet packet is decomposed into several signals of different frequencies by improved fast Fourier transform. The characteristic information of industrial user load signal is extracted effectively, which lays a foundation for determining the operation and cycle of various production processes.
The improved fast Fourier transform method makes use of the odd, even, virtual and real characteristics of discrete Fourier transform to improve the DFT [12]. In this study, the FFT extracted by time and the FFT extracted by frequency are included.
For finite discrete data $x(n)$, n = 0, 1,... N-1 DFT is defined as:

$$X(k) = \sum_{r=0}^{N-1} x(r) W_N^{rk} \quad k = 0,1,...,N-1, W_N = e^{-j\frac{2\pi}{N}}$$

In order to decompose a large point DFT into a small point DFT, the length of the sequence N must be a composite number. In this paper, N= 2m (m is a positive integer). The sequence $x(n)$ is decomposed into two groups according to odd and even terms by time-extracted FFT:

$$\begin{cases} x(2r) = x_1(r) \\ x(2r+1) = x_2(r) \end{cases} \quad r = 0,1,...\frac{N}{2}-1$$

Then the DFT of two N/2 points is:

$$X(2r) = \sum_{n=0}^{N/2-1} x_1(n) W_{N/2}^{nr}$$

$$X(2r+1) = \sum_{n=0}^{N/2-1} x_2(n) W_{N/2}^{nr}$$

3. Case Analysis of Non-intrusive Monitoring for Large Power Data Industry Users

Steel is an important traditional pillar industry in Henan Province. The production process of steel is complex, especially in the whole process steel industries, the production system is huge. By using the non-intrusive monitoring method provided in this study, the operation and cycle of the main production processes can be determined, and the industrial production process can be monitored in detail according to the electricity consumption situation of industries, thus providing technical means for monitoring the implementation effect of "de-productivity". It can also obtain the output of steel production for a period through the calculation of typical links and technological power capacity and provide technical support for supervision of key industrial users to reduce production capacity and energy consumption.

3.1. Preprocessing of Large Load Data in Steel Industries

The data preprocessing method is used to preprocess the load data, which can reduce the impact of some abnormal values and missing data, and more accurately reflect the real power consumption situation of users.

Taking the original load data of a steel industry in Henan Province (not multiplied by the comprehensive ratio) as an example, the data set collected by the meter on a certain day appears to be missing. As shown in Figure 3, the sampling time interval of the data set is 15 minutes, the missing time interval is 21:00-22:00, and a total of 5 values are missing.

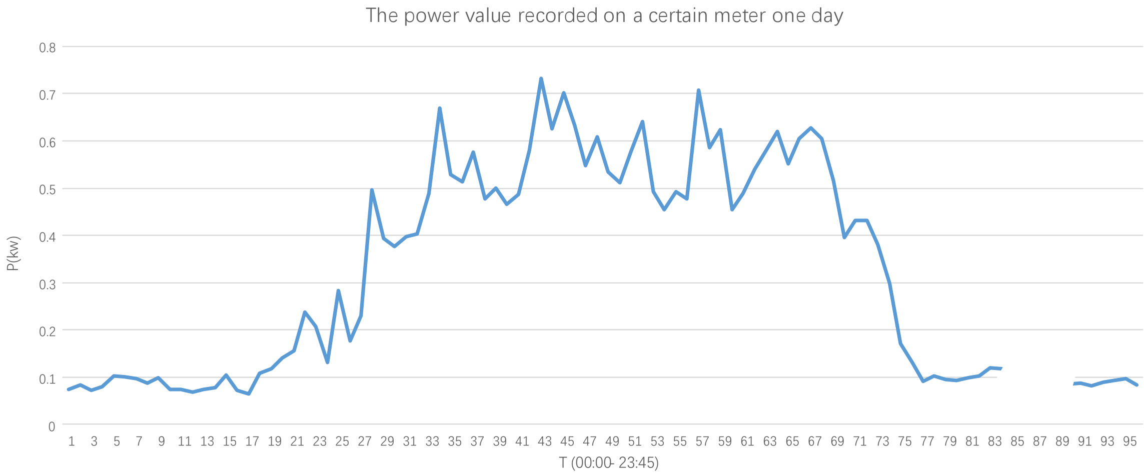

Figure 3. Raw data of ammeter.

According to the actual missing situation of data sets, the mapping method of adjacent data sets is selected to fill all missing data. The length of sliding window is set to 12, which means the missing data is filled by data sets within 3 hours, and the maximum missing rate is set to 50%. When the missing rate is greater than the set value, the missing data is not filled completely. In the above case, when the sliding window moves to 19:30, its window range is 79-90, and the current data missing rate is 5/12=42%<50%. It satisfies the condition of data completion. The data set after completion is shown in Figure 4.

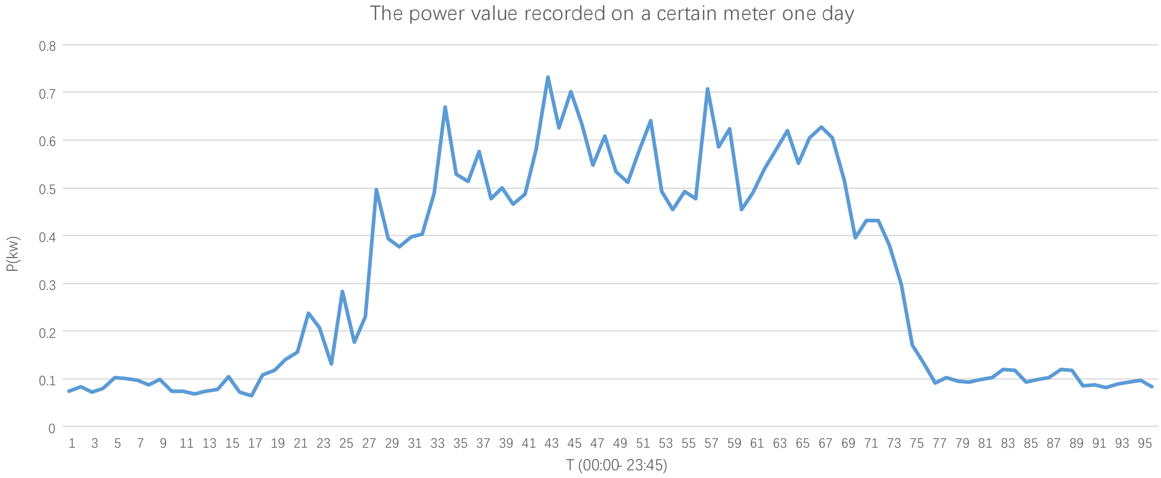

Figure 4. Completed ammeter data.

3.2. Decomposition of process flow in steel industry by non-intrusive technology

By preprocessing the data of electricity load from March to September in the steel industry, the original load data of electricity consumption in the industry is improved. Combining with the comprehensive ratio 264000. The sampling period is 5 minutes, with a total of about 63000 power points.

Wavelet packet decomposition in the third layer is used to decompose the original load signal of the industry, and the energy spectrum is calculated. The three-layers decomposition has 2, 4 and 8 bands, totaling 14 bands. The signal decomposition diagram of each band is shown in Figure 5.

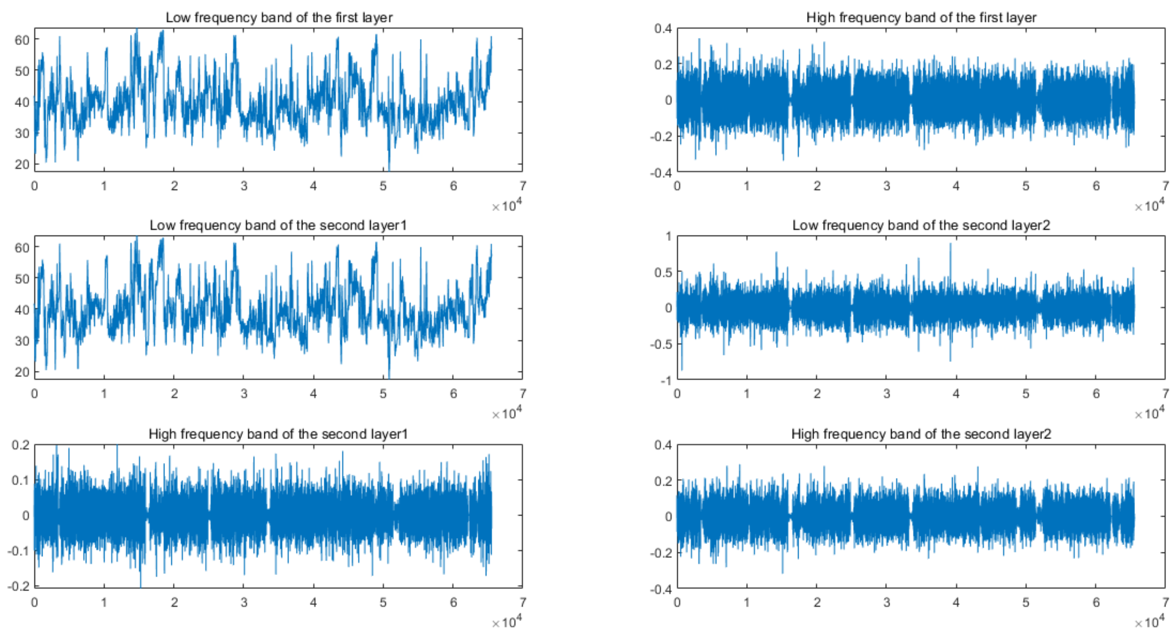

(a) Wavelet Packet Decomposition in the First and Second Layers

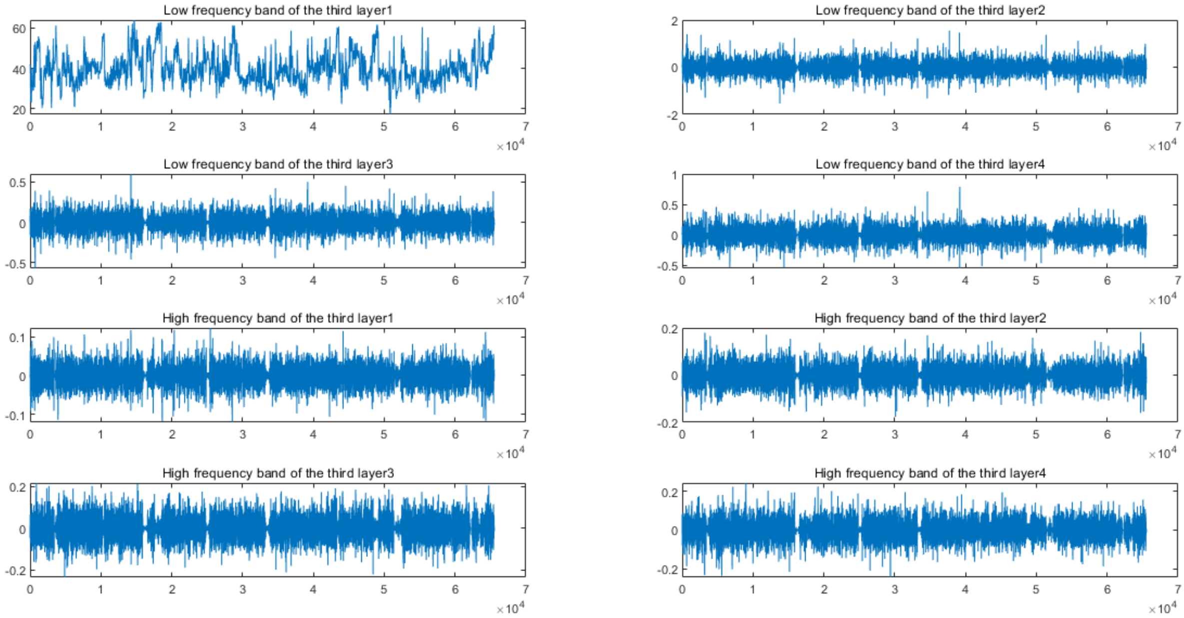

(b) Wavelet Packet Decomposition in the third Layer

Figure 5. Signal decomposition diagram.

The sampling period is 5 minutes, and the corresponding sampling frequency is 1/300. The signal of the third low frequency band 1 filters out the high frequency useless signal and contains most of the load signal information. The frequency band signal is decomposed by FFT to obtain the power spectrum information of steel industry, as shown in Figure 6. Through spectrum analysis, the frequency of rolling, steelmaking and ironmaking in this steel industry is about 1/1200Hz, 1/1800Hz and 1/3600Hz, and the period is about 20min, 30min and 60min, which is consistent with the actual production situation. After obtaining different process flow curves and calculating the average value of the waveform curve, the absolute value of the difference between each point and the average value is calculated, a reasonable threshold is set and the points whose absolute value is less than the threshold value and the slope is positive is screened out. If the point is greater than the average value, it is the starting point, and if it is less than the average value, it is the stop point. According to the decomposition of different process flow in the enterprise, the start-up and shutdown of each process flow in a one-day cycle are obtained as shown in Figure 7.

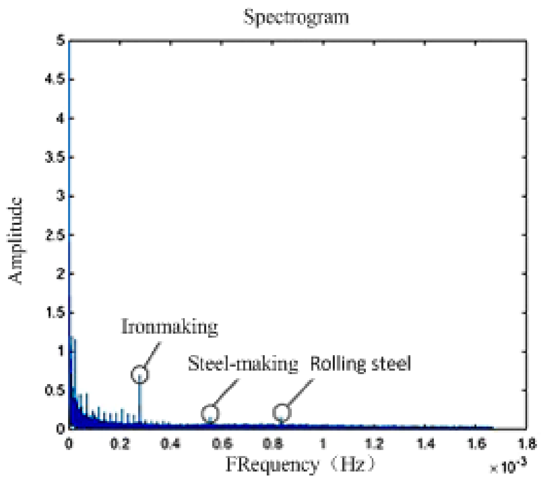

Figure 6. Spectral decomposition map of electricity consumption in steel plants.

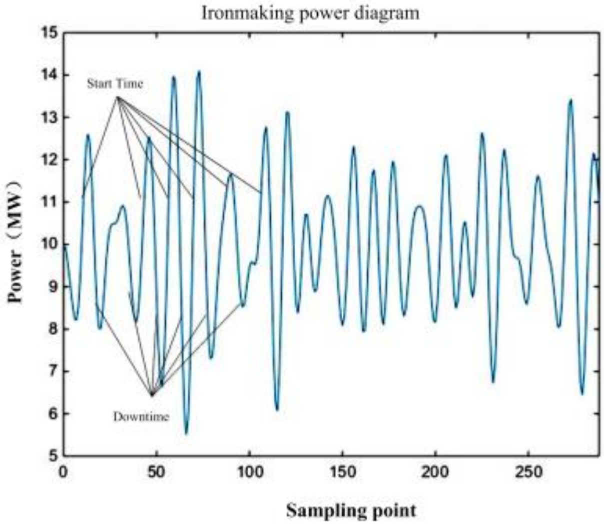

(a) Electric decomposition diagram for ironmaking

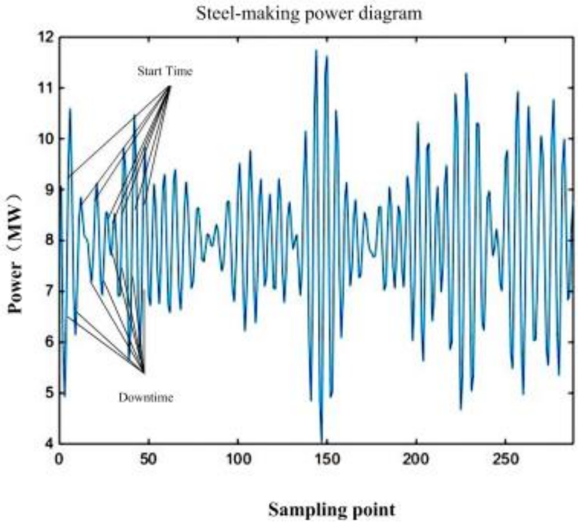

(b) Electric decomposition diagram for steelmaking

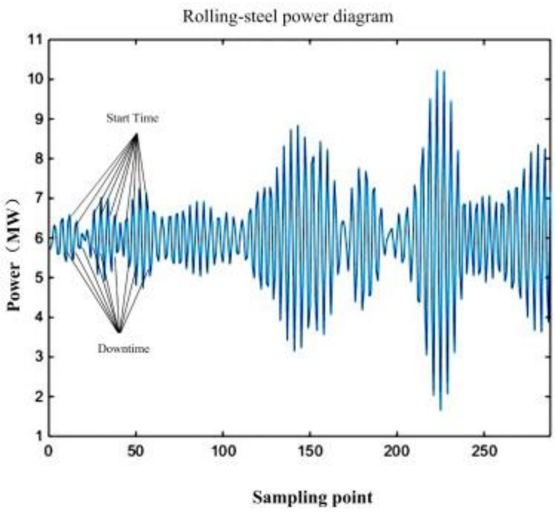

(c) Electrical decomposition diagram for steelrolling

Figure 7. Electrical decomposition diagram for each process.

IOP Conf. Series: Earth and Environmental Science **431** (2020) 012030 doi:10.1088/1755-1315/431/1/012030

Through non-intrusive decomposition of the process flow in steel plants, the industrial production process can be monitored in detail, so that the production situation of industries can be effectively monitored "remotely", and the occurrence of "should stop but not" production situation can be prevented, thus providing technical means for monitoring the implementation effect of "no capacity". Through non-invasive decomposition to judge the start-up and stop of each process, the operation status of each link can be more carefully grasped. According to the number of start-up and shut-down times per day and the output of each link in a single start-up operation, the daily output of each link can be preliminarily estimated. The results are compared with the average power consumption of steel and iron to calculate the production capacity and output, to grasp the production situation of enterprises more reliably and further test the implementation of "de-production capacity".

3.3. Analysis of Production Capacity and Output of Steel Industries

Usually, the electricity consumption of steelmaking and rolling links in steel industries accounts for about 40% of the total electricity consumption, and that of ironmaking links accounts for about 20% of the total electricity consumption.

According to the monthly electricity consumption information, the energy consumption of steel and iron produced by steel industry is estimated, as detailed in Table 1.

Table 1. Calculation of electricity consumption of steel produced by steel enterprises.

	March	April	May	June	July	August	September
Power consumption of steel production (MWh)	30608.04	34840.22	37348.53	37342.49	37633.43	35510.88	32982.25
Power consumption of iron production (MWh)	15304.02	17420.11	18674.26	18671.24	18816.71	17755.44	16491.12

Through visiting and investigating several steel industries and statistical data of relevant departments [13-15], it is shown that the power consumption per ton of steel and iron is 430-470 kWh and 180-220 kWh respectively. According to the monthly power consumption of steel industries and the power consumption per ton of steel and iron, the production range of steel and iron can be calculated, as shown in Table 2

Table 2. Estimation of output of steel enterprises.

		March	April	May	June	July	August	September
Steel production (Ton)	Maximum	71181.49	81023.71	86857.04	86843.00	87519.61	82583.45	76702.90
	Median	68152.49	77575.93	83161	83147.56	83795.37	79069.26	73438.95
	Minimum	65123.49	74128.14	79464.96	79452.11	80071.13	75555.07	70175.00
Iron production (Ton)	Maximum	85022.34	96778.41	103745.92	103729.14	104537.31	98641.34	91617.36
	Median	77293.04	87980.37	94314.47	94299.22	95033.92	89673.95	83288.51
	Minimum	69563.73	79182.33	84883.02	84869.30	85530.52	80706.55	74959.66

4. Conclusion

IOP Conf. Series: Earth and Environmental Science **431** (2020) 012030 doi:10.1088/1755-1315/431/1/012030

This paper studies the non-intrusive monitoring method for industrial users based on large data of electric power, realizes the effective decomposition of the main production processes of steel industries, and takes a steel industry in Henan as an example, realizes the decomposition of the main production processes such as ironmaking, steelmaking and rolling, determines the operation cycle of each process, and estimates the production capacity of the industry. Comparing the calculated capacity with the capacity limitation stipulated by the national policy, it is helpful for the supervisory department to control the production situation of industrial users and better implement the national policies and regulations. Non-intrusive monitoring of industrial users can help relevant departments monitor the production situation of industries according to real-time electricity consumption, and reasonably analyze the accomplishment of the goals of "de-productivity" based on relevant data. Then, by analyzing the production capacity and power consumption of industrial users, it can grasp the production level and energy consumption level of industrial users and provide indicators support for further formulation of the "de-productivity" target, form a "closed-loop policy" to guide industrial users to transform and upgrade to high-efficiency productivity, and can also help users understand their electricity consumption habits and main influencing factors, provide industrial users with electricity optimization suggestions, and further guide industrial users to use electricity scientifically, economize on electricity and improve their electricity efficiency. Therefore, through the research results of this paper, we can better grasp the implementation effect of key enterprises'policies such as capacity removal, energy saving and emission reduction, monitor the operation of enterprises, and provide key support for the formulation and adjustment of policy initiatives.

5. References

[1] Wu Xianli. Problems and Countermeasure of Supply Side reform in Henan's Industrial Field [J]. Journal of Luoyang Institute of Science and Technology (Social Science), 2018, 33(05): 34-38.
[2] Hart G W．Nonintrusive appliance load monitoring [J]．Proceedings of the IEEE，1992，80(12)：1870-1891．
[3] W.C. Bush, M. Bons, Marc. Nonintrusive End-use Monitoring in Europe[C]. 1998 DA/DSM Proceedings, London 1998
[4] W.C. Bush. Single Point End-use Energy Disaggregation (SPEED) [C]. Proceedings of the International End-Use Monitoring Symposium, Amsterdam, The Netherlands, September 1998
[5] Steven Drenker, Ab Dader. Nonintrusive Monitoring of Electric Loads[J]. IEEE Computer Applications in Power, 1999, 12(4)：47-51
[6] S.B. Leeb, S.R. Shaw, J.L. Kirtley. Transient Event Detection in Spectral Envelope Estimates for Nonintrugive Load Monitoring[C]. IEEE PES Winter Meeting, New York, January, 1995：95-105
[7] Robert W. Cox, LCDR Patrick L. Bennett, LCDR T. Duncan Mc Kay, et al. Using the Non-Intrusive Load Monitor for Shipboard Supervisory Control[C]. Electric Ship Technologies Symposium, 2007：523-530
[8] Robert Cox, Steven B. Leeb, Steven R. Shaw, et al. Transient Event Detection for Nonintrusive Load Monitoring and Demand Side Management Using Voltage Distortion[C]. Applied Power Electronics Conference and Exposition, 2006：1751-1757
[9] JG Roos, IE Lane, EC Botha, et al. Using Neural Networks for Non-intrusive Monitoring of Industrial Electrical Loads[C]. Instrumentation and Measurement Technology Conference, 1994, 3：1115-1118
[10] Wu Ting, Yan Guozheng, Yang Banghua. EEG feature extraction in brain computer interface based on wavelet packet decomposition [J]. Chinese Joumal of Scientific Instrument, 2007, 28(12):2230-2234.
[11] Li Shiling, Li Zhi, Li Hesheng. The Method of Roller Bearing Fault Monitoring Based on Wavelet Packet Engergy Feature [J]. Journal of System Simulation, 2003(1).
[12] Qian Hao, Zhao Rongxiang. Interharmonic Analysis Based on Interpolated FFT Algorithm[J].Proceedings of CSEE,2005, 25(21):87-91.

[13] Tian Jinglong. Energy consumption and energy saving analyses of top ten iron & steel plant[J].Energy of Metallurgical Industry,2007(06):3-7.
[14] Wang Weixing. Analysis on Energy Consumption Status and Energy Saving Potential of China's Iron and Steel Industry[J]. China Steel Focus, 2017(8):50-58.
[15] Liu Xiangbin. Study on Reasonable Production and Optimization of Electricity in Iron and Steel Enterprises[D].Northeastern University,2012

Acknowledgments
This work supported by the The National Natural Science Foundation of China (51607068); The Fundamental Research Funds for the Central Universities(2017MS090).

IOP Conf. Series: Earth and Environmental Science **431** (2020) 012031 doi:10.1088/1755-1315/431/1/012031

Study on stability feature extraction of power system using deep learning

D Y Shi[1,2], Y Lv[1], Z H Yu[1], G M Lu[1], H Y Dai[1], M Xie[1] and L L Zhang[1]

1 China Electric Power Research Institute, East Road of Qinghe Xiaoying 15#, Haidian District, Beijing 100192, China
2 Dept. of Electrical Engineering, Tsinghua University, Haidian District, Beijing 100084, China
E-mail: sdy@epri.sgcc.com.cn

Abstract. Dynamic security assessment (DSA) of power grids is widely used in dispatching operation systems, and calculation speed is one of its most important performance indicators. In this paper, a stability feature extraction method is proposed, which is useful for quick judgment of stability and assisted decision-making. Firstly, a simulation sample database is constructed based on historical online data and a deep learning model with least absolute shrinkage and selection operator (LASSO) is trained to pick both the high level and low level stability features. While a new operation mode needs to be evaluated, a fast search is implemented to obtain the most similar samples in the database using the chosen high level features; the final result will be determined comprehensively by the familiar samples. If the power grid is in critical condition, a decision-making will be done by using the low level features. The validity of proposed method is verified by the simulation using online data of Northeast Power Grid of China. It is proved that the method meets the requirements for speed and accuracy of online analysis system.

1. Introduction

In order to protect the transmission of electric energy reliability, China Power Grid has carried out many projects such as power transmission from west to east, national networking and UHV transmission, an extra-large-scaled AC / DC hybrid power grid has been accomplished in China[1]. With the expansion of grid-scale, the security and stability characteristics of power grid become more and more varied. In order to enhance the abilities to control the large grid operation, the DSA applications are deployed in all dispatching systems above provincial level [2-5], which is also unknown as online security and stability analysis. A comprehensive security analysis will be made by DSA every 15 minutes, which includes more than 1000 transient stability simulation of predefined faults, and needs extremely large calculation. However, calculation speed is the main performance index, as the analysis result will become meaningless without timeliness. As calculation quantity and speed are contradictory, some kinds of quick judgment technologies need to be proposed which could calculate the stability indicators with small calculation cost and only pick the real dangerous faults to make the simulation, so the computing resource will be saved and early warning time of DSA will be shorten.

With the operation of DSA system, a great amount of historical data has been produced, which both includes the power flow data and stability analysis result. There are many regularities and experiences contained in the historical data, which could be applied in quick judgment of online stability analysis

to improve the calculation speed and validity. Some analyses of quick judgment have already been made by using historical data and machine learning method [6-11].
In this paper, with the consideration that it is easy to find similar samples in the latest historical online data, the deep learning with LASSO and k-NN method are introduced to extract the stability features and make the quick judgment. It is proved that the method could shorten the calculation time significantly with slight decrease of accuracy, and meets the requirements of online analysis.
The rest of the paper is organized as follows: Section 2 introduces some related concepts, including online small signal stability, deep learning model and LASSO method; Section 3 describes the main ideas and analysis steps of the method; results are illustrated and evaluated in Section 4 using actual data; Section 5 concludes the paper.

2. Related concepts

2.1. Online small signal stability
Transient stability and small signal stability are the most time-consuming analyses in DSA. In this paper, we take online small signal stability for example; the process of transient stability is the same. The frequency and damping ratio of designated oscillation mode are the main indicators of small signal stability.
The online small signal stability analysis usually adopts eigenvalues method, which can be divided into three main steps [12]:

1) Linearization of the model. According to the current system operation point, linearize the dynamic models of power elements;
2) Solve eigenvalues and eigenvectors of the state matrix of power system;
3) The coherent generators and oscillation mode analysis. According to the result of eigenvector, we can determine the coherent generators, select the representative generator and analyse the corresponding typical oscillation modes.

At present, the online small signal stability analysis has been put into practical application, but there are still some drawbacks as follows:

- The computation time is too long. Take the online calculation data of real power system as an example, calculation time is usually 1-2 minutes, which is the longest of the online analysis.
- It is possible that the key oscillation mode can’t be found. Because the scale of the modern power system is too large, the dimension of state matrix is always very high, so it is impossible to get all the eigenvalues. In practice, the Rayleigh entropy iterative method is usually used to solve a small amount of eigenvalues between 30 and 200. So, it has the possibility that the eigenvalue of the key oscillation mode can’t be solved.

2.2. Deep learning model
In recent years, deep learning has obtained great development and became the research focus of artificial intelligence (AI) technologies. It is widely applied in image recognition, natural language processing and other fields. Deep learning is good at extracting features or regularities from massive data automatically and reflecting complicated mapping relationship, which meets the requirement of high dimensional, strong non-linear, strong coupling characteristics of power system stability problems.
Power system has a typically hierarchical structure, which is used for building the neural network of deep learning model: we take stations as the basic units and divide the whole system into three levels including district, provincial and regional; establishing the affiliation relationship between the three levels of network through topology analysis; use fully-connected neural network for each sub net and connect them together based on the affiliation to form the deep learning model. The deep learning model is shown in figure 1, which is called grids hierarchical net (GHNet).

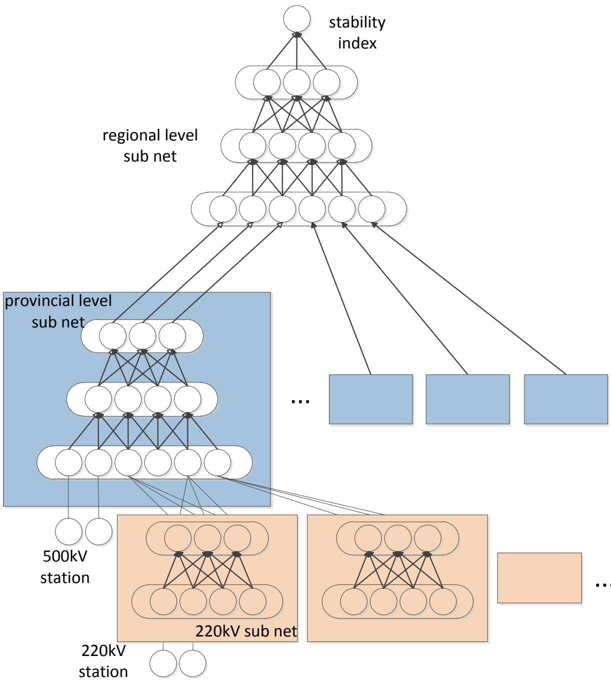

Figure 1. GHNet Structure.

2.3. LASSO

LASSO method adds a penalty function of L1-norm of parameters to the cost function of deep learning. It depresses the unimportant coefficients to zero or near zero, and leads to a more refined model. After training the model, the primary parameters will be more prominent, so that the features are extracted out. The cost function of deep learning model with LASSO is shown in formula (1).

$$J(X) = \frac{1}{N}\sum_{n=1}^{N}\left[y - f_{NN}(X)\right]^2 + \lambda\left\|W_1\right\|_1 \tag{1}$$

where N is the number of samples in each batch; y is the stability index obtained by simulation, like damping ratio of small signal stability; $f_{NN}()$ indicates the deep learning model; X is the input of neural network; W_1 is the first level trainable parameters of neural network; λ is a super parameter used for trade-off between the actual cost and the penalty value of parameter W_1.

In formula (1), the first part reflects accuracy of the model, which indicates the stability characteristics that the model "learned"; the second part reflects the compressibility for unimportant features. We only use L1-norm on the first layer (W_1), because it is the most direct indicator to pick stability features.

3. Methodology

A kind of fast searching algorithm is implemented in this paper using static state values of power system as its input and damping ratio as its predicting target. Because there are so many static state values that have different influences on the stability, it is impossible to use all of the static state values. Instead, the stability features must be the most influential ones that should be picked out by feature engineering. There are two kinds of feature engineering: model-driven method that uses professional domain knowledge and data-driven method that finds out relationships between data like machine learning. In this paper, the deep learning model with LASSO is proposed for feature engineering, and k-NN is used for quick judgment, the detailed process is as follows:

3.1. Step 1:Establish the historical database

1) Inputs

This step will be done with the operation of the DSA system. The online data is produced every 5 minutes, which both includes the power flow data and stability analysis result. The static state values used as the input of deep learning model are listed in table 1.

Table 1. Single Values.

Equipment Type	Static State Value	Symbol	Data Type
Generator	Running State	S_G	Integer
	Active Power	P_G	Float
	Voltage	V_G	Float
Station	Total Active Power of Load	P_L	Float
	Total Reactive Power of Load	Q_L	Float
DC Line	Active Power	P_{DC}	Float

2) Predicting target

We choose the Liaoning - Heilongjiang oscillation mode's damping ratio as the predicting object. The bigger damping ratio means the more stable power system. If the damping ratio is less than 3%, the Northeast Power Grid of China will be in critical condition. Because the damping ratio is a continuous value, the predicting task can be considered as a regression problem.

3.2. LASSO model training

LASSO algorithm is solved by iteration process:

1) Determine the input as well as the structure of the model, and then determine the dimensions of the parameter matrix W_1;
2) Define the cost function as formula (1);
3) Use the iterative method to minimize the cost function.

Where λ is a super parameter: a larger λ means emphasis on the penalty term of W_1, which may lead to a bigger actual error that unable to reflect the stability characteristics of the power grid. Therefore, the selection of λ is the key issue.

In this paper, the model is trained for many times to seek the optimal value of λ. When the penalty term is not considered ($\lambda = 0$), the error rate will be the lowest that is defined as the base line. The parameter λ can be equidistant values in exponential coordinate, for example 0.1, 0.01, 0.001, etc.

3.3. Feature selection

According to the characteristics of deep learning model, parameter matrix W_1 represents the weight of each input. The greater value means the more important input. The dimensions of the matrix W_1 are N_1*N_2, N_1 and N_2 are the numbers of neuron in layer1 and layer2. Therefore, the algorithm sums the absolute values of each row of the matrix W_1, and selects the largest number of the results as the stability features.

3.4. Time domain simulation

Calculate the real damping ratio result by small signal stability simulation to verify the method. Then, put the latest power flow data and real damping ratio result into the historical database for next prediction. Algorithm flow chart is shown in figure 2.

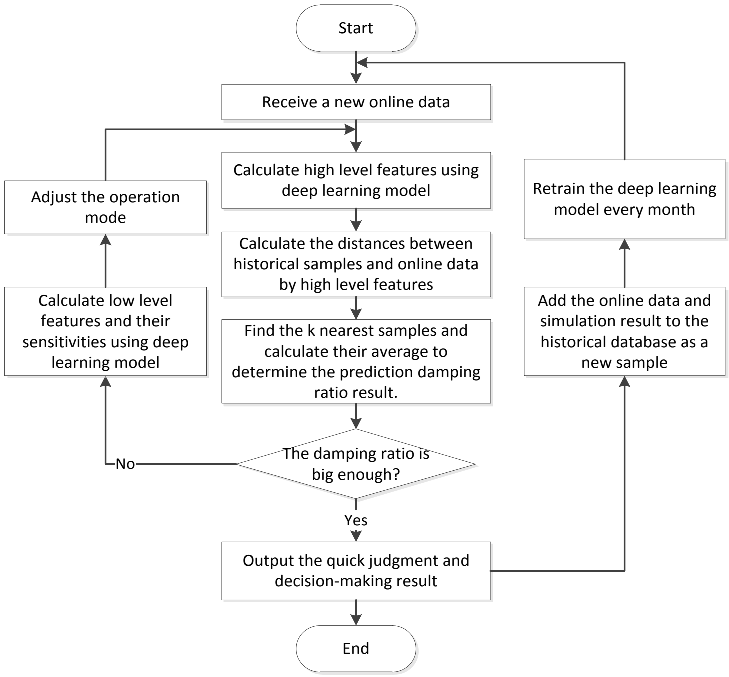

Figure 2. Algorithm flow chart.

4. Examples

The validity of proposed method is verified by simulation using online data of Northeast Power Grid of China. All the power element models above 220kV have been included in the online data. The number of input static state values is 1919, the predicting object is the damping ration of Liaoning - Heilongjiang oscillation mode.

4.1. Model training

Choose seven different parameter λ for model learning respectively: 0, 0.1, 0.01, 0.001, 0.0001 and 0.00001. The results are shown in table 2.

Table 2. Model performance with different λ.

λ	Error rate	Compression ratio
0（reference）	0.17%	1.18%
0.00001	0.23%	16.62%
0.0001	1.15%	62.17%
0.001	8.06%	79.42%
0.01	35.62%	85.14%
0.1	47.85%	61.83%

The error rate while λ=0.1 or λ=0.01 is obviously too large, indicating that the model cannot reflect the stability characteristics of the power grid, so it needs to be ignored. The rest results show that the error rate increases with the increase of λ, while the compression ratio of W_1 also increases as expected. We choose the LASSO model with λ=0.0001 as the best model.

4.2. Feature selection

We use the sum of the absolute value of parameter matrix W_1 to extract the low level features, and the results are shown in table 3. We use back propagation algorithm (BP) to calculate the sensitivities of the low level features with the online data at 10:00 on November 25, 5 of the largest positive and negative sensitivities are also shown in table 3. For convenience of comparison, we only pick out generator's active power features.

Table 3. Low level features.

Variable name	Weight of the feature	Sensitivity
HLJ.JX.#1	10.81	-0.001343
HLJ.JXER.#1	19.23	-0.000767
HLJ.JXER.#2	20.58	-0.000667
HLJ.JX.#2	15.90	-0.000639
HLJ.QTH.#1	8.23	-0.000473
LN.YSH.2#	9.83	0.000627
LN.QH.1#	12.98	0.000435
LN.YK.1#	8.86	0.000403
LN.GJZ.2#	9.17	0.000402
LN.DD.1#	10.53	0.000330

As the results shown in table 3, the sensitivities of generator’s active power in Liaoning are positive, and the sensitivities in Heilongjiang are negative. The results meet the characteristics of Northeast Power Grid, as the electricity power is mainly transmitted from Heilongjiang to Liaoning.

32 high level features can be calculated by deep learning model, because the number of neurons in the last hidden layer is 32.

4.3. Quick judgment
Take the online data at 10:00 on November 25 for example, 5 most similar samples are found by using high level features shown in table 4. The average of the 5 most similar samples is 0.207118, while the simulation result is 0.207084. The error rate is 0.016%, which is extremely low.

Table 4. The most similar samples.

No	Date time	Distance	Damping ratio
0	2018_11_25T10_00_00	0	0.207084
1	2018_11_25T09_45_00	7.068e-5	0.206563
2	2018_11_25T09_30_00	7.537e-5	0.206329
3	2018_11_25T10_20_00	7.653e-5	0.207589
4	2018_11_15T12_15_00	9.026e-5	0.207754
5	2018_11_15T20_35_00	9.227e-5	0.207353

Another interesting situation is that: some similar samples are not the closest ones in time, like 4 and 5 in table 4. It is due to the high dimensionality and high non-linearity of stability problem of power system.

4.4. Decision-making
We changed the operation mode of the online data at 10:00 on November 25 by using the low level features in table 3: reduce the active power of each generator with negative sensitivity by 10MW, and increase by 10MW otherwise. Our aim was to increase the damping ratio to make the power system more stable. The simulation result of damping ratio of new operation mode is 0.210108, which is increased as expected.

5. Conclusion
A deep learning model with LASSO is proposed to extract the high level and low level features based on historical database, which is very appropriate for online stability analysis. Simulation and experimental results verify the correctness and effectiveness of the proposed method. It is also necessary to make further improvements, such as:

1) Try more features that make influence on the stability of power system;
2) Rapid and valid method of determining the adjustment quantities;
3) Study on rapid and automatic methods for searching the optimal value of super parameter λ.

6. References

[1] Liu Z Y 2013 *Ultra-High Voltage AC & DC Grid* (Beijing: China Electric Power Press)
[2] Yan J F, Zhou X X, Shi D Y, et al. 2015 *Power System Online Dynamic Security Monitoring and Early-Warning Technology* (Beijing: China Electric Power Press)
[3] Tang Y, Wang Y T, Tian F, et al. 2012 Research and Development of Stability Analysis, Early-Warning and Control System for Huge Power Grids *Power System Technology* 36(7) pp. 1-11
[4] Sun S M, Xie C, Lv Y, et al. 2015 Power System Online Security and Stability Analysis Application Modes *Power System Technology* 39(10) pp. 2875-2881
[5] Yan J F, Yu Z H, Tian F, et al. 2008 Dynamic Security Assessment & Early Warning System of Power System *Proceedings of the CSEE* 28(34) pp. 87-93
[6] Guo T Y, Jovica V. Milanović 2014 Probabilistic framework for assessing the accuracy of data mining tool for online prediction of transient stability *IEEE Transactions on Power Systems* 29(1) pp. 377-384
[7] Athula D R, Francisco G, Kasun N, et al. 2010 Rotor angle instability prediction using post-disturbance voltage trajectories *IEEE Transaction on Power Systems* 25(2) pp. 94-956
[8] Turaj A, Soheil R 2013 Transient instability prediction using decision tree technique *IEEE Transactions on Power Systems* 28(3) pp. 3028-3037
[9] F R Gomez, A D Rajapakse, U D Annakkage and I T Fernando 2011 Support vector machine-based algorithm for post-fault transient stability status prediction using synchronized measurements *IEEE Transactions on Power Systems* 26(3) pp. 1474-1483
[10] Xu Y, Dong Z Y, Meng K, et al. 2011 Real-time transient stability assessment model using extreme learning machine *IET Generation, Transmission & Distribution* 5(3) pp. 314-322
[11] Xu Y, Dong Z Y, Zhao J H, et al. 2012 A reliable intelligent system for real-time dynamic security assessment of power systems *IEEE Transactions on Power Systems* 27(3) pp. 1253-1263
[12] Shi D Y, Lu G M, Gu L H, et al. 2013 Online Small Signal Stability Generator Group-Dividing Algorithm for Power System Based on Data Clustering *East China Electric Power* 41(11) pp. 2223-2228

Acknowledgments

Project is supported by National Key R&D Program of China(2017YFB0902604): On-line Safety Risk Prevention, Control and Intelligent Decision-making Technology for Large Power Grid.

Dongyu Shi received his B.S. and M.S. degree from Tsinghua University in 2003 and 2006 respectively. Currently, he is working in China Electric Power Research Institute (CEPRI). He participated as one of the principal researchers/developers in development of the dynamic security assessment (DSA) system, which is widely used in China. His research interests include power system dynamic security assessment, parallel computing, and machine learning.

2019 3rd International Conference on Power and Energy Engineering IOP Publishing
IOP Conf. Series: Earth and Environmental Science **431** (2020) 012032 doi:10.1088/1755-1315/431/1/012032

Application research of virtualization in life cycle management of nuclear power computers

Hongbao Han[1], Jinqiu Yang[2], Xiaohe Li[1], Shengzhi Liu[3] and Weiwei Pan[3]

1 Engineer, Suzhou Nuclear Power Research Institute, Shenzhen, CHN
2 Assistant, Suzhou Nuclear Power Research Institute, Yangjiang, CHN
3 Senior Engineer, Suzhou Nuclear Power Research Institute, Shenzhen, CHN
E-mail: yangjinqiu@cgnpc.com.cn

Abstract. At present, digital instrument control equipment and systems are widely used in nuclear power plants, in which computer is an important component of digital instrument control system. But the upgrading period of software and hardware system is very short. It is often faced with the shutdown of spare parts and the upgrade of software and hardware platform that can't support the original application software, which brings great challenges to the life management of computer. This paper expounds the application status of computer in the digital instrument and control system of nuclear power, the characteristics of life management, obsolescence solutions and risks, and introduces the virtual server technology. The application cases of Demineralized Water Production System (hereafter called SDA) booster upgrading project in a nuclear power plant are summarized, and the application scope and limitations of virtualization obsolescence management strategy are summarized. The practice shows that virtual server technology can effectively solve the problem of computer life cycle management in some cases, which is conducive to reducing costs and increasing efficiency, and improving the competitiveness of nuclear power.

1. Introduction

At present, digital instrument control system has been widely used in emerging nuclear power plants, and traditional instrument control system has been upgraded to digital instrument control system in existing power plants. Compared with traditional analog system, digital systems are more complex and contain more components, such as computers, HMI, internal data bus, communication network, etc. Maintenance and repair of digital equipment is basically not feasible. These factors also make the digital instrument and control system or products have the characteristics of limited life or easy outdated. Therefore, it is very important to incorporate these digital devices into the life cycle management research and develop a comprehensive and exclusive strategy or plan for the obsolescence of digital instrument and control system and products. [1] Among them, computer equipment is an important part of digital instrument and control system, which undertakes the tasks of human-machine interface, data storage and calculation and analysis. For example, DCS, a large-scale digital instrument and control system which integrates 4C technologies such as computers, and computer is widely used in its upper computer systems such as operator stations, engineer stations, servers and so on. In the digital instrument and control system, the life of computer technology innovation is facing more complex life cycle management issues.

2. Characteristic of computer life management in nuclear power plant

Computer is widely used in digital instrument and control system of nuclear power plant, such as LEVEL2 layer of NC-DCS system. It mainly includes operator station host, gateway host, communication station host, configuration engineer station, configuration server, maintenance engineer station, backup station host, POP host, NI/CI/computing server, history server and LEVEL3 getaway and so on. Such as SDA, EPP, TCS, KRT, KIS and other PLC system workstations. It can be seen that nuclear power plants have a large number of computers. The obsolescence and upgrading of computers is facing many difficulties and challenges, the details are as follows:

2.1 Hardware and software incompatibility

With the rapid development of computer hardware equipment, it's often faced with the problem of spare parts obsolescence, which needs to be upgraded with new hardware equipment. For the related operating system, application software and other software systems, there are no problems of failure and aging, but they are often incompatible with the upgraded hardware system. Moreover, software systems are upgraded in order to adapt the development of hardware and their own development needs. For example, the operating system may become obsolete in three years, while the distributed control system may become obsolete in six years. Therefore, when the hardware equipment is obsoleted and upgraded, it's often accompanied by the upgraded of software system, but the procurement cost of software is generally high.

2.2 Different life cycle

The life cycle of computer hardware is usually 5 years, plus spare parts in stock, which can run for about 10 years. The hardware life of the lower computer is generally 10 years, plus spare parts in stock, which can run for about 15 years. For the upper computer system closely related to the lower computer, such as the engineer station, when upgrading it, the lower computer system has not reached the end of its life, considering the cost problem, generally do not upgraded the whole system. The compatibility between the upgraded upper computer system and the lower computer system needs to be tested and evaluated, which has a certain risk. Therefore, computer obsolescence has different life cycle between upper computer and lower computer, the node of obsolescence time is inconsistences, and the risk of obsolescence is high.

For example, the NC-DCS system of nuclear power plant has been running for more than ten years since its design and debugging stage. The upper computer system has reached the end of its life. It is faced with the problems of lack of spare parts, shutdown of the manufacturer, slow response speed and high load. It is urgently needed to be obsoleted and upgraded. The preliminary general plan is that the computer hardware is upgraded from SUN Netra to x86 server, the system software version is upgraded, the operating system is upgraded Solaris from to Linux, and the logic/screen software is upgraded from V8.3/V4 to V8.5/V5. However, the lower computer has not yet reached the end of its life, considering the cost factor, it is impossible to upgrade the whole system for the time being. But at the end of the next machine life, the platform will be upgraded from AS5 to AS7. Compatibility problems caused by the obsolescence of the upper computer include: compatibility between the old version of engineering files and the new version of software system, compatibility between the compiled new version program and the old version of the lower computer, compatibility between the new version of the upper computer and the old version of the lower computer, compatibility between the upper computer system and the third party interface, etc. If the lower computer system is upgraded by stages and parts in the follow-up examination, the compatibility and construction solution of the system will be more complex and prominent.

2.3 Specialized software upgrade problems

In addition, some niche or special-purpose applications may face the situation that they have been phased out or not maintained and their sustainability cannot be guaranteed, so it is necessary to redesign the application files when upgrading the masterpiece.

In summary, the upgrading of computer equipment is inefficient, risky and costly. Computer elimination management is an unavoidable part of the technical life cycle of newly built and operated power plants. Through research and formulation of computer life cycle management plan, relevant objectives can be achieved, such as maximizing service life, maximizing usability, maintaining safety, minimizing risk, minimizing cost or improving efficiency.

3. Solution to computer obsolescence in nuclear power plant

It is of great significance to study the types, risks, solutions and scope of application of computer obsolescence for maintaining the safe and reliable operation and cost control of nuclear power plants. Among them, the traditional obsolescence of computer has the follow solutions: equivalent replacement, selection of longer obsolescence cycle hardware, defensive procurement of spare parts, etc. [2]

For example, HP ProLiant DL580 G5, a commercial server, was originally used in the history services of a nuclear power plant. Because this type of server is a commercial type and has fast updating and long period of power plant design and construction, the equipment has been obsoleted shortly after the unit is put into operation normally. And the relevant electronic components have been shut down, when the field equipment is damaged, it will not be able to be repaired or replaced, which has a great impact on the system function. The nuclear power plant uses Linghua industrial server as equivalent replacement and purchases sufficient spare parts. This industrial server has longer spare parts supply capacity than commercial computer, and can improve spare parts supply capacity for seven years.

However, these obsolescence solutions are only applicable to certain situations and will be subject to certain restrictions. For some special cases, such as the loss of industrial software authorization due to a long time, or the failure of a maintenance toll computer without permission to reinstall, the manufacturer refuses to provide support, even spare parts can`t be reinstalled at this time. In addition, the spare parts also has the same aging problems, the above-mentioned traditional solutions will not be able to solve.

This article will focus on the use of virtualization technology to solve the problem of computer obsolescence. Virtualization is through the simulation of hardware and software platforms, on which other software can be run. Virtualization, as a common practice in the field of information technology, is speeding up its entry into the digital instrument and control system to manage the software life cycle of the station directly.

4. Application research of virtual server in life cycle management of nuclear power plant

Virtualization server technology integrates the hardware resources of physical servers into logical resources, which virtual multiple independent virtual machines in one physical server, and allocates CPU, memory, disk, I/O card and other hardware resources to each virtual machine reasonably, thus saving hardware costs and improving resource utilization. With the wide application of virtualization technology, computer hardware manufacturers have begun to research on hardware. [3] With the continuous development of hardware-assisted virtualization technology, the operation of virtualization software is more agile and efficient.

Virtual server is a conventional design in IT industry, but it is seldom used in nuclear power digital control system. In this section, aiming at the enormous challenge of computer obsolescence and upgrading, a new idea and technical solution are introduced, taking the SDA upper computer upgrading project of a nuclear power plant as an application case.

4.1 The background of a nuclear power project

The SDA system of the nuclear power plant is a common system of the whole plant. The upper computer of its control system has been running for many years. The hardware of the system computer is aging, which often results in slow response and crash. Moreover, the main hardware of computer has been shut down, which seriously affects the reliability of the control system, so it`s urgent to upgrade the upper computer system. The original upper system frame diagram is shown in figure 1.

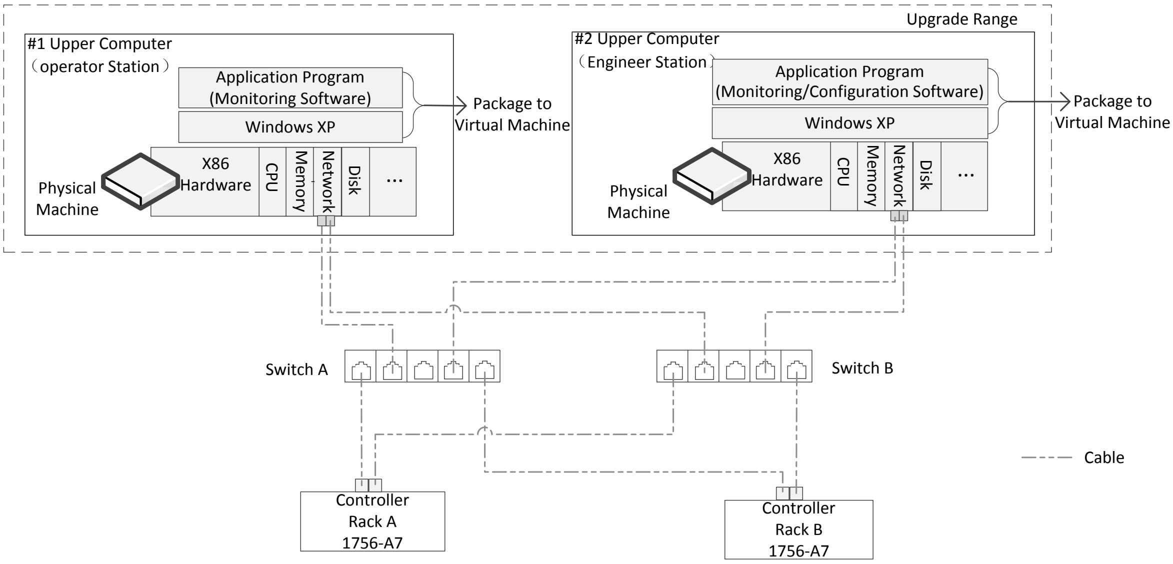

Figure 1 The original upper system frame diagram

The operating system of upper computer is Windows XP, and the monitoring display software is InTouch 10.0. Windows XP has been obsoleted, and the operating system is Windows 7 generally, but the version of original industrial configuration software is low (InTouch 10.0), which does not support windows 7system. Therefore, if the traditional upgrading solution is adopted, while upgrading the computer hardware, it is necessary to update the operating system to windows 7, update the monitoring display software to InTouch 10.6 or higher version, and update RS Logix5000 to version 16.0. The upgrading range is shown in the dashed line range.

4.2 *Virtual server upgrade solution*

This project chooses one physical server and two thin clients to build the upper computer network through two switching agencies. The system frame diagram is shown in Figure 2.

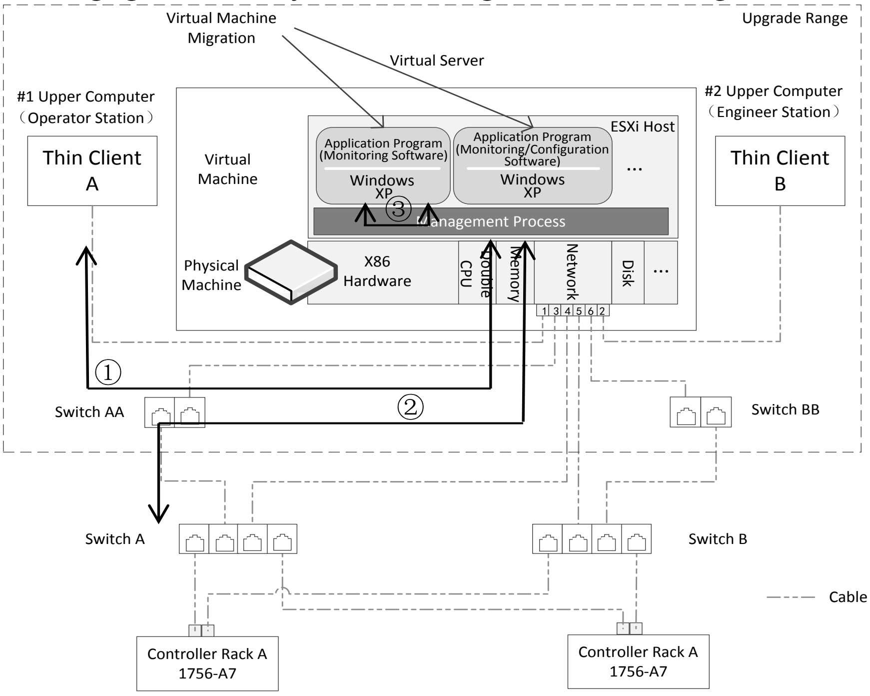

Figure 2 The frame diagram of virtual server upgrade

The virtual management software platform adopts Ware vSphere 6.0, and the physical server adopts hardware-assisted virtualization platform DELL Power Edge T series. This server uses Inter Xeon processor which supports virtualization to support the operation of virtualization software and make it run more smoothly. With modular design method, the main hardware is independent of each other, and disk, CPU, power module and memory are redundant configuration. When the server is free from failure, each hardware device handles the information by itself. If one of the hardware equipment fails, the system automatically transfers the data that the hardware equipment needs to process to redundant hardware equipment for processing, so as to ensure that there will be no outage when the equipment fails. After replacing the failed hardware, the system will return to the original operating state automatically.

Combining Figures 1 and 2, it can be seen that the upgrade plan is packaging the operating system and applications (industrial configuration software) in the original two computers, convert them into virtual machine files, and migrate them to the server platform seamlessly. Two virtual machines are running on one physical server, that is, two sets of operating systems and application software of the original engineer station and operator station. The thin client connects to the system through the switch and accesses the virtual machine in the server. Taking switch A as an example, the working mechanism of system signal flow is introduced as follows: thin client A calls the original operator station virtual machine, and the original operator station virtual machine returns relevant information to thin client A, as shown in solid line ①. The two virtual machines communicate with lower controller through the server and switch AA, as shown in solid line ②. The operator station virtual machine and the engineer station virtual machine communicate through the virtual switch inside the server, as shown in solid line ③.

After upgrade, the operator can not feel the difference between before and after the upgrade. The new system maintains all the monitoring functions of the original system. And because the main hardware of physical server is thermal redundancy, the operation of operator station and engineer station will not be affected when a hardware failure occurs, and the reliability of the system has been improved.

4.3 Comparison of virtualization and traditional solutions

Taking this project as an example, considering only the main factors, the traditional upgrading solution is compared with the virtual server solution. According to the foregoing, if adopting the traditional control solution, we need purchase two servers, two operating systems, two InTouch software and one RS logix5000 software. The comparison of the two solutions is shown in Table 1, and the detailed analysis is as follows.

- In the aspect of main hardware procurement, because of the low cost of thin client, the virtual server solution is slightly better. In addition, based on the main characteristics of virtual servers, the effect of Cost Reducing and Efficiency Increasing is more significant when the number of servers in the original system increases.
- In the aspect of main software procurement, because the procurement cost of application software is high relatively, the virtual server solution only needs purchase the virtual platform software, the cost is very low.
- In the aspect of upper computer life cycle, if virtualization solution is adopted in the last life cycle, the upgrade of the next life cycle will be low-cost and efficient, which also fully demonstrates the advantages of virtualization solution.

Through the above analysis and combining with the technical characteristics of virtual server, the following conclusions can be drawn:

- The more computer in the system, the greater the effect of cost reduction and efficiency increase.
- For computers adopting virtualization technology, the upgrade work at the next life cycle will become simple, cheap and efficient.
- It is also an excellent solution to the problems such as loss of application authorization and non-persistence of the special software.

- In addition, the virtualization solution will keep the original operating system and running view, and reduce human risk. Therefore, the application advantages of virtual server technology in nuclear power plants can be summarized as follows: low cost, high efficiency and low human risk.

Table 1 Comparison of traditional upgrade solution and virtual server upgrade solution.

Items involved	Main hardware procurement	Main software procurement	Total cost	Next life cycle	Winning solution
Solution 1: traditional solution	Two servers (about 50 thousand)	Two system software Two InTouch10.6 One RS Logix5000 （about 330 thousand）	380 thousand	Face the same problem	Solution 2
Solution 1: virtualization solution	One server Two thin client（about 30 thousand）	One VMware vSphere 6.0 platform software（about 6 thousand）	40 thousand	Substitute for physical servers	

5. Applicability and limitation of virtualization server solution

With the continuous improvement of virtual server technology, including better tools for backup, recovery and migration of data, computer hardware design more matching the operation of virtual machine. It is believed that the application of virtual server technology in nuclear power plants will be more and more, but virtualization strategy still has its applications and limitations.

5.1 Applications

The virtualization solution can be used to both old and new projects in nuclear power plant. For the old project, the whole operating system and application program on the obsolete server are migrated to the virtual environment through virtual technology, and the upgrade work becomes very simple. Taking the Daya Bay Nuclear power plant as an example, there are more than 20 servers of each unit at present, if using this technology, the cost will be saved by about 50%. If the virtual server solution is adopted in the new design system, the subsequent hardware upgrade and replacement will be a very simple thing, which greatly improves the maintainability of the system.

5.2 Limitations

When using virtualization solution, we should choose the computer hardware platform to support virtualization, and we need to train the maintenance worker of nuclear power plant to master the maintenance ability of this technology, the detailed description is as follows:

- Virtualized devices generally use workstations, servers and equipment with standard hardware-level interfaces supported by virtualization platform software. These standard hardware-level interfaces including Ethernet, RS232/485, USB, SATA and so on.
- The obtained virtualization platform software should support all specific hardware configurations and operating system versions.
- It should have the resources that can configure and manage a large number of parameters and configurations of virtualized software platforms, such as experienced maintenance worker list.

If the original hardware device or interface is retained in the system, the original system needs to be checked to confirm that the selected virtualization software platform supports all hardware functions. Before handing over users, it needs to be evaluated and tested. The following are specified:

- There are special hardware or interfaces in the original system environment, which are not supported by the virtualization software platform;
- The virtualization software platform should not interface with any system functions or have any impact on the system functions.

- It does not simply to guarantee the equivalence of underlying hardware and/or operating system configurations for virtualization. Hardware and/or operating system changes should be carefully evaluated and tested before debugging and handing over to users.

6. Conclusion

The application of computers in digital instrument and control systems of nuclear power plants in China is becoming more and more popular, while the research of computer life management is still in its infancy. With the rapid development of computer software and hardware technology, the speed of upgrading and transformation can`t catch up with the speed of software and hardware updating, which brings huge capital and manpower costs to the operators of nuclear power plants, and also brings certain safety and quality risks to the safe and reliable operation of nuclear power plants. Virtualization technology has innate advantages in cost reducing and efficiency increasing. It is also a recommended method of EPRI in the study of digital instrument management and obsolescence control of nuclear power plants. In this paper, through the application of virtualization strategy in the upgrade project of SDA control system in a nuclear power plant, the advantages of virtualization strategy are analyzed, and the applicability and limitations of virtualization strategy are briefly summarized. However, it is still necessary to study the application evaluation and testing of virtualization strategy in the future. However, with the continuous development of server virtual technology and real-time controller virtual technology, it is believed that there will be more and more applications in the field of nuclear power.

7. References

[1] Advanced Nuclear Technology: Guidance and Methodologies for Managing Digital Instrumentation and Control Obsolescence[R].EPRI FR- 3002002852.2014
[2] Application of VMware Esxi Virtualization Technology in Integration of Electric Power Information Resources [J] Hunan Electric Power.2012 (06):5-9
[3] Application of server virtualization technology in power system [J]. Science and Technology Information.2016 (27)

Acknowledgments

This paper has been completed. I sincerely thank all the leaders and colleagues who supported me during the completion of this paper. Their rigorous and earnest working attitude infected me with continuous hard work. Their selfless help enabled me to successfully complete the writing of this paper. At the same time, I would like to thank my parents and relatives for their silent support. In the future, I will work harder to achieve more excellent work performance and learning results.

Chapter 5:
Electrical Engineering and Automation

IOP Conf. Series: Earth and Environmental Science **431** (2020) 012033 doi:10.1088/1755-1315/431/1/012033

Power failure evolution model considering voltage stability

Jialin WANG[1], Qun YU[1] and Qi WANG[1]

1 College of Electrical Engineer and Automation, Shandong University of Science and Technology, Qingdao266590, Shandong Province, China
Email: wjl_94@163.com

Abstract. Voltage instability is often associated with power system blackout. In order to study the evolution mechanism of power failure and voltage instability in power failure, this paper proposes a new kind of power failure evolution model that considers voltage stability. The theory of static voltage stability analysis is introduced into the modelling. According to the simulation results of power failure in an IEEE39 system, the model proposed in this paper verifies the self-organized criticality of power network. It was also found that voltage instability lead to the increase of the frequency and scale of power failure. Furthermore, the frequency of load nodes in voltage instability accidents is calculated and the set of weak nodes is obtained.

1. Introduction

With the continuous development of the social economy, the interconnection of power grids is becoming a growing trend in power system development. As the scale of the power grid expands, system operation grows more complex, and the safe and reliable operation of power systems is affected. In recent decades, several power system blackouts have occurred around the world, resulting in huge economic losses. Generally, the evolution process of power failure includes two stages; the initial fault accumulation, rapid expansion of the fault area and the final stage of power failure. In the initial stage of power failure, some components exit the operation state due to short circuit failure, causing large-scale power flow transfer. In the stage of rapid expansion in the fault area, the power flow transfer causes an imbalance between the supply and demand of reactive power in the system, which may lead to voltage instability. In the final stage of power failure, the generator set adjacent to the unstable node may be out of step due to power imbalance. Voltage instability is one of the biggest factors that affects the development of power failure.

In recent years, in order to study the mechanism and reduce the risks involved in power failure, scholars have carried out a large number of studies and proposed a variety of power failure models. From the research methods, these models can be divided into two categories: those based on power flow analysis and those based on power grid topology analysis. The first type of model describes component characteristics through a probability model and mainly studies the overall characteristics of a power system, including OPA model [1], Hidden Failure model [2], Cascade model [3], SOC-power Failure model [4], and so on. The second model applies a complex network theory to analyse the topological characteristics of the power network, including a small-world network model [5] and scale-free network model [6]. Neither of the two models above consider the problem of voltage instability in power failure.

In order to describe the process of voltage instability, cellular automata theory is cited in the modelling of power failure. A cellular automata model is a discrete local dynamics model in time, space and state, and is mainly used in complex system simulation. Unlike general dynamics models, cellular automata are not determined by physical equations or functions, but by a series of rules. In cellular automata, all cells follow the same transformation rules. And the evolution of cellular automata is realized by using transformation rules to update the cellular state at every moment.

At present, cellular automata (CA) has been applied to many fields such as traffic flow simulation, forest fire spread simulation, and urban expansion simulation. In the literature [7], cellular automata theory was first applied to power failure modelling. In another study [8], fuzzy theory is combined with cellular automata theory to obtain the fuzzy cellular automata model. In the above model, the lines in the grid are taken as cells, while in this paper, the nodes in the power grid are taken as cells. Voltage is the basic parameter of the node. If the node is taken as a cell, it is convenient to introduce the theory of static voltage stability into the modelling of power failure.

The theory of static voltage stability is based on power flow calculation. The critical point of voltage instability is analysed through a variety of indicators, and the distance between the running point and the critical point is given. In this paper, the cell state is defined by voltage offset and voltage stability, so as to establish a power failure model based on cellular automata theory while considering voltage stability factors. This model is used to study the overall characteristics of the power grid. On the one hand, the self-organized criticality of the power grid is proved; on the other, the influence of voltage instability factors on the occurrence scale of power failure is studied. Then, in order to analyse the weak nodes in the network, the frequency of voltage instability of the nodes in the simulation is counted.

2. The components of cellular automata

2.1. The definition of cellular state

Nodes and lines are the basic components of a power grid. In this paper, any node cell in the cellular automaton can be expressed as follows:

$$C_i = i(i = 1, 2, \wedge, n) \tag{1}$$

where, n is the number of nodes in the grid, and i is the cell number. For each cell C_i, there is only one state at any given time. The set of cellular states is as follows:

$$S_i \in \{0,1,2\} \tag{2}$$

where, S_i is the state of cell numbered i. When S_i is equal to 0, the cell is in a state of normal. When S_i is equal to 1, the cell is in a state of emergency. When S_i is equal to 2, the cell is in a state of failure. In the process of cellular automata evolution, the transformation of cellular state is always unidirectional; that is, from normal state to emergency state and from emergency state to the instability state. The state of the cell depends on three factors: voltage stability, load rate, and degree.

2.1.1. Cellular state definition based on voltage stability.

1) Definition of the cellular normal state

According to the definition of voltage stability in the IEEE and CIGRE report [9], voltage stability means that the voltage of the system can be maintained or restored to the allowable range after a small or large disturbance. The maximum deviation of cellular voltage relative to nominal voltage is defined as ΔV. When the system is disturbed and the cell voltage offset to the nominal voltage is not greater than ΔV, the cell is in the normal state.

$$S_c = 0, (V_{\min} \le v \le V_{\max}, V_{\min} = V_{nomi} - \Delta V, V_{\max} = V_{nomi} + \Delta V) \tag{3}$$

where, V_{nomi} is the nominal voltage. $V_{\min}$ is the lower limit of normal range. $V_{\max}$ is the upper limit of normal range. v is the voltage of the node at a certain moment.

According to the power quality requirements, the absolute value of the positive and negative deviation of the voltage should not exceed 10% of the nominal voltage. Therefore, in this paper, the maximum voltage offset is set as 5%. The upper and lower limits of the normal range can be defined as follows:

IOP Conf. Series: Earth and Environmental Science **431** (2020) 012033 doi:10.1088/1755-1315/431/1/012033

$$V_{\min} = 0.95p.u., V_{\max} = 1.05p.u. \tag{4}$$

2) Definition of the cellular emergency and failure state

According to TAYLOR's definition of voltage instability [10], the result of voltage instability is overvoltage or low voltage. In this section, we define the emergency and failure state of the cell from the perspective of overvoltage and low voltage, respectively.

In the process of power failure, faults in electrical components or load shedding may cause over-voltage problems in some areas of the system, which may cause the insulation of the equipment to break down. Therefore, the over voltage problem is an important reason for the expansion of the scope of power failure. According to the analysis of overvoltage in power failure, the emergency and failure states of cell are defined as follows:

$$S_i = \begin{cases} 2, (V_{cr2} < v) \\ 1, (V_{\max} < v < V_{cr2}) \end{cases} \tag{5}$$

where, V_{cr2} is the maximum permissible value of voltage. When the cell voltage is greater than the upper limit of the normal range and less than the maximum allowable voltage, the cell is in the emergency state. When the cell voltage is greater than the maximum allowable voltage, the cell is in the failure state.

According to the regulation of overvoltage limit of an AC electrical device, the maximum allowable voltage of electrical equipment is different with different voltage grades. For example, for 110kV and 220kV systems, the power frequency overvoltage should not be greater than 1.3p.u. In this paper, the maximum permissible value of voltage is given as follows:

$$V_{cr2} = 1.3p.u. \tag{6}$$

In power failure, voltage instability can also cause low voltage in some areas. Therefore, the cell emergency and instability states are defined from the perspective of node voltage decrease as follows:

$$S_i = \begin{cases} 2, (V_{cr1} > V) \\ 1, (V_{\min} > V > V_{cr1}) \end{cases} \tag{7}$$

where, V_{cr1} is the minimum permissible value of voltage. When the cellular voltage is less than the lower limit of the normal range and greater than the minimum allowable voltage, the cell is in the emergency state. When the cell voltage is less than the minimum allowable voltage, the cell is in the failure state.

According to the theory of static voltage stability, the minimum permissible value of voltage is taken as the value at the nose point of the PV curve. The PV curve is a typical static voltage stability analysis method that can directly analyse the voltage stability of the cell. The operating state of cells in the power grid at each moment corresponds to a point on the PV curve, which is usually called the operating point. When the operating point of the cell is in the upper half of the PV curve, the voltage of operating point is higher than the minimum permissible value, and the cell is in a normal or emergency state. When the operating point is in the lower half of the PV curve, the voltage of the operating point is lower than the minimum permissible value, and the cell is in a state of instability. When the operating point of the cell is at the inflection point of the PV curve, the cell voltage is equal to the critical voltage, and the cell is in the critical instability state.

Generally, due to the different nodes corresponding to PV curves, the minimum permissible voltage value for different nodes varies. In this paper, the minimum permissible value of voltage is given as follows:

$$V_{cr1}(i) = V_{cpf}(i), (i = 1, 2, \wedge, n) \tag{8}$$

where, the $V_{cr1}(i)$ is the minimum permissible voltage of cell i. $V_{cpf}(i)$ is the voltage at the nose of the PV curve of cell i, which can be obtained by continuous power flow(CPF).

According to the above definition of cell state, the relationship between the cell state and the voltage limit is summarized and expressed on a PV curve, as shown in Figure 1.

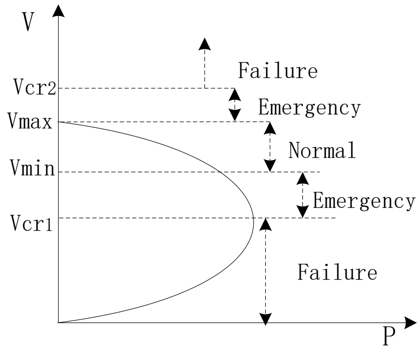

Figure 1. The relationship diagram between cell states and cell voltage limits.

2.1.2. Cellular state definition based on load rate.
Considering the thermal stability of the grid elements, the load carrying capacity of each node in the grid is limited. The node may fail if the load current passing through the node is greater than its permitted carrying capacity. The load rate of the node is defined as follows:

$$L_{Ci} = F_{Ci} / F_{Ci,\max} \tag{9}$$

where, F_{Ci} is the active power flow through the node. $F_{Ci,\max}$ is the limit of the active power transmission capacity of node.
According to the load rate of the cell, the normal, emergency and failure states of the cell are defined as follows:

$$S_c = \begin{cases} 0, (L_{C\min} < L_C < L_{Cnor}) \\ 1, (L_{Cnor} < L_C < L_{C\max}) \\ 2, (L_{C\max} < L_C) \end{cases} \tag{10}$$

where, $L_{C\min}$ is the minimum load rate of the node. L_{Cnor} is the normal load rate of node. $L_{C\max}$ is the maximum load rate of the node. The cell in different states has different values of failure probability. The cell fault probability model based on load rate is shown in figure 2. In this figure, $P_{\max}$ and $P_{\min}$ are the maximum and minimum shutdown probabilities, respectively.

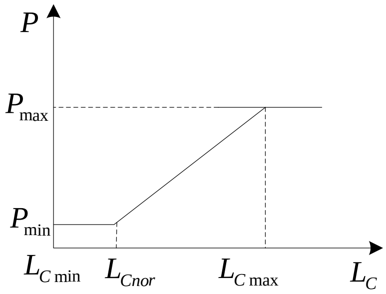

Figure 2. Cell failure probability model based on load rate.

2.1.3. Cellular state definition based on the degree.
In graph theory, the degree of a node is defined as the number of edges associated with that node. In the power grid, the degree of the electrical node is defined as the number of outgoing lines associated with the electrical node. For example, in figure 3, node 2 has two outgoing lines, so the degree of node 2 is two.

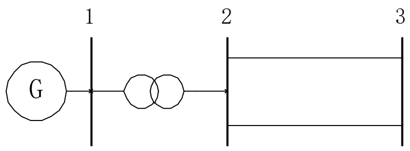

Figure 3. Three nodes system.

Cell states are defined based on the degree as follows:

$$S_c = \begin{cases} 0, (D = N) \\ 1, (0 < D < N) \\ 2, (D = 0) \end{cases} \tag{11}$$

where D is the degree of the node, and N is the degree of the node when the power grid is in the normal state. In power failure, when the outgoing line associated with the node fails and disconnects, the degree of the node decreases. When all the lines directly connected to the node are disconnected, the degree of the node is 0 and the cell is in the failure state. For example, in figure 1, when the line between node 2 and node 3 is disconnected, the node degree of node 3 is 0 and the node is out of service.

The degree of the node depends on the state of the outgoing line, and the state of the line depends on its load rate. The load rate of the line is defined as follows:

$$L_{Li} = F_{Li} / F_{Li,\max} \tag{12}$$

where, F_{Li} is active power flow over line i. $F_{Li,\max}$ is the maximum permissible value of active power flow over line i. The failure probability of the line is related to load rate range. The corresponding relationship between line load rate and line failure probability is shown in the figure 4.

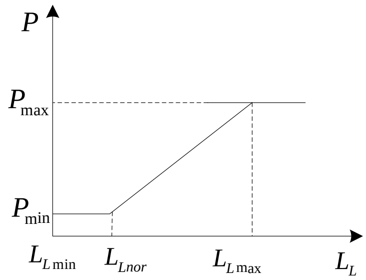

Figure 4. Line outrage probability model.

where, $L_{L\min}$ is the minimum load rate of the line, L_{Lnor} is the normal load rate of the line, $L_{L\max}$ is the maximum load rate of line, $P_{\max}$ is the maximum outrage probability of the line, and $P_{\min}$ is the minimum outrage probability of the line.

2.2. Definition of the cellular neighbour

The basic unit of a cellular automata is the cell. The state of the next moment of a cell is determined by the state of the cell itself and the state of its neighbour at the previous moment. In this paper, a node is defined as a cell. For two nodes directly connected by a line, any cell is the neighbour of another cell. In the three nodes system, node 1 and node 2 are neighbour cells to each other, so are node 2 and node 3.

2.3. Evolution rules of cellular automata

The power system is a complex system, and complex coupling relations exits between the components. When a component fails, it often affects the surrounding components as well. In cellular automata, cellular evolution rules need to be defined to describe the interaction between grid components in power failure. Specifically, according to the state of the cell itself and its neighbours at the current moment, the state of the cell at the next moment can be determined by the evolution rule. This paper defines the evolution rules of cellular automata from the perspective of voltage stability.

In the process of power failure, the induction motor and on-load tap changer (OLTC) are considered to be one of the important factors that results in voltage collapse. Due to dynamic components such as OLTC, the instability range is gradually expended. In this paper, the evolution rules of cellular automata are defined according to the characteristics of bus voltage variation in power failure.

Suppose cell i and cell j are neighbours to each other, when cell i is in a failure state due to voltage decrease, the minimum permissible voltage of cell j will be affected as follows:

$$V_{cr1,j}(t+1) = (1+\delta)V_{cr1,j}(t) \tag{13}$$

where, $V_{cr1,j}(t+1)$ is the minimum permissible voltage of cell j at the next moment. δ is a constant factor.

When cell i is in a state of instability due to overvoltage, the maximum permissible voltage of cell j will be affected as follows:

$$V_{cr2,j}(t+1) = (1-\delta)V_{cr2,j}(t) \tag{14}$$

where, $V_{cr2,j}(t+1)$ is the maximum permissible voltage of cell j at the next moment. δ is a constant factor.

3. Simulation and results

3.1. Analysis of power failure characteristics considering voltage instability

In order to verify whether the proposed grid cellular automaton model considering voltage instability is suitable for power failure simulation, the model was programmed and implemented in MATLAB.

The simulation progress is as follows: 1) Read the initial grid data. 2) Add disturbance to the power grid and calculate the AC power flow. 3) Calculate the state of each component of the power grid based on the power flow results. 4) Judge whether the topology of the power grid changes. If the grid topology changes, the power flow will be recalculated. If the topology does not change, the power flow will not be calculated. 5) Judge whether there are cells in the failure state. If there are cells in failure state, cellular automata will evolve according to the evolution rules. If no cells are in the failure state, the disturbance will continue to be added to the power system 6) Loss loads are counted.

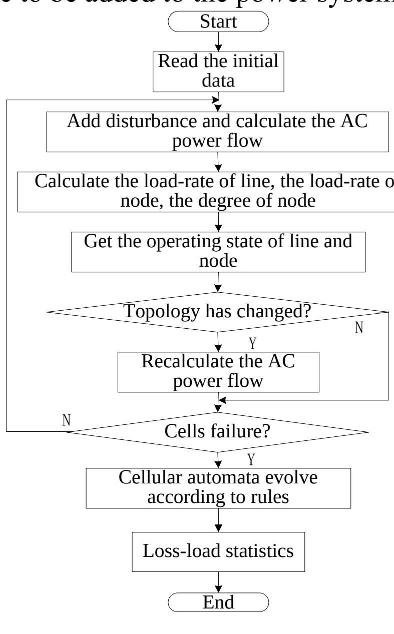

Figure 5. Power failure evolution model considering voltage instability.

In this paper, the model is used to simulate 200 power failure accidents in an IEEE39 system (Fig.9). Loss load is calculated and the loss load sequence of power failure is obtained in figure 6. In order to study the influence of voltage instability on power failure, the loss load sequence considers voltage instability is compared with the those without considering voltage instability.
Then, according to the loss load sequence, the number of power failure accidents under different loss load scales is counted. The logarithm of the scale of all power failure accidents and the corresponding number of power failure accidents are calculated, and the results are expressed in the scale-frequency double logarithm graph, that is, figure 7.

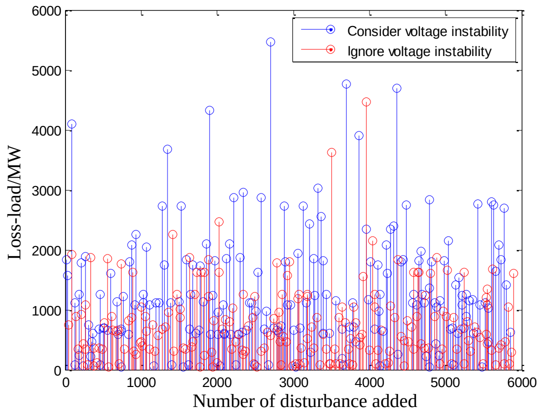

Figure 6. The loss-load sequence of power failure.

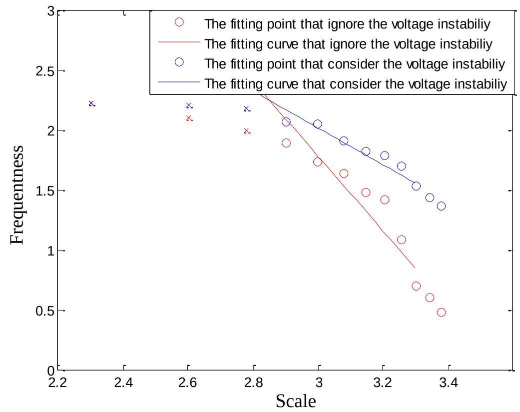

Figure 7. Scale-frequentness log-log graph.

The least square method is used to make linear regression for the fitting point at the tail, and the fitting curve regression equation and correlation coefficient of the scale of power failure taking into account the voltage instability factor are obtained:

$$\lg N_1 = 11.12 - 3.11 \lg r_1 \tag{15}$$

$$R_1 = -0.954 \tag{16}$$

The fitting curve regression equation and correlation coefficient of the scale of power failure, which ignores the voltage instability factor are obtained:

$$\lg N_2 = 6.63 - 1.54 \lg r_2 \tag{17}$$

$$R_2 = -0.968 \tag{18}$$

If significance level α is equal to 0.01, the threshold value $R_{0.01}$ is 0.7078. Based on the above critical value, the regression equation is verified as follows.:

$$|R_1| > R_{0.01}; |R_2| > R_{0.01} \tag{19}$$

Therefore, the two regression equations above are valid and the simulation results are credible. It can be seen from the analysis of figure 6 that, on the one hand, the self-organized criticality of the power grid is verified, and on the other hand, after considering the voltage instability factor, the occurrence frequency and scale of power failure accidents increase.

3.2. Statistical analysis of weak points

The model is used to simulate 16,000 power failure accidents and extract the failure node set related to voltage instability in each accident. In this paper, voltage instability of PV node is not considered. In IEEE39 system, nodes 1 to 29 are PQ nodes and the statistical results of failure frequency related to voltage instability are shown in figure 8.

IOP Conf. Series: Earth and Environmental Science **431** (2020) 012033 doi:10.1088/1755-1315/431/1/012033

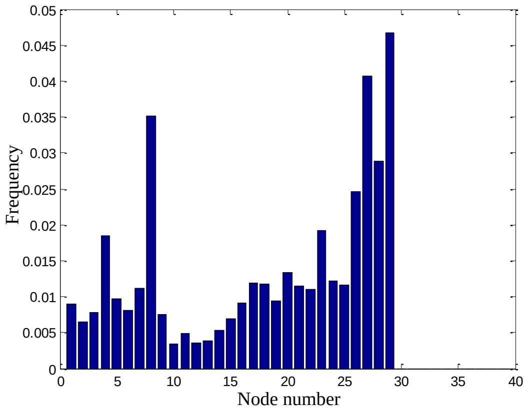

Figure 8. PQ node failure frequency statistics.

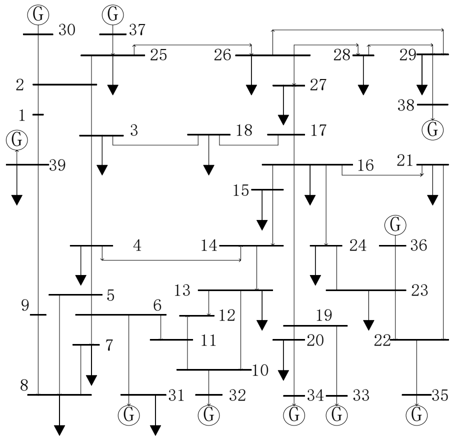

Figure 9. IEEE39 system.

According to the statistical results of failure frequency, No.8, No.27, and No. 29 have higher occurrence frequency. It can be seen from the analysis that in the IEEE39 node system, node 8 and node 29 are both located at the terminal region of the system, and their voltages are susceptible to load fluctuations.

4. Conclusion
Based on the original model, a power failure model that considers voltage stability is established in this paper. The proposed model is used to simulate power failure. The self-organized criticality of the power grid is verified and the driving effect of voltage instability in power failure is verified. The failure frequency of the node is counted. By analysing the statistical data, it was found that the failure frequency of node 8 and node 29 is higher than other nodes. Node 8 and Node 29, which is in the terminal region of the system, is more prone to voltage instability.
In this paper, the constant power load model is adopted. In the next stage of work, the induction motor model can be used to analyse the influence of load dynamic characteristics on power failure.

5. References
[1] Dobson I, Carreras B A, et al. An initial model for complex dynamics in electric power system blackouts [DB/OL]. 2014-02-01.
[2] Phadeke A G, Thorp J S. Expose hidden failures to prevent cascading outages [J]. IEEE Computer Application in Power, 1996, 9(3): 20-23.
[3] Nedic D P, Dobson I, Kirschena D S, et al. Criticality in a cascading failure blackout model [J]. Electrical Power and Energy Systems, 2006, 28(9).
[4] Yu Qun, Cao Na, Zhao Xiaonan. An improved model for self-Organized criticality in electric power system blackouts [C]. International Conference on Electric Utility Deregulation & Restructuring & Power Technologies, 2010.
[5] Watts D J, Strogatz S H. Collective dynamics of ‘small-world’ networks [J]. Nature, 1998, 393(6684): 440-442.
[6] Barabási A L, Albert R. Emergence of scaling in random networks [J]. Science, 1999, 286(5439): 509-512.
[7] Yu qun, Cao Na, Guo Jianbo. Simulation model of self-organized criticality characteristics of power system based on Cellular Automata [J]. Automation of Electric Power Systems, 2011, 35(21): 1-5.
[8] Yu qun, Min Zhang, Cao Na. Fault evolution model of power grid based on Fuzzy Cellular Automata [J]. Journal of Computer Applications, 2015, 35 (9): 2682-2686.
[9] IEEE/CIGRE joint task force on stability terms and definitions. Definition and classification of power system stability [J]. IEEE Trans on Power Systerms, 2004, 19(2): 1387-1401.

[10] CARSON W.TAYLOR. Power System Voltage Stability[M]. Beijing: China Electric Power Press, 2002.

Acknowledgments
This work was supported by the 2018 National Grid Corporation of Science and Technology Project "Interconnected power grid blackout early warning technology and system development based on multi-sand-pile theory".

IOP Conf. Series: Earth and Environmental Science **431** (2020) 012034 doi:10.1088/1755-1315/431/1/012034

Dynamic reactive power optimization method based on the transformer dummy node model

Aifeng Wang[1] and Hua Wei[1]

1 College of Electrical Engineering, Guangxi University, Nanning, China
E-mail: shynl@outlook.com

Abstract. This paper proposes a dynamic reactive power optimization method based on the transformer dummy node model. Compared to the method based on the traditional equivalent Π circuit, the proposed method adds the voltage at the dummy node as a variable, together with the voltage at the other side of the transformer, to express the voltage change on the two sides of the transformer. So the turn ratio of transformer is removed from variables, and the power flow equations of transformer branches do not contain turn ratio and its square, both the dimension of power flow equations and the number of non-zero elements in the Jacobian and Hessian matrix reduce, which decreases the calculative amount and accelerates the solution process. The test results of IEEE4, 14, 30 bus systems show that the proposed method obtains the same optimal solution with the traditional method but converges more quickly. With higher computational efficiency, the proposed method is suitable for the practical application of power systems.

1. Introduction

Dynamic reactive power optimization (DRPO) is of vital significance for the secure and economic performance of power systems since it could improve voltage quality and reduce network losses effectively. It is used to minimize transmission losses by determining all kinds of controllable variables, such as reactive power output of generators and shunt capacitor banks, taps of on-load tap changers (OLTC), etc, while satisfying some equality and inequality constraints including the power flow equations, upper and lower limits of variables, and the action number limits of controllable equipment.
Highly nonlinear of power flow equations, discretization of reactive power compensators and taps of transformers, and strong coupling of multi-period make the DRPO problem a large-scale, multi-period, and strongly coupled mixed-integer nonlinear programming problem that is difficult to solve directly.
One thinking of solving the DRPO problem is to eliminate coupling constraints among periods, so the DRPO problem converts into a series of static reactive power optimization problems. The literature [1] puts forward the concept of dynamic reactive power optimization, it divides the whole optimization time into a handful of long periods, and each long period is divided into several short periods. Discrete variables are fixed value in long periods, which limits the action number of discrete devices by long periods' division, the continuous variables adjust their values according to load change in short periods. However, the periods' division is generally dependent on the operating experience of dispatchers, with uncertainty, and the optimization results are often not satisfactory. The paper [2] add the adjusting cost of equipment to the objective function to form a multi-objective optimization problem together with the power losses of the system. Therefore the optimization at different periods is not interrelated each other. However, it is difficult to determine the adjusting cost of equipment.
Another way to solve the DRPO problem is to combine various algorithms to form a hybrid algorithm [3]. The DRPO problem is decomposed into two sub-problems: continuous variables optimization and discrete variables optimization. The interior-point method [4, 5] and the intelligent algorithm [6] are

used to iterate alternately to obtain the optimal solution of the problem, making full use of the respective advantages of the two algorithms.

Besides, researches improve solving efficiency by model transforming. In reference [7], the non-convex mixed-integer nonlinear programming for DRPO problem transforms into a convex mixed integer second-order cone programming problem, and dramatically reduces the complexity of the solution. In the literature [8], the DRPO problem is decomposed into three stages: relaxation solution, discrete variables solution and continuous variables solution, which simplifies the model and improves the solving efficiency of the problem.

In the traditional optimal reactive power flow (ORPF) method, the OLTC branches are represented by equivalent Π circuit. So the formulated power flow equations contain the variables of transformer ratios and the square of transformer ratios multiplied by the square of the voltage magnitudes, which increases the dimension of power flow equations and difficulty of solving Jacobian and Hessian matrix. At the same time, the equivalent Π circuit does not reflect the physical meaning of the OLTC branch and is difficult for people to understand, analyze, and remember.

The paper [9] proposes a rectangular form ORPF method based on the transformer dummy node model (TDNM). The OLTC branch is represented by an ideal transformer and its series impedance with a dummy node located between them. Instead of the transformer ratio variable, the voltage magnitude variable at the dummy node is used to express the transformation function of the ideal transformer. As a result, it simplifies the ORPF model and obtains a better calculation efficiency. However, under the rectangular form, a number, equal to the number of OLTC branches, of quadratic equality constraints were added to ensure that the voltage angles at two sides of the ideal transformer are identical. Meanwhile, the inequality constraints of the limits of transformer ratios become nonlinear from linear. The effect of simplification by applying the TDNM to the ORPF method weakens to some extent. A new ORPF method in mixed polar form based on TDNM was proposed in the paper [10]. Compared with the conventional ORPF method based on equivalent Π circuit, the power flow equations of the OLTC branches do not contain complicated items multiplied by the squares of variables, and drop from four-dimensional variables of the transformer equivalent Π circuit to three-dimensional variables. It simplifies the ORPF model efficiently and has a higher computational efficiency.

The ORPF methods based on TDNM proposed in the above literature improve the solving efficiency but cannot be used to guide the operation of power systems, because they consider taps of transformers as continuous variables. In actual power systems, taps of transformers are discrete variables and commonly has a service life expressed by limits of action number. An excess of actions will not only accelerate the aging of equipment but also increase the work intensity of the operators and running cost. Therefore, this paper proposes a DRPO method based on TDNM, considering taps of transformers as discrete variables and has limits of action number. At the same time, the interior point method, together with the branch and bound method, were employed alternately to solve the problem for continuous variables and discrete variables, respectively. Test results prove that the proposed method is effective.

The rest of this paper is organized as follows. Section 2 describes the DRPO method based on the traditional equivalent Π circuit. Section 3 proposes the DRPO method based on the TDNM. Section 4 analyzes the difference between the two DRPO methods. Section 5 discusses the performance of the proposed method, and conclusions drawn in section 6.

2. The DRPO method based on the traditional transformer equivalent Π circuit

2.1. The traditional transformer equivalent Π circuit

This paper considers the voltage magnitude changes of the OLTC branch, ignoring its phase changes. In the traditional transformer equivalent Π circuit (see Figure 1), the OLTC branch is between bus i and bus j, and the turn ratio of the OLTC branch is $1:k_{ij}$. The admittance of the OLTC branch is $\vec{y}_{\mathrm{T}ij} = G_{\mathrm{T}ij} + jB_{\mathrm{T}ij}$, the voltage at bus i and bus j are $\vec{v}_i = V_i \exp(\delta_i)$ and $\vec{v}_j = V_j \exp(\delta_j)$, Where $G_{\mathrm{T}ij}$ and $B_{\mathrm{T}ij}$ are the conductance and susceptance of the OLTC branch between bus i and bus j, while V_i, V_j, and δ_i, δ_j are the voltage magnitude and angle at bus i and bus j.

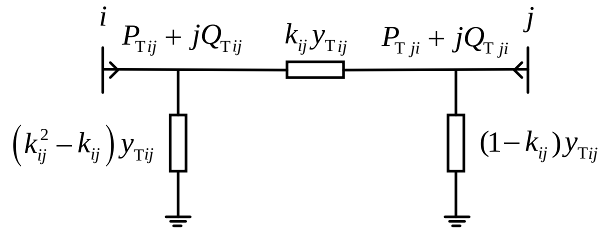

Figure 1. The traditional transformer equivalent Π circuit.

According to the power equation and the law of Kirchhoff, the active and reactive power flowing through the OLTC branch is:

$$P_{\mathrm{T}ij} = V_i^2 k_{ij}^2 G_{\mathrm{T}ij} - V_i V_j k_{ij} (\mathrm{G}_{\mathrm{T}ij} \cos(\delta_i - \delta_j) + \mathrm{B}_{\mathrm{T}ij} \sin(\delta_i - \delta_j)) \tag{1}$$

$$Q_{\mathrm{T}ij} = -V_i^2 k_{ij}^2 B_{\mathrm{T}ij} - V_i V_j k_{ij} (\mathrm{G}_{\mathrm{T}ij} \sin(\delta_i - \delta_j) - \mathrm{B}_{\mathrm{T}ij} \cos(\delta_i - \delta_j)) \tag{2}$$

$$P_{\mathrm{T}ji} = V_j^2 G_{\mathrm{T}ij} - V_j V_i k_{ij} (\mathrm{G}_{\mathrm{T}ij} \cos(\delta_j - \delta_i) + \mathrm{B}_{\mathrm{T}ij} \sin(\delta_j - \delta_i)) \tag{3}$$

$$Q_{\mathrm{T}ji} = -V_j^2 B_{\mathrm{T}ij} - V_j V_i k_{ij} (\mathrm{G}_{\mathrm{T}ij} \sin(\delta_j - \delta_i) - \mathrm{B}_{\mathrm{T}ij} \cos(\delta_j - \delta_i)) \tag{4}$$

2.2. The DRPO method based on the traditional transformer equivalent Π circuit

This paper mainly considers the optimization of the reactive power output of generators and taps of transformers, in which the reactive power output of generators are continuous variables, taps of transformers are discrete variables and have limits of action number. Assuming that N is the number of buses, M is the number of generators, U is the number of OLTC branches, and the optimization time, such as a day, is divided into T periods.

The mathematical model of the DRPO method is made up of the objective function, power flow equality constraints, and variables inequality constraints. The DRPO problem generally takes the minimum active power losses of the power system for a whole day as the objective function:

$$\min \sum_{t=1}^{T} P_{loss}^t = \sum_{t=1}^{T} \sum_{i=1}^{N} P_{Gi}^t - \sum_{t=1}^{T} \sum_{i=1}^{N} P_{Di}^t \tag{5}$$

Where P_{loss}^t is the active power losses of the system at the period of t; P_{Gi}^t is the active power output of generator at bus i at the period of t; P_{Di}^t is the active load at bus i at the period of t.

The power flow equality constraints can be expressed as:

$$\begin{aligned} & P_{Gi}^t - P_{Di}^t - V_i^t \sum_{j \in S_L} V_j^t (G_{\mathrm{L}ij} \cos \delta_{ij}^t + B_{\mathrm{L}ij} \sin \delta_{ij}^t) + (V_i^t)^2 \sum_{j \in S_{\mathrm{T}j}} (k_{ij}^t)^2 G_{\mathrm{T}ij} \\ & \quad - V_i^t \sum_{j \in S_{\mathrm{T}j}} V_j^t k_{ij}^t (G_{\mathrm{T}ij} \cos \delta_{ij}^t + B_{\mathrm{T}ij} \sin \delta_{ij}^t) + (V_i^t)^2 \sum_{j \in S_{\mathrm{T}i}} G_{\mathrm{T}ji} - V_i^t \sum_{j \in S_{\mathrm{T}i}} V_j^t k_{ji}^t (G_{\mathrm{T}ji} \cos \delta_{ij}^t + B_{\mathrm{T}ji} \sin \delta_{ij}^t) = 0 \end{aligned} \tag{6}$$

$$\begin{aligned} & Q_{Gi}^t - Q_{Di}^t - V_i^t \sum_{j \in S_{\mathrm{L}}} V_j^t (G_{\mathrm{L}ij} \sin \delta_{ij}^t - B_{\mathrm{L}ij} \cos \delta_{ij}^t) - (V_i^t)^2 \sum_{j \in S_{\mathrm{T}j}} (k_{ij}^t)^2 B_{\mathrm{T}ij} \\ & \quad - V_i^t \sum_{j \in S_{\mathrm{T}j}} V_j^t k_{ij}^t (G_{\mathrm{T}ij} \sin \delta_{ij}^t - B_{\mathrm{T}ij} \cos \delta_{ij}^t) - (V_i^t)^2 \sum_{j \in S_{\mathrm{T}i}} B_{\mathrm{T}ji} - V_i^t \sum_{j \in S_{\mathrm{T}i}} V_j^t k_{ji}^t (G_{\mathrm{T}ji} \sin \delta_{ij}^t - B_{\mathrm{T}ji} \cos \delta_{ij}^t) = 0 \end{aligned} \tag{7}$$

Where Q_{Gi}^t and Q_{Di}^t are the reactive power output of generator and the reactive load at bus i at the period of t; V_i^t, V_j^t, δ_i^t, δ_j^t are the voltage magnitude and angle of bus i and bus j at the period of t; $G_{\mathrm{L}ij}$ and $B_{\mathrm{L}ij}$ are the conductance and susceptance of the transmission line between bus i and bus j; k_{ij}^t is the turn ratio of the OLTC branch at the period of t; S_{L} is the set of transmission lines; $S_{\mathrm{T}j}$ is the set of buses at the k_{ij} side; $S_{\mathrm{T}i}$ is the set of buses at the other side of the OLTC branch; δ_{ij}^t is the phase difference between bus i and bus j at the period of t, $\delta_{ij}^t = \delta_i^t - \delta_j^t$.

The upper and lower inequality constraints of the variables are as follows:

$$\underline{P_{Gi}} \leq P_{Gi}^{t} \leq \overline{P_{Gi}} \tag{8}$$

$$\underline{Q_{Gi}} \leq Q_{Gi}^{t} \leq \overline{Q_{Gi}} \tag{9}$$

$$\underline{V_{i}} \leq V_{i}^{t} \leq \overline{V_{i}} \tag{10}$$

$$\underline{k_{ij}} \leq k_{ij}^{t} \leq \overline{k_{ij}} \tag{11}$$

Where $\underline{()}$ and $\overline{()}$ indicate the lower and upper limits of variables.
The equality constraints of adjusting transformers are as follows:

$$k_{ij}^{t} = \underline{k_{ij}} + M_{ij}^{t} k_{ij}^{step} \tag{12}$$

Where, M_{ij}^{t} is a positive integer, represents the tap position of transformer between bus i and bus j at the period of t ; and k_{ij}^{step} denotes the tap step size of the transformer between bus i and bus j .
The action number limit of the transformer tap between bus i and bus j satisfy the following inequality constraints:

$$\sum_{t=1}^{T-1} \left| M_{ij}^{t} - M_{ij}^{t+1} \right| \leq k_{ij}^{\max} \tag{13}$$

Where: $k_{ij}^{\max}$ is the maximum action number of the transformer tap between bus i and bus j in all day.

3. The DRPO method based on the transformer dummy node model

3.1. The transformer dummy node model

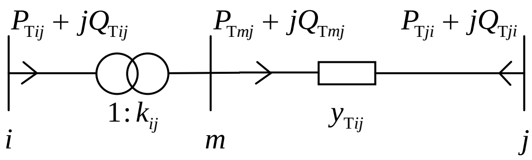

Figure 2. The transformer dummy node model.

The OLTC branch represented by an ideal transformer and its series admittance with a dummy node located between them, as shown in Figure 2. The ratio of the voltage magnitude at bus i to that at bus m is $1:k_{ij}$, and the voltage phases at two sides of the ideal transformer are identical, that is $V_m = k_{ij} V_i$ and $\delta_i = \delta_m$. In the following text of this paper, the voltage phase at bus m is replaced by the voltage phase at bus i . Thus the model is simplified.
Because there are no power losses consumed on the ideal transformer, the power at two sides of the ideal transformer is equal. According to the power equation and the law of Kirchhoff, the active and reactive power flowing through the OLTC branch can be expressed as:

$$P_{\mathrm{T}ij} = P_{\mathrm{T}mj} = V_m^2 G_{\mathrm{T}ij} - V_m V_j (\mathrm{G}_{\mathrm{T}ij} \cos(\delta_i - \delta_j) + \mathrm{B}_{\mathrm{T}ij} \sin(\delta_i - \delta_j)) \tag{14}$$

$$Q_{\mathrm{T}ij} = Q_{\mathrm{T}mj} = -V_m^2 B_{\mathrm{T}ij} - V_m V_j (\mathrm{G}_{\mathrm{T}ij} \sin(\delta_i - \delta_j) - \mathrm{B}_{\mathrm{T}ij} \cos(\delta_i - \delta_j)) \tag{15}$$

$$P_{\mathrm{T}ji} = P_{\mathrm{T}jm} = V_j^2 G_{\mathrm{T}ij} - V_j V_m (\mathrm{G}_{\mathrm{T}ij} \cos(\delta_i - \delta_j) + \mathrm{B}_{\mathrm{T}ij} \sin(\delta_i - \delta_j) \tag{16}$$

$$Q_{\mathrm{T}ji} = Q_{\mathrm{T}jm} = -V_j^2 B_{\mathrm{T}ij} - V_j V_m (\mathrm{G}_{\mathrm{T}ij} \sin(\delta_i - \delta_j) - \mathrm{B}_{\mathrm{T}ij} \cos(\delta_i - \delta_j)) \tag{17}$$

3.2. The DRPO method based on the transformer dummy node model

The objective function of this method is also equation (5). The constraints include power flow equality equations (18) - (19), upper and lower limits of variables inequality equations (8) - (10), and the inequlity constraints (20) of the voltage magnitude at the dummy node, the equality constraints (21) about the relationship between turn ratios of adjustable transformers and the voltage magnitude at both sides of the ideal transformer, and the action number limits equation (13) of the transformer taps.
The power flow equations are as follows:

$$\begin{aligned} &P_{Gi}^t - P_{Di}^t - V_i^t \sum_{j\in S_{\mathrm{L}}} V_j^t (G_{\mathrm{L}ij}\cos\delta_{ij}^t + B_{\mathrm{L}ij}\sin\delta_{ij}^t) + (V_m^t)^2 \sum_{j\in S_{\mathrm{T}j}} G_{\mathrm{T}ij} \\ &\quad - V_m^t \sum_{j\in S_{\mathrm{T}j}} V_j^t (G_{\mathrm{T}ij}\cos\delta_{ij}^t + B_{\mathrm{T}ij}\sin\delta_{ij}^t) + (V_i^t)^2 \sum_{j\in S_{\mathrm{T}i}} G_{\mathrm{T}ji} - V_i^t \sum_{j\in S_{\mathrm{T}i}} V_m^t (G_{\mathrm{T}ji}\cos\delta_{ij}^t + B_{\mathrm{T}ji}\sin\delta_{ij}^t) = 0 \end{aligned} \tag{18}$$

$$\begin{aligned} &Q_{Gi}^t - Q_{Di}^t - V_i^t \sum_{j\in S_{\mathrm{L}}} V_j^t (G_{\mathrm{L}ij}\sin\delta_{ij}^t - B_{\mathrm{L}ij}\cos\delta_{ij}^t) - (V_m^t)^2 \sum_{j\in S_{\mathrm{T}j}} B_{\mathrm{T}ij} \\ &\quad - V_m^t \sum_{j\in S_{\mathrm{T}j}} V_j^t (G_{\mathrm{T}ij}\sin\delta_{ij}^t - B_{\mathrm{T}ij}\cos\delta_{ij}^t) - (V_i^t)^2 \sum_{j\in S_{\mathrm{T}i}} B_{\mathrm{T}ji} - V_i^t \sum_{j\in S_{\mathrm{T}i}} V_m^t (G_{\mathrm{T}ji}\sin\delta_{ij}^t - B_{\mathrm{T}ji}\cos\delta_{ij}^t) = 0 \end{aligned} \tag{19}$$

Here V_m^t is the voltage magnitude at the dummy node m at the period of t.
The upper and lower limits of the voltage amplitude at the dummy node m is as follows:

$$\underline{k}_{ij} V_i^t \le V_m^t \le \overline{k}_{ij} V_i^t \tag{20}$$

The relationship between turn ratios of adjustable transformers and the voltage magnitude at both sides of the ideal transformer is as follows:

$$V_m^t / V_i^t = \underline{k}_{ij} + M_{ij}^t k_{ij}^{step} \tag{21}$$

4. Comparison of the two DRPO methods based on different transformer models

Compare the two DRPO methods based on different transformer models, the numbers of inequality constraints of the two methods are equal, and all constraints are linear, which has little impact on the solution efficiency. The difference in equality constraints is the main factor that affects the solving speed of the two methods. The equality constraints of the DRPO method based on transformer equivalent Π circuit (referred as 'the traditional method') include equations (6)-(7) and (12), the equality constraints of the DRPO method based on TDNM (referred as 'the proposed method') include equations (18)-(19) and (21). According to $k_{ij}^t = V_m^t / V_i^t$, Equations (6)-(7) and (12) can deduce equations (18)-(19) and (21). So the two methods are mathematically equivalent.

Table 1. The expressions of active power flowing through the OLTC branch under the two methods

	The first item	The second items	Number of variables/ Dimension of equation
The traditional method:Equation (6)	$(V_i^t)^2 (k_{ij}^t)^2 G_{\mathrm{T}ij}$	$-V_i^t V_j^t k_{ij}^t (G_{\mathrm{T}ij}\cos\delta_{ij}^t + B_{\mathrm{T}ij}\sin\delta_{ij}^t)$	5/4
The proposed method:Equation (18)	$(V_m^t)^2 G_{\mathrm{T}ij}$	$-V_m^t V_j^t (G_{\mathrm{T}ij}\cos\delta_{ij}^t + B_{\mathrm{T}ij}\sin\delta_{ij}^t)$	4/3

Power flow equations (18)-(19) have fewer variables and lower dimension than equations (6)-(7). The difference of power flow equations between the two methods reflects in the expressions of power flowing through the OLTC branches. If the branch between bus i and bus j is an OLTC branch, the expressions of active power flowing through the OLTC branch under the two methods are shown in Table 1. The proposed method has four variables, one less than five variables of the traditional method. The dimension of equation (18) is three, one less than four, the dimension of equation (6). In the same way, the active power flow equation at bus j in the proposed method has fewer variables and lower dimension than the traditional method. Similarly, the reactive power flow equation (19) has fewer variables and lower dimension than equation (7). If there is a total number of U on-load tap changers, and total T periods, the proposed method could reduce 2UT variables than the traditional method.

In this paper, the problem is decomposed into two sub-problems: continuous variables optimization and discrete variables optimization. The interior-point method is widely preferred to solve continuous subproblem. The number of non-zero elements in Jacobian and Hessian matrixes of the expressions of power flowing through OLTC branches in the proposed method is less than that in the traditional method, so its calculation amount decreases. Take the losses expressions consumed on the OLTC branch in the power flow equations of the IEEE4 bus system as an example, (see Figure 3 and Figure 4), the number of non-zero elements in Jacobian and Hessian matrixes of the proposed method is four and nine less than the traditional method respectively.

	$\delta_1 V_1$	$\delta_2 V_2$	$\delta_3 V_3$	$\delta_4 V_4$	K
$\partial P_1/\partial x$	J J		J J		J
$\partial Q_1/\partial x$	J J		J J		J
$\partial P_2/\partial x$					
$\partial Q_2/\partial x$					
$\partial P_3/\partial x$	J J		J J		J
$\partial Q_3/\partial x$	J J		J J		J
$\partial P_4/\partial x$					
$\partial Q_4/\partial x$					

(a)

	$\delta_1 V_1$	$\delta_2 V_2$	$\delta_3 V_3$	$\delta_4 V_4$	V_{1m}
$\partial P_1/\partial x$	J		J J		J
$\partial Q_1/\partial x$	J		J J		J
$\partial P_2/\partial x$					
$\partial Q_2/\partial x$					
$\partial P_3/\partial x$	J		J J		J
$\partial Q_3/\partial x$	J		J J		J
$\partial P_4/\partial x$					
$\partial Q_4/\partial x$					

(b)

Figure 3. For IEEE4 bus system, the Jacobian matrix of expressions of active power flowing through the OLTC branches of the two DRPO methods. (a) The traditional method. (b) The proposed method.

	$\delta_1 V_1$	$\delta_2 V_2$	$\delta_3 V_3$	$\delta_4 V_4$	K
δ_1	H H		H H		H
V_1	H H		H H		H
δ_2					
V_2					
δ_3	H H		H H		H
V_3	H H		H H		H
δ_4					
V_4					
K	H H		H H		H

(a)

	$\delta_1 V_1$	$\delta_2 V_2$	$\delta_3 V_3$	$\delta_4 V_4$	V_{1m}
δ_1	H		H H		H
V_1					
δ_2					
V_2					
δ_3	H		H H		H
V_3	H		H H		H
δ_4					
V_4					
V_{1m}	H		H H		H

(b)

Figure 4. For IEEE4 bus system, the Hessian matrix of expressions of active power flowing through the OLTC branches of the two DRPO methods. (a) The traditional method. (b) The proposed method.

It does not contain turn ratio and the square of turn ratio in the proposed method, which is more concise than the traditional method. Moreover, the voltage magnitude at the two sides of the ideal transformer reflects directly the physical significance of the transformer, which makes the proposed method easier to understand, analyze, and remember.

5. Numerical test and discussion

5.1. Test systems and environment

This paper assumes that there are 24 periods in one day, and load at per period follows the load curve shown in Figure 5. Take IEEE 4, 14, 30 bus systems [11] as examples to discuss the performance of the two methods. All the values of test systems calculate in the form of per-unit. The voltage magnitude of all buses are between 0.9 and 1.1, and the turn ratios in per-unit of the OLTC branches are all discrete values, such as 0.9, 0.95, 1.0, 1.05, 1.1.

All the test systems simulate in an HP PC-compatible computer, whose CPU is an Intel Core i5-6500, 3.20GHz, four cores, and its RAM is 8GB. All methods were modeled using the commercial software GAMS (General Algebraic Modeling System). The two DRPO methods were modeled as mixed-integer nonlinear programming problems while interior point method solver and SBB solver were respectively employed to solve the problem for continuous variables and discrete variables. The convergence Gap of integer optimization is 0.01.

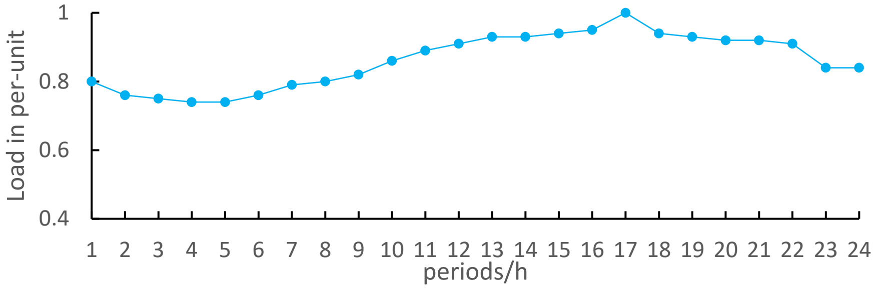

Figure 5. The curve of load in per-unit at 24 periods.

5.2. Effectiveness analysis of the proposed method

Table 2 lists the results of IEEE4, 14, and 30 bus systems under the two DRPO methods. The optimal value of active power losses calculated by the two methods is the same with each other, which proves that the two methods are equivalent. Compared with the traditional method, the proposed method has a smaller iteration number, shorter calculation time.

Table 2. The test results of the two DRPO methods.

	The traditional method			The proposed method		
	Optimal value(per-unit)	Caculation time(s)	Iteration number	Optimal value(per-unit)	Caculation time(s)	Iteration number
IEEE4	0.2301	0.984	518	0.2301	0.969	467
IEEE14	1.0948	5.343	1088	1.0948	5.282	1085
IEEE30	0.2251	18.469	1995	0.2251	16.141	1772

Table 3. The reduction of active power losses for IEEE30 bus system by using the proposed method.

The fixed turn ratio value	Active power losses under fixed turn ratio	Percents of active power losses reduction by using the proposed method
0.90	0.4312	47.8%
0.95	0.2833	20.5%
1.00	0.2261	0.44%
1.05	0.2443	7.86%
1.10	0.3562	36.8%

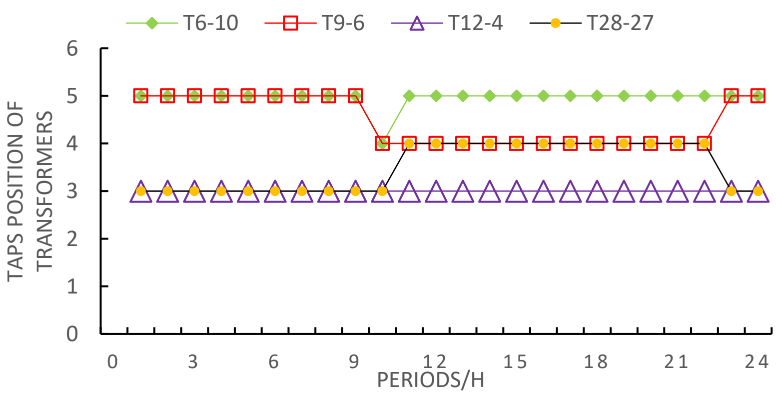

Figure 6. Taps positions of transformers for the IEEE30 bus system.

After optimization by using the proposed method, the active power losses reduce than before optimization. Taking IEEE30 bus system as an example (see Table 3), assuming that all turn ratios are set 0.9 before optimization, then the active power losses in per-unit of the system are 0.4312, while the

active power losses in per-unit by using the proposed method is 0.2251, decreases by 47.8 percents than before optimization. In the same way, the proposed method can also reduce the active power losses of the system when the transformer ratio is other fixed values, such as 0.95, 1.0, 1.05, and 1.1.
Figure 6 shows the tap positions of each transformer of the IEEE30 bus system after optimization using the proposed method. Transformer taps adjust their positions according to changes of load, and all transformer taps satisfy limit of action number.

6. Conclusion
This paper proposes a dynamic reactive power optimization method based on transformer dummy node model, considering taps of transformers as discrete variables and have limit of action number. Compared with the traditional method, the proposed method has fewer variables and lower dimension of equations. Besides, the number of non-zero elements in Jacobian and Hessian matrixes of the expressions of power flowing through OLTC branches in the proposed method is less than that in the traditional method, which decreases the calculation amount. The test results of IEEE4, 14, 30 bus system show that the proposed method is mathematically equivalent to the traditional method, and has higher calculation efficiency. The proposed method can effectively optimize the reactive power distribution of power systems, improve the safe and economic operation level of the power grid.

7. References
[1] Sharif, S.S. and J.H. Taylor 1998 *Dynamic optimal reactive power flow* p 3410-14.
[2] ZHANG, Y., et al., *Research on dynamic modeling for reactive power optimization under real-time circumstance.* Power System Technology, 2004. 28(12): p. 12-15.
[3] WEI, Y., L. FANG and C.Y. CHUNG, *A hybrid gengtic algotithm-interior point method for optimal reactive power flow*. IEEE Transactions on Power Systems, 2006. 21(3): p. 1163-1169.
[4] Liu, M., S.K. Tso and Y. Cheng, *An extended nonlinear primal-dual interior-point algorithm for reactive-power optimization of large-scale power systems with discrete control variables.* IEEE TRANSACTIONS ON POWER SYSTEMS, 2002. 17(4): p. 982-991.
[5] Wei, H., et al., *An interior point nonlinear programming for optimal power flow problems with a novel data structure.* IEEE TRANSACTIONS ON POWER SYSTEMS, 1998. 13(3): p. 870-877.
[6] Wen, Z. and L. Yu-tian, *Adaptive Particle Swarm Optimization and Its Application in Reactive Power Optimization.* Power System Technology, 2006. 30(8): p. 19-24.
[7] Lai, X., et al., *Dynamic Reactive Power Optimization Method Based on Mixed Integer Second-order Cone Programming.* Automation of Electric Power Systems Press, 2017. 41(17): p. 37-42.
[8] Qin, H., et al., *Three-stage dynamic reactive power optimization algorithm considering constraints of control device action times.* Electric Power Automation Equipment Press, 2018. 38(9): p. 179-186.
[9] Yan, W., et al., *A new optimal reactive power flow model in rectangular form and its solution by predictor corrector primal dual interior point method.* IEEE Transactions on Power Systems, 2006. 21(1): p. 61-67.
[10] Wei, H., C. Lin and Y. Wang, *The optimal reactive power flow model in mixed polar form based on transformer dummy nodes.* IEEJ TRANSACTIONS ON ELECTRICAL AND ELECTRONIC ENGINEERING, 2018. 13(3): p. 411-416.
[11] *Power system test case archive* [R/OL]. [2019-5-20]. http://www.ee.washington.edu/research/pstca/ index.html.

Acknowledgments
The work is supported by the National Nature Science Foundation of China (NSFC) (51667003).

IOP Conf. Series: Earth and Environmental Science **431** (2020) 012035 doi:10.1088/1755-1315/431/1/012035

Analysis of average-closing-speed for medium-vacuum circuit breaker from theoretical calculation aspects

Lijie Sun[1,2], Yanqing Peng[1], Yong Liu[2], Gang Wang[1,2] and Xibao Sun[3]

1School of Electrical Engineering and Automation, Xiamen University of Technology, Fujian Xiamen, China
2ABB(China）Co., Ltd. Power Product Medium Voltage Technology Center, Fujian Xiamen, China
3State Grid Xuzhou Power Supply Company
Email: 710521402@qq.com

Abstract. Average closing speed is an important indicator for evaluating the performance of CB, in order to calculate the average closing speed of the spring operating mechanism of the medium voltage vacuum circuit breaker, the paper establishes a simplified model of CB mechanism, combined with the kinetic energy theorem, and obtains the average closing speed by analyzing the equivalent mass and energy of the mechanism. In order to verify the correctness of the proposed method, the paper establishes a CB simulation model to obtain the simulated average closing speed. In the calculation of the energy of the open-off phase, the paper adopts a segmentation calculation method, which divides the closing process into the open-distance phase and the over-travel phase, and the calculated average closing speed is more accurate. This theoretical calculation method provides a theoretical basis for the research and development of the medium-voltage vacuum CB spring operating mechanism, and plays a positive role in related research and development work.

1. Introduction

The average closing speed of CB refers to the moving speed of the moving contact of CB during the closing process [1].In the actual design, the average closing speed is usually taken as the average speed of the moving contact at the 70% distance from the opening distance to the point of the closing point. If the average closing speed is too fast, it will cause some damage to the vacuum interrupter, which is an important indicator for evaluating the performance of the circuit breaker.

At present, the research on the average closing speed is mainly through calculating the energy change of the whole closing process, and using the kinetic energy theorem to calculate the closing speed [2].This is a full-scale averaging method that can only be used for approximate calculations. The spring operating mechanism is complicated, and the average closing speed obtained by the whole-average calculation method is far from the actual closing speed, which can not meet the needs of the current design.

The closing process is divided into two stages: open distance and overtravel. Firstly, the paper establishes a simplified model of the circuit breaker mechanism, and then calculates the energy change from the start of the closing to the displacement of the moving contact to 70% of the opening distance, the change of the mechanical energy from the start of the closing to the closing point, and the equivalent mass of the mechanism. Finally, the article uses the kinetic energy theorem to calculate the average closing speed. This calculation method divides the closing process into several stages and can calculate the average closing speed more accurately.

IOP Conf. Series: Earth and Environmental Science **431** (2020) 012035 doi:10.1088/1755-1315/431/1/012035

2. Establishment of simplified model for spring operating mechanism of medium voltage vacuum circuit breaker

The article selects a spring operating mechanism of medium voltage vacuum circuit breaker with a rated voltage of 12kV and rated short circuit breaking current of 31.5kA as the research object.
Firstly, the simplified model of the circuit breaker mechanism is established by using the 3D modeling software SolidWorks. After that, in order to facilitate the calculation, the connecting rod is simplified into a straight line, and finally a simplified model of the circuit breaker transmission mechanism is obtained, as shown in Figure 1:

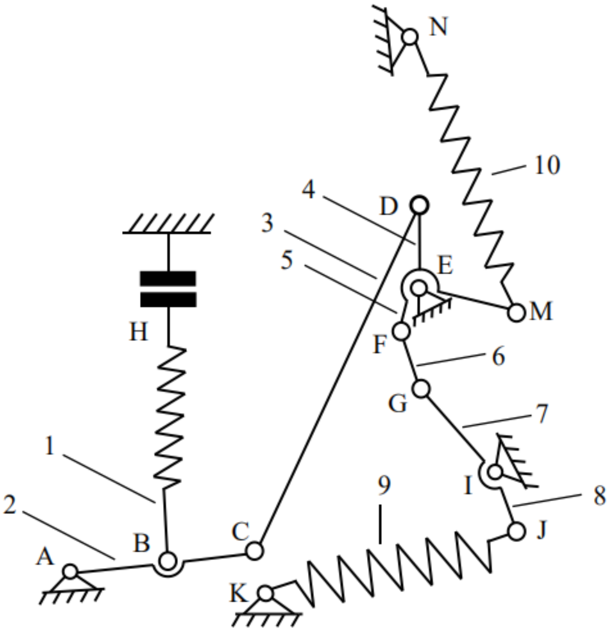

Figure 1. Simplified model of circuit breaker mechanism.

In the Figure 1: 9 represents the energy storage spring; 8 represents the link 8; 2, 3, 4, 5, 6, and 7 represent links 2, 3, 4, 5, 6, and 7; 10 represents the opening spring; 1 represents the moving contact portion.
During the closing process, after the circuit breaker receives the closing command, the energy storage spring releases the energy to push the connecting rod 8 to rotate. The link 8 drives the main shaft to rotate through the four-bar mechanism. When the main shaft rotates, the insulating rod is driven by the four-bar mechanism to move the moving contact. Move upward until the closing operation is completed, and at the same time, the opening spring is elongated with the rotation of the main shaft, and the opening spring stores energy to store energy for the mechanism opening [3].

3. Theoretical calculation of average closing speed of medium voltage vacuum circuit breaker

3.1. Calculation of speed ratio

Since the research goal of the article is to calculate the average closing speed of the moving contact, the article takes B point as the equivalent point and calculates the speed ratio of the remaining points relative to point B.
In the calculation, the fixed points A, E and I are used as fulcrums, and the speed ratio calculation is not involved. The speeds of points B, C, D, F, G and J are represented by v_b、v_c、v_d、v_f、v_g and v_j.
According to the different transmission modes of the mechanism, the mechanism transmission can be divided into two types:
(1) The link rotates at the same angular speed of the same rotating shaft
At this time, the speed of the mechanism is inversely proportional to the length of the mechanism [4].
Since the points A, E and I are the rotating shafts, We can get:

$$v_c = (L_2 / L_{AB}) v_b \tag{3.1}$$

In the formula: L_2 represents the length of the link 2; L_{AB} represents the distance from point A to B.

$$v_f = (L_5 / L_4) v_d \tag{3.2}$$

In the formula: L_5 represents the length of the link 5; L_4 represents the length of the link 4.

$$v_j = (L_8 / L_7) v_k \tag{3.3}$$

In the formula: L_8 represents the distance from point I to J; L_7 represents the length of the link 7.

(2) Four-bar linkage

In the organization, ACDE and EFGI are two four-bar mechanisms,We can use the closed triangle rule to find the speed ratio of the transmission rod [5].

Taking the point D speed as an example: v_c is perpendicular to the link 2, v_d is perpendicular to the link 4, we make the vertical speed so that it is perpendicular to the link 3, and construct a triangle by using the vertical speed and v_c, v_d, as shown in Figure 2:

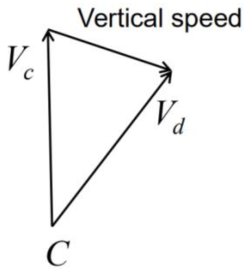

Figure 2. Closed triangle rule.

Then we can use the closed triangle rule to find v_d / v_c.

Similarly, we can use v_f, v_g and the vertical velocity of the link 6 to construct a closed triangle, then we can find v_f /v_g.

By substituting the various institutional parameters into the formula, we can find the speed ratio of the circuit breaker closing process, as shown in Table 1:

Table 1. Mechanism speed ratio.

Node number	Node speed	speed ratio	ratio
B	v_b	v_b/v_b	1
C	v_c	v_c/v_b	2.59
D	v_d	v_d/v_b	5.08
F	v_f	v_f/v_b	2.08
G	v_g	v_g/v_b	2.56
J	v_j	v_j/v_b	1.93

3.2 Equivalent mass calculation

3.2.1 Substitute quality

From a theoretical point of view, according to the different modes of movement of components, the substitution quality can be divided into the following three types:

- Parts for linear translation: the substitute quality of such parts can be considered to be concentrated at any point of the part.For example, the mass of part 1 can be directly equivalent to point B.
- Parts that rotate around a fixed axis: According to the principle of conservation of moment of inertia, the alternative quality of such parts can be concentrated at any point of the part.For example, The mass of the link 2, 4, 7 can be equivalent to points C, D, G.
- Complex parts that do parallel plane motion: These parts are usually approximated and the mass

is equivalent to both ends of the part[6].For example, The mass of the link 3 can be equivalent to points C, D;The mass of the link 6 can be equivalent to the points F, G.

3.2.2 Node quality

The two components are connected together by a pin. We call the pin joint a node. By calculating the replacement mass, most of the parts can be concentrated on the nodes [7].

3.2.3 equivalent quality

By calculating the mass of the substitute and the mass of the node, the mass of the part is concentrated on several nodes, and the motion of each node is v_a, v_b…, then the kinetic energy of the whole moving part is[8]:

$$A_d = \frac{1}{2}m_A v_A{}^2 + \frac{1}{2}m_B v_B{}^2 + \frac{1}{2}m_C v_C{}^2 + \cdots = \frac{1}{2}[m_A + m_B(\frac{v_B}{v_A})^2 + m_C(\frac{v_C}{v_A})^2 + \cdots]v_A{}^2 = \frac{1}{2}mv_A{}^2 \quad (3.4)$$

In the formula: m is the equivalent mass to be calculated.

Through the SolidWorks software, the mass and moment of inertia of each component, axle pin, spring, etc. can be obtained. Combined with the above-mentioned equivalent mass solution method, the node quality is shown in Table 2:

Table 2. Node quality.

Node	Components							
	1	**2**	**3**	**4**	**6**	**7**	**8**	**9**
B	5.1							
C		0.41	1.24					
D			1.24	0.35				
F					0.03			
G					0.03	0.03		
J							0.11	0.32

Known node mass and mechanism speed ratio, according to the equivalent mass formula:

$$m = m_A + m_B(\frac{v_B}{v_A})^2 + m_C(\frac{v_C}{v_A})^2 + \cdots \quad (3.5)$$

The equivalent mass of the available circuit breaker mechanism at point B is 62Kg.

3.3 Energy calculation

There are mainly five kinds of forces in the closing process to provide energy for closing. The energy storage spring and the contact self-closing force are used to drive the circuit breaker to close, and the opening spring, gravity and overtravel spring block the circuit breaker to close. The overtravel spring acts in the overtravel phase of the circuit breaker and does not need to be considered in the calculation of the energy in the open phase [9].

Through the simplified model of the circuit breaker established by SolidWorks, we can analyze the change of the length of the energy storage spring and the opening spring when the moving contact is at different positions, and then find the energy provided by each load force for closing.

In the article, the distance of the circuit breaker is 12mm, and the length of the energy storage spring and the opening spring are analyzed when the contact is started at the closing, displacement is 8.4mm, and the joint is just closed.As shown in Table 3.

After calculating the displacement of the energy storage spring, the opening spring and the moving contact, the energy storage spring is set to work W_1, the opening spring is W_2, the contact self-closing force is W_3, the gravity work is W_4, according to the spring work formula, The self-closing work formula and the gravity work formula can be used to obtain W_1, W_2, W_3, and W_4.

In addition, since the friction of the mechanism will lose some energy during the transmission process, the calculation is complicated. In engineering practice, it is generally expressed as mechanical efficiency. The average value η is generally 0.6 to 1, due to the spring action. There are many parts in the mechanism, and the energy loss in the transmission process is large. Therefore, the article takes η =0.9 for theoretical calculation [10].

Table 3. Mechanism displacement.

Contact displacement （mm）	Energys torage spring length （mm）	Energy storage spring displacement （mm）	Opening spring length（mm）	Opening spring displacement （mm）
0	133.68	0	189.58	0
8.4	142.87	9.19	213.70	24.12
12	148.69	15.01	24.12	35.54

Therefore, the energy change formula in the closing phase is：

$$W = \eta(W_1 + W_3 - W_2 - W_4) \tag{3.6}$$

The closing energy of the moving contact at the closing position of the closing position, displacement of 8.4 mm and the position of the just-integrated point is shown in Table 4:

Table 4. Institutional energy change.

Displacement	Energy				
	W_1	W_2	W_3	W_4	W
0	0	0	0	0	0
8.4	31.64	11.36	3.02	0.43	20.58
12	53.92	18.52	4.32	0.61	35.20

3.4 Average closing speed calculation

The kinetic energy theorem formula is:

$$W = \frac{1}{2}\mathrm{m}v^2 \tag{3.7}$$

In the formula: W represents the energy of the closing; m represents the equivalent mass of the institution; v represents the closing speed.

The closing energy and the equivalent mass of the mechanism have been obtained above, and the data is substituted into the kinetic energy theorem formula, which can be concluded as follows:The speed of the moving contact when the displacement is 70% of the opening distance is 0.83m/s.The speed at which the movable contact is displaced to the just-engaged point is 1.07 m/s.The movement of the moving contact during the closing phase can be approximated as an equal acceleration motion, and the average closing speed can be approximated as the average of the two, that is, the average closing speed is 0.95m/s.

4. Simulation analysis of average closing speed based on Adams

The virtual prototype is used to simulate the closing of the spring operating mechanism of the medium voltage vacuum circuit breaker, and the simulation results of the closing speed are obtained. Thecorrectness of the analytical method is verified by comparing the theoretical closing method and the average closing speed obtained by the simulation method.

4.1 Establish a simplified model of medium voltage vacuum circuit breaker

The modeling ability of Adams is weak. It is difficult to guarantee the three-dimensional model of medium voltage vacuum circuit breaker mechanism directly with Adams. The position and coordination of the mechanism are difficult to guarantee. Therefore, the article adopts professional 3D modeling software SolidWorks modeling, and then imports into Adams, The simplified model of the circuit breaker established in the paper is shown in Figure 3.

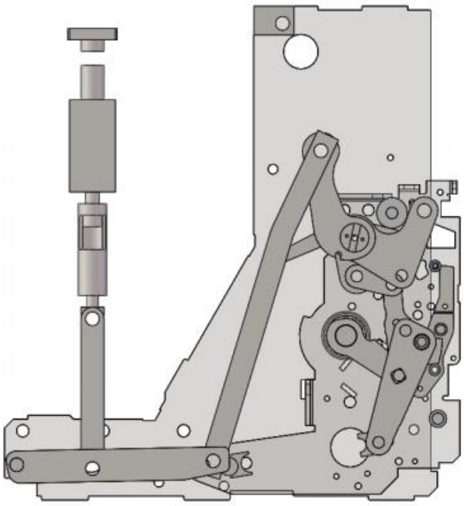

Figure 3. simplified model of the circuit breaker.

4.2 Adams simulation analysis

Introduce the established circuit breaker model into Adams, add constraints and spring drive to the mechanism, build a virtual prototype, and then simulate and analyze the virtual prototype closing process. The simulation results are shown in Figure 4:

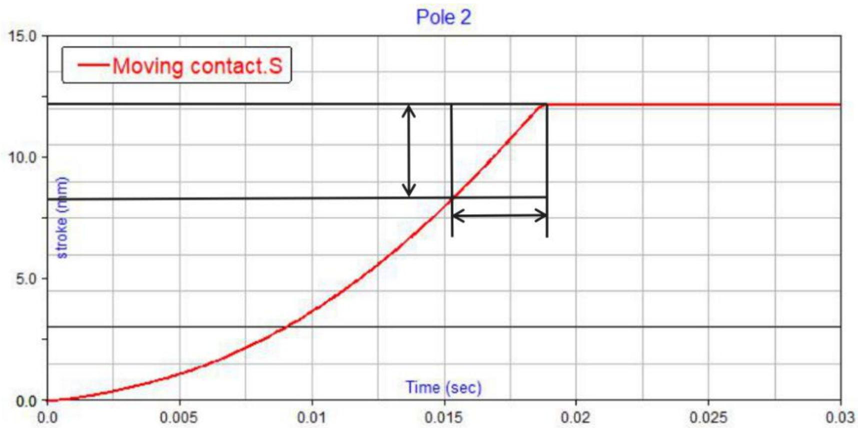

Figure 4. Closing simulation curve.

It can be seen from Figure 4 that when the moving contact displacement is 8.4 mm, the closing time is 0.0153 s, and when the moving contact moves to the just-integrated point, the closing time is 0.019 s, so the average closing speed of the simulation is 0.97m/s.

Comparing the calculation results with the simulation results, it can be concluded that the average closing speed obtained by the two methods is very close and the error is within a reasonable range, which verifies the correctness of the theoretical solution method.

5. Conclusion

- The article analyzes the average closing speed of the spring operating mechanism of the medium voltage vacuum CB from the theoretical point of view. Provide a theoretical basis for the design and development of circuit breakers.
- The article establishes a virtual prototype through ADAMS, and verifies the correctness of the theoretical analysis method by simulation.
- In the analysis of energy, a segmentation method is adopted. The article divides the closing process into the open phase and the overtravel phase, and then calculates the energy of different

IOP Conf. Series: Earth and Environmental Science **431** (2020) 012035 doi:10.1088/1755-1315/431/1/012035

phases in the open phase.This method of segmentation reduces the error of theoretical calculations.

- There are still many shortcomings in the analysis of the average closing speed. For example, when calculating the friction of the mechanism, the article only approximates the mechanical efficiency. If the friction of the mechanism can be analyzed in detail, the theoretical analysis results will be more accurate.

6. References

[1] Xu G Z 2000 Principle and Application of High Voltage Circuit Breaker of *Tsinghua University Press* **04** 124-168.
[2] Ren X L, Gao H L and Tian H W 2018 Parametric Modeling and Optimization of Circuit Breaker Spring Actuator of *Mechanical Design & Manufacturing* **02** 142-145.
[3] Yuan W 2001 Spring operating mechanism of high voltage circuit breaker *Mechanical Industry Press* **02** 23-65.
[4] LIU G J, CHEN J C 2012 Optimal Design of Circuit Breaker Linkage Mechanism of *Electrical and Energy Efficiency Management Technology* **08** 6-8.
[5] Deng B, Deng H X 2018 Optimal Design of Double Four-bar Mechanism for Spring Actuator of Circuit Breaker of *Machinery & Electronics* **08** 41-45.
[6] Gu G Q 2015 An Analysis Method of Transmission Ratio of Circuit Breaker Transmission Mechanism of *High Voltage Apparatus* **5** 123-127.
[7] Zhi B, Yan X and Liu B 2018 Design and Test of Vacuum Circuit Breaker with Hybrid Fast Operating Mechanism of *High Voltage Engineering* **06** 1791-1799.
[8] Kim,Young Shik 2013 Development of a Molded Case Circuit Breaker with a Spring-Actuated Linkage Based on Multi-Body Dynamics Analysis of *Advanced Materials Research* **711** 299-304.
[9] Tang J, Lu S, Xie J et al 2017 Contact Force Monitoring and Its Application in Vacuum Circuit Breakers of *IEEE Transactions on Power Delivery* **99** 1-1.
[10] Jang J S, Yoon C G, Ryu C Y et al 2015 Optimization of the Switch Mechanism in a Circuit Breaker Using MBD Based Simulation of *The Scientific World Journal* **2015** 1-7.

Acknowledgments

This work was supported by the Fujian Provincial Natural Science Foundation Project (GrantNo.2019J01867).

Load restoration strategy considering the recovery state of power plants in system restoration stage

Shengjun Wu[1], Xinzhen Feng[2], Qian Zhou[1], Hongfen Cui[2] and Hongyi Li[3]

1 Electric Power Research Institute of State Grid Jiangsu Electric Power Company, Jiangsu, China
2 China Electric Power Research Institute, Beijing, China
3 Nanjing University of Science and Technology, Jiangsu, China
E-mail: hongyi_lee27@njust.edu.cn

Abstract. Load restoration is important for reducing outage time and loss of smart grid after a blackout. Load recovery strategy of network reconfiguration is maximizing load amount during system restoration without considering the startup characteristic of thermal plants, which may result in the time-delay of hot-start generators and decrease the efficiency of power system restoration. In order to increase the restoration efficient of network reconfiguration stage, this paper proposes a load restoration strategy considering the recovery state of power plants based on logical preference description language (LPDL). Firstly, the load selection constraint determined by the recovery state of power plants in each time step is formulated by LPDL. Then, a non-linear optimization model for load restoration during network reconfiguration is established with the load selection constraint. Artificial Bee Colony algorithm (ABC) is employed to obtain the optimal load restoration scheme. Finally, the New England power system is employed to demonstrate the validation of the proposed method.

1. Introduction

Due to the advance control technology and widespread interconnection, the reliability is higher. But when the power system working on the limit states for the economic operation, it also has the risk of large area blackout which is caused by natural disasters or occasional faults [1, 2]. Several large area blackouts have happened in the past few years, such as India blackout in 30 July 2012, Japan blackout in 14 March 2011, Brazil and Paraguay blackout in 10 November 2010, which have caused millions of people out of electric service. After the blackout, it’s necessary to restore power supply quickly to decrease the loss caused by blackout. Therefore, the load restoration strategy is very important for power system restoration.

Power system restoration can be divided into three stages: preparation, system restoration (or network reconfiguration), and load restoration [3, 4, 5]. A large number of researches have been focused on load restoration strategy in load restoration stage. In this stage, major generators and backbone transmission lines have been restored and power supply is sufficient, optimal objective is to recover load as fully and rapidly as possible under the promise of constraints. With the ramp rate constrains of generators, the load restoration will last for several hours and be accomplished through step-by-step load pickup. For each small load pickup step, a mathematical model is formulated in [6] to determine the maximum restorable load of a substation while considers transient voltage constraint. A mixed-integer nonlinear load restoration model with AC power flow and reserve constraints during load restoration is formulated in [7]. A combinatorial optimization model taking the sequencing problem of load restoration into account is proposed in [8]. With the development of wide area monitoring system

(WAMS) and synchrophasor technology, a mathematical model to estimate the maximum restorable load is presented in [9] which employs WAMS data. A two-stage hierarchical method is presented in [10] to recover maximum possible level of loads, which includes the optimization of amount and location and real-time executing and monitoring. Besides above researches of load restoration powered by backbone transmission system, load restoration in distribution system and the microgrid also has got a lot of attention. A load restoration algorithm based on distributed multi agent is adapted for microgrid in [11]. An optimization model for the load restoration incorporating DGs is proposed in [12, 13].

In the network reconfiguration stage, in order to stabilize generating units, balance reactive power and provide satisfactory voltage profiles, a reasonable amount of important load will also be recovered simultaneously at the stage of network reconfiguration [14]. The optimization of restorable load under security constraints can accelerate the restoration of power system. A load restoration strategy coordinating the unit restoration with load restoration is proposed and an extended black-start multi-objective optimization model is established in [15]. An optimization model of load restoration considering load restoration cost, load characteristics, load importance and the influence of the load restoration on the succeeding network reconstruction is formulated in [16]. Load restoration is employed as a control method for standing phase angle reduction in [17]. A two-stage optimization model of network reconfiguration and load recovery is proposed in [18] including a MILP model optimizing transmission line charging and load pick-up and a nonlinear model minimizing the restoration duration.

In above researches, all the loads in blackout system are employed for restoration during network reconfiguration, while extra lines will recover the loads, which are not in the restored path. Due to the startup characteristic of thermal plants, additional restoration time may result in time-delay of hot-start generators and decrease the efficiency of power system restoration, meanwhile, thermal plant is required to start within maximum hot-start time or beyond minimum cold-start time. In addition, there is a time interval between maximum hot-start time and minimum cold-start time, and it is necessary to recovery as many loads as possible during the interval. That is, the loads, which can be recovered, are different from the recovery state of power plants.

To improve the efficiency of power system restoration, a new strategy for load restoration considering recovery state of power plants is proposed in this paper. Firstly, logical preference description language (LPDL) is employed to formulate the load selection constraint that can determine the load to be recovered in each time step. Then, a nonlinear optimization model for load restoration during network reconfiguration is established to maximize the weighted capacity of load restoration. The maximum power constraint of each load, power flow constraint and other constraints are taken into account. The artificial bee colony(ABC) algorithm obtains the optimal load restoration scheme. Finally, the load recovery strategy is applied in fixed and optimized system restoration path of different power systems to validate the performance.

2. Load selection constraint based on logical preference description language

Logical preference description(LPD) is a new research field of artificial intelligence [19], which can be employed to make decisions according to different preferences where users may have preferences on different goals under different circumstances. In this paper, the loads to be recovered at each time step is determined by the recovery state, and LPDL is employed to select the loads satisfying the requirement of different recovery state.

According to current researches, many qualitative preference problems can be solved on the premise of the following conditions:

- A set V of Boolean variables is given.
- A set B of propositional formulas which means background knowledge is given.
- A set F of propositional formulas which means the preferences among goals is given.
- A set S of preference strategies is given.

2.1. Logical preference description language

LPD is developed by Gerhard Brewka in order to represent complex qualitative preferences among problem solutions [20]. LPDL consists of ranked knowledge bases (RKBs) and preference strategies. RKBs are adapted to represent the relative importance of different goals, while preference strategies are defined to express complex preferences among models, which represent problem solutions.

2.1.1. Ranked knowledge bases.

RKB is a set of propositional formulas together with a total preorder. It can be expressed as a set of *(f, r)*, where *f* is a propositional formula and *r* is the rank of *f*, *r* is a non-negative integer, $f_1 \geq f_2$, if $r_1 \geq r_2$.

2.1.2. Preference strategies.

Preference strategies consist of basic strategy identifiers {T, κ, ⊆, #} and standard propositional connectives {∧, ∨, >, −}. Basic strategy identifier T is used in this paper to express the preference among loads. The strategy T can be described that T prefers m_1 over m_2 whenever the most important goal satisfied by m_1 is more important than the most important goal satisfied by m_2.

Based on the above knowledge, a basic preference description can be expressed as K^s, where *s* is a basic strategy identifier, *K* is a RKB.

In order to illustrate LPDL, assuming that RKBs are defined as follows: K={(a, 3), (b, 2), (c, 1)}.

Different models are defined according to RKBs, for example, *ab* means that in this model a, b are true, while c is false: M_1=*abc*; M_2=*ac*; M_3=*bc*; M_4=*ab*; M_5=*a*.

If the basic strategy identifier T is adapted to express the preference among models, the LPD is K_T. Based on this LPD, $M_1 >_T M_3$, because the rank of the most important goal satisfied by M_1 is 3, while M_3 is 2; while $M_1 \not>_T M_2$, because the rank of M_1 and M_2 are both 3. Similarly, $M_2 >_T M_3$, $M_4 >_T M_3$, $M_2 \not>_T M_4$, $M_1 \not>_T M_5$⋯The non-dominated models are M_1, M_2, M_4 and M_5, the preference structure among models can be illustrated in figure 1 (arrows point to strictly preferred models):

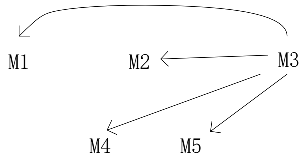

Figure 1. Strict preferences among models.

2.2. Selecting Loads to Be Recovered Based on Logical Preference Description Language

During network reconfiguration, the preferences among loads are determined by recovery state of power plants at each time step. If there are any power plants can be recovered in hot-start time interval, only the loads on optimal path can be restored, because the restoration of loads out of the optimal path will expand system restoration time. Otherwise, hot-start time may be missed and generator can be started until cold-start time due to the start-up character of generator. In contrast, if there are not any power plants can be recovered in hot-start time interval, the loads neighbouring the optimal path way can be restored to maximize the restorable load.

As to the analysis above, the distance from load to optimal restoration path determines the priorities of load. The loads in the blackout system can be divided into three categories according to their positions: the load on optimal restoration path, the load on neighbouring paths and the load far from the optimal restoration path. In order to avoid the recovery of extra lines outside optimal path which may affect the efficiency of network reconfiguration, the preference rank of the load on optimal restoration path is the highest. If generator can start in hot-start time interval, the preference ranks of other loads are lower. If recovery state of generators is in the time interval between maximum hot-start time and minimum cold-start time, the preference rank of load on neighbouring path is also the highest. The load which is far from the optimal restoration path has lower preference rank.

We can represent this information using the following RKBs:

$$\begin{cases} K_1 = \{(A,2),(B,1),(C,1)\} \\ K_2 = \{(A,2),(B,2),(C,1)\} \end{cases} \tag{1}$$

IOP Conf. Series: Earth and Environmental Science **431** (2020) 012036 doi:10.1088/1755-1315/431/1/012036

where K_1 is a set of preferences if generator can start in hot-start time interval, K_2 is another set of preferences if generator is not ready to start until the critical minimum time. A, B, C are the positions of loads relative to the optimal restoration path. A means that load is on optimal restoration path, B means that load is neighboring optimal path, C means that load is far from optimal restoration path.
The loads selecting constraint can be represented as the LPD expression:

$$\begin{cases} K_1^{\mathrm{T}} & if \quad t_i \le T_{ic\max} \quad or \quad t_i \ge T_{ic\min} \\ K_2^{\mathrm{T}} & if \quad T_{ic\max} < t_i < T_{ic\min} \end{cases} \tag{2}$$

where t_i is the time that cranking power has delivered to generator i, T_{icmax} is the critical maximum time interval of generator j and T_{icmin} is the critical minimum time interval.

3. Problem formulation

3.1. Objective function
Load restoration during network reconfiguration can be divided into several time steps. The maximum restorable load of each time step is determined by the cranking power of generators at this time step. This paper establishes an optimization model for load restoration, where the optimization target is to maximize the weighted capacity of load restoration:

$$\max f = \sum_{i=1}^{n} \sum_{j=1}^{m_i} \omega_{ij} x_{ij} P_{Lij} \tag{3}$$

where f is the weighted recovery capacity, n is the load bus to be recovered at each time step. In this paper, we divide a load bus into several components, m_i is the number of components of bus i. ω_{ij} is the weight of jth load of bus i. x_{ij} is the status of load bus, 1 means jth load of bus i has recovered, otherwise value is 0. P_{Lij} is capacity of jth load at bus i which is waiting for recovering.

3.2. Constraints
During system restoration, several constraints are required to be comprehensively taken into account, in order to ensure system security during restoration. The constraints can be listed as follows:

3.2.1. The maximum capacity of load restoration constraint.

$$\begin{cases} \sum_{i=1}^{n} \sum_{j=1}^{m_i} x_{ij} P_{Lij} < \Delta P_{\Sigma} \\ \Delta P_{\Sigma} = \sum_{i=1}^{N_G} (P_{Gi}(t+\Delta t) - P_{Gi}(t)) \end{cases} \tag{4}$$

where the load restoration at a time step is shown on the left of inequality, ΔP_{Σ} indicates the increment of power output， which can be calculated from the power output curve. P_{Gi}(t) is the power output of generator i, which can be obtained from [21].

3.2.2. The maximum capacity of load restoration considering transient frequency at each time step.
The maximum capacity of load restoration considering transient frequency at each time step is to ensure transient frequency within allowable ranges.

$$P_{L\max} = \Delta f_{\max} \sum_{i=1}^{n_G} \frac{P_{Ni}}{df_i} \tag{5}$$

where $\triangle f_{max}$ is 0.5Hz in this paper， df_i is transient frequency response of unit i, its value is mentioned in reference [16].

3.2.3. Steady state power flow constraints.

$$\begin{cases} P_{di} = V_i \sum_{j=1}^{N} V_j (G_{ij} \cos\delta_{ij} + B_{ij} \sin\delta_{ij}) = 0 \\ Q_{di} = V_i \sum_{j=1}^{N} V_j (G_{ij} \sin\delta_{ij} - B_{ij} \cos\delta_{ij}) = 0 \end{cases} \tag{6}$$

where P_{di} and Q_{di} are injection active and reactive power to bus i, V_i is voltage of bus i, G_{ij} and B_{ij} are conductance and susceptance between bus i and bus j respectively, δ_{ij} is the phase angle between V_i and V_j, N is number of buses.

3.2.4. Loads selecting constraint.

$$\begin{cases} K_1^{\mathrm{T}} & if \;\; t_i \le T_{ic\max} \;\; or \;\; t_i \ge T_{ic\min} \\ K_2^{\mathrm{T}} & if \;\; T_{ic\max} < t_i < T_{ic\min} \end{cases} \tag{7}$$

If the time that cranking power has delivered to generator i is within the maximum hot-start time T_{icmax} or beyond the minimum cold-start time T_{icmin}, the loads to be recovered will be selected according to the preference strategy K_1^{T}. If generator i is not ready to receive cranking power until the minimum cold-start time, the preference strategy K_2^{T} will be adapted to select loads to be recovered.

3.3. Model solving

The optimization model for load restoration proposed in this paper can be described as a 0-1 knapsack problem, which has been proved to be a nondeterministic polynomial complete (NPC) problem. Intelligent optimization algorithm is widely employed to solve this kind of problem. Compared with other swarm intelligence, such as genetic algorithm (GA) and particle swarm algorithm (PSO), ABC algorithm is of strong robustness, high searching accuracy and efficiency [22,23]. With its rapid convergence rate, less control parameters, high quality of solutions, strong robustness and global search capability, ABC algorithm has successfully applied in many areas, such as artificial neural network, power system optimization, engineering design, combinatorial optimization and so on. Therefore, ABC algorithm is applied to solve the optimization problem in this paper.

4. Case study

4.1. Example system and parameters

In order to verify the efficiency of the proposed strategy for load restoration, the 10-unit 39-bus system is employed for case studies. Suppose that generator in node 30 is a black start unit, which is a pumped storage power plant. Other units are all thermal power units, whose primary parameters are shown in table 1. The components of each load bus and their load capacity are shown in appendix. Start-up time of each line is 4min. In order to ensure that spinning reserve capacity is enough, assuming that unit 30 is a balancing machine whose maximum power output is 80% of its rated power.

4.2. Simulation Environment and Case Study

The generator start-up sequence is assumed to be obtained by dispatchers. The start-up sequence is 37-33-35-34-32-31-38-39-36. The optimal restoration scheme based on the proposed load restoration strategy at each time step is shown in table 2.

In the first four time steps, generators can start in maximum hot start time interval, according to the loads selecting constraint, loads on the optimal restoration path and in the recovered system are selected to be recovered. The restoration scheme at each time step is optimized based on ABC algorithm. In the fifth time step, generator 32 cannot start within maximum hot-start time. And loads neighboring the optimal path can also be recovered during the time interval between maximum hot-start time and minimum cold-start time, which will not affect the start-up time of other generators. In the last four time steps, start-up time of generators is beyond the minimum cold-start time, the increment of power output will be distributed to the loads on the optimal restoration path and in the recovered system.

Table 1. Parameters of generators.

Node Num.	P_G (MW)	P_{cr} (MW)	K_i (Pe%/min)	T_{cmax} (min)	T_{cmin} (min)	T_{PR} (min)
30	350	-	2.0	-	-	-
31	1145	68.7	1.0	45	180	10
32	750	52.5	1.0	45	180	10
33	750	67.5	1.0	60	180	10
34	660	46.2	0.8	60	180	10
35	750	75	1.0	60	180	10
36	660	52.8	1.0	60	180	10
37	640	38.4	0.8	40	180	10
38	930	46.5	1.0	40	180	10
39	1100	88	0.8	45	180	10

Table 2. Load restoration scheme at each time step obtained by proposed strategy.

Generator start-up sequence	Recovered load	Fitness value	Start-up time of generators /min
37	25(1)(3)	16.6	12
33	3(1)(3)(4), 18(1)(3)(4), 16(1)(2)(3)	72.46	36
35	21(1)(4)	18.32	48
34	21(6)	36.5	56
32	3(2)(5)(6)(7)(8)(9), 25(2)(5)(6), 18(2)(5), 16(4)(5)(6)(7)(8), 21(2)(3)(5)(7), 20(1)(2)(3)(4)(5)(6)(7)(8)(9)(10(11), 4(1)(3)(4)(6)(7)(8)(9)(10)(11), 12(1), 15(1)(2)(3)(5)(6), 27(1)(2)(3)(4)(7), 24(3)(4)(5)(6)(7), 26(1)(2)(3)(5)(6)(7)(8)(9)	1060.3	180
31	/	0	192
38	31(1), 29(1)	9.31	200
39	24(2), 26(4), 39(1)(4)	28.03	208
36	4(2), 24(1), 23(3), 39(2)(3)(13)	107.16	216

Table 3. Load restoration scheme at each time step obtained by old strategy.

Generator start-up sequence	Recovered load	Fitness value	Start-up time of generators /min
37	3(4), 25(1), 26(3)	24.52	12
33	3(3), 26(2)(5), 4(1)(2), 18(1), 28(1), 27(1), 16(3), 24(2), 20(1)(2)	91.11	40
35	3(2)(8), 25(3)(5), 26(4)(7)(9)(10), 4(7)(8)(9)(10), 18(2)(6), 28(2)(4)(6), 27(2)(3)(4), 16(1)(4), 15(1)(6), 21(3)(6)(7), 24(3)(5), 20(3)(4)(7)(8)(9), 29(2)(6), 23(3)	554.065	180
34	26(1)	2	199
32	25(2), 23(5), 12(1)	70.74	215
31	20(11)	82	231
38	7(4)	23.04	235
39	8(2)(6), 21(1)	60.1	247
	39(13)	80	251

4.3. Comparison and Analysis

According to the old restoration strategy, all the loads can be recovered at each time step without considering the recovery state of power plants, the optimal restoration scheme at each time step is

shown in Table 3. As we can see from the two tables, all the generators have regenerated at 216min according to the strategy proposed in this paper. While in table 3, all the generators have regenerated at 251min because of the recovery of extra lines outside the optimal path, which results in the time-delay of hot-start generators. It obviously illustrates that the improved strategy is much better in restoration time.
What's more, figure 2 shows the comparison of the load restoration capacity based on two strategies, the capacity of load restoration based on the strategy proposed in this paper is much larger. Therefore, the results demonstrate that the proposed strategy is highly efficient.

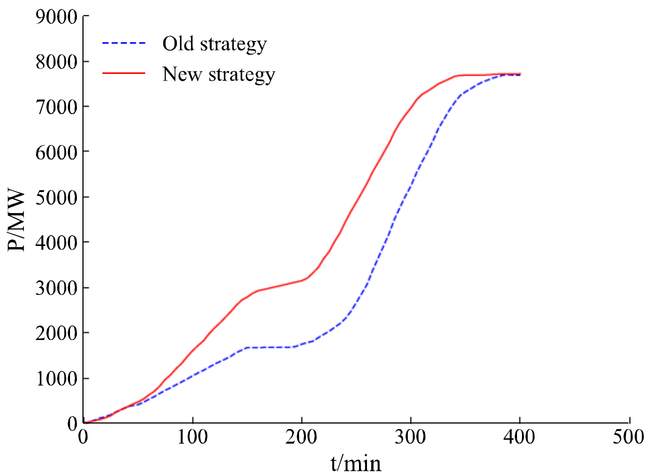

Figure 2. The comparison of load restoration capacity based on two strategies.

5. Conclusion

In order to improve the efficiency of power system restoration, a new strategy for load restoration considering critical minimum and maximum time intervals of generators, which will not lead to the additional restoration time of extra lines, is proposed in this paper. Logical preference description language is adapted to describe the selection of loads. An optimization model with consideration of weighted capacity of load restoration is established and the Artificial Bee Colony Algorithm is adapted to solve it. The simulation results validate the effectiveness of the proposed strategy, which can increase the capacity of load restoration and improve the efficiency of network reconfiguration.

6. References

[1] Andersson G, Donalek P, Farmer R, et al. "Causes of the 2003 major grid blackouts in North America and Europe, and recommended means to improve system dynamic performance", *IEEE Trans. Power. Syst.*, vol. 20, pp. 1922-28, April. 2005.
[2] Wu F F, Moslehi K, Bose A. "Power system control centers: past, present, and future", *Proc. of the IEEE*, vol. 93, pp. 1890-1908, November. 2005.
[3] Shi L B, Ding H L and Xu Z. "Determination of weight coefficient for power system restoration", *IEEE Trans. Power. Syst.*, vol. 27, no. 2, pp. 1140-41, May. 2012.
[4] Zeng S Q, Lin Z Z, Wen F S and Ledwich G. "A new approach for power system black-start decision-making with vague set theory", *Int. J. Electr. Power and Energy Syst.*, vol. 34, pp. 114-120, November. 2012.
[5] Fink L H, Liu K L and Liu C C. "From generic restoration actions to specific restoration strategies", *IEEE Trans. Power. Syst.*, vol. 10, pp. 745-52, May. 1995.
[6] Qu H and Liu Y. "Maximizing restorable load amount for specific substation during system restoration", *Int. J. Electr. Power & Energy Syst.*, vol. 43, pp. 1213-20, May. 2012.

[7] Qin Z J, Hou Y H, Liu C C, Liu S S and Wei S. "Coordinating generation and load pickup during load restoration with discrete load increments and reserve constraints", *IET Gener. Trans. & Distrib.*, vol. 9, pp. 2437-46, July. 2015.
[8] Qu H B, Yin M L and Lin S. "Load restoration optimization during last stage of network reconfiguration", *2014 China Int. Conf. Electr. Distrib.*, Shenzhen, 2014, pp. 1075-79.
[9] Liu W J, Lin Z Z, Wen F S and Ledwich G. "A wide area monitoring system based load restoration method", *IEEE Trans. Power. Syst.*, vol. 28, pp. 2025-34, May. 2013.
[10] Gholami A and Aminifar F. "A hierarchical response-based approach to the load restoration problem", *IEEE Trans. Smart Grid*, 2015(Early Access).
[11] Xu Y L and Liu W X. "Novel multiagent based load restoration algorithm for microgrids", *IEEE Trans. Smart Grid*, vol. 2, pp: 152-161, March. 2011.
[12] Wang Q C, Shi L B, Yan X W and Yao L Z. "An optimal strategy for load recovery considering renewable energy resource integration", in *Int. Conf. Renew. Power Gener.*, 2015, pp. 1-4.
[13] AM El-Zonkoly. "Power system single step restoration incorporating cold load pickup aided by distributed generation", *Int. J. Electr. Power & Energy Syst.*, vol. 35, pp. 186-193, 2012.
[14] Sun W, Liu C C and Zhang L. "Optimal generator start-up strategy for bulk power system restoration", *IEEE Trans. Power. Syst.*, vol. 26, pp. 1357-1366, August. 2011.
[15] Gu X P and Wang D J. "Investigation on extended black-start schemes of power system considering reasonable load restoration", in *IEEE PES Asia-Pacific Power and Energy Engineering Conf.*, 2014, pp. 1-5.
[16] Zhong H R, Gu X P and Zhu L X. "Optimization of load restoration during network reconfiguring process of black-start restoration", *Power Syst. Pro. Control*, vol. 39, pp. 26-32, September. 2011.
[17] Ye H and Liu Y T. "A new method for standing phase angle reduction in system restoration by incorporating load pickup as a control means", *Int. J. Electr. Power & Energy Syst.*, pp. 664-674, May. 2013.
[18] Liao S W, Yao W, Han X N, Wen J Y and Hou Y H. "Two-stage optimization method for network reconfiguration and load recovery during power system restoration", in *IEEE Power & Energy Society General Meeting.* 2015, pp. 1-5.
[19] Wright G H. "The logic of preference". 1963.
[20] Brewka G A, "rank based description language for qualitative preferences", in *ECAI.* 2004, pp. 303-307.
[21] Gu X P and Zhong H R. "Optimisation of network reconfiguration based on a two-layer unit-restarting framework for power system restoration", *IET Gener. Trans. & Distrib.*, vol. 6, pp. 693-700, July. 2012.
[22] Karaboga D and Basturk B. "On the performance of artificial bee colony (ABC) algorithm", *Appl. Soft Computing*, vol. 8, pp. 687-697, June. 2008.
[23] Karaboga D and Akay B. "A comparative study of artificial bee colony algorithm", *Appl. Mathematics and Computation*, vol. 214, pp. 108-132, 2009.

IOP Conf. Series: Earth and Environmental Science **431** (2020) 012037 doi:10.1088/1755-1315/431/1/012037

Simulation modeling study on short circuit ability of distribution transformer

Zhang Shiling[1] **and Gong Lin**[1]

1 State Grid Chongqing Electric Power Company Chongqing Electric Power Research Institute, Chongqing, China
E-mail: 526793305@qq.com

Abstract. Under short circuit condition, the oil immersed distribution transformer will endure combined electro-thermal stress, eventually lead to the mechanical damage of the inner winding of distribution transformer, therefore it is necessary to study the short circuit ability of the oil immersed distribution transformer. In this paper, the typical current waveform of the distribution transformer under the short-circuit condition is analyzed theoretically. The short circuit fault simulation model of distribution transformer is built on the MATLAB/Simulink simulation platform, the short circuit waveform of the single phase, double phase and three phase short circuit is obtained. Further on the ANSYS simulation platform, three dimensional solid modeling of the three-phase five column transformer is carried out, the harmonic and transient field are applied to analyze the magnetic field distribution of the key components in distribution transformer under the short circuit condition, the internal cause of large short-circuit force in the winding of the distribution transformer under the short circuit condition is analyzed to certain extent. The results of the modeling and simulation show that the three phase short circuit current is larger than the single-phase and bi-phase short circuit current. Its value is 1.45 times the normal running current, which is the gradual damping asymmetrical short-circuit current. Magnetic induction intensity is in-homogeneous in the circumferential direction of the core column, and the degree of in-homogeneity varies along height. The magnetic density distribution under the short circuit condition is more than 6 times as much as the the normal condition. From the point of view of simulation modeling, short circuit ability of the oil immersed distribution transformer is analyzed, distribution characteristics of short circuit current and magnetic field of oil immersed distribution transformer under short circuit condition have been obtained, the theoretical reference value of the state characteristics and protection measures of oil immersed distribution transformer under the overload condition can be provided.

1. Introduction

In process of operation, transformers may be impacted by short-circuit current as well as various over-voltages. For example, when the transformer is in normal operation, the secondary side of transformer will suddenly be short-circuit fault, and the large over-current will appear in the winding. Under the action of short-circuit current, on the one hand, it will cause huge electric force in each part of transformer, on the other hand, it will make the temperature of transformer winding rise rapidly. Although this process lasts for a short time, it is severe test to the stability and heat resistance of transformer withstanding short-circuit. Short-circuit test is the mechanical strength endurance test of transformer under strong current [1]. It is examination of the comprehensive technical ability and technological level of transformer manufacturing. Therefore, short-circuit test is the special test item. If power transformer is damaged by short circuit in the operation of the system, it will lead to the large area of power outage, and its maintenance period will be more than half a year, which will cause huge losses. At the same time, it is very difficult to repair damaged transformer winding on site. The repair of transformer is not only limited by the lifting conditions of the site, but also stringent to climatic environment and seasonal requirements [2]. It is difficult to meet the requirements of the maintenance process on site. It is almost impossible to repair the damaged transformer winding in good condition on site. Many transformers are short-circuit faulted [3].

The most transformer faults are caused by inter-turn and inter-phase short-circuit. Short-circuit fault of transformer will produce the short-term over-current which intrudes into transformer winding. It will produce large electromagnetic force between the winding of the transformer and lead to transformer winding deformation. At the same time, a large amount of heat will be generated after over-current passes through the winding of transformer. Under the superposition of heat, the insulation of transformer is damaged, which leads to the transformer outage and the large-scale blackout. Therefore, it is necessary to check the short-circuit current withstanding level of the transformer before it is put into operation or in process of transformer operation. At present, only a few national test stations are able to complete large transformer short-circuit test under short-circuit conditions. However, the establishment of the test station requires a large initial investment, and during test process, the factory or repaired transformer should be sent to the test station for short-circuit capability test. The test cost is high. The internal structure of the transformer winding is shown in Figure 1. For small-capacity distribution transformer, it is necessary to develop complete set of the short-circuit test device to realize on-site verification of short-circuit capacity of transformer. It can be seen that development of complete set of short-circuit test device of the distribution transformer can better solve the timeliness and rapidity of the on-site test, and has the good application prospect [4,5].

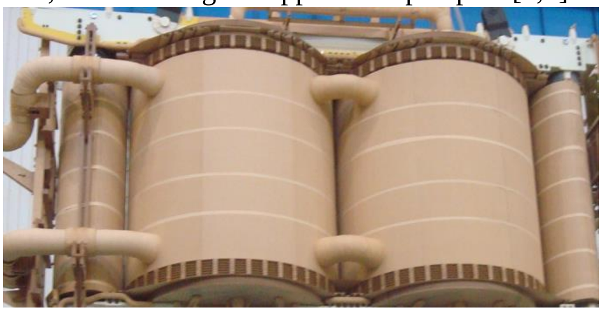

Figure 1. The internal structure of transformer winding

Distribution transformer will produce huge short-circuit force in winding in case of the sudden short-circuit. If the transformer design is not perfect and short-circuit resistance is not enough, such short-circuit force will cause damage to winding insulation and structural parts, affect the insulation performance of the transformer, and make winding loose, twisted and deformed, and lead folded. Even whole winding collapses, or the winding burns down due to the inter-turn short circuit caused by insulation damage [6]. In view of this, this paper firstly deduces analytical formula of short-circuit resistance of distribution transformer, and gets the typical waveform of short-circuit current of distribution transformer based on the theoretical formula. The short-circuit lumped circuit model of transformer winding is established in the MATLAB/SIMULINK computing environment, waveform characteristics of current in different types of short-circuit conditions are simulated. A three-dimensional finite element simulation model of transformer winding is established. The short-circuit current waveform is applied to finite element model. The magnetic density distribution characteristics of transformer winding under the short-circuit condition are obtained. From the point of view of simulation modeling, the short-circuit resistance of the oil-immersed distribution transformer is theoretically analyzed, and the oil-immersed distribution is obtained. The distribution characteristics of short-circuit current and the magnetic field of the electric transformer under short-circuit condition provide theoretical reference for the understanding the state characteristics and protection measures of oil-immersed distribution transformer under over-load condition.

2. Theoretical Analysis of Short Circuit Resistance of Distribution Transformer

The short-circuit electro-dynamic force is proportional to the square of the short-circuit current after the short-circuit of low-voltage side port of the transformer. In the calculation of winding strength, the maximum electromagnetic force on the winding is used, so it is important to determine the peak value of short-circuit current corresponding to the maximum electromagnetic force. There are two parts in short circuit current: periodic component and non-periodic component. The magnitude of non-periodic component is related to the instantaneous occurrence of short circuit [7]. In calculation of electromagnetic force of transformer winding, not only the leakage magnetic field should be accurately analyzed, but also the short-circuit current should be determined. In the process of the transformer operation, there are various short-circuit conditions. The three-phase short-circuit at the low-voltage side port is the most serious damage to the winding. The relevant transformer standards also stipulate that the three-phase short-circuit electromagnetic force at the low-voltage side port is used as design checking calculation condition. Therefore, the simplified equivalent circuit of the transformer with three-phase short circuit at the low-voltage side port is shown in Figure 2.

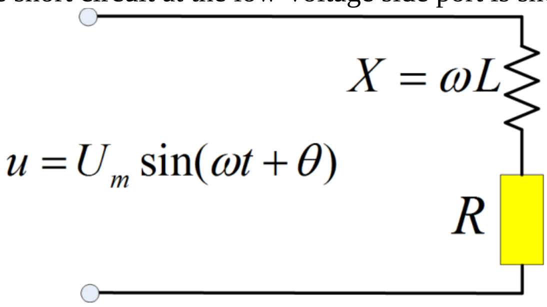

Figure 2. Simplified equivalent circuit of transformer winding

Let the applied voltage of the equivalent circuit shown in Figure 2 to be:

$$u = U_m \sin(\omega t + \theta) \quad (1)$$

According to principle of electrotechnics, the expression of steady-state current i_1 is as follows:

$$i_1 = \sqrt{2} I_0 \sin(\omega t + \theta - \varphi) \quad (2)$$

$$I_0 = \frac{U_m}{\sqrt{2}Z} = \frac{U_m}{\sqrt{2}\sqrt{(\omega L)^2 + R^2}} \quad (3)$$

In formula i_0, the effective value of short-circuit steady-state current and the phase angle of the power supply voltage in short-circuit are respectively calculated. Before short-circuit occurs, the transformer may be in load operation, but because the load current is much smaller than the short-circuit current, it is usually omitted. The sudden short-circuit of transformer is assumed to occur under no-load condition. After sudden short-circuit of the transformer, the short-circuit current in winding is equal to the sum of steady-state component and transient component. The expression of short-circuit current is as follows:

$$\begin{aligned} i_k &= i_1 + i_2 = \\ &\sqrt{2} I_0 [\sin(\omega t + \theta - \varphi) - \sin(\theta - \varphi) \exp(-\frac{R}{X}\omega t)] \end{aligned} \quad (4)$$

In general transformers, the formula at this time (4) can be simplified as follows:

$$\begin{aligned} i_k &= i_1 + i_2 = \\ &\sqrt{2} I_0 [-\cos(\omega t + \theta) + \cos(\theta) \exp(-\frac{R}{X}\omega t)] \end{aligned} \quad (5)$$

The typical short-circuit current wave-forms are obtained from expression (5) as shown in Figure 3.

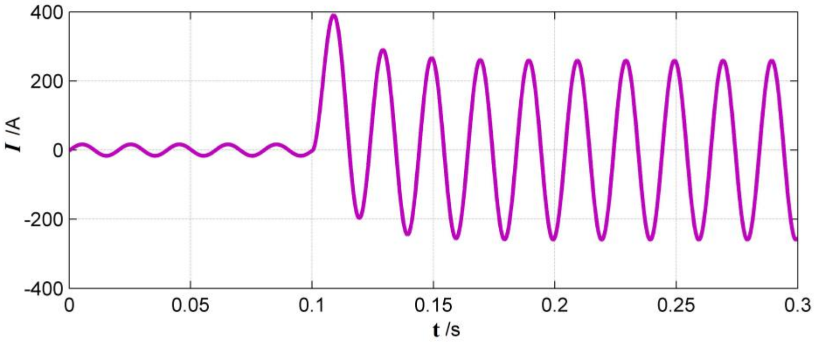

Figure. 3 Typical waveform of short circuit current

Table.1 The value of the coefficient *F*

X/*R*	1	2	4	6	8	10	14
F	1.51	1.76	2.09	2.27	2.38	2.46	2.55

As can be seen from Figure 3, if duration of short-circuit test current is long enough, asymmetric current containing first peak value will change to the square root of symmetric current *I*. The deviation of peak current obtained in the test should be less than 5% and deviation of symmetric current should be less than 10%. The test should be carried out when the phase current reaches the maximum asymmetric value. The first peak of asymmetric test current (kA) is calculated according to formula (6):

$$\hat{i} = I \times k \times \sqrt{2} = I \times F \tag{6}$$

In Formula (6), asymmetric short-circuit current coefficient *F* is determined according to the data in Table 1. Under the sudden short circuit condition of distribution transformer, the total current of short circuit current and its steady component act on transformer winding, which causes the average temperature of the transformer winding to rise. The temperature rise of transformer winding is related to the duration of short-circuit current and multiple of steady-state short-circuit current. When secondary side of the transformer is short-circuit suddenly, the short-circuit current flowing through the winding can reach several times or even tens of times of the rated current. Short-circuit loss of transformer is tens to hundreds of times of the rated operation.

3. Theoretical short-circuit current waveform simulation of distribution transformer

Using the three-phase saturated transformer module in Sim Power Systems, the simulation models of current and short-circuit current for no-load closing of SF10-90000/220 transformer are established in the Matlab7.0/Simulink. The transformer module in simulation model chooses three-phase double-winding saturated Yn/D11 transformer module to simulate and analyze the short-circuit current of single-phase, two-way and three-way short-circuit to ground respectively. The solution method used in the simulation is ode23tb. The simulation model in Simulink is shown in Figure 4.

Figure 4 includes the equivalent power supply, distributed transmission lines, transformers and the power system loads. The grounding fault of the transmission system is simulated by slitting switch, and current variation of the transformer's high voltage winding is emphasized in the simulation process. The short-circuit over-current situation is illustrated by the simulation results. Figure 5 is the typical current waveform of transformer after short-circuit. It can be seen that after single-phase, double-phase and three-phase short-circuit occurs, the short-circuit current increases tens of times instantaneously from the normal operation condition, and the current characteristics are quite different under the three conditions: under single-phase short-circuit condition, the A-phase current increases instantaneously, but the B-phase and C-phase current increases slightly. Under the condition of two-phase short circuit, the increase of A and C phase currents is larger than that of B phase currents; under the condition of three-phase short circuit, the increase of A phase, B phase and C phase amplitudes is larger, so the current under the condition of three-phase short circuit is the most stringent and the winding damage of distribution transformer is most serious. It is explained by single-phase short-circuit that the short-circuit current of windings reaches 225A from the transient peak current 327A to steady-state short-circuit current 225A generally undergoes the 3-4 current waveform periods, i.e. 0.06-0.08s, and the *F* value of asymmetric short-circuit current coefficient is about 1.45, which is mainly caused by the decay process of the non-periodic component of short-circuit current.

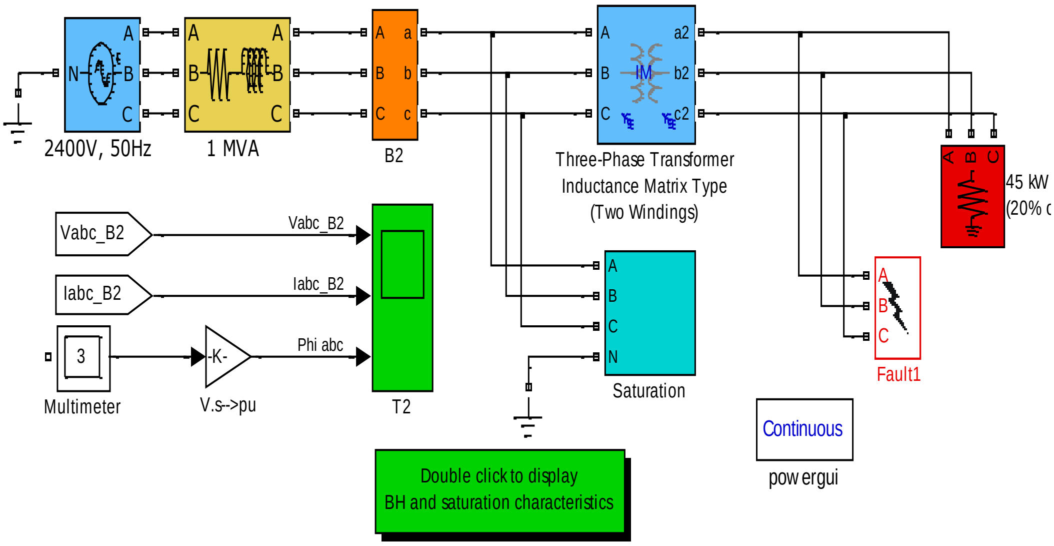

Figure.4 Matlab/Simulink calculation model

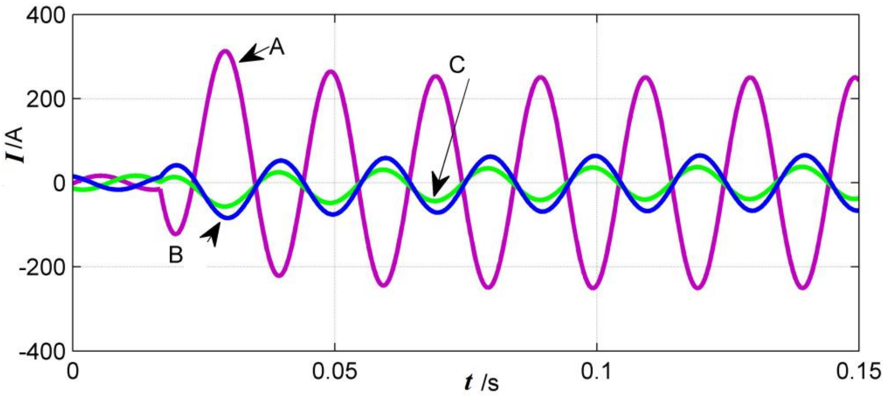

（a）Single phase short circuit

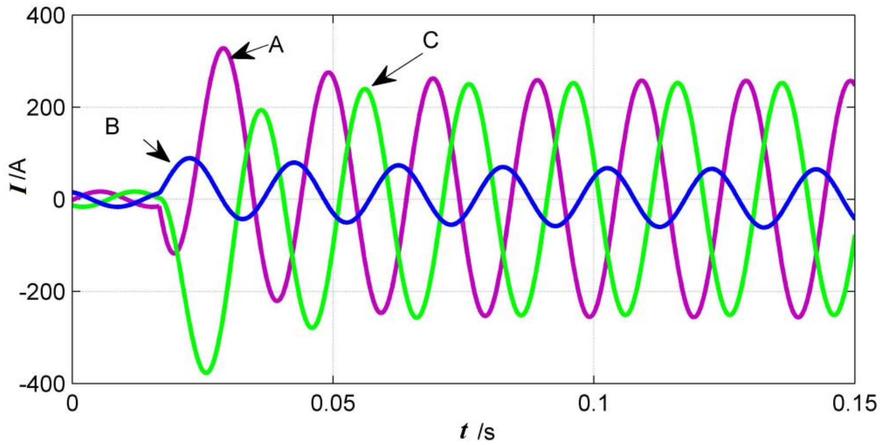

（b）Dual-phase Short Circuit

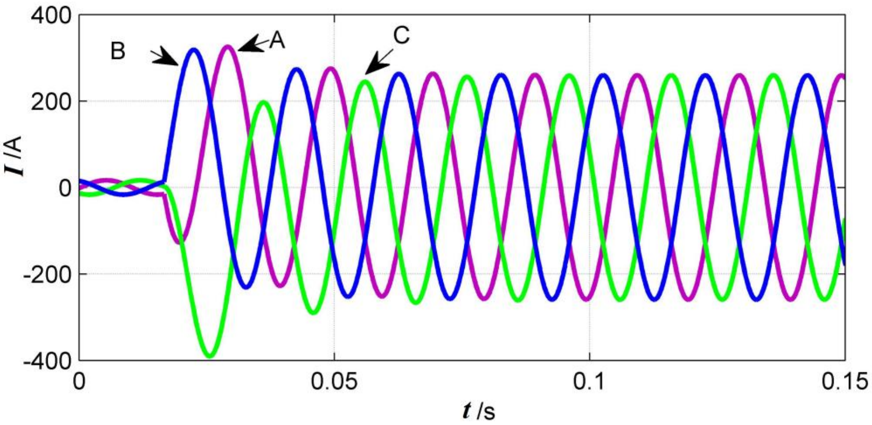

（c）Three-phase short circuit

Figure.5 Waveform of short circuit current

Therefore, if only mechanical effect of short-circuit current on the winding of distribution transformer under the short-circuit condition is examined, the short-circuit current of 0.5s is usually applied. If thermal effect of transformer winding under short-circuit current is further examined, the short-circuit current of transformer should be applied for long time to meet long-term thermal effect on the oil-paper insulation of the transformer.

4. Theoretical Finite element electromagnetic analysis of distribution transformer winding short circuit

In ANSYS environment, field-circuit coupling FEM calculation of transient electromagnetic field of three-phase five-column transformer under short-circuit condition is carried out. Taking three-phase five-column transformer as example, three-dimensional finite element simulation model is established under the ANSYS simulation environment. Figure 6 shows that the model considers the components of the mixed insulating oil, transformer winding, iron core, pulling plate, clamp, oil tank and electromagnetic shielding. The permeability of insulating oil is considered to be 1, and the winding of transformer is considered to be 1. The permeability and resistivity of the core are 1 and 1120,1 and 0.909e-6 for the clamp, 400 and 0.173e-6 for tank, 1 and 2.21e-8 for the electromagnetic shield, respectively. In ANSYS, three-dimensional simulation model is partitioned by finite element method as shown in Figure 7.

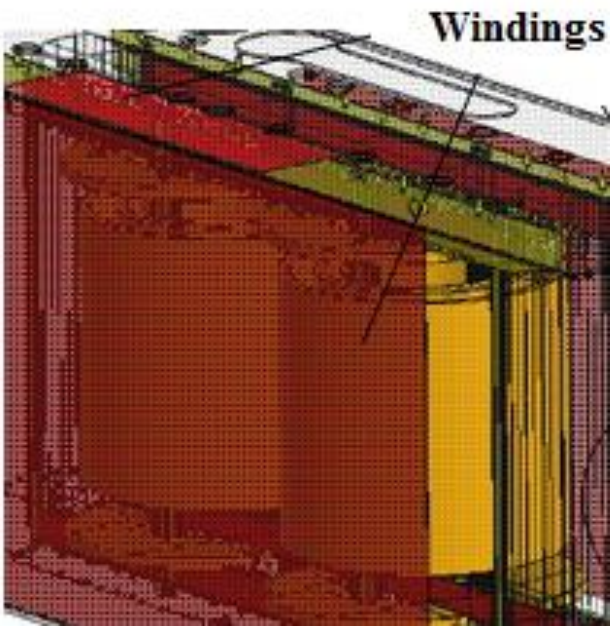

Figure.6 Model of the transformer winding

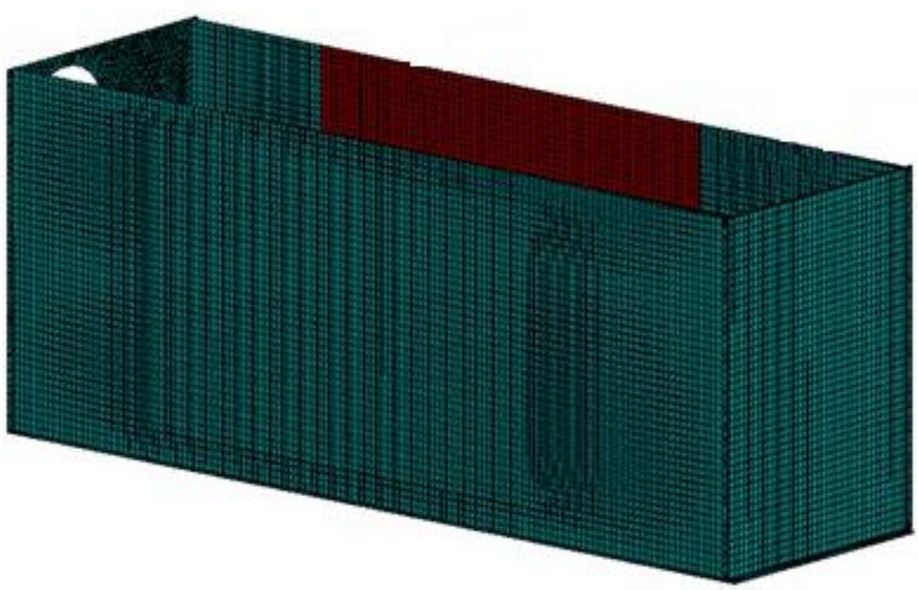

Figure.7 Finite element division of transformer model

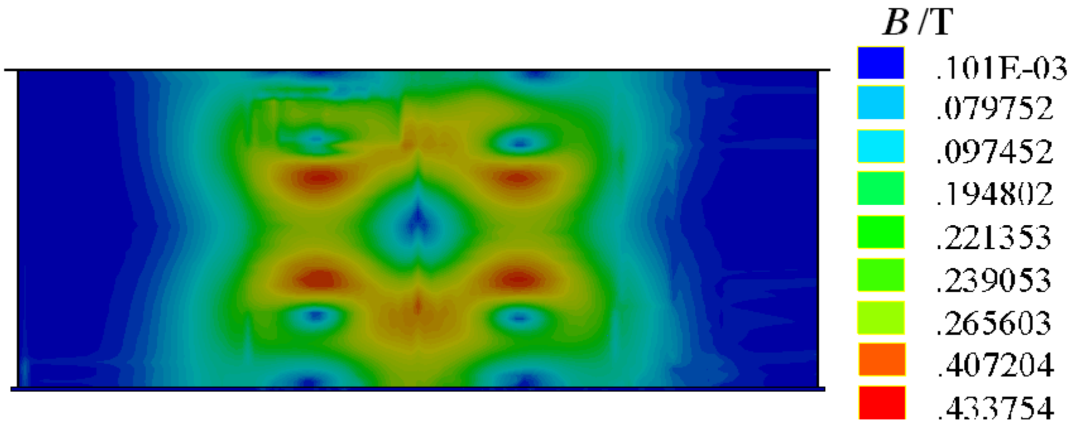

Figure.8 Eddy current distribution in transformer tank

The high voltage winding and the low voltage winding are considered simultaneously in transformer winding. Scanning method is used for meshing, free meshing method is used for iron core part, and the set frequency is 50 Hz in resonance method. Using ANSYS finite element software and APDL language programming, secondary development is carried out[8]. After meshing, the total number of units is 274927. The eddy current loss of transformer external tank is focused on. The total value of eddy current loss is 19722.5885W. The distribution of eddy current is shown in Figure 8. The eddy current loss distribution cloud chart in Figure 8 shows that heat source of the oil tank during the operation of the transformer is mainly induced eddy current heating under the current-carrying condition of the internal winding, and the eddy current distribution of the oil tank is extremely uneven under the short-circuit condition. On the other hand, the distribution of magnetic lines of transformer components is focused on as shown in Figure 9. The figure shows that under the action of sudden short-circuit current, the magnetic lines of transformer components are mainly distributed in the core and winding parts, and the distribution of magnetic lines near middle of the core is relatively dense, and the magnetic lines at both ends are divided.

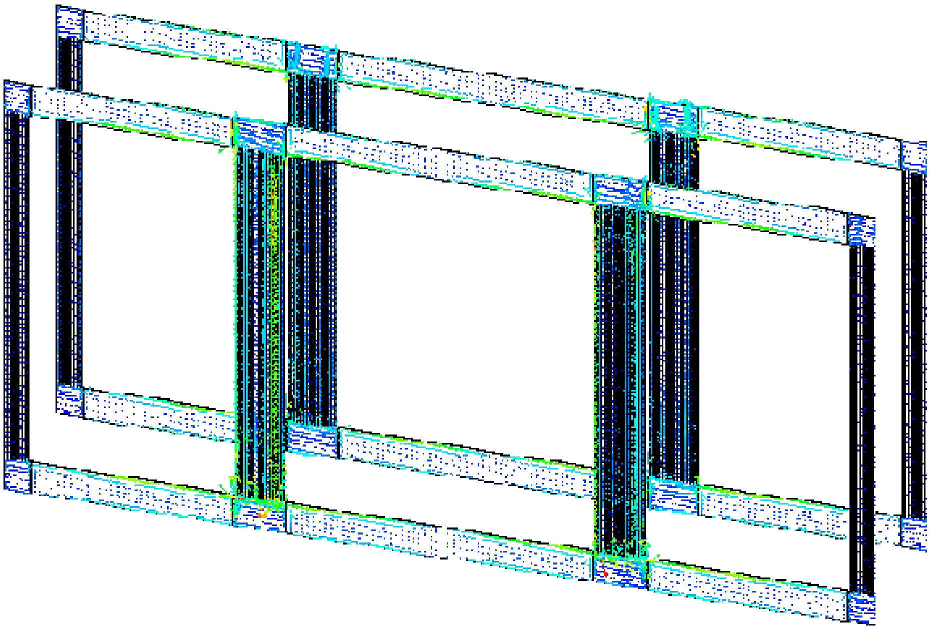

Figure.9 Magnetic line distribution in transformer component

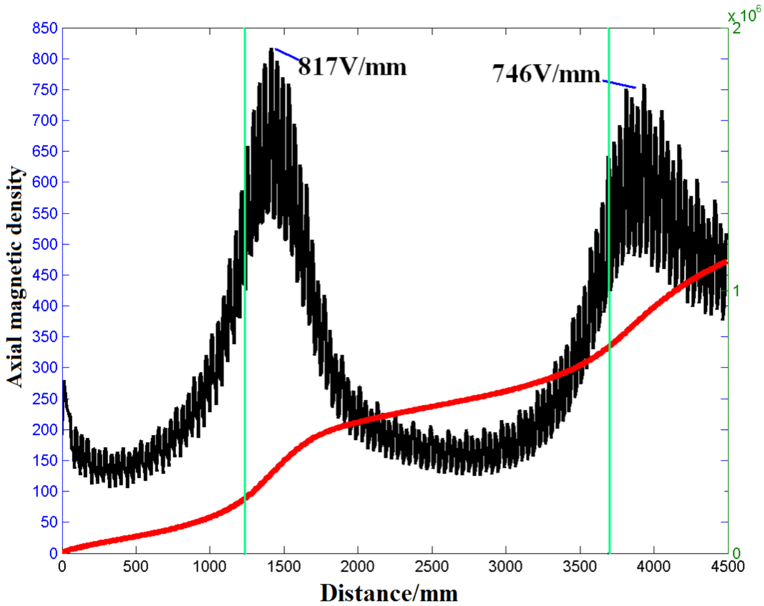

Figure.10 Axial magnetic density distribution of winding

At the same time, the axial magnetic density distribution of transformer winding is intercepted as shown in Figure 10. Figure 10 shows that the distribution of the axial magnetic density line is not uniform. There are two peaks and a trough in the middle, which is mainly affected by the metal structure such as the iron core and yoke. The key parameters such as asymmetric component duration and overshoot coefficient of short-circuit current waveform of distribution transformer are analyzed from the viewpoint of theoretical analytical formula and the simulation calculation model[9,10]. At the same time, the stress of winding magnetic line under short-circuit condition is analyzed by three-dimensional finite element simulation calculation model.

5. Conclusion

In this paper, the key parameters such as the asymmetric component duration and the overshoot coefficient of the short-circuit current waveform of distribution transformer are analyzed from viewpoint of theoretical analytic formula and the simulation calculation model. At the same time, the distribution and force of the winding magnetic line under short-circuit condition are analyzed by three-dimensional finite element simulation calculation model. The results show that the three-phase short-circuit current is larger than the single-phase and the double-phase short-circuit current, its value is 1.45 times of normal operation current, and it is asymmetric short-circuit current with gradual attenuation. The distribution of the magnetic induction intensity in the circumferential direction of iron core column is not uniform, and the degree of non-uniformity varies with height, and the magnetic density is divided under the short-circuit condition. From the point of view of FEM modeling, anti-short-circuit capability of the oil-immersed distribution transformer is analyzed theoretically. The distribution characteristics of short-circuit current and the magnetic field of oil-immersed distribution transformer under the short-circuit condition are obtained.

6. References

[1] Li Sheng-nan, Liu Shuang, Liu Jie et al. Calculation of current in winding of transformer with short circuited turn[J]. Transformer, 2017, 54(10): 1-4.
[2] Liu Yu,Zhang Jingzhuo, Lu Hailiang et al. Excitation inrush current test and simulation analysis of transformer in no-load closing switching[J]. High Voltage Apparatus, 2017,53(10)：117-123.
[3] Zhang Bo, Li Yan. Radial stability of large transformer windings under multiple inrush conditions [J]. Transactions of China Electrotechnical Society, 2017, 32(2)：71-76.
[4] Fan Lidong, Liu Jun, Zhang Anhong. Evaluation of short-circuit dynamic stability of amorphous alloy distribution transformer[J]. Transformer, 2017，54(12)：1-11.
[5] Zhao Lihua, Liu Danhua, Zhang Zongxi et al. Overload capability analysis and structure optimization of hybrid insulation system oil immersed transformer[J]. Water Resources and Power, 2017，35(10)：180-183.
[6] Wang Zheng, Zhao hengwei, Liu Qiancheng et al. Case analysis of transformer outlet short circuit fault based on multiple test[J]. Transformer, 2017，54(11)：56-60.
[7] Li Xinhai, Zeng Xinxiong, Liu Jianhui et al. Study on anti-short-circuit ability of transformer based on the zero loss deep current limiting technology [J]. High Voltage Apparatus, 2017, 53(10): 111-116.
[8] Wang Huan, Li Yan. Calculation and analysis of short circuit strength of large-scale power transformer windings considering residual stress[J]. Electric Power Automation Equipment, 2018，38(1)：105-109.
[9] Yang Yi, Liu Shi, Tian Feng et al. Simulation for transformer wingding vibration characteristics under short circuit impact[J]. Journal of Xi’an jiaotong university, 2017，51(10)：19-26.
[10] Zhang Peng, Wang Fochi, Zhou Ruoqi et al. Analysis and disgnosis of 220kV transformer winding short-circuit fault[J]. Transformer, 2017,54（11）：68-72.

Acknowledgments

Authors wishing to acknowledge assistance of “Research on key technology of hybrid insulating oil transformer” founded by State Grid Corporation of China .

IOP Conf. Series: Earth and Environmental Science **431** (2020) 012038 doi:10.1088/1755-1315/431/1/012038

Analysis of DC inter-electrode fault overvoltage in AC/DC hybrid power system

Rongfu ZHONG[1], Siwei WAN[1], Yunfeng XIA[1], Dongliang WEI[1], Wenzhi HE[1]

1 Dongguan Power Supply Bureau of Guangdong Power Grid Corporation, Dongguan, Guangdong, China
E-mail: zrf4832887@163.com

Abstract. AC/DC hybrid power system has become an important distribution system for high-proportion distributed renewable energy consumption and multi-energy supply. Among the DC-side fault overvoltage, the inter-electrode fault overvoltage is the most harmful to the system. In order to analyze the principle of overvoltage generation, this paper establishes a mathematical model for AC/DC hybrid power system, and researches the mechanism of inter-electrode fault overvoltage generation on the DC side of the system, and builds a Matlab/Simulink simulation model so that gets the simulation analysis results of 10kV DC and ±375V DC side in the system. The research shows that the system high-frequency mathematical model relation which obtained according to the mathematical mode is belongs to the coupled nonlinear time-varying system. The DC-side overvoltage development can be divided into three stages: after happening of the fault until the converter station is locked, after the converter station is locked until the fault is removed, after removal of the fault until the converter station is unlocked. Through modeling and simulation, it is verified that the development process of overvoltage is consistent with the theoretical analysis. According to the research conclusion, the method of 'arrester + parallel resistance + grounding device' is proposed to protect the DC side overvoltage of the system.

1. Introduction

It has become a trend that a large amount of distributed energy access to AC/DC power systems in the process of global energy revolution [1, 2], and renewable distributed energy plays an increasingly important role in the proportion of energy in the distribution system [3, 4]. With the rapid development of generalized DC loads such as inverter air conditioners and IT loads, traditional AC power distribution systems have many power conversion links and low efficiency[5, 6], while AC/DC hybrid power systems have AC/DC hybrid power supply. It meets the advantages of AC/DC energy access, less power conversion, simple structure and high efficiency, and has gradually become the preferred power supply system for various energy-using scenarios such as data centers, industrial parks, office and living parks[7, 8, 9]. Power electronic transformers are the key equipment for commutation in AC/DC hybrid power systems. Fully-controlled power electronic devices are used to realize bidirectional flow of AC and DC power [10, 11, 12]. Due to the existence of sophisticated devices and complex control of power electronic devices, the pressure and overcurrent capability are poor, so it is of great significance to carry out the DC side fault analysis in the system, especially the interpole faults with large faults [13, 14], so as to propose effective overvoltage protection measures.

Some researches have been carried out on the overvoltage of flexible DC systems in China. The internal overvoltage generation mechanism of Zhoushan multi-terminal flexible DC transmission project is simulated and analyzed. The overvoltage mechanism of the AC/DC side of the converter

station is analyzed in detail [15]. The DC overvoltage after the short-circuit fault of the DC line of the Zhangbei flexible DC power grid and the receiving converter station is analyzed, and the dynamic process of the DC system overvoltage before and after the DC breaker action is obtained [16]. Reference [17] analyzed the single-phase ground fault of the converter valve side busbar with the most over-voltage of the converter valve station, the short-circuit fault of the converter valve, the fault of the top of the converter valve to the ground, the grounding fault of the DC bus, and the ground fault of the DC line. A ±10kV two-terminal flexible DC distribution network is taken as an example for the AC side DC distribution network AC side fault, grid side fault, converter area fault, DC line area fault, and access equipment area fault[18]. The fault voltage of the class is simulated and analyzed. The above overvoltage analysis is mainly for the flexible DC system and its converter valve device, and the voltage level is relatively high. At present, the DC side overvoltage of the AC/DC hybrid power system with the power electronic transformer as the key equipment has not been studied.
In order to solve the DC side overvoltage problem of AC/DC hybrid power system, the new AC/DC hybrid power system structure with power electronic transformer is used to analyze the fault overvoltage mechanism on the DC side, and establish a mathematical model. The simulation of the inter-electrode fault of 10kV DC and ±375V DC is carried out, and the DC-side overvoltage protection principle and protective measures of AC/DC hybrid power system are proposed.

2. AC/DC hybrid power system

The AC/DC hybrid power system uses two power electronic transformers as the key equipment, covering 10kV AC, 10kV DC, 380V AC, ±375V DC, and which is connected by four voltage grade busbars. Among them, 10kV AC and 10kV DC are distribution voltages, and 380V AC and ±375V DC are used voltages. The 10kV DC bus and ±375V DC bus are connected to the renewable energy photovoltaic system, and the 380V AC bus is connected to the wind power system and the CSP system. The 10kV AC bus, 380V AC bus and ±375V DC bus are all powered to the load and are equipped with an uninterruptible power system (UPS) to provide stable and reliable power. The system can access a variety of distributed energy sources and different voltage level loads, enabling efficient consumption of regional distributed energy and meeting the power requirements of different types of loads. The AC/DC hybrid power system is shown in Figure 1.

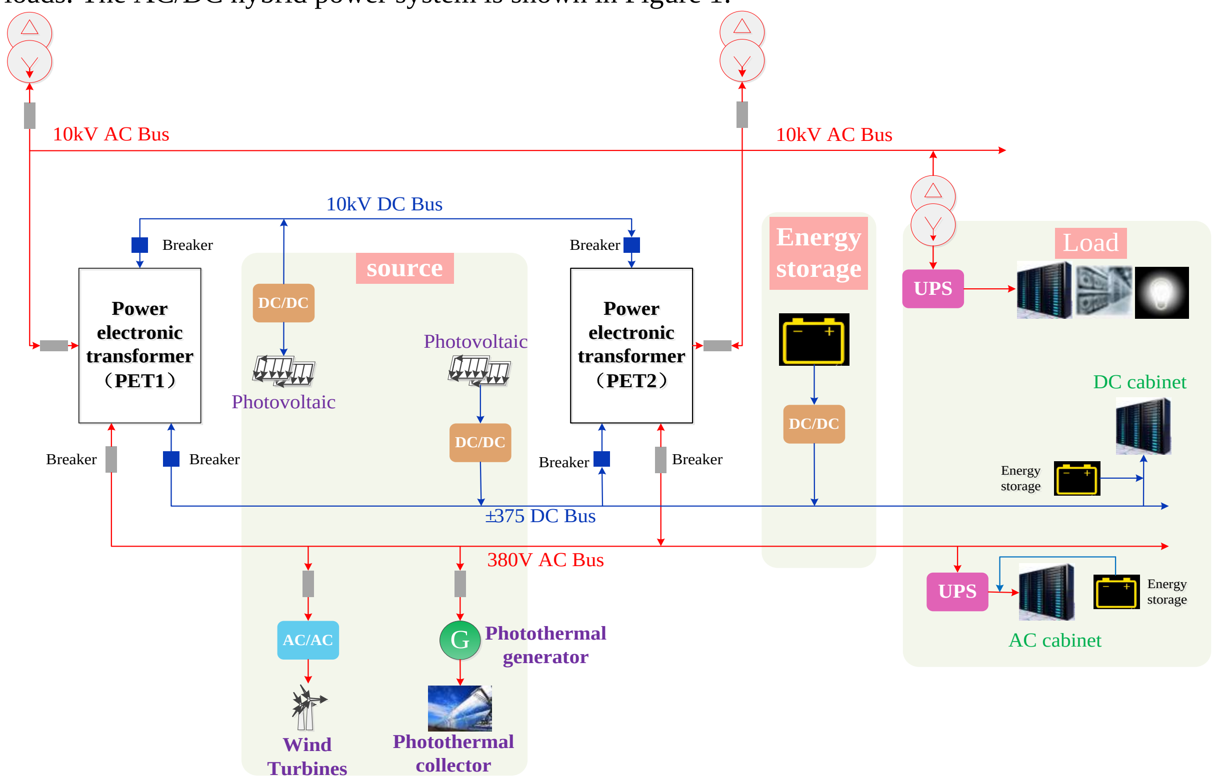

Figure 1 AC/DC hybrid power system

The AC/DC hybrid power system is a system with high renewable energy ratio access, and the power electronic transformer is used as the key equipment. The system overvoltage characteristics are different from the traditional power system overvoltage. In order to protect the system from overvoltage and keep the system stable, it is of great significance to carry out research on overvoltage of AC/DC hybrid power system. In the overvoltage analysis, there are unipolar ground overvoltage, lightning overvoltage, operating overvoltage, and inter-electrode fault overvoltage. Among them, the most influential system is the inter-pole fault over-voltage. Therefore, this paper focuses on the formation mechanism of the system-to-pole fault over-voltage and gives protective measures.

3. Mathematical model

In order to facilitate analysis of the overvoltage, the power electronic transformer is treated as a voltage source converter (VSC) according to the AC/DC hybrid power system structure of figure 1. Thus, a structural diagram of a two-port AC/DC hybrid power system is obtained, as shown in figure 2. This process does not affect the analysis of the mechanism of system overvoltage generation.

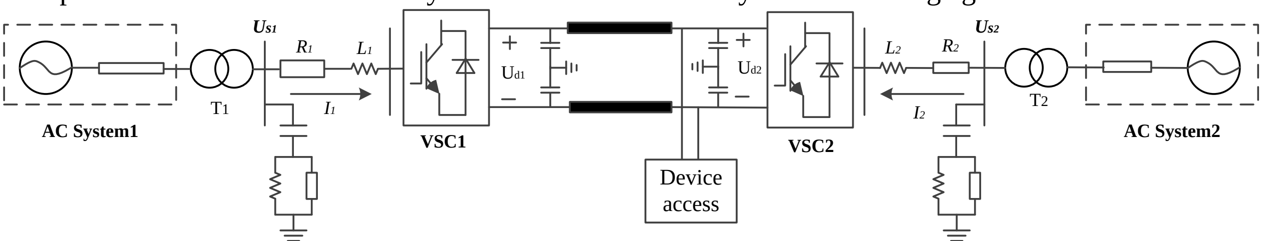

Figure 2 Structure diagram of two-port AC/DC hybrid power system

For the convenience of analysis, the following assumptions are made for the AC/DC hybrid power system. 1) The AC system on both sides takes the same voltage amplitude, but the initial phase and frequency of the voltage can be inconsistent. The three-phase AC voltage is sinusoidal. 2) Both the converter transformer and the commutating reactor are linearly symmetrical, regardless of their saturation state, and the transformer winding near the converter side adopts the "△" connection method, so there is no zero sequence component in the system. 3) The commutation reactance and equivalent loss of each phase in the two systems are symmetric. 4) The converters on both sides of the system have symmetry, that is, they all adopt a three-phase two-level topology, and the switching devices and other corresponding passive components are completely identical.

In order to further simplify the analysis, considering that the secondary side of the transformer adopts the "△" wiring mode, which is no zero-sequence component path in the system. Figure 2 can be simplified to some of the circuits shown in Figure 3.

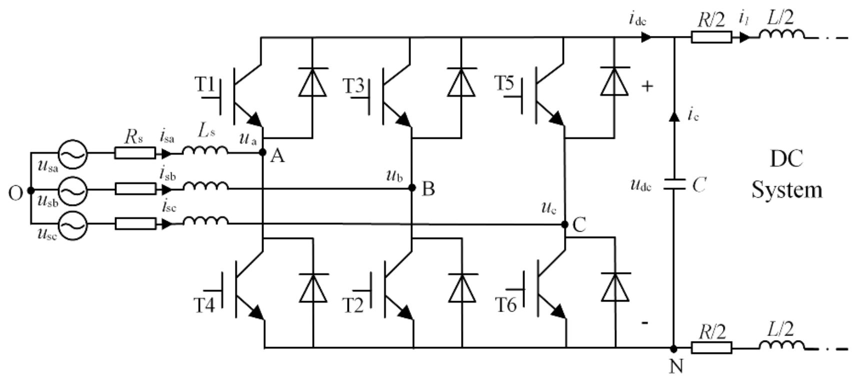

Figure 3 Three-phase voltage converter structure

If not specified, the side system of the AC/DC hybrid system is used for analysis. According to Kirchhoff's law, the voltage equation of phase A in Figure 3 can be obtained.

$$L\frac{\mathrm{d}i_{\mathrm{sa}}}{\mathrm{d}t}+R_{\mathrm{s}}\cdot i_{\mathrm{sa}}=u_{\mathrm{sa}}-\left(u_{\mathrm{AN}}+u_{\mathrm{NO}}\right) \tag{1}$$

Let the upper arm switching function of phase A be Sa and the lower arm switching function be $S_a{}'$. The upper arm of the A phase is closed and the lower arm is opened When Sa=1 and $S_a{}'=0$, then there is $u_{AN}=u_d$. The upper arm of the A phase is opened and the lower arm is closed when Sa=0 and $S_a{}'=1$, then there is $u_{AN}=0$, there is a relationship $S_a+S_a{}'=1$. There are $i_{sa}+i_{sb}+i_{sc}=0$ in the three-phase three-wire system. in addition, there is $u_{sa}+u_{sb}+u_{sc}=0$ when the three-phase AC system voltage is symmetrically balanced. It is now substituted into formula (1).

$$u_{NO}=-\frac{u_d\cdot(S_a+S_b+S_c)}{3} \tag{2}$$

Substituting the formula (2) into the formula (1) gives the following formula.

$$L\frac{di_{sa}}{dt}+R_s\cdot i_{sa}=u_{sa}-\frac{u_d\cdot(2S_a-S_c-S_b)}{3} \tag{3}$$

$$L\frac{di_{sb}}{dt}+R_s\cdot i_{sb}=u_{sb}-\frac{u_d\cdot(2S_b-S_a-S_c)}{3} \tag{4}$$

$$L\frac{di_{sc}}{dt}+R_s\cdot i_{sc}=u_{sc}-\frac{u_d\cdot(2S_c-S_a-S_b)}{3} \tag{5}$$

There is the following differential relationship on the DC side of the system.

$$C\frac{du_d}{dt}=(S_a\cdot i_{sa}+S_b\cdot i_{sb}+S_c\cdot i_{sc}) \tag{6}$$

Equations (3)~(6) constitute the high-frequency mathematical model of the system. It can be obtained that the current per phase of the system is determined by the three-phase switching function, so it is a nonlinear time-varying system coupled with each other.

4. The overvoltage generation mechanism of DC inter-electrode fault

According to Fig. 2, the equivalent circuit of the two-port AC/DC hybrid power distribution system can be obtained, as shown in Fig. 4. In the figure, I is a DC current power supply. I_1 is a DC side photovoltaic current power supply. C_N is a overvoltage absorbing capacitor of neutral point bus. D is a single-phase conduction diode of analog VSC. R_1 and C_1 are respectively resistance and capacitance of converter stations. L is a smoothing reactor of DC system. C_3 is a storage capacitor. R, L, C are the unit impedance values of the DC side, respectively.

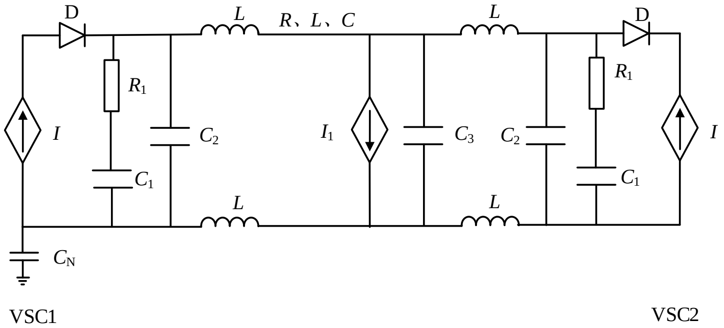

Figure 4 Equivalent circuit of of two-port AC/DC hybrid power system

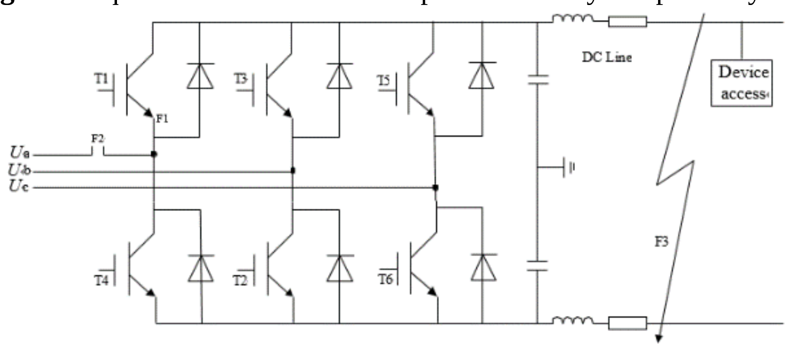

Figure 5 Inter-electrode fault on the DC side of the system

The most serious fault in the AC/DC hybrid distribution network system is the two-pole short-circuit fault, so the overvoltage caused by the two-pole short-circuit fault is mainly analyzed. The AC side and the DC side will simultaneously feed the fault current to the fault point When the fault occurs. Considering that such a large fault current in the actual system will burn the insulated gate bipolar transistor (IGBT) in the converter. The IGBT in the actual engineering has a reliable self-protection function, which causes the DC fault to occur. It can be turned off immediately. However, although the self-protection function of the IGBT does not burn it in the event of a DC fault, the short-circuit current is still supplied to the AC and DC sides after the IGBT inside the VSC is turned off due to the presence of the freewheeling diode. This not only jeopardizes the freewheeling diode itself, but also causes the DC side fault to be completely isolated, affecting the safe and reliable operation of the grid.

Starting from the internal structure of the VSC, considering the self-protection function of the IGBT, an inter-electrode fault F3 as shown in Fig. 5 occurs on the DC side of the system. Since the IGBT will be turned off immediately due to the self-protection function due to the fault, which is assumed that the IGBT is immediately turned off after the fault occurs for the convenience of analysis.

The development process of overvoltage on the DC side is divided into three phases. The first stage, the DC voltage U_{dc} is greater than the AC side line voltage at the beginning of the fault. At this time, the DC side fault current will be discharged mainly from the DC capacitor to the short circuit point. Among them, L_1 is the bridge arm reactance, C_1 is the VSC DC side shunt capacitor, L_0 is the DC side equivalent reactance of the discharge loop, R_0 is the DC side equivalent resistance of the discharge loop, and R_1 and C_1 are the converter station resistance and capacitance, respectively. It can be seen from Fig. 3 that the dynamic process of this stage can be expressed as differential equation (7).

$$LC\frac{\mathrm{d}^2u_{\mathrm{dc}}}{\mathrm{d}t^2}+RC\frac{\mathrm{d}u_{\mathrm{dc}}}{\mathrm{d}t}+u_{\mathrm{dc}}=0 \tag{7}$$

Since the equivalent resistance on the DC side is small, the damping is generally satisfied $R<2L/C$, so the discharge of the capacitor C is an underdamped oscillation process. It can be obtained that the DC capacitor discharge is a second-order under-damped oscillation process, and the capacitor voltage attenuates the oscillation zero-crossing. At the same time, since the short-circuit current supplied by the AC side in this stage is only the continuous current of the AC reactor, no overcurrent occurs in the AC side and the inverter. On the DC side, an overcurrent occurs due to the discharge of a large capacitor.

The second stage, when U_{dc} drops to the AC side line voltage, the AC side power supply will begin to feed the fault current through the diode to the fault point. At this time, the conduction of the diode is based on the natural commutation principle of the uncontrolled rectifier bridge, so the process can be referred to as a diode natural commutation phase. At this stage, the AC power source and the DC capacitor are simultaneously discharged to the fault point, and the diode has a commutation process of alternately turning on and off. Each time this commutation process occurs, the dynamic process is re-solved once. The initial conditions are determined by the previous commutation process. Taking T1 and T2 conduction as an example, the flow path of the fault current is as shown in figure 6.

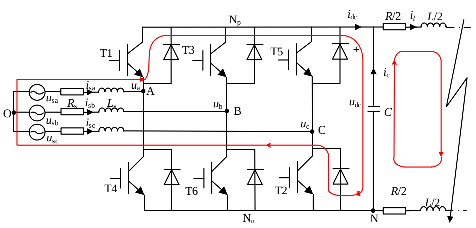

Figure 6 the flow path of fault current

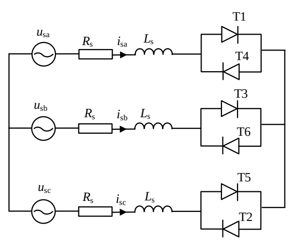

(a) Equivalent circuit of AC side

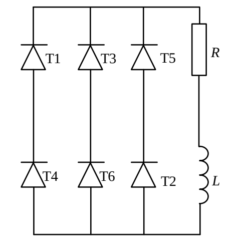

(b) Equivalent circuit of DC side

Figure 7 Equivalent circuit of the diode full conduction phase

The i_{sa} 、 i_l 、 u_{dc} are the state variables in the figure. Solving the multivariate state equation (8) can obtain the transient solution of AC and DC current and DC voltage under this condition.

$$\begin{bmatrix} \dot{i}_{sa} \\ \dot{i}_l \\ \dot{u}_{dc} \end{bmatrix} = \begin{bmatrix} -\frac{R_s}{L_s} & 0 & -\frac{1}{2L_s} \\ 0 & -\frac{R}{L} & \frac{1}{L} \\ \frac{1}{C} & -\frac{1}{C} & 0 \end{bmatrix} \begin{bmatrix} i_{sa} \\ i_l \\ u_{dc} \end{bmatrix} + \begin{bmatrix} \frac{1}{2L_s} \\ 0 \\ 0 \end{bmatrix} u_{sac} \tag{8}$$

The capacitor is in a charging state and the voltage is raised when the input and output power of the converter station is unbalanced. The following formula can be obtained when the A phase and the C phase are turned on according to Fig. 6,

$$u_A(t) + u_{ap}(t) + u_{dc}(t) + u_{cn}(t) - u_C(t) = 0 \tag{9}$$

Where, $u_A(t)$ is the instantaneous phase A voltage of the converter station outlet. $u_C(t)$ is the instantaneous phase voltage of the C-phase of the converter station. $u_{AC}(t)$ is the instantaneous phase voltage between phase A and phase C. $u_{ap}(t)$ is the instantaneous voltage of the phase A diode. $u_{cn}(t)$ is the instantaneous voltage of the C-phase diode. The capacitor starts to charge When the A phase and the C phase are turned on. Therefore, it is known from the formula (9). DC overvoltage will occur during the charging process of the capacitor. The waveform of the overvoltage will pulsate because the diodes of each phase are alternately turned on.

The third stage, the back EMF of the DC side short-circuit reactance will cause the six diodes in the VSC to be turned on when the DC capacitor voltage U_{dc} decays and oscillates through zero. Thereby a first-order discharge loop is formed on the DC side. The DC capacitor voltage is clamped to 0 by the diode. Therefore, the Np and Nn potentials of Figure 6 are equipotential, and the AC power supply circuit can be equivalent to Figure 7(a).

$$\begin{cases} U_{d+} = U_a + U_b + U_c \approx 0 \\ U_{d-} = U_a + U_b + U_c \approx 0 \\ U_d = U_{d+} + U_{d-} \approx 0 \end{cases} \tag{10}$$

Where, U_{d+} is the DC side positive voltage of the converter station. U_{d-} is the negative voltage of the converter station. U_i(i=a, b, c) is the outlet phase voltage of the AC side of the converter station. Therefore, the circuit shown in Figure 7(b) is completely symmetrical. The AC side is equivalent to a three-phase short circuit. Therefore, this stage can be decomposed into two parts of the AC side three-phase short circuit and the DC side side discharge, as shown in figure 7. Set the DC voltage zero crossing time to zero time. The A phase voltage on the AC side is expressed as $u_{sa} = U_m \sin(\omega t + \phi_0)$. The instantaneous value of phase A current is I_{a0}. The instantaneous value on the DC side is I_0'. The fault current flowing through the diode during this process can be obtained according to Figure 7.

$$\begin{cases} i_{T1} = \frac{1}{3} i_l + \frac{1}{2} i_{sa} \\ i_{T4} = \frac{1}{3} i_l - \frac{1}{2} i_{sa} \end{cases} \tag{11}$$

The above analysis shows that the current i_l of the DC link in this phase is an attenuation. The current i_{sa} supplied by the AC side consists of an attenuation component and a sinusoidal steady-state component. Therefore, the attenuation component decreases with i_l and i_{sa}. The sinusoidal steady-state component has the potential to cause a zero-crossing of the current flowing through the diode. Once the current of any of the six diodes crosses zero, the three-phase symmetrical short-circuit state of the AC side at this stage is destroyed. This phase ends and enters the natural commutation phase of the diode.

5. Simulation analysis

In the Matlab/Simulink environment, a two-phase AC/DC hybrid power system was built. The topology wiring diagram of system is shown in Figure 2. There are two VSC converter stations, and station 1 and station 2 are both fixed DC voltage control. The distributed power supply that is connected is exemplified by a photovoltaic power supply. The DC load is replaced by a DC resistor. According to the foregoing analysis, the two-pole short-circuit fault overvoltage of the 10kV and ±375V DC busbars is analyzed.

5.1 The inter-electrode fault overvoltage simulation of 10kV DC side

Two-pole short-circuit fault is introduced on the 10kV DC side when the system runs stably to 1s. The corresponding simulation curve is shown in Figure 8.

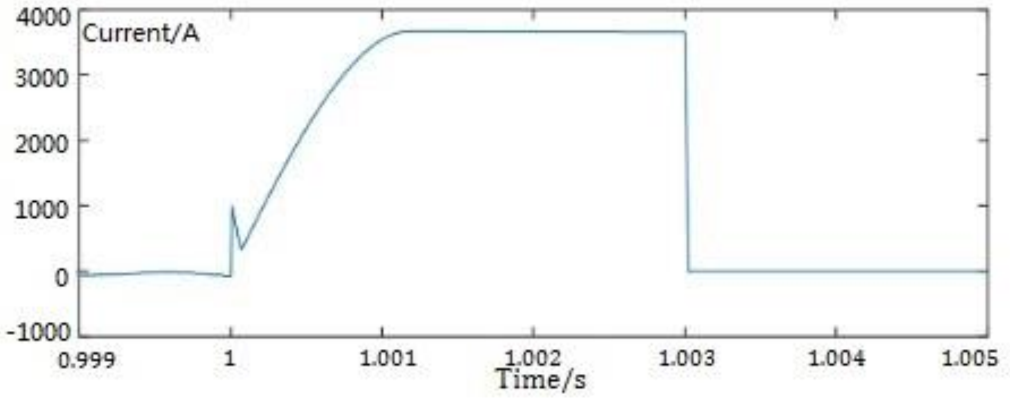

(a) 10kV DC port current

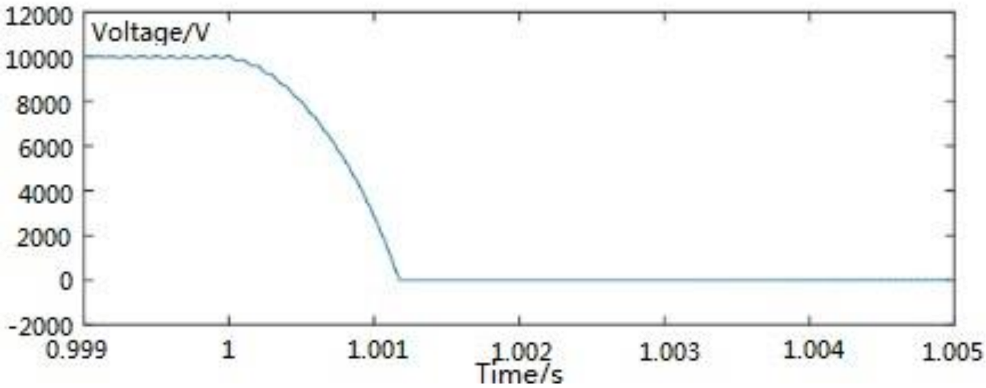

(b) 10kV DC port voltage

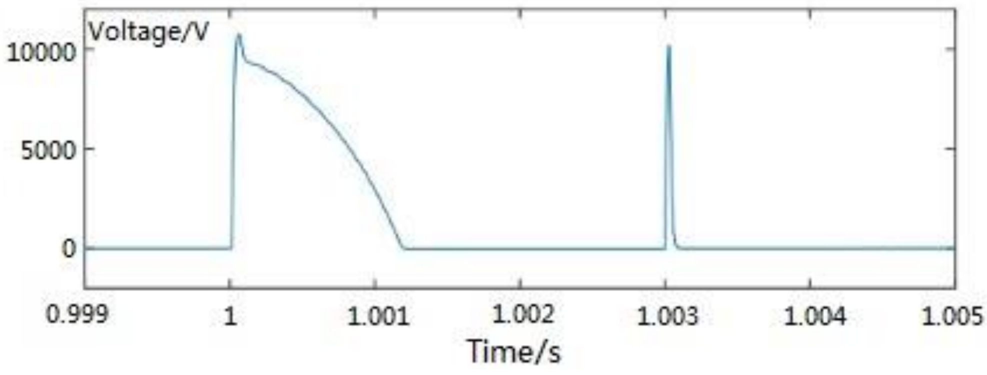

(c) 10kV DC FCC voltage

Figure 8 Simulation waveform of 10kV DC inter-pole short circuit fault

It can be seen from the simulation curve of figure 8 that the development process of the overvoltage on the DC side is divided into three stages. The first stage, time is from 1s to 1.00119s. A fault current controller (FCC) is connected to the 10kV DC side. 10~19 μs after the fault occurs, the short-circuit current will trigger the overcurrent protection of the FCC. The FCC is put into its current limiting reactance unit to suppress the rising speed of the short circuit current. At the same time, a breaking command is issued to isolate the entire 10kV area to match the actions of other DC fault isolation devices. Therefore, the short-circuit current at the exit of the 10kV line rises at the moment of failure,

IOP Conf. Series: Earth and Environmental Science **431** (2020) 012038 doi:10.1088/1755-1315/431/1/012038

and the fault current controller is input to limit its rising speed at 10 μ s. The short circuit current drops, and the short-circuit current rises slowly and reaches a maximum value of 3680A. The second stage, time is from 1.00119s to 1.003s. The AC side current quickly changes to a three-phase short-circuit current when the DC voltage drops to zero. Since the fault is not removed, the DC voltage will remain at zero and the DC current will remain at its maximum. The third stage, 1.003s and beyond. 3 seconds after the failure, the FCC completes the breaking. The voltage at the FCC is again sharply increased to a value of nearly 10 kV, and immediately drops to zero immediately after the action is completed. The overvoltage that appears here is an operating overvoltage.

5.2 The inter-electrode fault overvoltage simulation of ±375V DC side

After the ±375V DC system enters the steady state, an inter-electrode short-circuit fault is introduced at time 1.5s. After the fault occurs, the current-limiting reactance of all fault current controllers is applied to suppress the rise of the short-circuit current. After 1ms, the differential protection is activated and the circuit breaker is instantly disconnected. Thereby the fault area is isolated.

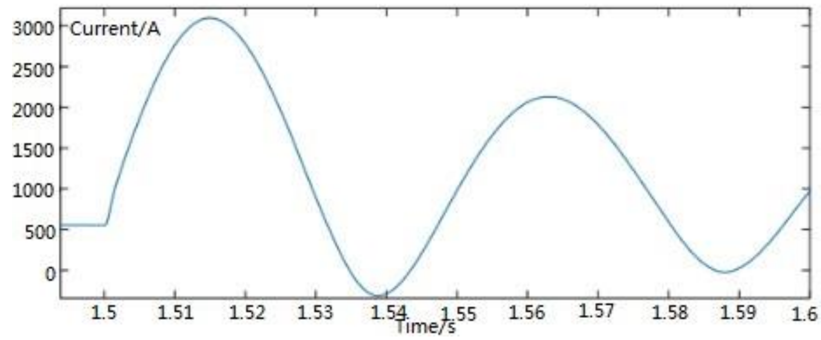

a) ±375V DC port current

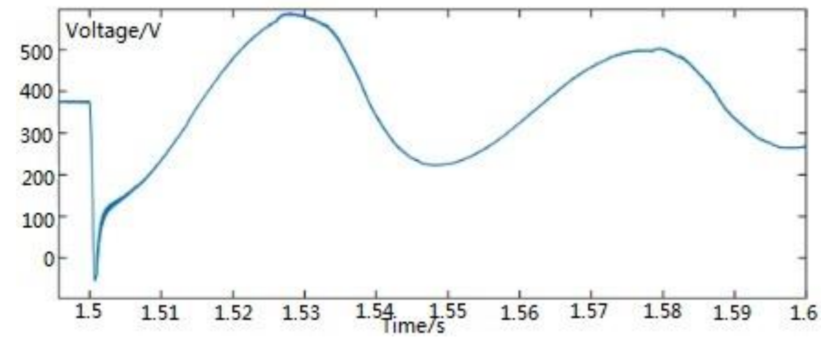

(b) ±375V DC port voltage

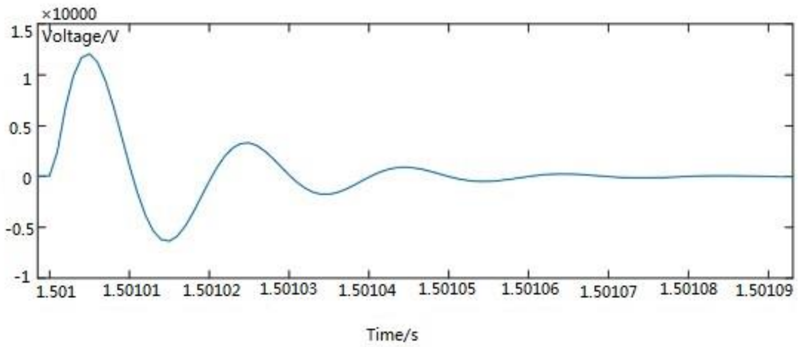

(c) Circuit breaker port voltage

Figure 9 Waveform diagram after ±375V DC side inter-pole short circuit fault

After the ±375V DC-side inter-pole short-circuit fault occurs, the port current, voltage, and breaker port voltage waveforms are as follows. As can be seen from Figure 9(a), the current rise speed and peak value of the ±375V DC port are suppressed due to the presence of the current limiting reactance of the fault current controller. As can be seen from Figure 9(b), the AC power source and the DC capacitor are discharged together to the fault point. The ±375V DC port voltage continues to drop to around zero. After the circuit breaker is activated, the fault line is cleared, the capacitor is in a charging state, and the input and output power are unbalanced. This leads to an increase in voltage with an extreme value of 588.72V. As can be seen from Figure 9(c), the circuit breaker action causes a high overvoltage at its port, with a maximum amplitude of 12000V.

5.3 Overvoltage protection measures

Modern power systems often use a gapless metal oxide surge arrester (MOA) as a critical device for overvoltage protection. Under normal conditions, the arrester has a high impedance characteristic and exhibits a low impedance characteristic when an overvoltage is applied. Due to the nonlinear nature of the arrester, it can only pass the current caused by the overvoltage without generating the power frequency follow-up current. A reasonable lightning arrester configuration can not only effectively protect the equipment in the converter station, but also improve the reliability of the system. It also reduces the cost of equipment and is optimal in terms of technology and economy.

According to the characteristics of the over-voltage across the DC side, a lightning arrester can be installed to protect against the hazard caused by the DC side overvoltage. The resistor can be connected in parallel with the arrester to limit the overvoltage amplitude. The lightning arrester is connected to the grounding device to effectively introduce a large current into the earth, which is called the ‘arrestor + parallel resistance + grounding device’ method.

6. Conclusion

The overvoltage research is carried out on AC/DC hybrid power system in the paper. According to the above research, the following conclusions can be obtained. The AC/DC hybrid power system with power electronic transformer has many advantages for power supply in various parks. It can access a variety of distributed energy sources and different voltage level loads. Achieve efficient consumption of regional distributed energy and meet the power supply requirements of different types of loads.

When an inter-pole short circuit fault occurs on a 10kV DC line, the voltage drops to zero and the current reaches 3680A. When an inter-pole short circuit fault occurs on a ±375V DC line, the circuit breaker port voltage reaches 12000V and the current reaches 3000A.

The problem of fault overvoltage between the DC side of the system can be solved by the method of ‘arrester + parallel resistance + grounding device’. That is, the lightning arrester and the resistor are connected in parallel, and the lightning arrester and the grounding device are reliably grounded to protect against the danger of overvoltage.

7. References

[1] Dong Chaoyang, Zhao Junhua, Wen Fuzhen,et al. From Smart Grid to Energy Internet: Basic Concepts and Research Framework[J]. Automation of Electric Power Systems, 2014, 38(15): 1-11.

[2] Sun Hongbin, Guo Qinglai, Pan Zhaoguang. Energy Internet: Idea, Architecture and Frontier Outlook[J]. Automation of Electric Power Systems, 2015, 39(11): 3005-3013.

[3] Ma Wei, Zhou Xiaoxin, Shang Yuzhen, et al. Energy Internet concept, key technologies and development models [J]. Power Grid Technology, 2015, 39(11): 3014-3022.

[4] Zhang Guorong, Chen Xiayu. A Summary of the Future Development of Energy Internet[J]. Electric Power Automation Equipment, 2017, 37(01): 1-7.

[5] Dong Xiaofeng, Su Yirong, Wu Jian, et al. Design and engineering demonstration of active distribution network supporting urban energy Internet[J]. Proceedings of the CSEE, 2018, 38(S1): 75 -85.

[6] Pu Tianjiao, Liu Kewen, Chen Naishi, et al. Urban energy Internet architecture based on active distribution network and its key technologies [J]. Chinese Journal of Electrical Engineering, 2015, 35(14): 3511-3521.

[7] Qi Wei, Wang Keyou, Li Guojie, et al. Layer and Distributed Optimal Scheduling of AC/DC Hybrid Active Distribution Network[J]. Proceedings of the CSEE, 2017, 37(07): 1909 -1918.

[8] Zhu Yongqiang, Jia Lihu, Cai Bingqian, et al. Overview of Topology and Basic Control Strategies for AC/DC Hybrid Microgrid[J]. High Voltage Engineering, 2016, 42(09): 2756-2767.
[9] Zhang Wei, Tang Wei, Liang Jun, et al. Power-voltage coordinated control of AC/DC hybrid medium voltage distribution network based on VSC[J]. Proceedings of the CSEE, 2016, 36(22): 6067 -6075.
[10] Zhao Zhengming, Feng Gaohui, Yuan Liqiang,et al. Development of power router and its key technologies[J]. Proceedings of the CSEE, 2017, 37(13): 3823-3834.
[11] Li Zixin, Gao Fanqiang, Zhao Cong, et al.Summary of Power Electronic Transformer Technology Research[J]. Proceedings of the CSEE, 2018, 38(05): 1274-1289.
[12] Ma Weimin, Wu Fangzhen, Yang Yiming, et al. Current Status and Application Prospects of Flexible DC Transmission Technology[J]. High Voltage Engineering, 2014, 40(08): 2429-2439.
[13] Tang Guangfu, Luo Xiang, Wei Xiaoguang. Multi-terminal HVDC and DC grid technology[J]. Proceedings of the CSEE, 2013, 33(10): 8-17+24.
[14] Tang Guangfu, He Zhiyuan, Pang Hui. Research, Application and Development of Flexible DC Transmission Engineering Technology[J]. Automation of Electric Power Systems, 2013, 37(15): 3-14.
[15] Deng Xu, Wang Dongju, Shen Yang,et al. Transient Overvoltage in Converter Station of Zhoushan Multi-End Flexible DC Transmission Project[J]. Power system protection and control, 2013, 41(18): 111-119.
[16] Li Yingbiao, Bu Guangquan, Wang Wei,et al. Analysis of DC overvoltage during short circuit of DC line in Zhangbei soft power grid project[J]. Proceedings of the CSEE, 2017, 37(12): 3391 -3399+3666.
[17] Zhang Zheren, Xu Zheng, Xue Yinglin. Research on overvoltage protection and insulation coordination of MMC-HVDC system[J]. Power System Protection and Control, 2013, 41(21): 58-64.
[18] Su Yijing. Research on Overvoltage Simulation and Equipment Insulation Coordination of DC Distribution Network [D]. Hangzhou: Zhejiang University, 2018.

Acknowledgments
Funding organisation: Supported by National Key Research and Development Program 2017YFB0903205.

IOP Conf. Series: Earth and Environmental Science **431** (2020) 012039 doi:10.1088/1755-1315/431/1/012039

Research on energy efficiency management method of AC/DC hybrid distribution system

Juan ZHOU[1], Wenjing XIE[1], Yunfeng XIA[1], Feng XUE[1], Junni SU[1]

1 Dongguan Power Supply Bureau of Guangdong Power Grid Corporation, Dongguan, China
E-mail: zhou_juanjane@126.com

Abstract. With the increasingly serious problems of fossil energy crisis and environmental pollution, vigorous development of Distributed Renewable Energy has become an important means of energy structure reform and energy consumption transformation. On the distribution side, AC/DC hybrid distribution system has been widely studied for its advantages of accessing multiple types of energy, satisfying diversification energy demand, realizing multi-energy complementation and improving grid security. The energy efficiency evaluation and management of AC/DC hybrid system are of great guiding significance to the planning and design of AC/DC system. However, traditional energy efficiency management mainly reduces primary energy consumption by saving electricity. For AC/DC systems with multiple distributed energy sources, it is difficult to reflect the efficiency level of the whole system by considering a single technology or a single part of energy efficiency management. Aiming at the characteristics of AC/DC hybrid distribution system, this paper studies the energy efficiency management method of the system. Firstly, combined with energy efficiency evaluation and system economic analysis, energy efficiency evaluation index of AC/DC hybrid distribution system are formulated. Secondly, the energy efficiency management method is studied through the study of adjustable load, transferable load and different types of load overall management method. Then the method of combining power quality and energy efficiency is studied. Finally the interaction between source and load is studied to improve the energy efficiency of the system. The energy efficiency management method proposed in this paper can fully tap the potential of load adjustable and energy saving, improve the comprehensive energy utilization efficiency of the system, which provides a basis for the engineering application of AC/DC hybrid power grid.

1. Introduction

In recent years, with the changes of the social environment such as energy security, climate crisis and environmental protection, many countries have implemented the changes of energy structure and energy consumption[1-3]. Energy internet, which is a integrated energy system with multiple energy sources has become the trend of energy development. As an important unit of energy internet, AC/DC distributed system not only contains multiple types of energy input to meet the diversified energy needs, but also promotes the matching of supply and demand within the system and enhances the security of power grid. With the improvement of power market and the widespread application of communication and measurement facilities, load optimization brought by demand-side participation has become an important factor that cannot be ignored in the planning and operation of energy interconnected AC/DC distributed system[4]. Considering the multi-energy coordination and optimization of energy supply and demand, AC/DC distributed system can not only achieve multi-energy complementation, but also give full play to the comprehensive regulation potential of demand response and energy storage equipment, promote the absorption of Distributed Renewable energy, and achieve high coupling between supply and demand[5].

The traditional energy management of distribution network usually achieves the goal of energy saving and consumption reduction by means of the transformation of process and equipment[6-8]. This method only pays attention to the energy saving of partial process technology, and lacks the scientific management of the energy efficiency of the whole system. According to the common energy use scenarios of AC/DC hybrid distribution network and the characteristics of multi-energy interaction, this paper proposes a calculable and replicate energy efficiency management method for AC/DC hybrid distribution system[9-12]. It includes the design of indicators for energy efficiency evaluation, system energy efficiency management method and energy efficiency management platform.This scheme can realize the efficient utilization of Distributed Renewable Energy and multiform energy storage, optimize the allocation of resources and improve economic efficiency, and help to alleviate the situation of increasing scarcity of traditional fossil energy, make full use of green energy and realize energy transformation.

2. Architecture design of AC/DC hybrid distribution system

This paper designs an AC/DC hybrid distribution system. As shown in Figure 1, the system includes photovoltaic system, wind power generation, photothermal power generation and thermal utilization system, and storage system. Through multi-port power electronic transformer, the distribution system has formed four voltage levels: 10kV AC and 10kV DC, 380V AC and ±375V DC.

The structure has the following advantages:

- It improves the reliability, flexibility and economy of operation and facilitates redundancy expansion through parallel expansion of power electronic transformers.
- On the power side, distributed renewable energy can flexibly select different voltage levels according to the size of capacity, which is conducive to renewable energy.
- On the load side, the generalized DC energy equipment represented by IT load, frequency conversion air conditioning, DC lighting and electric vehicle can be directly connected to the DC power grid, which reduces the loss of the converter link and improves the energy efficiency of the system.

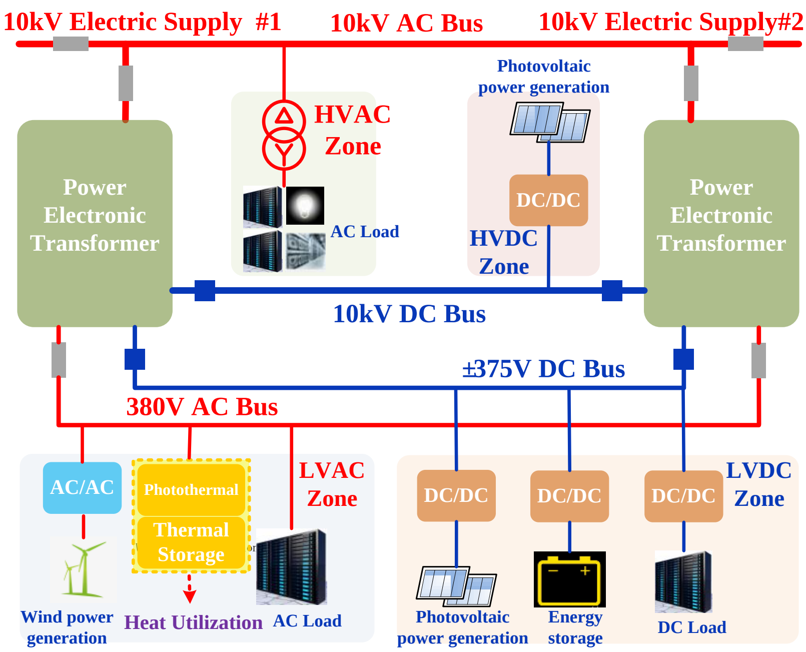

Figure 1. Architecture of AC/DC Hybrid Distribution System

3. Design of energy efficiency evaluation index

3.1. Energy efficiency evaluation index for each part of AC/DC hybrid distribution system

AC/DC distributed energy system can be divided into three parts: energy supply side, energy transmission channel and energy consumption side. According to the characteristics of these three parts, this paper formulates corresponding energy efficiency evaluation index[13].

3.1.1. Energy supply side

The power supply of AC/DC hybrid distribution network includes photovoltaic, wind, photothermal, storage, heat storage, generator, lithium bromide absorption chiller and other distributed power sources. Its energy efficiency index can be divided into two categories: process energy efficiency index and economic energy efficiency index[14]. The process energy efficiency index includes primary energy utilization rate and energy conversion efficiency, which can be obtained by optimizing energy saving of equipment and reducing multiple AC/DC converter links.Economic energy efficiency index includes initial investment cost, operation and maintenance cost and life expectancy, which can be optimized by means of energy efficiency management.

3.1.2. Energy transmission channel

AC/DC hybrid distribution network system realizes energy transmission and distribution through power electronic transformer and distribution line[15]. The energy efficiency evaluation object of energy transmission channel mainly focuses on the loss index of distribution line and power electronic transformer.

3.1.3. Energy consumption side

The energy efficiency evaluation index of the energy consumption side is embodied in the aspects of power consumption and power quality.

3.2. Comprehensive energy efficiency evaluation index

For a highly coupled system with multiple distributed energy sources and purchased electricity input, convert, consumption and storage, the energy efficiency of a single technology or link alone is not enough to reflect the efficiency level of the whole system, and the whole system needs to be considered as a whole to examine its energy efficiency level.

Considering that the whole AC/DC system, input can be divided into two types: outsourced electricity and distributed primary energy. The outsourced electricity includes fossil energy generation and renewable energy generation[16]. Distributed primary energy is mainly consist of solar energy and wind energy. The output power includes heat energy and cold energy. The comprehensive energy efficiency evaluation index of AC/DC distribution system can be defined as the ratio of total cold, heat and electricity to the input of fossil energy. The greater the ratio of total electricity to fossil energy input, the higher the energy efficiency.

The energy conversion path of AC/DC distribution system is shown in Fig. 2. The energy input of the system can be divided into two types: outsourced electricity and distributed primary energy. The outsourced electricity includes fossil energy generation and renewable energy generation. Distributed primary energy is mainly consist of solar energy and wind energy. Many kinds of energy, such as photovoltaic, wind power, photothermal and so on, are transformed into cold, heat and electricity which directly consumed by users through AC-DC hybrid distribution system. In the figure, Characters on the upper and left sides of the energy streamline represent the energy input or power input through the path.[17] Characters on the lower and right sides of the energy streamline represent the efficiency of energy conversion through the path.

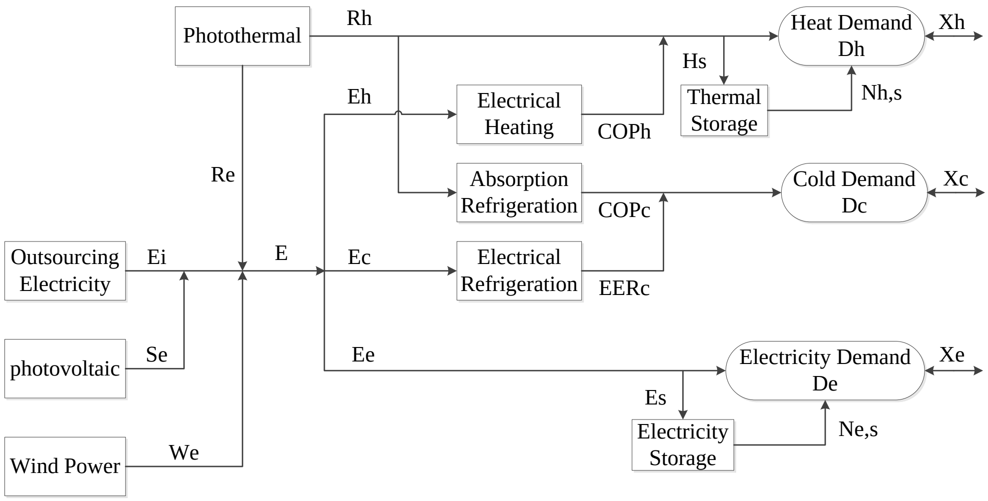

Figure 2. Energy Conversion Path Map

Considering such factors as energy storage loss, solar energy utilization and outward supply, the cooling D_c', heat $D_h'$and electricity D_e'required by the system can be expressed by equation (1) to equation (3)

$$\boldsymbol{D_c' = D_c + X_c} \tag{1}$$

$$\boldsymbol{D_h' = D_h + H_s(1 - N_{h,s}) + X_h - R_h} \tag{2}$$

$$\boldsymbol{D_e' = D_e + E_s\left(1 - N_{e,s}\right) + X_e} \tag{3}$$

Where D_c,D_h, $D_e$are the system demand of cooling,heat and electricity; X_c,X_h, X_e are the outward supply energy;E_s,H_s are the capacity of energy storage;Nh,s,Ne,s are the conversion efficiency of energy storage;X_h X represents direct utilization of heat.

The energy supply and demand balance equation of distributed energy system is shown in equation(4) to (6)

$$\boldsymbol{E_i = E - S_e - W_e - R_e} \tag{4}$$

$$\boldsymbol{E = E_h + E_c + E_e} \tag{5}$$

$$\boldsymbol{E_e = D_e'} \tag{6}$$

Where E_i, S_e,W_e,R_e are outsourced electricity, photovoltaic energy, wind energy, photothermal energy; E, E_c,E_h,E_e are the total energy, cooling, heat and electricity required by the system

The comprehensive energy efficiency of multi-energy complementary distributed energy system is defined as the ratio of total demand for cold, heat and electricity to fossil energy input (converted into equivalent standard coal). Its comprehensive calculation formula is shown in equation (7).

$$\boldsymbol{\eta_t = \frac{D_c'+D_h'+D_e'-H_s(1-N_{h,s})-E_s(1-N_{e,s})-R_h}{(E_h+E_c+E_e-S_e-W_e-R_e)\theta_e}} \tag{7}$$

4. Research on energy efficiency management method

From the energy efficiency evaluation index, we can see that the main way to improve the energy efficiency of the supply side is to increase the output of distributed energy, and to ensure that the network is fully absorbed as far as possible.[18-20] The main way to improve the energy efficiency of the supply side is to improve the energy efficiency of the equipment; the energy loss of the distribution side is mainly determined by the distribution lines and power electronic transformers; therefore, this paper focuses on the energy efficiency management of energy consumption side. The typical application scenarios of distributed distribution network include data center, industrial user and resident user. In this paper, by analysing the load situation in three kinds of power consumption scenarios, the energy efficiency promotion methods on the user side are excavated to form the energy efficiency management strategy.

4.1. Energy efficiency management method for controllable load

From the management point of view, the load on the energy consumption side can be divided into adjustable load, transferable load, uncontrollable load and important load. The first two kinds of terminal adjustable load and transferable load are the key contents of energy efficiency optimization management. The adjustable load power is variable and the working time cannot be moved. The power of the transferable load is fixed and the working time is controllable. Through the analysis of load characteristics of key equipment in AC/DC hybrid distribution system, adjustable load equipment mainly includes lithium bromide refrigeration unit, DC air conditioning, charging pile, LED lamp, elevator, and transferable load mainly includes production line equipment of industrial enterprises.

4.1.1. Lithium bromide refrigeration unit and DC Air conditioning

Air conditioning load accounts for 10% of grid load in summer. Reasonable setting of minimum start-up temperature of air conditioning can reduce energy consumption. When the temperature is lower than the limit, the system can automatically shut down; and the start and stop of air conditioning units can be considered by setting appropriate intervals.

4.1.2. Charging pile

Electric vehicle charging is managed according to peak and valley electricity price and SOC status of electric vehicle battery, and charging pile is arranged to charge during load Valley period.

4.1.3. LED lamp

Intelligently adjust the brightness of the lamp and turn it on or off by sensing the intensity of illumination and the daily activity time of the staff.

4.1.4. Elevator

According to the statistics of the elevator's running load, the most frequently used elevator and the period of high frequency use, combined with the staff's working time, the most reasonable use time is planned for different elevators, so as to reduce the energy waste of no-load or less-load elevators.

4.1.5. Production line equipment of industrial enterprises

The production line of industrial enterprises consists of different processes, which have different atmospheric loads. The energy consumption of each process can be analysed by collecting the electricity consumption data of the production and processing products. Under the condition that the production process is unchanged, the high energy consuming process can be adjusted in the valley period. The low energy consuming processes are produced in peak or peacetime periods. By rationally adjusting the production time, time and manpower of each process, we can achieve the purpose of saving production costs by staggering peak power consumption, help users to calculate the cost of electricity consumption, realize economic electricity consumption, and improve the level of energy saving and emission reduction.

4.2. Energy efficiency management in peak load period

There is a kind of high energy consuming enterprise in AC/DC hybrid distribution system, whose power consumption accounts for a large proportion of the total power consumption. When the power

supply of the system is insufficient during peak load period, if the effect of power limitation is obvious, and the overall energy efficiency of the system can be significantly improved. The optimal management strategy of load limitation in peak load period can be divided into two stages:
In the first stage, considering the gap allocation scheme of energy efficiency during peak load period, and taking the scale competition mechanism as the basis, the energy efficiency maximization model is constructed to determine the interruptible capacity allocation scheme of each high energy consuming enterprise.
The second stage is the real time operation stage, which divides users into uncontrollable high energy users, terminal control loads through smart meters and important loads of continuous power outage. Aiming at maximizing energy efficiency, minimizing switching operation times and minimizing important loads and interruptible outages, an optimization model of load management is constructed to form an optimal power limit sequence. Under the condition of ensuring the safety of power grid, the number of blackouts should be reduced, the power supply of important loads should be guaranteed, and the overall energy efficiency of the system should be improved.

5. Economic Analysis of Energy Efficiency Management

In AC/DC hybrid distribution system, the power sources in the system are renewable energy sources, and the output energy is partly controllable. On the premise of maximizing the output of distributed energy, the optimization of system economy is considered as the purpose of energy efficiency management.

5.1. Distributed power generation

In addition to the demand for load in the system, when the load in the system can not be absorbed, it can also sell electricity to the external network, which can directly obtain economic benefits.

5.2. Heat storage and power storage

Energy storage system can absorb electricity at low price, release electricity at high price, and transfer electricity to create economic value through time domain.

5.3. Adjustable load

Adjustable loads such as lithium bromide absorption refrigerators and charging piles can obtain economic compensation or preferential tariffs by interrupting load, reducing load or transferring peak load, and reduce electricity consumption expenditure.

5.4. Additional economic value of the system

As an important part of the distribution network, the system can participate in the competition of the power market as a whole after integrating resources, including demand-side response, ancillary service market, open spot electricity market and so on, so as to obtain greater economic value.

6. Conclusion

This paper presents an energy efficiency evaluation method and an energy efficiency management method for AC/DC hybrid distribution system. Firstly, an AC-DC hybrid distribution system based on power electronic transformer is introduced, which can meet the demand of power side and user side. Then, the energy efficiency evaluation methods of each part of the AC/DC system and the comprehensive energy efficiency evaluation methods of the system are analyzed. By analyzing the characteristics of energy consumption of different loads, the energy efficiency management of energy consumption side is mainly studied. Finally, from the economic point of view, the interaction between source and load is studied to improve the energy efficiency of the system. The energy efficiency management method proposed in this paper promote the effective interaction between the source network and energy storage, improve the comprehensive energy utilization efficiency of the system,

IOP Conf. Series: Earth and Environmental Science **431** (2020) 012039 doi:10.1088/1755-1315/431/1/012039

and provide a solution for energy efficiency management of multi-energy complementary AC/DC distribution system. In the future, energy efficiency management software will be developed according to the energy efficiency management scheme proposed in this paper.

7. References

[1] Loh P C，Li D，Chai Y K,et al．Hybrid AC–DC Microgrids With Energy Storages and Progressive Energy Flow Tuning[J]．IEEE Transactions on Power Electronics，2013，28(4)：1533-1543.

[2] Jin C，Loh P C，Wang P，et al．Autonomous operation of hybrid AC-DC microgrids[C]// Sustainable Energy Technologies (ICSET)，2010 IEEE International Conference on．IEEE，2011.

[3] Guerrero J M，Vasquez J C，Matas J，et al．Hierarchical Control of Droop-Controlled AC and DC Microgrids—A General Approach Toward Standardization[J]．IEEE Transactions on Industrial Electronics，2011，58(1)：158-172.

[4] Xie Ning，Zeng Jie，Xu Qi，et al．Overview of AC/DC hybrid distributed renewable energy system[J]．Southern Power System Technology，2017，11(9)：30-35(in Chinese)．

[5] Eneko U，Barrena A J．Hybrid AC/DC microgrids-part I：review and classification of topologies[J]．Renewable and Sustainable Energy Reviews，2015(52)：1251-1259．

[6] Eneko U，Jon Andoni B．Hybrid AC/DC micro grids-part II： review and classification of control strategies[J]．Renewable and Sustainable Energy Reviews，2015(52)：1123-1134．

[7] Eghtedarpour N，Farjah E．Power control and management in a hybrid AC/DC microgrid[J]．IEEE Transactions on Smart Grid，2014，5(3)：1494-1505．

[8] Nejabatkhah F，Li Y W．Overview of power management strategies of hybrid AC/DC microgrid[J]．IEEE Transactions on Power Electronics，2015，30(12)：7072-7089．

[9] Zhao Chuanhong，Weiss M，Mester A，et al．Power electronic transformer (PET) converter：Design of a 1.2MW demonstrator for traction applications[C]．Proceedings of 2012 International Symposium on Power Electronics Power Electronics，Electrical Drives，Automation and Motion．Sorrento，Italy：IEEE，2012：855-860．

[10] Huang A Q，Crow M L，Heydt G T，et al．The Future Renewable Electric Energy Delivery and Management (FREEDM) system：the energy internet[J]．Proceedings of the IEEE，2011，99(1)：133-148．

[11] Li Zixin，Wang Ping，Chu Zunfang，et al．Research on medium- and high-voltage smart distribution grid oriented power electronic transformer[J]．Power System Technology，2013，37(9)：2592-2601(in Chinese)．

[12] Gao Fanqiang，Li Zixin，Wang Ping，et al．Prototype of smart energy router for distribution DC grid[C]．Proceedings of the 17th European Conference on Power Electronics and Applications．Geneva，Switzerland：IEEE，2015：1-9．

[13] Suzuki A，Akagi H．HVDC Circuit Breakers Combining Mechanical Switches and a Multilevel PWM Converter：Verification by Downscaled Models[J]．IEEE Transactions on Power Electronics，2018，PP(99)：1-1．

[14] MA Zhao．R&D status and prospects of HVDC circuit breakers[J]．Smart Grid，2013，1(01)：12-16．

[15] Wen W，Wang Y，Li B，et al．Transient Current Interruption Characteristics of a Novel Mechanical DC Circuit Breaker[J]．IEEE Transactions on Power Electronics，2018，PP(99)：1-1．

[16] CHEN Zhengyu，YU Zhanqing，LÜ Gang，et al．Researches on 10 kV DC hybrid circuit breaker based on IGCT series[J]．Proceedings of the CSEE，2016，36(2)：317-326．

IOP Conf. Series: Earth and Environmental Science **431** (2020) 012039 doi:10.1088/1755-1315/431/1/012039

[17] QU Ru，ZHANG Xiangyu，CHEN Zhengyu，et al．IGCT series voltage-sharing technology for DC breaking[J]．High Voltage Engineering，2018，44(02)：409-416．
[18] ZHANG Fan， YANG Xu， REN Yu，et al．Voltage balancing circuit for series-connected IGBTs in solid-state breaker[J]．Proceedings of the CSEE，2016，36(3)：656-663．
[19] Dong Zhaoyang，Zhao Junhua，Wen Fushuan，et al．From smart grid to energy internet：basic concept and research framework[J]．Automation of Electric Power Systems，2014，38(15)： 1-11．
[20] Ma Zhao，Zhou Xiaoxin，Shang Yuwei，et al．Exploring the concept， key technologies and development model of energy internet[J]．Power System Technology，2015，39(11)：3014-3022．

Acknowledgments
Funding organisation: Supported by National Key Research and Development Program 2017YFB0903205.

IOP Conf. Series: Earth and Environmental Science **431** (2020) 012040 doi:10.1088/1755-1315/431/1/012040

Effect of magnetic field configuration on Faraday MHD accelerator

Lai Li[1], Xi Lu[2], Guiping Zhu[3], Hulin Huang[3] and Xidong Zhang[4]

1 College of Energy and Power Engineering, Nanjing University of Aeronautics and Astronautics, Nanjing 210016, China
2 Shanghai Key Laboratory of Deep Space Exploration Technology, Shanghai 201109, China
3 College of Astronautics, Nanjing University of Aeronautics and Astronautics, Nanjing 210016, China
4 College of Energy and Power Engineering, Nanjing Institute of Technology, Nanjing 211167, China
E-mail: zhuguiping@nuaa.edu.cn

Abstract. This works aims at the study of a Faraday electric accelerator with the plasma of argon used as the working gas, which is pre-ionized by nuclear energy. The electron density of plasma is above $10^{20}/m^3$. Different configurations of magnetic field are numerical studied to obtain the influences on the plasma ionization and flowing characteristics. A relatively higher velocity and electron number density are obtained in monotonically decreasing magnetic field generated by magnet with a shorter length. When the plasma flows through the magnetic field generated by 75-mm magnets, the outflow velocity is 2040 m/s, which is higher than 2016 m/s when the plasma flows through the magnetic field generated by 100-mm magnets.

1. Introduction

The concept of electric propulsion has been gaining increasing attentions since it was brought up by Tsiolkovsky in 1903 and Goddard in 1906, respectively [1]. The principle of electric propulsion systems is the acceleration of propellant by using electrical fields, currents, and magnetic fields [2]. Four electric propulsion technologies are mainly studied today including electro-thermal [3], electromagnetic, electro-static and the mixed type. Acceleration of charged ions using static electric fields [4, 5] is categorized into electrostatic acceleration. Current carrying quasi-neutral plasma using electromagnetic Lorentz forces [6, 7] is named electromagnetic acceleration. There are so far two major concerns on the studies of the above-mentioned electromagnetic, electrostatic and mixed type propulsion technologies. One of the concerns is the way and effectiveness to realize the ionization of working gas. The other critical issue is the ejection of ionized plasma by using the electrical power.

The duration of voyage in deep space exploration is required to be as short as possible due to voyage influence, survival needs, safety and endurance of the astronauts. For effective operation of the manned deep space exploration and orbit manoeuvring, it is necessary to minimize the fuel load and increase load capacity. Furthermore, high thrust propulsion is required to shorten the time of orbit manoeuvring and voyage. The thrust of most current electric propulsion technologies is infinitesimal, the value of which ranges from tens to hundreds of mN. To alleviate the contradiction, high-power electric propulsion is gaining increasing interests for shortening the duration of orbit manoeuvring and space travel, as well as carrying enough propellant for voyage.

With electrostatic-type propulsion, Hall effect thrusters are being constantly improved and developed towards high power and thrust. Under the condition of low magnetic field strength and 200-500 V discharge potential, the testing of NASA-457Mv2 stationary plasma thruster showed the achievement of the maximum thrust of 2.5 N with a maximum power of 50 kW [8]. A configuration of nesting multiple discharge channel was developed by NASA and investigated by groups of Jacobson [9] and McVey [10]. The proof of concept work on the X2 NHT (Nested Hall thruster) showed that such a configuration met or exceeded the performance of conventional single-channel thrusters [11]. A 100-kW class laboratory-model NHT known as the X3 was researched by University of Michigan in order to extend the NHT concept to higher operating powers with a wider throttling range [12].

Magnetoplasmadynamic thrusters (MPDT) produce thrust through the acceleration of ionized propellant species using electromagnetic force. The propellant, which initially may be a gas, liquid, or solid state, is ionized by the current arc in MPDT. Paccani et al. discussed the operation and performance of a quasi-steady, ablative MPDT with four different polymer propellants [7]. The highest thrust and thrust-to-power ratio were provided by Tyflon, whereas Hyflon offered the lowest values of these working parameters. Choueiri et al. [13] carried out the measurements of thrust for various mass flow rates for propellant gas, such as argon, xenon, hydrogen and deuterium. Corresponding to the mass flow rate of 0.5 to 6 g/s, the thrust can be obtained between 5 and 120 N. Miyazaki et al. [14] conducted experiments for thrust performance evaluation at an input power of 1 MW. The best performance of stable operating condition is obtained for an Argon propellant with a mass flow rate at 1.8 g/s.

To summarize, many experts have widely carried out research on thrusters propulsion performance under different acceleration principles, various channel structures and sorts of working fluids. However, most of those studies are realized under a uniform magnetic field or a single magnetic field configuration. For performance optimization, this paper mainly discussed the effect of different magnetic field configurations on a Faraday MHD electromagnetic accelerator. Noble gas Argon is used as the working medium assumed to be heated and pre-ionized by the nuclear energy before flowing into the channel and being accelerated by the Lorenz force through the applied electric field and magnetic field.

2. Numerical model

Fig. 1 shows schematic of the simulation domain with the channel active length at 200 mm. Ten pairs of electrodes with width of 10 mm are placed on the right and left surface of the channel. Channel height and width increase along the flow direction with a divergence angle of 1 degree. Inlet width and height are 20 mm and the outlet ones are 27 mm. The magnetic field is generated by magnets integrated on the upper and lower sides. The length of the magnet is M_x, the width is M_y and the distance between the magnets is H.

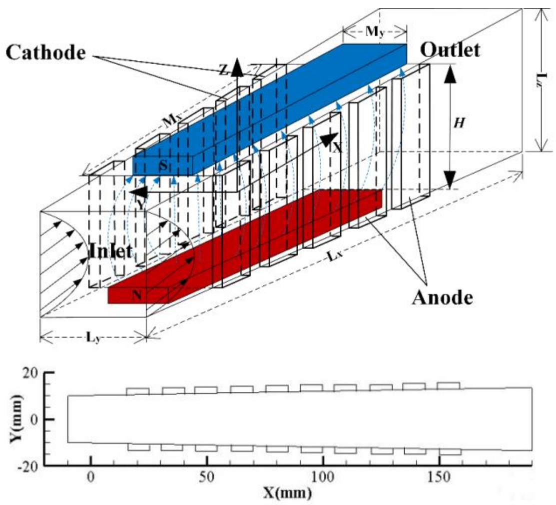

Figure 1. Schematic of simulation domain.

Pure argon is used as working gas in the simulations. The non-equilibrium argon plasma in the channel consists of ions, electrons and atoms under a two-temperature model [15, 16] which is described by the combination of state equations and Maxwell equations. Navier-Stokes equations include Lorentz force term and energy equation with energy exchange term are solved by Large Eddy simulation (LES) method. Non-slip and constant-temperature wall condition is used. Segmented Faraday connection is used for the electrodes. The intensity of electrical field is 5000 V/m between the anode and cathode. Table 1 shows the working conditions of the seed-free argon plasma used in the simulations. The verification of the simulation code has been accomplished in our previous work [17].

Table 1. Conditions used in simulations.

Working gas	Argon
Total inflow pressure	0.64 mPa
Total inflow temperature	6701 K
Inlet electron temperature	8000 K
Magnetic flux density	0.5-2.1 T

2.1. The equations for heavy particles

a. Continuity equation:

Continuity equation can be written as follows

$$\frac{\partial \rho}{\partial t} + \nabla \cdot (\rho \mathbf{u}) = 0 \tag{1}$$

where ρ is gas density, $\mathbf{u}$ is the flow velocity.

b. Momentum equation:

$$\frac{\partial \rho \mathbf{u}}{\partial t} + \nabla \cdot (\rho \mathbf{u}\mathbf{u}) = \mathbf{J} \times \mathbf{B} - \nabla p + \nabla \cdot \boldsymbol{\tau} \tag{2}$$

The notation $\mathbf{J}$ is the current density, $\mathbf{B}$ is the magnetic flux density, p is the static pressure, $\boldsymbol{\tau}$ is the viscous stress

c. Energy equation:

$$\frac{\partial E_s}{\partial t} + \nabla \cdot (E_s + p)\mathbf{u} = \mathbf{J} \cdot \mathbf{E} - \nabla \cdot \mathbf{q} + \nabla \cdot (\tau \mathbf{u}), \quad E_s = \rho\left(c_V T + \frac{1}{2}\mathbf{u}^2\right) \tag{3}$$

where $\mathbf{E}$ is the electric field, E_s is the total energy, c_V is the constant volume specific heat, T is the static temperature, $\mathbf{q}$ is the conductive heat flux.

2.2. The equations for ions and electrons

a. Conservation of ion number density:

$$\frac{\partial n_i^+}{\partial t} + \nabla \cdot n_i^+ \mathbf{u} = \dot{n}_i^+ = k_{fi} n_e n_i - k_{ri} n_e^2 n_i^+, \quad n_e = \sum_i^{ion} n_i^+ \tag{4}$$

where n_i^+ is the number density of argon ions, n_e is the number density of electron, n_i is the number density of argon atom. The three-body recombination rate coefficient k_r is determined by $k_r = k_{rh} k_{ro} / (k_{rh} + k_{ro})$ [16], where $k_{rh} = 1.09 \times 10^{-20} T_e^{-9/2}$ and $k_{ro} = 3.33 \times 10^{-44}\left(\frac{135300}{T_e} + 2\right)\exp\left(\frac{47800}{T_e}\right)$.

The ionization rate coefficient k_f is derived on the basis of the principle of detailed balance with the Saha equilibrium: $k_f n_i n_e = k_r n_i n_e^2$, $k_f = k_r \times \frac{g_i}{g_0}\left(\frac{2\pi m_e k T_e}{h^2}\right)^{3/2} \exp\left(-\frac{\varepsilon_i}{kT_e}\right)$, where g_i is the statistical weight of the ground state of the ion, g_0 is the statistical weight of the ground state of the neutral argon atom, ε_i is ionization potential of argon atom, the subscripts e and i and the superscript $+$ denote the electrons, neutral atoms and ionized particles, respectively.

b. Energy equation for electron:

$$\frac{\partial U_e}{\partial t}+\nabla\cdot\left(U_e\mathbf{u}_e\right)=\frac{|\mathbf{J}|^2}{\sigma}-p_e\nabla\cdot\mathbf{u}_e-3n_ek\left(T_e-T\right)\sum_h^{heavy}\frac{m_e}{m_h}\bar{\nu}_{eh}$$
$$p_e=n_ekT_e,\ \ U_e=\frac{3}{2}n_ekT_e+n_i^+\varepsilon_i \tag{5}$$

where, U_e is the electron energy, u_e is the velocity of electrons, m_h is the mass of heavy particle, m_e is the mass of electron, p_e is the electron pressure, k is Boltzmann constant, T_e is electron temperature, ε_i is the ionization energy. The LES-Smagorinsky model is applied as turbulence model to solve the equations of (1), (2) and (3) for the description of the fluid flow.

2.3. Governing equations for electrical-magnetic

a. Generalized Ohm's law:

$$\mathbf{J}+\frac{\beta}{|\mathbf{B}|}\mathbf{J}\times\mathbf{B}=\sigma\left(\mathbf{E}+\mathbf{u}\times\mathbf{B}\right),\ \ \sigma=\frac{e^2n_e}{m_e\bar{\nu}_{eh}} \tag{6}$$

In the equation, $\bar{\nu}_{eh}=\sum_h^{heavy}n_hQ_{eh}c_e$ is the average momentum transfer collision frequency for an electron e with a heavy particle h, where Q_{eh} is the energy-averaged momentum transfer cross section, $C_e=\sqrt{8kT_e/\pi m_e}$ is the mean electron velocity for a Maxwellian distribution and σ is the electrical conductivity.

b. Maxwell equations:

$$\nabla\times\mathbf{H}=\mathbf{J}+\frac{\partial\mathbf{D}}{\partial t},\ \ \nabla\cdot\mathbf{B}=0,\ \ \nabla\times\mathbf{E}=-\frac{\partial\mathbf{B}}{\partial t},\ \ \nabla\cdot\mathbf{D}=\rho_e \tag{7}$$

Since the charge is assumed as neutrality and magnetic Reynolds number is quite small, the Maxwell equations are simplified as follows:

$$\nabla\times\mathbf{E}=0,\ \ \nabla\cdot\mathbf{J}=0 \tag{8}$$

In equation (8), $\mathbf{E}$=-$\nabla\mathit{\Phi}$ is the electric field, where $\mathit{\Phi}$ is the electrical potential.

c. Equations of external magnetic field

Distribution of external magnetic field $\mathbf{B}_0=\left(B_{0x},B_{0y},B_{0z}\right)$ is governed by Biot-Savart law:

$$B_{0x}=\gamma\sum_{k=\pm1}\sum_{j=\pm1}\sum_{i=\pm1}\left(ijk\right)\text{artanh}\left[\frac{y-0.5jM_y}{r\left(i,j,k\right)}\right] \tag{9}$$

$$B_{0y}=\gamma\sum_{k=\pm1}\sum_{j=\pm1}\sum_{i=\pm1}\left(ijk\right)\text{artanh}\left[\frac{y-0.5iM_x}{r\left(i,j,k\right)}\right] \tag{10}$$

$$B_{0z}=\gamma\sum_{k=\pm1}\sum_{j=\pm1}\sum_{i=\pm1}\left(ijk\right)\left(\text{-arctan}\left[\frac{\left(x-0.5iM_x\right)\left(y-0.5jM_y\right)}{\left(z-0.5kH\right)r\left(i,j,k\right)}\right]\right)$$
$$r\left(i,j,k\right)=\left[\left(x-0.5iM_x\right)^2+\left(y-0.5jM_y\right)^2+\left(z-0.5kH\right)^2\right]^{1/2} \tag{11}$$

Equations (4) and (5) are solved by means of the user defined functions code. The elliptic equations for the potential derived from equations (6) and (7) are solved by MHD model of Fluent. The set of the above equations is solved numerically by means of the first-order upwind scheme.

3. Results and discussions

The induced electric potential $U=u_x B_{0z} d$ (B_{0z} is the magnetic flux density, d is the distance of electrodes) is produced by the conductive flow under the magnetic field. As both B_{0z} and d are constant, the induced electric potential increases with the velocity. Hence, the induced potential in the region with higher exit velocity may exceed the external potential and lead to deceleration of the flow. Appropriate reduction of magnetic flux density in higher velocity regions may alleviate the contradiction. The electromagnetic acceleration motion is numerically studied in this paper under different magnetic field intensities.

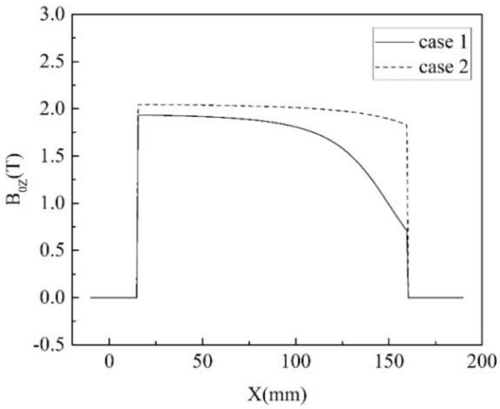

Figure 2. Distribution of external magnetic field along the center line of X direction.

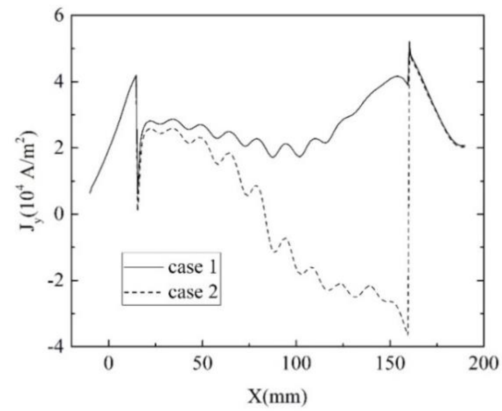

Figure 3. Distribution of current density of y direction along the center line of X direction.

The distribution of the magnetic flux density along the center line of the channel is shown in Fig. 2. The solid line represents the magnetic field generated by a short magnet (M_x=75 mm). The dashed line represents the magnetic field generated by a long magnet (M_x=100 mm). For convenience, we define the simulation under the short magnets condition as case 1 and the simulation under the long magnets condition as case 2. Both of the external magnetic fields are confined to the 15-160 mm region.

3.1. The characteristics of the plasma

From equation (6), the current density of y direction is obtained as $J_y = \sigma\left(E_y - u_x B_{0z}\right)$. Even the velocity increases, the current density J_y is still positive in case 1 due to the insignificant induced potential $\mathbf{u}\times\mathbf{B}$ in the decay magnetic field. The intensity of the magnetic field in case 2 exhibits small changes. On the contrary, the electric field $u_x B_{0z}$ produced by the induced potential $U=u_x B_{0z} d$ is higher than E_y generated by the external potential, which leads to a negative value of the current density (from 85 mm to160 mm in Fig 3). The distribution of electric power $P_g = \mathbf{J}\cdot\mathbf{E}$ along the center line of the mainstream has the same trend with the current density. Available electric power in case 1 is higher than that in case 2. Therefore, the energy for ionization in case 2 is less than that in case 1.

The pre-ionization electron number density of gas at the inlet is about 1×10^{20}/m^3. The electron number density shown in Fig. 4 changes between 0.975×10^{20} and 1.03×10^{20} /m^3 in two cases. The electron number density in case 2 is smaller than that in case 1 due to lack of the ionization energy. From Fig. 5, the electric conductivity varies from 13 to 106 /ohm-m in two cases. With no magnetic field, case 1 and case 2 share the same trend of electric conductivity. But the distinction of electric conductivity is significant in the electromagnetic region, where the value is smaller in case 1 than that in case 2.

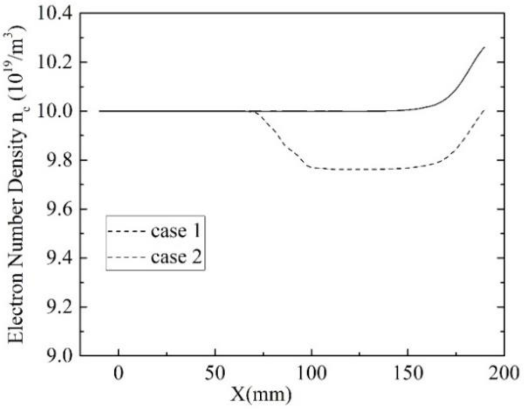

Figure 4. Distribution of electron number density along the center line of X direction.

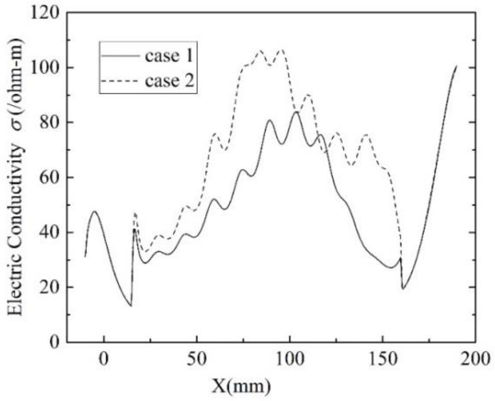

Figure 5. Distribution of electric conductivity along the center line in X direction.

3.2. The characteristics of the flow

The acceleration of mainstream velocity u_x mainly depends on the generated Lorentz force. Meanwhile, the intensity of the current density J_y mainly varies with u_x. Lorentz force $F_x = J_y B_{0z}$ determines the distribution of electric conductivity of the flow, which plays an important role to the distribution of current density. In addition, Lorentz force F_x varies with the current density J_y. Fig 6 is the contour of current density in two cases. With the increasing of velocity in the channel in both cases, current density in case 2 declines to be negative in the range of 85 mm to 160 mm, Fig 6 (b). The corresponding Lorentz force in this range becomes negative in case 2 (Fig 7(b)), which stands for reverse direction to the flow. As the value of B_{0z} in case 1 decreases monotonically from 1.98 to 0.75 T, the current density stays in positive although the velocity increases, hence, the Lorentz force is still with the same direction of flow from Fig 7(a).

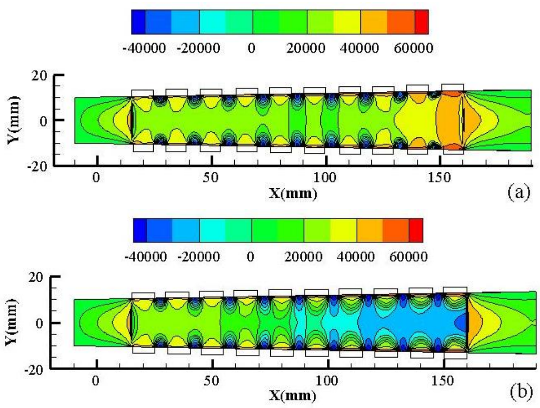

Figure 6. Contour of current density at Z=0 plane: (a) case 1, (b) case 2.

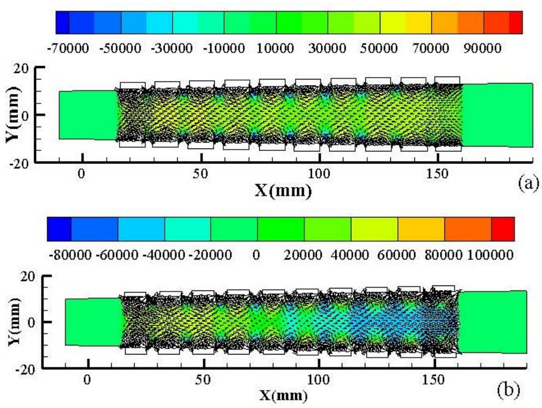

Figure 7. Contour and vector of Lorentz force at Z=0 plane: (a) case 1, (b) case 2.

Fig 8 shows that Lorentz force stays in positive due to the positive value of the current density J_y along the center line of X direction in case 1. The Lorentz force declines to be negative at the location of 85 mm in case 2. However, the Lorentz force is consistently positive near the electrodes areas because of the injection of electric energy. It is indicated that the negative current cannot form a path out of the electrode although Lorentz force is in opposite direction of the flow in case 2 resulted by greater value of the external potential than the induced potential. Therefore, the plasma in case 2 is ultimately accelerated.

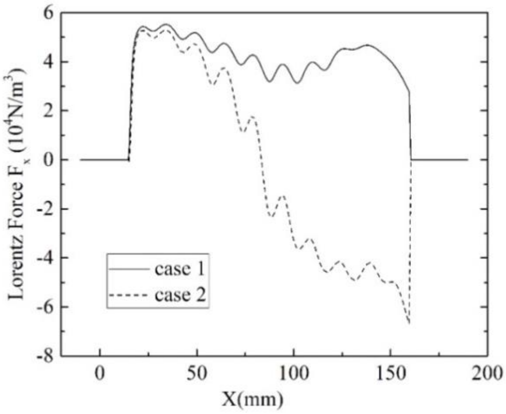

Figure 8. Distribution of Lorentz force in x direction along the center line of X direction.

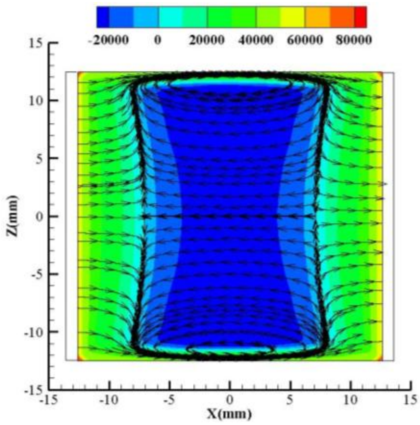

Figure 9. Contour and streamlines of electric current at X=140 mm plane: case 2.

Fig 9 shows the Eddy streamlines of the electric currents which is formed by the induced potential suppressed by external potential. As previously described, electric currents generated by the external potentials still flow in and out of the electrodes and detour past the eddy of electric currents. As a result, the plasma in case 2 is still accelerated, but the acceleration effect is weakened by the induced potential, which offsets part of the external electric energy. The acceleration effect of two cases can be observed in Fig 10. Obvious separation of two lines appears at the location of 85 mm. The velocity at the outlet are 2040 m/s in case 1 and 2016 m/s in case 2, respectively.

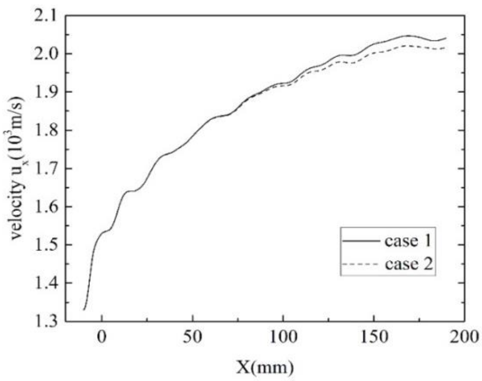

Figure 10. Distribution of velocity in X direction along the center line.

4. Summary

Influences of different magnetic field configurations on Faraday MHD accelerator are numerically studied in this paper. The noble argon plasma is used as working gas and its electron number density is about 1×10^{20}/m^3 at the inlet. Ionization and acceleration characteristics are mainly discussed under two magnetic fields, which are generated by long and short length of magnets, respectively. Both the applied external electric fields are 5000 V/m. The ionization and acceleration effects are weakened due to the offset of larger induced potential $\mathbf{u}\times\mathbf{B}$ appeared in the magnetic field generated by long magnets. The electron number density varies between 0.975×10^{20}/m^3 and 1×10^{20}/m^3 at magnetic field generated by 100 mm length magnets. The electron number density is kept over than 1×10^{20}/m^3 at magnetic field generated by 75-mm magnets. With 75-mm magnets, the exit velocity is 2040 m/s, which is higher than 2016 m/s in field generated by 100-mm magnet. Further research will be carried out to apply different external potentials under different magnetic field configurations in order to optimize acceleration effect.

5. References

[1] E. Y. Choueiri, "A Critical History of Electric Propulsion_ The First 50 Years (1906-1956)," *Journal of Propulsion & Power,* vol. 20, no. 2, pp. 193-203, 2004.

[2] R. J. Cassady, R. H. Frisbee, and J. Gilland, H., "Recent advances in nuclear powered electric propulsion for space exploration," *Energy Conversion & Management,* vol. 49, no. 3, pp. 412-435, 2008.

[3] C. Joyner, D. Levack, and S. Borowski, "Development of a Small Nuclear Thermal Propulsion Flight Demonstrator Concept that Is Scalable to Human Missions," in *48th AIAA/ ASME/SAE/ASEE, Joint Propulsion Conference &Exhibit,* Atlanta, Georgia, 2012.

[4] A. L. Ortega, and I. G. Mikellides, "The importance of the cathode plume and its interactions with the ion beam in numerical simulations of Hall thrusters," *Physics of Plasmas,* vol. 23, no. 4, pp. 295-865, 2016.

[5] P. J. Wilbur, V. K. Rawlin, and J. R. Beattie, "Ion Thruster Development Trends and Status in the United States," *Journal of Propulsion and Power,* vol. 14, no. 5, pp. 8, 1998.

[6] D. Ichihara, T. Uno, H. Kataoka, J. Jeong, A. Iwakawa, and A. Sasoh, "Ten-Ampere-Level, Applied-Field-Dominant Operation in Magnetoplasmadynamic Thrusters," *Journal of Propulsion and Power,* vol. 33, no. 2, pp. 360-369, 2017.

[7] G. Paccani, U. Chiarotti, and W. D. Deininger, "Quasisteady Ablative Magnetoplasmadynamic Thruster Performance with Different Propellants," *Journal of Propulsion & Power,* vol. 14, no. 2, pp. 254-260, 1998.

[8] G. C. Soulas, T. W. Haag, and D. A. Herman, "Performance test results of the NASA-457M v2 Hall thruster," in *48th AIAA/ASME /SAE /ASEE Joint Propulsion Conference & Exhibit,* Atlanta, USA, 2012, pp. 3940.

[9] D. T. Jacobson, D. H. Manzella, R. R. Hofer, and P. Y. Peterson, "NASAs 2004 Hall thruster program," in *40th Joint Propulsion Conference and Exhibit cosponsored by the AIAA, ASME, SAE, and ASEE*, Fort Lauderdale, Florida, 2004.

[10] M. J. B, P. A. S, and B. E. J. . *Multichannel hall effect thruster,* U. S. Patent, 2005.

[11] R. Liang, and A. D. Gallimore, "Far-Field Plume Measurements of a Nested-Channel Hall-Effect Thruster," in *49th AIAA Aerospace Sciences Meeting including the New Horizons Forum and Aerospace Exposition*, Orlando, Florida, 2011.

[12] R. Florenz, A. D. Gallimore, and P. Y. Peterson, "Developmental Status of a 100-kW Class Laboratory Nested channel Hall Thruster," in *32nd International Electric Propulsion Conference*, Wiesbaden,Germany, 2011.

[13] E. Y. Choueiri, and J. K. Ziemer, "Quasi-Steady Magnetoplasmadynamic Thruster Performance Database," *Journal of Propulsion and Power,* vol. 17, no. 5, pp. 967-976, 2001.

[14] K. Miyazaki, S. Takenaka, I. Funaki, and H. Horisawa, "Experimental Study of a 1-MW-Class Quasi-Steady-State Self-Field Magnetoplasmadynamic Thruster," in *The 33rd International Electric Propulsion Conference*, The George Washington University, 2013.

[15] M.Mitchner, and C. H. Kruger., *Partially Ionized Gases* Wiley, New York, 1973.

[16] M. Tanaka, T. Murakami, and Y. Okuno, "Plasma characteristics and performance of magnetohydrodynamic generator with high-temperature inert gas plasma," *IEEE Transactions on Plasma Science,* vol. 42, no. 12, pp. 4020-4025, 2014.

[17] L. Li, H.-l. Huang, and G.-p. Zhu, "Numerical Simulations for a Partial Disk MHD Generator Performance," *Energies,* vol. 11, no. 1, pp. 127, 2018.

Acknowledgments

This research was supported by the Shanghai space science and Technology Innovation Fund (Grant No. SAST2016030) Project of Nanjing Institute of Technology (Grant No. YKJ201524), and the Natural Science Foundation of Jiangsu Province (Grant No. BK20160775).

IOP Conf. Series: Earth and Environmental Science **431** (2020) 012041 doi:10.1088/1755-1315/431/1/012041

Application of attitude sensor in torque measurement of isolator switch

Zhaoqiang Zeng[1], Wenqi Mao[2], XiaoLei Zhou[1], YouJian Mao[3], Jia Peng[2]

1 State Grid Hunan Electric Power Co., Ltd. Maintenance Company, Changsha, China
2 State Grid Hunan Electric Power Co., Ltd., Changsha, China
3 Jiangsu Rugao High Voltage Electrical Appliances Co., Ltd., Nantong, China
E-mail: zzq7314@126.com

Abstract. Attitude sensor has excellent angle measurement function. Aiming at the current situation that it is difficult to measure rotation angle in on-line monitoring of isolator torque, this paper studies the structure, technical parameters and algorithm of attitude sensor suitable for measuring rotation angle, and develops corresponding application software, which can automatically plot relational curve of the torsion and spindle rotation angle. So that the on-line monitoring of torque can be realized

1. Introduction

The transmission parts of outdoor disconnector are exposed to the sun and rain directly in the atmosphere. They are easy to be corroded, contaminated with dust and lubrication failure and jam, which often leads to inseparable faults and seriously threatens the safe and reliable operation of the power grid.[1-2] However, the jamming of transmission parts is not formed overnight, it is a slow process from quantitative change to qualitative change. Only by monitoring the degree of jamming at any time, can the occurrence of disconnector accidents be eliminated or reduced when the jamming is enough to affect the alarm and timely maintenance of disconnector before the switch is switched on and off.

The jamming of transmission parts of disconnector will inevitably lead to the increase of operating torque of motor mechanism, so monitoring the main shaft torque of motor mechanism can directly reflect the change degree of jamming. By realizing on-line monitoring and diagnosis of mechanical jamming of disconnector, reliable scientific basis is provided for condition maintenance and early detection and treatment of mechanical jamming. [3]

At present, there is no ideal measurement method for the rotation angle of outdoor high-voltage disconnector in the industry. Real-time measurement of rotation angle is not accurate and reliable enough, and often can not cooperate with the on-line measurement of torque, which affects the on-line monitoring of mechanical load and fault location judgment [4]. The attitude sensor scheme makes it possible to install the isolator torque online measuring device in the box. This greatly improves the accuracy and reliability of the on-line torque monitoring device.

The attitude sensor is tied to the spindle and rotates with the spindle to measure the spindle rotation angle. Its small size and high precision can be installed in the mechanism box, which greatly improves the reliability.

2. Working principle of attitude sensor

Attitude sensor is a high-performance three-dimensional motion attitude measurement system based on micro-electro-mechanical system (MEMS). It includes three-axis gyroscope, three-axis accelerometer (IMU), three-axis electronic compass and other auxiliary motion sensors. Through the embedded low-power ARM processor, the calibrated angular velocity, acceleration, magnetic data, etc. are output. The motion attitude is measured by the quaternion-based sensor data algorithm, and the real-time output is quaternion and Euler. Zero-drift three-dimensional attitude data represented by angular equivalents. When used for angle (azimuth) measurement, its internal circuit calculates the angular velocity integral (special algorithm) out of azimuth, and converts it into digital signal output[5-6].
In recent years, the importance of attitude angle measurement in aviation, navigation and other military equipment has become increasingly prominent. As an important tool for attitude angle measurement, attitude sensors have attracted much attention. The high-precision sensors used in national defense and military affairs have excellent performance and are generally expensive. Some of them are even large in size and weight, which can not meet the needs of civil products for attitude measurement products. For the spindle angle measurement of disconnector, the real-time measurement of three-dimensional attitude angle by using a low-cost and cost-effective MEMS device to design a three-dimensional attitude sensor is enough to meet the requirements [7].
The error of attitude sensor used in this paper is less than 0.5 ℃ in static test and less than 2 ℃ in dynamic test. The attitude sensor can measure the attitude angle of the carrier at any time and state relative to the reference coordinate system, and the error analysis and compensation module is added to make it as far as possible not to be disturbed by external magnetic field, temperature change and other factors. Because of its small size, it fully meets the requirement of attitude sensor for torque measuring device of disconnector mechanism.

3. Application of attitude sensor in torque measuring device

The isolator torque measuring device is composed of torque measuring module, angle measuring module, wireless receiving module and industrial computer. The two measuring modules collect the signals of the main shaft torque and rotation angle of the operating mechanism respectively. Because the spindle rotates (+180 degrees) when the mechanism is switched on and off, the cable is easy to break if the sensor signal is transmitted by cable. Therefore, the torque and angle signals are transmitted by wireless communication. The wireless receiving module input the signal processing to the computer, and display the operating torque, spindle rotation angle and other mechanical characteristics parameters under the special tool software processing, and automatically draw the torque-angle (M-theta curve). The measurement data can be saved and uploaded to the computer for further analysis by special software. The principle of the device is shown in Figure 1 and the structure of the device is shown in Figure 2.

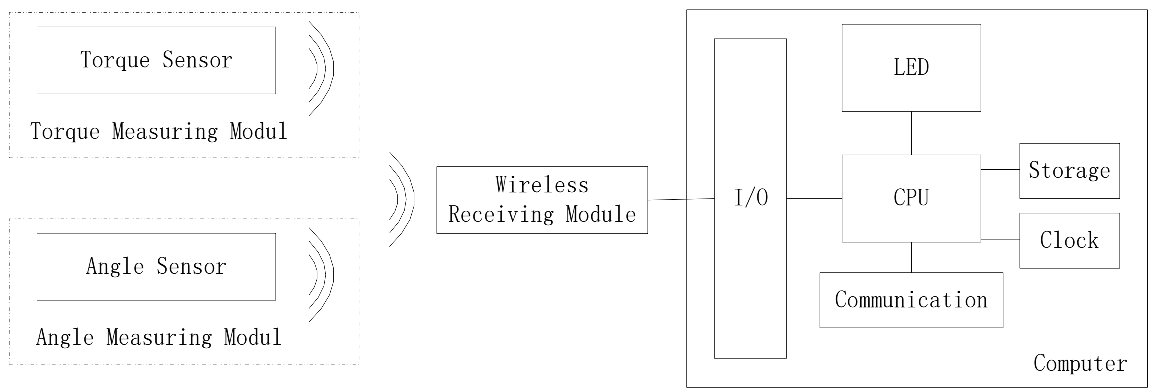

Figure 1. Figure of the principle of the device

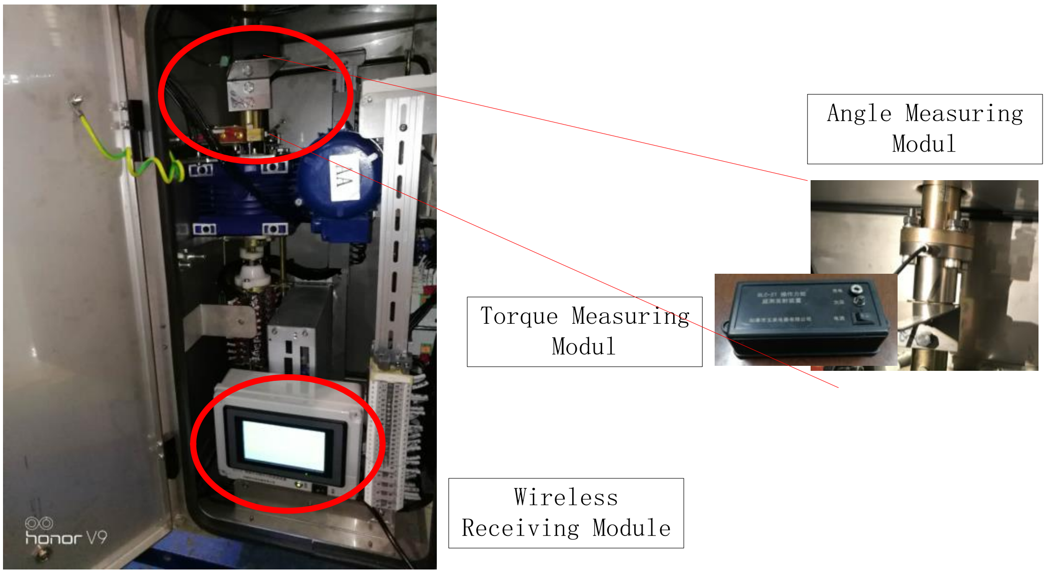

Figure 2. Figure of the structure of the device

The angular measurement module is composed of attitude sensor, single chip computer, power supply module and wireless transmission module. Its principle is shown in Fig. 3. The main functions are signal acquisition and wireless corner signal transmission.

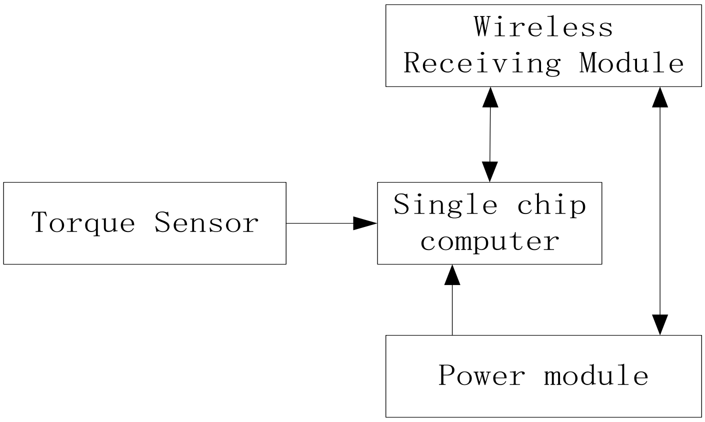

Figure 3. Figure of the principle of the angular measurement module

The main function of the wireless receiving module is to communicate with the measuring device and send the data of the attitude sensor and the torque sensor to the computer through the interface circuit for subsequent processing. It includes power supply module, wireless receiving module, single chip computer and output interface circuit. Its schematic diagram is shown in Fig. 4. In addition, in the receiving module, the direction signal given by the attitude sensor should be used to automatically judge whether the disconnector is switched on or off, which is accomplished by software.

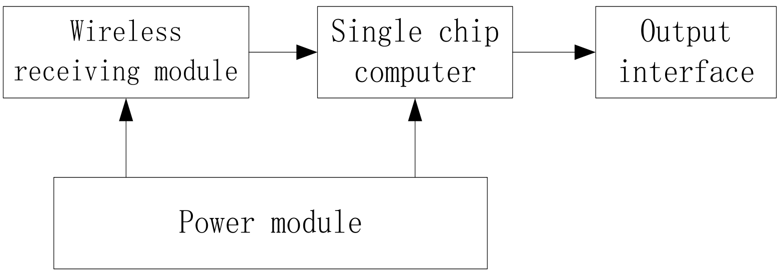

Figure 4. Figure of the principle of the wireless receiving module

Torque and rotation angle measurement devices collect the signals of operating mechanism torque and spindle rotation angle respectively. These signals are input to the computer, and processed by special tool software. The mechanical characteristic parameters such as operating torque and spindle rotation angle are displayed, and the torque-rotation angle (M-theta curve) is drawn automatically. Then the measurement is made by using diagnostic software. The curves of the torque obtained are compared with those of the same historical curve in the same coordinate system. The influence of various factors on the relationship curve was studied, such as corrosion, lubrication failure, spring pressure change, rotation angle change and so on. The reason of the change of the torque and the early warning value are analyzed, and the corresponding maintenance guidance is obtained.

4. Conclusion

At present, there is no ideal measurement method for the rotation angle of outdoor high-voltage disconnector in the industry. Real-time measurement of rotation angle is not accurate and reliable enough, and often can not cooperate with the on-line measurement of torque, which affects the on-line monitoring of mechanical load and fault location judgment. The attitude sensor scheme makes it possible to install the isolator torque online measuring device in the box. This greatly improves the accuracy and reliability of the on-line torque monitoring device.

To realize the automatic monitoring of the operating torque of disconnector, as long as there is switch-off operation, there will be data feedback, which can objectively, accurately and timely control the operating status of disconnector. Through the real-time coordination of the rotation angle and the torque, the expert diagnosis system can detect the hidden trouble and position very early, which not only improves the shape of disconnector. The level of state maintenance also improves the level of safe operation of power grid.

5. References

[1] Jingchun Cui, Dalu Yuan, Gao Song 2006 Operatan Analysis and Its Perfection for HV Switch Switch Disconnector *J. Electrical Equipment.***7** 4

[2] Mingxue Sheng, Zhiqing Wang, Gao Song 2010 Cause analysis and treatment of commen faults of outdoor high-voltage disconnector *J. High Voltage Appatatus*.46 10

[3] Xin Lei, Nan Xu, Yang Li, Meng He, ShaoWei Wang, Jia Chen 2018 Mechanical ConditionMonitoring and Diagnosis System of Isolation Switch *J. Electricity and Energy*.39 6

[4] Honda Dong, Shitao Feng, Tao Huang, Saipeng Zhang, Zhicheng Ge, Yuhang Shi 2018 Analysis of Detection Methods and Typical Mechanical Faults of High Voltage Disconnectors *J. Electrician technology*.4 37

[5] Xinjun Chen, Xiaoping Liu, Ruoli Dai, Haoyang Liu 2011 MEMS Multi-sensor Embedded Attitude Measurement System *J. Microcontrollers & Embedded Systems*.10

[6] Chunjun Wu, Binghong Zhou 2013 Wireless Attitude Measurement System Based on MEMS *J. Instrument Technigue and Sensor*.8

[7] Yanni Ma 2015 *The Design of Three-dimension Attitude Sensor* (Xian: Xian Technological University) chapter 2 pp 6–9

Acknowledgments

This research was supported by Science and Technology Project of State Grid Corporation of China (Grant No. 5216A0180003).

Optimization of the slotted liners parameters during dual tubing steam injection process

Peng Li[1], **Yanyu Zhang**[1, *], **Hang Hu**[1], **Yunlong Liu**[1], **Yang Liu**[2], **Huijuan Chen**[3]

1 School of Petroleum Engineering, China University of Petroleum (East China), Qingdao 266580, China
2 Research Institute of Petroleum Exploration and Development, Beijing 10083, China
3 Shanghai Institute of Applied Mathematics and Mechanics in Shanghai University, Shanghai, 200072, China
Email: yyzhang@upc.edu.cn

Abstract. To study the distribution of steam parameters along the wellbore and the influence of slotted liners parameters on the effect of reservoir uniform preheating during the dual tubing steam injection process. Based on the structural characteristics of screen pipe completion and the simultaneous steam injection technology of long and short tubing, a coupled numerical model of fluid flow and heat transfer in reservoir and wellbore was established, and the model was solved by full implicit finite difference method and iterative technique. The results show that when the density, width and length of the slotted liners increase from 350 to 550/m, 0.20 to 0.40 mm and 35 to 75 mm, respectively, the difference of steam quality at the two ends of steam convergence position in the annuli increases by 0.41%, 2.26% and 1.71%, and the reservoir heating uniformity decreases by 1.49%, 2.68% and 2.08%, respectively. Optimizing the slotted liners parameters and reducing the steam quality difference at the convergence position of annuli can improve the uniform heating degree of reservoir along the horizontal wellbore.

1. Introduction

Heavy oil is one of the most important energy resources, and it is mainly distributed in the United States, Canada, China and Venezuela. With the increasing difficulty in the development of conventional oil and gas resources, it is of great significance to develop heavy oil resources [1-4]. However, due to the reservoir heterogeneity and variable mass flow in horizontal wellbore, uneven reservoir heating is the main reason for low reservoir reserves utilization [5-10]. As the slotted liners parameters have an important influence on the distribution of steam parameters along horizontal wellbore and the uniformity of reservoir heating in the process of dual tubing steam injection process. Therefore, it is of great significance to explore the effect of slotted liners parameters during dual tubing steam injection process.

At present, dual tubing steam injection technology has been widely used in the development of heavy oil reservoirs. However, the relevant research on this technology is still lacked. In recent years, Wu et al. [11] and Sun et al. [12, 13] have established fluid flow and heat transfer models in dual tubing steam injection wellbore, and predicted the distribution of key parameters in the long tubing (LT) and annuli. However, these models are analytical models, and neglected the effect of changes of reservoir physical parameters with time and slotted liners parameters on reservoir heating.

In this paper, based on the structural characteristics of screen pipe completion and the simultaneous steam injection technology of long and short tubing, a new model of dual tubing steam injection process was established, and the model was solved by full implicit finite difference method and iterative technique. This study can provide a theoretical reference for optimizing the parameters of slotted liners and improving the uniformity of reservoir heating.

2. Reservoir governing equations

The mass conservation equation for each phase (oil, water, and steam) can be derived as follows:

$$\nabla\cdot\left(\rho_{\mathrm{o}}\frac{\alpha kk_{\mathrm{ro}}}{\mu_{\mathrm{o}}}\nabla\left(P_{\mathrm{o}}-\rho_{\mathrm{o}}\mathrm{g}D\right)\right)+\rho_{\mathrm{o}}q_{\mathrm{o}}=\frac{\partial}{\partial t}\left(\rho_{\mathrm{o}}S_{\mathrm{o}}\varphi\right) \tag{1}$$

$$\nabla\cdot\left(\rho_{\mathrm{w}}\frac{\alpha kk_{\mathrm{rw}}}{\mu_{\mathrm{w}}}\nabla\left(P_{\mathrm{w}}-\rho_{\mathrm{w}}\mathrm{g}D\right)\right)+\rho_{\mathrm{w}}q_{\mathrm{w}}+m_{\mathrm{c}}=\frac{\partial}{\partial t}\left(\rho_{\mathrm{w}}S_{\mathrm{w}}\varphi\right) \tag{2}$$

$$\nabla\cdot\left(\rho_{\mathrm{g}}\frac{\alpha kk_{\mathrm{rg}}}{\mu_{\mathrm{g}}}\nabla\left(P_{\mathrm{g}}-\rho_{\mathrm{g}}\mathrm{g}D\right)\right)+\rho_{\mathrm{g}}q_{\mathrm{g}}-m_{\mathrm{c}}=\frac{\partial}{\partial t}\left(\rho_{\mathrm{g}}S_{\mathrm{g}}\varphi\right) \tag{3}$$

Considering the heat exchange between the wellbore and the reservoir, a modified energy conservation equation is developed as follow [5-7]:

$$\begin{aligned}\nabla\cdot\left(\lambda_{\mathrm{R}}\nabla T\right)+\nabla\cdot\left(\sum_{i=\mathrm{o,w,g}}\rho_i H_i\frac{kk_{ri}}{\mu_i}\left(\nabla P-\rho_i\mathrm{g}\nabla D\right)\right)-Q_{\mathrm{loss}}+Q_{\mathrm{H}}+\\+Q_{\mathrm{well}}=\frac{\partial}{\partial t}\left[\left(1-\varphi\right)\rho_{\mathrm{R}}c_{\mathrm{R}}T+\varphi\sum_{i=\mathrm{o,w,g}}S_i\rho_i U_i\right]\end{aligned} \tag{4}$$

To describe the equilibrium relationship between steam and water, the steam-water equilibrium equation is given as follow [14].

$$T=T_{\mathrm{S}}(P) \tag{5}$$

Where α is the unit conversion coefficient; P is the pressure, Pa; q is the unit volume flow rate, $\mathrm{m^3/(m^3\cdot s)}$; S is the saturation; k is the relative permeability, $\mathrm{um^2}$; μ is the viscosity, Pa·s; ρ is the density, $\mathrm{kg/m^3}$; m_{c} is the condensate steam mass flow rate per unit volume, $\mathrm{kg/(m^3\cdot s)}$; φ is the porosity of the reservoir; g is gravitational acceleration, $\mathrm{m/s^2}$; λ_{R} is the heat conductivity coefficient of rock, W/(m·°C); Q_{loss} is the heat loss rate to the boundary layer, J/s; Q_{well} is the heat loss rate from wellbore to the reservoir, J/s; U is the internal energy, J/kg; ρ_{R} is the rock density, $\mathrm{kg/m^3}$; H is the enthalpy, J/kg; T is the reservoir temperature, °C.

3. Wellbore governing equations

3.1. Steam flow model in the LT

The steam mass flow rate remains unchanged in the LT. According to the mass conservation principle, the mass conservation equation is given by:

$$\frac{\mathrm{d}m_{\mathrm{l}}}{\mathrm{d}l}=\pi r_{\mathrm{li}}^2\frac{\mathrm{d}(\rho_{\mathrm{l}}v_{\mathrm{l}})}{\mathrm{d}l}=0 \tag{6}$$

The momentum conservation equation for steam flow in the LT is derived as follow:

$$\frac{\mathrm{d}P_{\mathrm{l}}}{\mathrm{d}l}+\frac{\tau_{\mathrm{l}}}{\pi r_{\mathrm{li}}^2\mathrm{d}l}=-\frac{\mathrm{d}(\rho_{\mathrm{l}}v_{\mathrm{l}}^2)}{\mathrm{d}l} \tag{7}$$

The energy conservation equation is developed as follow:

$$\frac{\mathrm{dQ_l}}{\mathrm{d}l}=-\frac{\mathrm{d}}{\mathrm{d}l}\left[m_{\mathrm{l}}\left(h_{\mathrm{l}}+\frac{v_{\mathrm{l}}^2}{2}\right)\right] \tag{8}$$

3.2. Steam flow model in the annuli

During dual tubing steam injection process, the steam mass flow rate in the annuli is not a constant, and the mass conservation equation for steam flow in the annuli can be written as:

$$\frac{\mathrm{d}m_{\mathrm{a}}}{\mathrm{d}l}=-m_{\mathrm{af}} \tag{9}$$

The momentum conservation equation for steam flow in the annuli is given as:

$$\frac{\mathrm{d}P_{\mathrm{a}}}{\mathrm{d}l}+\frac{\tau_{\mathrm{a}}}{\pi r_{\mathrm{ai}}^2\mathrm{d}l}=-\frac{\mathrm{d}(\rho_{\mathrm{a}}v_{\mathrm{a}}^2)}{\mathrm{d}l} \tag{10}$$

The energy conservation equation in the annuli is presented as follow:

$$\frac{\mathrm{d}Q_{\mathrm{a}}}{\mathrm{d}l}-\frac{\mathrm{d}Q_{\mathrm{l}}}{\mathrm{d}l}+m_{\mathrm{af}}\left(h_{\mathrm{a}}+\frac{v_{\mathrm{ar}}^{2}}{2}\right)=-\frac{\mathrm{d}}{\mathrm{d}l}\left[m_{\mathrm{a}}\left(h_{\mathrm{a}}+\frac{v_{\mathrm{a}}^{2}}{2}\right)\right] \tag{11}$$

Where m_{l} and m_{a} are the steam mass flow rate in the LT and annuli, respectively, kg/s; dl is the length of the microsegment, m; m_{af} is the steam injection rate, kg/(m·s); r_{li} and r_{ai} are the equivalent radius of the LT and annuli, respectively, m; v_{l} and v_{a} are the steam flow velocity in the LT and annuli, respectively, m/s; ρ_{l} and ρ_{a} are the steam density in the LT and annuli, respectively, kg/m^3; P_{l} and P_{a} are the steam pressure in the LT and annuli, respectively, Pa; τ_{l} and τ_{a} are the friction force in the LT and annuli, respectively, N; h_{l} and h_{a} are the steam enthalpy in the LT and annuli, respectively, J/kg; v_{ar} is the radial steam injection velocity, m/s; Q_{l} and Q_{a} are the heat exchange rate in the LT and annuli, respectively, J/s.

3.3. Coupled equations

The reservoir model and wellbore model can be coupled by steam injection rate from the annuli to the reservoir is presented as follow:

$$m_{\mathrm{g}}=\rho_{\mathrm{a}}\cdot J\cdot\left(P_{\mathrm{a}}-P\right)\cdot I_{\mathrm{s}} \tag{12}$$

Where J is the well index; I_{s} is the steam absorption index; and P is the reservoir pressure, Pa.

4. Results analysis

With the developed new model, the profiles of steam quality and reservoir temperature along the horizontal wellbore are obtained as shown in Figure.1-6. The input parameters for simulation are listed in Table 1.

Table 1. Basic data used in the calculations

Parameters	Values	Parameters	Values
Reservoir top depth /m	180	Reservoir thickness /m	20
Reservoir pressure /MPa	0.22	Reservoir temperature /℃	10
Porosity /%	33	Oil saturation /%	75
Horizontal permeability /(10^{-3}um^2)	2700	Vertical permeability /(10^{-3}um^2)	1890
Length of horizontal wellbore /m	850	Reservoir thermal diffusivity /(m^2/h)	0.004
Steam pressure/(MPa)	2.0	Steam quality	0.95

4.1. Width of the slotted liners

As shown in Figure.1 and 2. It can be seen that with the increase of the slot width, the steam quality in the LT is almost unchanged, this is because the steam flow rate in the LT is a constant. However, the steam quality in the annuli decreases, because with the width of the slotted liners increasing, more steam is injected into the reservoir, which leads to more heat loss. When the width of the slotted liners increases from 0.20 to 0.40 mm, the difference of steam quality at the two ends of steam convergence position increases from 2.03% to 4.29%, increased by 2.26%. Influenced by the difference of steam enthalpy between two ends of steam convergence position, the ratio of maximum reservoir temperature to average reservoir temperature along wellbore increases from 1.007 to 1.034, increasing by 0.027, and the reservoir uniform heating degree decreases by 2.68%. Therefore, reducing the width of the slot and choosing suitable injected steam quality of short and long tubing can reduce the difference of steam quality at the two ends of annuli convergence position, which is conducive to the reservoir uniform heating along the horizontal wellbore.

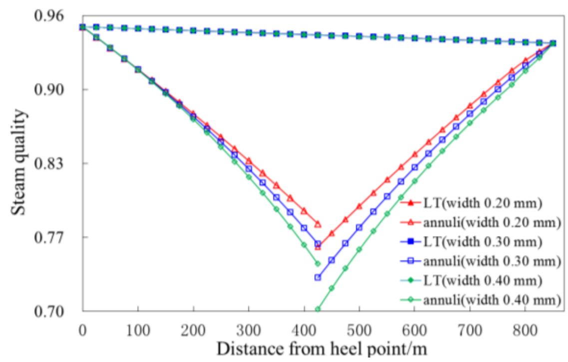

Figure 1. Distribution of steam quality along the wellbore with different slotted liners widths

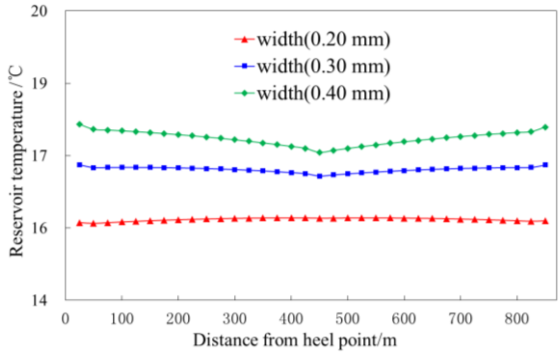

Figure 2. Distribution of reservoir temperature along the wellbore with different slotted liners widths

4.2. Length of the slotted liners

As shown in Figure.3 and 4. It is found that with the increase of the slot length, the steam quality in the LT is almost unchanged, this is because the steam flow rate in the LT is a constant. However, the steam quality in the annuli decreases, because with the length of the slotted liners increasing, more steam is injected into the reservoir, which leads to more heat loss. When the length of the slotted liners increases from 35 to 75 mm, the difference of steam quality at the two ends of steam convergence position increases from 2.31% to 4.02%, increased by 1.71%. Influenced by the difference of steam enthalpy between two ends of steam convergence position, the ratio of maximum reservoir temperature to average reservoir temperature along wellbore increases from 1.008 to 1.029, increasing by 0.021, and the reservoir uniform heating degree decreases by 2.08%. Therefore, reducing the length of the slot and choosing suitable injected steam quality of short and long tubing can reduce the difference of steam quality at the two ends of annuli convergence position, which is conducive to the reservoir uniform heating along the horizontal wellbore.

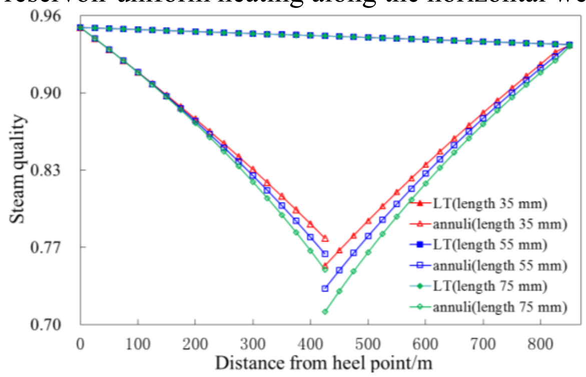

Figure 3. Distribution of steam quality along the wellbore with different slotted liners lengths

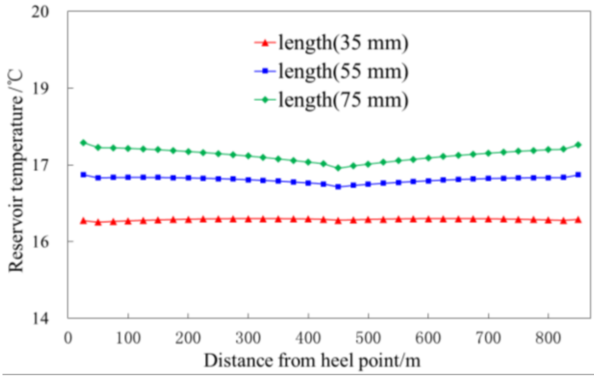

Figure 4. Distribution of reservoir temperature along the wellbore with different slotted liners lengths

4.3. Density of the slotted liners

As shown in Figure.5 and 6. It is observed that with the increase of the slot density, the steam quality in the LT is almost unchanged, due to the steam flow rate in the LT is a constant. However, the steam quality in the annuli decreases, because with the density of the slotted liners increasing, more steam is injected into the reservoir, which leads to more heat loss. When the density of the slotted liners increases from 350 to 550/m, the difference of steam quality at the two ends of steam convergence position increases from 3.18% to 3.59%, increased by 0.41%. Influenced by the difference of steam enthalpy between two ends of steam convergence position, the ratio of maximum reservoir temperature to average reservoir temperature along wellbore increases from 1.002 to 1.017, increasing by 0.021, and the reservoir uniform heating degree decreases by 1.49%. Therefore, reducing the density of the slot and choosing suitable injected steam quality of short and long tubing can reduce the difference of steam quality at the two ends of annuli convergence position, which is conducive to the reservoir uniform heating along the horizontal wellbore.

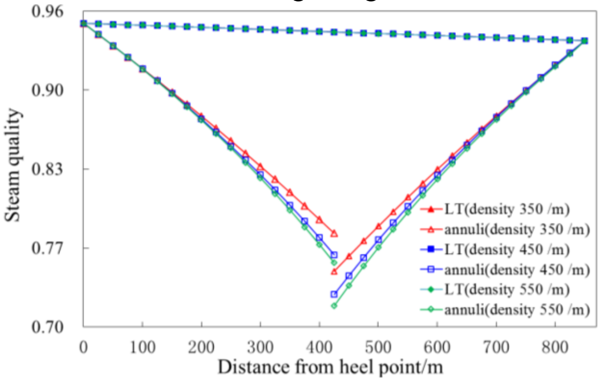

Figure 5. Distribution of steam quality along the wellbore with different slotted liners densities

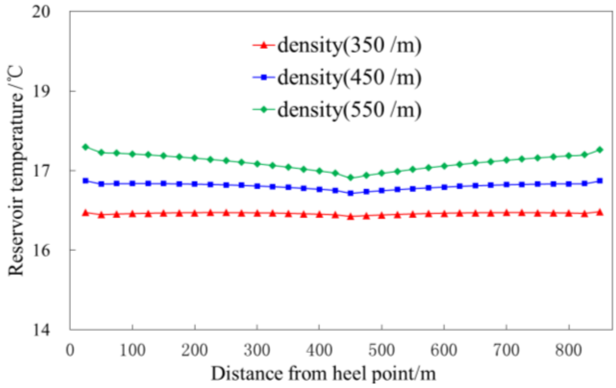

Figure 6. Distribution of reservoir temperature along the wellbore with different slotted liners densities

5. Conclusions

(1) The new coupled numerical model can predict the distribution of key thermal parameters of steam along the wellbore under different slotted liners parameters in the process of dual tubing steam injection.

(2) With the increase of slotted liners' density, width and length, the difference of steam quality at both ends of steam convergence position in the annuli increases, while the uniformity of reservoir heating decreases gradually.

(3) During the dual tubing steam injection process, choosing appropriate steam injection parameters can reduce the steam quality difference at the annuli convergence position, which is beneficial to uniform reservoir heating.

In this paper, a numerical model for optimizing the slotted liners parameters during dual tubing steam injection process is developed for the first time. This study can provide some important suggestions for oilfield development. The authors' following work will focus on: (1) the distribution of key parameters along the horizontal wellbore; (2) the optimization of the steam injection parameters, etc.

6. References

[1] Huang S J, Xia Y, Xiong H, et al. A three-dimensional approach to model steam chamber expansion and production performance of SAGD process [J]. International Journal of Heat and Mass Transfer, 2018, 127: 29-38.

[2] Huang S J, Cao M, Xia Y, et al. Heat and mass transfer characteristics of steam in a horizontal wellbore with multi-point injection technique considering wellbore stock liquid [J]. International Journal of Heat and Mass Transfer, 2018, 127: 949-958.

[3] Sun Xiaofei, Zhang Yanyu, Duan Xuewei, et al. A study on mechanisms and numerical simulation of secondary foamy oil by gas injection in heavy oil reservoirs [J]. OIL & GAS GEOLOGY, 2017(02): 391-399.

[4] Zhang Shuxia, Liu Fan, Mu Baoquan. An experimental study on enhanced heavy oil by steam flooding and chemical assisted steam flooding [J]. OIL & GAS GEOLOGY, 2017(05): 1000-1004.

[5] Chen Huijuan, Li Mingzhong, Di Qinfeng, et al. Numerical simulation of the outflow performance for horizontal wells with multiple steam injection vavles [J]. ACTA PETROLEI SINICA, 2017, 38(6): 696-704.

[6] Chen Huijuan, Li Mingzhong, Liu Chunmiao, et al. Inflow performance of slotted horizontal wells in cyclic steam simulation process [J]. Journal of Central South University (Science and Technology)，2016, 47(6)：2037-2044.
[7] Li M Z, Chen H J, Zhang Y Y, et al. A coupled reservoir/wellbore model to simulate the steam injection performance of horizontal wells [J]. Energy Technology, 2015, 3(5): 535-542.
[8] Lin Riyi, Qi Shangchao, Shen Wenli, et al. Study on parameters of steam injection in SAGD circulating preheating section. Journal of China University of Petroleum (Edition of Natural Science), 2018, 42(1): 134-141.
[9] Dong X H, Liu H Q, Pang Z X, et al. Flow and heat transfer characteristics of multi-thermal fluid in a dual-string horizontal well [J]. Numerical Heat Transfer, Part A: Applications, 2014, 66(2): 185-204.
[10] Dong Xiaohu, Liu Huiqing, Pang Zhanxi, et al. Model for steam properties in parallel-tubing horizontal wells of heavy oil reservoir [J]. Journal of Central South University (Science and Technology), 2014, 45(03): 939-945.
[11] Wu Yongbin, Li Xiuluan, Sun Xinge, et al. Key parameters forecast model of injector wellbores during the dual-well SAGD process [J]. Petroleum Exploration and Development, 2012, 39(04): 481-488.
[12] Sun F R, Yao Y D, Li X F, et al. A numerical model for predicting distributions of pressure and temperature of superheated steam in multi-point injection horizontal wells [J]. International Journal of Heat and Mass Transfer, 2018, 121: 282-289.
[13] Sun F R, Yao Y D, Li G Z, et al. An improved two-phase model for saturated steam flow in multi-point injection horizontal wells under steady-state injection condition [J]. Journal of Petroleum Science and Engineering, 2018, 167: 844-856.
[14] Mozaffari, S, Nikookar, M, Ehsani, M.R, et al. Numerical modeling of steam injection in heavy oil reservoirs. Fuel. 2013, 112, 185-192.

Acknowledgements
This work was financially supported by the National Natural Science Foundation of China (Grant No. 51704190), and the National Science and Technology Major Project (Grant No. 2016ZX05031-002).

IOP Conf. Series: Earth and Environmental Science **431** (2020) 012043 doi:10.1088/1755-1315/431/1/012043

Comparison of optimal reactive power flow model in the polar form and the mixed polar form

Aifeng Wang[1], Hua Wei[1], and Guohui Huang[1]

1 College of Electrical Engineering, Guangxi University, Nanning, China
E-mail: shynl@outlook.com

Abstract. This paper establishes the optimal reactive power flow (ORPF) model in the polar form and the mixed polar form. The analysis shows that the ORPF model in the polar form not only has less calculation amount of equality constraints than the ORPF model in the mixed polar form, but also has more concise expressions, which makes it easier to understand, analyze, and remember. The test results of IEEE30, 118, 300, 1047 bus systems show that the ORPF model in the polar form obtains the same optimal value and iteration number as the ORPF model in the mixed polar form, but its calculation time is shorter, and the solving efficiency is higher. With the increasing scale of modern power system, the calculation time of ORPF problem rises, so it is necessary to improve its solving efficiency. The ORPF model in the polar form is more suitable for power system analysis and calculation because of its high solving efficiency.

1. Introduction

Optimal reactive power flow (ORPF) is an essential work for improving the operational security and economy of power systems. It determines all kinds of controllable variables, such as reactive power output of generators and shunt capacitors, turn ratios of on-load tap changers (OLTC), etc., and minimizes transmission losses or other objective functions, while satisfying a given set of physical and operating constraints.

The rectangular form [1-3], the polar form [4-6], and the mixed polar form [7-9] widely apply to optimal power flow (OPF) and ORPF problems of power systems. Papers [10, 11]compare power flow calculation in the polar form and the rectangular form. There are many advantages to express bus voltages in the polar form. Firstly, in the actual power system, only the voltage magnitude and phase can be measured, but not the real and imaginary parts of the voltage. Secondly, voltage in the polar form can also reflect physical significance: the difference of voltage magnitude is related to the transmission of reactive power, and the difference of voltage phase is related to the transmission of active power. Thirdly, the power flow expression in the polar form is more concise than that in the rectangular form, which is convenient for people to understand, analyze and remember. Expressing bus voltage in the polar form and the mixed polar form both have the advantages mentioned above. However, there is no literature comparing models in the mixed polar form and the polar form. Therefore this paper establishes the ORPF models in the mixed polar form and the polar form, and compares the solving efficiency of the two models in order to find which one more suitable for power systems. Test results indicate that the ORPF model in the polar form has higher solving efficiency than the ORPF model in the mixed polar form.

The rest of this paper is organized as follows. Section 2 describes the ORPF model in the mixed polar form. Section 3 introduces the ORPF model in the polar form. Section 4 analyzes the difference

IOP Conf. Series: Earth and Environmental Science **431** (2020) 012043 doi:10.1088/1755-1315/431/1/012043

between the two models. Numerical tests are performed and discussed in section 5. Conclusions are drawn in section 6.

2. The ORPF model in the mixed polar form

2.1. The power equations in the mixed polar form of the on-load tap changer

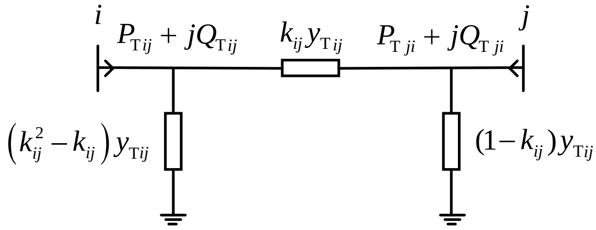

Figure 1. The transformer equivalent Π circuit.

This paper considers the voltage magnitude changing of the OLTC branch, ignoring its phase changing. In the ORPF model, the OLTC branch is represented by equivalent Π circuit, as shown in Figure 1. The OLTC branch is between bus i and bus j, and the ratio of voltage magnitude at bus i to that at bus j is $1:k_{ij}$. The admittance of the OLTC branch, the voltage at bus i and bus j, were expressed in the mixed polar form as follows:

$$\overrightarrow{y_{\mathrm{T}ij}} = G_{\mathrm{T}ij} + jB_{\mathrm{T}ij} \tag{1}$$

$$\overrightarrow{v_i} = V_i e^{\delta_i} \tag{2}$$

$$\overrightarrow{v_j} = V_j e^{\delta_j} \tag{3}$$

Where $G_{\mathrm{T}ij}$ and $B_{\mathrm{T}ij}$ are the conductance and susceptance of the OLTC branch between bus i and bus j, while V_i, V_j and δ_i, δ_j are the voltage magnitude and phase at bus i and bus j.

According to the power equation and the law of Kirchhoff, the active and reactive power flowing through the OLTC branch is:

$$P_{\mathrm{T}ij} = V_i^2 k_{ij}^2 G_{\mathrm{T}ij} - V_i V_j k_{ij} (\mathrm{G}_{\mathrm{T}ij} \cos(\delta_i - \delta_j) + \mathrm{B}_{\mathrm{T}ij} \sin(\delta_i - \delta_j)) \tag{4}$$

$$Q_{\mathrm{T}ij} = -V_i^2 k_{ij}^2 B_{\mathrm{T}ij} - V_i V_j k_{ij} (\mathrm{G}_{\mathrm{T}ij} \sin(\delta_i - \delta_j) - \mathrm{B}_{\mathrm{T}ij} \cos(\delta_i - \delta_j)) \tag{5}$$

$$P_{\mathrm{T}ji} = V_j^2 G_{\mathrm{T}ij} - V_j V_i k_{ij} (\mathrm{G}_{\mathrm{T}ij} \cos(\delta_j - \delta_i) + \mathrm{B}_{\mathrm{T}ij} \sin(\delta_j - \delta_i)) \tag{6}$$

$$Q_{\mathrm{T}ji} = -V_j^2 B_{\mathrm{T}ij} - V_j V_i k_{ij} (\mathrm{G}_{\mathrm{T}ij} \sin(\delta_j - \delta_i) - \mathrm{B}_{\mathrm{T}ij} \cos(\delta_j - \delta_i)) \tag{7}$$

2.2. The ORPF model in the mixed polar form

This paper mainly considers the regulating of transformer taps and the reactive power output of generators. Its mathematical model is made up of the objective function, power flow equality constraints, variables inequality constraints, etc.

The ORPF problem generally takes the minimum active power losses of the system as the objective function:

$$\min P_{loss} = \sum_{i \in S_{\mathrm{G}}} P_{\mathrm{G}i} - \sum_{i \in S_{\mathrm{D}}} P_{\mathrm{D}i} \tag{8}$$

Here, P_{loss} is the active power losses of the system; P_{Gi} and P_{Di} are the active power output of generators and the active load at bus i; S_G is the set of generators; S_D is the set of loads.

The power flow equality constraints can be expressed as:

$$\begin{aligned} &P_{\mathrm{G}i} - P_{\mathrm{D}i} - V_i \sum_{j \in S_{\mathrm{L}}} V_j (\mathrm{G}_{\mathrm{L}ij} \cos\delta_{ij} + \mathrm{B}_{\mathrm{L}ij} \sin\delta_{ij}) + V_i^2 \sum_{j \in S_{\mathrm{T}j}} k_{ij}^2 G_{\mathrm{T}ij} \\ &- V_i \sum_{j \in S_{\mathrm{T}j}} V_j k_{ij} (G_{\mathrm{T}ij} \cos\delta_{ij} + \mathrm{B}_{\mathrm{T}ij} \sin\delta_{ij}) + V_i^2 \sum_{j \in S_{\mathrm{T}i}} G_{\mathrm{T}ji} - V_i \sum_{j \in S_{\mathrm{T}i}} V_j k_{ji} (\mathrm{G}_{\mathrm{T}ji} \cos\delta_{ij} + \mathrm{B}_{\mathrm{T}ji} \sin\delta_{ij}) = 0 \end{aligned} \tag{9}$$

$$
\begin{aligned}
&Q_{\mathrm{G}i}-Q_{\mathrm{D}i}-V_i\sum_{j\in S_{\mathrm{L}}}V_j(\mathrm{G}_{\mathrm{L}ij}\sin\delta_{ij}-\mathrm{B}_{\mathrm{L}ij}\cos\delta_{ij})-V_i^2\sum_{j\in S_{\mathrm{T}j}}k_{ij}^2B_{\mathrm{T}ij}\\
&\quad -V_i\sum_{j\in S_{\mathrm{T}j}}V_jk_{ij}(G_{\mathrm{T}ij}\sin\delta_{ij}-\mathrm{B}_{\mathrm{T}ij}\cos\delta_{ij})-V_i^2\sum_{j\in S_{\mathrm{T}i}}B_{\mathrm{T}ji}-V_i\sum_{j\in S_{\mathrm{T}i}}V_jk_{ji}(\mathrm{G}_{\mathrm{T}ji}\sin\delta_{ij}-\mathrm{B}_{\mathrm{T}ji}\cos\delta_{ij})=0
\end{aligned}
\tag{10}
$$

Where, $Q_{\mathrm{G}i}$ and $Q_{\mathrm{D}i}$ are the reactive power output of generators and the reactive load at bus i; $\mathrm{G}_{\mathrm{L}ij}$ and $\mathrm{B}_{\mathrm{L}ij}$ are the conductance and susceptance of the transmission line between bus i and bus j; S_L is the set of transmission lines; $S_{\mathrm{T}j}$ is the set of buses at the k_{ij} side of the OLTC branch; $S_{\mathrm{T}i}$ is the set of buses at the other side of the OLTC branch; δ_{ij} is the difference of phase between bus i and bus j, $\delta_{ij}=\delta_i-\delta_j$.

The upper and lower inequality constraints of the variables are as follows:

$$\underline{P_{\mathrm{G}i}}\le P_{\mathrm{G}i}\le\overline{P_{\mathrm{G}i}}\tag{11}$$

$$\underline{Q_{\mathrm{G}i}}\le Q_{\mathrm{G}i}\le\overline{Q_{\mathrm{G}i}}\tag{12}$$

$$\underline{V_i}\le V_i\le\overline{V_i}\tag{13}$$

$$\underline{k_{ij}}\le k_{ij}\le\overline{k_{ij}}\tag{14}$$

Where, $\underline{()}$ and $\overline{()}$ indicate the lower and upper limits of variables.

3. The ORPF model in the polar form

3.1. The power equations in the polar form of the on-load tap changer

According to the power equation and the law of Kirchhoff, the active and reactive power in the polar form flowing through the OLTC branch can be expressed as:

$$P_{\mathrm{T}ij}=V_i^2k_{ij}^2Y_{\mathrm{T}ij}\cos\alpha_{\mathrm{T}ij}-V_iV_jk_{ij}Y_{\mathrm{T}ij}\cos(\delta_i-\delta_j-\alpha_{\mathrm{T}ij})\tag{15}$$

$$Q_{\mathrm{T}ij}=-V_i^2k_{ij}^2Y_{\mathrm{T}ij}\sin\alpha_{\mathrm{T}ij}-V_iV_jk_{ij}Y_{\mathrm{T}ij}\sin(\delta_i-\delta_j-\alpha_{\mathrm{T}ij})\tag{16}$$

$$P_{\mathrm{T}ji}=V_j^2Y_{\mathrm{T}ij}\cos\alpha_{\mathrm{T}ij}-V_jV_ik_{ij}Y_{\mathrm{T}ij}\cos(\delta_j-\delta_i-\alpha_{\mathrm{T}ij})\tag{17}$$

$$Q_{\mathrm{T}ji}=-V_j^2Y_{\mathrm{T}ij}\sin\alpha_{\mathrm{T}ij}-V_jV_ik_{ij}Y_{\mathrm{T}ij}\sin(\delta_j-\delta_i-\alpha_{\mathrm{T}ij})\tag{18}$$

Where $Y_{\mathrm{T}ij}$ and $\alpha_{\mathrm{T}ij}$ are the admittance magnitude and phase of the OLTC branch between bus i and bus j.

3.2. The ORPF model in the polar form

The objective function of this model is also equation (8). The constraints include power flow equality equations (19) - (20), upper and lower limits of variables inequality equations (11) - (14).

The power flow equality constraints can be expressed as:

$$
\begin{aligned}
&P_{\mathrm{G}i}-P_{\mathrm{D}i}-V_i\sum_{j\in S_L}V_jY_{\mathrm{L}ij}\cos(\delta_{ij}-\alpha_{\mathrm{L}ij})+V_i^2\sum_{j\in S_{\mathrm{T}j}}k_{ij}^2Y_{\mathrm{T}ij}\cos\alpha_{\mathrm{T}ij}\\
&\quad -V_i^2\sum_{j\in S_{\mathrm{T}j}}V_jk_{ij}Y_{\mathrm{T}ij}\cos(\delta_{ij}-\alpha_{\mathrm{L}ij})+V_j^2\sum_{j\in S_{\mathrm{T}i}}Y_{\mathrm{T}ji}\cos\alpha_{\mathrm{T}ji}-V_i\sum_{j\in S_{\mathrm{T}i}}V_jk_{ji}Y_{\mathrm{T}ji}\cos(\delta_{ij}-\alpha_{\mathrm{T}ji})=0
\end{aligned}
\tag{19}
$$

$$
\begin{aligned}
&Q_{\mathrm{G}i}-Q_{\mathrm{D}i}-V_i\sum_{j=i}^{N}V_jY_{\mathrm{L}ij}\sin(\delta_{ij}-\alpha_{\mathrm{L}ij})+V_i^2\sum_{j\in S_{\mathrm{T}j}}k_{ij}^2Y_{\mathrm{T}ij}\cos\alpha_{\mathrm{T}ij}\\
&\quad -V_i^2\sum_{j\in S_{\mathrm{T}j}}V_jk_{ij}Y_{\mathrm{T}ij}\cos(\delta_{ij}-\alpha_{\mathrm{L}ij})-V_i^2\sum_{j\in S_{\mathrm{T}i}}Y_{\mathrm{T}ji}\cos\alpha_{\mathrm{T}ji}-V_i\sum_{j\in S_{\mathrm{T}i}}V_jk_{ji}Y_{\mathrm{T}ji}\sin(\delta_{ij}-\alpha_{\mathrm{T}ji})=0
\end{aligned}
\tag{20}
$$

Where $Y_{\mathrm{L}ij}$ and $\alpha_{\mathrm{L}ij}$ are the admittance magnitude and phase of transmission line between bus i and bus j.

4. Comparison of the two ORPF models

The objective function and inequality constraints are identical in the two ORPF models, which do not affect the solution efficiency. The difference in the equality constraints is the critical factor that affects the solving efficiency of problem. Comparing the equality constraints of the two ORPF models, equations (9) - (10) and equations (19) - (20) could deduce each other. Therefore the two models are mathematically equivalent, and the optimal reactive power flow model in the polar form has the following advantages:

The calculation amount of power flow equations in the polar form is less than that in the mixed polar form. Take the active power flow equation as an example, as shown in Table 1. From the third item to the seventh item of the equation (9) are different from that of equation (19), which is the main factor affecting the calculation amount. If there is a transmission line between bus i and bus j, the third term is included in the active power flow equation. The third term of equation (9) is obtained by combining of two quartic polynomials, while the third term of equation (19) only has one quartic polynomial, so the calculation amount of equation (19) is less than that of equation (9). If an OLTC branch is between bus i and bus j, for the bus i, the fourth and fifth items are added to the active power flow equation. Compared with equation (9), the calculation amount of the fifth term of equation (19) reduces, and the fourth item has an additional trigonometric function multiplier, which could increase the calculation amount. However, the trigonometric function multiplier of the fourth item is a fixed value for a certain OLTC, so it needs to be computed only once through the whole iteration process, and little impact on the entire amount of calculation. Overall calculation amount of the fourth and fifth items of the equation (19) is still less than that of the equation (9). For bus j, the sixth and seventh items add to the active power flow equation, and similarly, the calculation amount of the sixth and seventh items of equation (19) is less than that of equation (9).

In a word, the calculation amount of the active power flow equation in the polar form is less than that of the mixed polar form, and the calculation amount of the reactive power flow equation is similar. Also, the expressions in the polar coordinates are more concise and easier to understand, analyze, and remember.

Table 1. Comparison of active power flow equation of the two ORPF models

	The model in the mixed polar form: Equation(9)	The model in the polar form: Equation(19)
The first item	$P_{\mathrm{G}i}$	$P_{\mathrm{G}i}$
The second item	$-P_{\mathrm{D}i}$	$-P_{\mathrm{D}i}$
The third item	$-V_i \sum_{j\in S_{\mathrm{L}}} V_j (\mathrm{G}_{\mathrm{L}ij}\cos\delta_{ij} + \mathrm{B}_{\mathrm{L}ij}\sin\delta_{ij})$	$-V_i \sum_{j\in S_L} V_j Y_{\mathrm{L}ij} \cos(\delta_{ij} - \alpha_{\mathrm{L}ij})$
The fourth item	$V_i^2 \sum_{j\in S_{\mathrm{T}j}} k_{ij}^2 G_{\mathrm{T}ij}$	$V_i^2 \sum_{j\in S_{\mathrm{T}j}} k_{ij}^2 Y_{\mathrm{T}ij} \cos\alpha_{\mathrm{T}ij}$
The fifth item	$-V_i \sum_{j\in S_{\mathrm{T}j}} V_j k_{ij} (G_{\mathrm{T}ij}\cos\delta_{ij} + \mathrm{B}_{\mathrm{T}ij}\sin\delta_{ij})$	$-V_i^2 \sum_{j\in S_{\mathrm{T}j}} V_j k_{ij} Y_{\mathrm{T}ij} \cos(\delta_{ij} - \alpha_{\mathrm{L}ij})$
The sixth item	$V_i^2 \sum_{j\in S_{\mathrm{T}i}} G_{\mathrm{T}ji}$	$V_i^2 \sum_{j\in S_{\mathrm{T}i}} Y_{\mathrm{T}ji} \cos\alpha_{\mathrm{T}ji}$
The seventh item	$-V_i \sum_{j\in S_{\mathrm{T}i}} V_j k_{ji} (\mathrm{G}_{\mathrm{T}ji}\cos\delta_{ij} + \mathrm{B}_{\mathrm{T}ji}\sin\delta_{ij})$	$-V_i \sum_{j\in S_{\mathrm{T}i}} V_j k_{ji} Y_{\mathrm{T}ji} \cos(\delta_{ij} - \alpha_{\mathrm{T}ji})$

5. Numerical test and discussion

5.1. Test systems and environment

This paper takes IEEE30, 118, 300, 1047 bus systems [12] as examples to discuss the performance of the two ORPF models. The characteristics of bus systems are as shown in Table 2. All the test systems

calculate in the form of per-unit value, and the convergence precision is 10^{-6}. The voltage magnitude range is set between 0.9 and 1.1, and the adjustment range of the turn ratios are all 0.9-1.1 identically.
All the test systems simulate in an HP PC-compatible computer. The computer's CPU is an Intel Core i5-6500, 3.20GHz, four cores, and its RAM is 8GB. All models were tested using the commercial software GAMS (General Algebraic Modeling System). The two ORPF models are modeled as a nonlinear programming problem, and the interior point method solver is used to solve them.

Table 2. The characteristics of bus systems.

	Number of buses	Number of transmission lines	Number of transformers	Number of active power resources	Number of reactive power resources
IEEE30	30	37	4	6	6
IEEE118	118	168	11	16	54
IEEE300	300	302	107	21	69
IEEE1047	1047	1018	164	68	152

5.2. The test results analysis of the two ORPF models

Take IEEE30 bus system as an example, the optimal value (per-unit) of active power losses (see Table 3), turn ratios of the OLTC branches (see Table 4), output of active and reactive power resources, voltage magnitude and phase of buses (see Table 5) calculated by the two models are same with each other, indicating that the two models are mathematically equivalent.

Table 3. The test results of the two ORPF models.

	Optimization by the ORPF model in the mixed polar form			Optimization by the ORPF model in the polar form			Before optimization
	Optimal value(per-unit)	Caculation time(s)	Iteration number	Optimal value(per-unit)	Caculation time(s)	Iteration number	Active power losses(per -unit)
IEEE30	0.0122	0.125	12	0.0122	0.063	12	0.0126
IEEE118	0.7086	0.156	17	0.7086	0.125	17	0.713
IEEE300	3.2196	0.203	21	3.2196	0.156	21	3.5531
IEEE1047	2.4517	0.469	28	2.4517	0.437	28	2.5379

Table 3 shows that the optimal value (per-unit) of IEEE30, 118, 300, 1047 bus systems by using the two ORPF models are same. Assuming that turn ratios of each test system are all equal to 1.0 before optimization, the active power losses of each test system is reduced to some extent after optimization by using the two ORPF models. It illustrates that the two ORPF models both can effectively reduce the active power losses of the power system in the precondition of ensuring the voltage quality. In addition, the model in the polar form has the same iteration number as the model in the mixed polar form. However, its calculation time is shorter, and the solving efficiency is higher than the model in the mixed polar form.

Table 4. For IEEE30 bus system, the turn ratios of transformers computed by different models.

	The model in the mixed polar form	The model in the polar form
$k_{6,10}$	1.100	1.100
$k_{9,6}$	1.050	1.050
$k_{12,4}$	0.988	0.988
$k_{28,27}$	1.031	1.031

Table 5. For IEEE30 bus system, the output of active and reactive power resources, voltage magnitude and phase of buses computed by different models.

Bus number	The ORPF model in the mixed polar form				The ORPF model in the polar form			
	Voltage magnitude	Voltage phase	Active power resources	Reactive power resources	Voltage magnitude	Voltage phase	Active power resources	Reactive power resources
1	1.100	0.000	0.100	-0.049	1.100	0.000	0.100	-0.049
2	1.099	-0.003	0.225	0.059	1.099	-0.003	0.225	0.059
3	1.096	-0.007	-	-	1.096	-0.007	-	-
4	1.095	-0.007	-	-	1.095	-0.007	-	-
5	1.099	-0.003	1.042	0.199	1.099	-0.003	1.042	0.199
6	1.096	-0.004	-	-	1.096	-0.004	-	-
7	1.090	-0.012	-	-	1.090	-0.012	-	-
8	1.100	-0.001	0.462	0.364	1.100	-0.001	0.462	0.364
9	1.080	0.032	-	-	1.080	0.032	-	-
10	1.097	-0.019	-	-	1.097	-0.019	-	-
11	1.100	0.164	0.754	0.156	1.100	0.164	0.754	0.156
12	1.091	-0.023	-	-	1.091	-0.023	-	-
13	1.100	0.008	0.263	0.073	1.100	0.008	0.263	0.073
14	1.079	-0.036	-	-	1.079	-0.036	-	-
15	1.078	-0.037	-	-	1.078	-0.037	-	-
16	1.082	-0.027	-	-	1.082	-0.027	-	-
17	1.087	-0.025	-	-	1.087	-0.025	-	-
18	1.073	-0.041	-	-	1.073	-0.041	-	-
19	1.073	-0.041	-	-	1.073	-0.041	-	-
20	1.078	-0.036	-	-	1.078	-0.036	-	-
21	1.086	-0.028	-	-	1.086	-0.028	-	-
22	1.086	-0.028	-	-	1.086	-0.028	-	-
23	1.073	-0.042	-	-	1.073	-0.042	-	-
24	1.075	-0.044	-	-	1.075	-0.044	-	-
25	1.081	-0.055	-	-	1.081	-0.055	-	-
26	1.065	-0.061	-	-	1.065	-0.061	-	-
27	1.093	-0.057	-	-	1.093	-0.057	-	-
28	1.092	-0.009	-	-	1.092	-0.009	-	-
29	1.075	-0.075	-	-	1.075	-0.075	-	-
30	1.064	-0.089	-	-	1.064	-0.089	-	-

6. Conclusion

This paper establishes the optimal reactive power flow model in the mixed polar form and the polar form, then compares and analyzes them detailedly. The objective function and inequality constraints of the two models are identical, while the equality constraints are different. The optimal reactive power flow model in the polar form, not only has less calculation amount of equation constraints than the model in the mixed polar form but also has more concise expressions, which makes it easier to understand, analyze and remember. The test results of IEEE30, 118, 300, 1047 bus systems shows that the optimal solution and the optimal value of active power losses obtained by the two models are the same with each other, which indicates the two models are equivalent in mathematics. The optimal reactive power flow model in the polar form has the same iteration number as the reactive power flow model in the mixed polar form, but has shorter calculation time and higher solving efficiency, and more suitable for the calculation of various problems of power systems.

7. References

[1] Qin, Z., Y. Hou and Y. Chen, *Convex Envelopes of Optimal Power Flow with Branch Flow Model in Rectangular Form*. IEEE Power and Energy Society General Meeting PESGM. 2015.

[2] Luo, J., L. Shi and Y. Ni, *A Solution of Optimal Power Flow Incorporating Wind Generation and Power Grid Uncertainties*. IEEE ACCESS, 2018. 6: p. 19681-19690.

[3] Wei, H., et al., *An interior point nonlinear programming for optimal power flow problems with a novel data structure.* IEEE TRANSACTIONS ON POWER SYSTEMS, 1998. 13(3): p. 870-877.

[4] Liu, M.B., S.K. Tso and Y. Cheng, *An extended nonlinear primal-dual interior-point algorithm for reactive-power optimization of large-scale power systems with discrete control variables*. IEEE TRANSACTIONS ON POWER SYSTEMS, 2002. 17(4): p. 982-991.

[5] Xiao-qin, X. and W. Hua, *A reduced-space interior point method for transient stability constrained optimal power flow in polar coordinate.* Power System Protection and Control, 2012. 40(4): p. 14-19.

[6] Ke, P., H. Xue-shan and M. Xiang-xing, *Solution Principles Study of Nonlinear Correction Equations in Primal-Dual Interior Point Method for Reactive Power Optimization.* Power System Technology, 2006. 30(19): p. 59-65.

[7] Wei, H., C. Lin and Y. Wang, *The optimal reactive power flow model in mixed polar form based on transformer dummy nodes.* IEEJ TRANSACTIONS ON ELECTRICAL AND ELECTRONIC ENGINEERING, 2018. 13(3): p. 411-416.

[8] Yi, Y., X. Chu and Y. Liu, *Activating Reactive Power Support from Active Distribution Systems.* IEEE Power and Energy Society General Meeting PESGM. 2018.

[9] Pandey, A., et al., *Robust Power Flow and Three-Phase Power Flow Analyses.* IEEE Transactions on Power Systems, 2019. 34(1): p. 616-626.

[10] Bynum, M., et al., *Tightening McCormick Relaxations Toward Global Solution of the ACOPF Problem.* IEEE TRANSACTIONS ON POWER SYSTEMS, 2019. 34(1): p. 814-817.

[11] Zhang, C., et al., *A Mixed Interval Power Flow Analysis under Rectangular and Polar Coordinate System.* IEEE Transactions on Power Systems, 2017. 32(2): p. 1422-1429.

[12] *Power system test case archive* [R/OL]. [2019-5-20]. http://www.ee.washington.edu/research/pstca/ index.html.

Acknowledgments

The work is supported by the National Nature Science Foundation of China (NSFC) (51667003).

Equivalence analysis of multiple monitoring methods for partial discharge

Lu Fan[1], Zhenhua Shao[2], Hanxin Shen[3], Zezhong Li[1] and Lijie Sun[1]

1 School of Electrical Engineering and Automation, Xiamen University of Technology, No.600, Ligong Road, Jimei District, Xiamen, P.R.China
2 Department of Electrical Engineering, Minjiang University, Fuzhou, Fujian, P.R.China
3 School of OPTO-Electronic and Communication Engineering, Xiamen University of Technology, No.600, Ligong Road, Jimei District, Xiamen, P.R.China
E-mail:821534949@qq.com

Abstract. In order to study the relationship between the amplitude (mV) and the discharge (pC) of a typical fault of a tip discharge in a partial discharge. Therefore, three different groups of tip electrode models (tip-tip, tip-plate, tip-ball) were simulated. The relationship between magnitude and discharge volume and voltage was obtained by using amplitude detection method (Ultra High Frequency Method, Acoustic Emission Method and Transient Earth Voltage method) and Pulse Current Method respectively. Kendall correlation analysis found that the amplitude and the voltage of the AE Method in the three amplitude detection methods are closest to the variation trend of the discharge quantity and the voltage of the Pulse Current Method. Exploring the equivalence between the amplitude and the discharge of the most accurate detection means, the mathematical model with the best fit is the Sum of Sin Functions.

1. Introduction

In recent years, with the increasing demand for electricity from all walks of life, the power grid not only needs to provide a large amount of electricity, but also needs to ensure the quality of electricity. Switchgear as one of the important protection units, its stable operation determines the safety of more users, maintaining its normal operation is still a problem worth exploring. In switchgear cabinets, busbar and metal components are prone to lead to sharp partial discharge because of some problems such as inadequate fabrication such as burrs, too long screw and irregular chamfer. Long-term power frequency and high voltage will inevitably affect the normal operation of switchgear cabinets to a certain extent, so the detection of partial discharge is particularly important.

Nowadays, pulse current method is a mature method to detect partial discharge. Its principle is that the discharge inside high voltage insulation equipment causes charge transfer to generate current pulse in the experimental circuit, and then collects data and judges the degree of partial discharge according to the detected current pulse intensity. Pulse current method is one of the most original methods of partial discharge measurement. Up to now, it is still the mainstream method of partial discharge detection because of its abundant information of current pulse and its incomparable advantages in other detection techniques such as easy quantification. It is the only standard test method among countries, but it also has obvious disadvantages: (1) it is vulnerable to current interference, higher requirements for experimental environment, (2) low measurable frequency, narrow frequency band, (3) weak anti-interference ability, will become less sensitive with the increase of capacitance, (4) At present, it is mostly used in off-line detection projects.

In the process of partial discharge, not only pulse current, but also ultrasonic, light, gas and other substances can be produced. so other detection methods are becoming popular in recent years, such as Ultra High Frequency (UHF) method, Acoustic Emission (AE) method, Transient Earth Voltage (TEV) method and so on. The basic principle of UHF method is that when partial discharge occurs, it produces a very steep pulse current, whose rise time is less than 1ns, and excites electromagnetic waves with frequencies up to several GHz. Through UHF sensor, it can detect electromagnetic waves in the range of 300-3000MHz produced by partial discharge, so as to obtain information of location and intensity of partial discharge [1]. The advantage is that it is not interfered by the electromagnetic signal of the conventional frequency,it is not sensitive to the corona discharge interference in the air and the signal propagation attenuation is small. The principle of the AE method is that when the partial discharge produces sound wave, a kind of pressure will be formed instantaneously, and an ultrasonic pulse will be generated, the information of partial discharge can be obtained by using the sound wave detected by the ultrasonic probe in the range of 20-200 KHz. Its advantage is that it has better anti-interference ability, and is sensitive to the type of medium and is basically not affected by electrical interference [2, 3]. The detection principle of TEV method is a method of partial discharge judgment by detecting the transient ground voltage generated by partial discharge (so-called TEV is the electromagnetic wave generated by partial discharge propagates to the surface of equipment along the breakpoint of shielding structure, generates current on the surface, and then forms the induced voltage to the ground on the surface of equipment). The channel measurement frequency band is 10 kHz-100 MHz, which has the advantage that the electromagnetic signal has less attenuation during propagation along the surface of the object due to no significant interference source [4].
These methods rely on their respective advantages to compensate for the shortcomings of the pulse current method, and it is worthwhile to further explore these methods. Document [5] simulates and analyses the relationship between UHF method and pulse current method output under four typical fault models in GIS. Document [6, 7] explores the relationship between UHF signal calibration and discharge quantity of partial discharge fault types in oil. These studies only use UHF as an amplitude detection method, the detection method is relatively single, and the domestic research on the use of AE discharge detector is less. Using UHF, AE and TEV three kinds of amplitude detection methods to carry out experiments at the same time, we can study the results and accuracy of the three detection methods, and establish the equivalence function relationship with the pulse current method.

2. Analysis method

2.1 Kendall correlation analysis

In order to explore the correlation between the Amplitude-Voltage trend and the Discharge quantity-Voltage trend of the three amplitude detection methods, Therefore, the Kendall correlation coefficient was used to study in Matlab. In statistics, the Kendall correlation coefficient is a statistical value used to measure the correlation between two random variables. The correlation value is often expressed by τ. It tests the statistical dependence of two random variables by calculating the correlation coefficient. The kendall coefficient has a value range of -1 to 1. When τ is 1, it means that two variables have a highly consistent rank correlation, when τ is 0, it means that the two variables are independent of each other, when τ is -1 , indicating that the two variables have completely opposite level correlations[8].Therefore, among the three amplitude detection methods, the Amplitude-Voltage trend with τ closest to 1 is the most consistent with the Discharge quantity-Voltage trend, and the detection method is more accurate.

2.2 Fitting degree analysis

In order to explore the mathematical relationship between amplitude and discharge quantity, three mathematical models, Polynomial, Sum of Sin Functions and Exponential, were selected to compare the goodness of fit. The Polynomial function model is $y=\mathrm{a}x^2+\mathrm{b}x+\mathrm{c}$ .The Sum of Sin Functions model is $y=\mathrm{a}_1\sin(\mathrm{b}_1x+\mathrm{c}_1)+\mathrm{a}_1\sin(\mathrm{b}_1x+\mathrm{c}_1)$ .The Exponential function model is $y=\mathrm{a}e^{\mathrm{b}x}+\mathrm{c}e^{\mathrm{d}x}$.

Goodness of Fit is the fit of the regression line to the detected value, It mainly consists of Sum of Squares for Error (SSE), Root Mean Squared Error (RMSE), Coefficient of determination (R^2), and

Degree of Freedom Adjust (R^2_{adj}).

(1) Sum of Squares for Error(SSE) expression is

$$\mathrm{SSE} = \sum_{i=1}^{n} (y_i - \hat{y}_i)^2 \tag{2.1}$$

SSE represents the dispersion of observations and fitted values, and the closer the value is to 0, the better the degree of fit.Where n is the number of samples, y_i is the observed value, and $\hat{y}_i$ is the sample regression fitted value, which is the estimated value of the regression line.

(2) Root Mean Squared Error (RMSE) expression is

$$\mathrm{MSE} = \mathrm{SSE}/n = \frac{1}{n}\sum_{i=1}^{n} (y_i - \hat{y}_i)^2 \tag{2.2}$$

$$\mathrm{RMSE} = \sqrt{\mathrm{MSE}} = \sqrt{\mathrm{SSE}/n} = \sqrt{\frac{1}{n}\sum_{i=1}^{n} (y_i - \hat{y}_i)^2} \tag{2.3}$$

RMSE represents the deviation between the observed value and the sample value. The smaller the RMSE is, the closer it is to 0, the better the degree of fit.Among them, the MSE is the mean square error, which is the ratio of the sum of the squares of the data to be fitted and the fitted values to the number n of fittings.

（3）Coefficient of determination (R^2) expression is

$$\mathrm{SSR} = \sum_{i=1}^{n} (\hat{y}_i - \bar{y}_i)^2 \tag{2.4}$$

$$\mathrm{SST} = \sum_{i=1}^{n} (y_i - \bar{y}_i)^2 \tag{2.5}$$

$$R^2 = \frac{\mathrm{SSR}}{\mathrm{SST}} = \frac{\mathrm{SST}-\mathrm{SSE}}{\mathrm{SST}} = 1 - \frac{\mathrm{SSE}}{\mathrm{SST}} \tag{2.6}$$

R^2 represents the degree to which the data to be fitted is distributed around the regression line of the original data, and the larger the value, the closer to 1 indicates that the degree of fit is optimal.Where SSR is the sum of the squares of the difference between the fitted data and the mean of the data to be fitted, and SST is the sum of the squares of the difference between the data to be fitted and the mean.

（4）Degree of Freedom Adjust(R^2_{adj}) expression is

$$R^2_{adj} = 1 - \frac{\mathrm{SSE}/(\mathrm{n-k-1})}{\mathrm{SST}/(\mathrm{n-1})} \tag{2.7}$$

R^2_{adj} represents the corrected decision coefficient, and the closer the value is to 1, the highest the degree of fit.Where n-k-1 is the degree of freedom of the sum of squares of residuals, and n-1 is the degree of freedom of the sum of squares.

3. The relationship between pulse current method parameters and other detection parameters

According to the IEC60270 standard, the pulse current method expresses the degree of discharge by the apparent discharge quantity pC. UHF, TEV, and AE can represent the partial discharge intensity by the amplitude mV [9](can be converted to mV by the formula dB=20×log(mV)).

Referring to the common tip discharge types of switchgear cabinets, three common types of tip discharges were simulated: tip-tip discharge model, tip-plate discharge model and tip-ball discharge model [10].At the same voltage level, the PDS800 partial discharge detector and the JFD-251 partial discharge detector were used for detection,the amplitude and discharge quantity during partial discharge are obtained separately, so as to explore the equivalence relation between the two, and define the amplitude parameter as P(mV) and the discharge parameter as Q(pC).

3.1 Experimental process

Because the acrylic sheet has good insulation performance and the material is transparent and easy to observe, it is used as a bracket in the model.The pointed electrode is a cone having a bottom radius of

15 mm and a height of 40 mm, the spherical electrode has a diameter of 50 mm, the plate electrode has a length of 150 mm, a width of 120 mm, and a thickness of 10 mm.All the outer layers of the electrode are tightly covered with tin foil to ensure good electrical conductivity. On this basis, a set of partial discharge detection test platform for analog switchgear is built, as shown in Figure 1.

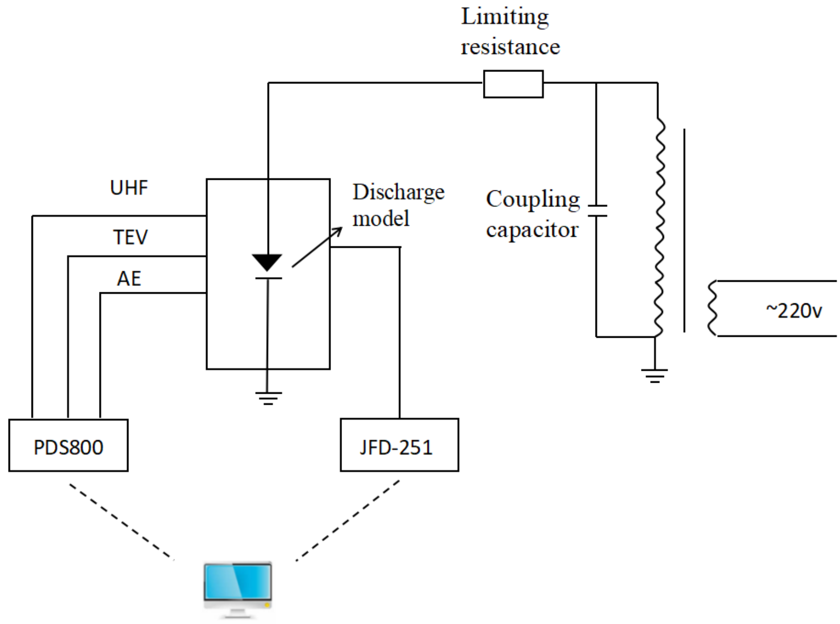

Figure 1. Wiring diagram of partial discharge detection by TEV,AE, UHF method and pulse current method

Maintain the three metal electrode models: tip-tip, tip-plate, and tip-ball spacing is 30mm. In the three pairs of models, the tip electrode is connected to the high voltage, and the other end is grounded. The voltage is slowly applied to observe the electrode phenomenon. The relationship between the applied voltage and the discharge quantity pC data and the data relationship with the amplitude mV at the same voltage are recorded.The data were analyzed and found that the trend of pC and mV values between the electrode models at the same voltage level was similar, so the fitting figure was analysed [11, 12].

3.2 Experimental results and analysis

3.2.1 Tip-tip discharge model

The relationship between the discharge quantity Q obtained by the pulse current method and the applied voltage U is as shown in Figure 2(a). It can be seen that the discharge quantity starts to increase sharply at 10 kV until the growth slows down at 17 kV and begins to stabilize until breakdown. UHF, TEV and AE are used to obtain the relationship between the amplitudes of P_{UHF},P_{TEV},P_{AE} and the applied voltage U. Since UHF and AE have small changes with respect to the amplitude of TEV at the same voltage, in order to better compare the discharge development trend measured by each detection method, the UHF and AE amplitude data are reasonably amplified by 1000 times and 40 times respectively. The new curve is placed in the figure as shown in Figure 2(b). It can be seen from the figure that the TEV method first detects the change of amplitude. The UHF method grows slowly at 17kV until breakdown, while the AE method shows a large increase at 19kV.

IOP Conf. Series: Earth and Environmental Science **431** (2020) 012044 doi:10.1088/1755-1315/431/1/012044

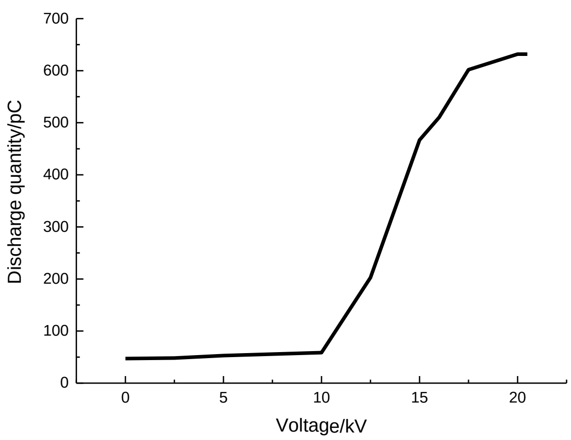

(a)Relationship between discharge quantity and voltage

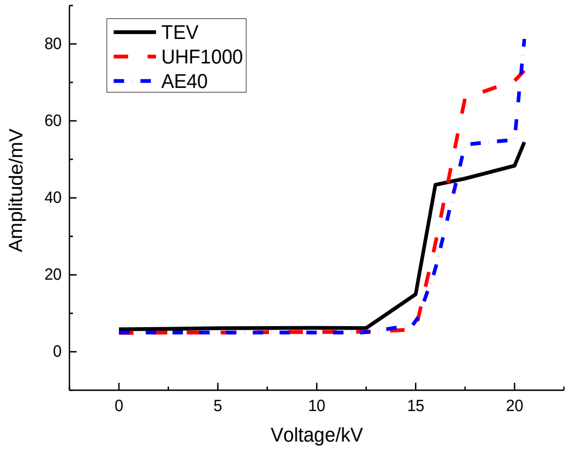

(b) The relationship between amplitude and voltage

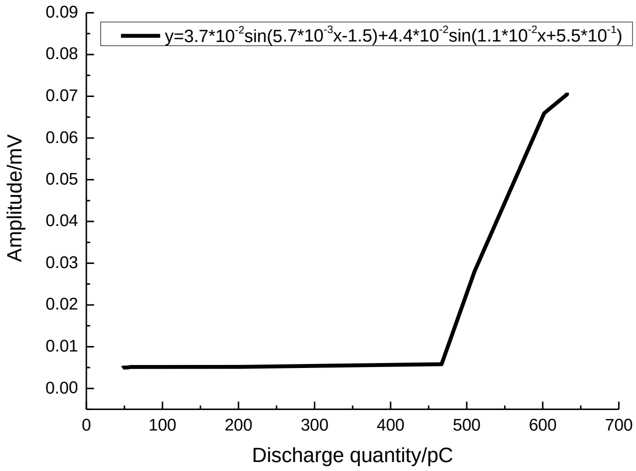

(c) Functional relationship between discharge quantity and amplitude of UHF detection method

Figure 2. shows the relationship between the feature quantities under the tip-tip model.

From Fig. 2(a) and (b), it can be observed that the trends of Q-U and P-U are roughly the same. The kendall coefficients of the three detection methods are τ_{AE*40}=0.9173,τ_{TEV}=0.9439,$\tau_{UHF*1000}$=0.9888,the more the τ value is closer to 1, the higher the correlation. Therefore, in the tip-tip discharge model, the discharge trend of the UHF method is closest to the trend of the pulse current method.The pulse current method parameter Q and the UHF method parameter P are fitted. The fitting conditions under the three mathematical models are shown in Table 1.The SSE and RMSE values of the Sum of Sin Functions are closest to 0, and R^2 and R^2_{adj} are most oriented to 1, so the Sum of Sin Functions has the best fit.And determine the best fit mathematical model of Q and P under the tip-tip model as Sum of Sin Functions , the fitting figure is shown in Figure 2(c).The model coefficients are $a_1=3.7\times10^{-2}$, $b_1=5.7\times10^{-3}$, c_1=-1.5, a2=4.4×10^{-2}, $b_2=1.1\times10^{-2}$, $c_1=5.5\times10^{-1}$.

3.2.2 Tip-plate discharge model

In the same way, under the tip-plate discharge model, the relationship between the discharge quantity Q obtained by the pulse current method and the applied voltage U is shown in Figure 3(a). It can be seen that Q starts to change slightly from 10kV, and begins to increase greatly at 12.5kV, and the 14kV growth rate begins to decrease. The UHF and AE amplitude data are reasonably magnified 1000 times and 10 times as a new curve added to the P-U relationship diagram as shown in Figure 3(b).The observation curve shows that TEV and UHF start to increase slightly at 10kV, AE starts to increase from 12kV, and the TEV curve begins to settle at 13kV.While AE and UHF increase in different ranges at 12 kV,it is difficult to see which P-U curve is more in line with Q-U curve by observation.

Table 1. The goodness of fit of the mathematical model under the tip-tip model.

Mathematical Model	Goodness of Fit			
	SSE	RMSE	R^2	R^2_{adj}
Polynomial	$4.2384e^{-4}$	0.007781	0.9495	0.935
Sum of Sin Functions	$1.008e^{-5}$	0.001587	0.9988	0.9973
Exponential	$2.3829e^{-4}$	0.0063	0.9716	0.9574

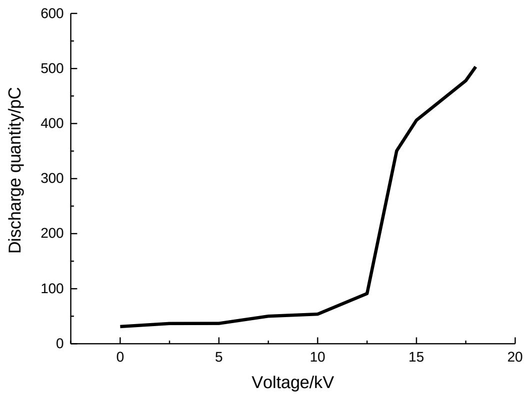

(a)Relationship between discharge quantity and voltage

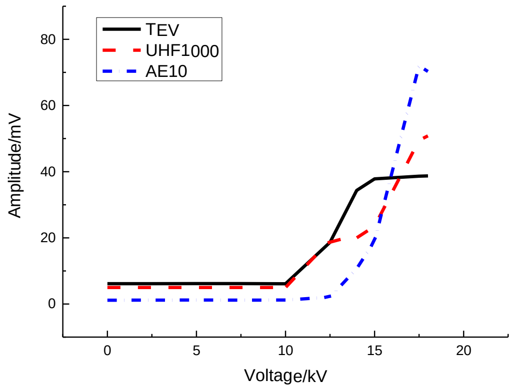

(b) The relationship between amplitude and voltage

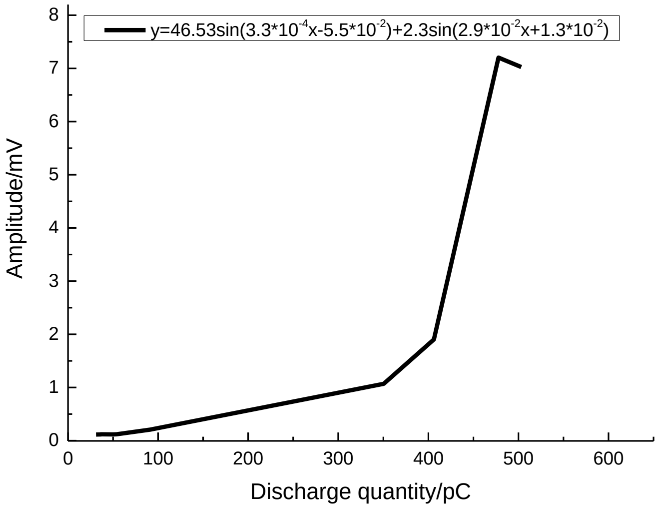

(c) Functional relationship between discharge quantity and amplitude of AE detection method

Figure 3. shows the relationship between the feature quantities under the tip-plate model

The kendall coefficient are τ_{AE*40}=0.8989, τ_{TEV}=0.822, $\tau_{UHF*1000}$=0.8819.Therefore, in the tip-plate discharge model, the discharge trend of the AE method is closer to the pulse current method.The pulse current method parameter Q and the AE method parameter P are fitted, and the fitting condition is as shown in Table 2.The SSE value and RMSE value of the Sum of Sin Functions are the smallest closest to 0, and R^2 and R^2_{adj} are most inclined to 1, and the fitting degree of the Sum of Sin Functions is optimal.It is determined that the best fit mathematical model of Q and P under the tip-plate model is

IOP Conf. Series: Earth and Environmental Science **431** (2020) 012044 doi:10.1088/1755-1315/431/1/012044

Sum of Sin Functions, and the fitting figure is shown in Fig. 3(c).The model coefficients are a_1=46.53，$b_1=3.3\times10^{-4}$， $c_1=-5.5\times10^{-2}$, a_2=2.3， $b_2=2.9\times10^{-2}$， $c_1=1.3\times10^{-2}$.

3.2.3 Tip-ball discharge model

Similarly, in the tip-ball discharge model, the relationship between the discharge quantity Q obtained by the pulse current method and the applied voltage U is as shown in Figure 4(a). It can be seen that the discharge quantity begins to increase slowly at 5kV until a large increase occurs at 15kV.The UHF and AE amplitude data are reasonably magnified 1000 times and 10 times as a new curve added to the P-U relationship diagram as shown in Figure 4(b).It can be seen that UHF first started the amplitude change at 5kV, but the fluctuations in the subsequent changes are quite different from the Q-U trend, and the AE started to increase significantly at 15kV.

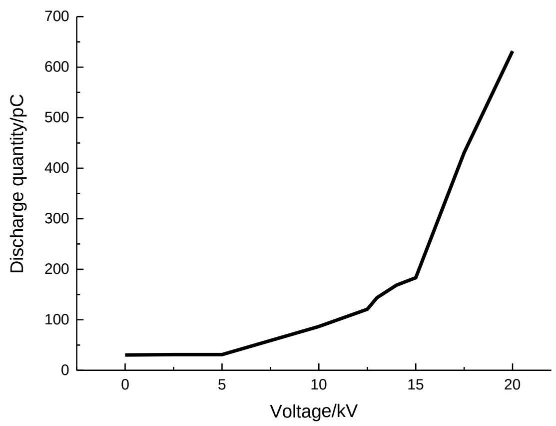

(a)Relationship between discharge quantity and voltage

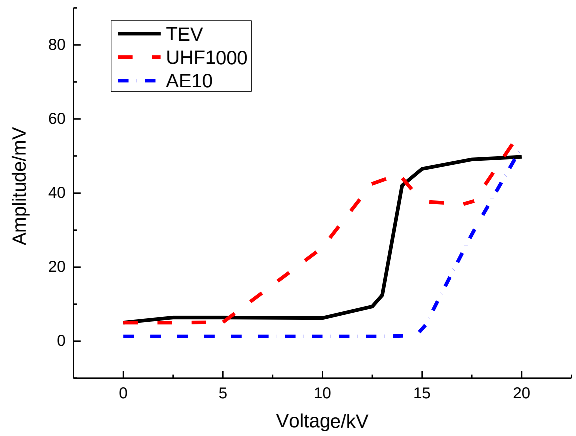

(b) The relationship between amplitude and voltage

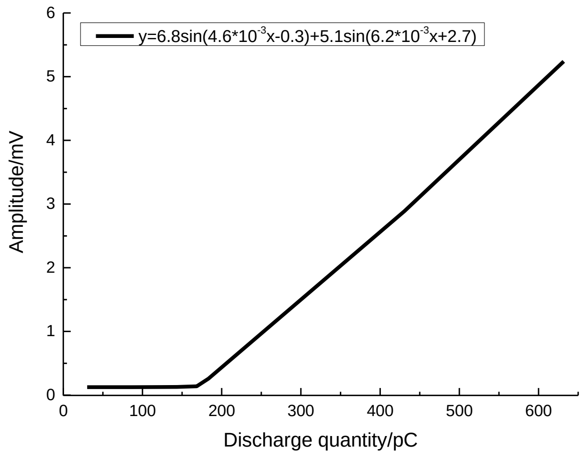

(c) Functional relationship between discharge quantity and amplitude of AE detection method

Figure 4. shows the relationship between the feature quantities under the tip-ball model

The kendall coefficient are τ_{AE*10}=0.977,τ_{TEV}=0.8989,$\tau_{UHF*1000}$=0.6591.It can be seen that in the tip-ball discharge model, the discharge trend of the UHF method has a large deviation from the pulse current method,but the discharge trend of the AE method is closest to the pulse current method.The pulse current method parameter Q and the AE method parameter P are fitted, and the fitting condition of each model is shown in Table 3.The SSE value and RMSE value of the Sum of Sin Functions are the smallest closest to 0, and R^2 and R^2_{adj} are most inclined to 1, and the fitting degree of the Sum of Sin Functions is optimal.It is determined that the best fit mathematical model of Q and P under the tip-ball model is Sum of Sin Functions, and the fitting figure is shown in Figure 3(c).The model coefficients are a_1=6.8， $b_1=4.6\times10^{-3}$， c_1=-0.3； a_2=5.1， $b_2=6.2\times10^{-3}$， c_1=2.7.

Table 2. Goodness of fit of mathematical models under the tip-plate model.

Mathematical Model	**Goodness of Fit**			
	SSE	RMSE	R^2	R^2_{adj}
Polynomial	3.5483	0.7120	0.9519	0.9381
Sum of Sin Functions	0.6862	0.4142	0.9907	0.9791
Exponential	2.9904	0.7060	0.9594	0.9391

Table 3. Goodness of fit of mathematical models under the tip-ball model.

Mathematical Model	**Goodness of Fit**			
	SSE	RMSE	R^2	R^2_{adj}
Polynomial	0.3289	0.2168	0.9880	0.9845
Sum of Sin Functions	0.0034	0.0290	0.9999	0.9997
Exponential	0.0232	0.0622	0.9992	0.9987

4. Conclusion

In the experiment, multiple test methods were used to test and collect data on three kinds of tip electrode models. The kendall coefficient is compared with the detection method which is the closest to the trend of pulse current method, and the optimal equivalence function relationship between amplitude (mV) and discharge quantity (pC) is fitted. The conclusion is obtained through research:

- The voltage was gradually applied to the experimental model, and the variation trend of the magnitude (mV) and discharge volume (pC) of the same kind of electrode model was similar.
- According to the Q-U and P-U trends of the three kinds of tip electrode models, the kendall correlation result indicates that the Acoustic Emission(AE) method is more accurate than the UHF method and the TEV method in PD detection with tip failure;
- According to the degree of fitting of the three mathematical models, the equivalence relationship between amplitude (mV) and discharge quantity(pC) is most consistent with the mathematical model of Sum of Sin Functions.

Therefore, based on the equivalence analysis using the tip discharge model, other fault defect models can be combined with other detection methods. This study is to find the best detection method for detecting other fault models, and to study the amplitude and discharge quantity. The functional relationship with a higher degree of fit provides the basis for research.

5. References

[1] Zhong L P,Ji S C and Cui Y J et al 2015 Study on Typical Defective Discharge Characteristics of Transformer and Its Charge Detection Technology of *High Voltage Electrical Appliance* **51** 15-21.

[2] Wang G R 2018 Method for detecting partial discharge of transformer of *Energy and Energy Saving* **10** 145-146.

[3] Shi W,Yang Z L and Huang Q X et al 2018 Study on the development characteristics of ultrasonic partial discharge of metal tip defects of different lengths in GIS of *High Voltage Electrical Appliance* **54** 80-85.

[4] Lv F C,Li D H and Wang Z J et al 2013 Partial Discharge Detection and Positioning of Switchgear Based on TEV and Ultrasonic of *Electrical Measurement and Instrumentation* **50** 73-78.

[5] Yang T, Wu J and Zhang G et al 2018 Experimental Research on Relationship between UHF Partial Discharge Signals and Discharge Quantity in GIS of *MATEC Web of Conferences* **208** 01002.
[6] LIU S C,Wang C and DU L 2017 Calibration of Local High-frequency Signals for Typical Defects in Transformer Oil of *High voltage technology* **43** 2983-2990.
[7] Cleary G P and Judd M D 2006 UHF and Current Pulse Measurements of Partial Discharge activity in Mineral oil of *Measurement and Technology* **153** 47－54.
[8] Hu C J 2013 Significance test of Kendall τ Correlation Coefficient under Small Sample of *Control Engineering* **20** 1195-1197.
[9] YAN Q 2016 Application and Research of Partial Discharge Online Monitoring System for High Voltage Switchgear of *North China Electric Power University*.
[10] YANG G W,WANG X and ZHANG W J et al 2014 Analysis of Common Insulation Fault Factors of 35kV Switchgear of *Electrotechnical* **3** 3-4.
[11] ZHAO X H,YANG J G and LU X L et al 2008 Comparison of partial discharge detection pulse current method and ultra-high frequency method in oil of *High Voltage Technology* **07** 1401-1404.
[12] LI H F, GAO Z B et al 2018 Study on TEV and Ultrasonic Partial Discharge Characteristics of Typical Defect Models of *Switchgear of Insulation Materials* **51** 81-86.

Acknowledgments
This work has been supported by the planning project of Xiamen Municipal Science and Technology Bureau (Grant No.3502Z20173034) and the Project of Fujian provincial bus and special vehicle R & D Collaborative Innovation Center (Grant No. 2016BJC004) and Industry-University Cooperation Project of Fujian Science and Technology Department:Power Lithium Battery Variable Rate Balanced Charging Management System(Grant No.2019H6024) and the Project of Graduate Science and Technology Innovation of Xiamen University of Technology.

Chapter 6:
Electronic Information Engineering

Estimating the boundary of the asymptotic stability region of Lotka–Volterra system by using the trajectory reversing method

Yi-Horng Lai[1] and Liang Fang[1]

1 School of Mechanical and Electrical Engineering, Xiamen University Tan Kah Kee College, China
E-mail: lai81.xujc@qq.com/ lai81@xujc.com

Abstract. This paper proposes a topological approach for plotting the boundary of the region of asymptotic stability (RAS) of Lotka–Volterra predator-prey system. First, stability analysis was used to determine the specific saddle point that has eigenvalues with one positive and two negative real parts in a linearized Jacobian matrix. A set of initial states located around the saddle point on the specific eigenplane spanned by the two stable eigenvectors was then selected. Finally, the trajectory reversing method was used and the trajectories that had initial states on the eigenplane delineated the boundary of the asymptotic stability region. The trajectories of the initial states that started from the opposite sides of the RAS exhibited different dynamic behaviour. The numerical simulation are presented to demonstrate the effectiveness of the proposed approach.

1. Introduction

Determining the boundary of an asymptotic stability region around an equilibrium point is a conventional technique in the study of nonlinear systems. The region of asymptotic stability (RAS) is defined as a set of initial conditions in which the system approaches a specific equilibrium point. The analysis of the RAS can clarify many nonlinear characteristics of a system. Studies have proposed numerous methods for finding the boundary of the RAS. These methods can be classified into two categories: Lyapunov and non-Lyapunov methods [1].

The Lyapunov method consists of two steps. First, Lyapunov's direct method is used to derive a Lyapunov function and prove the local asymptotical stability of an equilibrium point. Second, optimization techniques are used to enlarge the region defined by the Lyapunov function [2-3]. Because Lyapunov functions are not exclusive, an RAS estimated using a Lyapunov function is usually conservative. No conclusion can be reached regarding the actual boundary of the RAS [4].

Most non-Lyapunov methods are based on topological approaches. The stability characteristics of a nonlinear system can be determined by analysing the type of equilibrium point of the linearized system. There are three types of equilibrium points: sink, source, and saddle points. Saddle points have specific dynamic behaviours that are distinct from those of sink and source points. For example, if some of the initial points are determined to be in the neighborhood of a saddle point, parts of the trajectories converge to the saddle point when the time is increasing or reversing, but others do not. Therefore, these converging trajectories can be used to form the surface of a stability boundary. The estimation of the boundary of an RAS in the second-order system using the trajectory reversing method has been demonstrated previously [5-6]. For presenting a clear boundary for an RAS in a three-dimensional space, Lee and Han proposed the phase portrait method, in which some special sets of initial points are selected on the surface spanned by the stable eigenvector of the saddle point; the trajectory reversing method is then used to make the trajectories form a manifold of the RAS in a nonlinear system [7].

The Lotka–Volterra systems are crucial mathematical models. They are the proper starting point for numerous classes of models in ecology, biology, physics, and chemistry. Numerous interesting dynamic behaviours (e.g., global asymptotic behaviour, bifurcation, and phase space analysis) of Lotka–Volterra systems have been identified [8-10]. In addition, the conditions of chaotic dynamics were evaluated by using equilibria analysis [11]. However, few studies have discussed the boundary of RAS or the edge of chaotic attractors in Lotka–Volterra systems. The technique for determining the exact basins of chaotic attractors when a chaotic attractor and a stable equilibrium point coexist in phase space has seldom been investigated. Clarify the clear boundary of RAS can be used to predict the dynamic characteristics of initial states.

This study analysed the stability characteristics of equilibrium points and determined the actual boundaries of the RAS in the three-dimensional Lotka–Volterra predator-prey system. First, the necessary conditions for the saddle point and the RAS are introduced. Furthermore, the three-dimensional Lotka–Volterra predator-prey system is presented and the stability properties of the equilibrium points are investigated. Last, the numerical results for plotting the boundary of an RAS are given.

2. Method

Consider a third-order autonomous system expressed by

$$\dot{X} = F(X), \tag{1}$$

where $X = [x_1 \quad x_2 \quad x_3]^T$ and $F(X) = [f_1(X)\ f_2(X)\ f_3(X)]^T$.

Linearizing the third-order system at an equilibrium point X_{ep}, the Jacobian matrix can be written as

$$A = \begin{bmatrix} \frac{\partial f_1}{\partial x_1} & \frac{\partial f_1}{\partial x_2} & \frac{\partial f_1}{\partial x_3} \\ \frac{\partial f_2}{\partial x_1} & \frac{\partial f_2}{\partial x_2} & \frac{\partial f_2}{\partial x_3} \\ \frac{\partial f_3}{\partial x_1} & \frac{\partial f_3}{\partial x_2} & \frac{\partial f_3}{\partial x_3} \end{bmatrix}. \tag{2}$$

Assume that the column vector V_{Ri} and the row vector V_{Li} satisfy the following equations

$$A \cdot V_{Ri} = \sum_{i=1}^{3} \lambda_i \cdot V_{Ri}. \tag{3}$$

$$V_{Li}^T \cdot A = \sum_{i=1}^{3} \lambda_i \cdot V_{Li}^T. \tag{4}$$

where λ_i is the eigenvalues of A; V_{Ri} is named the right eigenvector of A. Likewise, V_{Li}^T is named the left eigenvector of A.

Rewrite Eq. (3) and (4) as

$$A \cdot V_R = V_R \cdot D \Longrightarrow V_R^{-1} \cdot A = D \cdot V_R^{-1}. \tag{5}$$

$$V_L^T \cdot A = D \cdot V_L^T. \tag{6}$$

where D is a diagonal matrix if all the eigenvalue of A are different.

Comparing Eq. (5) and (6), it can be seen that

$$V_L^T = V_R^{-1} \Longrightarrow V_L^T \cdot V_R = I. \tag{7}$$

Assume the boundary of the RAS in the phase space is the manifold surface passing through a saddle point. Using linearizing process at a saddle point, this boundary will be a tangent plane of the manifold surface at this saddle point. Suppose that the manifold including the point $(\hat{x}_1, \hat{x}_2, \hat{x}_3) = 0$ has the normal vector V^T. Then

$$V^T \cdot \hat{x} = 0. \tag{8}$$

Because all the states on this plane must satisfy the Eq. (1), we have

$$\frac{d}{dt}(V^T \cdot \hat{x}) = 0 \Rightarrow V^T \cdot \dot{\hat{x}} = 0 \Rightarrow V^T \cdot A \cdot \hat{x} = 0. \tag{9}$$

Referring to Eq. (6), if we want to satisfy Eq. (8) and (9) simultaneously, we have

$$V^T \cdot A \cdot \hat{x} = \lambda \cdot V^T \cdot \hat{x} \Rightarrow V^T \cdot A = \lambda \cdot V^T. \tag{10}$$

Eq. (10) indicates that V^T must be the left eigenvector of Jacobian matrix A. Therefore, the manifold surface with normal vector V^T can be spanned by the two stable right eigenvectors.

According to the preceding analysis, the procedure for identifying the boundary of the RAS is as follows:

Step 1: Find all the equilibrium points ($F(X) = 0$).

Step 2: Find the specific saddle point having one positive and two negative real parts of eigenvalues in the linearized Jacobian matrix. Then calculate the left eigenvectors that are associated with the eigenplane spanned by the two stable eigenvectors of the saddle point.

Step 3: Select a set of initial points around the saddle point on the eigenplane.

Step 4: Utilize the backward integrations of the system equation and plot all the reversing trajectories in phase space.

3. Stability analysis of the three-dimensional Lotka-Volterra system

Consider the three-dimensional Lotka-Volterra predator-prey system [12]:

$$\frac{dx_1}{dt} = ax_1 - bx_1x_2 + ex_1^2 - sx_1^2x_3, \tag{11}$$

$$\frac{dx_2}{dt} = -cx_2 + dx_1x_2, \tag{12}$$

$$\frac{dx_3}{dt} = -px_3 + sx_1^2x_3. \tag{13}$$

The Jacobian matrix of the predator-prey system is

$$A_p = \begin{bmatrix} a + 2ex_1 - bx_2 - 2sx_1x_3 & -bx_1 & -sx_1^2 \\ dx_2 & -c + dx_1 & 0 \\ 2sx_1x_3 & 0 & -p + sx_1^2 \end{bmatrix}. \tag{14}$$

Consider the following system parameters: a=1, b=1, c=1.2, d=1, e=2, p=3 and s=2.7. The predator-prey system has five equilibrium points E_i^p : E_1^p =(0,0,0), E_2^p =(-0.5,0,0), E_3^p =(-1.054,0,0.3893), E_4^p=(1.054,0,1.0921) and E_5^p=(1,3,0). The corresponding eigenvalues of the Jacobian matrix (14) evaluated at equilibrium points are: λ_1= −3, λ_2 = −1, λ_3=1 for E_1^p (a saddle having two negative eigenvalues); λ_1= −1, λ_2= −1.5, λ_3= −2.325 for E_2^p (a stable node having three negative eigenvalues); λ_1= −3.1266, λ_2=2.1256, λ_3= −2.054 for E_3^p (a saddle having two negative eigenvalues); λ_1=0.5409, λ_2= −0.5+4.2894j, λ_3= −0.5-4.2894j for E_4^p (a spiral-saddle having two complex eigenvalues with negative real part); λ_1= −0.3, λ_2= 1+1.414j, λ_3= 1−1.424j for E_5^p (a spiral-saddle having two complex eigenvalues with positive real part).

Both spiral-saddle points E_4^p and E_5^p are the chaotic attractor. The interaction between these two chaotic attractors is responsible for the chaotic dynamics of the system. Regarding the saddle point E_3^p, the two stable eigenvectors are related to the stable manifold separating the boundary of RAS of the unstable region and the stable equilibrium point E_2^p.

4. Numerical simulation of an RAS

Regarding the saddle point E_3^p, the left eigenvector related to the positive eigenvalue is V_L=[0.572, 0.144, −0.807] , which can be defined the normal vector of the tangent plane of boundary of RAS at E_3^p.

Regarding the neighborhood of the saddle point E_3^p, by employing the backward integration method for selecting a set of initial conditions on the tangent plane, the boundary of the RAS manifold can be found, as shown in Fig. 1. For example, Fig. 2 shows that the trajectories with initial points (-0.8, 0.031, 0.69), (-1.71, 0.058, 0.185) in the unstable region (upper side of RAS) will diverge to infinity. However, Fig. 3 shows that the trajectories with initial points (-0.8, 0.031, 0.59), (-1.71, 0.058, 0.085) in the stable region (opposite side of RAS) will converge to the equilibrium point E_2^p. Therefore, the boundary in Figure 1 is really the boundary of RAS of Lotka-Volterra predator-prey system.

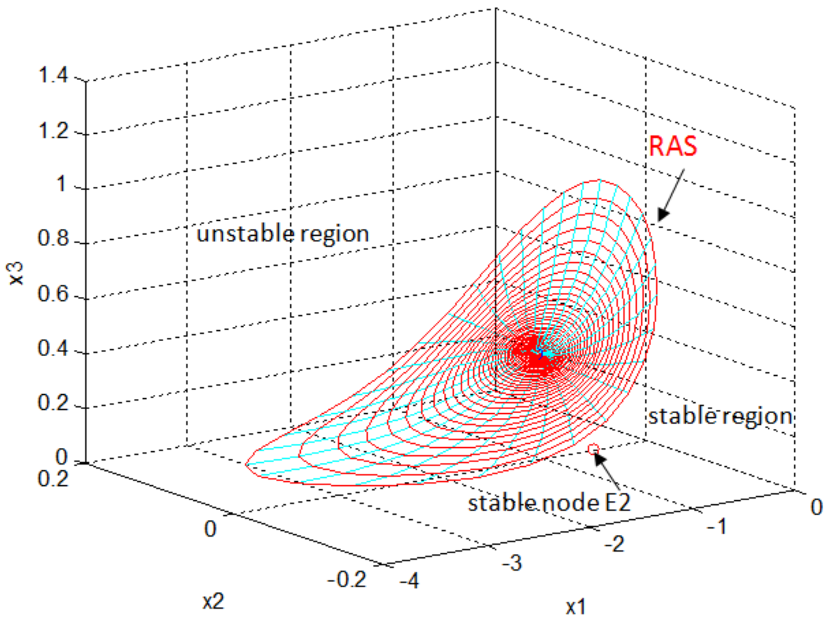

Figure 1. The boundary of RAS of the Lotka-Volterra predator-prey system.

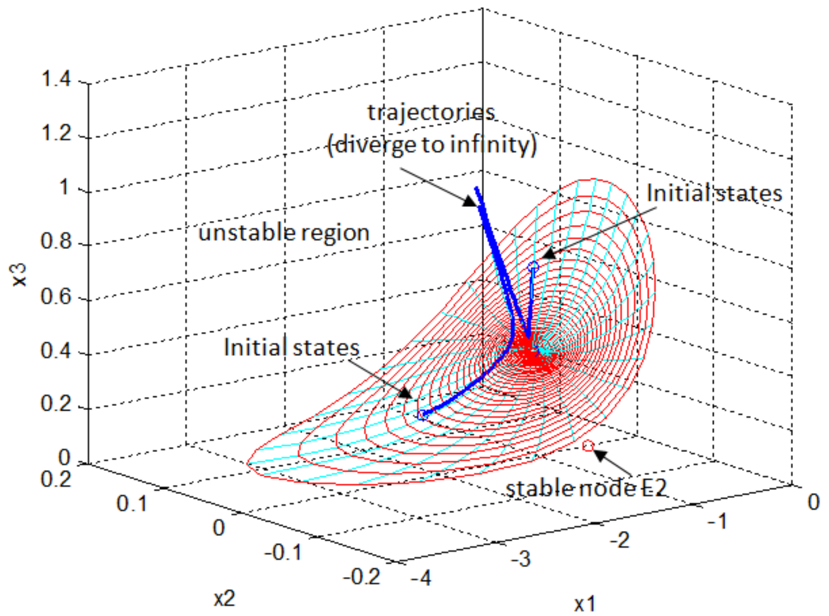

Figure 2. The trajectories with initial states on the unstable region (upper side of RAS).

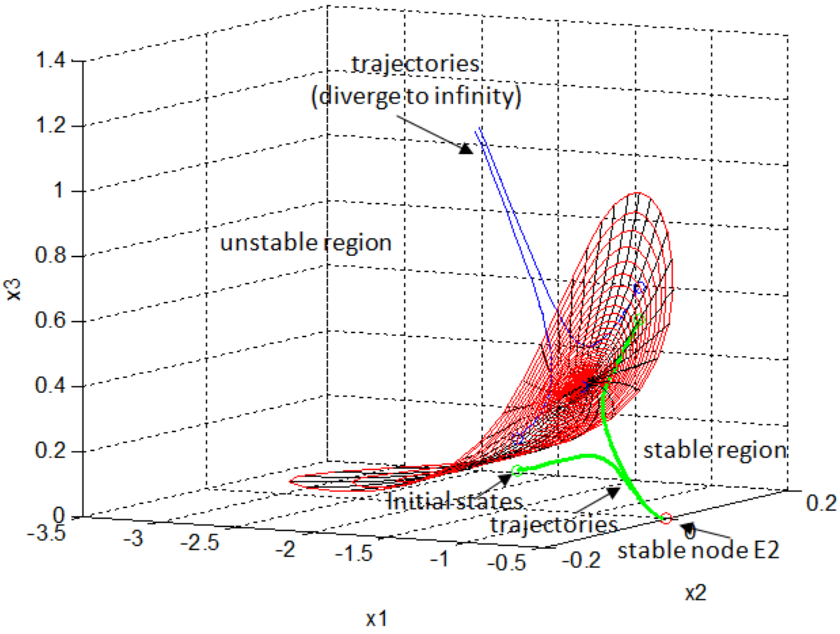

Figure 3. The trajectories with initial states on the stable region (opposite side of RAS).

5. Conclusion

In this paper, stability analyses of the third-order Lotka–Volterra predator-prey system are conducted. The boundary of the RAS of the system is plotted using the trajectory reversing method. The trajectories of the initial states starting from opposite sides of the RAS exhibit different dynamic behaviour. The simulation results verify the effectiveness of the proposed method.

6. References

[1] Armiyoon, A.R. and Wu C.Q. 2015 Nonlinear Dyn. **79** 275.
[2] Tan, W.H. and Packard A. 2008 IEEE Trans. on Autom. Control 53 565.
[3] Chesi, G. 2009 Automatica **45** 1536.
[4] Pang, G. and Zhang K. 2015 Int. J. Control **88** 484.
[5] Noldus, E. and Loccufier M. 1995, Int. J. Control **61** 917.
[6] Jerbi, H., Braiek N. and Bacha A. 2014 Arabian J. Sci. Eng. **39** 3841.
[7] Lee H. K. and Han K. W. 2000 IEEE Trans. Nucl. Sci. **47** 2693.
[8] Tian, J., Yu Y. and Wang H. 2014 Math. Probl. Eng. **2014** 1.
[9] Starkov, K.E. and Krishchenko A.P. 2014 Communications in Nonlinear Science and Numerical Simulation **19** 1486.
[10] Danca, M.-F. 2010 Applied Mathematics and Computation **216** 2107.
[11] Itik M. and Banks S.P. 2010 Int. J. Bifurcation and Chaos **20** 71.
[12] Petras, I. 2011 Fractional-Order Nonlinear Systems: Modeling, Analysis and Simulation (Springer Berlin Heidelberg).

Acknowledgments

This paper was supported by Education Department of Fujian Province (no. FBJG20180093) and Construction Project of Mechanical Engineering Application-oriented Discipline in Fujian Province.

IOP Conf. Series: Earth and Environmental Science **431** (2020) 012048 doi:10.1088/1755-1315/431/1/012048

Comparison of corrosion characteristics of conductive concrete

Tian Xu[1], Pei Feng[1], Liu Xin[1], Jia Lulu[1], Deng Chenxing[1], Yang Pinghao[2] and Cheng Hongbo[2]

1 State Grid Jiangxi Electric Power Co., Ltd. Electric Power Research Institute, Nanchang, China
2 School of Electricity and Automation Engineering, East China Jiaotong University, Nanchang, China
E-mail: creatortx@163.com

Abstract. Conductive concrete has great application potential in grounding and electromagnetic shielding. To verify the effect of conductive concrete on the corrosion of grounded metals, several conductive concrete with different conductive phase, such as Q235 carbon steel, galvanized steel and stainless steel, were prepared. The conductive concrete test specimens are immersed in red soil leachate, their open circuit potential, potentio-dynamic polarization and electrochemical impedance spectroscopy were measured by electrochemical method. Corrosion behaviour of different grounding metals in conductive clays with different conductive phase are compared based on the pre-mentioned three indicators. The results show that conductive concrete can reduce the corrosion of grounded mental effectively compared with ordinary concrete, galvanized steel has better corrosion resistance than Q235 carbon steel, graphite-based conductive concrete can protect the grounding metal better than stainless steel-based conductive concrete, and high conductive phase content can make a low metal corrosion.

1. Introduction

With the power grid expansion, the construction of grounding grids under harsh environmental has become more and more common [1-2], the grounding metal faces more and more corrosion threat. The corrosion will break the grounding conductors, which will cause the ground potential rise and threaten the safety of workers and equipment. The corrosion of grounded metals has become one of the important reasons affecting the stability and safety of power systems [3-5].

Conductive concrete has lower soil resistivity and better gelation performance [6-8]. When applied to the grounding of the tower for power system, the grounding resistance can be effectively reduced. At the same time, because the conductive cement is weakly alkaline, it will form a certain protective effect on the grounding metal. However, the corrosion characteristics of the grounded metal in conductive concrete environment are still less analyzed, and the anti-corrosion effect is still unclear. Therefore, from the perspective of electrochemical corrosion, the electrochemical corrosion test of grounded metal in conductive cement was designed by the principle analysis of open circuit potential, dynamic potential polarization curve and electrochemical impedance spectroscopy. Corrosion behavior and regularity of both Q235 carbon steel and zinc in different graphite and stainless steel proportion conductive concrete

2. Corrosion principle of grounding electrode

The grounding metal is affected by various complicated factors such as humidity, temperature, pH value, soil quality and microorganisms in the soil. The corrosion of the surface is inevitable, which can be roughly divided into micro-cell corrosion and electrolytic corrosion.

A large amount of electrolytes such as acid-base salts are generally dissolved in the soil moisture, and the grounded metal is buried therein, which causes microbattery reaction, thereby leading to the corrosion on metal surface [9]. Taking the galvanized steel commonly used in the tower grounding as an example, the metal zinc on the surface loses electrons in the electrolyte solution to form soluble zinc ions:

$$Zn - 2e \rightarrow Zn^{2+} \tag{1}$$

When electron enters the solution, if the solution is acidic, the electron will combine with the hydrogen ion in the solution to generate hydrogen and escape on the impurity. If the solution is neutral or alkaline, the electron will combine with the oxygen in the solution to produce hydrogen and oxygen. And then root ions, oxygen corrosion occurs.

$$2H^{+} + 2e \rightarrow H_2 \uparrow \tag{2}$$

$$O_2 + 2H_2O + 4e \rightarrow 4OH^{-} \tag{3}$$

Throughout the process, due to the movement of electrons, a string of current is generated between the impurities and the metal zinc to form a battery effect.

Red soil is usually dark red, mostly acidic, with a surface and center pH between 5.0 and 5.5. In this environment, the grounded metal is prone to corrosion and the corrosion rate is fast, and certain improvement measures are needed.

3. Evaluation index and testing method for grounding metal corrosion

In order to evaluate the corrosion behavior of metals, the corrosion characteristics of metals were evaluated by three indicators: open circuit potential, dynamic potential polarization curve and electrochemical impedance spectroscopy.

Open Circuit Potential Method (OCP) refers to the electrode potential when the current density is zero, which is essentially the potential difference between the working electrode and the reference electrode without load [10]. It can measure the total potential difference between the corrosion micro-potential of the grounded metal material and the reference electrode without the applied current. The greater the potential difference, the tendency of corrosion occurs. The measurement of the open circuit potential is relatively simple.

The potentiodynamic polarization method is to set the scan rate by determining the initial potential and the termination potential, and then electrochemically measure the constituent three-electrode system. The corrosion rate of the grounding metal in the conductive cement is obtained by analyzing the data of the current and the potential [11], therefore, it can reflect the speed of metal corrosion.

The electrode potential and the applied polarization current density generally satisfy the Tafel equation:

$$\left|\Delta E\right| = -b_A \lg i_{corr} + b_A \lg i_{Ai} \tag{4}$$

$$\left|\Delta E\right| = -b_c \lg i_{corr} + b_c \lg i_{ci} \tag{5}$$

The polarization curve of the strong polarization region on $E - \lg i$ the semi-logarithmic coordinate is linear. According to this, the Tafel straight line can be obtained, and the straight line is extrapolated to E_{corr} , and in the horizontal axis, the corrosion current i_{corr} can be calculated from the value $\lg_{icorr}$ corresponding to the upper point.

In addition to the open circuit potential and the polarization curve, the impedance spectroscopy can also describe the corrosion of the metal. It refers to the sinusoidal variation of the current (or potential) flowing through the electrochemical system over time under small amplitude conditions. Simultaneously measure the change of the corresponding system potential (or current), or directly measure the AC impedance (or admittance) of the system, analyze the reaction mechanism of the electrochemical system and the relevant parameters of the calculation system [12]. The polarization resistance can be measured by the impedance spectrum method, and the larger the polarization resistance, the better the corrosion resistance [13]. Besides, the process and principle of corrosion can also be judged by the shape of the electrochemical impedance spectrum.

4. Corrosion test and comparison for grounded metal in conductive concrete

Based on ordinary Portland cement and fine sand, graphite (500 mesh, carbon content 99% or more), stainless steel fiber (316L, diameter 0.035 mm, length 8-12 mm) were added as a conductive phase material. Conductive concrete with different conductive phase content were prepared by changing the mass ratio of the conductive phase to the Portland cement, the contents are shown in Table 1.

Table 1. Conductive phase material proportion.

Stainless fiber（%）	Graphite（%）
0	0
1	30
1.5	35
2	40
2.5	50
3	55

The conductive phase material was mixed according to the ratio of Table 1 and vibrated, the grounded metal was vertically inserted into the center of the test piece. The samples were placed in a curing box for 24 hours, and maintained for 28 days before demolded, thus the 100mm*100mm*100mmm test sample were made.

Q235 carbon steel and galvanized steel are used to test, their open circuit potential, polarization curve and impedance spectrum are measured by using the electrochemical workstation. The results are shown in figure 1 to figure 3.

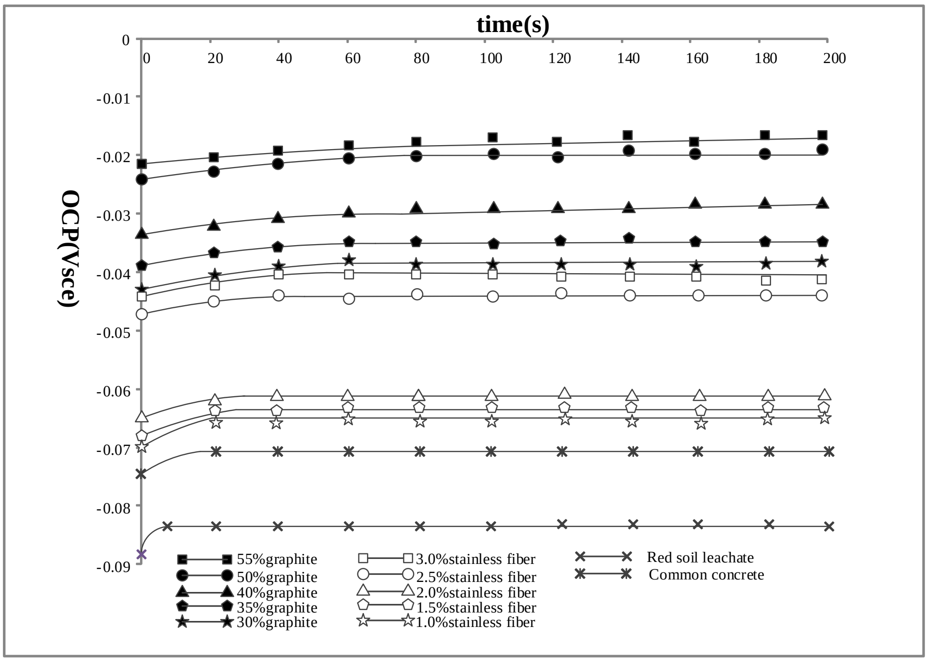

(a) Q235 carbon steel sample OCP results

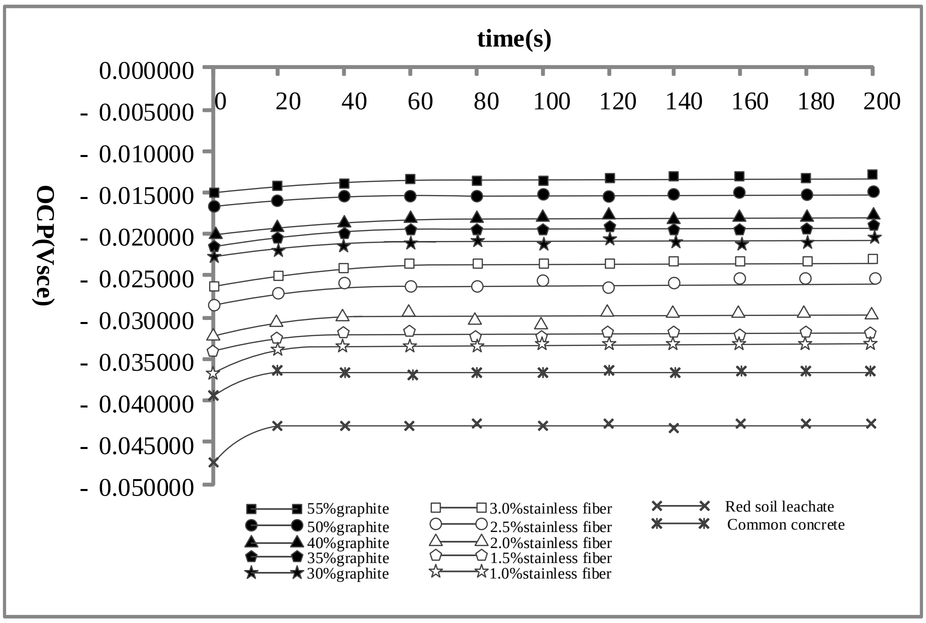

(b) Galvanized steel sample OCP results

Figure 1. OCP testing results.

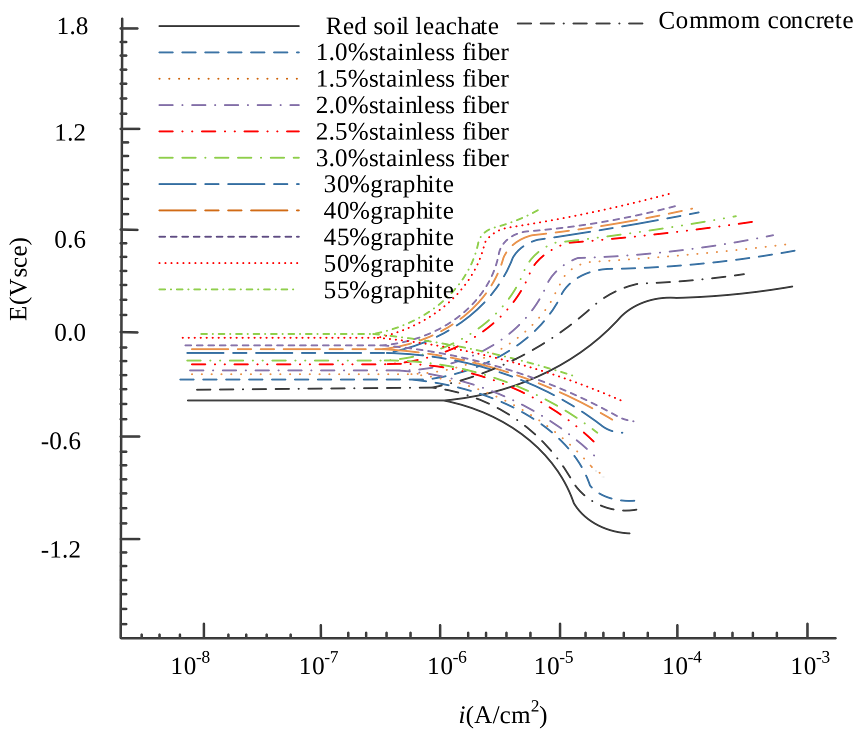

(a) Q235 carbon steel sample dynamic potential polarization curves

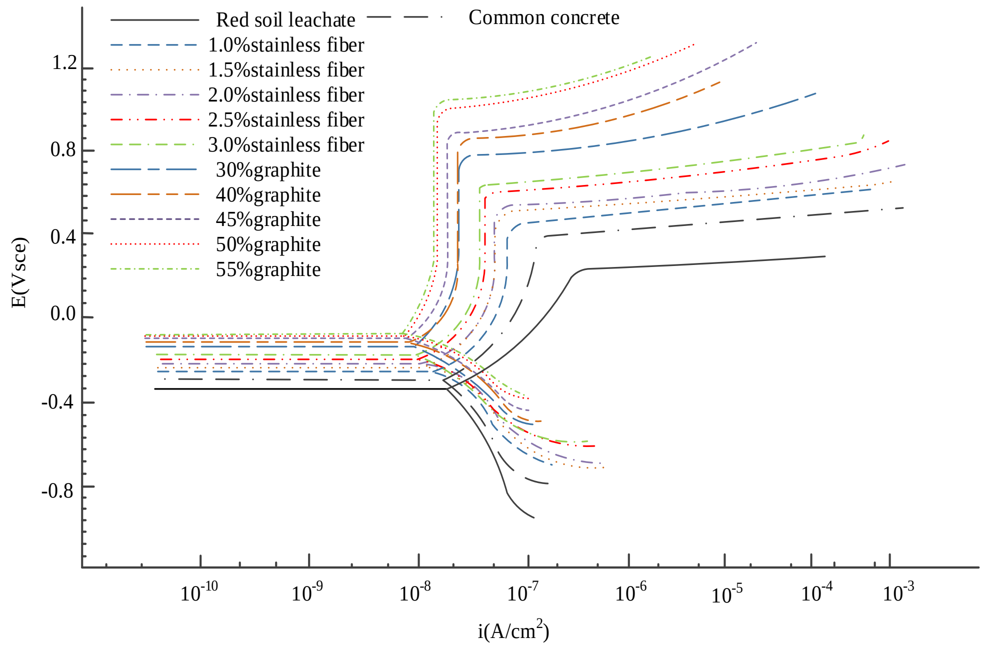

(b) Galvanized steel sample dynamic potential polarization curves

Figure 2. Dynamic potential polarization curve results.

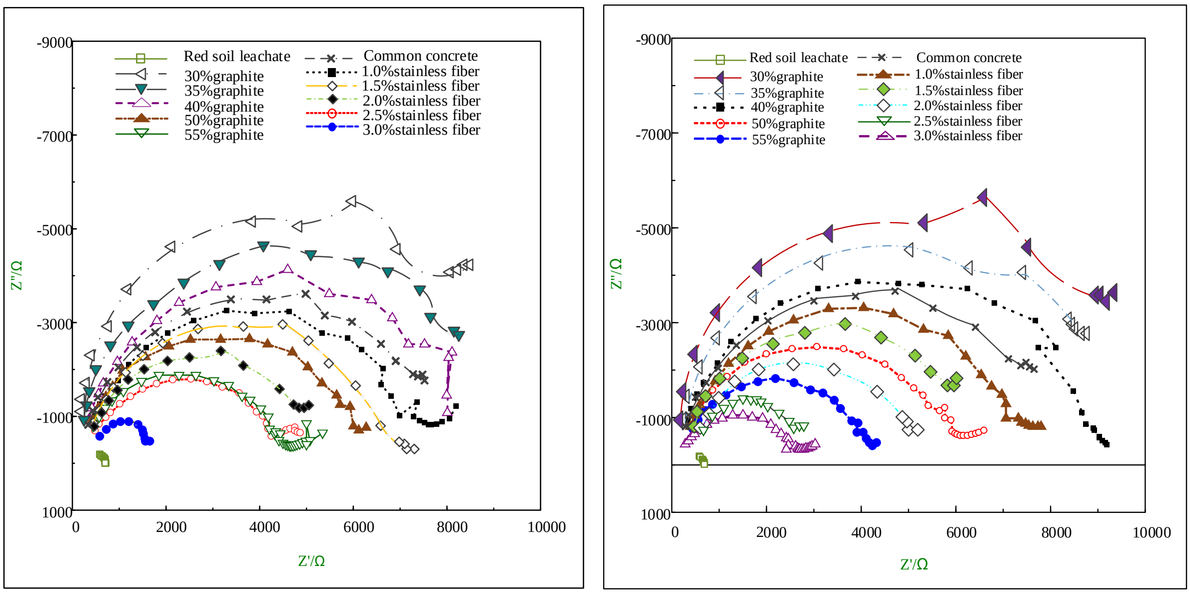

(a)Q235carbon steel results (b) Galvanized steel results

Figure 3. Electrochemical impedance spectroscopy testing results.

4.1. Corrosion behavior comparison under different soil environments

It can be seen that the metal electrode has lower open circuit potential in the red soil leaching solution than in the concrete. It shows that conductive concrete can greatly reduce the corrosion sensitivity of metal to the environment. Taking polarization curves into consideration, we can find that the corrosion potential of the red soil leaching solution is the lowest and the corrosion current is the largest. From chemical impedance spectroscopy observation, we can see that the chemical arc impedance radius of the red soil leaching solution is very small compared with that of the concrete, indicating that the corrosion resistance of the grounded metal in the red soil environment is relatively poor.

Taken together, red soil has the strongest corrosive ability in four different soil environments, followed by ordinary concrete, while graphite-based conductive concrete has the weakest corrosion ability.

4.2. Comparison of corrosion characteristics of different metals

It can be seen from figure 1(a) that the performance of the ‘pregnancy period’ of each group is consistent with the open circuit potential. The performance of the graphite group is superior to that of the stainless steel fiber group.

Under the conditions of red soil leachate, the test results of the potentiostatic polarization curves of the test pieces of each group are shown in figure 2(a). The corrosion potential of the Q235 carbon steel specimens coated with conductive cement is higher than that of the control group.It can be seen from figure 2(a) that as the content of the conductive phase increases, the passivation region of the polarization curve also gradually increases, which is consistent with the monitoring result of the open circuit potential. So the Q235 carbon steel has a slower corrosion rate in the graphite-based conductive cement.

The part of the figure 3(a) clearly constitutes the semicircular inductive arc is a result of the high frequency region. It can be seen that as the graphite content increases, the radius of the inductive arc gradually decreases. It is worth noting that the conductive cement group with stainless steel fiber is not as good as the ordinary concrete group in corrosion durability, which is probably because the chemical properties of stainless steel fiber are more active than ordinary concrete aggregates, when experimental current increases or there is an increase in time, corrosion does happen. It can be concluded that the application of conductive cement can improve the corrosion resistance of Q235 carbon steel in red soil environment and improve its anti-corrosion ability. However, unlike the two indicators of open circuit potential and polarization curve, there is no change in the corrosion resistance of the metal in the conductive cement. As the amount increases, the corrosion durability will decrease.

4.3. Corrosion behavior comparison under different conductive phase contents

Different graphite content (30%, 35%, 40%, 50%, 55%)and different stainless steel fiber content (1%, 1.5%, 2%, 2.5%, 3%) (galvanized steel / carbon steel, according to the analysis in session 4.2),the results of the open circuit potential, polarization curve and chemical impedance spectrum can help understand of the influence of the conductive phase content on the corrosion of the metal. With the increase of the amount of graphite or stainless steel fiber, the open circuit potential is gradually positive, and the open circuit potential is more obvious when the graphite content is 50%. In the stainless steel fiber group, the open circuit potential is more significantly improved when the stainless steel fiber content is 2.5%. This shows that the addition of two conductive phase materials reduces the possibility of corrosion of the coated Q235 carbon steel.

5. Conclusions

(1) In general, the degree of corrosion of grounded metals in ordinary concrete, soil leachate and conductive cement can be arranged as: soil leachate > ordinary concrete > conductive cement.

(2) Open-circuit potential monitoring and other three types of tests show that compared with Q235 carbon steel, galvanized steel has lower corrosion tendency, less corrosion rate and stronger corrosion resistance in conductive cement.

(3) With the increase of the content of conductive phase, the corrosion tendency of grounded metal in conductive cement is getting lower and lower, the corrosion rate is getting smaller and smaller, but the corrosion resistance is getting worse. The above three indicators are obviously stronger than the performance of grounding metals in ordinary concrete or soil leaching solution. The test results show that the conductive cement has the best protection effect on the grounded metal when the graphite content is 50% or the stainless steel fiber content is 2.5%. Compared with stainless steel fiber, graphite as a conductive phase material to prepare conductive cement is more conducive in protecting the grounding metal.

IOP Conf. Series: Earth and Environmental Science **431** (2020) 012048 doi:10.1088/1755-1315/431/1/012048

6. References

[1] Zhou L J, He Z J, Chen Y, et al. Impact of grounding conductor corrosion on grounding resistance of grounding mesh and improvement method[J]. Journal of the China railway society, 2018, 40(2):39-44.
[2] Wei W, Wu X Q, Ke W, et al. Research progress on corrosion and protection of grounding grid materials[J]. Corrosion science and protection technology, 2015, 27(3):273-277.
[3] Liu S N, Wang C, Deng J L, et al. Epoxy based conductive anti-corrosion coatings for grounding grid[J]. Journal of Chinese society for corrosion and protection, 2015, 35(6):510-518.
[4] Hua G R, Li W H, Guo Y Y. Corrosion rate prediction of Q235 steel in Hainan substation grounding grid based on neural network models[J]. Corrosion and protection, 2017, 38(8):573-577.
[5] Meng X M, Wang L M, Chen S M, et al. Research status and prospect of grounding material in power engineering[J].New chemical materials, 2016(9):10-12.
[6] Li T F, Luo R C, Pan J W, et al. Analysis of influence of resistance reducing material on electrical performance parameters of vertical DC ground electrode[J]. Insulators and surge arresters, 2018(1):132-136.
[7] Niu J G, Xian R C, Sun X F, et al. Influence of grounding material and structure on the resistance of tower grounding grid in urban distribution overhead lines[J]. Science technology and engineering, 2018, v. 18; No.453(20):121-127.
[8] Gao Z Q, Cao X B, Du J L, et al. Study on the effect of vertical rod on reducing tower's inpulse grounding resistance[J]. High voltage apparatus, 2018(4):182-187.
[9] Li J, Su H, Yan A J, et al. Research of acid soil corrosion resistant new steels for grounding grid[J]. Corrosion science and protection technology, 2015, 27(2):116-122.
[10] Wen D J, Zhao Y H, Tang L L, et al. Effect of high-pressure torsion on corrosion behavior of GW83K magnesium alloy[J]. Materials review, 2017, 38(5):6-12.
[11] Zou S Y, Zhou X L, Cui X, et al. Effect of electroless copper plating on surface of SiCp on corrosion resistance of Si Cp/Al composites[J]. Transactions of materials and heat treatment, 2017, 358(5):6-12.
[12] Wang J, Jia M Y, Yang C H, et al. On completeness of EIS equivalent circuit analysis for electrochemical corrosion process[J]. Journal of Chinese society for corrosion and protection, 2017,37(06):479-486.
[13] Qiao H X, Lu C G, L Q, et al. Experimental study on corrosion resistance of erinforced concrete based on different cementitious materials[J]. Bulletin of the Chinese ceramic society, 2018, 37(1):25-34.

IOP Conf. Series: Earth and Environmental Science **431** (2020) 012049 doi:10.1088/1755-1315/431/1/012049

Wavelet-based baseline correction optimization algorithm for SF6 spectral signal

Liu Wenfeng[1], Wang Yanting[1], Liu Liang[1], Yao Mingshu[2], Xu Xiaofeng[2], Gao Jing[2] and Wang Liang[2]

1 Taipingwan hydroelectric power plant, China
2 Shenyang Institute of Engineering, China
E-mail: 2727820196@qq.com

Abstract. SF6 gas is widely used in various power equipment. In this paper, a baseline correction algorithm based on spectral detection method based on optimal wavelet basis is proposed. The algorithm selects the optimal wavelet base, removes the strong spectrum information by threshold method, eliminates the influence of continuum fitting, and performs the least squares fitting on the residual signal to obtain the continuum, and removes the continuum from the original spectrum to obtain the required Line spectrum. The accuracy of the quantitative analysis of the line spectrum intensity after processing is greatly improved, and the baseline is effectively estimated and corrected, and the fitting accuracy is higher than the traditional iterative wavelet baseline correction algorithm.

1. Introduction
The SF6 insulating gas is a mixture system with uncertain components. The concentration of many components to be tested is very low, which requires high sensitivity of the analytical method [1-3]. Absorbing spectral signals of insulating gases often exhibit baseline drift and tilt under the influence of source, instrument background, and sample size. A variety of derivatives also cause a complex background image of the spectral signal, coupled with the measurement environment and the background spectral drift caused by the change of conditions, so that in addition to noise, the spectral data also has a continuum of low-frequency gradual change. The line spectrum is superimposed on the continuum, so that the intensity of the line cannot be truly reflected, which is not conducive to the extraction of the line, which limits the accuracy of the quantitative analysis. Therefore, the use of baseline correction algorithms to remove continuum is one of the key techniques for spectral analysis.

2. The theoretical basis optimizing
Due to the complex physical causes of baseline drift, it is difficult to establish an accurate model of the continuum. Considering the environment and other factors, the background spectrum is a low-frequency signal with relatively stable trend, and the line spectrum is mainly located in the high frequency band [4]. Therefore, using the difference between the two, a curve fitting method is used to obtain an approximate continuous spectrum curve. These methods essentially extract the continuous slowly varying signal in the spectrum by smooth operation. The influence of the strong line makes the fitted continuum not accurate enough in the vicinity, away from the baseline, and deviates from the peak of the line, thus limiting the extraction of the line and the determination of the parameters. Wavelet with its tight support and multi-resolution characteristics, has attracted researchers at home and abroad to study the application of baseline correction [5].

IOP Conf. Series: Earth and Environmental Science **431** (2020) 012049 doi:10.1088/1755-1315/431/1/012049

In this paper, a baseline correction algorithm based on the optimal wavelet basis is proposed. By constructing the cost function, the best wavelet base is selected to represent the signal in the wavelet library generated by the SF6 mixed gas spectral signal, so that the spectral signal is decomposed by the wavelet base. According to the characteristics of the continuum and spectral peaks in the energy distribution, the decomposition coefficients of the spectral signals under the optimal wavelet basis are thresholded, the peak signal components of the energy concentration are eliminated, and the residual signal is subjected to least squares fitting to extract the continuum. signal. After removing it, a spectral line spectrum can be obtained. Applying the algorithm to the sr absorption spectrum signal of insulating gas can accurately estimate the baseline fluctuation potential and effectively correct the baseline drift phenomenon.
Figure 1 shows a schematic diagram of the wavelet library space for signal decomposition. Each of these small squares represents the time-frequency space occupied by the decomposition of the signal under a particular basis function. It can be seen that the width of the entire line represents the room space, and the frequency from low to high is shown from left to right. For the spatial decomposition scale, l is the sequence number of the space V0.Each column represents the decomposition scale of the previous column, and the decomposition scale plus one. As long as the selected subspace does not cover the length of one line, it can be used as a set of orthogonal bases of space to completely represent the signal of the space.

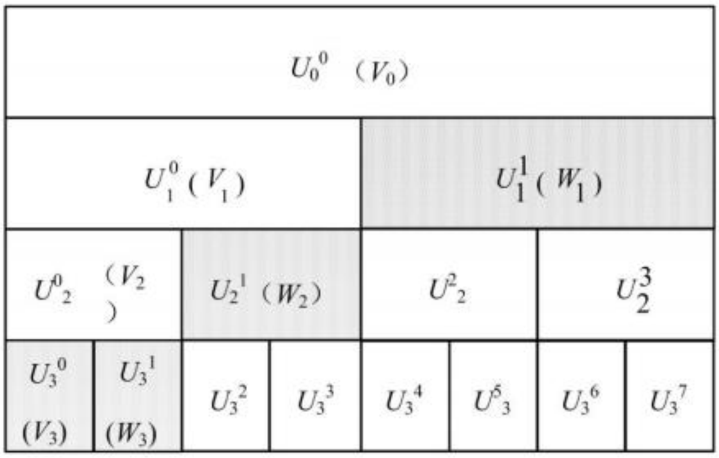

Figure 1. Wavelet frequency domain space.

It can be seen that the standard wavelet transform performs multiple resolutions on the low frequency part of the signal to achieve multi-resolution analysis. This is not in line with the need to extract the spectral absorption band. The best method for dividing the wavelet space should be selected according to the characteristics of the analyzed signal, that is, the optimal basis is selected. The specific step is to determine the search method, and search for the wavelet bases that constitute the optimal basis in the entire wavelet library according to the rule that minimizes the cost function.

3. Baseline correction algorithm

This paper proposes a baseline correction algorithm based on the optimal wavelet basis. The main idea is to use the best wavelet base before the continuous spectrum fitting, so that the correlation peak energy in the wavelet coefficients is concentrated in a few scales, and then the threshold method is used to eliminate the strong.

3.1. Algorithm implementation steps

The basic steps of the baseline correction algorithm for the SF6 insulating gas spectral signal based on the optimal wavelet basis are as follows.

(1) Generate a wavelet library
When the scale is small enough, the spectral data to be processed can be assumed, and the scaling function is approximated as a function, so the sampling sequence f(n), n = 1, 2,..., N, which is considered to be f(t), is the wavelet packet function.
Let fm,l(n) denote the decomposition coefficient of f(n) in the lth subspace of dimension m, where m = 1, 2,..., M, l = 1, 2,..., 2m, then from the above assumptions, there are f0, 0 (n) = f(n), and the wavelet library of M = 4 is calculated according to the calculation formula of the wavelet packet.
(2) Calculating the cost function
Construct the cost function V(m, l) to reflect the concentration of signal energy in the wavelet coefficients. The cost function is solved for the decomposition coefficient of each base of the signal in the wavelet library.
(3) Search for the optimal basis
The optimal base is searched in the wavelet library in the order of e-tops. The principle is to minimize the total cost function of the wave base. At this time, the wavelet coefficients of the signal decomposition have the highest energy concentration.
(4) Threshold method to remove peak components
The threshold operation is used to search for the strong band on the wavelet decomposition coefficient f..l(n) of each optimal basis.

$$H(f_{m,l}(n),\ h) = \begin{cases} f_{m,l}(n), & |f_{m,l}(t)| \geqslant h \\ 0, & |f_{m,l}(t)| < h \end{cases} \tag{1}$$

$$h = 3\sigma_{m,l}$$

where the threshold is taken.
The above operation considers the wavelet coefficients larger than the threshold to be dominated by the strong band components, and the others are retained.
(5) Inverse transform to obtain a signal that removes peak components
After the threshold processing, the interference of the strong band to the fitted continuum is substantially eliminated. The wavelet coefficients are reconstructed on a scale-by-scale basis, and finally the spatial wavelet coefficients are obtained after removing the strong bands.
(6) Fitting the continuum and then obtaining the line spectrum
The continuum of the fit is obtained by a least squares fitting algorithm. The continuum is subtracted from the original signal f(n), which is the baseline corrected line spectrum.

3.2. Sequence length problem of wavelet packet transform
Conventional wavelet packet transform algorithms usually use the definition of inner product. In the calculation process, the data will become shorter and shorter, which often makes the subsequent processing algorithms difficult to obtain better results due to insufficient quantity. The traditional convolution type wavelet packet transform algorithm keeps the length of the decomposed data consistent with the original spectral data. The wavelet packet decomposition formula is as follows.

$$\begin{aligned} f_{m+1,2l}(n) &= \frac{1}{2}\sum_{k\in Z} h(k) \bullet f_{m,l}(n - 2^m k) \\ f_{m+1,2l+1}(n) &= \frac{1}{2}\sum_{k\in Z} g(k) \bullet f_{m,l}(n - 2^m k) \end{aligned} \tag{2}$$

where m is the scale of the decomposition, l is the subspace in the entire function space, h(k) is the low-pass filter coefficient, and g(k) is the high-pass filter coefficient corresponding to the wavelet packet reconstruction formula.

$$f_{m,l}(n) = \frac{1}{2}\sum_{k\in Z} h(k) \bullet f_{m+1,2l}(n+2^m k) + \frac{1}{2}\sum_{k\in Z} g(k) \bullet f_{m+1,2l+1}(n+2^m k) \tag{3}$$

where h(k) and g(k) represent the conjugate of h(k) and g(k), respectively.

3.3. Selection of cost function

Since the information to be extracted mainly exists in the form of a peak, which appears as a modulus maxima in the wavelet space, a cost function is constructed to count the number of modulus maxima exceeding a certain threshold value, in all wavelet coefficients constituting the wavelet base. When the number of modulus maxima exceeding the threshold is the smallest, it is considered that the energy of the spectral signal is most concentrated at this time, and the selected wavelet base is the optimal wavelet base.

It can be seen that the key to solving is to determine the threshold. A more reasonable consideration is to weight the variance e of the noise contained in the wavelet coefficients at each node in the wavelet library. As a threshold, it can generally take 3~5.

3.4. Optimal basis search method

Search in order from bottom to top.

First, mark the lowest layer (m = 4 each node, initialize the optimal base.

Then, for each layer 2m nodes, two or two groups, compare the sum of the two node cost function values of each group from the bottom to the top and the corresponding node cost function value of the previous layer; if the former is greater than the latter, Then remove the labels of the two nodes in the lower layer and replace them with the nodes of the higher layer. Otherwise, the sum of the costs of the two nodes in the next layer replaces the cost function value of the corresponding node in the previous layer, but the label is not processed.

Compare from bottom to top layer by layer (scale) until all scales are processed.The wavelet base corresponding to all the nodes marked is the optimal wavelet base.

This method can quickly and efficiently search for the optimal basis.

4. Experimental results and discussion

This section verifies the performance of the proposed SF6 insulating gas spectral signal baseline correction algorithm through experiments. For comparison, the effect of using the iterative wavelet for baseline correction is first given, as shown in Fig. 2.

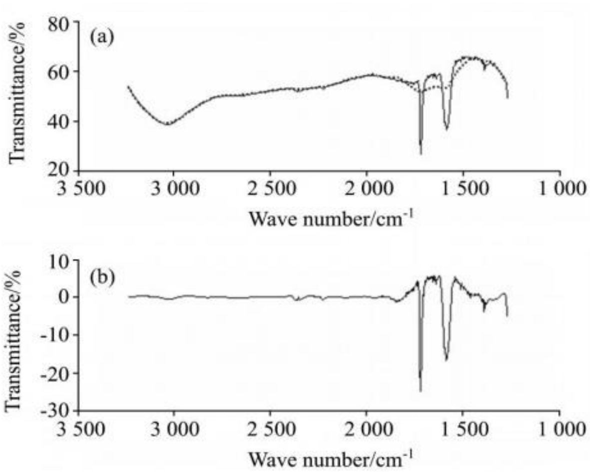

Figure 2. Baseline image of interactive wavelet.

The solid line in Fig. 2(a) is the absorption spectrum curve of the insulating gas SF6 after use in the wavenumber of 3240-1265 cm-1, and the broken line is the continuum extracted by the iterative wavelet method.It can be seen that the intensity of the absorption peaks at 1716 and 1585 cm-1 in the spectral signal is large, which affects the accuracy of the baseline correction, resulting in the continuum of the region near the strong absorption peak deviating significantly from the true baseline, and the error is large.Fig. 2(b) is a line spectrum diagram after removing the continuum spectrum. In the part outside the absorption peak region, the spectrum is relatively flat, and the change basically reflects the spectral absorption intensity. In the strong absorption band, the peak of the peak signal is Significant drift, peak intensity no longer truly reflects the absorption of the mixed gas to be tested, can not be applied to the application of quantitative analysis of components in the subject.

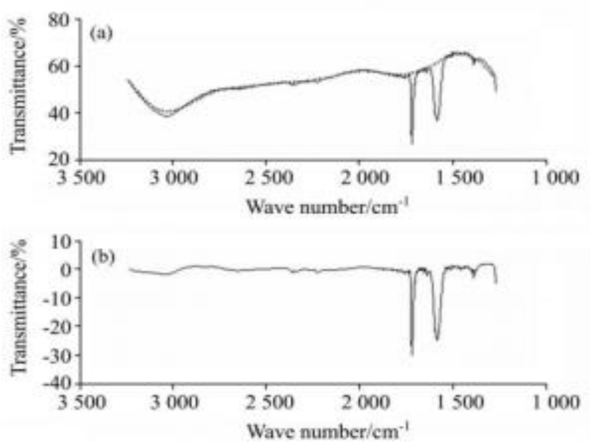

Figure 3. Best wavelet baseline image.

Figure 3 shows the experimental effect of continuous spectrum removal using the optimal wavelet basis method.The solid line in Fig. 3(a) is the same spectral curve as described above, and the broken line is the continuous spectrum extracted by the optimal wavelet basis method.It can be seen that the fitting operation basically eliminates the interference of the strong band and accurately estimates the trend of the baseline fluctuation.Figure 3(b) is a spectrum of the SR mixed gas with the effect of removing the continuum. The baseline is relatively stable, and the peaks can be clearly identified. The spectral width and intensity accurately reflect the true absorption spectrum of the gas to be tested. Definitive and quantitative applications.In addition, the optimal wavelet base concentrates the signal energy on a few wavelet scales. The threshold method can be used to remove the peak interference with high energy. This overall threshold operation makes the algorithm have higher computational efficiency.

5. Summary

In this paper, the best wavelet basis is used to correct the baseline signal of SF6 insulating gas. Compared with the existing baseline correction method, the algorithm removes the strong spectrum information before the continuous spectrum fitting, avoids the influence on the fitting, and makes the algorithm accurate to the baseline; according to the SF6 insulating gas spectrum signal itself Features, adaptively select the best base for time-frequency signal analysis, high computational efficiency, and good robustness. The experimental results show that the optimal wavelet base correction algorithm accurately fits the baseline of the power insulation gas spectral signal, and extracts the spectral line information effectively from the original spectrum signal. The algorithm is accurate and reliable, and it is the online performance monitoring of the power insulating gas SF6. And spectral techniques for power equipment fault diagnosis provide algorithm support.

6. References

[1] Xiong Chengji. Image threshold denoising algorithm based on wavelet transform [J]. Science and Technology, 2019 (20): 62.

IOP Conf. Series: Earth and Environmental Science **431** (2020) 012049 doi:10.1088/1755-1315/431/1/012049

[2] Wang Zhen. Research on background deduction and quantitative algorithm of partial discharge decomposition components in SF _ 6 [D]. Chongqing University, 2011.
[3] Yao. Study on chromatographic peak background deduction and overlapping signal separation of partial discharge decomposition products in SF_6 [D]. Chongqing University, 2009.
[4] Dong Yue. On-line monitoring and vibration signal analysis of SF_6 high voltage circuit breaker [D]. Shanghai Jiaotong University, 2008.
[5] A High-performance Small Signal Amplifier [J].Journal of Northeast Agricultural University(English Edition),2005(02):141-145.

IOP Conf. Series: Earth and Environmental Science **431** (2020) 012050 doi:10.1088/1755-1315/431/1/012050

Energy self-sufficient sensor node for long range wireless networks

P Bolte[1] and U Witkowski[1]

1 South Westphalia University of Applied Sciences, Electronics and Circuit Technology, Luebecker Ring 2, 59494 Soest, Germany
E-mail: bolte.philipp@fh-swf.de

Abstract. Wireless networks can have different architectures depending on the application context. In this paper, we concentrate on a wireless network that supports a gateway to a server being accessible from the internet. Many typical related applications can be found in IoT and Industry 4.0. Focus of this paper is on the design of a sensor node that is energy self-sufficient and supports the LoRa communication standard. By using LoRa long range wireless communication of up to several kilometres range becomes possible. Therefore, large areas can be covered by using multiple sensor nodes. Special attention had been on low-power design aspects to run the node with rechargeable battery and small photovoltaic cell only. Example application is ambient monitoring and support of an aquaponics project.

1. Introduction

Sensor networks are used in many applications ranging from small size local networks to large size networks having many nodes and covering large areas [1, 2]. An example application for a small size network is a body sensor network connecting only a few nodes able to measure ECG activity, SpO2 rate and context information as accelerations, temperatures and humidity [3]. Here, main design focus was on small size and high energy efficiency, i.e. low power consumption. Therefore, used radio technology was ZigBee operating in 2.4 GHz band. Larger networks are used e.g. for habitat monitoring, security surveillance, inventory control [4] or also for mobile applications like traffic control and vehicle monitoring [5]. Depending on the application context, specific focus has to be on aspects as node and network architecture and topology, energy supply and low power, scalability, node localization features, routing, and Quality of Service (QoS).

Due to the significant advances in microelectronics and radio technology the fields IoT (Internet of Things) and Industry 4.0 became an important area of wireless attached sensors and sensor networks integrating several sensors of same or different modality [6]. Besides the data collection in classic sensor networks, the data processing in IoT applications is an important feature. E.g., by applying big data analysis schemes and techniques from machine learning also complex data sets can be analysed to assist the user of a network or a technical system in decision making [7]. Typical to many IoT and Industry 4.0 applications is the remote access to the system and the data via internet. For this, the sensor system has to integrate a gateway to transmit data to a server or to receive control commands in a bidirectional manner.

Our sensor node is intended to capture sensor data of different modality and to transmit this data to a gateway that realizes the access to a server in the internet. Design requirements are coverage of medium to large areas by using a long-range communication system supporting wireless transmission range up to several kilometres. The node has to be low power using a small buffer battery only. The energy self-sufficiency is realized by integrating a small photovoltaic cell. As transmission technology,

LoRa (Long Range) has been chosen. Together with LoRaWAN it supports network communication features by using a low power routing protocol [8]. The network node integrates a LoRa transceiver module with 868 MHz RF frequency. A gateway device from The Things Network is used as infrastructure to connect to the internet. The first application for our node is environment monitoring, i.e. measuring of ambient temperature and humidity as well as fine dust concentration. A more complex application is an urban farming project: aquaponics. This is the combination of aquaculture with fishes and hydroponics, a concept of soil-less growing of plants [9]. The developed sensor node can support several other applications by integrating application specific sensors. E.g., it could be the monitoring of energy systems as decentralized photovoltaic systems as well as wind or hydro power stations.
This paper is organized as follows: After the introduction in section 1 the features of the LoRa communication system as well as the networking support provided by LoRaWAN are explained in section 2. The sensor node that has been developed is presented in section 3. This node is used in an example application to sense and to transmit ambient data. In section 4 the example application with the developed sensor node is introduced and some details on implemented software stack and performance data are presented. In addition, the remote display of collected sensor data is demonstrated. The paper is concluded in section 5.

2. RF communication: LoRa and LoRaWAN

The LoRa standard describes a proprietary direct sequence spread spectrum (DSSS) modulation developed by Semtech that is commonly used in IoT applications. The additional LoRaWAN technology introduces a medium access control (MAC) layer and a message routing layer on top of the LoRa physical layer. The LoRaWAN protocol stack is suitable for long-range communication in contrast to protocols like Wifi, Bluetooth or ZigBee [10]. LoRaWAN outperforms traditional cellular networks like GSM, 3G and LTE when comparing power consumption and hardware complexity.

2.1. LoRa

The LoRa standard describes the lower physical layer of data transmission that is used in the proposed sensor network (SN). A data frame is built from the raw payload by adding a preamble, a header and a payload CRC [11]. The preamble is required by the receiver to detect the start of transmission. The header includes all information required to process the payload and is expanded by adding redundant bits to achieve a forward error correction (FEC) with a fixed code rate (CR). The payload and its CRC utilize FEC as well but with a variable CR that is defined in the header. The complete packet is transmitted using a modified DSSS coding. Each bit of the data frame is replaced by a sequence of bits (chips) to increase the signal bandwidth. The resulting chip stream is transmitted using chirp spread spectrum (CSS) by a continuously varying frequency. The center frequency and bandwidth (BW) are adapted to the regulatory requirements of a certain region. The Spreading Factor (SF) describes the ratio of chiprate to bitrate. This approach offers the narrow band interference rejection of DSSS while eliminating the requirement of a precise reference clock due to coding based on frequency variation rather than a fixed frequency [12].

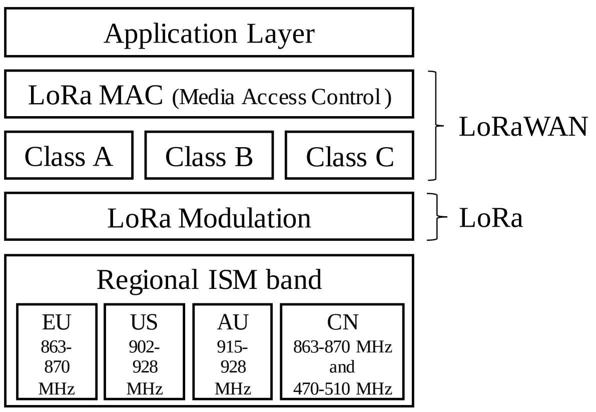

Figure 1. Layer based architecture of the LoRa communication system integrating LoRa and LoRaWAN layers with support of different ISM bands (based on [13])

The range of communication modules using the LoRa standard depends on the transmission power, the bandwidth, the spreading factor and the antenna characteristics. A distance of more than 2 km in non-line of sight (NLOS) conditions can be reached without significant packet loss [14]. The air-time of a message of given size is proportional to the SF and reciprocal with the BW. A trade-off between maximum range and data rate, respectively number of devices needs to be found.
LoRa defines mainly the modulation technique, the number of available channels, the channel bandwidth, transmission power and the frequency bands used for transmission. All these parameters depend on the region LoRa is applied. As shown in Figure 1 different ISM frequency bands are used in different regions of the world. As a result, also the data rate varies.

2.2. LoRaWAN

An additional layer needs to be added to the LoRa physical layer to address MAC and routing of messages. For this purpose, the LoRaWAN standard was utilized in this paper. It defines the data format and timing of message exchange between the end-devices (here sensor nodes – SN) and the gateways [8]. The used frequency band and channel plan depends on the region where the network is hosted and is described by LoRaWAN standard as well [15]. Figure 2 shows an example network arrangement.

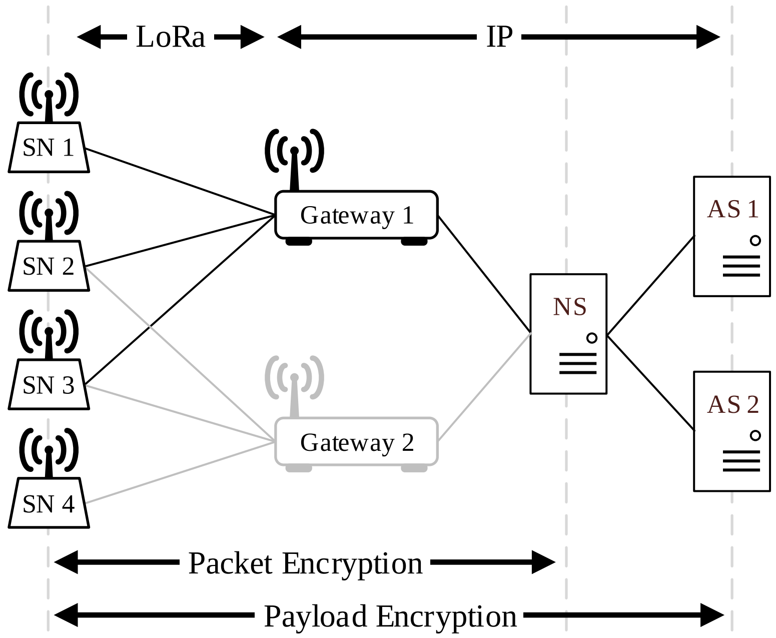

Figure 2. Example LoRaWAN network

The network supports a large number of end-devices, respectively sensor nodes for this application. All end devices must support at least all class A functionality. End-devices that implement class A begin the message exchange on a certain event (e.g. completion of a sensor measurement). The payload is sent as an uplink message over LoRa. The uplink message is received by all gateways that are in range of the SN. The gateways transmit the received message to a network server (NS) over traditional IP which does a deduplication of multiple incoming messages from the same SN. The payload is redirected to an application server (AS) over IP. The specific AS that is used is defined by the node during the network join procedure. The application is able to send a response to the uplink message. The NS decides based on the link quality which gateway is used for the transmission of the downlink message. There are only two time slots (RX1, RX2) shortly after the transmission of the uplink message at that a class A end-device is listening for downlink messages. It is only possible to send data to an end-device during these time slots. This further implies that data can only be sent to an end-device after the end-device did a transmission. The LoRaWAN standard also implements AES based data encryption to increase network security. The messages are encrypted by the network session key (NwkSKey) and include a message integrity check (MIC) between the end-device and the NS to prevent replay attacks. The payload of the message is encrypted using the application session key (AppSKey). The LoRaWAN standard includes the over-the-air activation (OTAA) method that generates the session keys on the AS based on a single application key (AppKey). The AS transmits the generated NwkSKey to the NS of the provider. A third-party network operator is not able to decrypt the payload because the AppSKey is only known by the end-device and the AS. This approach has shown some weaknesses. LoRaWAN does not provide perfect forward secrecy and the join procedure is prone to replay attacks [16]. The LoRaWAN cannot be used in environments where subsequent decryption of data has fatal consequences.

3. Sensor node architecture

This paper proposes a universal sensor node (SN) architecture that can be used for a variety of applications. A SN is made of a base board and optional expansion boards. The base board integrates all general components while the extension boards contain all application specific parts. Multiple expansion boards can be stacked onto the extension header of the base board. The components of the base board are shown in Figure 3. It is theoretically possible to operate an SN in its minimal configuration, i.e. without an expansion board because all essentials components are already included on the base board.

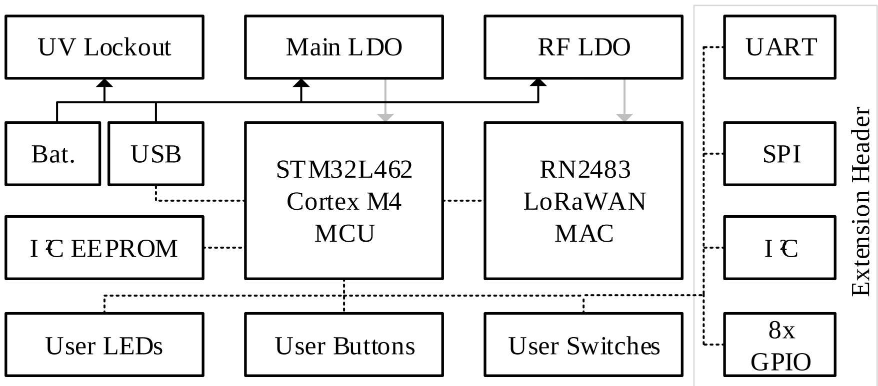

Figure 3. Structure of the sensor node

3.1. STM32L462 MCU

The used STM32L462 microcontroller (MCU) from STMicroelectronics is based on the commonly used ARM Cortex M4 architecture with an integrated FPU. The MCU is optimized for low-power applications but also includes a massive amount of peripherals. The power consumption depends on the set clock frequency and the enabled peripherals and can be further reduced by a variety of low-power modes with a different trade-off between power consumption, start-up time and available wakeup sources.

3.2. RN2483 LoRaWAN modem

The Microchip RN2483 modem is used for the LoRaWAN communication. This system-on-module (SoM) includes the LoRa modem as well as the LoRaWAN protocol stack. The communication to the host MCU is realised using an UART interface. A PCB antenna was placed on the sensor node PCB that is connected to the antenna pin of the RN2483 module.

3.3. Power supply

One major part of the SN design is the power supply scheme. The system was designed to run on a single rechargeable 3.7V LiPo battery allowing flexible battery life up to multiple years on a single charge depending on the application. The used LiPo battery with a capacity of 2200 mAh is capable of driving big loads in contrast to very cheap non-rechargeable 3V lithium cells, which is required by some applications. The battery is charged using an on-board battery charger supplied by the USB port. A separate LDO with enable input is used to supply the LoRaWAN modem reducing the stand-by current by disabling the modem when not needed. A hardware under-voltage lockout is integrated that disables all voltage domains if the battery voltage drops under a defined threshold to prevent damage to the LiPo battery.

3.4. User Controls
The SN board includes 3 user controllable LEDs, 2 programmable buttons and 2 DIP switches. These peripherals are accessible by the software through the board support package (BSP). In the developed example application, the LEDs are used to indicate the device state, the buttons enable special boot modes (USB storage mode, configuration reset) and the DIP switches define the used SF of the LoRa modem.

3.5. Expansion Header
The 20 pin expansion header includes multiple supply voltages, one UART, one I2C and one SPI interface and 8 GPIO signals. All GPIO signals are 5 V tolerant and can be mapped to ADC channels to read analog voltages from 0 to 3.3 V. It is intended to stack the expansion boards with the application specific circuit on top of the SN board but it is also possible to connect the boards using a ribbon cable if the package space is constraint.

3.6. Firmware
A basic firmware was developed for the SN, which includes the BSP for the user IOs, a driver for the RN2483 LoRaWAN modem, a SWO (serial wire output) based logging, a configuration parser and a sample application. The logging module outputs debugging messages over the SWO of the debug probe to simplify debugging.

A configuration parser is integrated to allow the integration of user configurable parameters. The configuration file is structured into sections and can hold a variable number of parameters (float or string type) and is stored as a text file in the I^{2}C EEPROM. The EEPROM is FAT formatted and can be accessed through the USB interface. This makes it easy to access the configuration file by a standard computer and to edit it, no programming cable is required. The stored configuration is parsed at system reset. A sample application is supplied with the firmware to simplify the development of a custom application. The sample application cyclically measures the battery voltage and transmits it over the LoRaWAN network. The LoRaWAN parameters can be set using the defined configuration file.

4. Node setup and environmental sensing
The example application presented in this paper is inspired by projects like luftdaten.info and hackAIR that are citizen science platforms, which collect fine-dust measurements from SN operated by citizens [17]. In these projects, an ESP8266 WiFi MCU development board plus breakout boards are used. Drawback is the WiFi communication that is not power efficient and does not have long transmission range. Additionally, stationary power supply is used what significantly limits outdoor applications without having certain technical infrastructure. Our proposed sensor architecture can be used to operate an improved energy self-sufficient fine-dust SN with an increased range by replacing the WiFi infrastructure by LoRaWAN and by PV based charging option as well as low-power design.

4.1. Hardware setup
For the introduced application with sensing of fine-dust concentration and other environmental parameters the base board is expanded by a sensor driver board integrating a Sensirion SPS30 fine dust sensor, a DHT22 temperature and relative humidity sensor, a photovoltaic (PV) expansion board and a 5W PV cell, as shown in Figures 4 and 5.

IOP Conf. Series: Earth and Environmental Science **431** (2020) 012050 doi:10.1088/1755-1315/431/1/012050

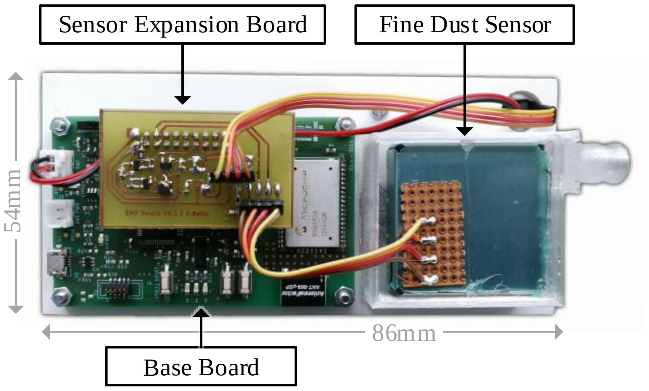

Figure 4: Environmental sensor (top view) with base board integrating LoRa and expansion board for sensor interconnect

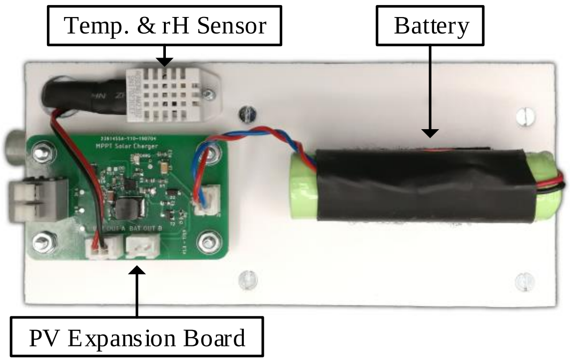

Figure 5: Environmental sensor (bottom view) with temperature and humidity sensor and PV board for PV MPPT and charge control

The sensors are connected to the sensor expansion boards that is stacked on top of the base board using the expansion header. An additional step-up voltage regulator with controllable enable input is used to generate the 5V sensor supply voltage.

The PV expansion board integrates a maximum power point tracking (MPPT) battery charger that is supplied by the PV cell. The output of the expansion board is connected to the battery input of the main board. The LiPo battery is connected to terminal of the expansion board instead. All components are fitted onto a carrier board that is inserted into a pipe with 2 bent end pieces. The whole unit can be mounted onto usual rainwater downpipes using a pipe clamp.

4.2. Software stack

The SN measures the current fine-dust particle concentration of different particle sizes (PM1, PM2.5, PM4, PM10 [18]), the current temperature, humidity and battery voltage every 5 minutes. It transmits the measured values using The Things Network (TTN) LoRaWAN network infrastructure. The total payload length is 46 bytes containing single precision float values representing particle mass concentration and particle number concentration for each of the 4 particle size ranges, the particle number concentration of PM0.5, and the average particle size and 16 bit long integer values for the battery voltage, humidity and temperature. The data is captured from the MQTT broker of TTN into a MariaDB database using a Node-RED graphical programming interface. The gathered data is processed and visualized using the Grafana dashboard.

4.3. Performance

The measurement of the fine-dust particle concentration requires a constant airflow through a measuring chamber. The sensor needs to be active for about 15 seconds to gather valid data. During this time, the LoRaWAN modem joins the network. The data is sent after both measurement are done and the modem is ready after enabling. During the active phase of around 20 seconds, the SN draws an average current of 80mA. In idle phase, the current consumption drops below 1mA. The sensor node is able to run for 14 days on a single battery charge without recharging. The 5W PV module is easily capable of recharging the battery even facing poor solar radiation. Therefore, a robust long-term self-sufficient operation is possible.

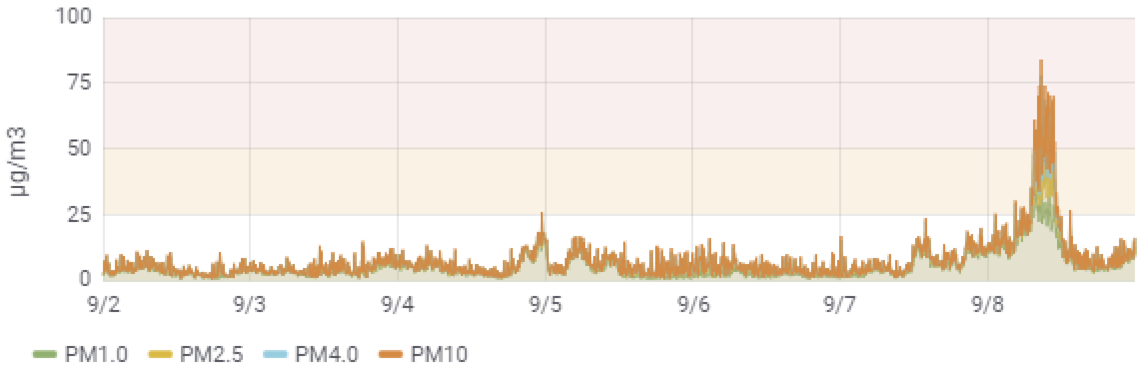

Figure 6: Particle concentration measurements for a period of one week

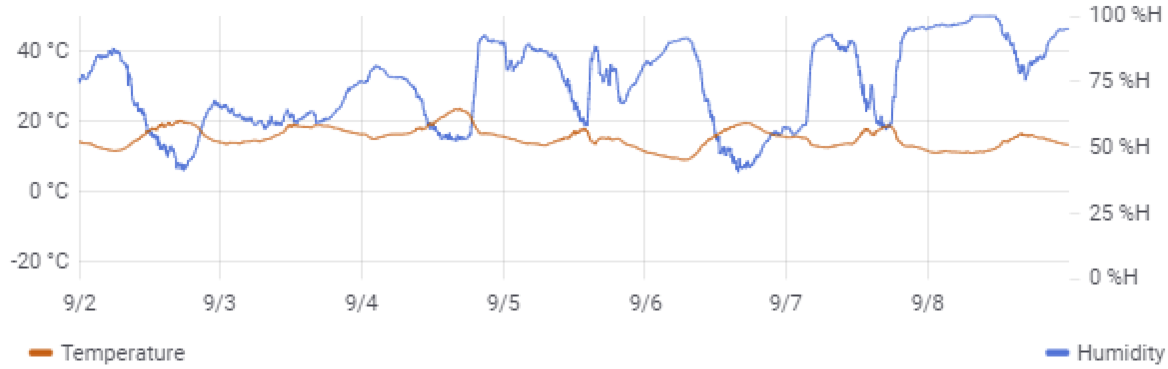

Figure 7: Temperature and humidity measurements for a period of one week

Figures **6** and **7** show the gathered sensor data for a period of one weak. The value for PM2.5 concentration had a maximum of 59.2 µg/m³ and an average of 6.51 µg/m³. The PM10 concentration had a peak of 83.8 µg/m³ and an average of 7.488 µg/m³. With exception of one short period the 24h particle concentration falls short the limit of 25 µg for PM 2.5 and 50 µg PM10 defined by the WHO [19]. The temperature was between 8.9 ℃ and 23.6 ℃ with an average of 15.2 ℃. The relative humidity range was between 40.5% and 99.9% with an average of 73.3%.

5. Conclusion

Objective of this paper was the design of a long-range sensor node that supports self-sufficient operation for months or even years by combining accumulator and PV cell and using low-power modes. Application context is environment sensing with focus on fine-dust, temperature and humidity. To realize long-range wireless transmission the LoRa standard has been used by integrating a LoRaWAN modem into the designed hardware. The hardware concept of the sensor node follows a modular approach. Therefore, different types of sensors can be easily integrated into the node to adapt the sensor node for various applications. The LoRa wireless communication supports transmission ranges of several kilometers enabling coverage of large areas. Via a LoRa gateway, sensor data is transmitted to an internet located server, which supports IoT applications. Users can easily access the sensor data remotely from any place.

6. References

[1] Yick J and Mukherjee B and Ghosal D 2008 Wireless sensor network survey *Computer Networks* pp 2292–2330

[2] Buratti C and Conti A and Dardari D and Verdone R 2009 An Overview on Wireless Sensor Networks Technology And Evolution *Sensors* (vol 9 no 9) pp 6869–96,

IOP Conf. Series: Earth and Environmental Science **431** (2020) 012050 doi:10.1088/1755-1315/431/1/012050

[3] Lo B and Thiemjarus S and King R and Yang, G-Z 2005 Body Sensor Network - A Wireless Sensor Platform for Pervasive Healthcare Monitoring *3rd International Conference on Pervasive Computing*
[4] Li C and Zhang H and Hao B and Li J 2011 A survey on routing protocols for large-scale wireless sensor networks *Sensors* 11(4) pp 3498-526
[5] Ramasamy V 2017 Mobile Wireless Sensor Networks: An Overview, Wireless Sensor Networks - Insights and Innovations *IntechOpen* DOI 10.5772/intechopen.70592
[6] Kocakulak M and Butun I 2017 An overview of Wireless Sensor Networks towards internet of things *IEEE 7th Annual Computing and Communication Workshop and Conference (CCWC)* DOI 10.1109/CCWC.2017.7868374
[7] Minteer A 2017 Analytics for the Internet of Things (IoT) *Packt Publishing*
[8] LoRa Alliance 2015 LoRaWAN Specification (IoT) *https://lora-alliance.org/resource-hub*
[9] Goddek S and Delaide B and Mankasingh U and Ragnarsdottir K and Jijakli H and Thorarinsdottir R 2015 Challenges of Sustainable and Commercial Aquaponics *Sustainability 7(4)* pp 4199-224
[10] Phung K H, Tran H, Nguyen Q, Truong T H and Nguyen T L 2018 Analysis and Assessment of LoRaWAN *2nd International Conference on Recent Advances in Signal Processing, Telecomunication & Computing* pp 241–246
[11] Semtech 2013 SX1272/3/6/7/8: LoRa Modem Designers Guide *https://www.semtech.com*
[12] Semtech 2015 AN1200.22 LoRa Modulation Basics *https://www.semtech.com*
[13] IoT Gateways.eu 2018 LoRaWAN *https://industrialgateways.eu/lorawanhome*
[14] Augustin A, Yi J, Clausen T and Townsley W M 2016 A Study of LoRa: Long Range & Low Power Networks for the Internet of Things *Sensors* vol 16 no 9 DOI 10.3390/s16091466
[15] LoRa Alliance 2017 LoRaWAN 1.1 Regional Parameters *https://lora-alliance.org/resource-hub*
[16] You I, Kwon S, Choudhary G, Sharma V and Seo J T 2018 An Enhanced LoRaWAN Security Protocol for Privacy Preservation in IoT with a Case Study on a Smart Factory-Enabled Parking System *Sensors* vol 18 no 6 DOI 10.3390/s18061888
[17] Kosmidis E, Syropoulou P, Tekes S, et. al. 2018 hackAIR: Towards Raised Awareness about Air Quality in Europe by Developing a Collective Online Platform *ISPRS Int. Geo-Inf.* vol 7 no 5 DOI 10.3390/ijgi7050187
[18] Srimuruganandam, Bathmanabhan, Nagendra S and Madanayak S 2010 Analysis and interpretation of particulate matter – PM10, PM2.5 and PM1 emissions from the heterogeneous traffic near an urban roadway *Atmospheric Pollution Research* (vol 1 no 3) pp 184–194
[19] WHO Regional Office for Europe 2005 *WHO Air quality guidelines for particulate matter, ozone, nitrogen dioxide and sulfur dioxide* (Denmark: World Health Organization)

IOP Conf. Series: Earth and Environmental Science **431** (2020) 012051 doi:10.1088/1755-1315/431/1/012051

Metrics of energy consumption in software systems: a systematic literature review

S Ergasheva[1,2,] I Khomyakov[1,2], A Kruglov[1,2] , G Succi1[2]

1 Innopolis University, Innopolis, Russia
2This research project is carried out under the support of the Russian Science Foundation Grant No 19-19-00623.
E-mail: a.kruglov@innopolis.ru

Abstract. The current situation when using tight time frames and frequently changing requirements when creating software dictates the need to create a system for monitoring energy consumption at any stage of production of a software product. At the first stage, we need to evaluate the state-of-the-art on this topic. To this goal, we conducted a systematic literature review. During the review more than 500 studies were observed and 124 of them were selected for detailed analysis. Among these papers, 169 metrics were derived and assessed from the point of their applicability within invasive software development process analysis. The study demonstrates the relevance of the questions posed and shows the immaturity of the area. There is no evolutionary study and the possibility of assessment at any stage of the development of a software product. The data show the importance and relevance of technical work and the importance of its further development.

1. Introduction

Given the sharp growth of IT systems and their impact on worldwide energy consumption, energy efficiency is becoming a real concern. It is estimated that the energy consumption of the ICT sector will reach 433 GW in 2020, meaning more than 14.5% of worldwide power consumption [1]. Therefore, it is essential to have precise figures of the current energy consumption of computer and mobile devices and how much of this is due to the software running on them, to understand how to reduce their power consumption and design future energy efficient equipment.

In order to provide a novelty approach on the energy efficiency assessment of the software product, we decide to focus on the development process analysis and related software metrics. For the data collection process, we will use non-invasive tools for monitoring the process of software development. A set of metrics for measuring software (source code), and the development process can be adjusted [2]. The toolkit integrates with major software development environment and office applications, so developers are not distracted from the main workflow. This technology has been successfully tested for problem analysis methodologies pair programming on software quality [3].

The project aims at building and validating a quantitative framework to guide the development and the evolution of sustainable software systems using a variety of metrics collected throughout the life-cycle of software systems, optimizing the performances of the systems under a variety of relevant factors, including efficient use of resources [4].

At the first stage of the project the metrics which describe, interpret and measure the value of resources software components of adaptive systems throughout their life cycle (design, implementation, operation) should be defined. These metrics will correlate with specific monitored resources, architectural elements and the behaviour of the system as a whole. To define a proper metrics, a systematic analysis of the state of the art should be performed, related to the main topics of the project: i.e., resource- and sustainable-wise metrics, pervasive and non-invasive data collection instruments, quality- oriented development support tools and methods, self-adaptation techniques and policies. As far as possible and depending on the characteristics of the available literature, this task will provide an organized body of empirical evidence with reference to the main themes of concern for the project.

For identification and analysis of relevant research literature, we formulated following 4 research questions (RQs):

- What are the existing studies on green metrics (energy consumption in mobile, embedded and cloud systems)?
- What is the classification of these metrics?
- What are descriptions and limitation of these metrics?
- What are the ways of collecting selected metrics?

2. Review protocol

We defined the search strategy based on the research questions and terms that helped us in studies selection to examine. The following approaches were used to build the search terms [5]:

- Derivation of major terms from the research questions.
- Identification of alternative spellings and synonyms for major terms.
- Identification of keywords in relevant papers or books.
- Usage of the Boolean OR to incorporate alternative spellings and synonyms.
- Usage of the Boolean AND to link the major terms.

For identification of primary research papers, the search string was generated based on the PICO (Population, Intervention, Comparison, Outcomes) approach. In the result of PICO strategy we defined following terms based on the research questions. Correlation of numerical quantities and search terms defined can be seen from the table 1.

Table 1. Search queries

Search query	Papers
Software (metrics OR measurements)(energy consumption OR energy efficiency OR power consumption)(mobile AND (devices OR phones OR development))	50
Software metrics for embedded systems in power consumption	11
Metrics of (power OR energy) consumption in (embedded OR cloud) systems	51
software metrics energy consumption mobile devices -wireless -radio	16
software metrics of energy consumption in smartphones	29
software metrics of energy consumption in mobile application development	23
software (metrics OR measurement) (energy consumption OR power management) (mobile devices OR mobile phones) -wireless -radio	21
software (metrics OR measurement) ((energy OR power) AND (consumption OR management OR reduction)) ((mobile AND (devices OR phones)) OR Smartphones) -wireless -radio	10
software (metrics OR measurement) (energy consumption OR power management) (mobile devices OR mobile phones) -wireless -radio	37
software (metrics OR measurement) ((energy OR power) AND (consumption OR management OR reduction)) ((mobile AND (devices OR phones)) OR Smartphones) -wireless -radio	16
software (metrics OR measurement) of (Energy OR Power) (consumption OR management OR Efficiency OR Reduction) in ((Mobile (device OR phone OR application development)) OR Laptop OR Smartphone) -wireless -radio	16
(software AND (metrics OR measurement) AND power AND (consumption OR management) AND ((mobile AND (device OR phone OR application development)) OR smartphone) NOT wireless NOT radio)	50
(software AND (metrics OR measurement) AND ((energy AND consumption) OR (power	92

AND management)) AND (embedded AND systems))	
Software (metrics OR measurement)(energy consumption OR power management) (cloud systems)	82

To execute the search on the research studies, we selected following free access literature libraries for automatized searches, namely:

- Google Scholar
- Scopus
- IEEE Xplore
- Web of Knowledge
- Digital library ACM
- Science Direct
- ResearchGate

Primary studies identification was performed based on the Snowballing instructions proposed in [5] which includes the steps:

1. Use the papers selected in automatic and manual searches as the initial set of selected studies;
2. Based on the selected studies, check references by looking at works of authors already included, since they obviously carry out relevant research in relation to their objectives;

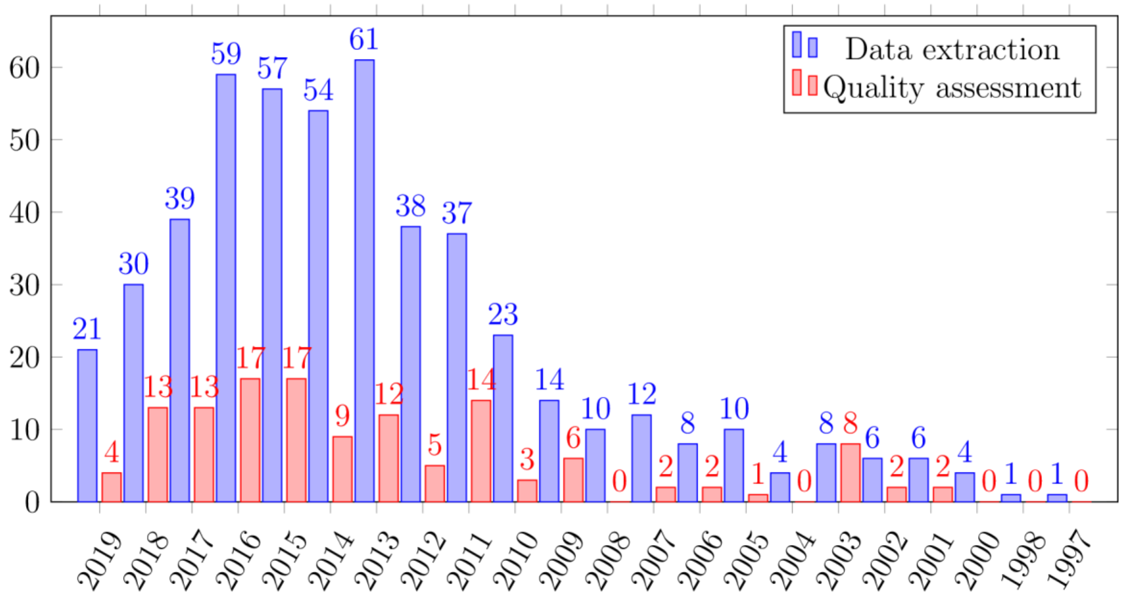

Figure 1. Papers related to the energy efficiency topic

3. Based on the set of documents found, check studies that cite the selected studies (forward snowballing).

This approach is conducted with the help of Google Scholar Database, since it captures more than individual databases. With the aim of selecting the most relevant articles for the study object, we included:

1. Articles that present Software measurements and discussion on metrics used for mobile, embedded and cloud systems;
2. Articles that contain related title, keywords and abstract to the research questions;
3. Major publications between 2000 and 2019.

During the research paper selection process, we applied exclusion criteria to eliminate duplication, not relevant and incomplete studies. If the study has been published in more than one conference or has more than one versions, then the most complete version was chosen. Furthermore, the studies that do not present the related information about the software measurements of mobile, embedded and cloud systems were not included. Besides, the patents and the studies in terms energy consumption of wireless network and radio connections were excluded from this SLR. According to the approach of

including the studies between 2001 and 2019, the representation of articles distribution by years is given in figure 1.
In the stage of quality assessment from the title, keywords and abstract, 75.4 % of primary studies were rejected, 23.6% of them were accepted and 1%was rejected for duplication. In the next stage of data collection, selected papers were completely reviewed and observed whether they do contribution in answering the research questions in the areas mobile, embedded and cloud systems. After the complete reading of the papers, they were classified into Tool, Process or Project metrics, Models and Methods, Empirical study and Best practises reviews. These classification of the papers gave complete understanding of which paper can answer which Research questions.
A Systematic Literature Review investigates metrics associated with power consumption of mobile, embedded and cloud systems. At first, the search keywords string was inserted. There were selected 504 primary studies from the digital library sources (see figure 1). Following this, the results were sorted with reading of title, keywords and abstract. We classified them in terms of suitability and relevance from 1 to 5 scale, where 124 studies were selected according to the high scale. Following this stage, complete reading of the articles was performed meaning that they answer the elaborated research questions. Besides, the studies that were not available and not applicable which discusses hardware metrics were derived separately for exclusion procedure. The ranking of selected studies according to the scale depicted in table 2.

Table 2. Experts ranking results

NotApl	1	2	3	4	5	NA
134	68	56	86	82	38	39

3. Results

In the previous section, the results of data extraction of primary studies were described. In this section the further analysis of the extracted data is discussed in order to obtain the answers to the research questions. By analyzing the existing software metrics of mobile, embedded and cloud systems towards the power consumption and their classifications, the distribution of selected studies in the areas of Cloud, Embedded consisted 23.3% and 27.5% respectively. While the relevant studies in Mobile Devices took 49.2% of overall selected studies in the research (see figure 2).
Besides, we want to find out descriptions and some limitations of the metrics encountered during the SLR. Then the types of tools for collecting these metrics will be analysed.

What are the existing studies on energy consumption in mobile, embedded and cloud systems?

The figure 1 shows the graphical distribution of the selected papers derived by years.

What is the classification of these metrics?

From the refined set of studies the exhausting set of metrics was derived. Overall number of energy efficiency metrics mentioned in literature is 169. In order to distinguish the focus of these metrics, their classification was performed. Based on the review of the studies, the metrics were classified into one of the following category:

- hard metrics, which are related to physical measurement of energy consumption by different components of a system
- code metrics, which are related to analysis of the software code itself
- run-time metrics, which are related to the dynamic analysis of the applications, e.g. analysis of the byte code
- indirect metrics, which are commonly related to the particular energy efficiency model
- process metrics, which are related to the analysis of the software development process
- others, which are focused on the specific parts of the systems' operation

The distribution of the metrics according to the given classification is given in figure 3.

IOP Conf. Series: Earth and Environmental Science **431** (2020) 012051 doi:10.1088/1755-1315/431/1/012051

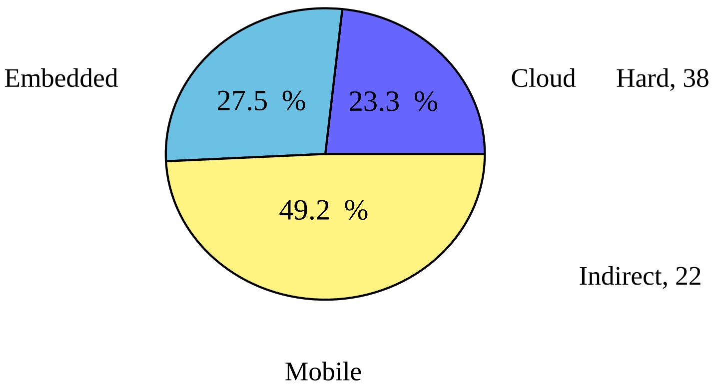

Figure 2. Papers' distribution by topic

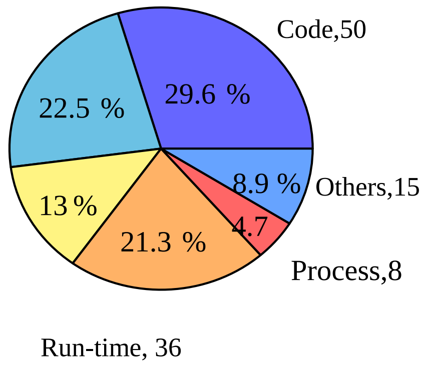

Figure 3. Analyzed metrics classification

What are descriptions and limitations of these metrics?

The goal of this SLR is to analyze existing metrics for energy efficiency assessment, which can be applied in the project. The goal of the project is to develop framework which will be focused on the analysis of the software metrics excluding direct measurement of hardware parameters, and be applicable to any mobile, embedded or cloud system. Thus, among the giving classification the only two groups suitable for software framework are code and process metrics. The description of the derived software and process metrics are given in table 3.

Table 3. Code metrics for energy efficiency

#	Metric	Description	Source
1	Control flow-graph	Graphical representation of control flow or computation during the execution of programs or application.	[6]
2	Sorting Algorithm Type	The approach of saving through software by choosing the appropriate sorting algorithm.	[7]
3	Performance tips	Strategies that can be used to conserve and extend the battery life.	[8]
4	Software energy metric	Software energy metric (SEM) which corresponds to the number of executed assembly instructions and the number of memory accesses to the date memory.	[9]
5	Nesting function	A function which is defined withing another function, the enclosing function. It was assigned for evaluation of software designs energy consumption of hierarchical measures(EIC, MAC).	[9]
6	Sequencing function	It is calculated based on the control flow-graph. $I(F;F_1;F_2;\dots;F_n) = \sum I(F_i)$	[9]
7	Prime function	It is calculated based on the control flow-graph and defined as the number of basic mathematical operators (excluding division) plus the number of memory accesses in the statement.	[9]
8	Number of executed instructions	It corresponds to instruction execution within the processor and instructions fetches from the memory.	[9]
9	Number of Immediate sub-classes of a Class	It refers to the number of direct descendants of a class.	[10]
10	Coupling between Object	Number of classes coupled to a specific class.	[10]
11	Lack of Cohesion on Methods	Number of pairs of member functions with shared instance variables subtracted by the total pairs of member functions without shared instance variables.	[10] [11]
12	Efferent Couplings	Classes in the package that depend on the other packages.	[10][11]
13	Response For a Class	Number of methods of a specific class plus number of other class methods called by the methods of this class.	[10]
14	Abstractness	Ratio of the number of abstract classes in the analyzed package to the total number of classes in the analyzed package.	[10] [11]
15	Instability	Ratio of efferent coupling to total coupling.	[10] [11]
16	Attribute Hiding Factor	These metrics measure how properties like variables and methods are encapsulated in a class. A private property is completely hidden.	[10]

17	Coupling Factor	Number of actual method overrides divided by the maximum number of possible method overrides.	[10]
18	Weighted Methods per Class	Aggregate of complexities of methods in a class. When complexities are equal, number of methods defined in each class.	[10] [11]
19	Loops	For and While loops in the source code.	[12]
20	Code smell	Internal Setter, Leaking Thread, Member ignoring method and Slow Loop consume up till 87 times more than methods affected by other code smells.	[12]
21	Cyclomatic Complexity	It counts the number of flows through a piece of code.	[11]
22	LOC	Lines of code.	[13]
23	Invocation	The number of executions of a program or function.	[8]
24	Field access	Number of accesses to object fields.	[8]
25	Array length	Number of accesses to the array length operation.	[8]
26	Number of Static Attributes	The number of attributes that contain the same value for each object (all instances of the class).	[11]
27	Specialization Index	Indicate the average of the specialization index, defined as NORM * DIT / NOM	[11]
28	Normalized distance	This metric from Main Sequence calculate by $\mid A + I - 1 \mid$, this number should be small, close to zero for good packaging design.	[11]
29	Depth of Inheritance tree	(DIT) is the distance from class Object in the inheritance hierarchy.	[11]
30	Number of Packages	Number of packages in the code.	[11]
31	Number of overridden Methods	This metric shows the total number of methods in the selected scope that are overridden from an ancestor class	[11]
32	Number of Static Methods	Number of methods whose signatures differ is known as overloading. Single return value.	[11]
33	Nested Block Depth	This metric is the number of statement blocks that are nested due to the use of control structures (branches, loops)	[11]
34	Number of Parameters	Number of formal parameters being passed onto the function	[11]
35	Development productivity	How many outputs can be produced per unit time. It is measured as size divided by time.	[14]
36	Defect density	Number of defects found per unit size of product. It is measured as Defects divided by size.	[14]
37	Defect removal efficiency	The percentage of defects removed during the phase. Calculated as Defects removed within the phase divided by total defects.	[14]
38	Cost performance index	This metric indicates the degree to which actual time spent is meeting time commitments	[14]
39	Size estimation errors	Indicator to which degree the estimate matches the actual size: (Actual size - Planned size)/Planned size.	[14]
40	Life cycle Cost Metric	Relation between efforts needed for redesigning an application for energy consumption optimization vs. the potential energy savings	[15]
41	Quality of Service Metric	It includes the following parameters: Availability, Throughput, Response Time, Process Time/Job Duration, Reliability, Recoverability, Workload, Application Performance Metric	[15]

What kind of tools are used for collecting these metrics? A number of tools for collecting energy consumption metrics were found from selected studies. Some of the found tools are used while collecting metrics of the product, process or both of them. Found tools and their descriptions are provided.

MEMT - It allows the development of plugins for automatic tuning where the design makes a reference to Periscope Tuning Framework, as described in the paper [16].

PETrA - Power Estimation Tool for Android is software-based tool developed to measure the power consumption of mobile apps at a method-level granularity [17].

PUPiL - a hybrid software/hardware power capping system. It is based on a novel decision framework. To ensure a power cap, PUPiL navigates nodes - choices about how to use a particular resource in a decision framework [18].

JADE - a system that adds sophisticated energy-aware computation offloading capabilities to Android apps. Jade monitors device and application status and automatically decides where code should be executed [19].

GEMMA - GUI Energy Multi-objective optiMization for Android apps. It generates color palettes using a multiobjective optimization technique, which produces color solutions optimizing energy consumption and contrast while using consistent colors with respect to the original color palette [20].

Green Advisor - a first of its kind tool that systematically records and analyzes an application's system calls to predict whether the energy-consumption profile of an application has changed [21].

ePRO-MP - profiles and optimizes both performance and energy consumption of multi-threaded applications running on top of Linux for ARM11 MPCore-based embedded systems. It does not require power consumption equipment and uses regression-based energy model [22].

LEMON - Lemon is a server/client based monitoring system for a very large scale infrastructure. On every monitored node, a monitoring agent is launched and this communicates using a push/pull protocol with sensors [23].

ANEPROF - Android systems's tool that can obtain function-level power distribution and distinguish the power consumption among threads, Java methods, and JVM services and also addresses how to correctly associate power logs with Android system's behaviours [24].

4. Discussion

This section represents various findings of our Systematic Literature Review(SLR) and draw some conclusions. The 504 papers in the areas like Mobile, Embedded and Cloud systems were under study consideration that investigate energy consumption. The Systematic Literature Review's aim was to identify Green metrics and their classification with descriptions and limitations, and the types of tools to collect these metrics. The results of the review shows that the studies that investigate Energy efficiency in Mobile systems constitutes more than Embedded and Cloud systems. In fact, that as young fields, energy efficiency surveys in Cloud and Embedded systems require more research studies where it became common in recent years to pay more attention to them.

From 124 studies 17 of them focused on experimenting existing best practises and conducting empirical studies for better understanding of existing techniques efficiency of energy metrics. In the paper [13], there were taken into consideration six popular mobile applications, where the authors observed whether the battery of the mobile device can last up to approximately an extra hour if the applications are developed with energy-aware practices. While in [25], there was conducted an empirical study of the effects of 18 code obfuscations on the amount of energy consumed by executing a total of 21 usage scenarios spread across 11 Android applications on four different mobile phone platforms.

Whereas, 54 studies such as [26] and others were concentrated on proposing new or improved Models and Frameworks for mapping software design to power consumption. Where the importance of energy efficiency was described in early analysis of software design and have significant impact on energy conservation achievement.

Furthermore, the tools to collect Green metrics were considered to capture types of Tools in the observed research papers. In the paper [27], the tool under consideration the dynamic energy consumption estimator showed high estimation accuracy and effectiveness as it selected the suitable energy consumption estimator for various mobile application programs. Moreover, the paper [21] considered precision, recall, specificity, and F-measure, proposing the GreenAdvisor tool that uses the application's system-call profile to warn developers about possible changes in the application's energy consumption profile by using Rule of Thumb. However, our study did not consider the complete understanding of Tools' functions and working conditions.

The main concentration during the SLR was to identify the metrics related to the software code metrics defined in the study [28] excluding hardware metrics. In the paper [29], methods affected by 4 code smell types, Internal Setter, Leaking Thread, Member ignoring method and Slow Loop consume up till 87 times more than methods affected by other code smells. Refactoring of these code smells reduced energy consumption in all situations. While in [30], they explored the memory usage and the bytecode executed during an operation. They found that choosing the wrong Collections type, as indicated by their profiles, can cost even 300% more energy than the most efficient choice.

5. Conclusion

Systematic Literature Review conducted within this project clearly shows the urgency of the software energy efficiency issue and its proper and operative analysis in particular. In general, all studies could be devoted into the real measurement and model-based measurement, as it was proposed in [24]. Direct measurements involve usage of third-party hardware tools to read actual energy consumption by different modules and components of the software or entire hardware-software systems.

Metrics, related to this area of energy efficiency analysis were separated into hard metrics group. These metrics are not in scope of the given project, as far as our goal is to develop framework for invasive analysis of the software development process. Thus, the product and process metric, related to the software quality analysis should be the main focus of further research. Based on the analysis of these metrics (table 3) it could be concluded that the group of process metrics has not properly observed yet. One of the reason for it is the absence of the tool for sufficient analysis of the development process. Usually, such process involves participation of the developer [31], and we faced with the problem of subjective measurement and time costs increasing due to the task switching. Developing of the framework which provides an invasive measurement of the development process could result in bunch of metrics showing development effort patterns. The combination of the developers' behavior patterns and code metrics could result in highly precise model for the in situ analysis of the developing product. Thus, the development of framework for invasive process measurement as well as developing of the model for mapping process and code metrics to the actual energy efficiency of the software product will be the subject of the further research.

6. References

[1] Vereecken W, Heddeghem W, Deruyck M, Puype B, Lannoo B, Joseph W, Colle D, Martens L and Demeester P 2011 Power consumption in telecommunication networks: Overview and reduction strategies *IEEE Communications Magazine* **49** 62–9

[2] Pedrycz W, Succi G, Sillitti A and Iljazi J 2015 Data description: A general framework of information granules *Knowledge-Based Systems* **80** 98–108

[3] Coman I D, Sillitti A and Succi G 2008 Investigating the usefulness of pair-programming in a mature agile team *Lecture notes in business information processing* (Springer Berlin Heidelberg) pp 127–36

[4] Corral L, Sillitti A and Succi G 2015 Software assurance practices for mobile applications - A survey of the state of the art *Computing* **97** 1001–22

[5] Kitchenham B, Brereton O P, Budgen D, Turner M, Bailey J and Linkman S 2009 Systematic literature reviews in software engineering a systematic literature review *Information and Software Technology* **51** 7–15

[6] Hao S, Li D, Halfond W G J and Govindan R 2013 Estimating mobile application energy consumption using program analysis *Proceedings of the 2013 international conference on software engineering* ICSE '13 (Piscataway, NJ, USA: IEEE Press) pp 92–101

[7] Verma M and Chowdhary K R 2018 Analysis of energy consumption of sorting algorithms on smartphones *SSRN Electronic Journal*

[8] Li D and Halfond W G J 2014 An investigation into energy-saving programming practices for android smartphone app development *Proceedings of the 3rd international workshop on green and sustainable software - GREENS 2014* (ACM Press)

[9] Chatzigeorgiou A and Stephanides G 2002 *Software Quality Journal* **10** 355–71

[10] Bangash A A, Sahar H and Beg M O 2017 A methodology for relating software structure with energy consumption *2017 IEEE 17th international working conference on source code analysis and manipulation (SCAM)* (IEEE)

IOP Conf. Series: Earth and Environmental Science **431** (2020) 012051 doi:10.1088/1755-1315/431/1/012051

[11] Keong C K, Wei K T, Ghani A A A and Sharif K Y 2015 Toward using software metrics as indicator to measure power consumption of mobile application: A case study *2015 9th malaysian software engineering conference (MySEC)* (IEEE)
[12] Vasile C V, Pattinson C and Kor A-L 2018 Mobile phones and energy consumption *Green IT engineering: Social, business and industrial applications* (Springer International Publishing) pp 243–71
[13] Cruz L and Abreu R 2017 Performance-based guidelines for energy efficient mobile applications *2017 IEEE/ACM 4th international conference on mobile software engineering and systems (MOBILESoft)* (IEEE)
[14] Gwak T-H and Jang Y-J 2006 An empirical study on sw metrics for embedded systems
[15] Kipp A, Jiang T and Fugini M 2011 Green metrics for energy-aware IT systems *2011 international conference on complex, intelligent, and software intensive systems* (IEEE)
[16] Liu W, Zhou J, Gong B, Dai H and Guo M 2018 Improving the energy efficiency of data-intensive applications running on clusters *International Journal of Parallel, Emergent and Distributed Systems* 1–14
[17] Nucci D D, Palomba F, Prota A, Panichella A, Zaidman A and Lucia A D 2017 Software-based energy profiling of android apps: Simple, efficient and reliable? *2017 IEEE 24th international conference on software analysis, evolution and reengineering (SANER)* (IEEE)
[18] Zhang H and Hoffmann H 2016 Maximizing performance under a power cap: A comparison of hardware, software, and hybrid techniques *SIGPLAN Not.* **51** 545–59
[19] Qian H and Andresen D 2015 Reducing mobile device energy consumption with computation offloading *2015 IEEE/ACIS 16th international conference on software engineering, artificial intelligence, networking and parallel/distributed computing (SNPD)* (IEEE)
[20] Linares-Vásquez M, Bavota G, Cárdenas C E B, Oliveto R, Penta M D and Poshyvanyk D 2015 Optimizing energy consumption of GUIs in android apps: A multi-objective approach *Proceedings of the 2015 10th joint meeting on foundations of software engineering - ESEC/FSE 2015* (ACM Press)
[21] Aggarwal K, Hindle A and Stroulia E 2015 GreenAdvisor: A tool for analyzing the impact of software evolution on energy consumption *2015 IEEE international conference on software maintenance and evolution (ICSME)* (IEEE)
[22] Wonil C, Hyunhee K, Wook S, Jiseok S and Jihong K 2009 EPRO-mp: A tool for profiling and optimizing energy and performance of mobile multiprocessor applications *Scientific Programming* **17** 285–94
[23] Marian B, Ivan F, Nicholas H, Hector L T, Daniel L, Miroslav S and Denis W 2011 LEMON - LHC era monitoring for large-scale infrastructures *Journal of Physics: Conference Series* **331** 052025
[24] Chung Y-F, Lin C-Y and King C-T 2011 ANEPROF: Energy profiling for android java virtual machine and applications *2011 IEEE 17th international conference on parallel and distributed systems* (IEEE)
[25] Sahin C, Wan M, Tornquist P, McKenna R, Pearson Z, Halfond W G J and Clause J 2016 How does code obfuscation impact energy usage? *Journal of Software: Evolution and Process* **28** 565–88
[26] Mendonça J, Andrade E and Lima R 2019 Assessing mobile applications performance and energy consumption through experiments and stochastic models *Computing*
[27] Lim K-H and Lee B-D 2014 History-based dynamic estimation of energy consumption for mobile applications *16th international conference on advanced communication technology* (Global IT Research Institute (GIRI))
[28] Gurbuz H G and Tekinerdogan B 2016 Software metrics for green parallel computing of big data systems *2016 IEEE international congress on big data (BigData congress)* (IEEE)
[29] Palomba F, Nucci D D, Panichella A, Zaidman A and Lucia A D 2019 On the impact of code smells on the energy consumption of mobile applications *Information and Software Technology* **105** 43–55

[30] Hasan S, King Z, Hafiz M, Sayagh M, Adams B and Hindle A 2016 Energy profiles of java collections classes *Proceedings of the 38th international conference on software engineering - ICSE 16* (ACM Press)
[31] Anon 2009 *The personal software process sm (psp sm) body of knowledge (version 2.0)* (Carnegie Mellon University)

Acknowledgements
This research project is carried out under the support of the Russian Science Foundation Grant № 19-19-00623.

IOP Conf. Series: Earth and Environmental Science **431** (2020) 012045 doi:10.1088/1755-1315/431/1/012045

Research on epoxy-based nanocomposites with high energy density and charge-discharge efficiency filled with TiO_2 nanofibers

Bo Kong[1], YongPeng Meng[1], SiYu Chen[1], YuShuan Gao[1], YongHong Cheng[1] and WenKe Wang[1]

1 The State Key Lab of Electrical Insulation for Power Equipment, Xi'an Jiaotong University, Xi'an, China
E-mail: kb1996@stu.xjtu.edu.cn

Abstract. Capacitor films with high energy density are critical to energy storage. However, the energy density of state-of-the-art commercial capacitor films are limited by their low dielectric permittivity. In this study, epoxy-based nanocomposite films are prepared by filling with TiO_2 nanofibers. Results show that nanocomposite films have larger discharge energy density because of the significant increase in dielectric permittivity, which caused by the additional interface polarization and space charge polarization. And a superior charge-discharge efficiency is achieved in the composite films at the same time due to the low dielectric loss. In addition, the composites also keep a high breakdown strength because of the dispersion of the nanofibers. The discharge energy density of 5.19 J/cm^3 with the efficiency of 80% is achieved at 470 MV/m in the nanocomposites containing 2wt% nanofibers. The excellent energy density and charge-discharge efficiency of epoxy-based nanocomposites offer a promising opportunity for future researches and industrial application.

1. Introduction

The development of new renewable energy has attracted a lot of attention, but these energy sources are often scattered and discontinuous. Therefore, how to effectively store them has become a hot topic. In addition, high-quality energy storage devices are also necessary for electric vehicles and various electronic devices. Film capacitors are highly concerned because of the advantages of high power density and fast discharge rates [1]. However, the commonly used biaxially oriented polypropylene (BOPP) films are limited by the low energy density of only 1-2 J/cm^3 [2]. Hence, the achievement of films for energy storage capacitors with high energy density is crucial.

The energy density (*Ue*) of the dielectric is an important parameter to characterize the energy storage properties, which represents the energy stored in unit volume of the dielectric material. Theoretically, the energy density is expressed as $U_e = \int EdD$, which is determined by the applied electric field (E) and the electric displacement (D) [3]. And the electric displacement is related with electric filed and permittivity (ε). The energy density is usually obtained by testing the electrical displacement–electric field loop (D-E loop), as shown in figure 1.

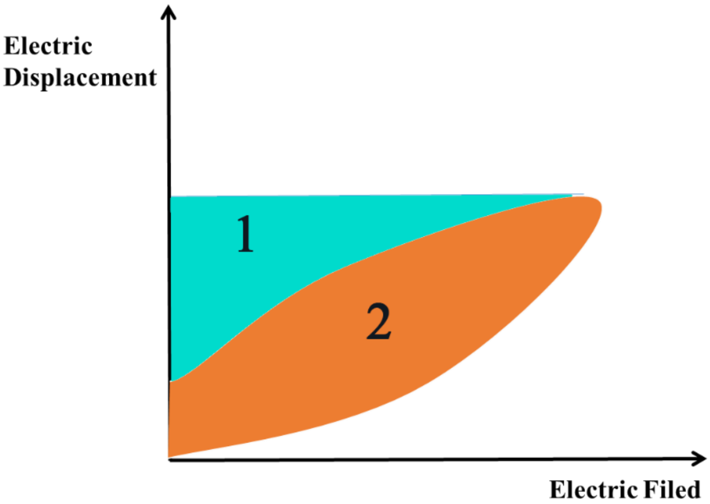

Figure 1. The D-E loop of dielectric.

The D-E loop in figure 1 represents a complete charge-discharge process of the dielectrics, and also implies the relationship between *D* and *E*. The sum of the region 1 and region 2 represents the charge energy density (indicated by W_1), and the region 1 (indicated by W_2) represents the discharge energy density, which is also defined as the energy density of the material. The charge-discharge efficiency (η) is expressed with equation (1). The region 2 indicates the energy that cannot be released during the charge-discharge process. For nonlinear dielectrics, it is mainly related to residual polarization. And for linear dielectrics, it is related with leakage current and dielectric loss [4].

$$\eta = \frac{W_2}{W_1} \tag{1}$$

The strategies to improve energy density of material is to enhance the permittivity, breakdown strength (E_b) and charge-discharge efficiency. The nanodoping is a positive approach to increase permittivity, which is commonly used in the existing researches. Lin X (2016) prepared nanofibers of TiO_2 coated $BaTiO_3$ by coaxial electrospinning, and achieved the high energy density of 10.94 J/cm^3 in the nanocomposites based on Poly (vinylidene fluoride) (PVDF) [3]. Wang Y (2017) prepared sandwich-structured nanocomposites, and the middle layer of pure PVDF is reported to effectively improve the breakdown strength and charge-discharge efficiency [5].

However, it is difficult for PVDF-based nanocomposites to maintain excellent efficiency, which is also paramount to industrial applications [6]. Therefore, it is indispensable to seek a new type of polymer films with high energy density and great charge-discharge efficiency. In comparison, epoxy resin has higher permittivity than BOPP, better breakdown strength and efficiency than PVDF. It is also appreciated for the favorable industrial application prospects.

In this paper, epoxy resin was selected as the polymer matrix and TiO_2 nanofibers (TO nf) prepared by hydrothermal method were added to improve the energy storage performance. As a result, the dielectric permittivity increases significantly and the dielectric loss is limited in the nanocomposites. In addition, the composite films keep a high breakdown strength and a large discharge energy density is achieved with high charge-discharge efficiency. The outstanding energy storage density and charge-discharge efficiency give epoxy-based nanocomposites the opportunity to be applied in the field of future capacitor films.

2. Experiments

For the preparation of the TO nf, 1.5 g of TiO_2 powder was firstly dispersed in 80 ml of 10 M NaOH solution in a 100 ml Teflon autoclave. Then the autoclave was heated to 200 ℃ and kept for 24 h. After cooled to room temperature, the powder was washed with deionized water and then soaked with a 0.2 M diluted hydrochloric acid for 3 h. After that, the powder was washed with deionized water for several times. And then the powder was calcined at 500 ℃ for 2 h to form TO nf. The morphologies of the nanofibers were observed by scanning electron microscopy (SEM) and transmission electron microscopy (TEM). Moreover, structural characterization was performed by X-ray diffraction (XRD) to identify the crystal structure.

For the fabrication of the composite films, TO nf were proportionally added to the hardener and ultrasonically dispersed for 30 minutes after dried at 60 ℃ for 24 h. Next, the mixture was degassed at vacuum at room temperature for 15 minutes and then completely mixed with an appropriate amount of epoxy resin. It should be noted that the epoxy resin was placed in a vacuum oven at 60 ℃ for 1 h in advance to remove moisture and bubbles. Then the composites were hot pressed and cured at 80 ℃ for 2 h to form films. In this research, nanocomposite films with different mass fraction were prepared and the thickness was ranged from 10um to 16um. The morphologies of the composites were observed by optical microscope.

For electrical properties tests, gold electrodes were sputtered on both sides of the films. All samples were dried at 60 ℃ for 24 h before tested. Both the dielectric permittivity and the dielectric loss of the nanocomposite films were measured by a Concept 80 Broadband Dielectric Spectrometer at room temperature, and the frequency was ranged from 10^{-1} to 10^{6} Hz. The D–E loops were measured at 100 Hz by a Polarization Loop and Dielectric Breakdown Strength Tester, and the breakdown strength of the film was also tested by this instruments.

3. Results and discussions

The TiO_2 nanofibers were prepared by hydrothermal method, and epoxy-based nanocomposite films was obtained by hot pressing method. Figure 2a and figure 2c show the microstructure of the nanofibers observed by SEM and TEM. The nanofibers maintain a wire structure with diameter of about 200 nm and length of about 10 μm, as shown in figure 2a. Figure 2c demonstrates that the nanofibers are distinct polycrystalline structures. The crystal structure of the prepared TiO_2 was identified as an anatase crystal form by comparing the XRD of the nanofiber, which is shown in figure 2b with a standard PDF card.

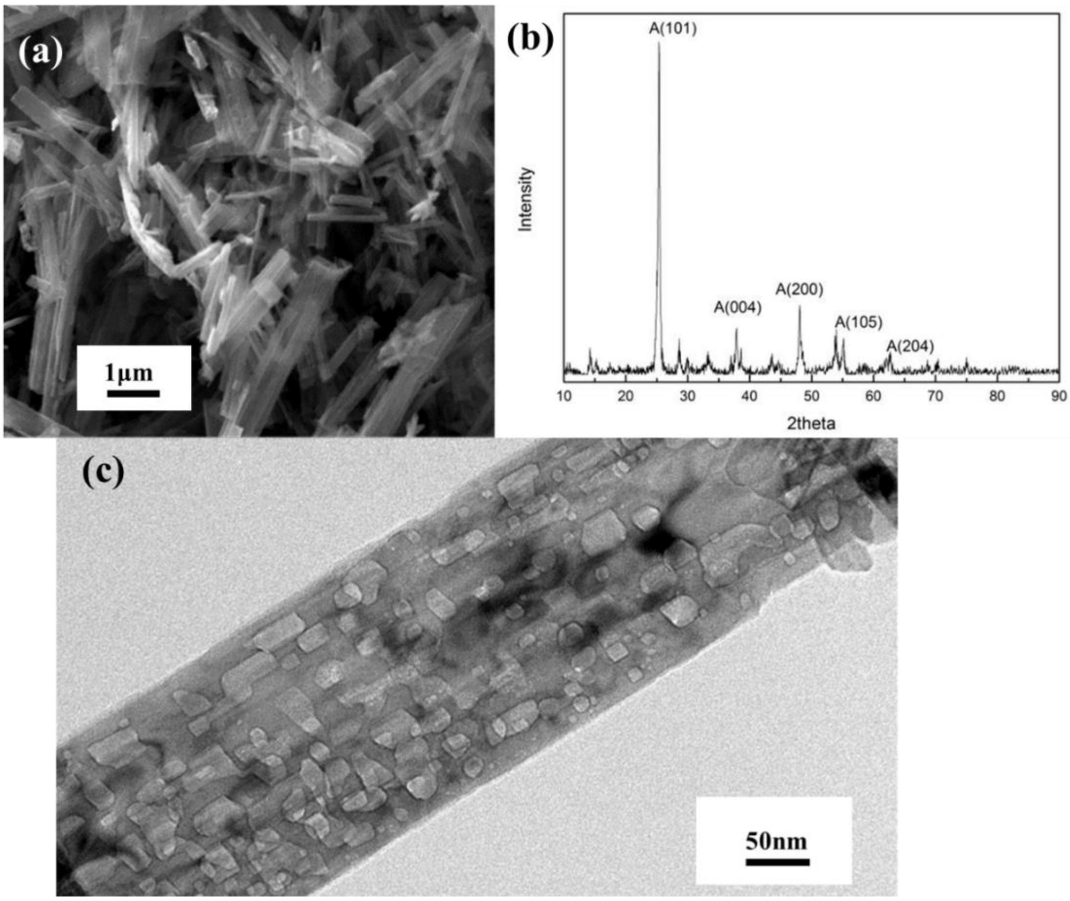

Figure 2. (a) SEM image, (b) XRD pattern and (c) TEM image of the TiO_2 nanofibers.

In previous researches, agglomeration tends to occur in the nanocomposites due to the large specific surface area and high surface activity of nanofillers [7]. The agglomeration of the nanofibers exacerbates the distortion of the electric field, thereby greatly impairing E_b and η of the composite films. Consequently, a high energy density cannot be achieved, without alleviating the agglomeration of the nanofibers. In this paper, the nanofibers were dispersed in the hardener by ultrasonic dispersion. The dispersion of the nanofibers is uniform and no significant agglomeration observed, as shown figure 3c. Meanwhile, figure 3a and figure 3b demonstrate the excellent film formation and flexibility of epoxy films and composite films.

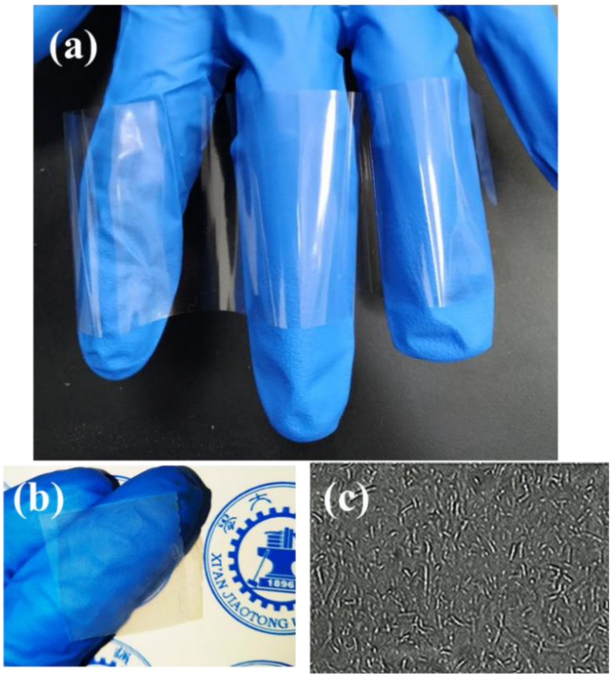

Figure 3. (a)The epoxy film. (b) The nanocomposite film. (c) The morphology of nanocomposites with 1wt% TO nf.

It can be seen that the doping of TO nf significantly enhances the permittivity of composite films from figure 4a. At the frequency of 100 Hz, the permittivity of the epoxy film is only 4.83, while the composite film containing 2wt% TO nf reaches 5.58. The high permittivity of TO contributes to it, which induce huge electric displacement under external electric field. More importantly, a special region with strong interfacial interaction is formed between the nanofibers and the epoxy matrix. The interfacial polarization and space charge polarization greatly enhances the electric displacement and permittivity [8]. However, the additional polarization generated by the nanofibers and the interface region also increases the dielectric loss of the composite film, as shown in figure 4. Despite this, nanocomposites still keep low dielectric loss below 0.045, due to the good compatibility of nanofibers with epoxy and the properties of epoxy resins as dielectric.

Both the increase in permittivity and the low dielectric loss are advantageous for improving the energy density of nanocomposite films. At the same time, high breakdown strength is also critical for energy density. In general, nanodoping causes distortion of the electric field inside the composites, leading to a drop in breakdown strength. However, a good dispersion allows the composite films to maintain a high breakdown strength. In addition, the huge aspect ratio of the nanofibers is also beneficial for the breakdown strength, which causes the nanofibers to overlap with each other and the electric field applied in the vertical direction to decrease [9]. Besides, Figure 4b show that the breakdown strength of composite films loading 0.5wt% TO nf reaches 496 MV/m., the nanocomposites with 2wt% TO nf still maintain the breakdown strength of 412 MV/m.

It is reported that the applied electric field of the capacitor film required for electric vehicles is 200 MV/m, so the discharge energy density under this field is quite important [10]. The commercial BOPP film has an energy density of only 0.4 J/cm^3 at this field. As a comparison, the epoxy film reach 0.79 J/cm^3 at this field and maintain a charge-discharge efficiency near 100%, as shown in figure 5. And the composite films doped with TO nf maintain an efficiency of more than 90% while increasing the energy density. The composite films containing 2wt% TO nf have an efficiency of 97%, and achieve an energy density of 0.98 J/cm^3, almost 2.5 times that of BOPP.

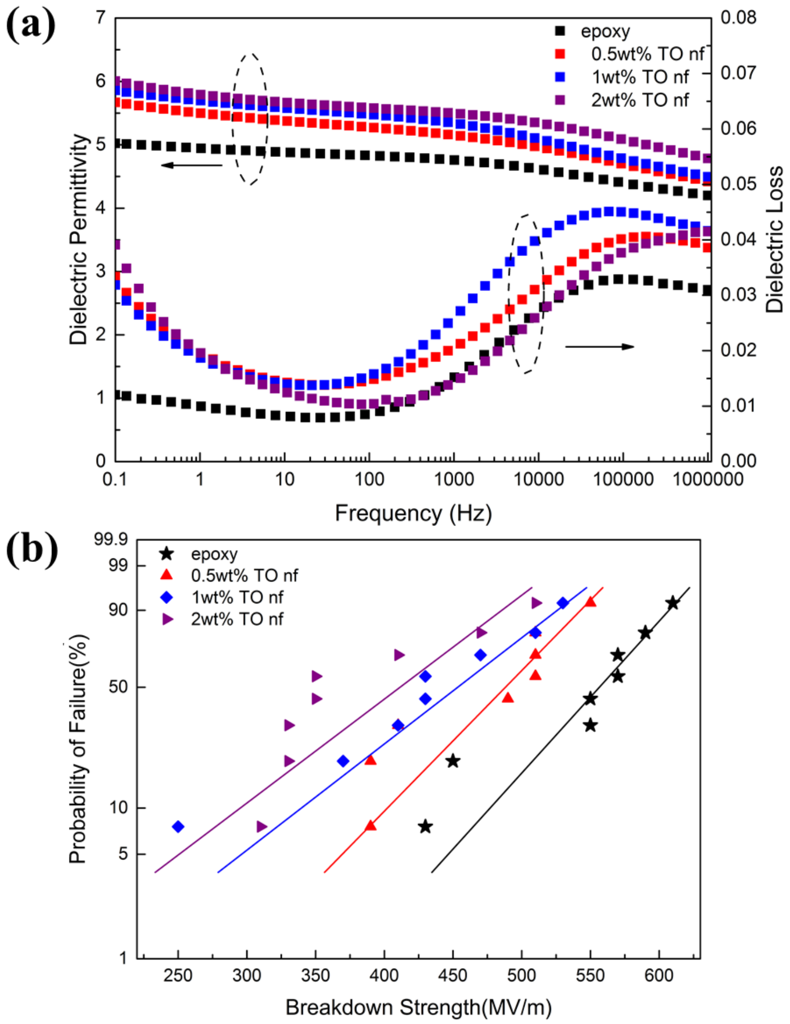

Figure 4. (a) The dielectric permittivity and dielectric loss of nanocomposites at different mass fraction. (b) Failure probability of breakdown strength deduced from Weibull distribution for nanocomposites with different mass fraction of nanofibers.

The energy density of the composite films was improved significantly due to the increase in dielectric permittivity. Meanwhile, the composites maintain a low loss to ensure high charge-discharge efficiency. These are critical to the application of film capacitors. It can be seen from figure 5 that the nanocomposite with 0.5wt% TO nf reaches an energy density of 4.78 J/cm^3 at 470 MV/m, and maintains a high efficiency of 90%. Besides this, a higher energy density of 5.19 J/cm^3 is achieved at 470 MV/m in the composite loading 2wt% TO nf, which is 17.7% higher than the epoxy films in the same electric filed. In addition, an efficiency of 80% is obtained, due to the low dielectric loss below 0.045, as shown in figure 4.

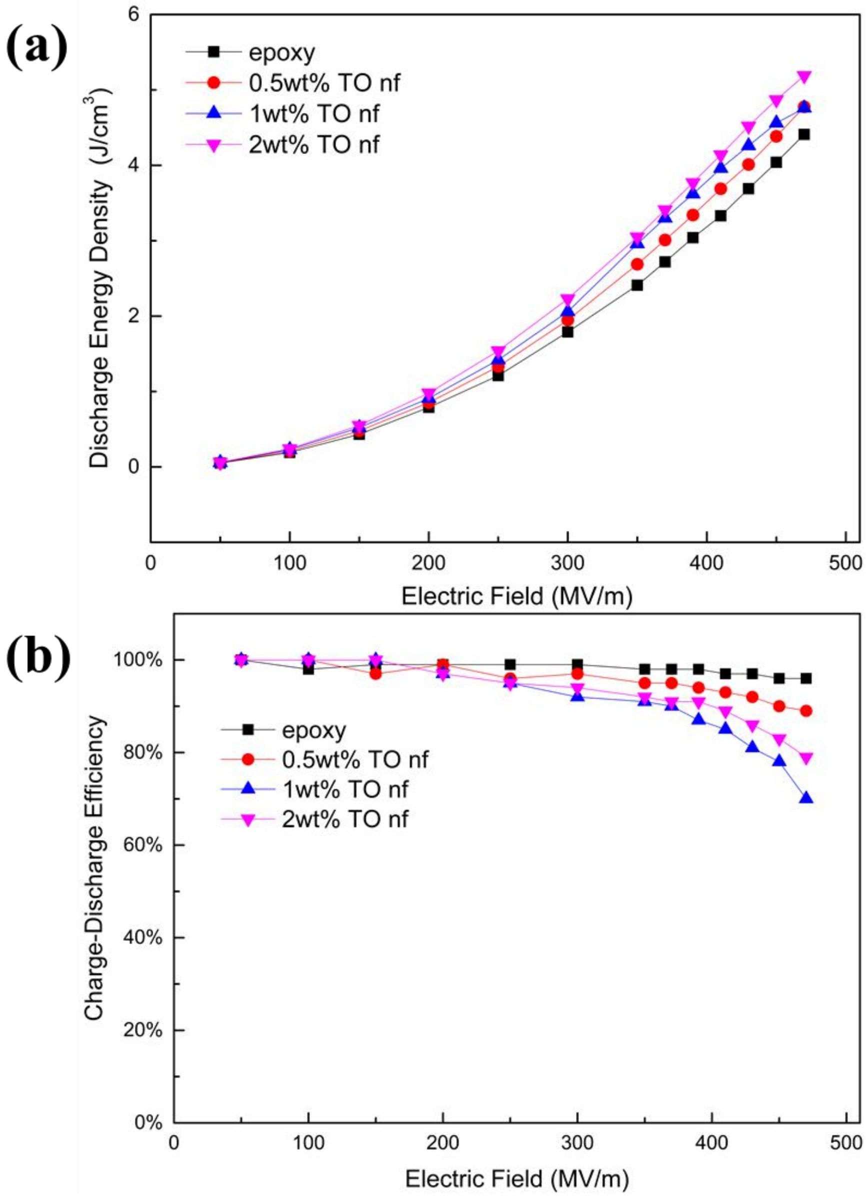

Figure 5. (a) Discharge energy density and (b) charge-discharge efficiency of epoxy nanocomposites with different mass fraction of nanofibers.

4. Conclusions

The addition of nanofibers significantly enhances the dielectric permittivity due to the high dielectric permittivity of TO and the additional polarization and electric displacement at the interfaces. Meanwhile, the nanocomposites also reach an excellent charge-discharge efficiency because of the low dielectric loss. Besides this, a high breakdown strength is also achieved because of the good dispersion of nanofibers. A high energy density of 5.19 J/cm^3 is achieved in the nanocomposites with 2wt% TO nf with an efficiency of 80% at 470 MV/m. Epoxy-based nanocomposites have excellent charge-discharge efficiency and high energy density. Therefore, they have the potential to become an alternative to capacitor films. Moreover, future study can focus on the effect of structures of epoxy resin and hardener on the energy storage properties, to find one most suitable for future capacitor films.

5. References

[1] Hasan N S, Hassan M Y and Majid M S 2013 *Renewable & Sustainable Energy Reviews* **21** 237-247

[2] Liu J, Tian G and Qi S 2014 *Materials Letters* **124** 117-119
[3] Lin X, Hu P and Jia Z 2016 *Journal of Materials Chemistry A* **4** 2314-2320
[4] Han K, Li Q and Chanthad C 2015 *Advanced Functional Materials* **25** 3505-3513
[5] Wang Y, Cui J and Yuan Q 2015 *Advanced Materials* **27** 6658-6663
[6] Wen H, Xiao W and Wen X 2012 *IEEE Transactions on Vehicular Technology* **61** 2950-2964
[7] Xu H and Gao L 2003 *Journal of the American Ceramic Society* **86** 203-205
[8] Zhang X, Shen Y and Zhang Q 2015 *Advanced Materials* **27** 819-824
[9] Liu S, Zhai J and Wang J 2014 *Acs Applied Materials & Interfaces* **6** 1533-40
[10] Li Q, Liu F and Yang T 2016 *Proceedings of the National Academy of Sciences* **113** 9995-10000

Acknowledgments
This work was supported by the Innovation Research Group of NSFC (51521065), National Natural Science Foundation of China (51677143), and the Research Foundation of State Key Laboratory of Electrical Insulation and Power Equipment (EIPE14107). The authors thank Ms. Feng and Mr. Zhang for their help in experiments.

IOP Conf. Series: Earth and Environmental Science **431** (2020) 012046 doi:10.1088/1755-1315/431/1/012046

Research on key technologies of high voltage and large capacity static synchronous series compensator control system

Peie Yuan[1], Xiang Wang[1], Guofu Chen[1], Xiaoguang Jia[1], Fengjiao Dai[1], Zhiyong Yu[1] and Yingpei Wang[1]

1 State Key Laboratory of Advanced Power Transmission Technology, Global Energy Interconnection Research Institute Beijing, China
E-mail:haixia28@sina.com

Abstract. With the rapid development of economy, the structure of power grid is becoming more and more complex, which has brought about uneven distribution of power flow, limited transmission capacity and the decline of power quality. The application of new static synchronous series compensator can quickly and effectively regulate power flow, suppress sub-synchronous oscillation and enhance system stability on the basis of guaranteeing transmission capacity. In practical engineering application, the design of control system and the realization of control algorithm are very important. In this paper, the control system of 220 kV 30MW self-excited SSSC device is developed based on the control and protection platform of serial RapidIO technology. Firstly, the main topology structure of SSSC is introduced, and the two-stage DC voltage stabilization and upper steady-state operation control strategy of SSSC using fast response control method which simultaneously regulates modulation ratio and trigger angle are expounded. Secondly, the dual redundancy control system architecture is designed, and the control system implementation scheme is designed. Finally, the RTDS power in the loop experimental system is designed, and the control algorithm is verified by RTDS experiments. The experimental results show that the control strategy and control system implementation scheme adopted in this paper can realize smooth start-up and exit of SSSC device and flexible regulation of power flow. The developed control system can satisfy the long-term reliable and stable operation of the system, especially the design of redundancy mechanism, and increase the reliability of the device operation. Follow-up static synchronous series compensator project and even FACTS project provide reference.

1. Introduction

With the rapid development of economy and the scale of new energy added, the structure of power grid is becoming more and more complex, which brings about problems such as uneven distribution of power flow, limited transmission capacity and decline of power quality. The application of a new type of Static Synchronous Series Compensator (SSSC) can quickly and effectively regulate power flow, suppress sub-synchronous oscillation and enhance system stability on the basis of guaranteeing transmission capacity. It has the advantages of flexible control and simple structure, and has been applied more and more widely [1, 2].

In recent years, scholars at home and abroad have made fruitful achievements in SSSC research [3-6]. In literature [7], a stable start-up strategy is proposed in UPFC project. The start-up of the series part depends on the parallel external devices to increase the start-up time. The paper [8, 9] considers that the unbalanced power exchange on the DC side is the fundamental cause of the unbalanced voltage, and gives the corresponding DC side capacitor voltage balance method for trapezoidal wave modulation. In reference [10], the unbalanced state of chain reactive power compensator is studied, and the idea of decoupling control is put forward. It can be used for reference in SSC, especially the decoupling control between upper and lower control. Reference [11] introduces the quasi-steady state model of SSSC in H-bridge cascade structure. The impedance compensation domain is analyzed by constant impedance control, but the control mode is too single. Literature [12] compares three kinds of control ideas considering the unbalanced capacitor voltage of H-SSSC, and proposes a comprehensive control strategy which can adjust the modulation ratio and trigger angle simultaneously with rapidity. However, most of these studies remain at the theoretical level, and lack of engineering application practice. Controller design for SSSC is rarely mentioned. Therefore, the high performance SSSC control system and its control strategy for engineering need to be further studied.

Referring to the above research results, the control system of 220 kV 30MW self-excited SSSC device is developed by using the control and protection platform based on serial RapidIO technology. Firstly, the main topology of SSSC is introduced, and the upper steady-state operation control strategy of two-stage DC voltage stabilization and constant active power operation control for SSSC is proposed. Secondly, based on the control and protection platform of serial RapidIO technology, a dual redundancy architecture control system and its engineering implementation scheme are designed. Finally, the RTDS power in the loop experiment system is designed, and the control algorithm is verified by the RTDS experiment, which proves the accuracy of the control strategy and the stability and reliability of the control system.

2. Principle and topology

SSSC is a series compensator based on synchronous voltage source. It provides a voltage which is 90° different from the line current and independent of the line current. It is equivalent to connecting a reactance in series on the transmission line. Therefore, by controlling the voltage amplitude of the SSSC device injection system, the equivalent impedance of the SSSC is controlled, so that the effective impedance of the transmission line can be changed, and finally the purpose of regulating the power flow is achieved. At this kind of circumstance, SSSC and power network exchange only reactive power.

According to the research of SSSC's main topology from domestic and foreign scholars, when the system is unbalanced, three single-phase H-bridges have the advantage of single-phase voltage and current control being more flexible than three-phase bridges, so the SSSC selects the three-phase H-bridge cascaded main topology in this project. AS show in figure 1, it consists of controller(KZ),series value(HB),DC capacitor(C),filter(L),bypass thyristor(TBS),coupling transformer(T), circuit breaker1(QF1), circuit breaker2(QF2), circuit breaker3(QF31). Because the coupling transformer is connected in series on the Transmission Line, the series value is also effectively connected in series to the Transmission line, and series compensation can be realized. The main function of bypass thyristor is: when the series valve is exited, the controller simultaneously issues a command to close the bypass switch and contact the bypass thyristor. Since the bypass thyristor is touched quickly, the series valve can be bypassed very quickly, and after the bypass switch is closed. The circuit breaker is mainly used for the switching of the SSSC. When the SSSC is working normally, the AC breaker QF1 is disconnected, the valve outlet side breaker QF2 is closed, and when the system is faulty, the SSSC is removed from the grid. Each phase converter valve is cascaded by 9 H-bridge modules.

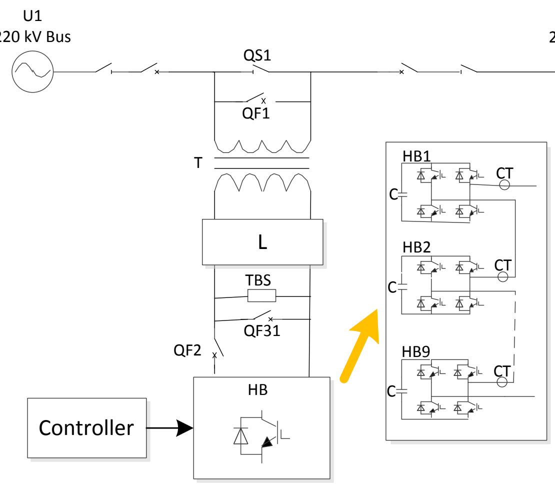

Figure 1. Schematic diagram of the SSSC topology.

3. Research on control technology

3.1. Control strategy research

3.1.1. Startup strategy

Controlling the phase of the output voltage of the inverters is the same as the phase of the injected current, which can ensure that the inverters are pure resistance in the process of charging from the external system, so it does not consume reactive power and has the highest charging efficiency. This way can also be called the "resistance" mode of SSSC, that is, the full active PWM rectification mode. The expression of equivalent resistance of full active PWM rectifier charging output is as follows:

$$R = \frac{U(t)}{I(t)} = \frac{mV_{dc}}{I_P} \tag{1}$$

Among them, R is the injection equivalent resistance, m is the modulation ratio, U (t) is the output voltage of the inverter, I (t) is the injection system current, and V_{dc} is the DC bus voltage.
It is assumed that the injection equivalent resistance is small and the line current remains unchanged during the charging process. In the process of charging, the DC voltage increases continuously until the set value, so the modulation ratio m is inversely proportional to the DC voltage in the control. Through the detection link, the modulation ratio can be calculated by formula (1). At the initial stage of charging, the parallel diode in H bridge is used to pre-charge the DC capacitor, and then the PWM rectifier is carried out.

3.1.2. Steady-state control

Combined with H-SSSC steady-state model, when the total conversion ratio of coupling transformer is 1, Then the DC capacitance equation of series compensation line:

$$C\frac{dU_{ci}(t)}{dt} = S_{\omega}(t)\sin(\omega t + \varphi) \tag{2}$$

Where, C is the DC side capacitance value. U_{ci} is the capacitance voltage of the ith module, and φ is the angle between line current and compensation voltage. S_{ω} is defined as a switching function.

$$S_{\omega}(t) = m_i \sin \omega t \tag{3}$$

Where, m_i is the modulation ratio. Then the DC side capacitance voltage can be obtained.

$$V_{ci}(t) = \frac{I_L m_i}{4C_{\omega}}[2\omega t\cos\varphi + \sin\varphi - \sin(2\omega t + \varphi)] + V_{ci}(0) \tag{4}$$

I_L corresponds to the current RMS of AC line at this time, It is known that its DC component $\overline{V}_{dc}$ is:

$$\overline{V}_{dc} = \frac{I_L m_i}{4C_\omega}[2\omega t \cos\varphi + \sin\varphi] + V_{ci}(0) \tag{5}$$

And the line current:

$$I_L = \frac{\left|\overrightarrow{U_1} - \overrightarrow{U_2}\right|}{\left|X_L - X_{ref}\right|} = \frac{\sqrt{U_1^2 + U_2^2 - 2U_1U_2\cos\delta}}{\left|X_L - X_{ref}\right|} \tag{6}$$

Where,U1 and U2 are voltage values on both sides of AC line respectively. X_L is the Line impedance, X_{ref} is the reference value of line impedance.
It can be seen that the DC side capacitance voltage is positively correlated with the angle φ and modulation ratio m when the line current and capacitance value are constant. The DC side capacitance voltage can be controlled by controlling the angle φ. At this time, the compensation voltage is not strictly vertical to the line current. Instead, there is a difference in angle δ_1:

$$\delta_1 = k_p\left(NU_{cref} - \sum_{i=1}^{N}U_{ci}\right) + k_i\int\left(NU_{cref} - \sum_{i=1}^{N}U_{ci}\right)dt \tag{7}$$

Where: δ_1 is the regulation angle during SSSC startup or operation, K_p and k_i are PI control loop parameters, N is the number of submodules, U_{cref} is the capacitor voltage reference value.

3.1.3. Voltage equalization control

Two-stage DC voltage stabilization is to realize DC capacitor voltage balance control by upper and lower layer hierarchical control. The control strategy of calculating modulation ratio m and phase angle α is defined as upper control, and the control strategy of calculating modulation ratio m_i and phase angle α_i by balancing control algorithm is called lower control. If there is no balance control algorithm, all cascade modules use m and α directly, and each module after adding balance control algorithm uses their respective m_i and α_i.
The purpose of second order dc stable voltage is to obtain modulation ratio and firing angle each sub-module. the correction formula of the secondary voltage regulation:

$$\begin{cases} m_i = m\sqrt{1 + \left(\dfrac{U_{ci} - U_{cref}}{U_{ci}}\right)^2} \\ \alpha_i = \alpha + \arctan\dfrac{U_{ci} - U_{cref}}{U_{cref}} \end{cases} \tag{8}$$

Where, m_i is the modulation ratio of ith sub-module, α_i is the firing angle of ith sub-module, m is the modulation ratio of whole series value, α is the firing angle of whole series value.
It can be seen that by combining the direct PI control of the DC-side capacitor voltage with the separate adjustment of the modulated waves of each module, the H-bridge SSSC responds faster according to the fast response control method. Combined with the constant active power control method, the overall control block diagram is shown in Figure 2.

IOP Conf. Series: Earth and Environmental Science **431** (2020) 012046 doi:10.1088/1755-1315/431/1/012046

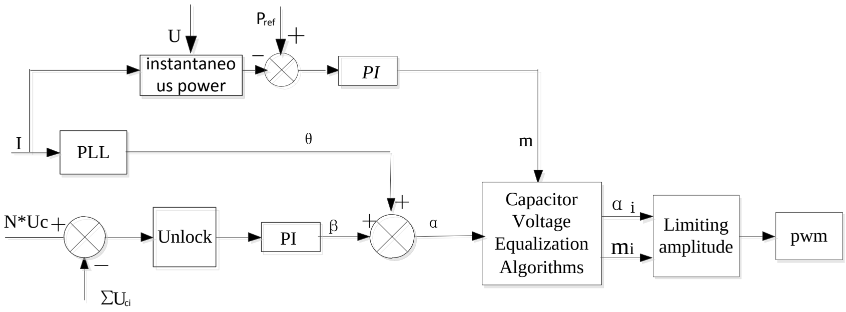

Figure 2. The general block diagram of control.

Figure 2 shows the instantaneous active power calculated by collecting the voltage and current values of the line, and the instantaneous active power is compared with the reference power value P_{ref}, and the reference modulation ratio m is generated by PI control. The difference between the total capacitance of the module and the reference value of the capacitor voltage is obtained by the PI link to obtain the first-order DC voltage regulation angle β. At this time, the overall energy of the H-bridge cascade is balanced, thereby avoiding the overall overcharge. The two-stage voltage regulation finally obtains the modulation ratio m_i and the firing angle α_i of each sub-module, ensuring that a single sub-module does not overcharge and achieve voltage equalization. Then the CPS-SPWM modulation strategy is applied to obtain the trigger pulse of each module of the H-bridge level, and the IGBT is controlled to be turned on and off, and the corresponding output voltage is compensated.

3.2. Dual redundant control system architecture

The figure 3 show the control system structure of SSSC. The control system adopt the way of separate configuration, with high-speed fiber-optic communication between the two to exchange information. In order to improving the reliability of control system, each set of control is equipped with a separate acquisition chassis, and the control system has adopted two sets of redundant configuration, control (A) and control (B) is master-slave redundant configuration, namely only the master control system is in working statement at any time, the slave control system is in stand-by statement. Once the main control system fails, the "master-slave" switching is immediately performed: “master” change to “slave”, “slave” change to “master”. In the time of “master-slave” switching does not affect the normal operation of the converter.

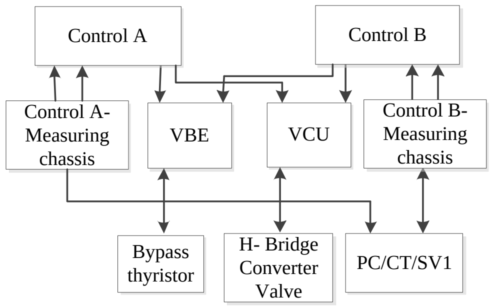

Figure 3. The system structure of SSSC’s control system.

So the SSSC’s control system consists of control A, control B, value-controlled (VBC), value-based electronics (VBE).

3.3. Control system design

Based on the H-bridge cascade topology, SSSC adopts two-stage DC voltage regulator three- stage hierarchical control strategy. The SSSC control system is divided into three levels: system level, device level and valve level. The three layers of control are coordinated to achieve specific compensation effects. The control arithmetic in SSSC project is realized as follows: system level control and device level control are implemented in the DSP TMS320C665x of the core CPU board in the control chassis. The valve level control is realized by the DSP TMS320C665x and FPGA in the core CPU board of the valve control VCU chassis. As shown in Figure 4.

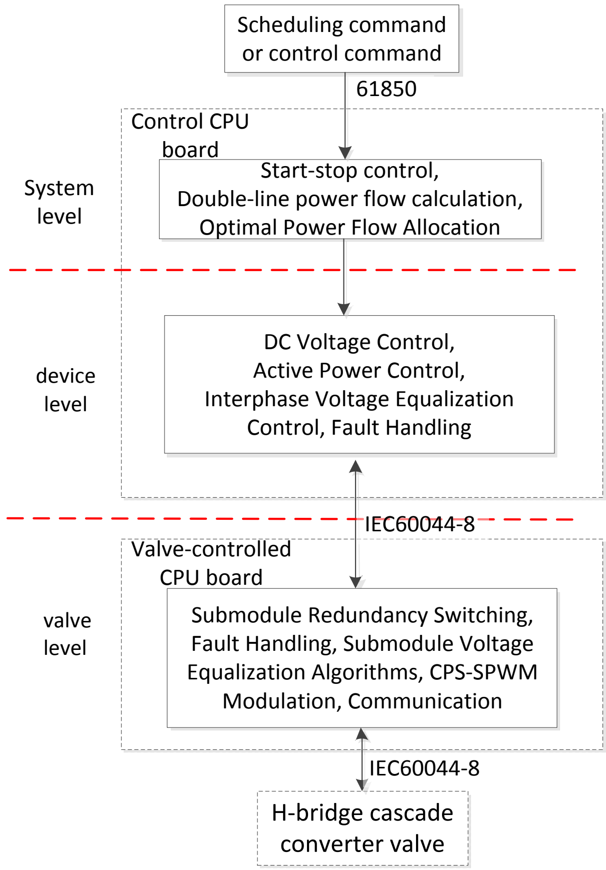

Figure 4. Schematic diagram of overall control scheme

In order to ensure the reliable operation of the control system and the implementation of the algorithm, the phase-to-phase voltage equalization algorithm is implemented in the main control program, and the sub-module voltage equalization algorithm is implemented in the valve control program.

The SSSC device receives control commands and scheduling commands from the remote dispatch center through the monitoring background and communication channel of the Shigezhuang substation. The monitoring background is connected to the system level through fiber optics, using the 61850 communication protocol. System-level control mainly includes equipment start-stop control, operation mode selection, two-wire power flow calculation, and power flow optimization distribution and other functions. According to the requirement of adjusting power flow or damping the subsynchronous oscillation, the power flow control target is proposed for the device, and the system level control obtains the final active power command Pref according to the control target, thereby realizing the optimal operation of the distribution network. Pref is the active command of the device level controller, and this active command cannot exceed the power limit of the line.

The device level control receives the system level control command Pref, completes the constant DC voltage control and the fixed active power control, respectively control the DC capacitor voltage and the output active power. At the same time, it completes the first-level DC voltage stabilization algorithm. The device-level control also carries out on-line fault monitoring.

The device level and valve level are connected by optical fiber and communicated by IEC60044-8 protocol. Valve level control mainly achieves three functions, one is sub-module voltage equalization control, the other is sub-module redundancy switching, and the third is CPS-SPWM modulation.

The final modulation wave of each sub-module is the result of three-phase addition of device-level algorithm, phase-to-phase voltage equalization algorithm and sub-module voltage equalization algorithm. Then, according to the CPS-SPWM modulation method, the trigger pulse of each sub-module is generated and sent to the sub-module of the valve.

4. Control system function test

4.1. The design of RTDS system

In this paper, RTDS real-time digital simulation system and SSSC control equipment are used to form a closed-loop simulation system. RTDS real-time simulation system used to simulate the primary equipment, such as AC Equivalent system, transformer, converter value, switch etc, the parameters are shown in Table 1 and Table 2. The SSSC's control system, which was tested, consists of control A, control B, value-controlled VBC, value-based electronics (VBE), background program of monitoring. SSSC's control system connect with digital real-time simulation system by the screen of interfaces(DIDO signal, analog and cables), and form a close-loop test system.

Table 1. The main parameters of Series transformer

Reference name	unit	value
capacity	MVA	30
ratio	1	10.2/22.7
Uk%	%	15

Table 2. The main parameters of H-bridge

Reference name	unit	value
Rated current	A	760
Rated voltage	k（phase）	11.4
Module number	\	9

The SSSC control system adopts a self-developed new platform. The core CPU board adopts the DSP + FPGA dual-chip architecture. The DSP adopts the TMS320C665x series chip, which is based on TI's KeyStone multi-core architecture, which can run at a core speed of up to 1.25 GHz. The FPGA uses the XILINX Kintex-7 series chip.

The connection between DSP and FPGA use the method, which is a data interaction between a multichannel low-speed port and a single-channel high-speed port, figure 5 show that, this realize the data interaction between several low-speed channels and a single high-speed channel, among them high-speed serial port is used SRIO protocol, low-speed channel consist of serial port, the difference interface in backboard, light port for input and output.

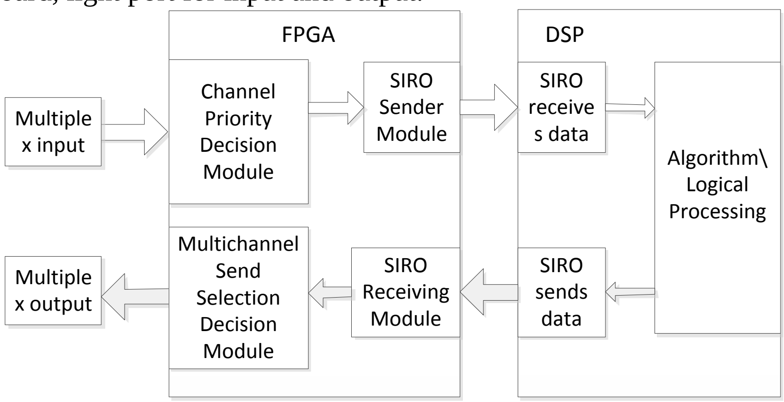

Figure 5. data interaction between multichannel low-speed port and single-channel high-speed port.

The FPGA chip is used to realize the link of data communication in bottom board, including multi-channel data acquisition and transmission, the fusion of the low-speed channels to the single-channel high-speed transmission, and the single-channel data classification and analysis to the different channels. The DSP chip is used to realize data processing and control algorithm on board, by high-speed serial port from FPGA obtain necessary data, complete data analysis and calculation in real-time, then send the calculation result to the FPGA by high-speed serial port, realize the Real-time communication with monitoring background and VBC.

By adopting advanced chips and efficient communication methods, the new platform can shorten the control cycle and reduce the delay in communication. The multi-channel to single-channel design is more compatible and portable, and can be reused and reduced the internal complex logic timing control, and increases system reliability. It provide the support in hardware for successful development of SSSC.

4.2. Self-excited starting test

Based on the two-stage DC voltage regulation strategy, a self-excited startup scheme suitable for SSSC devices is designed.

(1) Check if the system has access conditions for SSSC. That is, the line current is in a normal state and is greater than the starting value, and each device can operate normally.

(2) When the condition (1) is satisfied, close SSSC's the valve outlet side breaker QF2 and cut off the AC breaker QF1, At this time, the converter valve is in the locked state, At this time, the converter valve is in the locked state. Because there is a difference between the power supply amplitude and the phase angle at both ends of the SSSC device, the current flows through the parallel thyristor in both side of sub-module, converter value controller obtain the power by current CT.

(3) After the converter valve controller obtain the power successfully and stabilizes, the valve control returns the “control device allows input” to the main control, then the main controller unlocks the inverter and enters the zero voltage state, which is control upper bridge arm connecting and under bridge arm disconnecting, the DC side capacitor voltage is stabilized at a small voltage value, and the SSSC outlet voltage is a voltage drop of the transformer leakage reactance.

(4) Dc voltage operating, the DC side capacitor voltage is charged following the control curve until the capacitor voltage reach the rated reference value. In this process, when DC voltage reaches 600V, converter value is switched from CT to dc voltage.

(5) Power flow control operating, SSSC's operating module work in regulation statement.

(6) SSSC power flow control input, select SSSC operation mode to enter regulation operation.

The figure 6 show the wave of starting process:

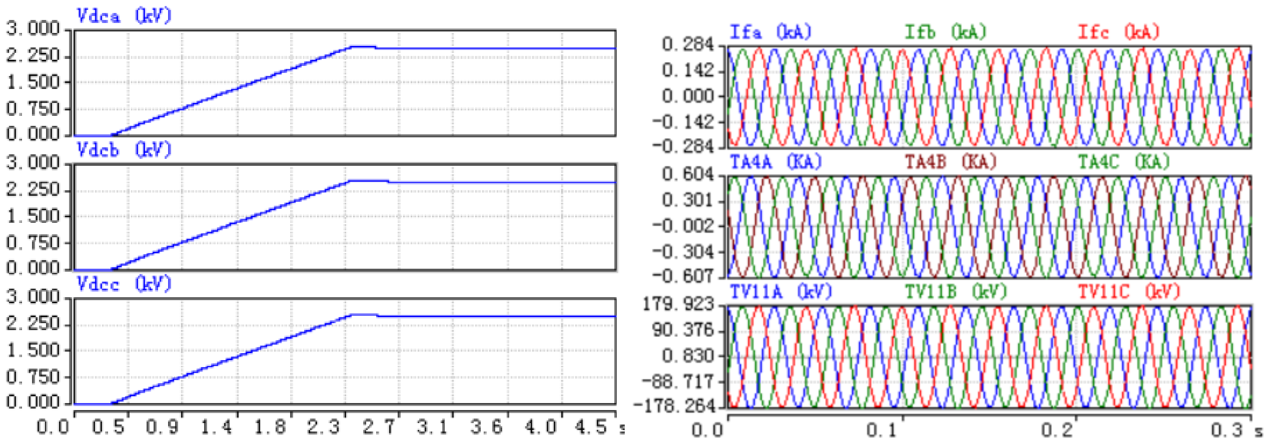

(a)the wave of dc voltage (b)the wave of current in bridge arm, line voltage and current

Figure 6. The wave of starting process.

Figure (a) is the wave of dc voltage of each sub-module, after equipment is started, the capacitor is charged according to the slope set in the program. Figure (b) is the waveform of the bridge arm current and line voltage and current. The experimental results show that during the startup process, the

IOP Conf. Series: Earth and Environmental Science **431** (2020) 012046 doi:10.1088/1755-1315/431/1/012046

capacitance voltage of each sub-module rises to the rated 2.5kV with a set slope, and the bridge arm current and line voltage and current have no impact. After reaching stability, the capacitor voltage of each module fluctuates around 2.5kV, and the fluctuation range does not exceed 0.1kV.

4.3. Capacitor voltage equalization algorithms test

In order to verify the correctness of the capacitor voltage equalization algorithm, the RTDS model parameters are modified. According to the technical parameters of capacitors, the capacitance error does not exceed 5%. The capacitance of the first four modules of phase A is set to 4200uF, the capacitance value of phase B is set to 4000uF, and that of the last four modules of phase C is set to 3800 uF. The experimental waveform of capacitor voltage equalization is shown in Figure 7.

The experimental results show that when there are differences in capacitance both phases-to-phases and each sub-module, the maximum difference of capacitance voltage between each sub-module is 0.1% in steady state, and the three-phase voltage of the network side of series transformer maintains balance, which meets the design requirements. The correctness and validity of the capacitor voltage equalization algorithm are verified.

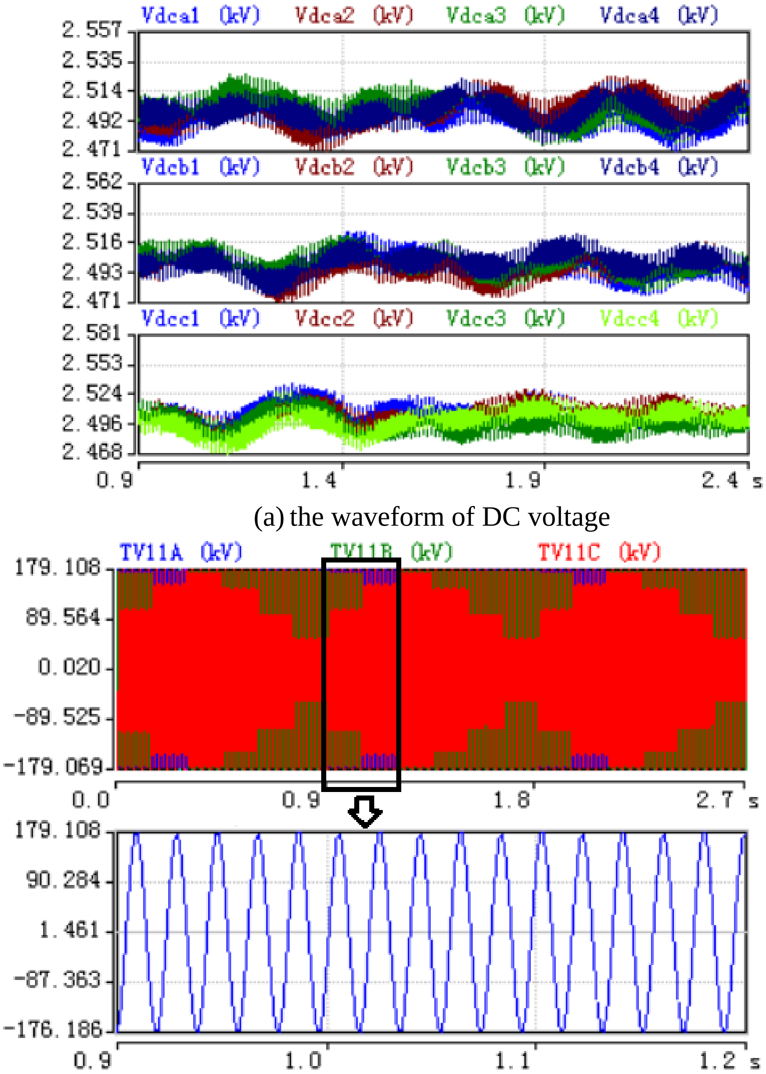

(a) the waveform of DC voltage

(b) the waveform of transformer network side voltage

Figure 7. Waveform of Capacitor Voltage Equalization Algorithm.

4.4. Dynamic performance test

Figure 8 is the waveform of power step test. In the experiment, the active power instruction of the line jumps from 170 MW to 270 MW, and the change

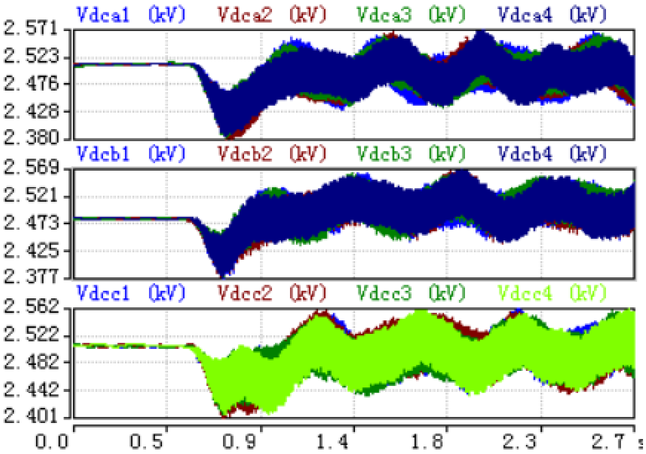

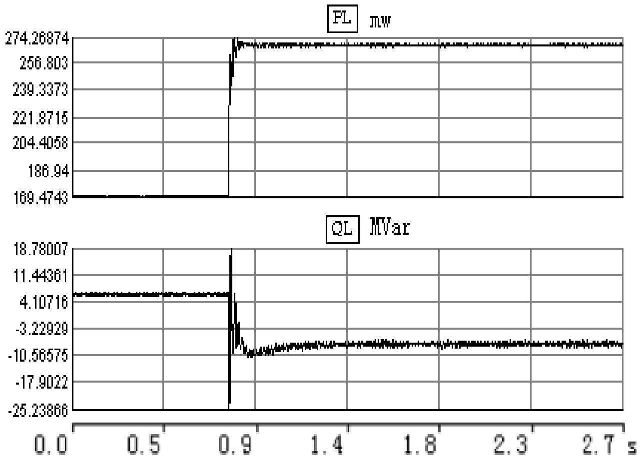

rate of the power instruction is 1 p.u. / 1 point.

(a)the waveform of DC voltage (b)Waveform of Active and Reactive Power Flow

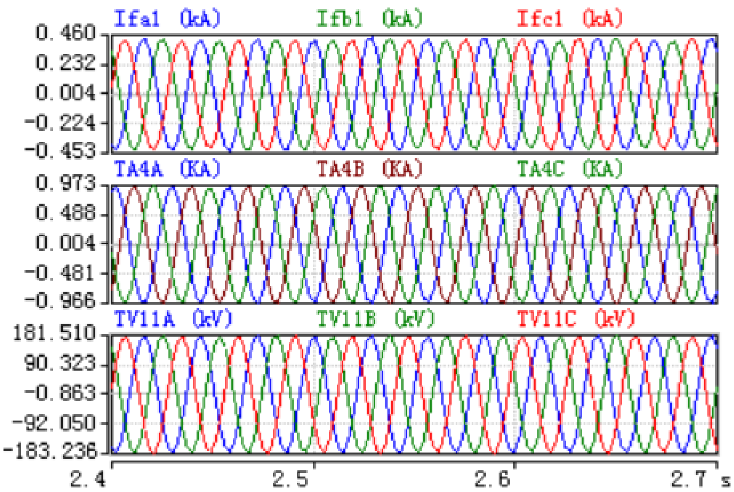

(c)the waveform of transformer network side voltage

Figure 8. Power step (170-270MW) simulation waveform.

Dynamic experimental results show that in the process of the power step, the active power of the line is stabilized in the power flow instruction, the capacitor voltage of the sub-module is stabilized in the rated voltage, the bridge arm current, system current and voltage have no impact, and the system runs normally. It proves that the fast response control method has good instantaneous characteristics and can satisfy the fast and stable response characteristics of H-bridge cascade SSSC as reactive power compensation device to power flow regulation, thus verifying the correctness of the control system and its algorithm.

5. Conclusion

(1) The self-developed control platform uses advanced chips and efficient communication mode, which improves the calculation speed, shortens the control cycle, reduces the communication delay, and can meet the long-term reliable and stable operation of the system. It provides hardware support for the successful development of the SSSC control system.

(2) The dual redundancy mechanism SSSC control system developed in this paper increases the reliability of the device. The application of two-stage DC voltage stabilization algorithm and fast

response control method can realize smooth start-up and exit of SSSC device, and adjust the power flow flexibly in real time according to the demand of power flow adjustment or damping of sub-synchronous oscillation. The practicability and reliability of the designed SSSC control system are further verified.

In a word, the development of Tianjin SSSC control system and the successful operation of the device can provide reference for the follow-up project of static synchronous series compensator and even FACTS project in China.

Science and Technology Project: Research on Real-time Communication Technology for Localization of Power Electronic Device Control and Protection System

6. References

[1] ZHOU Junyu. Review of the applications of static synchronous series compensator in powersystem[J]. *Electrotechnical Application*. 2006, 25 (4):51-54,118(in Chinese).

[2] HE Da-yu. FACTS technology and new progress in the development of its controllers[J]. *Automation of Electric Power Systems*, 1997, 21(2): 1-6.

[3] Javeed Kittur,Saikumar H. Y, Sharath Raj S. Y. Comparative analysis of robust PSS and robust supplementary modulation controller for SSSC [J]. *Biennial International Conference on PESTSE*, 2016,16(8):4673-6658.

[4] F. J. Chivite-Zabalza,P. Izurza,G. . Calvo, M. A. Rodriguez. Modelling and control of a Series Static Synchronous Compensator using low-frequency, fixed-modulation index techniques [J]. *IEEE Power Electronics,Machines and Drives*,2014,17(2):1-6.

[5] Wei Wenhui,Song Qiang,Teng Letian,et al. Research on anti-fault dynamic control of static synchronous compensator using cascade multilevel inverters[J]. *Proceedings of the CSEE*, 2005,25(4):19-24(in Chinese).

[6] Zhao Jianjun, Guo Jianbo, Zhou Xiaoxin. The steady state performance analysis and mathematical model of static synchronous series compensator[J]. *Electric Powe,*2005,38 (10):11-14.

[7] Han, B.,Baek,S.,Kim,H.,Karady,G.Dynamic characteristic analysis of SSSC based on multibridge inverter. *IEEE Transactions on Power Delivery*,2002,17(2):623-629.

[8] Yusuke Fukuta, Giri venkatataramanan. DC bus ripple minimization in cascaded H-dridge multilevel converters under staircase modulation.*37th IAS Annual Meeting*, 2002, 3:1988-1993.

[9] Fang Zheng Peng, McKeever J. w. ,Adms D. J..A power line conditioner using cascade multilevel invertes for distribution systems. *IEEE Transactions on Industry Applications*, 1998, 34(6):1293-1298.

[10] Y. Wang, Y. Chai,J. Tang,X. Yuan and C. Xia,'' DC voltage control strategy of chain star STATCOM with second — order harmonic suppression,'' *in lET Power Electronics*,2016,14(9):2645-2653.

[11] ZHAO Yang. Study on static synchronous series compensatorcontrol strategy and subsynchrnous resonance mitigation[D].*Beijing, China: North China Electric Power University*, 2009.

[12] LU Zhengang, SONG Jieying, SONG Fangfang ,et al. Main parameter design and control technology of cascaded H-bridge SSSC[J]. *Smart Grid*,2017,**5**(6):536-543.

The study of intelligent transport systems management of convoy of unmanned vehicles with a lead vehicle with the purpose of increase of efficiency of cargo transportation

D. Endachev[1], A. Kolbasov[2*] and K. Karpukhin[3]

1 Deputy CEO, NAMI Russian State Scientific Research Centre, Moscow, Russia
2 Head of research devision, NAMI Russian State Scientific Research Centre, Moscow, Russia
3 Project Director, NAMI Russian State Scientific Research Centre, Moscow, Russia
*Email: Aleksey.kolbasov@nami.ru

Abstract. This material describes the development of an intelligent transport system for controlling the movement of a column of unmanned vehicles with a leading pilot vehicle in order to increase the efficiency and safety of freight and passenger transportation in remote regions of the North of Russia, as well as in the Arctic and Antarctic. The obtained scientific results allow us to move on to the creation of new types of freight and passenger vehicles that can move unmanned modes over long distances, but at the same time, the possibility of direct human intervention remains. The introduction of this type of vehicles will improve the efficiency of freight and passenger transportation, reduce fuel consumption by predicting the traffic situation and increase the safety of transportation on public roads. The materials describe the circuit diagram of the components of the slave and leading intelligent vehicle, give mathematical models of some control systems and describe the tests that confirmed the operability of this type of vehicle. Tests have shown the adequacy of mathematical models and the complete autonomy of driven vehicles that follow the lead.

1. Introduction

The development of unmanned freight vehicles (UFV) among the world's leading automakers is considered one of the most promising areas. The leaders in this area, actively competing among themselves, are the American companies Waymo (a division of Google Corporation, Figure 1) and Otto (a division of Uber Technologies, Figure 1) formed in 2016. Other leading UFV developers are Volvo Trucks (Sweden) and Daimler (Germany).

A characteristic feature of the developments carried out by the aforementioned companies is the re-equipment of the production car in the UFV while maintaining the ability to control it with a driver, in connection with which the UFV retains the driver's cab and the controls of the base chassis [1-2].

It should be noted that the Otto division was organized with the aim of developing equipment and software for adapting operated trucks to autonomous control, and, for example, the well-known UFV Oshkosh TerraMax model, introduced in 2004, is an example of the application of the universal technology of unmanned control TerraMax UGV on standard tactical army car. Automakers such as Daimler and Volvo are developing in their UFV prototypes (Figure 1) automatic control technologies that have been tested on production vehicles as Advanced Driver Assistance Systems (ADAS). In November 2017, the world's leading manufacturer of electric vehicles Tesla Inc (USA) introduced a prototype of the electric cargo vehicle Tesla Semi (Figure 1) with a carrying capacity of 36 tons, equipped with an autopilot system. Tesla Semi is an original chassis with a single driver's cab, equipped with a traction battery pack and four electric motors, each of which drives one of the wheels of the rear bogie. Traction batteries provide a range of 500 miles (804 km). The autopilot system includes a standard set of functions for driver assistance systems (ADAS), including lane keeping, and also provides the ability to change lanes. Thus, the presented prototype is not fully UFV, however, according to the development company, by 2020 it is expected to mass production of a fully autonomous freight electric vehicle [3].

Figure 1. Top: Waymo Track, Otto, Volvo Trucks; Button: Daimler, Oshkosh TerraMax, Tesla Semi**.**

It is believed that the use of UFV in the column is the most effective, in which it is expected to achieve the following results:

- improving road safety, since the negative impact of the human factor, which according to statistics is the cause of almost 80% of road accidents, is minimized;
- achieving savings of up to 20% of fuel;
- increase in transportation productivity by 1.3–1.4 times;
- ensuring comfortable working conditions for drivers in driven trucks;
- minimization of harmful effects on the environment;
- reducing the need to maintain a large staff of professional drivers with high pay;
- the ability to integrate unmanned transport systems into the technological process of enterprises, primarily large transport and logistics centers, ports, etc., ensuring their continuous round-the-clock operation.

2. Prerequisites and means to solve the problem.

The specific climatic conditions of most of the territory of Russia [4], the state of the road infrastructure, as well as the current legislation, do not allow us to expect the appearance of UFV on public roads in the near future. About 70% of the territory of the Russian Federation belongs to the regions of the Far North, and more than 20% is located beyond the Arctic Circle [5]. Areas of the Far North, including the Arctic shelf, are rich in minerals, the development of which is not sufficiently effective, including due to the poor development of the transport system. Road transport is most common in the absence or limited ability to use a network of railways, airfields, waterways. The increase in road transport requires a wider use of all-terrain vehicles and is a prerequisite for the development of the northern regions. Given these factors, it can be assumed that for Russia, the development of off-road unmanned vehicles should also be the main direction in the field of UFV. It is in the regions of the Far North that the commissioning of unmanned ground transportation systems (primarily transport columns) should provide increased efficiency and safety of all-season cargo transportation between settlements, strongholds of enterprises of the fuel and energy complex, etc.
The road climatic conditions of the Arctic zone of the Russian Federation are characterized by the following features [6-7]:

• abnormally low temperatures (up to -60 °C), which complicate the starting of engines and limit the normal functioning of the technical means of autopilots;
• severe off-road driving conditions that allow the vehicle to be used only in winter conditions;
• reference-free terrain, which impedes visual determination of the location of the pilot vehicle along the route;
• snow drifts that do not allow recognition of road markings and impede the functioning of vision devices;
• constancy of limited visibility in polar night conditions;
• unpredictable influence of the geomagnetic situation and the state of the troposphere and ionosphere of the Earth at polar latitudes on the conditions for uninterrupted reception of satellite navigation signals.

3. Description of the column of unmanned vehicles

Convoy of unmanned freight vehicles (CUFV) (with a leading manned vehicle) can have any configuration in accordance with its purpose and may include a different number of unmanned links, which, in turn, can be different types of cargo vehicles (Figure 2).

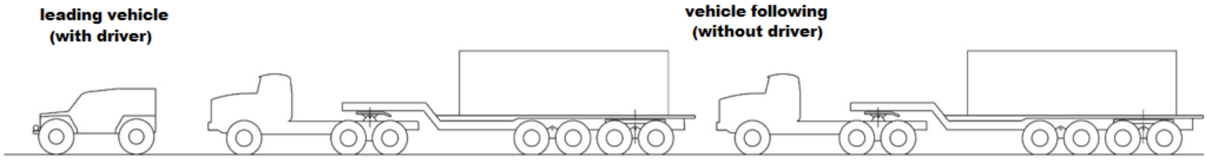

Figure 2. Diagram of a column of unmanned trucks with a leading vehicle.

The motion control system of the leading manned vehicle CUFV receives information about the location and trajectory of movement of the CUFV from wheel speed sensors, the GPS navigation module CH-5707 and strapdown inertial navigation system. Input data from the listed devices are processed in the microprocessor unit MCS. After that, the navigation problem is solved, the current vector of control actions on the UFV is determined, and road signs are identified according to the data of the navigation system[8]. The received data is transmitted to the command and navigation terminal for deciding on the management of the column.

Using the communication module, the command terminal conducts a constant exchange of telemetry information with UFV, the next in the column and generates directive commands for UFV.

Special software for the vehicle control system has been developed for UFV:
• stabilization of UFV on the trajectory set by the leading pilot vehicle;
• stabilization of speed and distance UFV in the column;
• automatic braking of the UFV in the convoy before obstacles;
• control of directional stability and prevention of capsizing of UFV in a column;
• monitoring tire pressure in the UFV column;
• emergency stop UFV in the convoy.

Auxiliary algorithms do the job of logging the system, exchanging data between the blocks that make up the system, and its functional units.

In all vehicles, algorithms for working with GPS / GLONASS receivers and strapdown inertial navigation system modules are implemented. The MCS of the slave CUFV receives information from the following telemetry sources:
• from the host UFV;
• from wheel speed sensors;
• from the navigation module satellite navigation system;
• from means of technical vision and video processing unit.

According to the results of the work, the following MCS algorithms were developed:
• stabilization of UFV on the trajectory set by the leading pilot vehicle;
• stabilization of speed and distance UFV in the column;
• automatic braking of the UFV in the column before the obstacle;
• control of directional stability and prevention of capsizing of UFV in a column;

• monitoring tire pressure in the UFV column;
• emergency stop UFV in the convoy.

Auxiliary algorithms do the job of logging the system, exchanging data between the blocks that make up the system, and its functional units. So, according to data from navigation systems and processed video information, the UFV stabilization algorithm on the trajectory works. According to data from technical vision and wheel speed sensors, algorithms for stabilizing the speed and distances of UFV, automatic braking in front of an obstacle, and emergency stop in the column work [9].

4. Description of unmanned vehicle convoy control algorithms

Various mathematical models and algorithms have been developed for the control and interaction of the links of an intelligent convoy of freight vehicles:

• a mathematical model of the longitudinal motion of the center of mass of the driven UFV;
• mathematical model of brake deceleration;
• a mathematical model for controlling the course of the followers of the UFV;
• intelligent MCS control algorithm;
• traction control algorithm;
• brake control algorithm;
• course management algorithm;
• an algorithm for the interaction of vehicles in a convoy.

The practical use of these mathematical models involves the identification of their parameters using experimental data and data on the technical characteristics of vehicles. Settings for control algorithms should also be determined by the results of test tests of the control system in various operating modes.
Mathematical models of the longitudinal motion of the center of mass, an algorithm for controlling brake mechanisms, as well as an algorithm for the interaction of intelligent vehicles moving in a column are described earlier [10]
Below are models of deceleration retardation, course control models driven by the UFV course control algorithm.

4.1. Description of the mathematical model of brake deceleration

In the mathematical model, the brake deceleration equation is described as:

$$a_T(U_3) = \begin{cases} m_0^{-1}\sum_{i=1}^{4} k_{3i}U_3\,, \text{если } 0 \le U_3 \le U_{3\text{гр}}; \\ m_0^{-1}\sum_{i=1}^{4} k_{3i}U_{3\text{гр}}\,, \text{если } U_3 > U_{3\text{гр}}, \end{cases} \quad (1$$

$k_{3i} = 10^5 S_{Ti}R_{Ti}k_{sTi}R_{di}^{-1}P_{Tmax}$ – brake gain of the i-th wheel;

S_{Ti} – total area of brake cylinders of the i-th wheel, m^2;

R_{Ti} – radius of the brake disc (drum) of the i-th wheel, m;
R_{di} – dynamic radius of the i-th wheel, m;
k_{sTi} – coefficient of sliding friction of the i-th brake disc (drum);
P_{Tmax} – maximum pressure in the hydraulic system, bar;
m_0 – vechicle mass, kg;
$U_{3\text{гр}}$ – the boundary value of the control action on the brake system.

The adopted numbering of the wheels corresponds to the remoteness of the wheel from the driver's seat in the car with a left-side steering wheel layout. So, the front left wheel i = 1, the front right i = 2, the rear left i = 3 and the rear right i = 4.
Brake force$F_{Ti}, 1 \le i \le 4$ in the contact spot, limited by the sliding friction force F_{TSi}, are defined as $F_{Ti} = k_{3i}U_3$.
The boundary values of the control actions $U_{3\text{гр}i}$ are determined from the conditions of equal braking forces F_{Ti} and the maximum values of the sliding friction forces F_{TSi} taking into account the redistribution of weight on the wheels of the front and rear axles during braking and on the wheels of the left and right sides when cornering for a car with a track gauge a and wheel base b:

IOP Conf. Series: Earth and Environmental Science **431** (2020) 012052 doi:10.1088/1755-1315/431/1/012052

$$\begin{cases} F_{Ti} = k_{3i} U_{3\text{гр}i}; \\ F_{TSi} = F_{Ni} k_{Si}^*, \end{cases}$$

At $\alpha_T = 0$:

$$F_{Ni} = m_i g + 0{,}5 C_{Ti} b^{-1} \sum_{i=1}^{4} R_{di} k_{3i} U_{3\text{грi}} + 0{,}5 C_{ci} m_0 b^{-1} a^{-1} h_m V_m^2 \Psi_c,$$

where $C_{Ti} = \begin{cases} 1, if\ 1 \le i \le 2; \\ -1, if\ 3 \le i \le 4; \end{cases}$

$\mathrm{C}_{ci} = \begin{cases} 1, if\ i = 1, 3; \\ -1, if\ i = 2, 4; \end{cases}$

m_i – mass attributable to i-th wheel;
Ψ_c – steering angle;
k_{si}^* – the maximum value of the sliding friction coefficient of the i-th wheel.
The boundary value of the total brake control $U_{3\text{гр}}$ is defined as the minimum of 4 and 1:

$$U_{3\text{гр}} = \min\{U_{3\text{гр}1}, U_{3\text{гр}2}, U_{3\text{гр}3}, U_{3\text{гр}4}, 1\}, \text{where} \tag{2}$$

$$U_{3\text{грi}} = [m_i g + 0{,}5 C_{ci} m_0 b^{-1} a^{-1} h_m V_m^2 \Psi_c] k_{Si}^* \cdot \left[k_{3i} - 0{,}5 C_{Ti} b^{-1} k_{Si}^* \sum_{i=1}^{4} R_{di} k_{3i} \right]^{-1}.$$

In a correctly designed brake system $U_{3\text{гр}1} = U_{3\text{гр}3}$ at
$a_T = a_{Tmax} \approx k_S^* \cdot g$ and the ratio of $\alpha = k_{33} \cdot k_{31}^{-1}$ equally:
$\alpha = [m_3 \cdot m_0^{-1} g - 0{,}5 b^{-1} \cdot R_d a_T] \cdot [m_1 \cdot m_0^{-1} g + 0{,}5 b^{-1} \cdot R_d a_T]^{-1}$.

In this case $\sum_{i=1}^{4} k_{3i} = 2k_{31}(1+\alpha)$ and coefficient brake booster $k_{31} = k_{32}$ и $k_{33} = k_{34}$ defined as:

$$\begin{cases} k_{31} = 0{,}5(1+\alpha)^{-1} a_{Tmax} m_0; \\ k_{33} = \alpha \cdot k_{31}, where \end{cases}$$

$a_{Tmax} = 0.5 \cdot V_m^2 \cdot \Delta L_S^{-1}$;

ΔL_S – stopping distance determined from experimental data of braking from speed V_m.
Maximum brake deceleration value a_{Tmax} determined from the equation:

$$a_{Tmax} = m_0^{-1} \sum_{i=1}^{4} k_{3i} U_{3\text{гр}}.$$

4.2 Description of the mathematical model of the slave course control UFV

To solve the problem of controlling the course of the driven UFV, according to the data received from the wheel speed sensors, calculation of the heading angle estimate$\dot{\Psi}_m$, is required, this value in general form is obtained from the formula:

$$\dot{\Psi}_m = \omega_m + \Delta\omega_m, \tag{3}$$

Where ω_m – angular frequency of rotation of the center of mass at the bend, rad/sec;
$\Delta\omega_m$ – additional component of the angular frequency of rotation of the center of mass during drifts and drifts of wheels, rad/sec,

Formula (3) is a mathematical model of the dynamics of the heading angle.

The angular frequency of rotation of the center of mass at the bend is identified by a virtual sensor of the parameters of the center of mass as:

$\omega_m = V_m R_m^{-1} = b^{-1} V_m \Psi_C$,

Where R_m – bend radius, b – car wheelbase, V_m – longitudinal velocity of the center of mass, m/sec;
Ψ_C – steering angle.

Equation solution we write in the form:

$$\Psi_m(t) = b^{-1} \int_{t_0}^{t} V_m(\tau) \Psi_C(\tau) d\tau + \int_{t_0}^{t} \Delta\omega_m(\tau) d\tau + \Psi_m(t_0). \tag{4}$$

IOP Conf. Series: Earth and Environmental Science **431** (2020) 012052 doi:10.1088/1755-1315/431/1/012052

This solution describes the dynamics of the course angle behavior as a function of the speed and angle of rotation of the steered wheels.

4.3 Development of a course management algorithm.
The mathematical model of the dynamics of the heading angle is described by formula 4. For the formation of the heading control algorithm, we write the formula (4) in a discrete form:

$$\Psi_m(k) = \Psi_m(k-1) + b^{-1}\int_{t_{k-1}}^{t_k} V_m(\tau)\Psi_C(\tau)d\tau + \int_{t_{k-1}}^{t_k} \Delta\,\omega_m(\tau)d\tau$$

To control the steering trapezoid of the car, we consider a computer control scheme for the angle of rotation of the steered wheels Ψ_m (Figure 3):

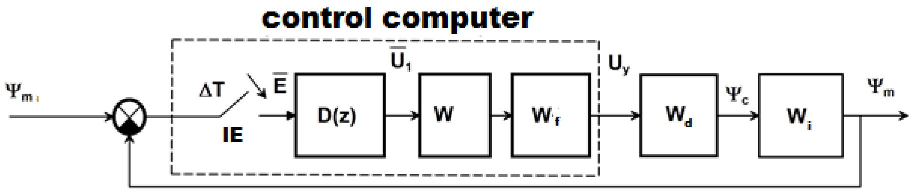

Figure 3 – The scheme of computer control of the angle of rotation of the steered wheels.

The input parameter in the system Ψ_m is set based on the solution of the navigation problem performed by the high-precision navigation system and the estimation of the location error on a given motion path.
The control circuit contains an electric motor for the power steering connected to the reversible electronic keys controlled by a computer. The controller program is implemented on a navigation computer, which receives information about the parameters of movement, speed and angle of rotation of the steered wheels, generates and transfers control actions to the electronic keys with a PWM signal. The computer part of the system contains a pulse element (IE), performing quantization of signals in time with a period ΔT, the transfer function of the controller
$D(z) = k_c k_{full}^{-1}(1-z^{-1})\Delta T^{-1}$, delay element $W(p) = e^{-p\Delta T}$ for the time of data exchange with the navigation computer, latch with transfer function $W_{\text{ф}}(p)$. The continuous part of the system in the form of a reversible electric power steering motor appears to be an integrating link. $W_{\text{д}} = k_0 p^{-1}$ c gain factor k_0, connects the output signal in the form of an angle of rotation Ψ_C with the input signal in the form of a control voltage U_{y}.
The finite-difference equation of the engine in discrete time:

$$\Psi_C(k) = \Psi_C(k-1) + \Delta T k_0 U_{\text{y}}(k-1); \tag{5}$$

The equivalent circuit of a computerized course control system includes an additional link: an integrator of course change $W_{и}$, with a coefficient $W_{и}(p) = b^{-1}V_m/p$. The original system in the continuous part contains two integrators in series and can potentially be prone to undamped oscillations. To give the system an exponential stability, a differential controller with

$$D\ \ (z) = k_c k_{\text{общ}}^{-1}(1-z^{-1})\Delta T^{-1}:$$
$$U_1(k) = [U(k) - U(k-1)]\Delta T^{-1}, \tag{6}$$

where $U(k) = k_c k_{\text{full}}^{-1}(k)E(k)$;
$k_{\text{full}} = b^{-1}V_m(k)\Delta T k_0$;
$E(k) = \Psi_{m\,\text{ЗАД}}(k) - \Delta\Psi_m(k)$;
k_c – custom coefficient.

5. Tests convoy of unmanned vehicles.

Tests of the intellectual convoy of freight vehicles took place in August 2019 at the NITSIAMT FSUE "NAMI" automobile training ground using the following unique scientific facilities: "Scientific-research complex of road structures for testing and fine-tuning of automotive equipment

Avtopolygon" (No. 499886) and "Computer information -measurement system of active safety "INCA-SPORT" "(No. 507727).

During the research tests, a check was carried out for compliance with the functions of the control system to the basic requirements of the technical specifications in terms of special functions: trajectory construction by a leading pilot vehicle:

- stabilization of UFV on the trajectory set by the leading vehicle;
- stabilization of speed and distance of UFV in the column;
- automatic braking of unmanned vehicles in a convoy in front of an obstacle;
- control of directional stability and prevention of capsizing of UFV in a column;
- recognition of road signs by the leading pilot vehicle;
- tire pressure monitoring in the UFV column;
- emergency stop UFV in the column.

Figure 4 – Convoy of unmanned trucks during the test

The construction of the trajectory by the leading pilot vehicle of the UFV column in the column transport control system is carried out according to the integrated navigation system (satellite and wheel) and, in the presence of road markings, according to the data from the video camera. Figure 5 shows the image of the arrival map with the constructed path of the leading pilot vehicle according to the integrated navigation system. Analysis of the arrival map shown in Figure 5 allows us to conclude that when constructing the trajectory by the leading pilot vehicle, the error in constructing the trajectory was less than 0.5 m at a vehicle speed of 30 km/h. The total length of the route was 673 meters. Start and finish points fell.

Tests of the function of stabilizing the speed and distance of the UFV in the convoy were carried out on a straight section of the dynamometer road of the Dmitrov auto test site at a speed of 7 km/h. The distance between the slave UFV and the lead pilot vehicle was measured using a long-range radar mounted in front of the slave UFV. Figure 6 shows the timing diagrams of the test of the stabilization function of the speed and the UFV distances in the column.

Analysis of time charts shows that when driving in the mode of stabilization of speed and distances, the distance between cars during the movement was on average 11-14 meters, and the error of stabilization of speed did not exceed 1 km/h. The distance after joint braking was 2.4 meters.

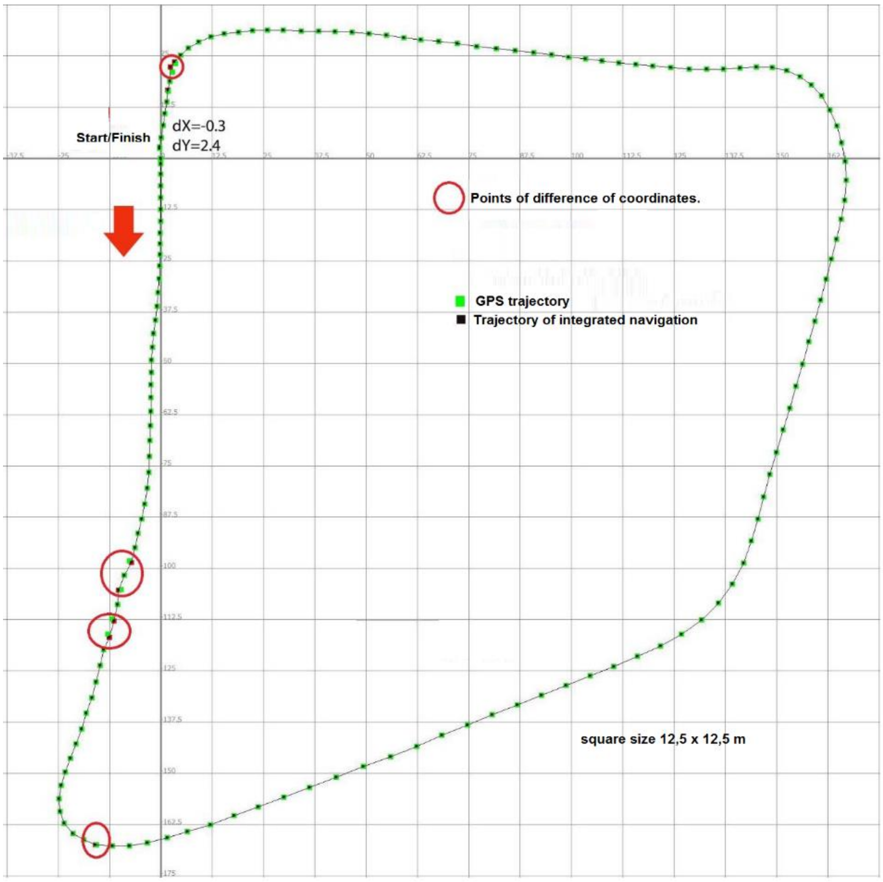

Figure 5 – Test Result: test map of the driving vehicle with indication of deviations from the specified route.

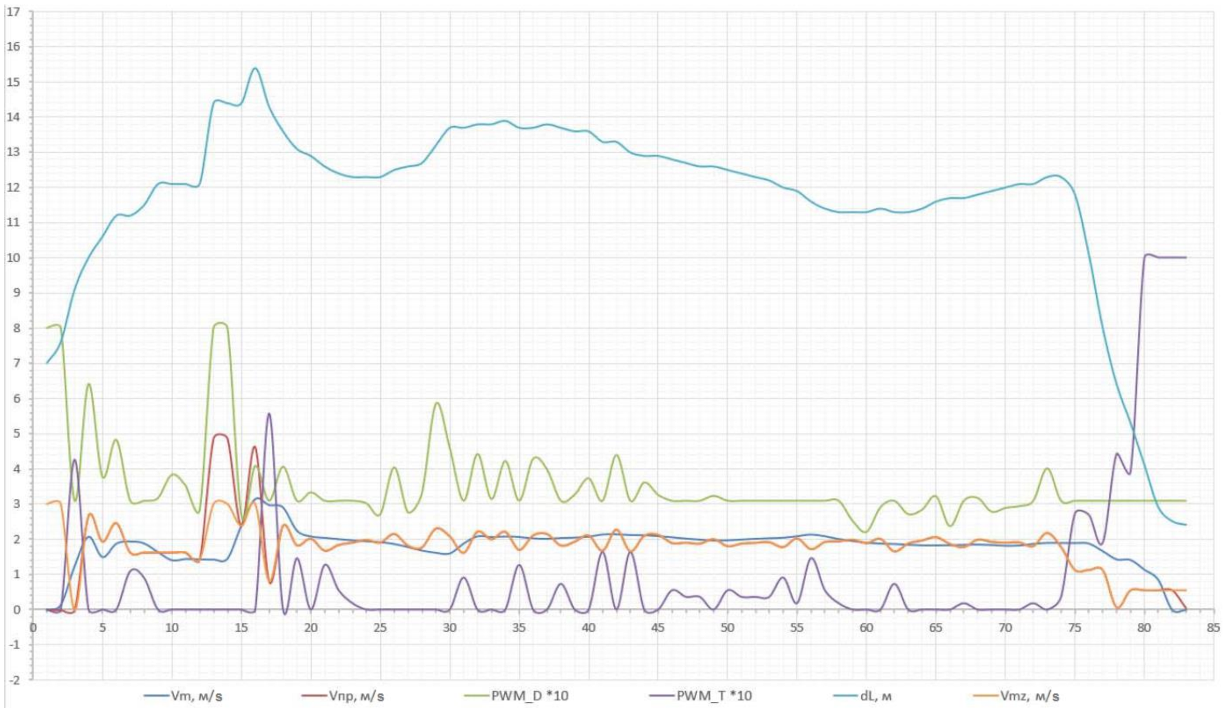

Figure 6 – Timing diagrams of the test of the stabilization function of the speed and distance of unmanned vehicles in the column.

6. Conclusion

The analysis of the results of research tests of the prototype column transport control system of the cars of the leading pilot and driven UFV allows us to conclude that the prototype column transport control system as a whole meets the requirements of the technical specifications.

7. References

[1] Rabbou M. A., El-Rabbany A. Non-linear filtering for precise point positioning GPS/INS integration //The International Archives of Photogrammetry, Remote Sensing and Spatial Information Sciences. – 2014. – T. 40. – №. 2. – p. 127.

[2] Lombacher, J., Hahn, M., Dickmann, J., Wöhler, C. (2017, March). Object classification in radar using ensemble methods. In Microwaves for Intelligent Mobility (ICMIM), 2017 IEEE MTT-S International Conference on (pp. 87-90). IEEE

[3] Erhan D., Szegedy C., Toshev A., and Anguelov D. Scalable Object Detection Using Deep Neural Networks. In Proceedings of the 2014 IEEE Conference on Computer Vision and Pattern Recognition (CVPR 14). IEEE Computer Society, Washington, DC, USA, p. 2155-2162.

[4] Katanaev N.T., Kolbasov A.F., A system of forecasting changes in meteorological factors in order to improve road safety, The "Žurnal AAI" №4, 2016, p. 38-40.

[5] Malhotra N., Charlton, S., Starkey, N. and Masters, R. Driving speed choice: The role of conscious monitoring and control (reinvestment) when driving. Transportation Research Part F Traffic Psychology and Behaviour, Available online 24 June 2017, pp. 1-14.

[6] S. Patil, G. Kahn, M. Laskey, J. Schulman, K. Goldberg, and P. Abbeel. Scaling up gaussian belief space planning through covariance-free trajectory optimization and automatic differentiation. In Intl. Workshop on the Algorithmic Foundations of Robotics, 2014.

[7] Saikin A.M., Buznikov S.E., Karpukhin K.E. The Analysis of Technical Vision Problems Typical for Driverless Vehicles, Research Journal of Pharmaceutical, Biological and Chemical Sciences. 2016. Vol. 7. № 4. p. 2053-2059.

[8] Shadrin S.S., Ivanov A.M., Karpukhin K.E Using Data From Multiplex Networks on Vehicles in Road Tests, in Intelligent Transportation Systems, and in Self-Driving Cars,. Russian Engineering Research. 2016. Vol. 36. № 10. p. 811-814.

[9] Buznikov S.E., Endachev D.V., Karpukhin K.E., Saykin A.M., Terenchenko A.S. Development of Russian driverless electric vehicle, International Journal of Mechanical Engineering and Technology. 2017, Vol. 8, Issue 12, p. 955-965.

[10] Saykin A., Endachev D., Ph.D., Karpukhin K., Kolbasov A. Research of intelligent transport systems management of convoy of unmanned vehicles with the lead pilot vehicle for work in the north of the russian federation in thearctic and Antarctic/ Trans and Motauto World. 2018. № 1. C. 37-40.

[11] Karungaru S., Nakano H., and Fukumi M.. Road Traffic Signs Recognition Using Genetic Algorithms and Neural Networks. International Journal of Machine Learning and Computing, Vol. 3, No. 3, 2013, p. 31

Acknowledgements

This material was prepared based on the results of applied scientific research and experimental developments, which are carried out with the financial support of the Ministry of Education and Science of Russia. The Agreement number is No. 14.625.21.0043. The unique identifier of the project is RFMEFI62517X0043.

Chapter 7:
Electricity and energy

IOP Conf. Series: Earth and Environmental Science **431** (2020) 012055 doi:10.1088/1755-1315/431/1/012055

Day-ahead optimal scheduling of integrated energy system with electric heat pump

Nianchu Zhang[1], Qi Wang[1], Ming Ni[2,3,4], Manli Li[2,3,4] and Zheng Zhang[1]

1 Nanjing Normal University (College of Electrical and Automation Engineering), Nanjing, China
2 NARI Group Corporation (State Grid Electric Power Research Institute), Nanjing, China
3 NARI Technology Co. Ltd., Nanjing, China
4 State Key Laboratory of Smart Grid Protection and Control, Nanjing, China
E-mail: 181802018@stu.njnu.edu.cn

Abstract. The regional integrated energy system is an effective way to realize energy cascade utilization and improve the flexibility and economy of the load side operation. Combine cooling heating and power (CCHP) system is a typical form of integrated energy systems. However, due to heat-load-based operation mode, the peak modulation capacity of CCHP units and the accommodation of renewable energy are limited. This paper explores methods of increasing the flexibility and economy of the system. An optimal scheduling model is proposed for integrated energy systems containing an electric heat pump, considering heating network characteristics. Simulation results show that the electric heat pump can help the system realize heat-and-power decoupling, improve the flexibility of the system and reduce the operating cost of the system.

1. Introduction

In China, the CCHP technology is developing rapidly. As the heating demand and integration of wind power grows, the flexibility and economy of the CCHP system should be focused [1]. The development of the park-level CCHP system is strongly supported by the government. Many integrated energy systems (IES) entities have been built and put into use, such as the demonstration project of CCHP system sitting in the ZOL Software Park Software Plaza. However, CCHP units usually operate in heat-load-based mode so as to give priority to the heating load. The electric power output is forced to be at a high level to follow the heating power output. As a consequence, the range of electric power output is narrowed and the peak modulation capacity of CCHP units is restricted. Therefore, research on improving flexibility and economy of CCHP system is urgently needed to make up for the current shortcomings.

Many scholars have proposed to improve the flexibility and economy of CCHP system by installing electric boilers or heat storage tanks for IES. In [2-3], electric heating boilers and heat storage tanks are used to improve the flexibility of the cogeneration system and promote wind power accommodation. However, the investment cost of the heat storage tanks is too high and the heat storage effect is not quite satisfied. The price of electric boilers is lower, but the heat loss is much larger than that of heat pumps [4].

Some studies have proposed to establish an operational model of CCHP system considering the heat storage characteristics of buildings and heating pipelines. In [5-8], a heat storage model of buildings is established considering the performance of radiators and the consumption of buildings to transfer the heat load to other periods. Although it doesn't require additional investment, its ability of adjusting is limited.

Compared with electric boilers, electric heat pumps (EHP) are much more energy-efficient. Therefore, the application of EHP in CCHP system is promising. At present, the research on the optimal scheduling of the CCHP system containing an electric heat pump is rarely.

This paper is organized as follows. The second section introduces the structure of the CCHP system containing an EHP and establishes the day-ahead optimal scheduling model. In section three, test case of integrated system is presented and the simulation results are analyzed. Section four is the conclusion of the work.

2. Day-ahead optimal scheduling model

2.1. Modeling of coupling units

2.1.1. Gas turbine (GT). The GT mathematical model is shown equation (1).

$$\begin{cases} P_{GT} = V_{HG} \cdot q_{HG} \cdot \eta_{GT} & \eta_{GT}^{s} = Q_{GT}^{s} / P_{GT} \\ Q_{GT}^{s} + Q_{GT}^{w} = V_{HG} \cdot q_{HG} \cdot (1\text{-}\eta_{GT}\text{-}\eta_{GT}^{loss}) & \eta_{GT}^{w} = Q_{GT}^{w} / P_{GT} \end{cases} \tag{1}$$

where P_{GT}, Q_{GT}^{s} and Q_{GT}^{w} represent the electric power output, steam heat power output and hot water heat power output, respectively. V_{HG} and q_{HG} represent the nature gas consumption and the unit calorific value of natural gas, respectively. η_{GT}, η_{GT}^{loss}, η_{GT}^{s} and η_{GT}^{w} represent power generation efficiency, energy loss rate, steam thermoelectric ratio, and hot water thermoelectric ratio, respectively.

2.1.2. Gas boiler (GB). The GB mathematical model is shown in equation (2).

$$\begin{cases} Q_{GB}^{s} + Q_{GB}^{w} = V_{HG} \cdot q_{HG} \cdot \eta_{GB} \\ \eta_{GB}^{s/w} = Q_{GB}^{s} / Q_{GB}^{w} \end{cases} \tag{2}$$

where Q_{GB}^{s} is the steam heat power output, Q_{GB}^{s} is the hot water output, η_{GB} is the steam heat power generation efficiency, and $\eta_{GB}^{s/w}$ is the steam-water ratio.

2.1.3 Heat recovery boiler (HRB). The HRB mathematical model is shown in equation (3).

$$Q_{WH}^{out} = Q_{WH}^{in} \cdot \eta_{WH} \tag{3}$$

where Q_{WH}^{in} and Q_{WH}^{out} represent the steam heat power input and output, respectively, $\eta_{WH}$is the energy conversion coefficient.

2.1.4. Electric refrigerator (ER). The ER mathematical model is shown in equation (4).

$$C_{EC} = P_{EC} \cdot COP_{EC} \tag{4}$$

where P_{EC} and C_{EC} represent the electric power input and the cooling power output, $COP_{EC}$is the cooling coefficient.

2.1.5. Steam operated absorption refrigerator (SOAR). A steam operated absorption refrigerator is used in the integrated system, and its mathematical model is shown in equation (5).

$$C_{CH/C}^{out} = Q_{CH/C}^{in} \cdot COP_{CH/C} \tag{5}$$

where $Q_{CH/C}^{in}$ and $Q_{CH/C}^{out}$ represent the heating power input and the cooling power output, $COP_{CH/C}$ is the cooling coefficient.

2.1.6. Electric heat pump (EHP).

$$C_{HP}^{out} = P_{HP} \cdot COP_{HP} \tag{6}$$

where C_{HP}^{out} and P_{HP} represent the electric power input and the heating power output, COP_{HP} is the heating coefficient.

2.2. Modeling of EH

The EH connects the energy input and output through the coupling matrix, which embodies the energy coupling relationship between the subsystems. The output matrix, the coupling matrix and the input matrix respectively correspond to the energy consuming unit, the coupling unit and the energy supply unit mentioned above. Based on the modeling of each unit equipment, this paper uses the concept of EH to model the IES [9]. The common mathematical expression of EH is shown in the figure 1.

$$\underset{\text{Output matrix}}{\underbrace{\begin{bmatrix} L_\alpha \\ L_\beta \\ \cdots \\ L_\omega \end{bmatrix}}_{L}} = \underset{\text{Coupling matrix}}{\underbrace{\begin{bmatrix} C_{\alpha\alpha} & C_{\beta\alpha} & \cdots & C_{\omega\alpha} \\ C_{\alpha\beta} & C_{\beta\beta} & \cdots & C_{\omega\beta} \\ \vdots & \vdots & \ddots & \vdots \\ C_{\omega\alpha} & C_{\omega\beta} & \cdots & C_{\omega\omega} \end{bmatrix}}_{C}} \underset{\text{Input matrix}}{\underbrace{\begin{bmatrix} P_\alpha \\ P_\beta \\ \cdots \\ P_\omega \end{bmatrix}}_{P}}$$

Figure 1. Mathematical model of energy hub.

The mathematical expression of EH can also be formatted as:

$$L = CP \tag{7}$$

where ***L*** and ***P*** respectively represent the output and output matrix of the energy hub, ***C*** is the coupling matrix. The equation (7) reflects the energy conversion relationship between the units in IES, and ***C*** can be determined therefrom.

2.3. Modeling of heating network transmission delay and temperature loss

According to [8], there is a significant difference in the transmission delay and energy transmission loss between the heating system and the electric power system. The transmission loss will increase the total demand of the system thermal power, and the transmission delay will cause the supply and demand out of sync, so that the optimal scheduling results of the entire system will also be affected. The transmission medium of the heating network is usually hot water or steam. The heating network is regulated by quality regulation method considering hydraulic conditions. The time delay caused by media transfer will contribute to a time delay in the transmission of heat power.

In the park-level integrated system, the distance between the heat sources and the heat load is not far, so the transient process of heat medium changing is very short. For the day-ahead optimal scheduling model, the scheduling period is one hour. It can be interpreted that the temperature of the medium has reached a fixed value and keep stable after one adjustment and before the next scheduling [8]. Supposing the heat power of the medium only radiated to the outside through the pipeline, the temperature from the heat source x at time t is shown in equation (8).

$$T_s^{'}(x,t) = \begin{cases} \dfrac{(T_{s0}^{'} - T_{s0})\exp\left(-\dfrac{x}{Rc\rho f}\right)}{\pi d_1^2 x/(4f)} t + T_{s0}\exp\left(-\dfrac{x}{Rc\rho f}\right) + \left[1-\exp\left(-\dfrac{x}{Rc\rho f}\right)\right] T_e, t \in \left[0, \pi d_1^2 x/(4f)\right] \\ T_{s0}^{'}\exp\left(-\dfrac{x}{Rc\rho f}\right) + \left[1-\exp\left(-\dfrac{x}{Rc\rho f}\right)\right] T_e, t \in \left[\pi d_1^2 x/(4f), +\infty\right] \end{cases} \tag{8}$$

IOP Conf. Series: Earth and Environmental Science **431** (2020) 012055 doi:10.1088/1755-1315/431/1/012055

where T_{s0}^{i} and T_{s0}^{i-1} respectively represent the temperature of the heating source at time t and t_{i-1}, R is the equivalent thermal resistance, c is the specific heat capacity, ρ is hot water density, Δt is the scheduling period, T_r and T_e respectively represent the backwater temperature and ambient temperature. Considering the characteristics analyzed above, the power requirements at the heat source can be derived and calculated according to [8].

2.4. Day-ahead optimal scheduling model

2.4.1. Objective function. This paper focuses on the operational cost of systems, regardless of the cost of equipment investment, maintenance or overhaul. The objective function is to minimize operating costs, which include the cost of purchasing electricity from the grid and the cost of purchasing natural gas.

$$\min C = C_e + C_g \tag{9}$$

$$\begin{cases} C_e = \sum_{t=1}^{n} c_e^t P_G^t \Delta t \\ C_g = c_g^t \sum_{t=1}^{n} \left(P_{CU}^t + P_{CH/C}^t + P_{GB}^t \right) \Delta t \end{cases} \tag{10}$$

where n is the number of the total scheduling period, i represent the ith period，Ce is the cost of purchasing electric power from the grid, Cg is the cost of the natural gas consumed.

2.4.2. Constraints on the CCHP units.

$$\begin{cases} P_{GT}^{\min} \le P_{GT} \le P_{GT}^{\max} \\ Q_{GB}^{\min} \le Q_{GB}^{s} \le Q_{GB}^{\max} \\ Q_{WH}^{\min} \le Q_{WH}^{out} \le Q_{WH}^{\max} \\ C_{EC}^{\min} \le C_{EC} \le C_{EC}^{\max} \end{cases} \begin{matrix} C_{CH/C}^{\min} \le C_{CH/C}^{out} \le C_{CH/C}^{\max} \\ C_{HP}^{\min} \le C_{HP}^{out} \le C_{HP}^{\max} \\ P_{PV}^{\min} \le P_{PV} \le P_{PV}^{\max} \end{matrix} \tag{11}$$

where subscript min and subscript max respectively represent the upper and lower limit of the output power, the constraints on the GT、GB、HRB、ER、SOAR、EHP、PV are represented in equation (11).

2.4.3. Constraints on ramping power.

$$\begin{cases} -P_{GT}^{down} \le P_{GT}^{t} - P_{GT}^{t-1} \le P_{GT}^{up} \\ -Q_{GB}^{down} \le Q_{GB}^{t} - Q_{GB}^{t-1} \le Q_{GB}^{up} \end{cases} \tag{12}$$

2.4.4. Constraints on battery operation.

$$\begin{cases} P_{\min}^{C} \le P_{ES,C} \le P_{\max}^{C} \\ P_{\min}^{D} \le P_{ES,D} \le P_{\max}^{D} \end{cases} \tag{13}$$

$$E_{i\min} \le E_i \le E_{i\max} \tag{14}$$

$$E(t+1) = (1-\sigma) E(t) + \left(P_C \eta_C - P_D / \eta_D \right) \Delta t \tag{15}$$

$$X(1,t) + X(2,t) \le 1 \tag{16}$$

The constraints on battery charging/discharging is shown in equation (13). The equation (14) represents the constraints on the battery state. The battery mechanism constrains is shown in the equation (15), where η_C and η_D respectively represented the charging/discharging efficiency. X(1，t) and X(2，t) shown in the equation (16) are all 0-1 variables, equation (16) represent the constraint that the battery can't be charged or discharged at the same time.

2.4.5. Power balance. The input and output power of cold, heat, and electricity should meet the balance.

3. Case study

3.1. Test system and scenarios

The test system proposed in this paper is presented in figure 2 and the simulation data used are presented in figure 3 according to [8, 10, 11]. In order to verify the effect of the EHP on improving the flexibility and economy of IES, this paper sets up two scenarios for comparative analysis. Scenarios 1: The system does not install an EHP; Scenarios 2: The system contains an EHP. The optimized scheduling results in the two cases were compared and analyzed, and the results are as follows.

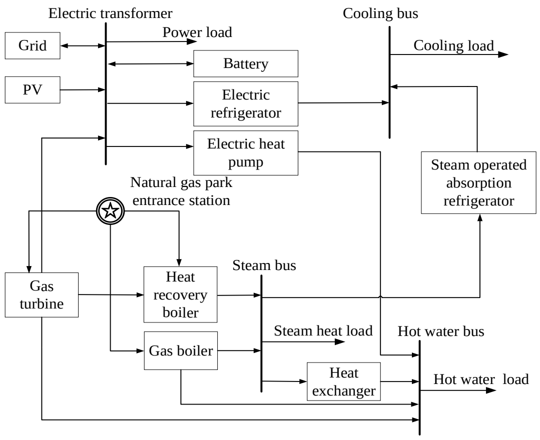

Figure 2. Modified test system (CCHP system containing an EHP).

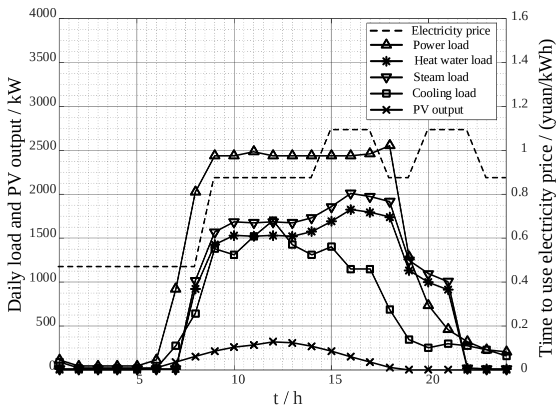

Figure 3. Predicted curves of system load and time of use electricity price.

3.2. Results

3.2.1. Operating cost. The optimized cost of the system operation in different scenarios is shown in table 1. The minimum operating cost of Scenario 1 is 40556.8 yuan, and the minimum operating cost of Scenario 2 is 34670.1 yuan. It can be seen that the operating cost of the system is greatly reduced due to the EHP.

Table 1. Comparison of operation cost.

Scenario	Electric Heat Pump installed or not	Operation cost (RMB)
1	No	40556.8
2	Yes	34670.1

3.2.2. Hourly power balance. The hourly power output of each unit for the two scenarios is shown in figure 4 to figure 11. Figure 3 shows that the heat load is at the peak during the period 9 to 19. In Scenario 1, the hot water power is provided by a gas boiler, a gas turbine, and a heat exchanger. In Scenario 2, the hot water power is provided by a gas boiler, a gas turbine, a heat exchanger, and an electric heat pump. It can be seen from figure 6 and figure 10 that the output of the gas boiler is greatly reduced during period 9 to 19. In the heat-load-based operation mode, when the heat load is large, the electric power output by CCHP unit will be excessive. However, the EHP can help solve this problem by converting electric power into heating power, so that the system will achieve heat-and-power decoupling. What's more, as shown in figure 7 and figure 11, during period 9 to 19, the heat power generated by GT is greatly reduced. This also illustrates that the EHP has helped the system achieve heat-and-power decoupling and has improved the flexibility of the CCHP system.

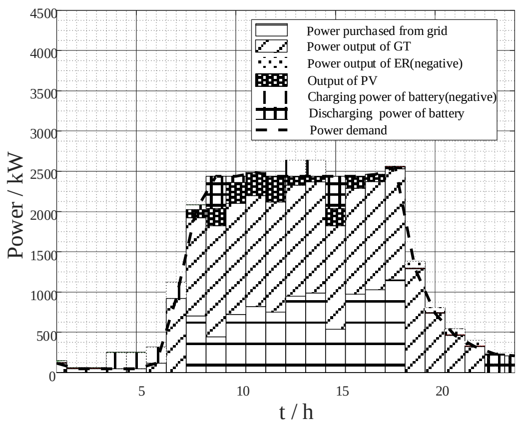

Figure 4. Optimal scheduling of Electric power without electric heat pump.

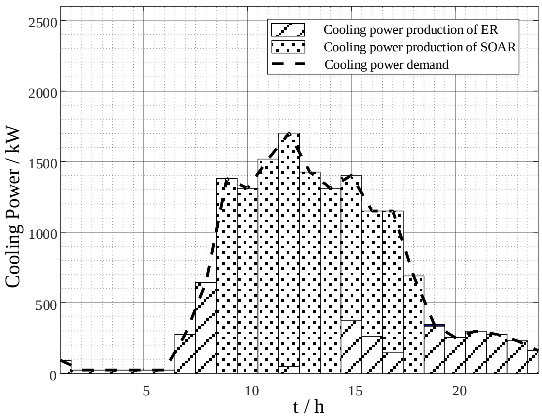

Figure 5. Optimal scheduling of cooling power without electric heat pump.

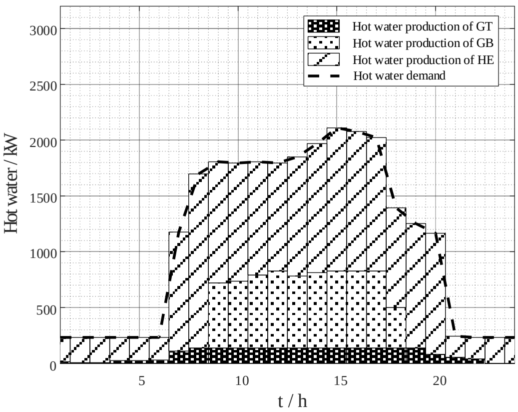

Figure 6. Optimal scheduling of hot water power without electric heat pump.

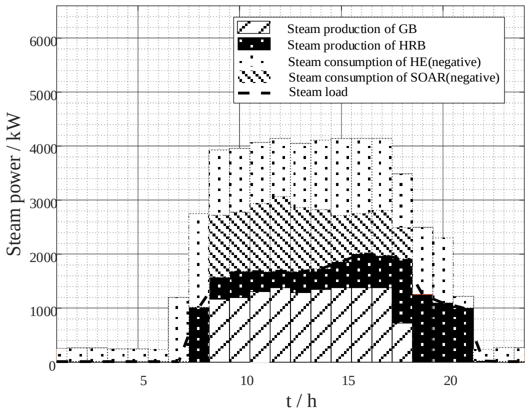

Figure 7. Optimal scheduling of steam power without electric heat pump.

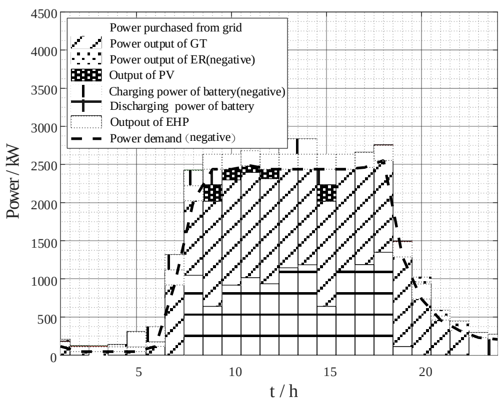

Figure 8. Optimal scheduling of Electric power with electric heat pump.

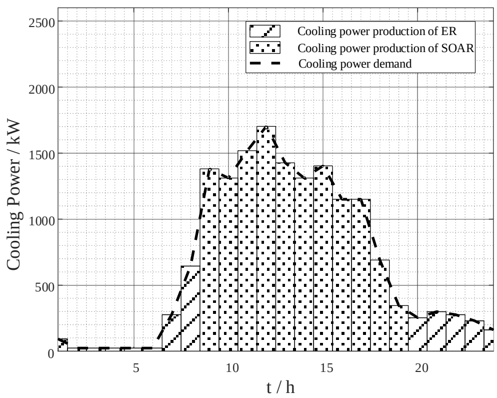

Figure 9. Optimal scheduling of cooling power with electric heat pump.

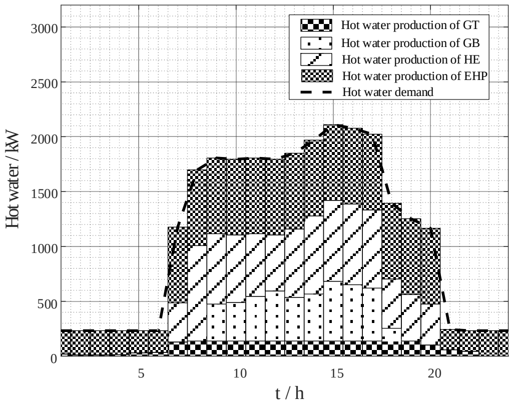

Figure 10. Optimal scheduling of hot water power with electric heat pump.

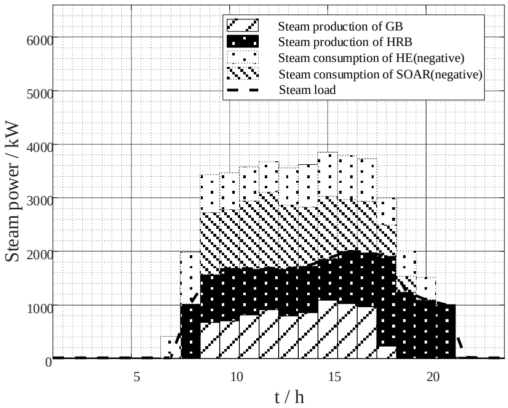

Figure 11. Optimal scheduling of steam power with electric heat pump.

4. Conclusion

A day-ahead optimal scheduling model for a CCHP system containing an EHP is proposed in this paper, and the effect of EHP is analyzed. The simulation results show that the EHP can effectively help the system realize “heat-and-power decoupling” by converting excess electric power into heating power, and improve the flexibility of CCHP system. The installation of the EHP greatly reduces the daily operating cost as well. It is verified that the EHP can improve the flexibility and economy of CCHP systems. In future work, wind power prediction will be considered to reduce wind power curtailment. Besides, the prediction of cold, heat and electric load will be attached importance to improve the robustness of the system.

5. References

[1] Kang H, Qun C. “Overall energy efficiency and flexibility retrofit scheme analysis of heat-power energy system,” *Thermal Power Generation*, 2018, 47(5): 14-21.

[2] Xinyu C, Chongqing K, Mark O, et al. “Power for wind power integration in china: modeling and implications,” *IEEE Transactions on Power Systems*, 2015, 30(4): 1848-57.

[3] Yong L, Yao Z, Yi T, et al. “Optimal stochastic operation of integrated low-carbon electric power, natural gas, and heat delivery system,” *IEEE Transactions on Sustainable Energy*, 2018, 9(1): 273-83.

[4] Quan L, Hao J, Tianyou C, et al. “Wind power accommodation by combined heat and power plant with electric boiler and its national economic evaluation,”. *Automation of Electric Power Systems*. 2014, 38(1): 6-12.

[5] Yuanhang D, Lei C, Qun C, et al. “Dispatch model for CHP with pipeline and building thermal energy storage considering heat transfer process,” *IEEE Transactions on Sustainable Energy*, 2019, 10(1): 192-203.

[6] Wei G, Jun W, Shuai L, et al. “Optimal Operation for Integrated Energy System Considering Thermal Inertia of District Heating Network and Buildings,” *Applied Energy*, 199(2017): 234-46.

[7] Shuai D, Chengfu W, Shijie X, et al. “Day-ahead optimal scheduling of electricity-gas-heat integrated energy system considering dynamic characteristics of networks,” *Automation of Electric Power Systems*, 2018, 42(13): 12-19.

[8] Shuai Y, Wei G, Xuesong Z, et al. “Effect of heating characteristics on ultra-short-term scheduling of integrated energy system,” *Automation of Electric Power Systems*, 2018, 42(14): 83-90.

[9] Weiliang W, Dan W, Hongjie J, et al. “Review of steady-state analysis of typical regional integrated energy system under the background of energy internet,” *Proceedings of the CSEE*, 2016, 36(12): 3292-305

[10] Yufei X. "Research on Scheduling Method of the Wind-power-heat Integrated System to Improve the Efficiency of Wind Power Utilization," 2018.

[11] Turk A, Zeng Q, Qiuwei W, et al. "Optimal Operation of Integrated Electrical, District Heating and Natural Gas System in Wind Power Dominated Power System," *International Journal of Smart Grid and Clean Energy*. 2013, 2(X): 1-10.

Acknowledgments

This work is supported by the "NARI Group Corporation-2018 Open Fund Project from The National Key Laboratory of Smart Grid Protection and Operation Control" (Grant No. SGNR0000GZJS1808076) and Postgraduate Research & Practice Innovation Program of Jiangsu Province (KYCX19_0807).

Modelling best fit-curve between China's production and consumption-based temporal carbon emissions and selective socio-economic driving factors

M. Jawad Sajid[1]

1 School of Management, Xuzhou University of Technology, Xuzhou, Jiangsu province, 221000, China
E-mail: jawad.jaws@outlook.com; 11910@xzit.edu.cn

Abstract. Production and consumption-based approaches are primarily used to determine emissions responsibility at industrial and national levels. China is the world's topmost emitter under both these approaches. Most of the literature especially for China mainly focuses on drivers of direct GHG emissions. This study based on the curvilinear analysis, models best-fit curves between these two emission types and selective driving factors. GDP, GDP/Capita and GNI best-fit curves didn't support EKC hypothesis for production-based emissions, while for consumption-based emissions their curves are in support of EKC. Population, population density, Urbanization, CO_2 intensity and urban population agglomeration all had non-linear best-fit curves. While energy use indicated a linear relation with production-based emissions and non-linear with consumption-based emissions. FDI and renewable energy consumption showed a non-linear negative relation with both emissions. Understanding of the non-linear relationship between vital driving factors and China's emissions under both approaches can help policymakers formulate more informed mitigation policies.

1. Introduction

Reducing GHG emissions is a global objective [1-3], but the increase in worldwide energy-based GHG emissions in 2017 has undermined the global emissions reduction objectives set out in the Paris agreement [4]. About 60% of global GHG emissions are CO_2 emissions [5]. Ever since the 'industrial revolution' CO_2 intensity in 'atmosphere' has greatly increased [6]. The current rate of global GHG emissions can affect the worldwide environment [7]. Carbon emissions from fossil fuel flames are the main cause of global warming [8]. Pursuing many nations to impose mechanisms for the decrease in the consumption of fossil fuels [9]. China is the world top emitter under production and consumption-based accounting approaches [10]. More than 50% of global outflow trade emissions are from China [11].

Two type of approaches including: consumption-based, where emissions are attributed to the region of final consumption [12-13], and production-based, where emissions are attributed to the region where they are produced irrespective of the fact where they are eventually consumed [14-16]; are extensively employed for calculation of global GHG emissions [17]. PBA, in theory, is similar to IPCC and other international agreements. But the IPCC approach has been strongly criticized because outsourcing mainly takes place between developed and developing nations [18]. This transferring of CO_2 emissions from developed to developing nations is a major problem, developed nation's emissions rise when trade adjustment is considered [19]. Therefore, consumption-based emissions of developed

IOP Conf. Series: Earth and Environmental Science **431** (2020) 012061 doi:10.1088/1755-1315/431/1/012061

nations are usually higher than their production-based emissions [20-21]. Regional accounting approach adopted by IPCC encourages direct imports between nations [22-23].

The type of accounting approach adopted deeply influence the allocation of CO_2 emissions responsibility [24]. Hence there is an international debate on approaches and allocation of responsibility for GHG emissions [25-26]. Calculations under PBA are uncomplicated, but it neglects global transport and carbon leakage problems [10]. On the other hand, the consumption-based approach is much fairer when assigning emissions accountability [27-28]. Consumption-based policy is objective and cost-efficient [29]. And it may be needed for sustainable environment [30]. It can help abate worldwide air contamination [31], stimulate ecological comparative advantages and dispersal of technology [32]. The consumption-based approach would pursue importers towards mitigation projects in regions from where they import merchandises [33]. The consumption-based approach also has some disadvantages which may be eliminated by exercising shared responsibility [10; 33-34].

There are three approaches to estimate best-fit curve between dependent (Y) and independent (X) variable: Linear regression, data transformations and curvilinear regression [35]. The curved trend in non-linear relations can be much better explained by non-linear functions for example 'quadratic or cubic' or transformation into a linear function [36]. But transforming data values using some common method of transformation and then performing linear regression may give different results then fitting a curve to un-transformed data, or we can find an equation best fitting our curved data using curvilinear regression [35]. For best fit, we have employed Polynomial, Compound, Growth, Logarithmic, S, Exponential, Inverse, Power and Logistic models.

Most of the current literature on driving factors of China's temporal emissions either focuses on the identification of these factors or their impact on direct emissions while the relationship of these factors with consumption and production based emissions are mostly being ignored. [37] Studied drivers of energy-related CO_2 emissions of 30 provinces of China. Used 'panel data and spatial econometrics models' for their study. [38] Calculated the factors of CO_2 emissions of Chinas business sector. Used VAR and STIRPAT models. [39] Studied the driving factor for China city level carbon emissions. Employed a series of 'dynamic distribution approaches and panel data models.' [40] Also investigated drivers of city level carbon emissions of China. [41] Calculated CO_2 emission decrease potential of Chongqing city of China. Employed LMDI, STIRPAT model' to forecast future carbon emissions.

[42] Researched drivers of energy-related carbon emissions of Beijing. Employed 'Input-output model and SDA to study drivers.' [43] Examined key drivers to predict carbon emissions of Hebei. Employed 'Bivariate correlation analysis, factor analysis, PSO-ELM.' [44] Considered the effect of population-related drivers on carbon emissions in 30 Chinese provinces.

This paper is novel in several aspects first of all non-linear regression analysis has rarely been applied to understand the relationship between different driving factors and carbon emissions of a country. Secondly, in general, there is not much literature available where the relationship between a country's direct (production-based) and carbon footprint (consumption-based) emissions and significant driving factors have been analysed. Finally, to the best of author's knowledge, there is no such attempt has been made to graphically model the relationship between both the direct and consumption-based emissions and important socioeconomic factors of China (which is the largest carbon emitter under both the approaches). In this study, the author has tried to fill this gap. The author estimated best-fit curves for both production and consumption-based emissions with selective key driving factors from 1970 to 2015. A comprehensive presentation of key driving factors temporal relationship with both type of emissions will help policymakers to devise better informed future mitigation policies for both PBA and CBA based emissions of China.

2. Experimental design, materials, and methods

The Data on consumption and production- based emissions of China from 1970 to 2015 was obtained from the Eora database which is based upon [45-46]. The relationship between following socioeconomic factors GDP [47-48], GDP per Capita [49-52], population [49; 51-54], population density [51], urbanization [47-50; 54], FDI [48; 53], energy consumption [55]; Urban agglomeration [56] coupled with consumption & production based yearly emission of China was found out. Plus, the author also included GNI, CO_2 intensity and Renewable energy consumption [57].

All socio-economic data is from 'The World Bank data bank' [58]. First, the presence of linear or linear-relationship between socio-economic factors (independent variables) and Production and consumption-based emissions (dependent variable) through residual plotting in SPSS was found out. From the graphs, it was apparent that a non-linear relationship exists between most of the socio-economic factors and PBA & CBA emissions. Bivariate correlation using the Pearson Coefficient is used to establish a relevant relationship between shortlisted variables and carbon emissions [55]. Pearson correlation is a parametric test for a linear relationship between two variable, is not useful for non-linear relation so alternatives should be considered [59].

3. Results

3.1. Model selection

The purpose of regression analysis is to check for influence, significance, and certainty of the factors [60]. The basic linear regression equation is:

$$Y=\alpha + \beta x \tag{1}$$

Where the value of dependent variable is represented by Y, α represents the constant and β represents the value of coefficient of regression and x is independent variable.

For the best fit, the author employed Polynomial, Compound, Growth, Logarithmic, S, Exponential, Inverse, Power and Logistic models to the data; eventually most of the factors best-fit curves in relation with production and consumption-based emissions were obtained through Polynomial model curve fitting. Different powers of x variable are respectively added to the equation to find out their effect on R^2 till no more noteworthy contributions can be obtained for the value of R^2, So on until the increase or change in R^2 is no more significant [35]. Starting by fitting linear regression equation *($y=\alpha+\beta x$)* to the data followed by:

$$Y^2 = \alpha + \beta_1 x + \beta_2 x^2 \tag{2}$$

$$Y^3 = \alpha + \beta_1 x + \beta_2 x^2 + \beta_3 x^3 \tag{3}$$

where Y^2 and Y^3 represent the values of the dependent variable at quadratic and cubic levels respectively.

3.1.1. Production-based emissions. Table 1, contains the details about the final selected models based upon the derivation of the highest R^2 values.

Table 1. Summary of selected models (production-based emissions).

Independent variable	Model type	R	R^2	Adjusted R^2	Std. Error of the Estimate
GDP	Cubic	.950	.903	.901	.666
GDP/Capita	Cubic	.953	.908	.905	.649
Population	Quadratic	.835	.698	.691	1.17
Population density	Quadratic	.835	.698	.691	1.17
Urbanization	Quadratic	.961	.923	.921	.594
FDI	Quadratic	.913	.833	.827	.880
GNI	Cubic	.950	.903	.901	.666
Energy use	Linear	.999	.999	.999	.072
Urban agglomeration	Cubic	.960	.923	.921	.594
CO_2 Intensity	Quadratic	.810	.656	.647	1.199
Renewable Energy Consumption	Inverse	.994	.989	.988	.226

The best-fit curves for the independent variables of GDP, GDP/Capita, GNI and Urban agglomerations were obtained under the cubic model. For Population, Population density, Urbanization, FDI and Carbon Intensity, the Quadratic model yielded the highest values of R^2. For both Population and Population density the Cubic model between these two variables and Production-based emissions of China, could not be tested due to near-collinearity among model terms. Additionally, due to the existence of the non-positive values, the Logarithmic and Power models could not be tested for the independent variable of FDI (Foreign direct investment). Best fit curve for the energy use and production based emissions was obtained under the Linear regression model. And finally for Renewable energy consumption, the best fit curve was obtained under the inverse model. The Cubic model could not be fitted for Renewable energy consumption due to near-collinearity among model terms. ANOVA null hypothesis for both linear and non-linear models was rejected at a significance of .000.

3.1.2. Consumption-*based emissions.* Table 2, contains the details about the final selected models based upon the derivation of the highest R^2 values.

Table 2. Summary of selected models (consumption-based emissions).

Independent variable	Model type	R	R^2	Adjusted R^2	Std. Error of the Estimate
GDP	Cubic	.996	.992	.991	.159
GDP/Capita	Cubic	.996	.992	.991	.159
Population	Quadratic	.924	.854	.848	.666
Population density	Quadratic	.924	.854	.848	.666
Urbanization	Cubic	.993	.986	.985	.207
FDI	Cubic	.915	.837	.820	.743
GNI	Cubic	.996	.992	.991	.160
Energy use	Cubic	.999	.998	.997	.081
Urban agglomeration	Cubic	.991	.982	.981	.236
CO_2 Intensity	Cubic	.928	.861	.854	.617
Renewable Energy Consumption	Power	.991	.982	.981	.066

Like production-based emissions, the highest R^2 values between the independent variables of GDP, GDP/Capita, GNI and Urban agglomerations and the consumption-based emissions were again obtained under the cubic model. Contrary to the best fit curve obtained under the Quadratic and Linear models respectively for the independent variables of carbon intensity, FDI, Urbanization and the energy use with production-based emissions, the best fit curves between these variables and the consumption-based emissions were obtained under the cubic model. For Population and Population density the best-fit curves were obtained under the Quadratic model. Finally, for Renewable energy consumption Power model produced the highest results. ANOVA test for both linear and non-linear regression models was significant at .000.

3.2. Rationalization of best-fit curves

Figure 1a and 1b contains the graphical presentation of the best-fit curves between production and consumption based emissions (dependent variable) and selective socio-economic factors (independent variables) from 1970-2015. GDP, GDP/Capita and GNI regression slopes are steeply concaved approaching last few observations it smoothens. Which means initially slight increases in GDP, GDP/Capita or GNI have seen a larger increase in China's PBA emissions while later on the opposite is true. Approaching end it is steeping again. Thus not supporting EKC hypothesis which advocates the presence of an inverted U-shaped relationship between a country's emissions and its economic progress. The same cannot be said about China's consumption-based emissions relation with GDP, GDP/Capita and GNI. Although their best fit curve is obtained under the cubic model but almost a semi-inverted U shaped regression curve can be observed between these economic factors and consumption-based emissions of China.

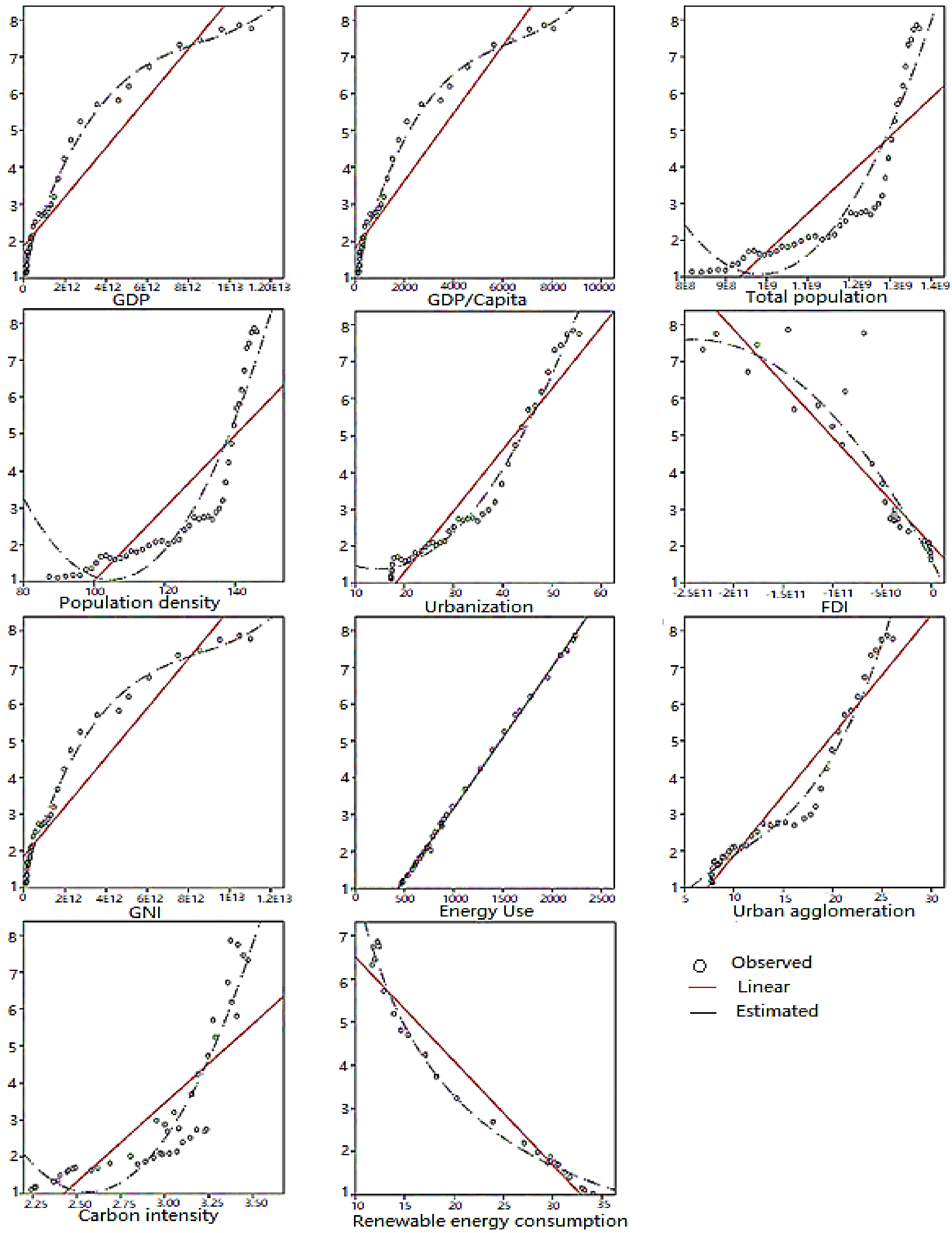

Figure 1a. Best-fit curves for Production-based emissions. Where, Y-axis presents PBA (dependent variable) emissions in 'Mt CO_2 per capita'; X-axis presents independent variables: GDP, GDP per capita and GNI (PPP) measured at (current US$), Population density (people per sq. km of land area), Population in urban agglomerations of more than 1 million, Energy use (Terajoules), Foreign direct

investment, net (BoP, current US$), Renewable energy consumption (% of total final energy consumption), and urbanization (% of total population).

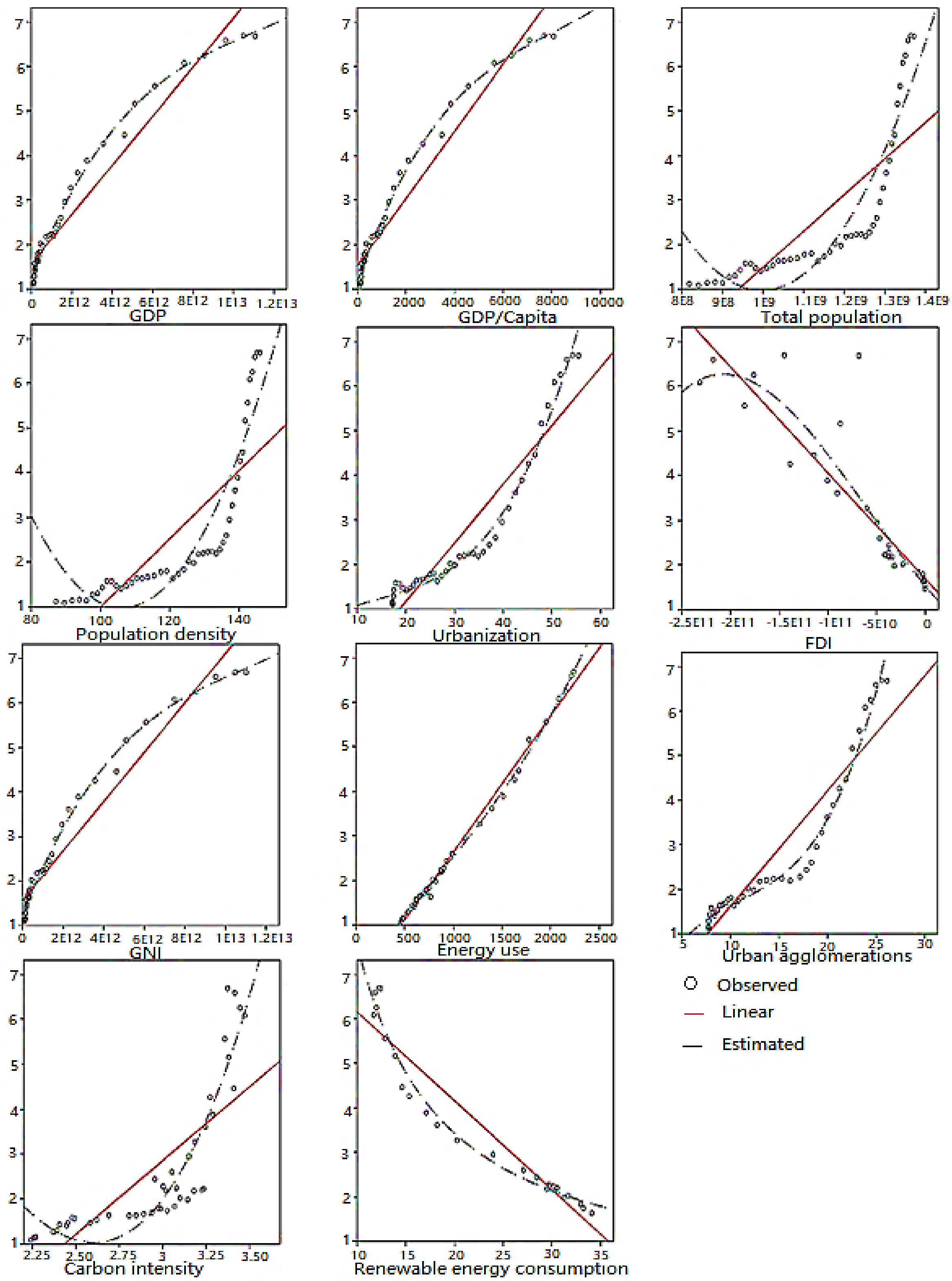

Figure 1b. Best-fit curves for Consumption- based emissions. Where, Y-axis presents CBA (dependent variable) emissions in 'Mt CO2 per capita'; X-axis presents independent variables: GDP, GDP per capita and GNI (PPP) measured at (current US$), Population density (people per sq. km of

land area), Population in urban agglomerations of more than 1 million, Energy use (Terajoules), Foreign direct investment, net (BoP, current US$), Renewable energy consumption (% of total final energy consumption), and urbanization (% of total population).

Total population and population density best-fit curves with both production and consumption based emissions have shown hockey stick shaped curves. Which employs that initial increases in China's population and population density didn't seem to be affecting its PBA and CBA emissions much. Afterward slight population increases have (holding other factors constant) resulted in larger increases in PBA and CBA based emissions. Which could be owing to the increased purchasing power of China's general population over time.

Very steeped slightly convexed best fit curves are obtained for production and consumption-based emissions and urbanization. Which means in the beginning increases in China's urbanization rate observed a lower rate of increases in its PBA and CBA emissions. Afterward slight increases in urbanization rate have resulted in large increases in PBA and CBA emissions. The same observation holds for best-fit curves between urban population agglomerations and PBA and CBA based emissions of China.

Energy use best-fit curve with China's production based emissions were obtained with linear model. Which means (holding other factors constant) every unit increase in energy use will result in .004 units increase in PBA emissions. While for consumption-based emissions its best fit curve was obtained at cubic level. Which with slight variations also indicate more or less a linear trend.

CO_2 intensity best-fit curves with both production and consumption-based emissions show hockey stick shaped patterns. While FDI and renewable energy consumption have shown negatively sloped best-fit curves with both production and consumption-based emissions. For FDI these curves are slightly concaved while for renewable energy consumption, these curves are slightly convexed.

4. Conclusion and policy implications

The purpose of this paper was to find out the best-fit curves between production & consumption-based emissions and vital socio-economic factors of the topmost carbon emitter China. Until now most of the literature takes in to account only direct emissions while ignoring these main two accounting approaches for GHG emissions. This paper will not only be helpful specifically to Chinese policymakers but also to other scholars and governments concerned with environmental mitigation. The main points for policy guidance are summarized below:

1) GDP, GDP/Capita and GNI best-fit curves with PBA emissions didn't indicate the presence of the EKC hypothesis. While their best-fit curves with CBA supported the presence of the EKC hypothesis and shown somewhat inverted semi U shaped curves. Which indicates that the Chinese government cannot allow unchecked growth based on the EKC theory, i.e., in the hope that after reaching a certain peak its emissions will come down with the further growth of its GDP. Our results indicated no clear presence of the EKC relationship between direct emissions of China and the GDP, GDP/Capita and GNI.
2) On the other hand, there is some evidence of the existence of the EKC curve between China's carbon footprint (consumption-based emissions) and these socio-economic factors. Which means with further economic growth (GDP, GDP/Capita and GNI), China's consumption-based emissions are expected to decrease. This indicates that China's rapid economic growth has resulted in decreasing degree of foreign carbon imports as compared to its carbon exports. Due to this reason, China as a nation can benefit from an emission accountability system based upon its carbon footprint (consumption-based) as compared to direct emissions. Consumption-based emissions accounting approach can also help the Chinese government to maintain its rapid economic growth while witnessing a decrease in its carbon footprint (after a certain point). Which as per this study's findings, would not be possible under a production-based approach (direct emissions).
3) It is recommended that the Chinese government should pursue the implementation of the consumption-based method under the IPCC and at other international forums. The consumption-based system also will particularly save China from the problem of the global carbon leakage. Not only China's consumption-based emissions are less than its production-based emissions but

also a consumption-based emissions accountability mechanism can help China achieve future economic growth while reducing its carbon footprint.

4) Population, population density and CO_2 emission intensity all have shown hockey stick shaped curves with both production and consumption-based emissions. Which means initially with an increase in these factors both the direct and consumption-based emissions did not increase significantly. But after some time a smaller amount of increase in population, population density, and CO_2 emission intensity have witnessed the larger amount of direct and consumption-based emissions. Which means the Chinese government at all costs should control future increases in population, population density, and CO_2 emission intensity.
5) Very steeped slightly convexed best fit curves were obtained for production and consumption-based with Urbanization and urban population agglomerations. It indicates that for mitigation of China's future emissions the rapid phenomenon of urbanization in China should be stopped or slowed as much as possible. The rural population should be discouraged to move to urban cities which is the main cause of conversion of the rural population into urban population in China. Furthermore, to reduce the impact of urban population agglomerations on both the production and consumption-based emissions urban infrastructures should be made more environmentally friendly, residents in the urban agglomerations should be encouraged to improve their consumption habits, etc.
6) Energy use has indicated a linear relation with China's production based emissions. Although, it's best fit curve with consumption-based emissions was obtained at cubic level but it was also more or less indicating an almost linear relationship with both the production and consumption-based emissions. Due, to this presence of almost a linear relation (direct relation) improvements in energy use structure and efficiency can help directly in the reduction of the China's consumption and production-based emissions. Chinese government can invest in technological advances to improve its overall energy efficiency.
7) Both FDI and penetration of renewable energy showed negatively sloped non-linear curves with production and consumption-based emissions. They might hold the key towards unlocking China's carbon mitigation potential. China has already shifted its attention towards more use of renewable energy to fulfil its energy needs. This process should be further supported and financed. Furthermore, more FDI could be attracted through tax breaks, subsidies and miscellaneous incentives.

5. References

[1] Q. Cao, W. Kang, M. J. Sajid, and M. Cao, "Measuring China's carbon emissions based on final consumption," Energy Procedia, vol. 152, pp. 853–862, 2018.

[2] Q. Cao, W. Kang, S. Xu, M. J. Sajid, and M. Cao, "Estimation and decomposition analysis of carbon emissions from the entire production cycle for Chinese household consumption," Journal of Environmental Management, vol. 247, pp. 525–537, Oct. 2019.

[3] M. Cao, W. Kang, C. Qingren, and M. J. Sajid, "Estimating Chinese rural and urban residents' carbon consumption and its drivers: considering capital formation as a productive input," Environment, Development and Sustainability, pp. 1–22, 2019.

[4] M. J. Sajid, Q. Cao, and W. Kang, "Transport sector carbon linkages of EU's top seven emitters," Transport Policy, vol. 80, pp. 24–38, May 2019.

[5] H. Vidyarthi, "An econometric study of energy consumption, carbon emissions and economic growth in South Asia: 1972-2009," World Journal of Science, Technology and Sustainable Development, vol. 11, pp. 182-195, 2014.

[6] C. Zhou, S. Wang and K. Feng, "Examining the socioeconomic determinants of CO_2 emissions in China: A historical and prospective analysis," Resources, Conservation & Recycling, vol. 130, p. 1– 11, 2018.

[7] M. Jaforullah and A. King, "The econometric consequences of an energy consumption variable in a model of CO_2 emissions," Energy Economics, vol. 63, p. 84–91, 2017.

[8] S. J. Davis and K. Caldeira, "Consumption-based accounting of CO_2 emissions," PNAS, vol. 12, p. 5687–5692, 2010.

[9] M. d. P. Pablo-Romero and A. Sánchez-Braza, "The changing of the relationships between carbon footprints and final demand: Panel data evidence for 40 major countries," Energy Economics, vol. 61, p. 8–20, 2017.
[10] J.-L. Fan, Y.-B. Hou, Q. Wang, C. Wang and Y.-M. Wei, "Exploring the characteristics of production-based and consumption-based carbon emissions of major economies: A multiple-dimension comparison," Applied Energy, vol. 184, p. 790–799, 2016.
[11] B. Liddle, "Consumption-based accounting and the trade-carbon emissions nexus," Energy Economics, vol. 69, p. 71–78, 2018.
[12] T. Wiedmann, "A review of recent multi-region input–output models used for consumption-based emission and resource accounting," Ecological Economics, vol. 69, pp. 211-222, 2009.
[13] J. Barrett , G. Peters , T. Wiedman, K. Scott , M. Lenzen, K. Roelich and C. L. Quéré, "Consumption-based GHG emission accounting: a UK case study," Climate Policy, vol. 13, pp. 451- 470, 2013.
[14] K. Steininger, C. Lininger, S. Droege, D. Roser, L. Tomlinsone and L. Meyerd, "Justice and cost effectiveness of consumption-based versus production-based approaches in the case of unilateral climate policies," Global Environmental Change, vol. 24, pp. 75-87, 2014.
[15] G. Atkinson, K. Hamilton, G. Ruta and D. V. D. Mensbrugghe, "Trade in 'virtual carbon': Empirical results and implications for policy," Global Environmental Change, vol. 21, pp. 563-574, 2011.
[16] A. Bows and J. Barrett, "Cumulative emission scenarios using a consumption-based approach: a glimmer of hope?," Carbon Management, vol. 1, pp. 161-175, 2010.
[17] J. Tian, H. Liao and C. Wang, "Spatial–temporal variations of embodied carbon emission in global trade flows: 41 economies and 35 sectors," Nat Hazards, vol. 78, p. 1125–1144, 2015.
[18] A. Malik and J. Lan, "The role of outsourcing in driving global carbon emissions," Economic Systems Research, vol. 128, pp. 168-182, 2016.
[19] K. Kanemoto, D. Moran, M. Lenzen and A. Geschke, "International trade undermines national emission reduction targets: New evidence from air pollution," Global Environmental Change, vol. 24, pp. 52-59, 2014.
[20] T. Wiedmann, R. Wood , J. C. Minx , M. Lenzen , D. Guan and Rocky Harris, "A CARBON FOOTPRINT TIME SERIES OF THE UK – RESULTS FROM A MULTI-REGION INPUT–OUTPUT MODEL," Economic Systems Research, vol. 22, pp. 19-42, 2010.
[21] G. P. Peters, J. C. Minx, C. L. Weber and . O. Edenhofe, "Growth in emission transfers via international trade from 1990 to 2008," PNAS, vol. 108, p. 8903–8908, 2011.
[22] S. J. Davis, . G. P. Peters and K. Caldeira, "The supply chain of CO_2 emissions," PNAS, vol. 108, p. 18554–18559, 2011.
[23] A. Skelton, D. Guan, P. G.P. and D. Crawford-Brown, "Mapping flows of embodied emissions in the global production system," Environmental Science and Technology, vol. 45, pp. 10516-10523, 2011.
[24] Z. Mi, Y. Zhang, D. Guan, Y. Shan, Z. Liu, R. Cong, X.-C. Yuan and Y.-M. Wei, "Consumption-based emission accounting for Chinese cities," Applied Energy, vol. 184, p. 1073– 1081, 2016.
[25] K. Steen-Olsen, J. Weinzettel, G. Cranston, A. E. Ercin and E. Hertwich, "Carbon, Land, and Water Footprint Accounts for the European Union: Consumption, Production, and Displacements through International Trade," Environmental Science & Technology, vol. 46, p. 10883–10891, 2012.
[26] D. Caro, F. M. Pulselli, S. Borghesi and S. Bastianoni, "Mapping the international flows of GHG emissions within a more feasible consumption-based framework," Journal of Cleaner Production, vol. 147, pp. 142-151, 2017.
[27] K. Feng, K. Hubacek, L. Sun and Z. Liu, "Consumption-based CO_2 accounting of China's megacities: The case of Beijing, Tianjin, Shanghai and Chongqing," Ecological Indicators, vol. 47, p. 26–31, 2014.

[28] J.-L. Fan, Y.-B. Hou, Q. Wang, C. Wang and Y.-M. Wei, "Exploring the characteristics of production-based and consumption-based carbon emissions of major economies: A multiple-dimension comparison," Applied Energy, p. 790–799, 2016.
[29] K. Steininger, C. Lininger, S. Droege, D. Roser, L. Tomlinsone and L. Meyerd, "Justice and cost effectiveness of consumption-based versus production-based approaches in the case of unilateral climate policies," Global Environmental Change, vol. 24, pp. 75-87, 2014.
[30] O. Fernández-Amador, J. F. Francois, D. A. Oberdabernig and P. Tomberger, "Carbon Dioxide Emissions and Economic Growth: An Assessment Based on Production and Consumption Emission Inventories," Ecological Economics, vol. 135, p. 269–279, 2017.
[31] D. Guan, J. Lin, S. J. Davis, . D. Pan, K. He, C. Wang, . D. J. Wuebbles, D. G. Streets and Q. Zhang, "Reply to Lopez et al.: Consumption-based accounting helps mitigate global air pollution," PNAS, vol. 111, p. E2631, 2014.
[32] G. P. Peters and E. G. .. Hertwich, "CO_2 Embodied in International Trade with Implications for Global Climate Policy," Policy analysis, vol. 42, pp. 1401-1407, 2007.
[33] G. P. Peters, "From production-based to consumption-based national," METHODOLOGICAL AND IDEOLOGICAL OPTIONS, vol. 65, pp. 13-23, 2008.
[34] M. Lenzen, J. Murray, F. Sack and T. Wiedmann, "Shared producer and consumer responsibility — Theory and practice," Ecological Economics, vol. 61, pp. 27-42, 2007.
[35] J. McDonald, Handbook of Biological Statistics, 3rd ed., Baltimore, Maryland: Sparky House Publishing, 2014.
[36] Minitab Inc., "Linear, nonlinear, and monotonic relationships," 2010. [Online]. Available: https://support.minitab.com/en-us/minitab/18/help-and-how-to/statistics/basic-statistics/supporting- topics/basics/linear-nonlinear-and-monotonic-relationships/. [Accessed 2018 February 2018].
[37] Q. Zhang, J. Yang, Z. Sun and F. Wu, "Analyzing the impact factors of energy-related CO_2 emissions in China: What can spatial panel regressions tell us?," Journal of Cleaner Production, vol. 161, pp. 1085-1093, 2017.
[38] A. Wang and B. Lin, "Assessing CO_2 emissions in China's commercial sector: Determinants and reduction strategies," Journal of Cleaner Production, vol. 164, pp. 1542-1552, 2017.
[39] S. Wang and X. Liu, "China's city-level energy-related CO_2 emissions: Spatiotemporal patterns and driving forces," Applied Energy, vol. 200, p. 204–214, 2017.
[40] C. Zhou and S. Wang, "Examining the determinants and the spatial nexus of city-level CO_2 emissions in China: A dynamic spatial panel analysis of China's cities," Journal of Cleaner Production, vol. 171, pp. 917-926, 2018.
[41] X. Tan, L. Dong, D. Chen, B. Gu and Y. Zeng, "China's regional CO_2 emissions reduction potential: A study of Chongqing city," Applied Energy, vol. 162, p. 1345–1354, 2016.
[42] J. Wei, K. Huang, S. Yang, Y. Li, T. Hu and Y. Zhang, "Driving forces analysis of energy-related carbon dioxide (CO_2) emissions in Beijing: an inputeoutput structural decomposition analysis," Journal of Cleaner Production, vol. 163, pp. 58-68, 2017.
[43] W. Sun, C. Wang and C. Zhang, "Factor analysis and forecasting of CO_2 emissions in Hebei, using extreme learning machine based on particle swarm optimization," Journal of Cleaner Production, vol. 162, pp. 1095-1101, 2017.
[44] Y. Wang, Y. Kang, J. Wang and L. Xu, "Panel estimation for the impacts of population-related factors on CO_2emissions: A regional analysis in China," Ecological Indicators, vol. 78, p. 322–330, 2017.
[45] K. Kanemoto, D. Moran and E. Hertwitch, "Mapping the Carbon Footprint of Nations," Environmental Science and Technology, p. 10.1021/acs.est.6b03227, 2016.
[46] K. Kanemoto, D. Moran, M. Lenzen and A. Geschke, "International Trade Undermines National Emissions Targets: New Evidence from Air Pollution," Global Environmental Change, vol. 24, pp. 52- 59, 2014.
[47] X. Ouyang and B. Lin, "Carbon dioxide (CO_2) emissions during urbanization: A comparative study between China and Japan," Journal of Cleaner Production, vol. 143, pp. 356-368, 2017.

[48] C. Zhou, S. Wang and K. Feng, "Examining the socioeconomic determinants of CO_2 emissions in China: A historical and prospective analysis," Resources, Conservation & Recycling, vol. 130, pp. 1-11, 2018.
[49] Q. Zhang, J. Yang, Z. Sun and F. Wu, "Analyzing the impact factors of energy-related CO_2 emissions in China: What can spatial panel regressions tell us?," Journal of Cleaner Production, vol. 161, pp. 1085-1093, 2017.
[50] A. Wang and B. Lin, "Assessing CO_2 emissions in China's commercial sector: Determinants and reduction strategies," Journal of Cleaner Production, vol. 164, pp. 1542-1552, 2017.
[51] C. Zhou and S. Wang, "Examining the determinants and the spatial nexus of city-level CO_2 emissions in China: A dynamic spatial panel analysis of China's cities," Journal of Cleaner Production, vol. 171, pp. 917-926, 2018.
[52] X. Tan, L. Dong, D. Chen, B. Gu and Y. Zeng, "China's regional CO_2 emissions reduction potential: A study of Chongqing city," Applied Energy, vol. 162, p. 1345–1354, 2016.
[53] S. Wang and X. Liu, "China's city-level energy-related CO_2 emissions: Spatiotemporal patterns and driving forces," Applied Energy, vol. 200, pp. 204-214, 2017.
[54] Y. Wang, Y. Kang, J. Wang and L. Xu, "Panel estimation for the impacts of population-related factors on CO_2 emissions: A regional analysis in China," Ecological Indicators, vol. 78, p. 322–330, 2017.
[55] W. Sun, C. Wang and C. Zhang, "Factor analysis and forecasting of CO_2 emissions in Hebei, using extreme learning machine based on particle swarm optimization," Journal of Cleaner Production, vol. 162, pp. 1095-1101, 2017.
[56] X. Xu, H. Huo, J. Liu, Y. Shan, Y. Li, H. Zheng, D. Guan and Z. Ouyang, "Patterns of CO_2 emissions in 18 central Chinese cities from 2000 to 2014," Journal of Cleaner Production, vol. 172, pp. 529-540, 2018.
[57] R. Roman, J. M. Cansino and J. A. Rodas, "Analysis of the main drivers of CO_2 emissions changes in Colombia (1990-2012) and its political implications," Renewable Energy, vol. 116, pp. 402-411, 2018.
[58] The World Bank, "The World Bank," 2019. [Online]. Available: databank.worldbank.org. [Accessed 20 January 2019].
[59] Kent State University Libraries, "SPSS Tutorials: Pearson Correlation," 2018. [Online]. Available: https://libguides.library.kent.edu/SPSS/PearsonCorr. [Accessed 16 February 2019].
[60] A. Gallo, "Harvard Business review," 2015. [Online]. Available: https://hbr.org/2015/11/a-refresher-on-regression analysis. [Accessed 18 February 2019].

IOP Conf. Series: Earth and Environmental Science **431** (2020) 012062 doi:10.1088/1755-1315/431/1/012062

Comparison of fuel consumption and emission characteristics of china VI coach under different test cycle

Hanzhengnan Yu*, Yu Liu and Jingyuan Li

China Automotive Technology and Research Center Co., Ltd., Tianjin, China
E-mail: yuhanzhengnan@catarc.ac.cn

Abstract. As the test cycle used for evaluating the fuel consumption and emission characteristics of the heavy-duty commercial vehicle in China will be replaced from C-WTVC to CHTC in a round 2020, the investigation on the variation of fuel consumption and emission test results after the replacement is well needed for further vehicle's development and calibration. In this paper, the fuel consumption and emission characteristics of a China VI coach under these two test cycles have been discussed and compared. Results showed that fuel consumption, CO, HC and NOx emissions of the test coach all increased after changing the test cycle from C-WTVC to CHTC, which were due to the low rotation speed and low torque operating points, and the aggressive and frequent acceleration under CHTC. In addition, Acceleration driving condition contributed most to the deterioration of fuel consumption, CO, HC and NOx emissions under CHTC, which attention should be especially paid in the further vehicle calibration.

1. Introduction

The coach is a kind of heavy-duty commercial vehicle which is used passenger transport among cities, towns and villages. In 2018, sales quantity of coach is up to 84420 units, which accounts for 42.5% of the overall sales quality of coach, public bus and school bus [1]. Furthermore, the fuel consumption and exhaust emitted accounts for a large proportion of the whole vehicle transportation due to its large curb weight and long driving distance. Therefore, the energy conservation and emission reduction of the coach cannot be ignored.

In current Chinese standard (GB/T 27840 and GB 17691), C-WTVC is the test cycle used for evaluating the fuel consumption and emission characteristics of the heavy-duty commercial vehicle [2-3]. Because that C-WTVC was developed according to the diving data in Europe, US and Japan [4], it was difficult to reflect the real driving characteristics of China resulting in the gaps of fuel consumption and emission levels between the real-road and regulation test. To solve this problem, China's Ministry of Industry and IT (MIIT) introduced China automotive test cycle (CATC) series in 2018 which was developed according the three years' real-road driving data of more than 5000 vehicles in 41 Chinses cities.

CATC series is divided into light-duty (CLTC) and heavy-duty commercial vehicle test cycles (CHTC). The CHTC series include 6 test cycles which are defined as bus test cycle (CHTC-B), coach test cycle (CHTC-C), light truck test cycle (CHTC-LT), heavy truck test cycle (CHTC-HT), tractor-trailer test cycle (CHTC-TT) and dumper test cycle (CHTC-D). CHTC series will be replace C-WTVC in GB/T 27840 and GB 17691 in a round 2020.

The replacement of the test cycle will certainly affect the measuring result of the fuel consumption and emission, so that research on the results comparison under different test cycles is well needed for further vehicle's development and calibration. In this paper, the fuel consumption and emission characteristics of a China VI coach under different test cycles have been discussed and compared.

2. Test apparatus and methods

2.1. Test vehicle

The test vehicle used in this investigation was a 9m coach which reached the China VI emission standard and the specifications have been summarized in Table 1. During the test, the vehicle load was set as 100%, and the total vehicle mass was 13000kg.

Table 1. Vehicle specification.

Parameters	Value
Length*width*height(mm)	8995*2500*3410
Curb weight(kg)	9800
Maximum design total mass(kg)	13000
Engine rated power(kW/rpm)	199/2100
Enigne maximum torque(N.m/rpm)	1000/1200~1700
Gear	6 Manual
Gear ratio	6.4/3.7/2.2/1.4/1.0/0.7

2.2. Diving cycle

In this paper, two driving cycles have been used in the tests, one was the C-WTVC and the other was CHTC-C and both cycles were divided into low, medium and high velocity parts, as shown in Figure.1.

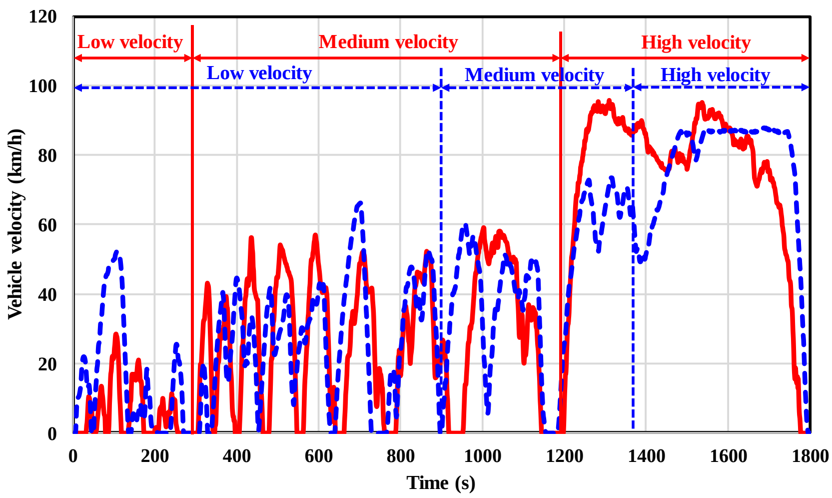

Figure 1. CHTC-C (red solid) and C-WTVC (blue dashed) test cycles.

The fuel consumption and emission results of the coach under C-WTVC were calculated by each part's value with weighing coefficients of 0.1 (low), 0.2 (medium), and 0.7 (high). The results of CHTC-C did not need the weighing calculation of each part. In addition, the main parameters of these two test cycles including driving duration, driving distance, average velocity etc. have been listed in Table.2 and of which Idling, constant, acceleration and deceleration driving conditions were defined in Table 3.

Results showed that the mean velocity of CHTC-C was lower than the C-WTVC (coach) although with a higher maximum velocity. Either the absolute value of maximum or mean acceleration/deceleration of CHTC-C was higher than C-WTVC (coach), which indicated a more aggressive driving style in China.

Table 2. Comparison of the main parameters of CHTC-C and C-WTVC (coach).

Main Parameters	CHTC-C	C-WTVC (coach)*
Driving Duration (s)	1800	485.5
Driving distance (km)	19.62	8.07
Max. velocity (km/h)	95.70	87.80
Mean velocity (km/h)	39.24	59.79
Max. acceleration (m/s^2)	1.25	0.87
Mean acceleration (m/s^2)	0.43	0.33
Min. deceleration (m/s^2)	-1.28	-1.00
Mean deceleration (m/s^2)	-0.48	-0.46
Iding condition (%)	18.22	5.24
Constant conditon (%)	33.00	59.88
Acceleration condition (%)	26.22	16.29
Deceleration condition (%)	22.56	18.59

* C-WTVC (coach) was the C-WTVC after weighted with weighing coefficients of 0.1 (low), 0.2 (medium), and 0.7 (high).

Table 3. Definition of Idling, constant, acceleration and deceleration driving conditions

Conditon	Acceleration (m/s2)	Velocity (m/s)
Iding condition	$-0.15 \leq a \leq 0.15$	$v<1$
Constant conditon	$-0.15 \leq a \leq 0.15$	$v \geq 1$
Acceleration condition	$a>0.15$	-
Deceleration condition	$a<-0.15$	-

The proportion of each driving condition presented that the proportions of CHTC-C's idling condition, acceleration and deceleration condition were all higher than C-WTVC (coach) resulting in a nearly 50% decrease of the proportion of constant condition compared to C-WTVC (coach).

2.3. Test system

The test system in this study consisted of heavy-duty chassis dynamometer, fuel consumption instrument, exhaust gas analyzer (HORIBA MEXA-7200DTR) and CAN analyzer. The exhaust gas analyzer was used to measure the vehicle's transient emissions of CO, HC and NOx, and CAN analyzer was used to monitor the rotation speed and output torque ratio of the diesel engine.

3. Results and discussion

3.1. Distributions of diesel engine operating points under different test cycles

To clearly explain the variations of fuel consumption and emission characteristics between these two cycles, the diesel engine operating points were compared first as shown in Figure.2.

Results showed that most of the operating points under CHTC-C were concentrated in the low rotation speed and low torque region (35.61%). While operating points under C-WTVC (coach) were concentrated not only in low rotation speed and low torque region (14.93%) but also the high rotation speed region (34.22%). The mean values of rotation speed and torque ratio under these two test cycles, as the yellow pots shown, also indicated that the distribution of the operating points under CHTC-C tend to the low rotation speed and low torque ratio region. This was mainly due to the higher idling condition proportion and lower mean velocity of the CHTC-C. It worth noting that operating points with high torque ratio (>80%) only appeared under CHTC-C, which was because of the higher output torque requirement due to both higher velocity and acceleration values.

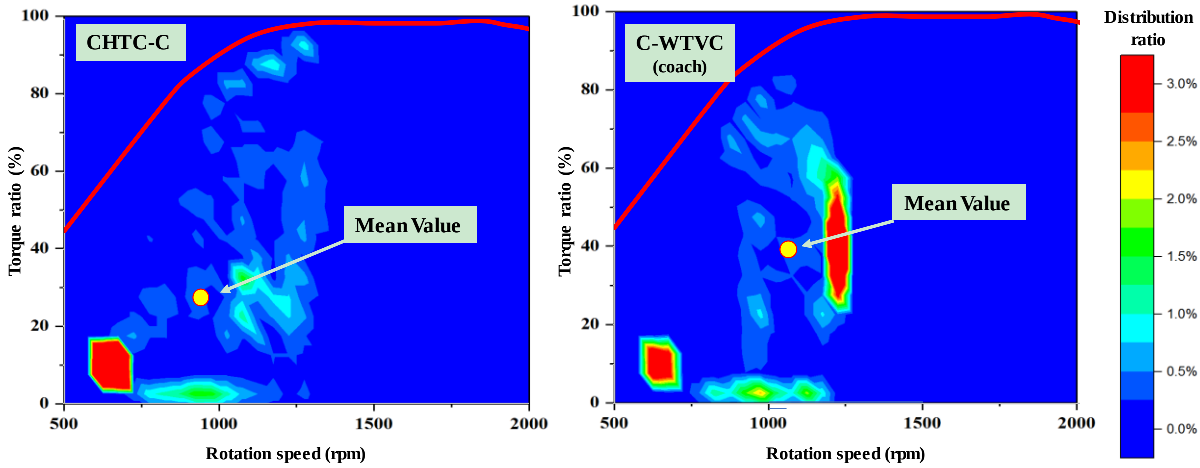

Figure 2. Diesel engine operating points under CHTC-C and C-WTVC (coach) test cycles.

3.2. Fuel consumption and emission characteristics under different test cycles

Figure.3 showed the fuel consumption and emission characteristics of the test coach under different test cycles. Results indicated that fuel consumption rate under CHTC-C were higher than C-WTVC (coach), 7.71%. For emission characteristics, all kinds of the emissions were higher under CHTC-C. The values of CO, HC and NOx emissions under CHTC-C increased 9.88%, 39.01% and 23.41% than C-WTVC's results, respectively.

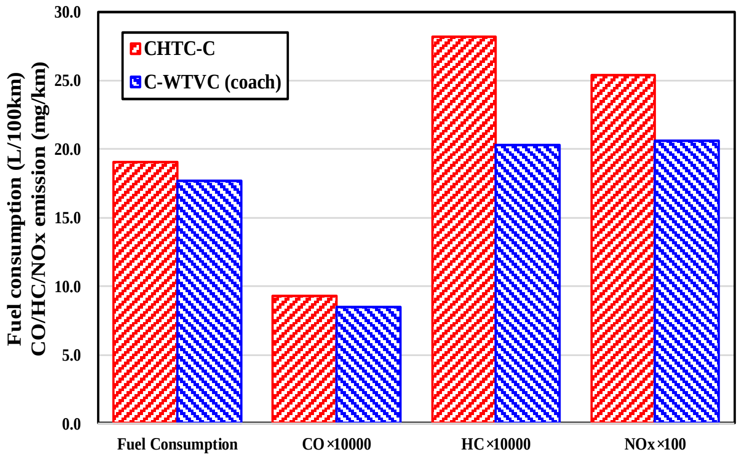

Figure 3. CHTC-C and C-WTVC (coach) test cycles.

The higher fuel consumption rate under CHTC-C could be attributed to the low rotation speed and low torque ratio distribution of the diesel engine operating points, which was away from the high efficiency region. Besides, higher acceleration value and proportion also caused more incomplete combustion of the injected fuel resulting in higher fuel consumption.

The mass generation of CO was due to either low combustion temperature or rich fuel-air mixture. The low rotation speed and low torque ratio distribution resulted in lower combustion temperature, and higher acceleration value and proportion led the rich fuel-air mixture distributed in the cylinder. These all increased the CO emissions under CHTC-C.

HC emissions was generated because of the insufficient fuel-air mixing and quenching, which was often occurred when vehicle accelerating. So, the higher acceleration value and proportion of CHTC-C were the main reasons caused the increase of HC emissions.

The increase of NOx emission under CHTC-C was mainly attributed to two reasons, one is the higher in-cylinder caused for the frequent acceleration, the other was the low convert efficiency of the SCR system due to the lower exhaust temperature which was related to the low rotation speed and low torque ratio operating point distribution.

3.3. Fuel consumption and emission share ratios of each driving condition under different test cycles
In this paper, the concept of share ratio was introduced to investigate the contribution of each driving conditions to the overall fuel consumption and emission, which was defined as the percentage of fuel consumption or emission gross under one driving condition (idling, constant, acceleration or deceleration condition) to the gross under the whole test cycle. The comparison of the share ratio of each driving condition under different test cycles was given in Figure.4

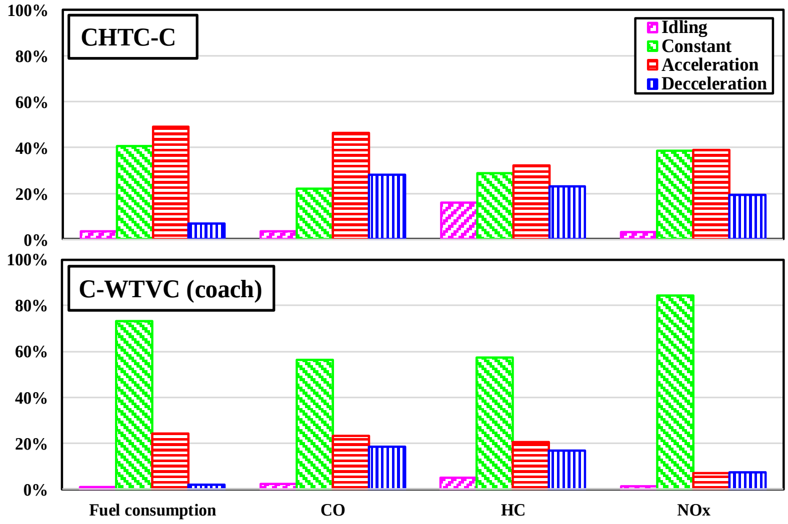

Figure 4. Fuel consumption and emission share ratios of each driving condition under different cycles.

Results showed that the share ratio of acceleration condition to the fuel consumption and overall emissions was the highest under CHTC-C, while was the constant condition under C-WTVC (coach). This was mainly attributed the difference of the driving condition proportions between these two cycles. To eliminate this effect, the share ratios were divided by duration of each corresponding driving condition, as shown in Figure.5.

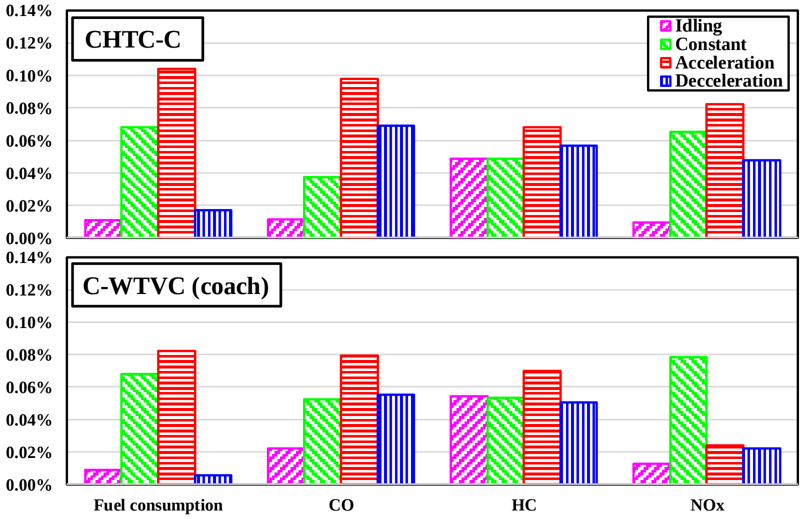

Figure 5. Fuel consumption and emission share ratios per second of each driving condition under different cycles.

From the values of fuel consumption and emission share ratio per second, it indicated that acceleration condition contributed most to the fuel consumption, CO emission and HC emission under both CHTC-C and C-WTVC (coach). Moreover, the values under CHTC-C were generally higher than C-WTVC (coach), which was because of the more aggressive acceleration driving styles of CHTC-C. The difference of the most contribution driving condition to NOx emission between these two cycles showed that higher acceleration was the main reason caused NOx generation under CHTC-C, while higher in-cylinder temperature caused by higher average velocity of the constant condition was the reason under C-WTVC (coach).

4. Conclusion

In this paper, the fuel consumption and emission characteristics of a China VI coach under CHTC-C and C-WTVC (coach) have been discussed and compared. The conclusion can be reached as the following.

1. The distribution of the diesel engine operating points under CHTC-C tend to the low rotation speed and low torque ratio region compared with C-WTVC (coach), and the operating points with high torque ratio (>80%) only appeared under CHTC-C.
2. The higher fuel consumption, CO, HC, and NOx emissions was obtained under CHTC-C, which were due to the low rotation speed and low torque operating points, and the aggressive and frequent acceleration.
3. Acceleration driving condition contributed most to the deterioration of fuel consumption, CO, HC and NOx emissions under CHTC, which attention should be especially paid in the further vehicle calibration

5. References

[1] http://www.find800.cn/c/2019/0123/70/121984.html.
[2] Fuel Consumption Test Methods for Heavy-Duty Commercial Vehicles (GB/T 27840-2011) 2011 Standardization Administration of China
[3] Limits and Measurement Methods for Emissions from diesel fuelled heavy-duty vehicles (CHINA VI) (GB 17691-2018) 2019 Ministry of Ecological Environment of China
[4] Chen L, Wang Z, Liu S and Qu L Using a chassis dynamometer to determine the influencing factors for the emissions of Euro VI vehicles 2018 *J Transportation Research Part D: Transport and Environment* **65**:564-73.

Acknowledgments

This study is supported by the National Key R&D Program of China (2018YFB0106402) and Research and Development of Chinese New Energy Automobile Products Test Driving Cycles (CATC).

IOP Conf. Series: Earth and Environmental Science **431** (2020) 012063 doi:10.1088/1755-1315/431/1/012063

Possible application of solar steam regeneration method in absorption air-conditioning system

YL Wu[1], F Cheng[1] and XW Li[1]

1 College of Power Engineering, Nanjing University of Science and Technology, Nanjing 210094, China
E-mail: good3000best@163.com

Abstract. In recent years, solar absorption air-conditioning system have become an important directions of solar energy utilization. Improving solar energy utilization efficiency can effectively solve the problems of energy crisis. In traditional thermal method, low efficiency suffer from the heat loss and the cost is expensive. To improve solar energy utilization efficiency, a solar steam regeneration method was proposed: with corresponding material structure that can locate solar energy in the event of evaporation and minimize heat loss. The material structure has a high absorption in the solar spectrum, thermally insulating, hydrophilic surfaces and interconnected pores which allows the fluid flow to and from the structure. The solar steam regeneration method can be used in solar absorption air-conditioning system. Models have been developed and some important parameters have been investigated. The influence of concentration and absorbent variety has been analyzed in the experiments. Preliminary testing of the evaporation process has been carried out. It found the solar energy utilization efficiency with solar steam method has potential to further increase by 2 or 3 times. The solar energy utilization efficiency of the solar steam regeneration system approached 46%. That indicates it a promising choice for solar desalination and absorption system.

1. Introduction

In the conventional method, solar energy usually heats the bulk liquid to a quite high temperature to generate water steam [1]. Low efficiency and the requirement for high optical concentration limit the utilization of solar energy. Recently, Chen et al have proposed a solar steam method to improve the efficiency of solar energy utilization for steam generation [2]. The method uses photo-thermal materials to localize the solar heat in the evaporation surface and thus decreases the thermal loss to bulk water [3]. It can improve solar thermal efficiency at low optical concentration in open air while generating steam [4].

At present, researches on the solar steam method mainly focused on exploring materials with high absorption in the solar spectrum [5]. There are no studies on absorbent solutions. This paper presents propose a solar steam method based absorption air-conditioning system. We have analyzed and discussed the regeneration process of three common absorbents in theory. Experiments have been made to test the regeneration rate of water for different absorbent solutions. The results show solar steam method can greatly improve the thermal efficiency at lower optical concentration. The experimental solar energy utilization efficiency of solar steam method based absorption system increase exponentially.

2. Materials and methods

2.1. Principle of the solar steam method

The original idea about solar steam method was first proposed by a research group led by Chen in 2014 [2]. Its core is to achieve thermal heating localization. With photo-thermal materials, solar heat will gather on the evaporation surface, which can reduce the heat loss and improve the energy utilization efficiency. This photo-thermal structure demands four characteristics: high absorption in the solar spectrum, thermally insulating, hydrophilic surfaces and interconnected pores which allows the fluid flow to and from the structure. Figure 1 shows the schematic diagram [6]. The porous structure serves as the light absorber; the cellulose wrapped expanded polyethylene foam serves as the thermal insulation. When the structure is illuminated by sunlight, the upper surface will efficiently convert the absorbed light into localized heat. Then the surface water will evaporate and rapidly escape into the air. This method can bring high thermal efficiency and produce high temperature vapor under the same optical concentration.

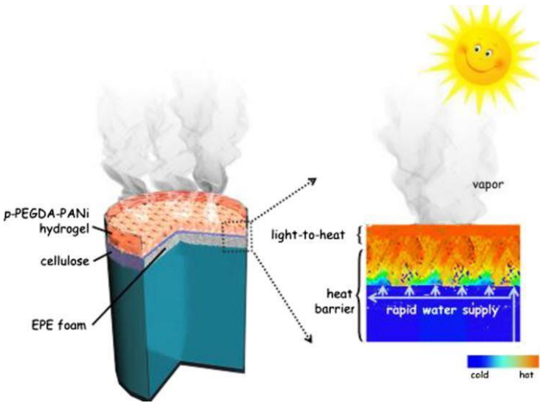

Figure 1. Schematic diagram [6].

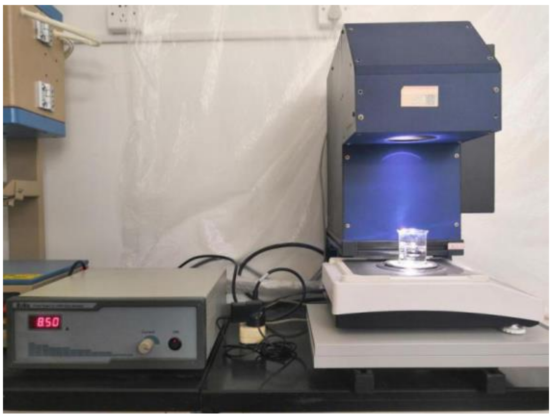

Figure 2. Experimental system.

2.2. Experimental system of the solar steam regeneration method

Figure 2 presents the configuration of the experimental platform. Three different absorbents are used in the experiment. We chose carbonized cunninghamia as the photo-thermal material. After treatment, the wood showed ultra-high absorptivity, low thermal conductivity, self-floating properties and high solar thermal efficiency [7]. Cunninghamia has good corrosion resistance and mechanical strength.

2.3. Performance estimation of the solar steam system

The solar energy utilization efficiency η of the whole system is:

$$\eta = \frac{Q_0}{G} = \frac{lm_a}{PS} \tag{1}$$

where l is the latent heat of water vaporization. P is the power density of solar illumination. S is the area of the material illuminated by sunlight.

By applying Eq. (1), we can analyze the utilization efficiency of the system.

2.4. Theoretical analysis of the solution regeneration

With the water vapor evaporating, the solution concentration becomes larger. It will inhibits the regeneration process. To maintain a same evaporation rate, it is necessary to consider increasing the solution temperature. One conception of the heating localization in the solar steam regeneration process is to reduce the liquid bulk to be heated. This measure can reduce the total energy provided to raise the liquid to a certain temperature. But actually, the less liquid leads to faster evaporation and faster concentration; so more energy must be provided to heat the solution to a higher temperature for maintaining the evaporation speed. Is the final result increased energy consumption or energy savings during the solar steam regeneration process?

Taking LiCl solution as an xeample, we first calculate the vapor pressure of LiCl solution of certain concentration, amount and temperature. The relative vapor pressure π can be calculated as [8]:

$$\pi \equiv \frac{p_{sol}(\xi, T)}{p_{H_2O}(T)} \tag{2}$$

p is the vapor pressure, ξ is the mass fraction of solute, T is the absolute temperature.

$$c_{p_{sol}}(T,\xi) = c_{p_{H_2O}}(T) \times (1 - f_1(\xi) \times f_2(T)) \tag{3}$$

$c_{p\,H2O}$ is the specific thermal capacity of water, c_{psol} is the specific thermal capacity of solution.
The energy consumed Q by heating the absorbent solution is：

$$Q = c_{p_{sol}} m_{sol} \Delta T \tag{4}$$

m_{sol} is the amount of the solution. ΔT denotes the temperature increase of the solution.

3. Results and discussion

3.1. Theoretical results of solution regeneration

Taking 500g of LiCl solution as an example. The initial solution temperature is 25℃ and heate it to 70℃. Here we take different percentages of the solution to calculate the concentration and vapor pressure. The vapor pressure of LiCl solution in 70℃ are displayed in Figure 3 (a). As it shows: the vapor pressure in 70℃ increases from 6.4898KPa to 16.7419KPa; Con_{LiCl} decreases from 41.7% to 28.5%. With the increases of concentration, the energy consumed Q_1 by heating the solution decreases from 5.6512KJ to 5.0814 KJ.

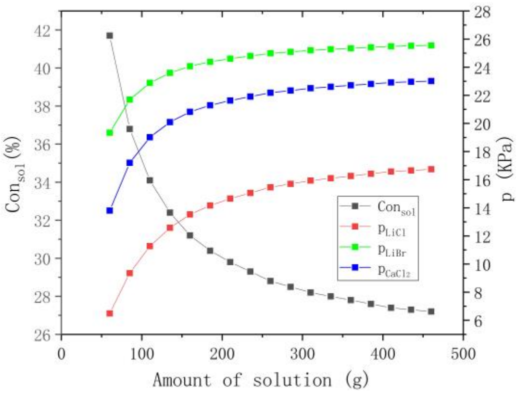

(a) The concentration and vapor pressure at 70℃

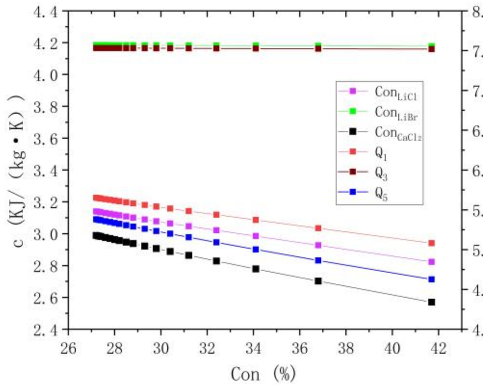

(b) The specific thermal capacity and energy consumed

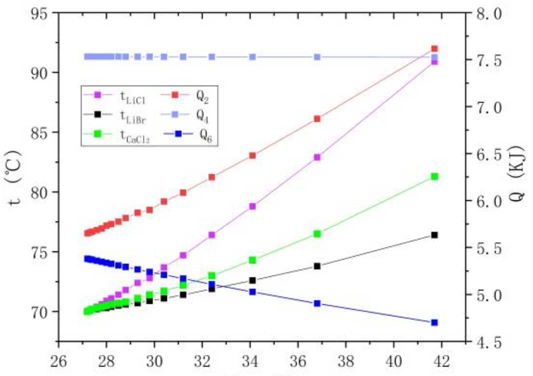

(c) The energy consumed and temperature

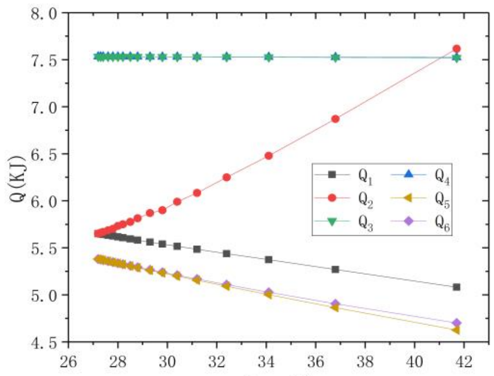

(d) The comparison of energy consumption

Figure 3. Theoretical results of different solutions.

IOP Conf. Series: Earth and Environmental Science **431** (2020) 012063 doi:10.1088/1755-1315/431/1/012063

To maintain the same regeneration speed, the solution must be heated to a higher temperature. Suppose the vapor pressure of different concentrations of LiCl solution is 16.7419KPa. Figure 3 (c) shows the temperature rises from 70℃ to 90.9℃ as Con_{LiCl} increases from 27.2% to 41.7%. The energy consumed Q_2 increases from 5.6512KJ to 7.6162KJ. Figure 3 (d) shows Q_1 is less than Q_2 for the same concentration. The difference between Q_1 and Q_2 enlarges as Con_{LiCl} increases. That indicates heating LiCl solution with smaller liquid body increased the total energy consumption. Similarly, the results of LiBr solution are shown in Figure 3. When heating LiBr and $CaCl_2$ solution with smaller liquid body achieve a final energy saving effect.

3.2. Experimental results

Figure 4 (a) shows the evaporation rate of LiCl solution. The evaporation rate based on the solar steam method rapidly increased in the first ten minutes, then it tended towards smoothly. Comparatively, the evaporation rate without the solar steam method had no distinct change. The evaporation rate based on the solar steam method is greater. Compared with the rate without the method, it had been raised by 260 percent. Figure 4 presents the evaporation rate with different concentrations. The evaporation rate of water kept on decreasing as Con_{LiCl} increased from 20% to 35%.

The comparison between the theoretical and experimental results are shown in Figure 5. Figure 5 (a) reveals the experimental evaporation rates. Figure 5 b presents the change law of the theoretical vapor pressure. The solution vapor pressure determines the evaporation rate. The trend of the change of the evaporation rate is correspondent with that of the theoretical vapor pressure. That indicates the theoretical analysis results are in good agreement with the experimental results.

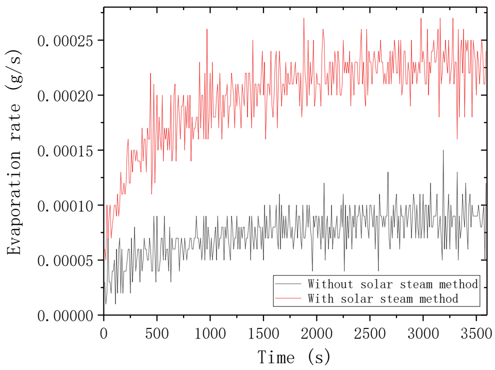

(a) Con_{LiCl} is 20%

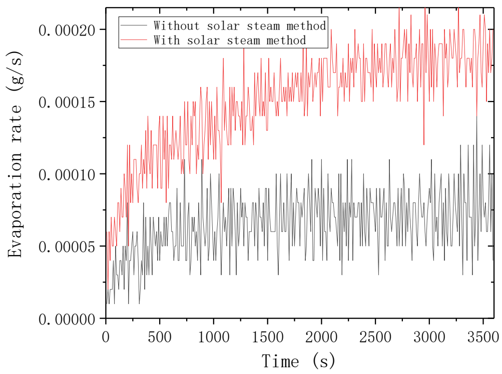

(b) Con_{LiCl} is 25%

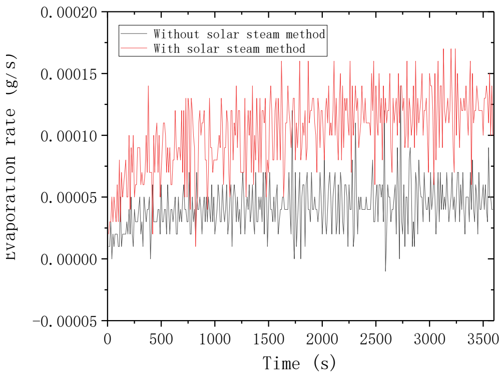

(c) Con_{LiCl} is 30%

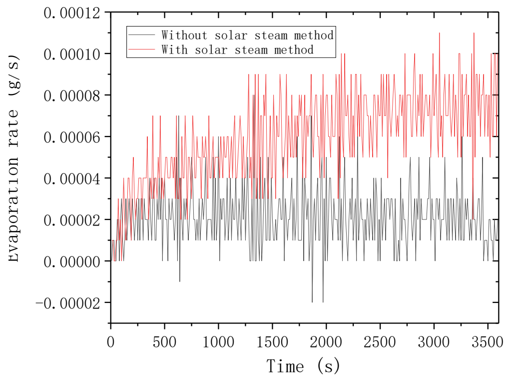

(d) Con_{LiCl} is 35%

Figure 4. The evaporation rate of LiCl solution with different concentrations.

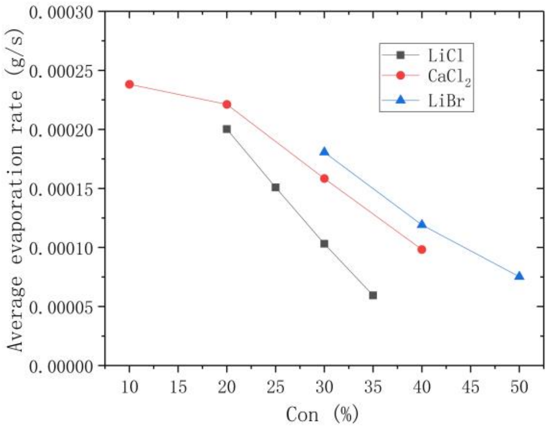

(a) Experimental evaporation rates

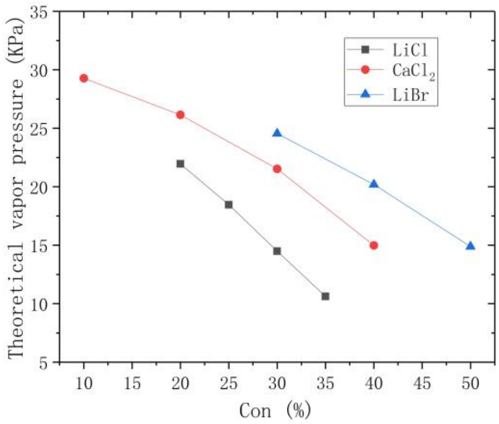

(b) Theoretical vapor pressure

Figure 5. Comparison of the theoretical and experimental results.

3.3. Solar energy utilization efficiency of the absorption system based on the solar steam method

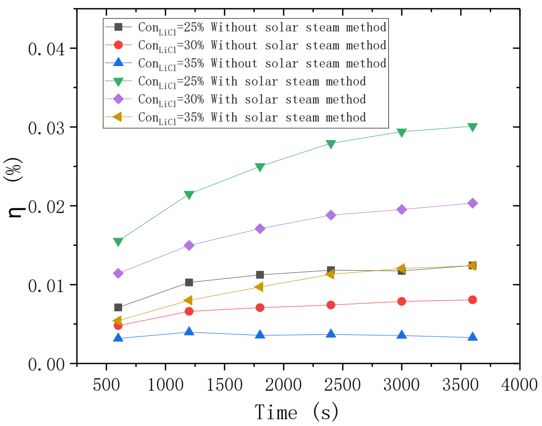

Figure 6. Solar energy utilization efficiency.

Figure 6 shows the solar energy utilization efficiency of LiCl solution. It can be found the solar energy utilization efficiency keeps increasing at the beginning. The solar energy utilization efficiency decreases with the increasing concentration. The maximum value reaches 30.1% and the average is 24.9%. The average value of the solar energy utilization efficiency is only 9.8% when Con_{LiCl} is 35%.

3.4. Discussion
The solar steam based system uses photo-thermal materials to achieve thermal heating localization. This manner can decrease the thermal loss to bulk water and achieve high efficiency steam generation. Cost is another advantage of the solar steam based system. The core of the absorption system is fabricated by a low-cost and ordinary materials. Solar energy utilization efficiency will decrease as the increases of the concentration.

4. Conclusions
The solar steam method based absorption system has many good features of the traditional solar absorption system. Moreover, the use of photo-thermal materials reduces the initial investment and maintenance cost. Primary experimental researches have exposed the new method can greatly increase the evaporation rate of solution at lower optical concentration. The solar energy utilization efficiency of LiCl solution reaches 30.1%. The experimental solar energy utilization efficiency is between 10%

and 40% under different solution concentrations. The solar energy utilization efficiency with the solar steam method increases by 2 or 3 times. The solar energy utilization efficiency is higher with lower absorbent solution concentration.

5. References

[1] Zhong JX, Huang CL and Wu DX 2019 *J. Int. J. Heat Mass Transf*. **128** 860-864.
[2] Ghasemi H, Ni G, Marconnet A M and Loomis J.2014 *J. Nat. Commun*. **5** 4449.
[3] Xue G, Liu K and Chen Q 2017 *J. ACS. Appl. Mater. Inter*. **15** 15052-15057.
[4] Yin Z, Wang H and Jian M 2017 *J. ACS. Appl. Mater. Inter*. **9** 28596-28603.
[5] Zhu MM, Yu JL, Ma CL and Zhang CY 2019 *J. Sol. Energy Mater. Sol. Cells*. **191** 83-90.
[6] Yin X, Zhang Y, and Guo Q 2018 *J. ACS. Appl. Mater. Inter*. **10** 10998-11007.
[7] Zhu M, Li Y and Chen F 2018 *J. Adv. Energy Mater*. 1701028.
[8] Conde M R 2004 *J. Int J Therm Sci*. **43** 367-382.

Acknowledgements

This research was supportted by the fund of National Natural Science Foundation of China under the contract No. 51676098. It was also supported by the grants from the fund of Natural Science Foundation of Jiangsu Province under the contracts No. BK20170095 and No. BK20160822. These supports are gratefully acknowledged.

IOP Conf. Series: Earth and Environmental Science **431** (2020) 012058 doi:10.1088/1755-1315/431/1/012058

Research on the working medium of the absorption air-conditioning system with a new regeneration method

YH Li[1], F Cheng[1] and XW Li[1]

1 College of Power Engineering, Nanjing University of Science and Technology, Nanjing 210094, China
E-mail: good3000best@163.com

Abstract. To be environmentally friendly and save energy, absorption air-conditioning system is a good attempt. However, plenty of heat waste in the regeneration limits its performance. For further application, the capacitive deionization (CDI) regeneration method has been proposed which works between the electrode pairs of the capacitor to achieve the interconversion between water and solution. Previous work shows the theoretical COP of the new system could reach up to 6 under certain conditions. Different absorbents have been calculated and experimented in this paper to find a most suitable absorbent to approach the highest possible COP. Different concentrations also has been considered. It is found that the COP of the CDI based system can attain 2 to 3. Experimental results agree well with theoretical results of the tendency of the system performance among different absorbents and different concentrations. There is some difference of the COP because the energy recovery rate in our experiment can not approach 50% which is calculated at 50% theoretically. In practical applications, the COP could be higher with energy recovery of CDI.

1. Introduction

The concepts and technologies of sustainable development of energy, water and environment have been discussed in many researches [1]. In the last decades, the energy consumption of buildings takes up more than 40% of the global energy consumption [2]. The energy supply of air-conditioning system account for 1/3 in buildings [3]. The conventional vapor compression system leads to some environmental problems, such as ozonosphere hole [4]. Absorption air-conditioning system is a good tempt, which can be supported by renewable energy and use water as refrigerant [5].

To improve COP, a capacitive deionization (CDI) method for absorption system has been proposed in our research: strong absorbent solution and pure water are acquired with the joint work of two CDI units so that the deionization and regeneration processes are completed between the electrode pairs of the capacitor [6]. The energy recovery ability of the capacitor has a great benefit to improve the system performance [7]. However, there is only theoretical result while the actual performance of the CDI based absorption system has not been tested [6]. So the paper researches on the theoretical analysis and practical experiment to test the actual performance of the system with different absorbents.

2. Materials and methods

2.1. Principle of the capacitive deionization regeneration system

Figure 1 is the principle of the capacitive deionization and regeneration process. In the deionization process, charging the electrodes, the ions in the salt water will move to the electrodes driven by the electric field force. We can acquire deionized water in the exit. As for regeneration step, along with canceling the electric supply, the original electric field will disappear so that the ions will release to the deionized water to get salt water again. In this way, using two CDI units, the deionization and regeneration processes can happen at the same time. With this method, the generator and absorber in the traditional absorption system can be instead. The other part of the system is the same with traditional system.

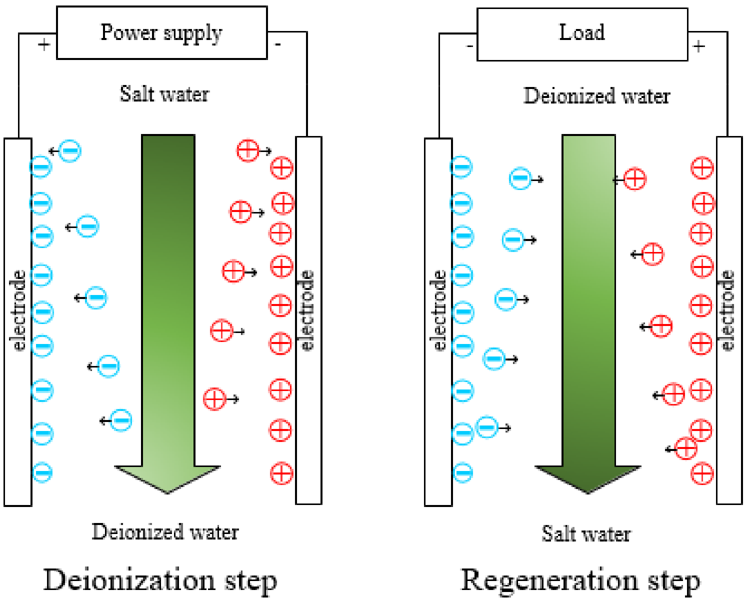

Figure 1. Principle of the capacitive deionization process.

2.2. Mass and energy models of the CDI regeneration process

In the absorption process, assume the mass of the absorbent solution flowing into the absorber per second is m_{ia}. The concentration of the solution is Con_{ia}. And the mass of the deionized water at the outlet of the absorber is m_{oa}. The concentration of it is Con_{oa}. Δm_w is the mass flow rate of the absorbed water vaper. In the regeneration process, m_{ir} is the mass flow rate of the absorbent solution flowing into the regenerator. Con_{ir} is the concentration of it. m_{or} is the mass flow rate of the regenerated solution at the outlet of the regenerator. The concentration is Con_{or}. Δm_s is the amount of the ions released from electrodes. Con_{ia} and Con_{or} are equal; Con_{oa} and Con_{ir} are equal. The mass balance equations are:

$$m_{ia} + \Delta m_w = m_{oa} \quad (1)$$

$$m_{ia}Con_{ia} = m_{oa}Con_{oa} \quad (2)$$

$$m_{ir} + \Delta m_s = m_{or} \quad (3)$$

$$m_{ir}Con_{ir} + \Delta m_s = m_{or}Con_{or} \quad (4)$$

As for the energy supply to the deionizer, there's the equation between Δm_s and current:

$$\frac{\Delta m_s}{M_s} = \frac{\lambda I}{zF} \quad (5)$$

λ is the charging efficiency. P_{de} is the energy demand. U is the supplied voltage. The total energy need for the CDI based system (P_{CDI}) is:

$$P_{CDI} = P_{de} - P_{rec} \quad (6)$$

The COP of the CDI based system is:

$$COP = \frac{Q_0}{P_{CDI}} = \frac{l_w \Delta m_w}{P_{de} - P_{rec}} = \frac{l_w \Delta m_w}{(1-\eta) P_{de}} = \frac{l_w \Delta m_w}{\frac{zF \Delta m_s U}{\lambda M_s}(1-\eta)} = \frac{l_w (1 - Con_{or}) \lambda M_S}{zFU(1-\eta) Con_{or}} \tag{7}$$

2.3. Experimental system

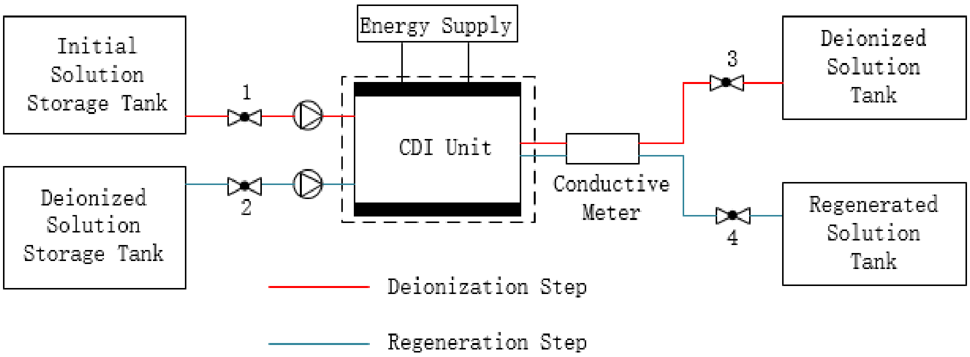

Figure 2. Simplified circuit of the experimental system.

We have designed a system to test the deionization and regeneration process. Figure 2 shows the simplified circuit of it First, open valves 1 and 3. The initial solution with certain concentration flows through the CDI unit driven by the pump with energy supply. The absorbed solution flows out is stored in the Deionized Solution Storage Tank. When the number displayed by the conductive meter is stable, it means the absorption ability of the CDI unit approach its highest limitation. Previous work finds the process lasts for 20 minutes. Then close valves 1 and 3 and open 2 and 4. Power off the CDI unit. The deionized solution flows through the unit. We can get regenerated solution at the outlet and store it in the Regenerated Solution Storage Tank.

3. Results and discussion

3.1. Theoretical performance of the CDI based system

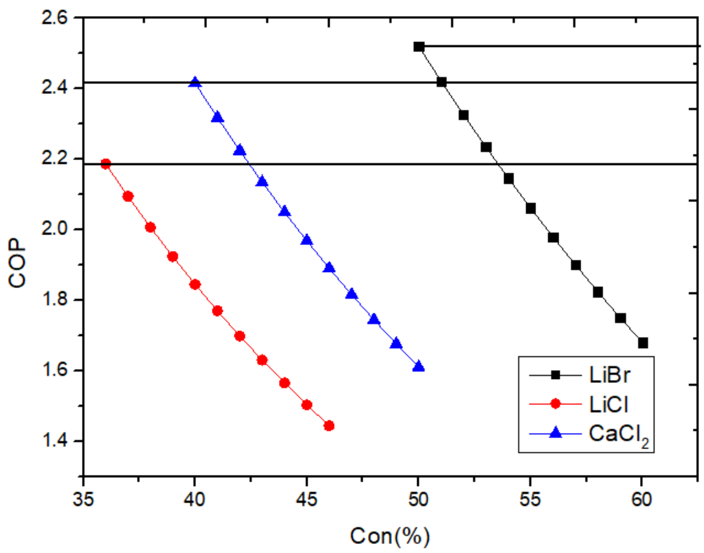

Figure 3. Theoretical COP of different absorbent systems.

With Eq. (7), COP can be calculated and the performance can be analyzed with different absorbents. Figure 3 presents the COP with different absorbents. COP changes along with the concentration of the regenerated solution. And the COP is higher with lower concentration. Because, the solution with low concentration doesn't need so much solutes added to it and reduce the energy demand in the absorption process. Within their respective working concentration ranges, the system COP with LiBr is the highest, which can reach 2.5. The COP with $CaCl_2$ is second, which is between 1.6 and 2.4. COP with LiCl is the last one, but it still can approach 2.18. The COP of the CDI based system with four absorbents is all better than traditional absorption air-conditioning system.

3.2. Experimental results

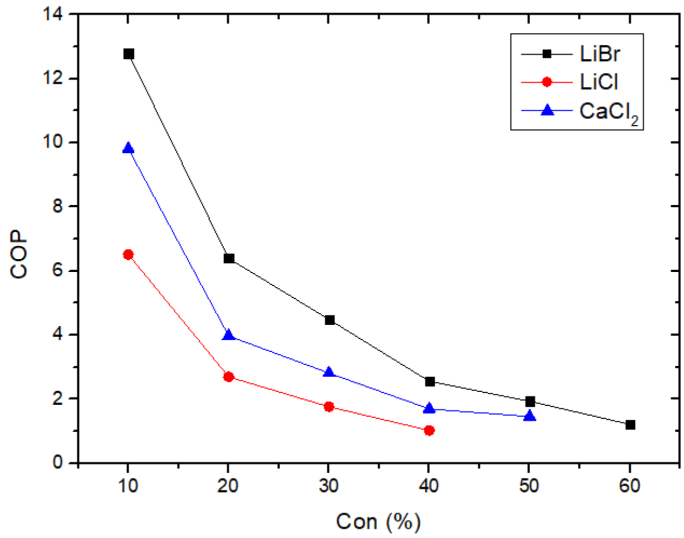

Figure 4. Experimental performance of different absorbent systems.

We can get the COP of the three systems, which are shown in Figure 4. The energy consumption of LiBr system is the highest, but its performance is still the best because its salt regeneration capacity is significantly higher than others. The COP of $CaCl_2$ system is also good because its salt regeneration capacity and energy consumption both are at a good level. According the usual working concentration of absorbents in traditional air-conditioning, LiBr system has the best performance in our experiment, which can approach above 2. It is a little lower than the theoretical result, but still higher than traditional system.

3.3. Discussion

CDI based system is a good alternative to improve the performance of absorption air-conditioning. Compared with traditional absorption system, it avoids the heat waste during the regeneration process and reduces the electric demand. Activated carbon is the widely used material of electrodes, which only costs about 0.89 dollars/m^2. It is very cheap. The most importantly, CDI based system has better performance. In our experimental system, the COP can reach up to 2. The energy recovery ability is a large advantage. By changing the electrode material and completing the energy recovery model, the energy recovery ability can be improved to get high COP of the system.

4. Conclusion

CDI based absorption system has been proposed to improve the performance. It has big advantages compared to the traditional absorption system. Some theoretical analyses have been carried out before. However, there is few experiment on the specific performance with different absorbents. So theoretical and experimental researches of different absorbents (LiBr, LiCl and $CaCl_2$) have been done in this paper.

According to the mass and energy model, the theoretical performance of different absorbents has been acquired. It is found that all the systems with the four absorbents have good performance. COP of LiBr system is the highest, which can attain 2.5 with 50% energy recovery ratio. It is worth mentioning that it can be much higher due to the energy recovery ability. Although the other three absorbent systems are not as good as LiBr system, their COP can also reach 2 in certain working conditions.

Experiments have been made to test the actual performance among different absorbent systems. The results show that previous theoretical results have certain reliability. With our experimental facility, LiBr system still has the highest salt regeneration capacity and COP, which can approach 1.94 under its usually worked concentration. While ensuring the ability to absorb water vapor in the absorber, properly reducing the concentration of the salt solution can increase the COP.

5. References

[1] Krajačić Gora, Duić Neven, and Vujanović, Sustainable development of energy, water and environment systems for future energy technologies and concepts 2016 *J. Energy Convers. Manag.* **125** 1-14

[2] Gao H, Kochb C and Wu YP, Building information modelling based building energy modelling: A review 2019 *J. Applied Energy*. **238** 320–43

[3] Ahmad A, Dadah R and Mahmoud S, Liquid Nitrogen energy storage for air conditioning and power generation in domestic applications 2016 *J. Energy Convers. Manag.* **128** 34-43

[4] Hou S, Li H and Zhang H, Open air–vapor compression refrigeration system for air conditioning and hot water cooled by cool water 2007 J. *Energy Convers. Manag.* **48(8)** 2255-60

[5] Ali Shirazia,b, Robert A Taylora and Graham L, Solar-powered absorption chillers: A comprehensive and critical review 2018 *J. Energy Convers. Manag.* **171** 59–81

[6] Li XW, Zhang XS, Wang H and Zhang Z, The potentials of capacitive deionization regeneration method for absorption air-conditioning system 2016 *J. Energy Convers. Manag.* **14**:303-311

[7] Zhao H, Zhang XS and Li XW, Research on actual performance and energy recovery characteristic of capacitive deionization regeneration method for absorption air-conditioning system 2018 J. *Energy Convers. Manag.* **171** 1549–59

Acknowledgments

This research was supportted by the fund of National Natural Science Foundation of China under the contract No. 51676098. It was also supported by the grants from the fund of Natural Science Foundation of Jiangsu Province under the contracts No. BK20170095 and No. BK20160822. These supports are gratefully acknowledged.

IOP Conf. Series: Earth and Environmental Science **431** (2020) 012059 doi:10.1088/1755-1315/431/1/012059

Hour-ahead photovoltaic power forecast using a hybrid GRA-LSTM model based on multivariate meteorological factors and historical power datasets

Biaowei Chen[1,2], Peijie Lin[1,2], Yaohai Lin[3], Yunfeng Lai[1,2], Shuying Cheng[1,2], Zhicong Chen[1,2], and Lijun Wu[1,2]

1 School of Physics and Information Engineering, and Institute of Micro-Nano Devices and Solar Cells, Fuzhou University, Fuzhou, China
2 Jiangsu Collaborative innovation Center of Photovoltaic Science and Engineering, Changzhou, China
3 College of Computer and Information Sciences, Fujian Agriculture and Forest University, Fuzhou, China
E-mail: linpeijie@fzu.edu.cn; yunfeng.lai@fzu.edu.cn

Abstract. Owing to the clean, inexhaustible and pollution-free, solar energy has become a powerful means to solve energy and environmental problems. However, photovoltaic (PV) power generation varies randomly and intermittently with respect to the weather, which bring the challenge to the dispatching of PV electrical power. Thus, power forecasting for PV power generation has become one of the key basic technologies to overcome this challenge. The paper presents a grey relational analysis (GRA) and long short-term memory recurrent neural network (LSTM RNN) (GRA-LSTM) model-based power short-term forecasting of PV power plants approach. The GRA algorithm is adopted to select the similar hours from history dataset, and then the LSTM NN maps the nonlinear relationship between the multivariate meteorological factors and power data. The proposed model is verified by using the dataset of the PV systems from the Desert Knowledge Australia Solar Center (DKASC). The prediction results of the method are contrasted with those obtained by LSTM, grey relational analysis-back propagation neural network (GRA-BPNN), grey relational analysis-radial basis function neural network (GRA-RBFNN) and grey relational analysis-Elman neural network (GRA-Elman), respectively. Results show an acceptable and robust performance of the proposed model.

1. Introduction

The consumption of energy is growing dramatically since the rapidly rhythm of human social activities. With the continuous consumption of fossil fuels such as coal, oil and natural gas, their extensive use has induced a significant global climate change. This environmental problem has become the focus of attention worldwide.

Over the past decades, in an increasing number of countries, such as the United States, Japan and China, the proportion of renewable energy in electrical market is increased dramatically. Among these renewable energies, solar photovoltaic (PV) power is one of the largest renewable energy resources on our planet, due to its benefits of being clean, inexhaustible and green. According to the REN21's 2019 report, in 2018, solar PV capacity additions were more than 100 GW for the first time, and the cumulative capacity reached 505 GW, an increase of 25% from 2017 [1]. However, like many other renewable energy sources., PV power depends highly on weather conditions. The instability of weather condition makes the output of PV power have strong randomness, fluctuations and intermittence. It not only brings big challenge to PV plant in electrical power dispatching and maintenance management, but also increases the cost of power generation. Therefore, these challenges should be urgently solved to enhance the inflexibility of PV plant.

Enhancing the prediction accuracy of PV power is a good way to improve the inflexibility of PV system [2]. Up to now, a good number of researches has been conducted to develop appropriate models in forecasting PV power generation with the targets of higher accuracy and minimum complexity with computational cost [3]. The time horizon of PV power forecast can be categorized as long-term (LT), short-term (ST), or very short-term (VST) [4]. The VST horizon is defined as several minutes to several hours. This kind of forecasting method would provide reference to unit commitment, scheduling, and dispatching of electrical power. In addition, it also enhances the security of grid operation [5]. The radical increase in the computer's power makes learning networks (LNs) based forecasting models always provide a more promising performance than physical methods and statistical approaches due to their potential abilities for data-mining and feature-extracting. Typical LNs applied in the studies of PV power forecast includes back propagation neural network (BPNN), radial basis function neural network (RBFNN), Elman neural network (Elman NN) and et al [6]. In addition, the numerical weather prediction (NWP) based prediction method has become the most popular research directions due to the higher accuracy and resolution of NWP [7]. In [8], based on multivariate meteorological factors and historical power datasets, the model applies grey relational analysis (GRA) algorithm and NWP meteorological information to select similar days as training-dataset, and the result shows the accuracy of day-ahead PV power forecasting has been improved.

It is clear that the forecasting accuracy of model as well as the cost of training-time can be improved by selecting datasets reasonably [9]. And GRA is an efficient algorithm to select the similarity time periods. In addition, the long short-term memory recurrent neural network (LSTM) also applied to handle time series forecasting task. In [10], the model applies LSTM to forecasting day-ahead solar irradiance, the merit of LSTM in time series task has been proved. However, the huge dataset dramatically increases the training time cost, which makes it unsuitable for VST PV power prediction. Thus, the GRA-LSTM hour-ahead PV forecasting method applies GRA to select the similar and optimal time periods of forecasting hour, and applies LSTM as LN to predict hour-ahead PV power generation output.

2. Architecture of the proposed model

2.1. Correlation between PV power output and input variables

The generation power of grid-connected PV power station is mainly related to the following factors: the meteorological factors, the working characteristics of PV module, the type and installation of PV cell. Due to the complexity of the inherent properties of grid-connected PV power plants, it is difficult to fully consider all the performance parameters in many practical engineering applications. However, in many studies [2,3,6,11], the importance of meteorological factors for PV generation have been proved. Thus, the $\rho_{x,y}$ is applied to analyze the influence of meteorological factors on the output power of PV power generation.

The $\rho_{x,y}$ is defined as follows:

$$\rho_{X,Y} = \frac{N\sum XY - \sum X \sum Y}{\left(N\sum X^2 - (\sum X)^2\right)^{1/2}\left(N\sum Y^2 - (\sum Y)^2\right)^{1/2}} \tag{1}$$

The Table 1 below shows the significance of different correlation values. And the Figure 1 represents the correlation of hourly PV power mean value (P_{mean}) with hourly typical meteorological mean value in different month, includes hourly mean value of air temperature (T_{mean}), hourly mean value of relative humidity (H_{mean}), hourly mean value of global horizontal radiation (G_{mean}) and hourly mean value of diffuse horizontal radiation (D_{mean}). In general, it can be seen that the correlation between different impact factors and PV output power change smoothly in different months. According to this, the proposed method applies these four factors as four vectors of the input eigenvector of training dataset. In addition, considering the ρ between G and P maintains in the highest level, the proposed model also selects G at every time point as the other vector of the input eigenvector.

Table 1. The significance of different correlation values

$\rho_{x,y}$ value	Significance
0.8-1.0	extremely strong correlation
0.6-0.8	strong correlation
0.4-0.6	medium correlation
0.2-0.4	weak correlation
0-0.2	very weak correlation

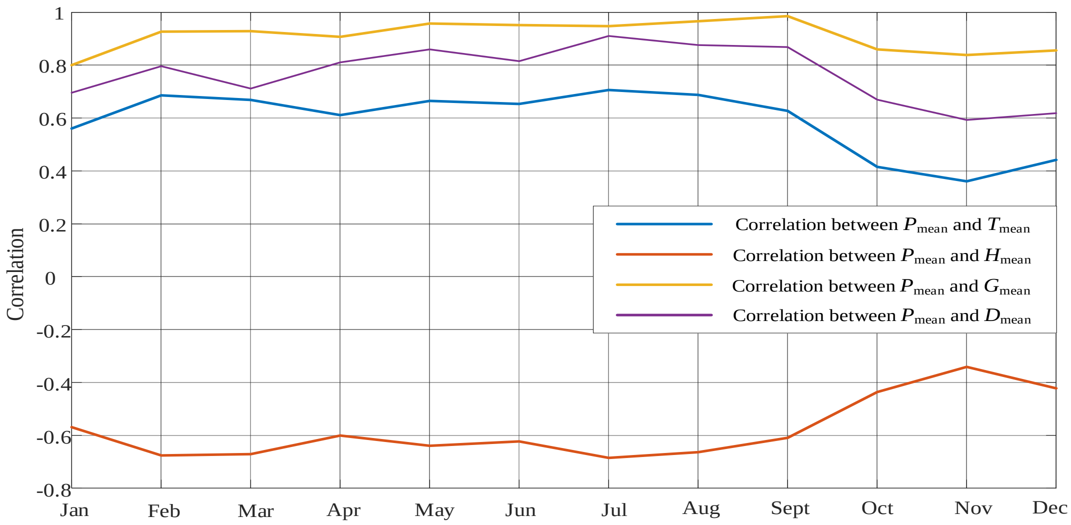

Figure 1. Correlation between hourly mean value of P and hourly mean value of different meteorological

2.2. Grey relational analysis

Cleaning and optimizing the training dataset of LNs can improve the accuracy as well as decrease the time-cost of forecasting models, the GRA is applied to select similarity and optimal similarity hours from history dataset. The basic idea of GRA algorithm is obtaining the correlation degree between the curve family of the original evaluation sequence set and the reference series according to the geometric similarity degree between them[8]. This analysis method seeks the numerical relation among the subsystems in a system, which provides a quantization for the changing situation of the system. The steps for comprehensive evaluation using GRA algorithm are as follows:

Step1: Obtain the analysis vector

Obtain the comparison sequence and the reference sequence. The reference sequence y and the comparison sequence x_i are defined as follows:

$$y=\{y(k)\mid k=1,2,...,n\} \tag{2}$$

$$x_i=\{x_i(k)\mid k=1,2,...,n\}, i=1,2,...m \tag{3}$$

where, n and m represent the dimension of the eigenvalues and the number of comparison sequence, respectively.

Step2: Nondimensionalize variables

Because it is hard to compare and obtain the accurate result when the dimensions of the system variables are different. Therefore, the data are generally dimensionless processing, and given by:

IOP Conf. Series: Earth and Environmental Science **431** (2020) 012059 doi:10.1088/1755-1315/431/1/012059

$$a_j^*(k)=\frac{A_j(k)-A_{\min}(k)}{A_{\max}(k)-A_{\min}(k)}, k=1,2,...m; i=0,1,2,...m; j=1,2,...,m+1 \tag{4}$$

where, $A_j(k)$ represents the combination matrix of the reference sequence and the comparison sequence, $A_{\min}(k)$ and $A_{\max}(k)$ are the minimum and maximum values of each column of the matrix, j represents the sum of the reference sequence and the comparison sequence quantities.

Step3: Calculate correlation coefficient $\xi_i(k)$

The $\xi_i(k)$ between $x_o(k)$ and $x_i(k)$ is given by:

$$\xi_i(k)=\frac{\min_i \min_k |y(k)-x_i(k)|+\rho \max_i \max_k |y(k)-x_i(k)|}{|y(k)-x_i(k)|+\rho \max_i \max_k |y(k)-x_i(k)|} \tag{5}$$

where, $y(k)$ and $x_i(k)$ represent the reference sequence and the comparison vector. ρ represents the resolution coefficient, here, ρ is 0.5.

Step4: Calculate correlation degree

Get the average of the correlation coefficients (that is, the points in the curve), as a quantitative representation of the correlation degree between the comparison sequence and the reference sequence. Correlation degree r_i is defined as follows:

$$r_i=\frac{1}{n}\sum_{k=1}^{n}\xi_i(k) \tag{6}$$

Step5: Sort correlation degree

The correlation degree is sorted according to the value, which reflects the relation of each comparison sequence relative to the reference sequence, calculate the correlation degree between the forecasting day and each sample in the same cluster sample sets. The hour with the highest correlation degree is determined as the optimal similarity hour, and the hours when the correlation degree is greater than a threshold $r_{\text{threshold}}$ is determined as similarity hours.

2.3. LSTM recurrent neural network

The Long-short term memory network, as one of the most advanced recurrent neural networks, has shown remarkable result in numerous time series learning tasks [10]. Fundamentally, there are three logic gate structures in every single cell, including forgetting gate, input gate and the output gate. And each operation process mainly includes four sub-operations. The formula corresponding to each part of the operation is as follows [12]:

Forget gate：

$$f_t=\sigma\left(W_f\bullet[h_{t-1},\ x_t]+b_f\right) \tag{7}$$

Input gate：

$$i_t=\sigma\left(W_t\bullet[h_{t-1},x_t]+b_i\right) \tag{8}$$

$$\tilde{C}_t=\tanh\left(W_C\bullet[h_{t-1},x_t]+b_C\right) \tag{9}$$

Merge process：

$$C_t=f_t*C_{t-1}+i_t*\tilde{C}_t \tag{10}$$

Output gate：

$$o_t=\sigma\left(W_o[h_{t-1},x_t]+b_o\right) \tag{11}$$

$$h_t=o_t*\tanh\left(C_t\right) \tag{12}$$

The cascade structure and cell sample of LSTM is shown in Figure 2.

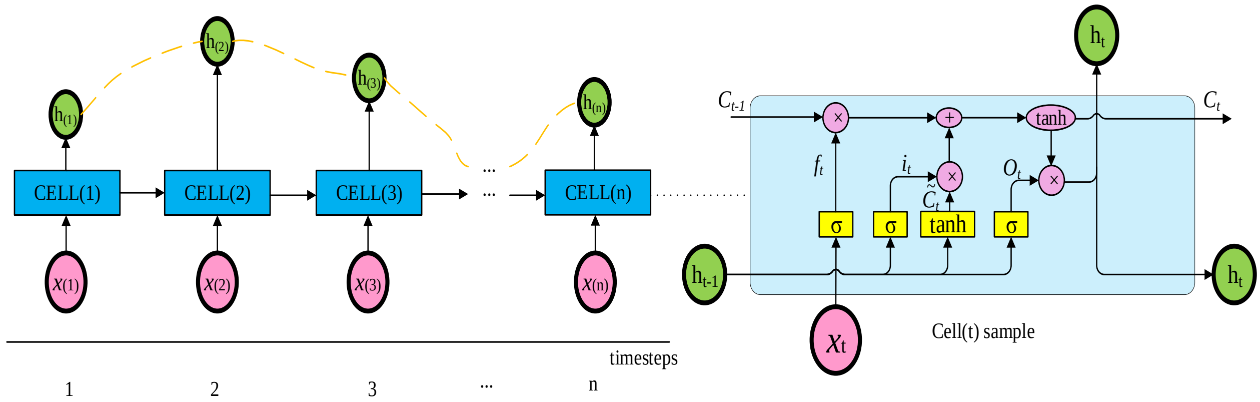

Figure 2. Cascade structure and cell sample of LSTM

where, h_t represents the output at time-step t, and x represents the input at time-step t

2.4. The implementation procedure of the GRA-LSTM model

The procedure of the GRA-LSTM model is shown in Figure 3. The detailed steps are described as follows:

Step 1: Collect the historical of power datasets and multivariate meteorological factors before forecasting hour. The multivariate meteorological factors include global horizontal radiation, diffuse horizontal radiation, relative humidity and air temperature.

Step 2: Preprocess the data, including abnormal data and normalization.

Step 3: Determine the similarity hours and the optimal similarity hour of the forecasting hour in the historical sample sets with GRA algorithm according to the meteorological characteristic (F_T) values of the forecasting hour. The y and x_i represent the eigenvector of forecasting hour and same-period hours of history dataset. The eigenvector F_T composed of (T_{start}, T_{mean}, T_{end}, G_{min}, G_{mean}, G_{max}), these parameters represent start, average, end value of temperature, and minimum, average, maximum value of global radiation, respectively.

Step 4: Collect the training samples, the threshold $r_{threshold}$ is set as 0.85. The training dataset include two main part. Include first 20 same time periods before forecasting day and first 10 samples of similarity hour samples, 30 samples in total. And the highest r_i sample is applied as optimal similarity hour.

Step 5: Determine the neuron numbers in the input, output and hidden layer, and initialize the threshold values and weights of LSTM RNN, respectively. The LSTM recurrent neural network is trained by using training hour samples, and the prediction model is obtained. In this study, h_t of LSTM is P_t, it representsthe power output at time-step t, and x_t is an eigenvector composed of (G_t, M_T), G_t represents global radiation at time-step t, M_T composed of (T_{mean}, H_{mean}, G_{mean}, D_{mean}) represent 4 meteorological factors in T hour period.

Step 6: Input the forecasting meteorological characteristic values ($M_{forecasting}$) of the forecasting hour and global radiation data (G_{best}) of optimal similarity hour into the prediction model to forecast the output power of the forecasting hour.

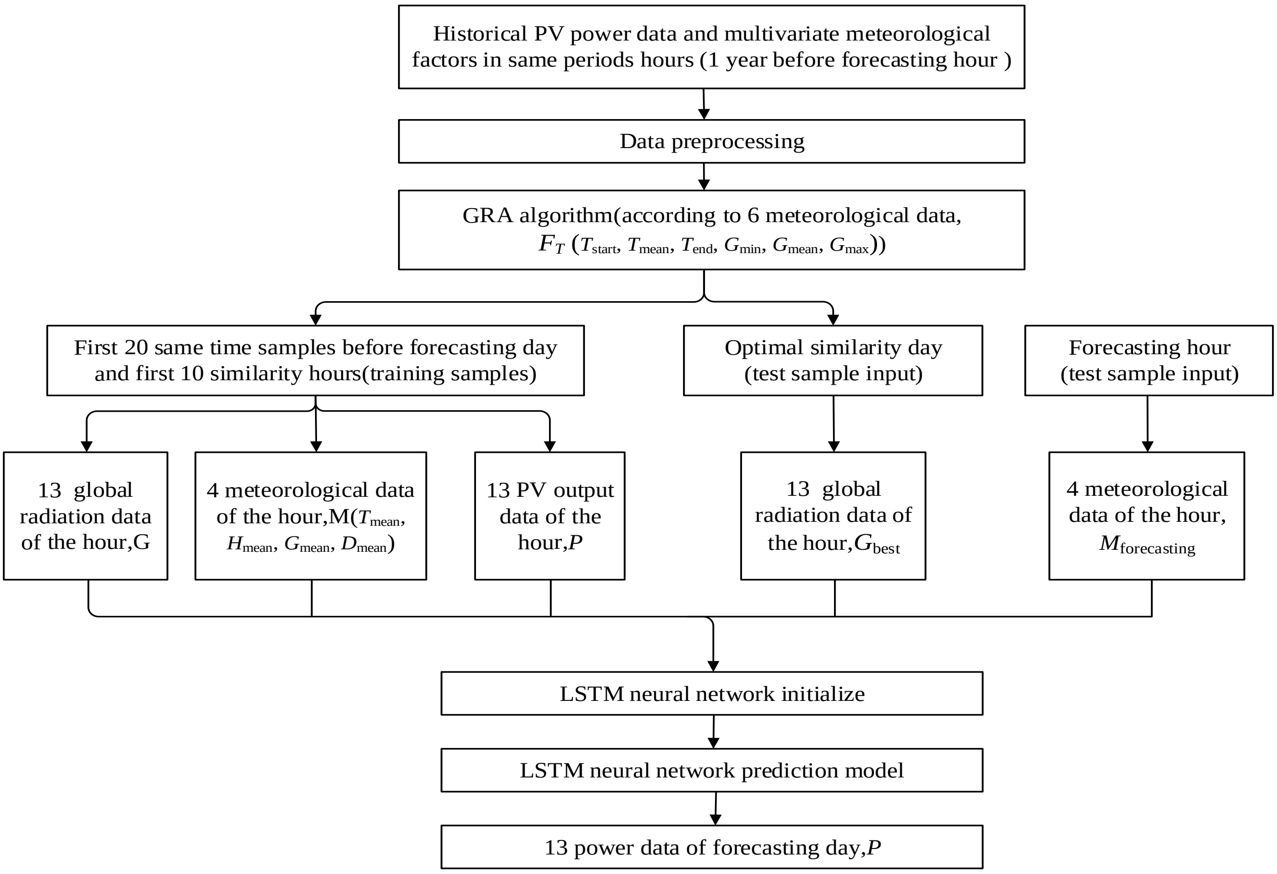

Figure 3 . Flowsheet of the proposed GRA-LSTM model

3. Experiment and discussions

3.1. Evaluation metrics

In order to verify the validity of the method. Three different evaluation metrics R^2, *RMSE*, and *MAPE*are applied to verify the prediction accuracy of the proposed model. These error metrics are defined as follows.
The R^2 is define as:

$$R^2 = \frac{\left(N\sum_{i=1}^{N} P_{f,i}P_{a,i} - \sum_{i=1}^{N} P_{f,i}\sum_{i=1}^{N} P_{a,i}\right)^2}{\left(N\sum_{i=1}^{N} P_{f,i}^{2} - \left(\sum_{i=1}^{N} P_{f,i}\right)^2\right)\left(N\sum_{i=1}^{N} P_{a,i}^{2} - \left(\sum_{i=1}^{N} P_{a,i}\right)^2\right)} \tag{13}$$

The *RMSE* is defined as：

$$RMSE = \left(\frac{1}{N}\sum_{i=1}^{N}\left(P_{f,i} - P_{a,i}\right)^2\right)^{1/2} \tag{14}$$

The *MAPE* is defined as：

$$MAPE = \frac{1}{N}\sum_{i=1}^{N}\left(\left|\frac{P_{f,i} - P_{a,i}}{\overline{P}_{a,i}}\right|\right)\times 100 \tag{15}$$

$$\overline{P}_{a,i} = \frac{1}{N}\sum_{i=1}^{N} P_{a,i} \tag{16}$$

Where $P_{f,i}$ and $P_{a,i}$ are the predict and practical PV output power of forecasting hour. $\overline{P}_{a,i}$ is the mean practical PV output power, and N is the sample point numbers in the PV power generation period which equals to 13 in this study.

3.2. Experiment result

The dataset of the PV systems from the Desert Knowledge Australia Solar Center (DKASC) is applied to verify the effect of the proposed forecast method. The multivariate meteorological factors (air temperature, relative humidity, global horizontal radiation and diffuse horizontal radiation) and historical power datasets from January 1, 2017 to November 30, 2018 are applied for the experiment. And the LSTM, grey relational analysis-back propagation neural network (GRA-BPNN), grey relational analysis-radial basis function neural network (GRA-RBFNN) and grey relational analysis-Elman neural network (GRA-Elman) are adopted as the comparison models. The forecasting curves by the GRA-LSTM forecasting model and the other forecasting comparison models are shown in Figure 4.

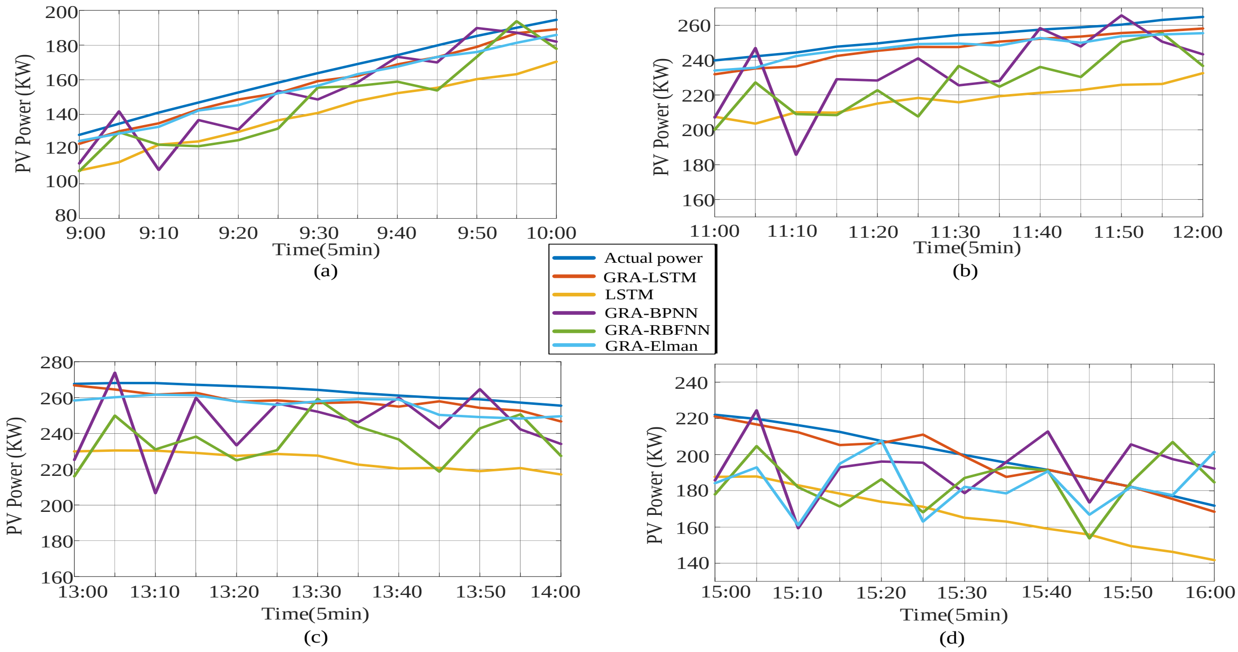

Figure 4. The forecasting cures of GRA-LSTM and comparison models: (a) 9 -10 o'clock;(b) 11-12 o'clock; (c) 13-14 o'clock;(d) 15-16 o'clock.

Figure 5 shows the corresponding absolute errors in different time periods. It is clear that the GRA-LSTM model-based prediction method has the best results in most cases.

In addition, to further test the performance of proposed model. The March 18, 2018 (summer in Australia), May 10, 2018 (autumn in Australia) and August 19, 2018 (winter in Australia), December 21, 2018 (spring in Australia) are selected as test days. And the Table 2 shows the prediction accuracy evaluation (includes the R^2, RMSE and MAPE) of forecasting result. Considering the proposed GRA-LSTM model-based forecast technology and the other comparative forecast approaches (LSTM, GRA-BPNN, GRA-RBFNN and GRA-Elman). It can be concluded that the proposed model results in better prediction accuracy: the *RMSE* and *MAPE* have 5.7766 kW and 2.2784% average values. The average *RMSE* enhancement of the GRA-LSTM model with respect to the previous comparative models is 66.57%, 42.81%, 71.54%, 47.91%, respectively. And the average *MAPE* enhancement is 70.42%, 46.01%, 72.73% and 54.24%, respectively. And considering the R^2 as given in Table 2, the LSTM has highest 0.9267 average value, it shows the outstanding time series learning ability of LSTM, however, the GRA-LSTM has better performance in robustness. Therefore, compared with comparative approaches. Synthetically, the proposed GRA-LSTM model is a novel and effective hour-ahead PV power generation prediction model.

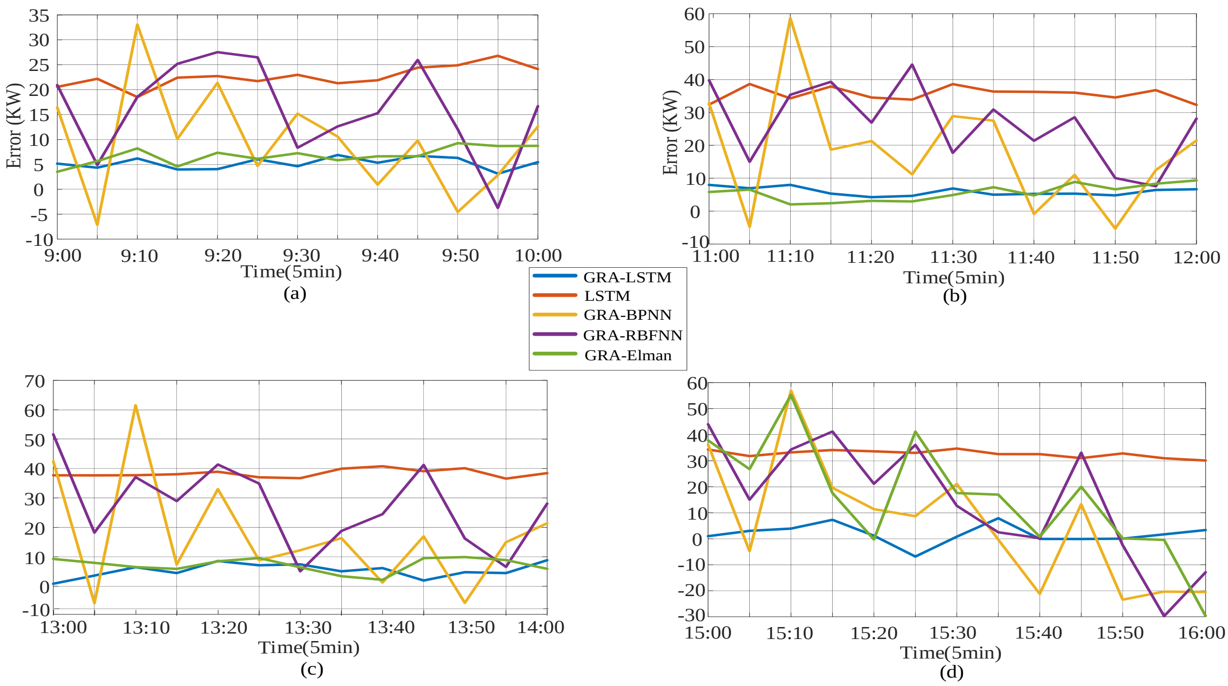

Figure 5.Absolute error curves in different time periods: (a) 9 -10 o'clock;(b) 11-12 o'clock; (c) 13-14 o'clock;(d) 15-16o'clock.

Table 2. Comparison of the prediction error by adopting various prediction methods.

	Model	Spring	Summer	Autumn	Winter	Average	Standard deviation
R^2	GRA-LSTM	**0.8891**	0.9065	0.9396	0.9011	0.9091	**0.0187**
	LSTM	0.8707	**0.9245**	**0.9683**	0.9435	**0.9267**	0.0359
	GRA-BPNN	0.4616	0.9238	0.9040	0.9220	0.8028	0.1972
	GRA-RBFNN	0.6098	0.9139	0.9538	0.9473	0.8562	0.1431
	GRA-Elman	0.6847	0.9890	0.9563	**0.9529**	0.8957	0.1226
RMSE(kW)	GRA-LSTM	**3.6194**	**6.0800**	7.3728	6.0343	**5.7766**	**1.3565**
	LSTM	7.2274	16.6588	13.250	31.9979	17.2835	9.1419
	GRA-BPNN	21.2371	8.6991	**6.6957**	**3.7780**	10.1025	6.6625
	GRA-RBFNN	10.6054	22.1715	17.6918	30.7319	20.3002	7.2992
	GRA-Elman	17.4779	13.7508	6.3992	6.7371	11.0912	4.7127
MAPE (%)	GRA-LSTM	**1.2109**	**2.3017**	3.0235	2.5776	**2.2784**	**0.6680**
	LSTM	2.3637	7.2106	6.6749	14.5652	7.7036	4.3846
	GRA-BPNN	8.4146	4.2270	**2.9075**	**1.3288**	4.2194	2.6304
	GRA-RBFNN	3.8040	10.6479	7.3737	11.5985	8.3560	3.0599
	GRA-Elman	7.4808	6.4619	3.0439	3.0102	4.9992	2.0048

4. Conclusion

A GRA-LSTM model-based method is proposed for hour-ahead PV power generation forecasting in this study. Four forecasting meteorological values are designed and are taken as the inputs of the prediction model along with the global horizontal radiation. To optimize the training dataset, the GRA algorithm is applied to select the similarity hours. Then the LSTM RNN is adopted to train the forecasting model. In addition, the datasets on the DKASC website are employed to verify the proposed method by comparing with four other models: LSTM, GRA-BPNN, GRA-RBFNN and GRA-Elman. The experimental results show that the smaller forecast error can be obtained by applying the proposed model, and the forecast accuracy and robustness of GRA-LSTM is superior to the compared models.

5. References

[1] REN21 2019 *Renewables 2019 Global Status Report* (Paris: REN21 Secretariat)
[2] Antonanzas J and Osorio N, et al. 2016 Review of photovoltaic power forecasting *Solar Energy* vol 136 pp 78-111
[3] Wang H and Lei Z, et al. 2019 A review of deep learning for renewable energy forecasting *Energy Conversion and Management* vol 198 p 111799
[4] Zheng L and Liu Z, et al. 2018 Very short-term maximum Lyapunov exponent forecasting tool for distributed photovoltaic output *Applied Energy* vol 229 pp 1128-113
[5] Das U K and Tey K S, et al. 2018. Forecasting of photovoltaic power generation and model optimization: A review *Renewable and Sustainable Energy Reviews* vol 81 pp 912-928
[6] Sobri S and Koohi-Kamali S, et al. 2018 Solar photovoltaic generation forecasting methods: A review *Energy Conversion and Management* vol 156 pp 459-497
[7] Wang F and Zhang Z, et al. 2019 Generative adversarial networks and convolutional neural networks based weather classification model for day ahead short-term photovoltaic power forecasting *Energy Conversion and Management* vol 181 pp 443-462
[8] Lin P and Peng Z, et al. 2018 Short-term power prediction for photovoltaic power plants using a hybrid improved Kmeans-GRA-Elman model based on multivariate meteorological factors and historical power datasets *Energy Conversion and Management* vol 77 pp 704-717
[9] Zhou H and Zhang Y, et al. 2019 Short-Term Photovoltaic Power Forecasting Based on Long Short Term Memory Neural Network and Attention Mechanism *IEEE Access* vol 7 pp 78063-78074
[10] Qing X and Niu Y 2018 Hourly day-ahead solar irradiance prediction using weather forecasts by LSTM *Energy* vol 148 pp 461-468
[11] Daniel K and Frank M, et al. 2019 Short-term and regionalized photovoltaic power forecasting, enhanced by reference systems, on the example of Luxembourg *Renewable Energy* vol 103 pp455-470
[12] Wang F and Yu Y, et al. 2018 Wavelet Decomposition and Convolutional LSTM Networks Based Improved Deep Learning Model for Solar Irradiance Forecasting *applied sciences* vol 8 p 1286

IOP Conf. Series: Earth and Environmental Science **431** (2020) 012060 doi:10.1088/1755-1315/431/1/012060

Online photovoltaic fault detection method based on data stream clustering

Yuqiao Cai[1,2], Peijie Lin[1,2], Yaohai Lin[3], Qiao Zheng[1,2], Shuying Cheng[1,2], Zhicong Chen[1,2], and Lijun Wu[1,2]

1 School of Physics and Information Engineering, and Institute of Micro-Nano Devices and Solar Cells, Fuzhou University, Fuzhou, China
2 Jiangsu Collaborative innovation Center of Photovoltaic Science and Engineering, Changzhou, China
3 College of Computer and Information Sciences, Fujian Agriculture and Forest University, Fuzhou, China
E-mail: linpeijie@fzu.edu.cn

Abstract. As the core component of solar power station, PV array is particularly important for safe and stable operation of the entire system. The existence of PV array faults for a long time can lead to potential danger of the entire PV system. Since the PV data is greatly affected by the environment, the continuous data stream generated during the operation of PV arrays can form clusters of arbitrary shape. When a PV fault occurs, new data streams can form a cluster that is different from the one under normal operation. Accordingly, this paper presents a model for online fault detection of PV arrays faults using data stream clustering approach. The real-time data stream of the PV arrays is transmitted to the diagnostic system through RabbitMQ server for online detection and data storage. The online density-based spatial clustering of applications with noise (DBSCAN) algorithm is used for clustering the data. Then, the faults are detected by judging whether new clusters are formed. The experiment result shows the effectiveness of the proposed method in grid-connected PV system.

1. Introduction

PV array is composed of several PV panels connected in series and parallel. The average life of PV panels is 20-30 years [1]. Solar power stations are often located in places of harsh environment. Therefore, PV arrays are easily affected by environmental factors, such as high temperature, strong wind, heavy rain and hail, which can cause corrosion or damage to the surface of PV components. Being exposed to ultraviolet light for a long time will accelerate the aging process of PV components. Faults in PV array include: short circuit fault, partial shading, aging degradation, open circuit fault, arc fault, hot spot, etc. In order to eliminate the impact of faults in PV array, conventional protection devices are usually installed on the DC side of PV array [2], such as overcurrent protection device (OCPD), ground fault detection and interrupter (GFDI), arc fault circuit interrupter (AFCI) and so on. However, it is difficult for conventional PV array protection devices to detect early-stage fault and adapt to a wide variety of fault types. Moreover, the MPPT technique implemented in inverter can also affect the effectiveness of these protection devices. Thus, an online PV fault detection system is one of the key issues that is needed to be solved urgently.

Recently, researchers have proposed some solutions to online fault diagnosis of PV arrays. Infrared thermal imaging equipment is applied to visually reflect the thermal image of the PV array. Specific image segmentation and feature recognition technology are used to find the temperature anomaly in the thermal image to define the fault type and location [3]. The advantage of the infrared image is that it has no effect on the structure of the PV array. However, for the limitations of the infrared image, such as high noise and uneven imaging, it is impossible to effectively distinguish the fault types when the PV array is complex [4]. When a component in PV arrays fails, the output voltage and output current of the entire array are affected. Comparing the actually measured IV curve under working conditions with the theoretical analysis results, the presence or absence of faults in the array can be accurately detected. The method of PV fault diagnosis based on machine learning (ML) is widely used in recent years. Generally, this method aims to apply artificial intelligence algorithm to process the electrical and environmental dataset detected by the sensors in PV array. After this, an accurate model is established to map the relationship between fault features and fault types. Then the faults are easily identified. The typical supervised ML algorithms applied in this field includes Decision Tree (DT) [5], Random Forest (RF) [6], Artificial Neural Network (ANN) [7], Support Vector Machine (SVM) [8], Extreme Learning Machine (ELM) [9], Probabilistic Neural Network (PNN) [10] and so on. The supervised ML methods rely on labeled data to build model, but it is too expensive to obtain the labels of large number of data. For data stream, the effectiveness of the supervised diagnostic method depends on the quality of the training data. Semi-supervised usually only needs to acquire a small number of labeled samples and unsupervised ML algorithms can work without labeled data. The more common semi-supervised and unsupervised ML algorithms are: Clusters based on density peaks [11], K-means clustering Class [12], Unsupervised probabilistic neural network [13]. Because of the continuous time sequence and variability of of PV arrays data stream, unsupervised method is more suitable for fault detection of data stream.

Generally, the PV array in operating is affected by environmental factors, thus the output under different environmental conditions represents a wide range of differences. Therefore, it is difficult to collect a large number of labeled samples for supervised online detection in practice. In this paper, an unsupervised online clustering detection method is proposed, which includes the transmission, storage and online detection part. The RabbitMQ is applied to design the transmission and storage part. This part transmits the collected PV data stream to the online detection system and stores it in the local hard disk or database. The online DBSCAN algorithm is adopted to cluster the normalized PV data in the online detection part. Then a fault is detected by judging whether the PV data stream forms a new cluster.

2. The proposed method of online detection

In this section, the design of RabbitMQ, online DBSCAN algorithm, the normalization method of PV data and the fault detection method proposed in this paper are introduced respectively.

2.1. RabbitMQ

AMQP (Advanced Message Queuing Protocol) is an application-level advanced message queuing protocol based on asynchronous processing. It is designed for message-oriented middleware and it is independent from language and development platform [14]. AMQP can provide a standard messaging service that enables communication between qualified client applications and messaging middleware agents. The AMQP model is shown in the figure 1, where P is the producer of the message, X is the message switch, and C is the recipient of the message. Since AMQP is Internet protocol, the producer, consumer, and message broker of the message are capable of existing on different platforms or devices in the process.

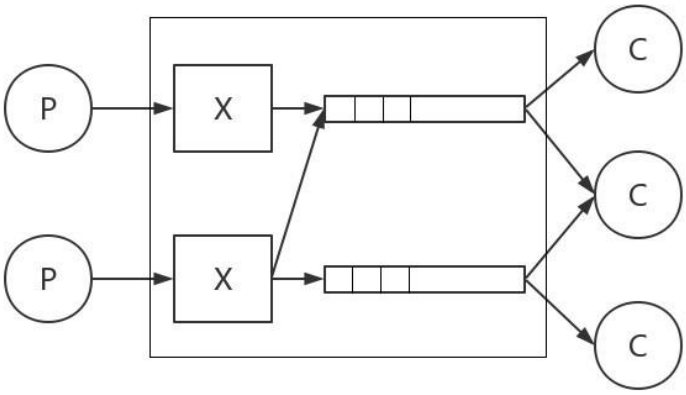

Figure 1. AMQP model

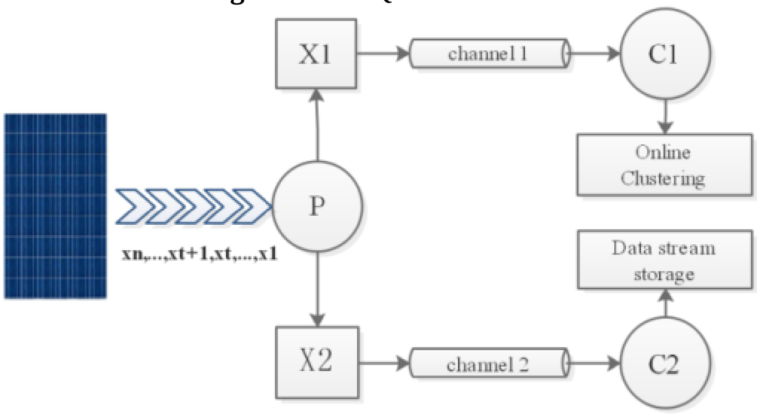

Figure 2. RabbitMQ system

RabbitMQ is a message broker software based on AMQP and written in Erlang. RabbitMQ can receive and deliver messages. As a medium for messaging systems, RabbitMQ can provide a common messaging and receiving platform for users' applications and ensure the security of messages transmission.

To realize the transmission and storage of real-time PV data, RabbitMQ is used to build a data stream transmission and storage system by its high availability cluster model. The platform for transmitting and storing PV data stream is presented in figure 2. Three virtual hosts are established on experimental PC, one for the producer and two for consumers. The real-time data stream of the PV array enters the RabbitMQ system, and the producer is responsible for transmitting the data stream to consumer 1 and consumer 2 at a certain set rate. Consumer 1 receives the PV data from the normalization process of the producer (see 2.3 for the normalization method), and then performs online detection of the normalized data stream using the online DBSCAN algorithm (online DBSCAN see 2.2). Consumer 2 receives the PV data transmitted from the producer, and the data can be stored in the local hard disk or database as needed.

2.2. Online DBSCAN algorithm

As one of the popular density-based clustering algorithm, the density-based spatial clustering of applications with noise (DBSCAN) is broadly used [15]. The main working mechanism is to collect samples with a certain density, storing them in a cluster, through which the degree of similarity among samples in the same cluster can reach a level that is as high as possible. The degree of difference between samples in different clusters is as large as possible. The DBSCAN algorithm is especially useful for processing large data sets with noise. The DBSCAN algorithm has been proven to be effective for analyzing large amounts of heterogeneous complex data [16]. In order to be adapted on the online clustering of data stream of PV data, the online DBSCAN algorithm is proposed. Compared with DBSCAN algorithm, the online DBSCAN algorithm can quickly analyze the existing clustering results when processing data stream. Online DBSCAN only updates the clusters in each clustering process by searching the clusters closest to the current data. Therefore, it reduces the time complexity and improves the efficiency of online clustering. In dealing with the problem of outliers, there may be data that were previously distinguished as outliers. After new data entering the system, some outliers may have the same data distribution as the currently existing clusters. After each clustering, if an outlier is found, it will iterate all current outliers to reaffirm whether there are new clusters formed by the outliers. So online DBSCAN algorithm can dynamically identify outliers and new clusters.

Some basic concepts about DBSCAN that will be used below are as follows:

Data vector: Assuming that the data stream arrives at time t, the n-dimensional data vector received by the system at time *t* is represented as $x_{\mathrm{t}} = \{x_1, x_2, ..., x_{\mathrm{n}}\}$.

eps neighborhood: A user-specified parameter *eps*>0 is used to specify the radius of the field for each object. The neighborhood of object *o* is a space centered on *o* and radius with *eps*.

minPts: The number of samples in the *eps* neighborhood of the object, it is also called the density threshold of the *eps* neighborhood of object.

Core point: For the specified object p, if the number of points contained in the *eps* neighborhood of *p* is greater than or equal to *minPts*, the object *p* is referred to as a core point.

The clustering process of the online DBSCAN algorithm is as follows:

(1) When x_t is entered the system, the DBSCAN compares the distance between x_t and the current cluster centers, and finds the cluster center closest to x_t ;

(2) Calculate the number of samples contained in the *eps* neighborhood of x_t , and compare it with the *minPts* set by the system. If the number is more than *minPts*, then integrate the sample as a core point into the current cluster, and then update the cluster center of the cluster;

(3) If the value is smaller than *minPts*, first determine whether the core point is included in the *eps* neighborhood of x_t . If it is included, the sample is integrated into the cluster where the core point is located, and the core point and cluster center of the cluster are updated. If not included, the sample is classified as an outlier;

(4) When a new outlier is found, the system iterates through all the outliers that currently exist, and determines whether there are a certain number of outliers to form a new cluster.

2.3. Normalization of PV data

The schematic diagram of a typical grid-connected PV system is shown in figure 3. The system usually includes $s \times p$ PV array, inverters, protection devices (OCPD and GFPD) and connection wires. In order to better analyze the PV data, the concept of a reference module, which is a PV panel independent from the PV array being used for testing, is introduced.

The component works in the same operating environment as the PV array under test (the same temperature and solar irradiance, etc.). It has the same component parameters with the PV array under test. The reference module is used to collect open circuit voltage (V_{OC}) and short circuit current (I_{SC}). The V_{OC} and I_{SC} of the entire PV array under test are estimated, and G indicates the irradiance on PV panel. In standard test condition (STC), $G_{\mathrm{STC}} = 1000$ W/m^2. Through the V_{OC} and I_{SC} of the array under test, the V_{MPP} and I_{MPP} can be normalized. The normalization method [17] is shown in equation (1).

$$\begin{cases} V_{\mathrm{NORM}} = \dfrac{V_{\mathrm{MPP}}}{s \times V_{\mathrm{OC\text{-}REF}}} \\ I_{\mathrm{NORM}} = \dfrac{I_{\mathrm{MPP}}}{p \times I_{\mathrm{OC\text{-}REF}}} \\ G_{\mathrm{NORM}} = \dfrac{G}{G_{\mathrm{STC}}} \end{cases} \tag{1}$$

Where V_{NORM} is the normalized voltage of the PV array under test, I_{NORM} is the normalized current, G_{NORM} is the normalized irradiance. $V_{\mathrm{OC\text{-}REF}}$ is the open circuit voltage of the reference module, $I_{\mathrm{SC\text{-}REF}}$

is the short circuit current of the reference module, and V_{MPP} and I_{MPP} are respectively voltage and current at which the PV array under test is operating at the maximum power point currently. *s* indicates the number of components in series, and *p* indicates the number of parallel strings of the PV array. The normalization method is simple in calculating, fast in processing, and the normalized PV data has strong discriminability.

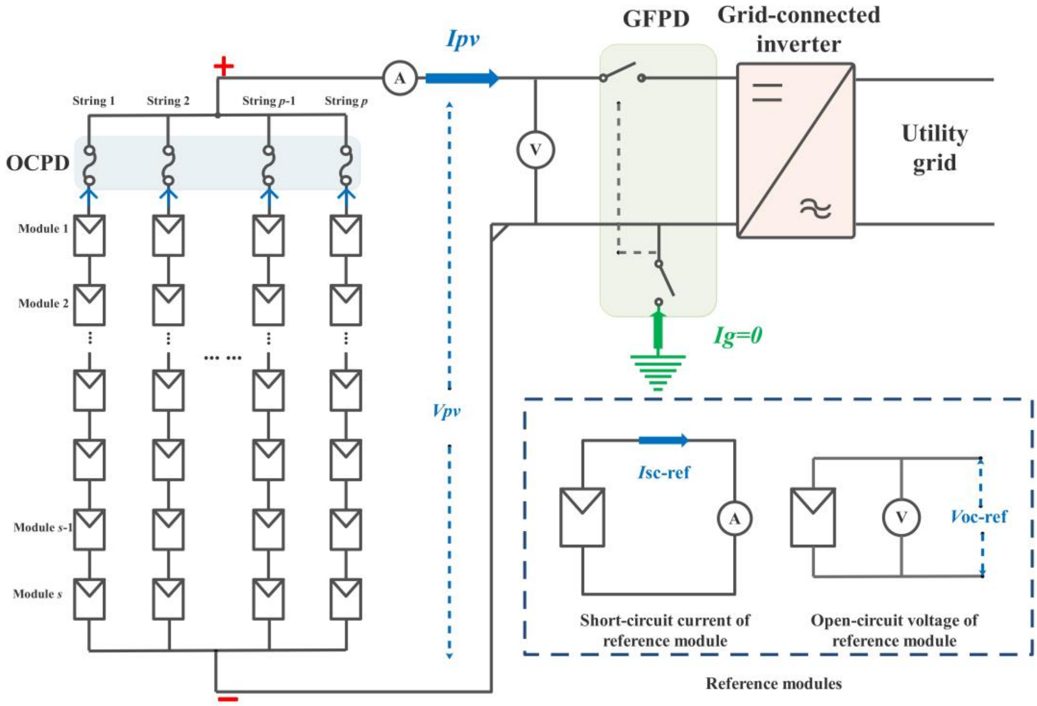

Figure 3. Schematic diagram of grid-connected PV system

During the operation of PV array, as the environmental factors change, the voltage (V_{MPP}) and current (I_{MPP}) at the maximum power point will change accordingly. The distribution of the V_{MPP} and I_{MPP} of the simulated PV array in the range of varying solar irradiance is shown in figure 4. The data of different states of the PV array have high overlap and cannot be effectively classified.

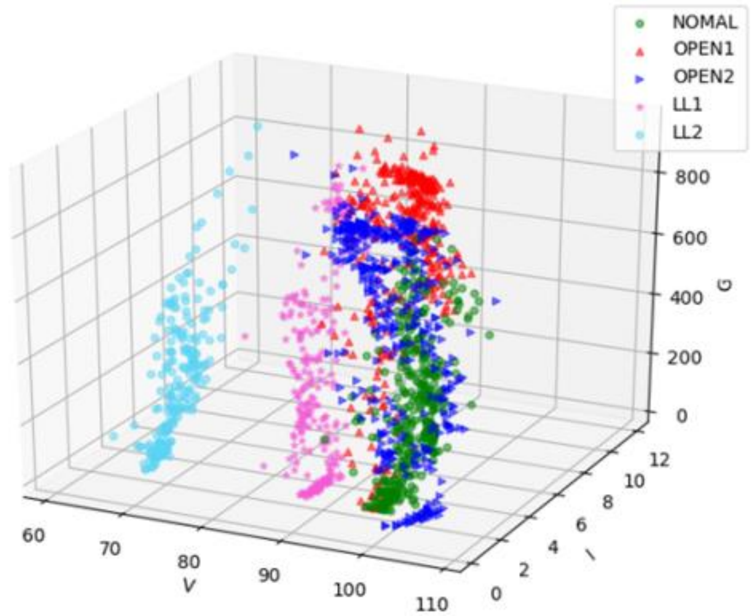

Figure 4. Unnormalized PV data

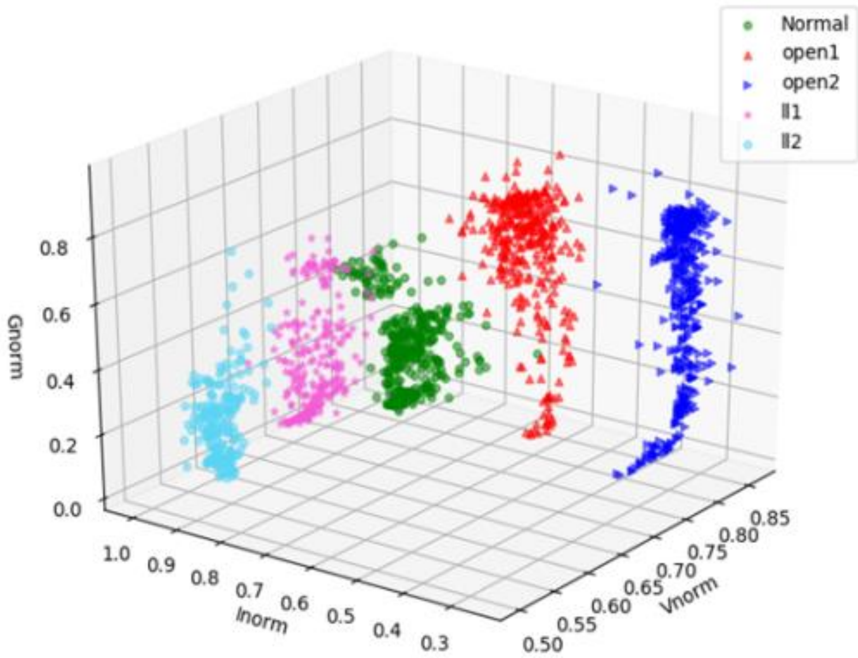

Figure 5. Normalized PV data

The normalized PV data are shown in the figure 5. It can be seen that the normalized PV data are clustered obviously, and the shape of the cluster is mostly columnar. Thus, density-based clustering algorithm is used to cluster such data.

2.4. Procedure of online detection

The flow of the online detection method for PV faults proposed in this thesis is shown in figure 6. The real-time data stream from the PV array enters the Rabbitmq system, which transfers the PV data into the online detection system and stores it. When outliers are defined, the system outputs outlier information; when a new cluster is recognised, it outputs new cluster information and alarms.

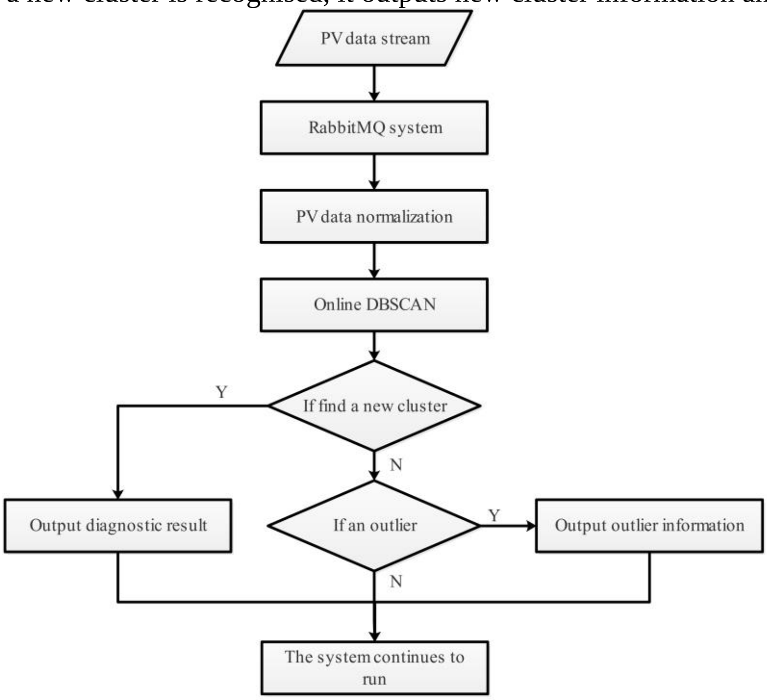

Figure 6. Flowchat of the proposed model

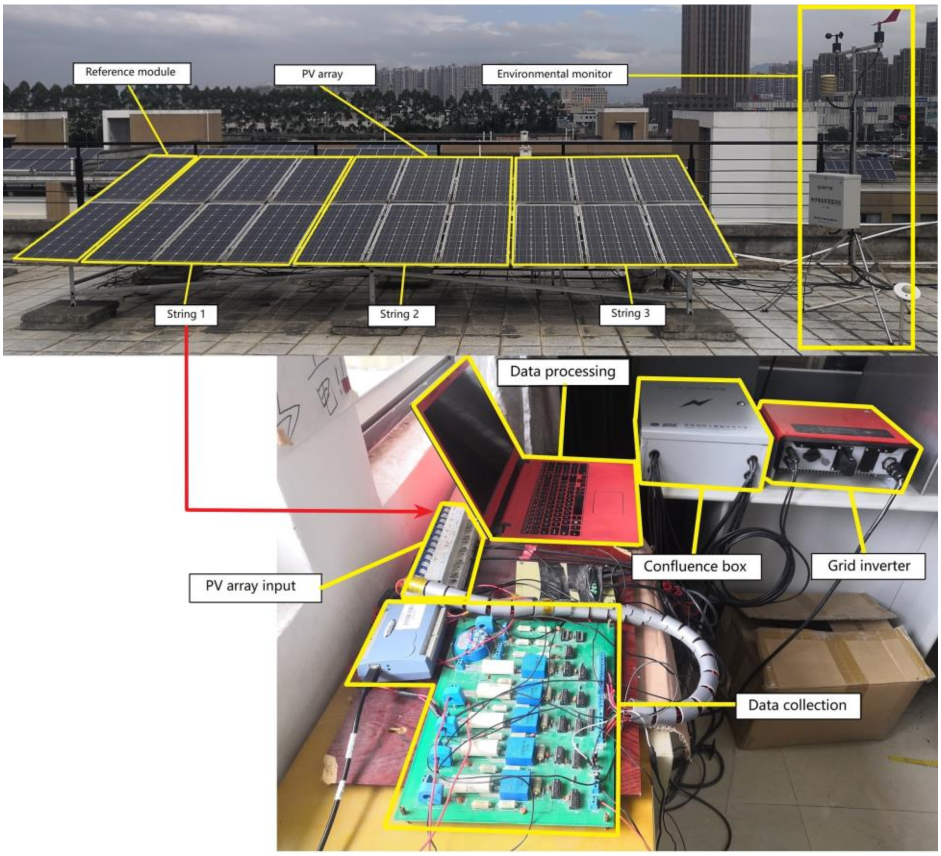

Figure 7. PV Experiment platform

3. Experimental results and analysis

In this section, we tested the effectiveness of the proposed method by using a 1.8 kW grid-connected PV system under actual operating conditions. As shown in figure 7, the PV array platform is a 3×6 PV array consisting of 6 identical PV modules connected in series as a string and 3 strings in parallel. Single crystal solar cells are used in PV modules. The output of the PV array is connected to a GW2500-NS PV grid-connected inverter through the confluence box. The detailed parameters of the PV array and inverter are shown in Table 1.

Table 1 Parameters of the PV array

DEVICE	DEVICE	PARAMETER
PV ARRAY *100*	*GL-*	STC： IMPP=17.1A,VOC=129V,ISC=18 Rated DC Power：2700W Maximum Input Voltage：500V
GRID INVERTER *GW2500-NS*	*Goodw*	Starting Voltage：80V Maximum Power Point Voltage Maximum DC Current：18A

Figure 8 shows how the diagnostic system distinguish outliers from a new cluster during fault detection, where the time interval between t_1 and t_0 is 51 seconds, *eps*=0.12, *minPts*=20. As shown in Figure 8(a), the diagnostic system first collects 50 normal running PV data to form an initial cluster, and then sets the OPEN1 fault (one strings of the PV array has an open circuit fault) on the running PV array after the diagnostic system runs for a period of time. The green dot and the red dot indicate the data of the normal working state and the outlier data by online DBSCAN, respectively. figure 8(a) is the diagnostic diagram of the PV array at time t_0. It can be seen from the figure that the detection system has discovered 6 outliers at time t_0. However, there are not enough outliers to diagnose a new cluster at time t_0, the system does not report the formation of a new fault, but it still outputs the outlier information. The specific information of each outlier can be obtained through the diagnostic system, including the formation time of the outliers and their corresponding array output values. figure 8(b) shows the detection results of the diagnostic system at time t_1. It can be found that a new cluster has been formed at time t_1, some of the outliers that are diagnosed at the time t_0 are included in the new cluster. When a new cluster is found, the diagnostic system outputs the formation time of the cluster, the current clustering center and the size of the cluster.

The detection results of the diagnostic system for different types of PV faults are shown in figure 9. figure 9(a) is the detection result when two PV strings of open circuits occur in the system (OPEN2). The output voltage of the PV array basically remains unchanged compared with the normal state, but the output current is significantly reduced as the number of open circuit strings increases. figure 9(b)-(c) are diagnostic results of faults in which the PV modules in the PV array are accidentally connected to the strings of the strings. figure 9(b) represents a case where one PV module is short-circuited (Line-Line 1), and figure 9(c) represents a case where two PV modules are short-circuited (Line-Line 2). The experiment result shows that four typical PV faults (OPEN1, OPEN2, Line-Line 1 and Line-Line 2) can be accurately detected.

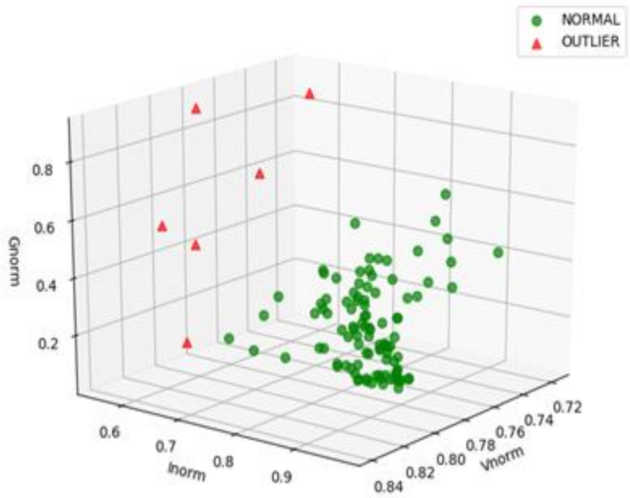

(a)

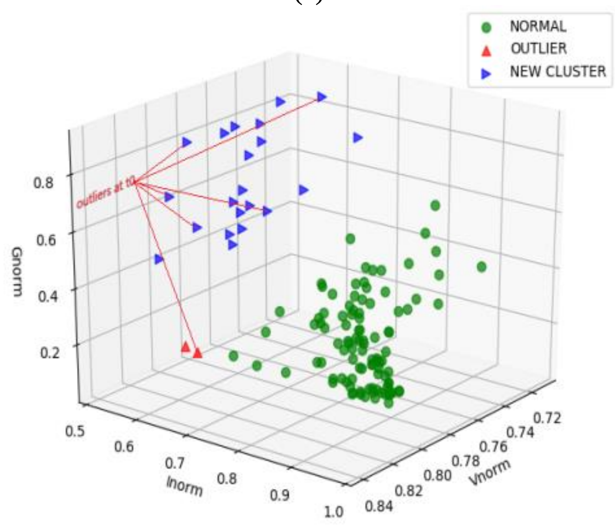

(b)

Figure 8. Detection of OPEN1 at different times (a) Clustering at time t_0; (b) Clustering at time t_1

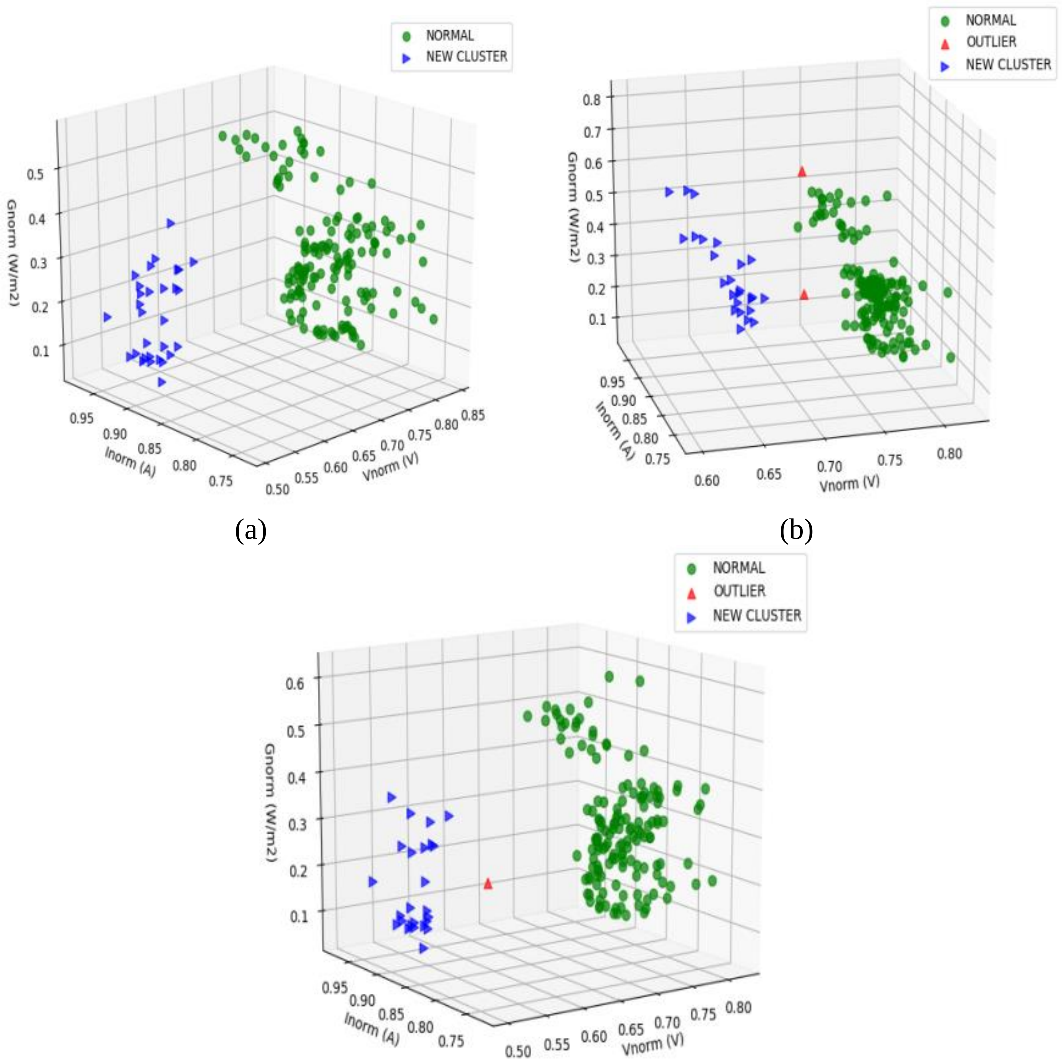

(a) (b)

(c)

Figure 9. Detection of different faults (a) OPEN2; (b) Line-Line 1; (c) Line-Line 2

4. Conclusion

In this paper, an online PV fault detection method based on data stream clustering is proposed. The effectiveness of the method is verified by a 1.8kW grid-connected PV system. This method uses RabbitMQ system to transfer and store PV data stream. The RabbitMQ system holds the advantages of high scalability and recoverability. The data collected can be processed in parallel and permanently retained. In the online clustering stage of PV data stream, the online DBSCAN algorithm can process the normalized PV data online efficiently, accurately distinguishing outliers from fault clusters. The detection system can define the typical electrical fault of PV arrays in time.

The detection system proposed in this thesis can only detects the typical electrical faults (open fault and short circuit fault) of the PV arrays. There is no further research on other fault types such as shadow fault and abnormal aging fault on PV arrays. Therefore, the future research work of this paper will comprehensively consider the online detection of various types of PV arrays faults under different working conditions, thus further improving the effectiveness of this detection method.

5. References

[1] Yang H, Wang H, et al. 2003 Status of photovoltaic industry in China *Energy Policy* vol 31 pp 703-707
[2] Alam MK, Khan F, Johnson J, Flicker J, et al. 2015 A comprehensive review of catastrophic faults in PV arrays: Types, detection, and mitigation techniques *IEEE J Photovoltaics* vol 5 pp 982–997.
[3] Pillai DS, Prasanth Ram J, Rajasekar N, et al. 2019 Extended analysis on line-line and line-ground faults in PV arrays and a compatibility study on latest NEC protection standards *Energy Conversion and Management* vol 196 pp 988-1001
[4] Dhoke A, Sharma R, Saha TK 2018 PV module degradation analysis and impact on settings of overcurrent protection devices *Solar Energ*y vol 160 pp 360-367
[5] Rabah B，Samir M. 2018 Fault detection and diagnosis based on C4.5 decision tree algorithm for grid connected PV system *Solar Energy* vol 173 pp 610-634
[6] Benkercha R, Moulahoum S, et al. 2018 Fault detection and diagnosis based on C4. 5 decision tree algorithm for grid connected PV system *Solar Energy* vol 173 pp 610-634.
[7] Chen Z, Han F, et al. 2018 Random forest based intelligent fault diagnosis for PV arrays using array voltage and string currents *Energy Convers & Manage* vol 178 pp 250-264
[8] Chine W, Mellit A, et al. 2016 A novel fault diagnosis technique for photovoltaic systems based on artificial neural networks *Renew Energy* vol 90 pp 501-512
[9] Fauzan HJ, Seongmun Oh, Jaesung J Development of photovoltaic abnormal condition detection system using combined regression and support vector machine *Energy vol 176* pp 457-467
[10] Chen Z, Wu L, Lin P, et al. 2017 Intelligent fault diagnosis of photovoltaic arrays based on optimized kernel extreme learning machine and I-V characteristics *Apply Energy* vol 204 pp 912-931
[11] Chen Z, Lin P, et al. 2017 A density peak-based clustering approach for fault diagnosis of photovoltaic arrays vol 204 pp 912-931
[12] Liu G, Zhu L, Wu X, Wang J 2019 Time series clustering and physical implication for photovoltaic array systems with unknown working conditions *Solar Energy* vol 180 pp 401-411
[13] Zhu H, Lu L, Yao J, Dai S, Hu Y 2018 Fault diagnosis approach for photovoltaic arrays based on unsupervised sample clustering and probabilistic neural network model *Solar Energy* vol 176 pp 395-405
[14] Maciej R, Krzysztof G, et al. 2014 *Conference on Computer Science and Information Systems,*Warsaw, Poland vol 2 pp 879-884
[15] Januzaj E, Kriegel H, Pfeifle M 2004 *European Conference on Principles of Data Mining and Knowledge Discovery Springer*, Berlin, Heidelberg pp 231-244
[16] Ester M, Kriegel H, Sander J and Xu X 1996 *Proceedings of the Second International Conference on Knowledge Discovery and Data Mining* Menlo Park CA pp 226－231
[17] Ye Z, Lehman B, Ball R, et al 2014 Graph-Based Semi-supervised Learning for Fault Detection and Classification in Solar Photovoltaic Arrays *IEEE Transactions on Power Electronics* vol 30 pp 2848-2858

IOP Conf. Series: Earth and Environmental Science **431** (2020) 012056 doi:10.1088/1755-1315/431/1/012056

Introduction and prospect of integrated energy service platform in industrial parks

Gu Feng[1], Xie Kai[1], Jin Hao[1] and Su Hengxun[1]

1 NR Electric Co.,Ltd, Nanjing, Jiangsu, China
E-mail: gufeng@nrec.com

Abstract. As a modern industrial division of labor and production area that adapts to market competition and industrial upgrading, the industrial park is a generation model for the country to actively plan and promote development. The integrated energy system of industrial parks is of great significance for improving energy efficiency, promoting large-scale development of renewable energy, improving the utilization of social infrastructure and energy supply, and achieving energy conservation and emission reduction targets. The combination of industrial parks and integrated energy service platform technologies can realize the coordinated operation and resource sharing of various energy systems, meet the individual needs of campus users, and provide diversified services for system maintainers, park managers, enterprises, and households. Based on the summary of the characteristics of the campus-type energy Internet, the paper studies the key technologies of its integrated energy service platform. The key technologies of information collection, source-charge prediction, multi-energy coordination scheduling and advanced application services of the company's latest integrated energy service platform are introduced, and suggestions for the development of integrated energy service platform in the park are put forward.

1. Introduction

Energy is the basic driving force for the development of the whole world economic growth, and the basis for human survival. The current energy security issues facing the world present new features and new changes that are significantly different from previous oil crises. It is not just a matter of energy supply security, but includes energy supply, energy demand, energy prices, energy transportation, energy use, etc. Comprehensive risks and threats, including security issues. [1] Improving energy efficiency, developing new energy sources, and strengthening the comprehensive utilization of renewable energy have become inevitable choices for solving the contradiction between energy demand growth and energy shortage in social and economic development projects. The integrated energy service under the energy Internet will promote the interconnection, intercommunication and mutual transfer of primary and secondary energy, realize the rational optimization and allocation of energy resources, promote the energy generation and consumption revolution, and promote the development of the real economy with good social and economic benefits. [2]

In recent years, the construction of industrial parks has become an important part of urban development, but there are also some problems in the construction of parks. [3] Due to the differences in the development of different energy systems, energy supply is often planned separately, designed separately, and operated independently. Lack of coordination has resulted in problems such as low energy utilization, weak overall security and self-healing capabilities of the energy supply system, resulting in difficulties in service management in the park and effective coordination between systems. The integrated energy service platform is a new energy system. [4] Through the deep integration of

IOP Conf. Series: Earth and Environmental Science **431** (2020) 012056 doi:10.1088/1755-1315/431/1/012056

Internet technology and energy technology, it provides effective support for the construction of smart parks. In order to enhance the core competitiveness of China's industrial parks, promote structural reforms in the energy sector, and develop based on the energy-based Internet thinking model and the development of new industrial parks, this paper mainly introduces the company's newly developed industrial park integrated energy service platform. [5]

With electricity as the core link of energy development, the energy strategy is mainly determined by various factors of production, the law of energy development and the unique characteristics of the power industry. [6] The energy supply of industrial parks will also be depended on electricity, and the realization of energy balance depends to some extent on the balance of power supply and demand. [7] Through the substitution of electric energy to realize the transformation of energy structure, the power generation is the focus of primary energy conversion and utilization. It can flexibly accept distributed power sources with multiple access points and other forms of energy, fully integrate distributed energy, integrate energy information widely, and promote primary energy. Clean and efficient development of resources and rational layout. [8] It introduces clean energy such as solar energy and wind energy, and replaces fossil energy by non-fossil energy through electricity, and adjusts with traditional municipal electric energy, gas, heat network and energy storage devices. [9] Its strategic transformation should include multiple aspects, namely, the transition from high-carbon energy structure to low-carbon type, extensive energy utilization to intensive and efficient, and energy service from one-way supply mode to intelligent interaction mode. [10]

In the rapid development stage of energy Internet and integrated energy services, our company has launched an integrated energy service platform for industrial parks in a timely manner and successfully put into operation in Wuxi Xingzhou Industrial Park. This paper focuses on the integrated energy service platform, combined with the actual project implementation, to show the latest development of the integrated energy service platform. Our company's latest industrial park integrated energy service platform has the following characteristics:

(1) Integrated design, system integration design, embody different connotations in different application scenarios, system realizes integrated architecture design of platform and application, establish integrated data center by using power grid panoramic view, and comply with relevant international standards Integrated design of the application. In the dispatch center, this integrated design is embodied in the integration of maintenance, data and models, and can realize the vertical integration of related applications.

(2) Standardization, each functional subsystem or functional module of the system is implemented in a modularized, standardized manner. The system platform follows the hardware equipment independence, grid model standardization, data communication standardization unified standards and norm construction, and facilitates the expansion of functions.

(3) Reliability, the platform provides a variety of system management services to support the application system to ensure its continuous, uninterrupted operation. In the case of no hardware failure and manual intervention on the duty equipment, automatic switching does not occur between the primary and backup applications. In the limit accident state of "single-machine single network", the data acquisition and processing functions ensure its integrity and correctness, and ensure that the basic functions of the system are not affected.

(4) Openness, the platform architecture has been fully considered in all aspects of design and function implementation to ensure system portability, scalability, interoperability and network connectivity, thus ensuring the openness of the system. The system is designed to comply with relevant international and industry standards and adhere to the principle of portability, which ensures that the system keeps up with the latest technology. Openness makes application integration in power system IT environments easier.

(5) Scalability, platform architecture design can ensure its continuous expansion and update, and constantly follow up the development of new technologies to meet the needs of users tomorrow. With standard features and tool sets, you can continuously upgrade and extend existing systems without affecting system uptime.

(6) Full support of C/S and B/S, the system not only realizes model and data integration and service, but also realizes integration and service of various application functions, and realizes sharing of various functions of the system. Implementation forms include C/S mode and B/S mode.

2. The overall structure of the park's integrated energy service platform

The integrated energy service platform of the industrial park needs to comprehensively control the energy flow, load flow, business flow and information flow in the industrial park in accordance with the characteristics of the integrated energy service platform, maximize the development and utilization of renewable energy, and improve the comprehensive utilization efficiency of energy. Provide users with economical, safe, reliable, convenient and efficient energy services to achieve grid-friendly, user-friendly construction of the park's energy interconnection system. The integrated energy service platform can create an open software and hardware platform and comprehensively optimize the management of energy, power grid and load according to the needs of different levels of users, taking into account various factors such as energy supply end characteristics, load type, energy-using equipment and operational personnel quality. Provide diversified services for the main body of the grid and the users on the user side, leading the trend of the construction of integrated energy service platforms. The overall architecture of the system is shown in Figure. 1. The overall architecture of the integrated energy service platform includes: information collection and control terminal subsystem, communication and storage system, function and application software system.

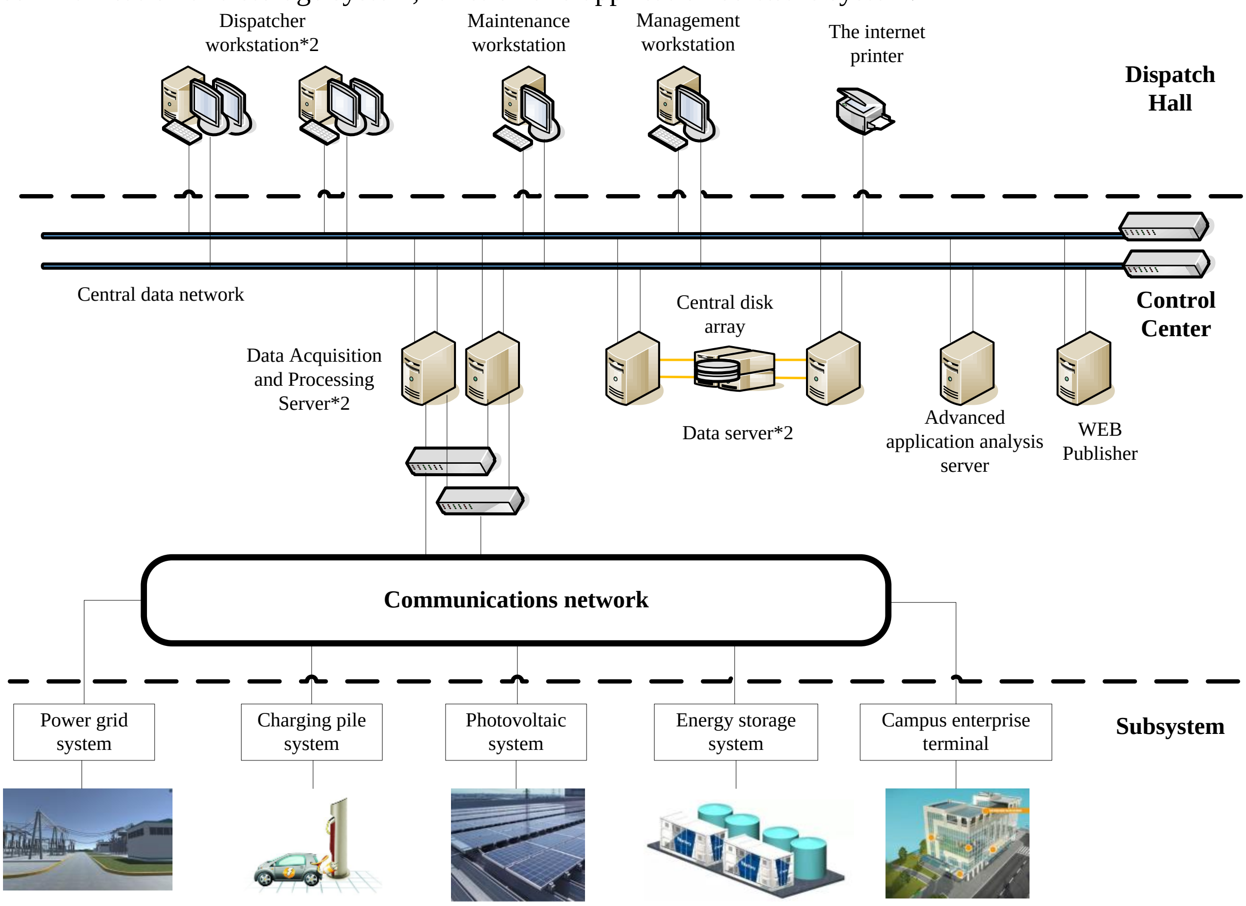

Figure 1. Overall architecture of the integrated energy service platform

The information collection and control terminal subsystem is mainly responsible for the data collection and processing of the grid, natural gas network, thermal network, power station, energy storage station and load information of each enterprise in the industrial park, and is uploaded to the central data collection server through the communication network. The intelligent user terminal can access various energy-consuming equipment, smart meters and sensor data in target buildings such as residents, businesses, and industries, and interact with the integrated energy service platform in real time. At the same time, the device can also switch and control the energy-consuming equipment in the target building.

The data collected by the underlying device is uploaded to the local subsystem server through fiber, wireless, etc., and the data is pre-processed, and the subsystem data can be viewed through the subsystem. The integrated energy service platform control center communicates with each subsystem through the communication network and collects all data to the control center server. Realize system status real-time monitoring, energy and load forecasting, energy-optimized scheduling, demand-side management, and advanced energy efficiency analysis.

The capabilities of the integrated energy services platform include device information collection and intelligent information processing, intelligent applications, advanced services, and intelligent decision making and control. Equipment information collection is effective measurement of power supply system, heating network, gas system, power generation, energy storage, users and other information and uploads to the data processing center through fiber or wireless communication channels for pre-processing and further analysis. Firstly, based on the measured data and historical data, the multi-time scale prediction of photovoltaic power generation, electric/heat/gas load is carried out, and the energy demand-scheduled model is established based on the integrated demand side response technology to carry out high-efficiency energy distribution. As one of the key means of market competition, service is the lifeline that determines whether the park can operate for a long time. Therefore, it is necessary to define the effective service content of the integrated energy service platform, including the core contents of energy efficiency, energy saving income and auxiliary income.

3. Key technologies of the park’s integrated energy service platform

3.1. Platform software architecture

A large number of distributed new energy photovoltaic, wind power and controllable load access requirements must be highly scalable. Different from the wide-area communication demand of the global energy Internet, the main characteristics of the communication of the integrated energy service platform of the industrial park are characterized by short communication distance, many interfaces and frequent interaction. Therefore, targeted solutions such as Ethernet, GPRS, LTE, Wifi, Zigbee and 4G/5G are more advantageous than fiber-optic communications suitable for long-distance information transmission.

The software architecture of the integrated energy service platform is shown in Figure. 2.In the software architecture of the integrated energy service platform, there are five layers, which are bottom-up:

1) Hardware platform layer: It can be various hardware platforms popular today, such as a computer that can be a RISC architecture or a computer with a CISC architecture; it can be a 32-bit machine or a 64-bit machine.

2) Operating system platform layer: The operating system can use a variety of popular operating systems, such as several mainstream UNIX, LINUX and Microsoft Windows.

3) Universal middleware layer: It enables the system to run on a variety of operating systems and hardware platforms, and has good portability. At the same time, it has scalability, heterogeneous systems, interoperability and so on.

4) Unified support platform layer: Provide a powerful and universal service, provide unified data management, high-performance real-time data access, coordinated human-computer interaction interface, network messaging, inter-process communication, system management, alarm and Events, data forwarding and other services. The various applications of the system are built on a unified data platform, an Internet/Intranet-based communication management subsystem, a fully graphical WEB-based user interface subsystem, a system management subsystem, and an alarm subsystem.

5) Application layer: On the unified support platform layer, realize the operation monitoring of power supply system, heating network, gas system, power generation system, energy storage system, user energy use; energy operation management; energy efficiency analysis management; optimization analysis and scheduling A series of software for training simulation with dispatchers. Each application

of the system adopts a modular design, and the user selects the required module to build the operating system according to the needs.

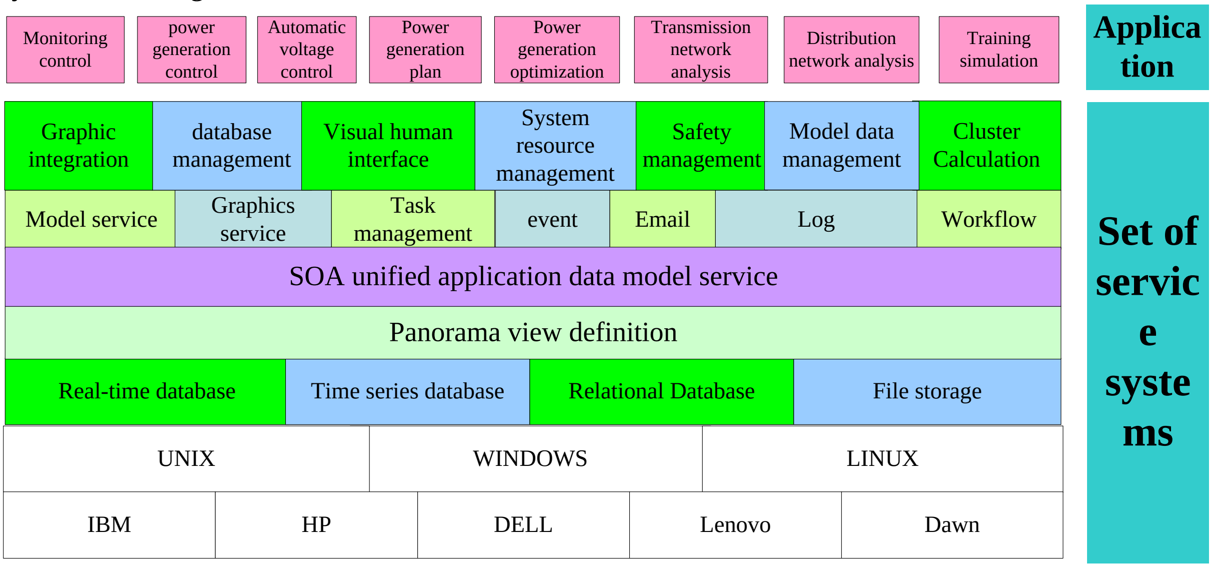

Figure 2. System software architecture

3.2. Data acquisition and monitoring SCADA

SCADA (Supervisory Control and Data Acquisition) is the basic application of the integrated energy service platform of the industrial park. It consists of front-end data acquisition devices and I/O nodes, SCADA nodes, network communication nodes, and historical nodes. SCADA functions include: data acquisition and processing, accident recall (PDR), alarm processing, and event sequence recording (SOE).

The system's data collection function supports information packet collection, wireless network mode information collection, and automatic data channel port-based duty function to achieve data collection for plant stations and soft handover to the active and standby channels. The pre-data collection server makes full use of the data network resources to reduce the dedicated line communication, and the network is the main one. The network and the dedicated line coexist and are mutually active, and comprehensively consider the lightning protection measures of the communication system.

The system shall be capable of acquiring and processing the following types of data: analog, electrical, state (including dual position), time sequential recording, protection device setting parameters and action signals, RTU reset signals. In order to ensure the reliability of information transmission, an error check code is used. The system can collect information of various RTUs and subsystems, receive forwarding data of monitoring systems such as EMS and centralized control stations of power supply companies, and data transmitted by GPS clocks, frequencies, UPS power supplies and other computer systems, and manually set data. The system can receive RTUs with different transmission protocols and different communication methods (synchronous, asynchronous, etc.), and there should be a specification library, such as the ministerial CDT protocol (new/old protocol and variant version), DNP3.0, IEC 60870-5-101, IEC 60870-5-103, IEC 60870-5-104, TASE2, 1801, S5, DISA, POLLING, MODBUS and other common domestic regulations can explain various specifications in more detail. The system not only supports basic serial port standards such as RS232, but also fully supports various serial port protocols; the supported protocols are: TCP/IP, PPP, SLIP, etc., to ensure the advancement of communication component technology.

3.3. Multi-optimal scheduling

Multi-energy optimization scheduling is responsible for comprehensive optimization and scheduling of multiple energy sources in the integrated energy service platform, which is an important means to achieve “multi-energy complementarity”. Fully analysis the utilization characteristics of various energy sources and evaluate the energy utilization efficiency under specific utilization forms. With the

energy supply and load forecasting information and equipment operating status as input data, construct the corresponding objective function according to the user's needs or the system optimization purpose of integrated energy. Select the appropriate optimization algorithm to solve the problem, generate multi-energy optimization operation strategy, and realize the multi-energy complementation of energy supply, energy storage and load in the network. According to the network topology and specific needs, the scheduling decision variables include: photovoltaic power generation, natural gas network gas supply; battery charge and discharge time and power; exchange with external electricity, gas, water and other energy; controllable load The amount of energy used, etc.
Different from traditional power system scheduling, the scheduling of integrated energy involves the interests of multiple entities and the mutual transformation of multiple energy sources. How to get the maximum comprehensive benefits is a problem that needs attention. At the same time, the energy Internet is the product of smart grid and energy structure reforms, and its operations must fully consider energy, environmental and social benefits. Therefore, the optimal scheduling of the integrated energy service platform must be a multi-objective optimization problem involving complex constraints.

3.4. Operational analysis application service

(1) Comprehensive decision analysis of electricity reliability. For the large-scale industrial enterprises accessing the integrated energy service platform (the highest voltage level is 110kV and above), the comprehensive decision analysis of power reliability can be analyzed by the following analysis methods, including power loss load statistics, power risk online analysis, and dispatch operation assistance. Decision-making, orderly electricity management, emergency plans and accident decision support. It can analyze the statistical loss caused by power outages, power outages and expected power outages, and provide a visual data display method. The power risk online analysis function module performs relevant analysis and judgment through network topology and real-time data, and comprehensively identifies, judges, analyzes, and classifies according to the characteristics of some common risks and custom risks, as well as risk triggering conditions and requirements. Present possible risks and provide accurate and comprehensive tips. This function can provide necessary reminders and auxiliary basis for scheduling related personnel to operate, troubleshoot, etc. Online risk analysis includes: important user monitoring, special operation mode monitoring, heavy equipment monitoring, accident risk analysis, and maintenance risk analysis.
(2) Power quality analysis and optimization. Power quality analysis and optimization functions should include voltage tolerance, voltage allowable fluctuations and flicker, three-phase voltage allowable imbalance, grid harmonics, etc., by comparing harmonics, voltage analysis and industry standard limits. This reveals existing and potential power quality issues, as well as safety issues associated with harmonics. Support standard value management such as harmonic voltage, harmonic current, harmonic content, harmonic content rate, harmonic order, total harmonic distortion rate, etc., can maintain and manage standard limits, including new indicators and their limits Add, delete, modify, view, etc. Support statistical queries for transient events, and query results can be used for transient event curve analysis and event statistics. Support standard deviation management such as voltage deviation, three-phase voltage unbalance, voltage fluctuation, voltage pass rate, over-voltage, etc., can maintain and manage standard limits, including adding, deleting, modifying, and viewing indicators and their limits. Wait.
(3) Analysis of energy efficiency evaluation. The electricity consumption KPI index should be based on the economic and security perspectives for the enterprise electricity consumption, and the KPI indicators should be used to find out the problems existing in the enterprise electricity, and provide data support for the enterprise to optimize energy. In combination with the company's electricity bills, the economic indicators have been developed with indicators such as power factor assessment indicators, demand assessment indicators, and peak-to-valley electricity costs. From the aspect of affecting the daily safety production of enterprises, the three-phase unbalance rate assessment indicators are mainly formulated. The user's energy consumption ranking in the district provides a list of users' electricity consumption and rankings in the district, which is convenient for understanding the electricity consumption of the whole district, real-time information of the major customers, and providing effective data support for the later grading services, providing large customers with

Personalized quality service to improve the satisfaction of large customers. The user energy consumption ranking in the district provides a list of users' electricity consumption and rankings in the district. It is easy to understand the distribution analysis of the industry's electricity consumption in the whole district. The enterprises are classified according to their industry categories, and the total electricity consumption of each industry is counted. Analysis the electricity structure in the district from an industry perspective. Through the industry's output value power consumption, it can assess the power consumption of output value of various industries, and provide horizontal benchmarking for various industries, providing vertical benchmarking functions for enterprises and industries. Monthly, the enterprise users will be provided with a monthly electricity analysis report to calculate the power consumption of the company last month and provide data evaluation basis from the perspectives of economy and safety. The analysis report describes in detail the daily electricity tariff for the previous month, the total electricity tariff for the month, the distribution of electricity consumption, the distribution of electricity tariffs, the economic and safe operation status of each transmission line of the enterprise, the economic operation status of the internal transformer of the enterprise, and the economic operation status of the whole company. In addition, the analysis report provides a preliminary diagnosis recommendation for the company based on historical experience.

3.5. Integrated services

Value-added services are an important manifestation of creating value for users. They are big data, cloud computing, and mobile Internet. They are important tools for energy demand side users on the basis of data panoramic display and application services. Services, user energy conservation and customized services, big data information value-added services, energy optimization management services, etc.

The comprehensive energy service platform of the industrial park should make full use of the power system reform and improve the business model of energy management, and continuously improve its competitiveness in a fully competitive energy market. On the one hand, it is necessary to meet the basic diversified energy needs of users; on the other hand, it is necessary to guide users to change their inherent consumption habits, provide innovative energy services and interactions, and provide professional services, management and operation and maintenance platforms based on online services. Information, streamlined, intelligent, and closed-loop interactive service models provide customers with comprehensive energy services throughout their life cycle.

4. Conclusion

The integrated energy service platform of the industrial park realizes multi-energy complementarity through the application of advanced new energy power generation management technology and multi-energy flexible conversion network such as electric-gas-heat/cold, and coordinates and optimizes the source network-charge by using advanced energy-efficiency analysis technology and communication network. - Energy flow and information flow between the stores. The industrial park-level energy service platform can provide support and auxiliary services to the grid, and can guide users to actively participate in energy regulation. Establishing an industrial park-type integrated energy service platform to realize the joint optimization of the public energy network-park energy network-user cluster/individual multi-level level is of great significance to promote the absorption of new energy and the efficient and safe operation of the network.

This paper analysis the characteristics of the integrated energy grid and the generalized energy Internet under the premise of clearly defining the scope of the integrated energy service platform of the industrial park. It points out the basic structure and key technical content of its energy efficiency management, which is existing and under construction. The demonstration project energy management model provides an effective reference and a clear construction direction. Our company's later research will focus on the realization of multi-functional platform construction and business model innovation, as well as energy conversion efficiency, energy router optimization and so on. We will continue to develop regional, building, hospital, school, industrial and mining enterprise sub-platforms based on customer needs, and enhance customer energy self-management capabilities. At the same time, it will continue to innovate the platform service model, segment the target customer groups, provide industry analysis for the industry, assist in the formulation of energy and industry policies, provide market potential analysis for energy service providers, and promote project cooperation; for equipment manufacturing enterprises and research units. Provide equipment energy efficiency analysis and promote technological innovation.

5. References

[1] Jia Hongjie, Wang Dan, Xu Xiandong, Yu Xiaodan, “Research on Several Issues of Regional Integrated Energy System” Automation of Electric Power Systems, pp. 198-207, July 2015.
[2] Zheng Zongqiang, Yan Mingyu, Peng Hui, Meng Yongliang, “Power System Regulation Distributed SCADA System Architecture and Key Technologies” Automation of Electric Power Systems, pp. 71-77,May. 2017
[3] Deng Wei, Ding Yi, Wang Yonghui , “Research on Energy Internet Architecture for Smart Campus” Electronic design engineering., pp. 110-113, Aug 2018.
[4] Li Bin, Cao Wangyu, Zhang Jie, Chen Songsong, “Multi-energy system trading system and key technologies based on heterogeneous blockchain” Automation of Electric Power Systems, pp. 183-193, April 2018.
[5] Chen Baisen, Liao Qingfen, Liu Dichen, Wang Wenyi, “Comprehensive evaluation indicators and methods for regional integrated energy systems” Power System Automation, pp. 174-182, April. 2018
[6] Ai Wei, Hao Ran, “Automation of Electric Power Systems” Electronic design engineering., pp. 2-10, Apri 2018.
[7] Tan Tao, Shi Jiaqi, Liu Yang, Zhang Jianhua, “The Characteristics of Campus Energy Internet and Key Technologies of Energy Management Platform” Power construction, pp. 20-30, Dec 2017.
[8] Yang Jincheng, Luo Jianbo, Kang Lihui, Shen Zhonghua. “Integrated energy services under the regional energy Internet architecture” Shanghai Energy Saving, pp. 137-146, March. 2017
[9] Xu Xiandong, Jia Hongjie, Yan Xiaolong, “Research on electric/gas/thermal hybrid power flow algorithm for regional integrated energy system” Proceedings Of The CSEE., pp. 3634-3642, April 2015.
[10] Qi Kaiping, Zhang Xiaoshun, Yu Tao., “Joint optimization scheduling of multi-energy systems based on knowledge migration Q learning algorithm” Automation of Electric Power Systems., pp.18-25, May 2017.Reference lists

Acknowledgments

Thanks to the company for providing technical support and personnel assistance. Thanks to the engineering staff of the Sin Chew Industrial Park Integrated Energy Service Platform Project.

IOP Conf. Series: Earth and Environmental Science **431** (2020) 012057 doi:10.1088/1755-1315/431/1/012057

Prospect analysis of high temperature air combustion technology for low calorific value coalbed methane in Liupanshui area of Guizhou province

Yu Zhou[1], Xiaowei Ji[1] and Jie Tang[1]

1 Liupanshui Normal University, College of Electrical Engineering, Department of Energy and Power Engineering, Liupanshui
E-mail:zhyu_86@163.com/86_zhyu@tongji.edu.cn

Abstract. China's coalbed methane resource is abundant, which ranks third in the world. The total amount of coalbed methane resources in Guizhou Province accounts for about 10% of China, which ranks second in the country. However, the utilization rate of coalbed methane in Guizhou Province is not only low, but also relatively single, especially the low calorific value coalbed methane extracted from underground mines which has a methane concentration of only 10-30%. And the main method to deal with low calorific value coalbed methane is discharging directly, which caused a huge waste of energy. High temperature air combustion technology (HTAC), which expands the utilization range of low calorific value fuels, has attracted wide attention due to its characteristics of extreme recovery of waste heat and ultra-low NOx emission. In this paper, the characteristics of high temperature air combustion of low calorific value coalbed methane are analyzed by theoretical and numerical calculation based on combustion theory and CFD method.

1. General situation of low calorific value coalbed methane in Liupanshui area

Coalbed methane (CBM), commonly known as "gas", refers to hydrocarbon gas [1-2], which is stored in coal seams, mainly composed of methane, adsorbed on the surface of coal matrix particles, partially free from coal pore or dissolved in coal seam water. It belongs to unconventional natural gas, and is a clean, high-quality energy and chemical raw material rising internationally in recent decades. At present, the global CBM reserves are about 124.8 trillion m^3, 90% of which are distributed in 12 major coal-producing countries. China's CBM reserves are about 30-35 trillion m^3, ranking third in the world [3-5]. The total amount of CBM resources in Guizhou Province is 3.15 trillion m^3, accounting for about 10% of the country, ranking the second in the country, after Shanxi [6-7]. Coalbed methane resources in Guizhou Province are mainly distributed in Liupanshui, Zhina and Northern Guizhou coalfields, accounting for 92.8% of the total coalbed methane resources in Guizhou Province [8-9].

According to statistics, the total amount of gas extracted from underground coal mines in Guizhou in 2009 is 674 million m^3, of which 83.92 million m^3 is used for power generation and as civil fuel. The utilization rate of gas in Guizhou Province is only 12.4%, most of which are discharged into the air as exhaust gas. In 2011, the utilization rate of Coalbed methane in Guizhou Province is 16% [10]. In 2016, the gas extraction rate in Guizhou Province is 231311.91 million m^3, and the utilization rate is 78711.34 million m^3. The utilization rate is only 34%, of which the utilization of gas power generation is 76726.83 million m^3, accounting for 97.5% [11] of the total utilization. From the above statistics, not only the utilization rate of CBM in Guizhou Province is low, but also the utilization form is relatively single, the main way of utilization is gas power generation, a small amount of which is used for civilian use.

At present, the way of CBM exploitation in Guizhou Province is mainly underground extraction, supplemented by surface extraction [12-13]. The concentration of methane in underground extraction CBM is only 10-30% which cannot meet the requirements of direct utilization, so it must be discharged into the atmosphere, resulting in huge energy waste. Take 2016 as an example, the annual CBM extraction volume in China is 173 billion m^3, of which underground gas extraction is one. With a utilization of 128 billion m3 and a utilization of 48 billion m3, the utilization rate is 37.5%, while the surface coalbed methane production is 45 billion m^3 and utilization of 42 billion m^3, the utilization rate is 93.3%. Therefore, it is of far-reaching significance to study how to utilize the low calorific value coalbed methane extracted from underground mine, improve the utilization rate of coalbed methane and turn waste gas into useful resources to alleviate the current energy shortage and optimize the energy structure.

2. High temperature air combustion technology

High temperature air combustion technology, also known as regenerative combustion technology, is a new type of combustion technology widely applied in developed countries since 1990s. Fig. 1 illustrates the principle of HTAC technology. The system consists of a pair of burners, regenerators, reversing valves and corresponding control systems. When the combustion-supporting air is fed by B burner, the air at ambient temperature is heated by the preheated high-temperature regenerator in B burner, then injected into the furnace and combusted with gas. After heat exchange in the furnace, the combustion-supporting air is discharged by A burner, the regenerator in A burner is heated at the same time. After appropriate time, through the switching function of the reversing valve, the combustion-supporting air is supplied by A burner, and the smoke is exhausted by B burner, so that the heat storage and heat release process can be completed again and again.

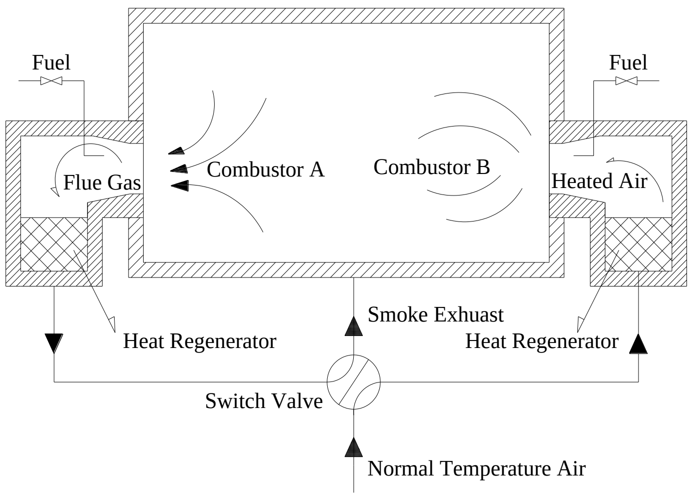

Figure 1 Schematic diagram of regenerative combustion technology

HTAC technology alternately stores heat and exhausts smoke through pairs of regenerative burners. The high temperature flue gas is strongly disturbed in the furnace and constantly changes its direction, which makes the temperature distribution in the furnace very uniform and avoids the appearance of local high temperature. At the same time, due to the regenerator's regenerative effect, the limit recovery of waste heat and the preheating of air are realized, the preheated air temperature usually can reach 1000 ~ 1400℃, which can save nearly 50% of the fuel [14] compared with the traditional combustion mode. In addition, in industrial furnaces using HTAC technology, fuel is burned in combustion-supporting air with oxygen concentration less than 21% through the organization of combustion conditions, thus reducing the production of NOx and environmental pollution.

3. Combustion theory calculation

IOP Conf. Series: Earth and Environmental Science **431** (2020) 012057 doi:10.1088/1755-1315/431/1/012057

3.1. Composition of coalbed methane

Based on the investigation of CBM storage status in southwestern Guizhou, this paper chooses several typical areas such as Jinjia mining area, Songsha mining area and Xingyi Chaoyang mining area for calculation and analysis. Among them, Jinjia mining area and Songsha mining area belong to Liupanshui. The composition of CBM in each area is shown in Table 1. The calculation results of low calorific value and high calorific value are also listed in the table. It can be seen that the coalbed methane in the above areas belongs to low calorific value fuels.

Table 1 Composition and calorific value of coalbed methane in different regions.

	Jinjia Mining Area	Songsha area	Chaoyang Mining Area, Xingyi
CH_4	20%	25%	30%
N_2	63%	61.5%	45.86%
CO_2	10.5%	2.2%	11.24%
C_2H_6	2.5%	3%	2%
C_3H_8	1.5%	0%	1.5%
C_4H_{10}	1%	0%	0%
CO	0%	6%	0%
O_2	0%	0.6%	0%
Other	1.5%	1.7%	1.5%
$H_l\left(kJ/m^3\right)$	10831.5	11099	12519
$H_h\left(kJ/m^3\right)$	11930	12200.6	13789

3.2. Explosion Limit

Explosion limit means that combustible materials and air must be uniformly mixed in a certain concentration range to form premixed gases and explode when confronted with fire source. The explosion limit is calculated by the following empirical formula.

The lower explosion limit: $$L_{\text{lower}}=\frac{100}{4.76(n\text{-}1)+1}\times 100\% \quad (1)$$

The upper explosion limit: $$L_{\text{upper}}=\frac{4\times 100}{4.76n+4}\times 100\% \quad (2)$$

In which: L_{lower} -- the lower explosion limit for combustible mixtures;

L_{upper} -- the upper explosion limit for combustible mixtures;

n --number of oxygen atoms required for complete combustion of 1 mol combustible gas.

The explosion limits of coalbed methane in Jinjia mining area, Songsha mining area and Chaoyang mining area in Xingyi are calculated. As shown in Table 2, the concentration of methane in low calorific value coalbed methane ranges from 20% to 30%, the explosion limit ranges from 11% to 48%, the explosion range is large. The explosion limit range is the smallest when the concentration of methane in coalbed methane is 25%.

Table 2 Calculation results of explosion limit.

	Jinjia Mining Area	Songsha area	Chaoyang Mining Area, Xingyi

Upper explosion limit	12.7%	15.8%	11.9%
Lower explosion limit	40.32%	39.7%	47.1%

3.3. Calorimeter temperature

A certain proportion of gas and air combustion, the heat includes two parts: one is the physical heat of gas and air (enthalpy of gas and air); the other is the chemical heat of gas (calorific value). If the combustion process is carried out under adiabatic condition, the two parts of heat are all used to heat the flue gas itself, the temperature that the flue gas can reach is called calorimeter temperature, and is calculated by formula (3).

$$\mathrm{t_c} = \frac{H_l + (c_g + 1.266\mathrm{c}_{H_20} d_g) t_g + \alpha V_0 (c_a + 1.266\mathrm{c}_{H_20} d_a) t_a}{V_{R0_2} c_{RO_2} + V_{H_2O} c_{H_2O} + V_{N_2} c_{N_2} + V_{O_2} C_{O_2}} \tag{3}$$

In which: H_l --Low calorific value of gas, kJ/m^3 (dry gas);

α --Excess air coefficient;

c_g、c_{H_2O}、c_a、c_{RO_2}、c_{N_2}、c_{O_2} --The average volume constant pressure heat capacities of gas, H_2O, air, triatomic gas, N_2 and O_2 from 0 to t_f℃, kJ/(m^3·k), respectively.

t_g 、 t_a --Gas and air temperature, ℃;

V_0 -- Theoretical air requirement, m^3 (dry air)/m^3 (dry gas);

V_{R0_2} 、 V_{H_2O} 、 V_{N_2} 、 V_{O_2} -- The volume of triatomic gas, water vapor, N_2, O_2 produced by fully burning 1 m^3 dry gas, m^3/m^3 (dry gas);

d_a、 d_g -- The moisture content of air and gas, kg/m^3,(dry air).

If the moisture content of air dg=10g/m3 (dry air), and the moisture content of coalbed methane is not counted. The calculating results of calorimeter temperature after complete combustion of coalbed methane at air temperature 1073K, 1173K and 1273K in three regions are shown in Table 3.

Table 3 Calorimeter temperature calculation results.

Air temperature（K）	Calorimeter temperature（K）		
	Jinjia Mining Area	Songsha area	Chaoyang Mining Area, Xingyi
1073	2260	2314	2321
1173	2263	2369	2381
1273	2385	2427	2439

From Table 3, when the combustion-supporting air temperature is 1023K, the calorimeter temperature of low calorific value coalbed methane in three mining areas can reach more than 2000K. With the increase of air temperature and methane concentration, the calorimeter temperature shows an upward trend, and the influence of air temperature on combustion temperature is more obvious of methane concentration.

4. Numerical simulation and comparative analysis with the theory calculation

The combustion process of low calorific value coalbed methane is simulated by CFD method. Assuming that the fuel is burned in a circular tube, the diameter is 200 mm, the length is 600 mm, the size of the gas and air inlets are 10 mm and 20 mm respectively, the air inlets are evenly arranged around the gas inlets, and the wall condition is adiabatic, the model is simplified to two-dimensional. The geometric structure and meshing of the model are shown in Figure 2. The model is meshed with structured grid, the mesh of air and gas inlets are partially densified.

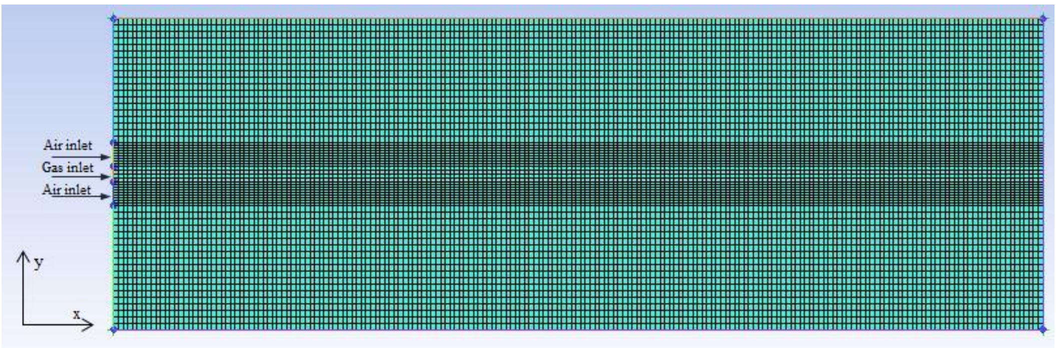

Figure 2 Geometric model and mesh generation

Taking Jinjia Coal Mine as an example, assuming that the inlet temperature of air is 1073K, the velocity is 2 m/s, the inlet temperature of gas is 300K and the velocity is 5 m/s, the steady-state numerical simulation of combustion process is carried out by using Eddy-Dissipation combustion model. The numerical results of combustion temperature, CH_4, O_2 and CO distributions are shown in Fig. 3-5 respectively.

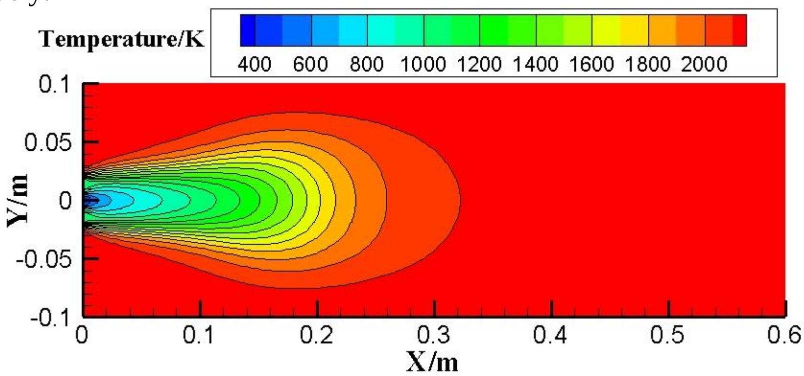

Figure 3 Contour of combustion temperature with 20% CH_4 Coalbed Methane

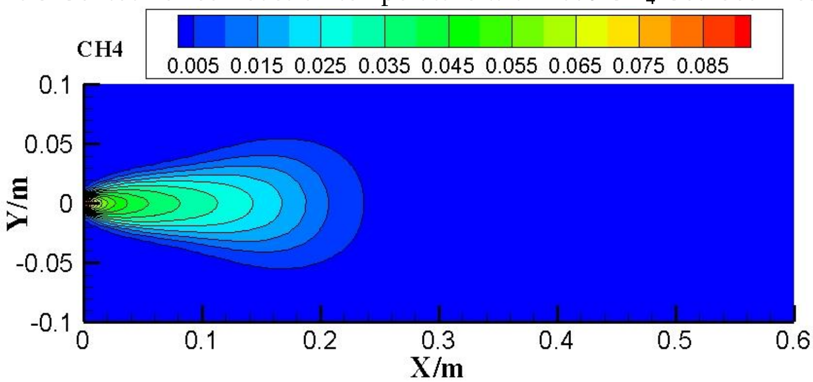

Figure 4 Contour of CH_4 concentration with 20% CH_4 Coalbed Methane

From Fig. 3, the outlet temperature of flue gas is 2180 K, the theoretical calculation value is 2260 K, and the error is 3.5%. The numerical simulation results are in good agreement with the theoretical calculation results. The numerical simulation results are slightly lower than the theoretical calculation values. The main reasons for the error are: (1) the loss of chemical incomplete combustion and the decomposition of flue gas components at high temperature are neglected in theoretical calculation;(2) The combustible components other than methane such as ethane in coalbed methane are neglected in numerical simulation.

From Fig. 4 to Fig. 5, the concentration of CH_4 and O_2 at the exit are close to 0, indicating that CBM and air are close to complete combustion, so does the CO concentration in Fig. 6.

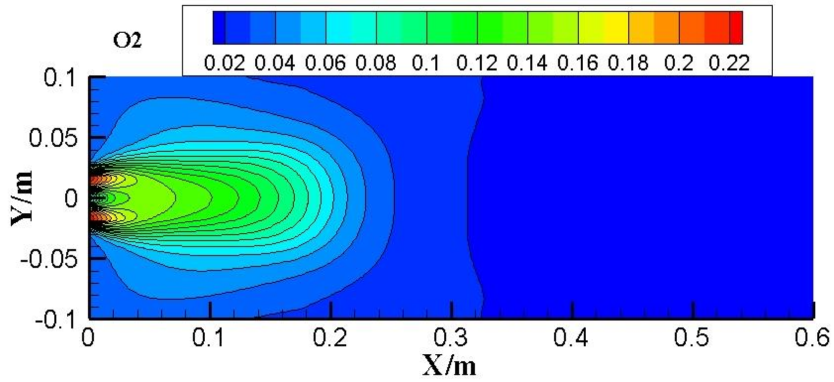

Figure 5 Contour of O_2 concentration with 20% CH_4 Coalbed Methane

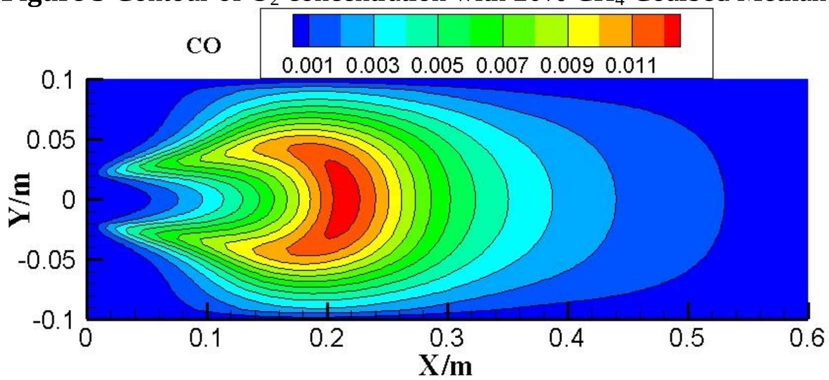

Figure 6 Contour of CO concentration with 20% CH_4 Coalbed Methane

Similarly, the numerical results of low calorific value coalbed methane in Songsha area and Chaoyang mining area in Xingyi are shown in Table 4, the numerical simulation value is always lower than the theoretical calculation value. The cause of the error has been analyzed in the previous part, and it will not be mentioned here. In addition, the higher the methane content in coalbed methane, the smaller the error between calculated and simulated values, and the error is within the allowable range.

Table 4 Comparison of theoretical and simulated combustion temperatures.

	Theoretical calculation value	Numerical simulation	relative error
Jinjia Mining Area	2260K	2180K	3.5%
Songsha area	2317K	2274K	1.8%
Chaoyang Mining Area, Xingyi	2326K	2304K	0.9%

5. Conclusion

In view of the present situation of rich CBM resources but low utilization rate, especially low calorific value CBM in Guizhou Province, combined with the characteristics of high temperature air combustion technology, the feasibility of applying high temperature air combustion technology to low calorific value CBM is analyzed theoretically and numerically in this paper.

(1) Through the investigation of Jinjia mining area, Songsha mining area and Xingyi Chaoyang mining area, most of the coalbed methane content is below 30%, which belongs to low calorific value fuel.

(2) When the concentration of methane in low calorific value coalbed methane ranges from 20% to 30%, the explosion limit ranges from 11% to 48%, the explosion limit range is large, and the explosion limit range is the smallest when the concentration of methane in coalbed methane is 25%.

IOP Conf. Series: Earth and Environmental Science **431** (2020) 012057 doi:10.1088/1755-1315/431/1/012057

(3) The theoretical calculation and numerical results of combustion of low calorific value CBM in high temperature air state are similar. When the temperature of combustion-supporting air is 1073K, the calorimeter temperature of combustion of low calorific value coal bed methane in three mining areas can reach more than 2000K. With the increase of air temperature and methane concentration, the calorimeter temperature shows an upward trend, and the influence of air temperature is more significant with the increase of the concentration of methane.

(4) The application of high temperature air combustion technology in the utilization of low calorific value CBM in Liupanshui area of Guizhou Province has a very broad prospect.

6. References

[1] Xie Wei, He Ting, Yang Ming, et al. Features and recovery technology of coal-bed gas in Guizhou[J]. Drilling and Production Technology, 2011, 34 (3): 58-60.

[2] Li Bobo, Yuan Mei, Ma Kewei. The utilization of methane and the analysis of influencing factors in Guizhou province [J]. Coal Mine Modernization, 2009 (5): 4-5.

[3] Tao S, Pan ZJ, Tang SL, Chen SD. Current status and geological conditions for the applicability of CBM drilling technologies in China: A review[J]. International Journal of Coal Geology, 2019.

[4] Qin Y, Tang X Y, Jian-Ping Y E, et al. Characteristics and Origins of Stable Carbon Isotope in Coalbed Methane of China[J]. Journal of China University of Mining & Technology, 2000, 29(2):113-119.

[5] Fu H, Tang D, Hao X, et al. Geological characteristics and CBM exploration potential evaluation: A case study in the middle of the southern Junggar Basin, NW China[J]. Journal of Natural Gas Science & Engineering, 2016, 30:557-570.

[6] Li S , Tang D , Pan Z , et al. Evaluation of coalbed methane potential of different reservoirs in western Guizhou and eastern Yunnan, China[J]. Fuel, 2015, 139:257-267.

[7] P Ren, H Xu, D Tang, Y Li, Z Chen, et al. Pore structure and fractal characterization of main coal-bearing synclines in western Guizhou, China[J]. Journal of Natural Gas Science and Engineering, 2019.

[8] Zhang Chunpeng, Wu Caifang, Li Teng, etc. Principal Component Analysis Method applied to evaluation on coalbed methane block selection [J]. Coal Science and Technology, 2016, 44 (08): 137-142.

[9] Gao Di. The prospect of 3 trillion cubic meters CBM development in Guizhou Province is vast [J]. Contemporary Guizhou, 2010 (20): 68-69.

[10] Huang Pei. Geological conditions and development and utilization situation of coal bed methane in Guizhou Province[J]. Clean Coal Technology, 2011, 17 (5): 104-105.

[11] Tang Yong. Present Situation and Foreground of Development and Utilization in Coalbed Methane in Guizhou [J]. Chemical Industry, 2017, 35 (5): 43-45.

[12] Yuan Mei, Li Xijian, Li Bobo, et al. Discussion of present situation of exploitation and utilization of coal bed gas resource in Guizhou Province [J]. Mining and Processing Equipment, 2008 (20): 11-13.

[13] Ma Shu, Luo Yong, Han Shixin, et al. [J]. The analysis of the situations and patterns of ground gas drainage of coal mine in Guizhou of China [J]. China Coal, 2016, 42 (3): 92-96.

[14] Zhou Yu, Qin Chaokui. Application Prospect of Natural Gas Regenerative Combustion Technology in Small-Size Heating Furnace [J]. Industrial Furnace, 2016 (6): 13-15.

Acknowledgments

Financial support for this work was provided by the Guizhou Provincial Education Department Foundation Project: Application study on High Temperature Air Combustion Technology in Low Calorific Value Coalbed Methane in Liupanshui Area (No. Qianjiaohe KY Zi[2018]373) and Research Initiation Fund of Liupanshui Normal University (LPSSYKYJJ201815) and (No.LPSSYKYJJ201814).

IOP Conf. Series: Earth and Environmental Science **431** (2020) 012053 doi:10.1088/1755-1315/431/1/012053

Trans-regional power trading optimization for promoting clean energy accommodation

Shi Xinhong[1], Yefei[1], Panjiajia[1], Zhangxu[1], Wang Gaoqin[1], Lv Jianhu [1]

1 China Electric Power Research Institute, No.8 Nanrui Road, Gulou District, Nanjing City, Jiangsu Province
E-mail: shixinhong@epri.sgcc.com.cn

Abstract. A trading decision-making method that uses electricity market means to promote clean energy accommodation is proposed. Making full use of load difference, peak-to-valley difference and time difference, a joint optimization model of clean energy purchasing-selling-transmission is established to promote clean energy accommodation, which considers the willingness of the recipient side, and satisfies the physical operation constraints of DC line. The model can set the power curve shape, in order to realize the lean decision of cross-regional trading power, and propose a practical accommodation plan. Based on the calculation of cross-regional power transactions between two regions in China, the validity of the model and scheme is verified.

1. Introduction

In recent years, the rapid development of clean energy is conducive to energy conservation, emission reduction and the sustainable development of China's economy. However, there are some problems in the development of clean energy [1-2]: the phenomenon of wind energy, solar energy, hydro energy abandonment is serious; wind power planning is not coordinated, the difficulty of peak and frequency regulation is increased. As the proportion of clean energy continues to grow, clean energy will be difficult to achieve local accommodation, cross-regional transactions and large-scale accommodation will be an effective way to solve problems [3-4]. At present, there are many mechanisms for promoting the development of clean energy. In the design of electricity market in various countries, the demand for clean energy accommodation is also fully considered, and efforts are made to promote the development of clean energy through the electricity market [5-6]. The idea of global energy internet is the key to clean replacement and electric energy replacement. It is a platform to ensure the efficient development of clean energy [7-8].

China has already carried out cross-regional power trading to promote clean energy accommodation in order to eliminate clean energy across regions and achieve optimal allocation of large-scale resources. However, the existing cross-region DC trading power curve is mostly determined by traders based on operational experience. It is difficult to realize the refined decision making of power generation and load in the purchase and sale areas, the full utilization of transmission channels. The literature [9] established a coordinated optimization model of wind-thermal and wind-hydropower considering grid security. Literature [10] analysed economic issues of wind power accommodation in and across provinces, and proposed market-based cross-province trading mechanism to promote the accommodation of wind power. In [11-12], the model of optimizing the accommodation capacity of new energy by DC tie line operation mode adjustment is proposed.

The paper optimizes the cross-regional clean energy trading power from the perspective of large-scale resource allocation. According to different regions and different power types, makes full use of existing transmission channels, further innovates trading methods to realize refined decision-making of cross-regional trading power. Practical plans for promoting reliable accommodation of clean energy through market-based approaches are studied.

2. Optimized model of cross-regional power trading curve for promoting clean energy accommodation

The model aims to improve the clean energy accommodation and improve the lean operation level of cross-regional power transactions. The objective function is that the clean energy accommodation of the sending domain is the largest.

$$\max \; CleanEnergy = \sum_{i_{ce},t} p_i(i_{ce},t,b) \cdot \mathrm{T}_{\mathrm{PrdMin}} \;/\; 60 \tag{1}$$

In formula (1), i_{ce} is clean energy unit; $p_i(i_{ce},t,b)$ is the output power of unit i_{ce} in area b at time, $\mathrm{T}_{\mathrm{PrdMin}}$ is the number of minutes included in a time interval.The optimization model considers the basic constraints of the actual operation of the power grid, such as: system operation constraints, unit operation constraints and network security constraints.

2.1. DC tie line physical operation constraints

In the paper, the physical operation constraints of the DC link are added to the model: tie line capacity constraint, tie line power rate change constraint, tie line continuous time power adjustment direction constraint, the tie line DC adjustment interval constraint [11].

2.2. Regional thermal power minimum operating mode constraint

The expression for the minimum operating mode constraint of the regional thermal power is:

$$\sum_{i_{tu}} \mathrm{I}_{\mathrm{sGU}}(i_{tu},g,b) \cdot U_{\mathrm{i}}(i_{tu},t,b) >= \mathrm{N}_{\mathrm{umMinOn}}(g,b) \tag{2}$$

$$\sum_{i_{tu}} \mathrm{I}_{\mathrm{sGU}}(i_{tu},g,b) \cdot P_{\mathrm{i}}(i_{tu},t,b) >= \mathrm{C}_{\mathrm{apMinOn}}(g,b) \tag{3}$$

$\mathrm{I}_{\mathrm{sGU}}(i_{tu},g,b)$ is 0-1 variable, $\mathrm{I}_{\mathrm{sGU}}(i_{tu},g,b)=1$ means unit i_{ce} of area b is in the unit group g ; $U_{\mathrm{i}}(i_{tu},t,b)$ is the on-off state of unit i_{ce} in area b at time t . $\mathrm{N}_{\mathrm{umMinOn}}(g,b)$ means the minimum units number of unit group g in area b , $\mathrm{C}_{\mathrm{apMinOn}}(g,b)$ means the minimum capacity of group g in area b .

2.3. Transaction power curve shape setting constraint

The shape of the DC tie line power will be constrained according to the experience of the transaction organization or the negotiation results of both buyers and sellers. the paper establishes the following constraints to optimize the peak-to-valley power curve.

2.3.1. Optimize the peak-to-valley ratio of fixed tie line power

$$P_{tieD}(i_{tie}) = R_D \cdot \mathrm{P}_{\mathrm{Max}}(i_{tie}) \tag{4}$$

$$P_{tieU}(i_{tie}) = R_U \cdot \mathrm{P}_{\mathrm{Max}}(i_{tie}) \tag{5}$$

$$R_U >= R_D \tag{6}$$

$$P_{tie}(i_{tie},t) = P_{tieU}(i_{tie}), \quad \textit{in which} \;\; \mathrm{I}_{sTieU}(t) = 1 \tag{7}$$

$$P_{tie}(i_{tie},t) = P_{tieD}(i_{tie}), \quad \textit{in which} \;\; \mathrm{I}_{sTieU}(t) = 0 \tag{8}$$

$P_{tieD}(i_{tie})$ is the power of tie i_{tie} during valley periods, $P_{tieU}(i_{tie})$ is the power of tie i_{tie} during peak periods, $\mathrm{P}_{\mathrm{Max}}(i_{tie})$ is maximum transmitted capacity of tie i_{tie} . R_D is the ratio of the valley-period power to the maximum transmitted power of the tie line. R_U is the ratio of the peak-period power to the maximum transmitted power of the tie line. $P_{tie}(i_{tie},t)$ is the power of tie i_{tie}. $I_{sTieU}(t)=1$ means t is in the peak periods. $I_{sTieU}(t)=0$ means t is in the valley periods.

2.3.2. Fixing Ratio of peaks and valleys of tie line power, optimizing peak and valley time

$$\sum_t U_{startUp}(i_{tie},t)=1 \tag{9}$$

$$\sum_t U_{startDown}(i_{tie},t)=1 \tag{10}$$

$$U_{tie}(i_{tie},t)=\sum_{t_1}^{t} U_{startUp}(i_{tie},t_1)\text{-}\sum_{t_1}^{t} U_{startDown}(i_{tie},t_1) \tag{11}$$

$$\begin{aligned} P_{tie}(i_{tie},t) &= U_{tie}(i_{tie},t)\cdot \mathrm{P_{TieMax}}(i_{tie})\cdot \mathrm{R_U}(i_{tie}) \\ &+\left(1-U_{tie}(i_{tie},t)\right)\cdot \mathrm{P_{TieMax}}(i_{tie})\cdot \mathrm{R_D}(i_{tie}) \end{aligned} \tag{12}$$

$U_{startUp}(i_{tie},t)$, $U_{startDown}(i_{tie},t)$ is 0-1 variables, it indicates that the tie line has not changed from a valley to a peak during the time period, and the tie line has not changed from a peak to valley during the t period; R_U and R_D is the valley and peak power ratio of the tie, $U_{tie}(i_{tie},t)$ is 0-1 variable; $U_{tie}(i_{tie},t)=1$ indicates the tie i_{tie} is in the peak periods at time t. $U_{tie}(i_{tie},t)=0$ indicates the tie i_{tie} is in the valley periods at time t.

2.4. Constraints about willingness of the receiving domain

The paper proposes to increase the willingness of receiving area to accept wind energy, including the receiving domain abandonment wind power does not increase, and the receiving domain purchase power fee dose not increase. The wind power abandonment of receiving area not increase constraint is as equation (13).

$$\begin{aligned} &\sum_t \left(P_{FW}(t,b)-\sum_{i_{wd}} P_i(i_{wd},t,b) \right) \\ &\le \sum_t P_{FW}(t,b)\cdot R_{AW}(b), \text{where} b\in \mathrm{S_{etBrchbuy}} \end{aligned} \tag{13}$$

$P_{FW}(t,b)$ indicates the forecasting wind power at time t, $P_i(i_{wd},t,b)$ indicates the output power of unit i_{wd} of the receiving area b, $R_{AW}(b)$ indicates the abandoned wind ratio of area b, $\mathrm{S_{etBrchbuy}}$ is the set of power purchase areas.

The economic constraints of the receiving domain are as follows:

$$\begin{aligned} &\mathrm{C_{TB}}(b)=\sum_{i,t} C_i(i,t,b)+S_i(i,t,b)+\sum_{i_{tie},t}(\mathrm{d_{tie}}(i_{tie},t,b)) \\ &\cdot P_{tie}(i_{tie},t)\cdot \mathrm{Pr_{tie}}(i_{tie},t,b)\cdot \mathrm{T_{PrdMin}}/60, \text{where}\, \mathrm{I_{sTieOp}}(i_{tie})\neq 0 \end{aligned} \tag{14}$$

$$\sum_b \mathrm{C_{TB}}(b)\le \mathrm{C_B}, \text{where} b\in \mathrm{S_{etBrchbuy}} \tag{15}$$

$C_i(i,t,b)$ is the generating cost of unit i in area b at time t, $S_i(i,t,b)$ is the starting cost of wind power unit i in area b at time t. $\mathrm{d_{tie}}(i_{tie},t,b)$ is the direction of tie i_{tie} in area b at time t. 1 indicates acceptance, -1 means send out. $\mathrm{Pr_{tie}}(i_{tie},t,b)$ is the price of tie i_{tie} in area b at time t. $\mathrm{I_{sTieOp}}(i_{tie})$ is 0-1 parameter, 1 indicates tie the power of i_{tie} is to be optimized.

3. Numerical analysis

Taking the cross-regional power transaction between two regions in China as an example, the two regions are connected by a DC transmission channel, and the actual capacity is 3000MW. The actual transaction power in the historical month is 1.98 billion kWh.

3.1. Consider the cost of accommodation, do not increase the trading power amount, optimize the trading power curve

Keep the transaction power amount between the sending end and the receiving end unchanged, do not increase the amount of abandoning wind and solar energy and the cost of purchasing electricity at the receiving end. Optimize the trading power curve between the two areas and calculate the maximum amount of wind power accommodated at the sending end.

A. Actual transaction situation.
B. Optimize trading power: fixed peak-to-valley ratio, optimize peak-to-valley time.
C. Optimize trading power: fixed peak and valley time, optimize peak-to-valley ratio.

3.1.1. Tie line power comparison

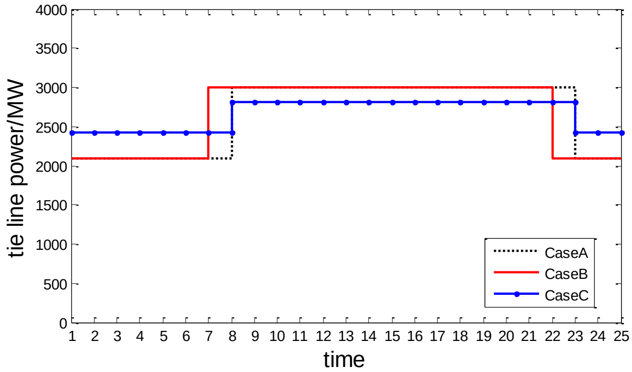

Figure 1. Comparison of trading power curves before and after optimization

3.1.2. Wind abandoning situation comparison

Table 1. The Maximum Clean Energy Accommodation of the Power Sending Area.

case	Wind abandon ratio	Monthly wind power accommodation(billion kwh)
A	15.59%	42.68
B	15.45%	42.75
C	13.91%	43.53

3.1.3. Economic comparison

Table 2. The Thermal Power Operation Cost of the Power Sending Side Compared with the Actual Trade.(billion kwh)

case	Power generation cost change amount	Electricity purchase costs change amount	Total cost change amount
A	-	-	-
B	0	0	0
C	-0.11	0	-0.11

Table 3 The Thermal Power Operation Cost of the Power Recipient side Compared with the Actual Trade (billion kwh)

case	Power generation cost change amount	Electricity purchase costs change amount	Total cost change amount
A	-	-	-
B	0	0	0
C	0	0	0

In this case, as showed in Figure 1, table 1, table 2 and table 3, the power of the tie line is unchanged from the actual transaction power without increasing the cost of the purchased power. After optimization calculation, the optimal peak-to-valley time of the tie line is optimized from 7:00-22:00 of the actual transaction to 6: 00-21:00, help send more than 0.07 billion kWh of clean energy, the optimal peak-to-valley ratio is optimized from 3000:2100 of actual transaction to 2807.75:2420.41, helping to send more than 85 million kWh of clean energy.

3.2. Consider the cost of receiving the terminal, increase the trading power, and optimize the trading power.

On the basis of the existing transactions, new transactions will be arranged, and the amount of electricity to be abandoned will not be increased, and the cost of purchasing electricity in the affected areas will not be increased. Optimize the trading power curve and calculate the maximum amount of wind power accommodation in the sending area.

A. Actual transaction situation;
B. Optimize trading power: fixed peak-to-valley ratio, optimize peak-to-valley time;
C. Optimize trading power: fixed peak and valley time, optimize peak-to-valley ratio.

3.2.1. Tie line power comparison

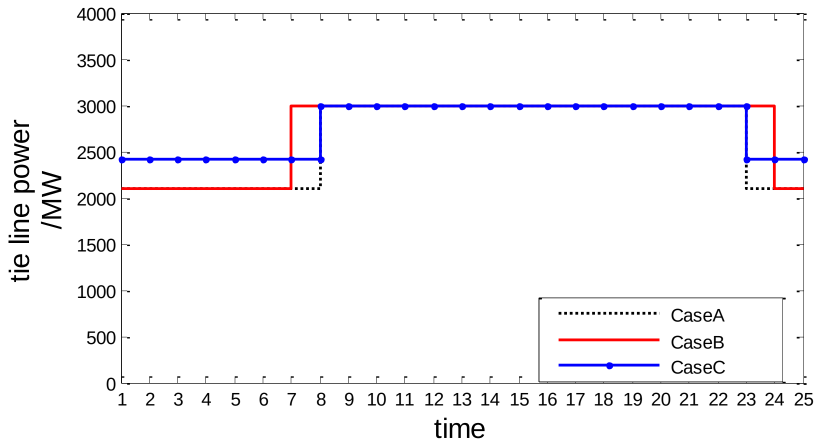

Figure 2. Comparison of trading power curves before and after optimization

3.2.2. Wind abandoning situation comparison

Table 4. The Maximum Clean Energy Accommodation of the Power Sending Area.

case	Wind abandon ratio	Monthly wind power accommodation(billion kwh)
A	15.59%	42.68
B	13.93%	43.52
C	13.79%	43.59

3.2.3. Economic comparison

Table 5. The Thermal Power Operation Cost of the Power Sending Side Compared with the Actual Trade (billion kwh)

case	Power generation cost change amount	Electricity purchase costs change amount	Total cost change amount
A	-	-	-
B	0.12	-0.29	-0.17
C	0.25	-0.3	-0.05

Table 6. The Thermal Power Operation Cost of the Power Recipient side Compared with the Actual Trade (billion kwh)

case	Power generation cost change amount	Electricity purchase costs change amount	Total cost change amount
A	-	-	-
B	-0.36	0.31	-0.04
C	-0.33	0.32	0

This case increases the transaction power without increasing the cost of the receiving end, as showed in Figure 2, table 4, table 5 and table 6, After calculation and analysis, the optimal peak-to-valley period of the tie line is optimized from 7:00-22:00 to 6:00-23:00 of the actual transaction. More than 0.84 billion kWh of clean energy was consumed; the optimal peak-to-valley ratio was optimized from 3000:2100 of actual transaction to 3000:2409.62, helping to send more than 91 million kWh of clean energy.

3.3. Optimize trading power regardless of the cost of receiving end

On the basis of the existing transactions, new transactions will be arranged, and the amount of electricity purchased by the abandoned areas will not be increased, and the cost of purchasing electricity in the affected areas will be increased. Optimize the trading power curve and calculate the maximum amount of wind power accommodation in the sending area.

A. Actual transaction situation;
B. Optimize trading power: fixed peak-to-valley ratio, optimize peak-to-valley time;
C. Optimize trading power: fixed peak and valley time, optimize peak-to-valley ratio.

3.3.1. Tie line power comparison

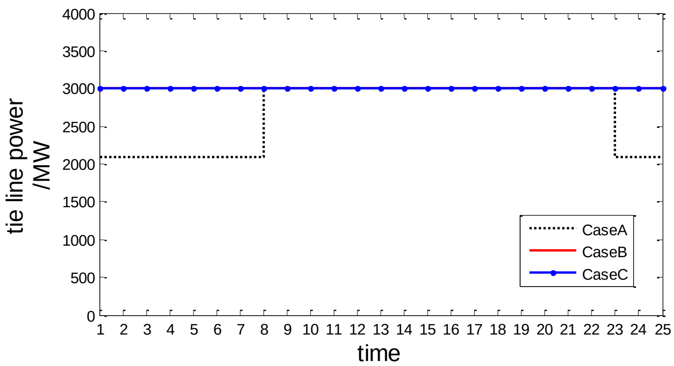

Figure 3. Comparison of trading power curves before and after optimization

3.3.2. Wind abandoning situation comparison

Table 7. The Maximum Clean Energy Accommodation of the Power Sending Area.

case	Wind abandon ratio	Monthly wind power accommodation(billion kwh)
A	15.59%	42.68
B	10.63%	45.19
C	10.63%	45.19

3.3.3. Economic comparison

Table 8 .The Thermal Power Operation Cost of the Power Sending Side Compared with the Actual Trade.(billion kwh)

case	Power generation cost change amount	Electricity purchase costs change amount	Total cost change amount
A	-	-	-
B	0.11	-0.88	-0.77
C	0.11	-0.88	-0.77

Table 9. The Thermal Power Operation Cost of the Power Recipient side Compared with the Actual Trade (billion kwh)

case	Power generation cost change amount	Electricity purchase costs change amount	Total cost change amount
A	-	-	-
B	8.31	0.94	9.26
C	8.31	0.94	9.26

This case optimizes the power and power of the tie line under the condition of increasing the cost of the receiving end, , as showed in Figure 3, table 7, table 8 and table 9. After calculation and analysis, the optimal peak-to-valley period is optimized from 7:00-22:00 of the actual transaction to full-channel operation, and the optimal peak-to-valley ratio is from The actual transaction of 3000:2100 is optimized to 3000:3000, full channel operation, helping to send more than 251 million kWh of clean energy.

4. Conclusion

The paper proposes a joint optimization model for purchasing and selling clean energy accommodation. The model considers the physical characteristics of the two ends of the DC tie line, and considers the willingness of the receiver and the experience of trading organizations. The method can promote the accommodation of clean energy, and provide technical means for inter-regional clean energy trading arrangements to improve the lean operation level of clean energy transactions.

In the paper, the daily trading scene is designed and deducted. If the scope is extended to the whole year, the load difference, peak-valley difference and time difference between the sending end and the receiving end have stronger complementary characteristics, and the work can be further carried out in the future.

5. References

[1] SHU Yinbiao, ZHANG Zhigang1, GUO Jianbo, et al. Study on Key Factors and Solution of Renewable Energy Accommodation [J]. Proceedings of the CSEE， 2017(01):4-12. (in Chinese).
[2] Xue Yusheng, Lei Xing, Xue Feng, et al. A review on impacts of wind power uncertainties on power systems[J]. Proceedings of the CSEE, 2014,3 4(29): 5029-5040(in Chinese).
[3] WANG Ningbo, WANG Jiandong, HE Shien． Cross G border accommodation method and transmission scheme of Jiuquan wind power[J]. Automation of Electric Power Systems, 2011, 35(22):82-89. (in Chinese).
[4] XU Wei, ANG Yu-lin, LI Zheng-guang, et al. Participation Mode of Large-Scale Jiuquan Wind Power Farm in Gansu Province to Electricity Market and Its Utilization Scheme [J]. Power System Technology，2010(6):71-77. (in Chinese).
[5] SHI Lianjun, ZHOU Lin, PANG Bo, Design Ideas of Electricity Market Mechanism to Improve Accommodation of Clean Energy in China[J]. Automation of Electric Power Systems, 2017(24):89-95. (in Chinese).
[6] ZOU Bin, ZHAO Yan, LI Xiaogang, et al.. Market Mechanism Research on Trans-Provincial and Trans-Regional Clean Energy Accommodation and Compensation[J]. Power System Technology，2016，40(4): 1087-1093 (in Chinese).
[7] LIU Zhenya, ZHANG Qiping, DONG Cun, et al. Efficient and Security Transmission of Wind, Photovoltaic and Thermal Power of Large-scale Energy Resource Bases Through UHVDC [J]. Projects Proceedings of the CSEE，2014, 34(16): 2513-2522 (in Chinese).
[8] Liang Xuming，Chen Guoping，Luo Dianqing, etal. A smart grid oriented architecture of operation and maintenance system based on centralized controlling and monitoring for inter-area HVDC power transmission project [J] Power System Technology 2011, 35(3):1-7.
[9] XU Fan, WANG Ying, YANG Jianping. et al. Generation Scheduling Model and Application for Wind-thermal Power System Considering Security Constraints[J]. Automation of Electric Power Systems, 2014.38（21）: 114-12. (in Chinese) .
[10] SHI Lianjun, ZHOU Lin, PANG Bo, Design Ideas of Electricity Market Mechanism to Improve Accommodation of Clean Energy in China[J], Automation of Electric Power Systems, 2017(24):89-95. (in Chinese).
[11] AHMADI-KHATIR A, CONEGO A J， CHERKAOUI R. Multi-area Unit Scheduling and Reserve Allocation under Wind Power Uncertainty[J], IEEE Trans on Power Sytems, 2014,29(1):1-10.
[12] ZHONG Haiwang, XIA Qing, DING Maosheng, et al.. A New Mode of HVDC Tie-lie Operation Optimization for Maximizing Renewable Energy Accommodation[J]. Automation of Electric Power Systems, 2015(3):36-42 (in Chinese).

Acknowledgments
This work was supported by the Science and Technology Foundation of the Science and Technology Foundation of State Grid Corporation of China “Research and Application of Global Planning Decision and Core Technology of Spot Electric Marke”.

Unit commitment of wind integrated power system considering optimal scheduling of reserve capacity

Liu Wenxue[1], Wang Liang[2], Zhang Bing[2], Ma Changhui[1] and Liang Zhengtang[1]

1 State Grid Shandong Electric Power Company Electric Power Research Institute Jinan, China
2 National Electric Power Dispatching and Control Center,State Grid Shandong Power Supply Company，Jinan，China
E-mail: liu_wenxue@126.com

Abstract. There are multiple uncertainties in the power system with wind farms, such as wind power output, load and forced outage of units, which lead to consider the spinning reserve capacity in unit commitment, which undoubtedly increases the difficulty of problem solving. In order to solve this problem, the fuzzy parameters of wind power output and load are obtained by using the error's fuzzy characteristics, and the mathematical model of generating unit combination is established to optimize the generator output and spinning reserve simultaneously by using the chance constraint, and the model is solved by using intelligent algorithm. The model fully analyses the cost difference of different units providing spinning reserve and the economic benefit of spinning reserve, aiming at minimizing the difference between the cost of generating reserve and the economic benefit of reserve, so as to maximize the overall economic benefit of the system. The feasibility and validity of the proposed model are verified by a 10-unit system with wind farms. The analysis shows that the model can reasonably consider reserve decision-making in unit commitment to deal with uncertainties in power system.

1. Introduction

Inspired by the Renewable Energy Law, the installed capacity of wind power in China has reached 114 million kW. However, the inherent intermittence and fluctuation of wind speed make a lot of errors in the prediction of wind power output, which has a great impact on the operation of the power grid [1-4].

The integration of large-scale wind power into power grid increases the uncertainty of unit commitment and the related risks of system operation, which makes the optimal allocation of spinning reserve capacity more complex. Considering the spinning reserve in unit commitment to response the system uncertainty has gradually become the focus of academic and engineering application research [5-14]. Document [5-7] defines various scenarios of the model according to the error distribution of the predicted value, forms the scenario tree of unit commitment prediction, and solves the problem on the basis of considering the spinning reserve. This kind of model requires a lot of computation to consider multiple cycle scenario trees. References [8-9] optimize the allocation of reserve under the condition of determining unit stop/start, without considering the influence of spinning reserve on unit commitment decision-making [10]. Reference [11-14] considers that under certain reliability level, the total reserve requirement of the system is determined in unit commitment, and there is no optimal allocation of reserve capacity among different units.

The above literature has made some progress in considering the unit commitment of spinning reserve, but the consideration of unit commitment and spinning reserve decision coordination is more in line with the operation nature of power system operation [15]. Reference [16-17] establishes an economic dispatching model for simultaneous optimization of generator output and reserve under power market conditions, but it does not analyze the reserve cost of single unit and the economic benefits of spinning reserve. Reference [18-19] establishes the optimal reserve allocation model of the system after wind power is connected, but only the probability of wind power and load error is taken into account in this paper, and the uncertainty of forced outage of generator units is not taken into account. Moreover, due to the influence of temperature, meteorology, statistical errors and absence of drainage law, the wind power output and load have fuzzy characteristics, so it is more reasonable to adopt the model of fuzzy parameters [20-22]. Literature [20-22] considers the role of spinning reserve in constraints, but no further study has been made on the cost, benefit and optimal allocation of spinning reserve.
In view of the multiple uncertainties in power system, the differential model of wind power output, load and forced outage of units is established. Based on the analysis of the cost of spinning reserve and the economic benefit of spinning reserve for single unit, the mathematical model of unit combination for optimizing the output of generators and spinning reserve is established. The improved clear equivalence class is used to deal with the credibility constraints, and the intelligent algorithm is used to solve the model. The feasibility and validity of the proposed model are verified by a 10-unit system with wind farms. The analysis shows that the model can coordinate the reserve decision-making in unit commitment to deal with uncertainties in wind power system.

2. Fuzzy variables and related fuzzy concepts in unit combination

When studying the fuzzy characteristics of load forecasting errors, the relative errors are usually used, and the membership function is expressed by Cauchy distribution. However, relative error will lose its guiding value when the load is low. This paper chooses absolute error to study the fuzzy model of load. The membership function of the fuzzy variable of load forecasting error is as follows:

$$\mu_{\Delta\tilde{P}_L} = \begin{cases} \dfrac{1}{1+\eta_L(\Delta P_L / P_L^{+})^2}, \Delta P_L \geq 0 \\ \dfrac{1}{1+\eta_L(\Delta P_L / P_L^{-})^2}, \Delta P_L < 0 \end{cases} \tag{1}$$

In the formula, P_L^+ 、 P_L^- the statistical average values of positive and negative errors are expressed respectively; η_L are weighted; the absolute errors of load forecasting are expressed as follows:

$$\Delta P_L = P_L - P_L' \tag{2}$$

In order to obtain the membership function of wind farm output power, the membership function of wind speed is obtained through the fuzzy characteristics of wind speed prediction error, and then the fuzzy model of wind farm output power is obtained based on the functional relationship between wind farm output and wind speed.
The fuzzy model of wind speed is the basis of active power model of wind farm. It is pointed out in literature that the error of wind speed prediction has the same fuzzy characteristics as that of load prediction.Ignoring the wake effect of wind turbines and the difference between wind turbines in wind farms, the total wind power of wind farms including typhoon turbines is:

$$W_{av} = N_W P_W \tag{3}$$

According to wind speed membership function and wind-work curve, the power of wind farm is a mixed type of fuzzy variable, and the fuzzy parameters of wind farm output can be obtained by the definition of membership degree[23].
The degree of membership of the continuous part is:

$$\mu_{0-r} = \mu\{W_{av} = P_W N_W\} \tag{4}$$

3. Cost-benefit analysis of reserve capacity

IOP Conf. Series: Earth and Environmental Science **431** (2020) 012054 doi:10.1088/1755-1315/431/1/012054

3.1. Cost analysis of reserve capacity

Assuming that the active power output P of generator is positive spinning reserve ΔP, the opportunity cost of providing reserve for a generator set is as follows [24] :

$$S = G' - G \tag{5}$$

According to the theory of marginal cost, the marginal cost of generating set providing positive spinning reserve is shown in the formula(6).

$$\gamma = \partial S / \partial \Delta P = \rho - b - 2aP - a\Delta P \tag{6}$$

In order to simplify the model, this paper does not consider the effect of time-of-use price on spinning reserve, that is, price is treated as a constant. Without considering the influence of spare capacity on spare cost,the formula can be simplified: $\gamma = \rho - b - 2aP$

According to the same idea, the negative spinning reserve cost can be calculated.

3.2. Benefit analysis of reserve capacity

In order to better analyze the benefits of spinning reserve for power grid stability and balance, the possibility of power unbalance is first expressed by variables, as shown in the formula:

$$Pet = \sum_{i=1}^{N_{Gt}} P_{Git} + W_{avt} - P_{Lt} \tag{7}$$

In the formula: N_{Gt} is the number of generating units opened in the unit combination cycle t; P_{Git} is the output of the i generating unit; and W_{avt} 、 P_{Lt} is the fuzzy variable of wind power output and load.The economic benefits of purchasing positive spinning reserve in power grid lie in improving the reliability of the system and reducing the power consumption which is not enough to meet the expected value, thus reducing the cost of power outage for users. Therefore, the economic benefits of the reserve can be expressed by the change of the outage cost of the users who purchase the reserve:

$$B_{s2t} = \alpha_1 \Delta E_{WAS} = \alpha_1 (E_{WASt,1} - E_{WASt,0}) = \alpha_1 \sum_{i=0}^{N_{Gt}} \Pr(A_i) \int_0^{D_t} Cr(Pet_i > r) dr \tag{8}$$

Formula: α_1 indicates the cost of wind energy waste per electric energy; and $E_{WASt,1}$ and $E_{WASt,0}$ is the expected value of wind energy waste for the purchase of reserve systems; D_t is the sum of negative rotation reserve for all generators without forced outage.

4. Model of unit commitment

4.1. The objective function

Based on the ideas in the literature, this paper takes the generator output and reserve capacity as optimization variables, and establishes a new unit combination model considering the reserve cost and benefit. The objective function of the model is:

$$\min f = \sum_{t=1}^{N_T} \sum_{i=1}^{N_G} [I_{it} f_i(P_{Git}) + I_{it}(1 - I_{i(t-1)}) S_{it}] + \sum_{t=1}^{N_T} [\sum_{i=1}^{N_G} I_{it}(\gamma_{1i} U_{it} + \gamma_{2i} D_{it}) - B_{s1t} - B_{s2t}] \tag{9}$$

Formula: P_{Git} is planning output for the unit i in the first dispatching cycle t ; I_{it} is starting-up state for the unit in the first dispatching cycle, starting-up state is 1, stopping state is 0; f_i is fuel cost function for the unit i; S_{it} is starting-up cost for the unit i in the t dispatching cycle; γ_{1i}, γ_{2i} is offer for the positive and negative spinning reserve capacity of the unit i respectively; U_{it}, D_{it} are up-regulation and reduce the reserve capacity of the unit i in the t dispatching cycle; and B_{s1t} and B_{s2t} are the economic benefits of the positive and negative spinning reserve during the scheduling cycle.

4.2. Constraint condition

Conventional generator constraints include upper and lower output limit constraints, reserve capacity constraints, ramp rate constraints and minimum start-up and shut-down time constraints[21].
During each unit combination cycle, the output of conventional units keeps power balance with the predicted value of wind power output and load output.

$$\sum_{i=1}^{N_{Gt}} P_{Git} + \overline{W}_{avt} - \overline{P}_{Lt} = 0 \tag{10}$$

In the formula, $\overline{W}_{avt}, \overline{P}_{Lt}$ are the predicted value of wind power and load output in the cycle, that is, the value of membership degree of wind power output and load fuzzy parameters is 1.
The positive reserve units can deal with the uncertainties of negative error in wind power forecasting, positive error in load forecasting and forced outage of conventional generators at a certain confidence level.

$$Pos\left\{Cr\{\sum_{i=1,i\neq j}^{N_{Gt}}(U_{it}+P_{Git}) \geq P_{Lt}-W_{avt}\} \geq \beta_1\right\} \geq \beta_2, t\in T \tag{11}$$

Formula: $0 \leq j \leq N_{Gt}$,number of outage generators (0 means no outage of generators); β_1, β_2 are Fuzzy and probabilistic confidence levels, respectively.
When the generator unit is forced to shut down, the power in the system is insufficient, and the significance of negative reserve is not obvious, so the chance constraints need not be considered. Negative reserve units can deal with uncertainties such as positive error and negative error in wind power forecasting at a certain confidence level.

$$Cr\{\sum_{i=1}^{N_{Gt}} D_{it} > \sum_{i=1}^{N_{Gt}} P_{Git} - P_{Lt} + W_{avt}\} \geq \beta_3, t\in T \tag{12}$$

Formula: β_3 is the level of fuzzy confidence.In order to ensure the safety of the system after the forced outage of generators, the generator can satisfy the power balance of the power grid without considering the spinning reserve response time, and has a certain spinning reserve. Its chance constraints are as follows:

$$\sum_{i=1,i\neq j}^{N_{Gt}} I_{it} P_{Gi\max} \geq \overline{P}_{Lt} - \overline{W}_{avt}, t\in T \tag{13}$$

Formula: β_4 is the level of fuzzy confidence.

4.3. The solution of model

The unit commitment problem proposed in this paper is a non-linear, high-dimensional, non-convex mixed integer programming problem with chance constraints. It is divided into two steps: decision-making of stop/start and joint decision-making of generator output and reserve scheduling. It is very difficult to solve by traditional optimization algorithms. Intelligent optimization algorithms, including genetic algorithm, simulated annealing, adaptive dynamic programming and particle swarm optimization, have achieved good results in power system unit commitment problems. In this paper, genetic algorithm is selected to optimize the start-up stop/start state of generating units. Particle swarm optimization is used to make joint decision on generator output and reserve.
Particle swarm optimization (PSO) is relatively simple in structure and fast in operation, so it is used for joint decision-making of generator output and reserve. For negative reserve chance constraints, this paper simplifies them into inequality constraints by using clear equivalence classes. For positive reserve chance constraints, because their random events are discrete, the probability of positive reserve chance constraints can be obtained by judging the fuzzy chance constraints under each random event condition, and then adding the probability of meeting the constraints. Then, the constraints are deal with by means of penalties.

5. Calculation and analysis of examples

5.1. The basic data and parameters

This paper chooses IEEE 10 system to study. The characteristic parameters and system parameters of generator set can be seen in reference [22]. The wind farm is connected to bus 20, and the rated capacity of a single typhoon unit is 2.0MW. There are 100 wind turbines. The wind speed of cut-in/rated/cut-out is 3, 13 and 25m/s, respectively. The wind speed and load forecasting values are shown in Table 1, respectively. Due to the high repeatability of load daily, the positive and negative prediction errors are 4% and 5% respectively. The daily regularity of wind speed is poor, with positive and negative prediction errors of 14% and 15%, and weights of 2.33. The price of electricity is 80, the cost of energy loss is 100, and the cost of wind energy waste is 50. This paper uses MATLAB programming to solve the problem. The maximum number of iterations is 100, the population number is 50, and the repeated optimization operation is 20 times.

5.2. The calculation results and analysis

Fuzzy confidence level is set to $\beta_1 = 92\%, \beta_2 = 96\%$, $\beta_3 = 92\%, \beta_4 = 92\%$. The optimal output, positive reserve capacity and negative reserve capacity of thermal power units are calculated by using the model proposed in this paper. Fig. 1, 2 and 3 show the optimal output, positive reserve capacity and negative reserve capacity of thermal power units.

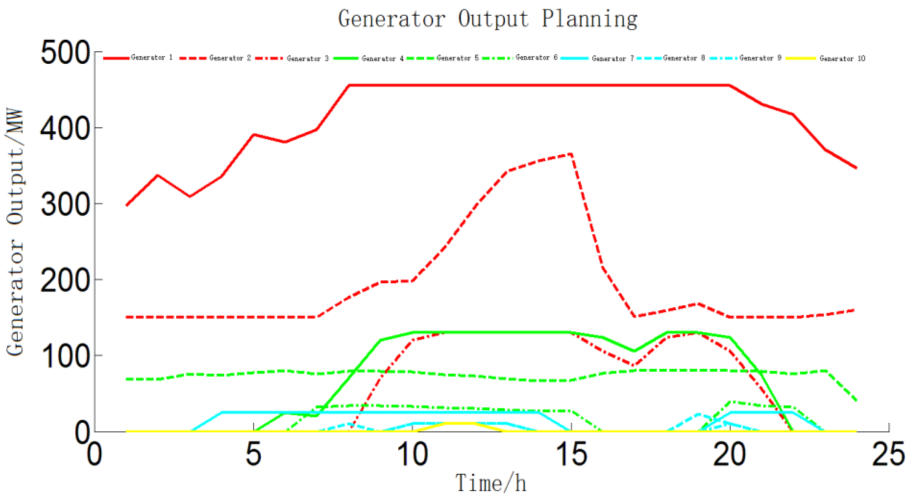

Figure 1. Unit commitment schedule

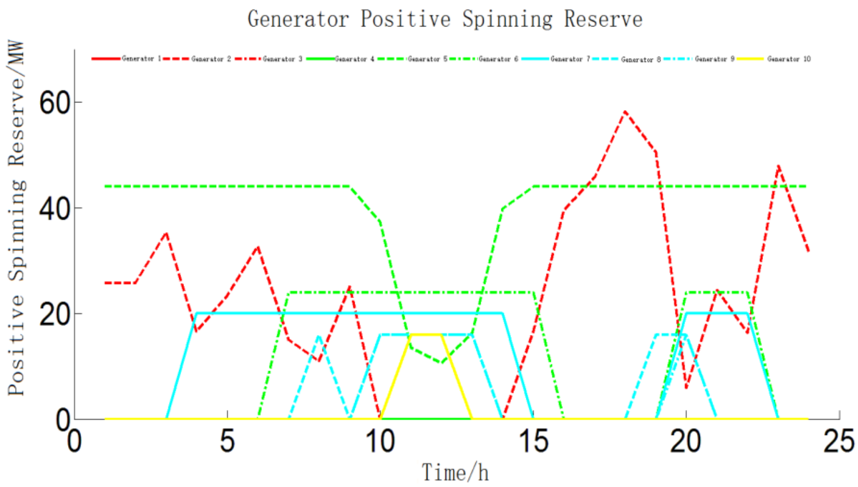

Figure 2. Positive spinning reserve schedule

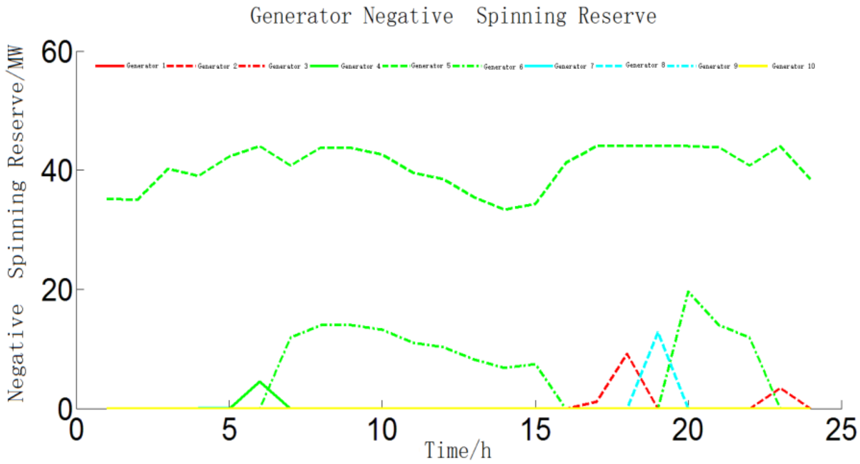

Figure 3. Negative spinning reserve schedule

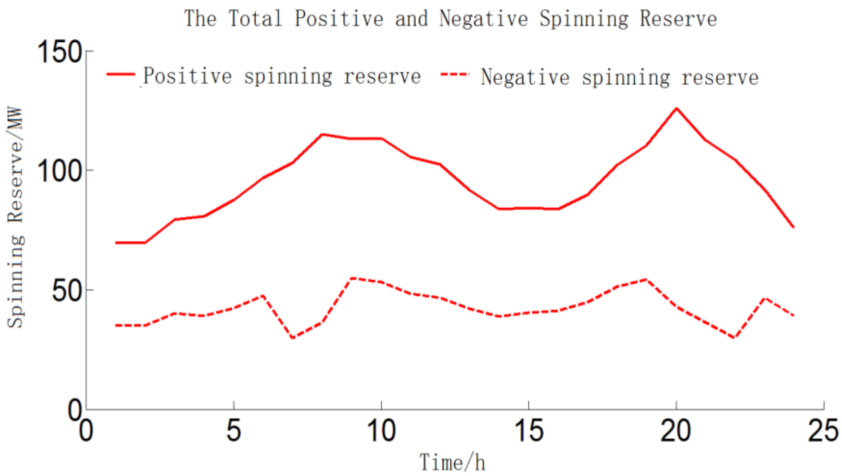

Figure 4. The total of spinning reserve capacity

Fig. 1 shows that under the influence of N-1 fault constraints, generators 1, 2 and 5 with lower overall generation cost and reserve cost are always in the open state. With the increase of load, the remaining generators will be opened from small to large according to the priority index under the condition of meeting the minimum start-stop time.

From Figure 2 and Figure 3, we can see that the reserve cost is an important basis for deciding the generator to provide reserve. In the forward spinning reserve plan, the reserve cost of generator 1 is higher, so it does not bear any reserve, while the cost of generator 2 and generator 5 is lower, so it bears more reserve capacity. When the remaining generators are opened over time, the reserve capacity is assumed according to the reserve cost. In the negative spinning reserve plan, the system needs very little reserve capacity, the generator 5 has been in the open state, and the negative reserve cost is low, so it undertakes most of the reserve.

The positive and negative spinning reserve capacity purchased by the system is shown in Fig4. Affected by both load forecasting errors and wind speed forecasting errors, the positive and negative reserve have similar trends, but the positive and rotary reserve is affected by the forced outage of generators, so it is higher than the negative spinning reserve. In the period 7-8 and 20-22, the negative reserve is significantly lower than the positive reserve, because in these two periods, the wind speed is super-rated, and the wind farm output is more likely to be rated capacity, so the impact of the reserve is also greater. Moreover, the probability of wind farm output exceeding rated power is 0, so the negative reserve is obviously reduced.

Table 2 shows the reserve capacity, reserve cost and reserve under different fuzzy and probabilistic confidence levels. As can be seen from the figure, with the increase of confidence level, the reserve capacity required by the system increases gradually, and the corresponding reserve cost and reserve income increase. In order to further study the cost-effectiveness of positive reserve, this paper defines the net income index of positive reserve as shown in the formula: $I_A = B_{s1} - U_{\cos t}$ (14)

The sixth item in the table is the net income under the confidence level. It can be seen that with the increase of the confidence level, the net income index first increases and then decreases. Therefore, in the actual system, if there is no compulsory requirement of confidence level, the fuzzy confidence level should be set to 90%, and the probability confidence level should be set to 95%. At this time, the reserve is passing through the highest net income.

Table 1. Positive reserve capacity, cost and benefit at different confidence levels

Fuzzy confidence	Probability confidence	Reserve capacity/MW	Reserve cost/$	Reserve benefits/$	Net income/$
86%	95%	892.5	51 914	183 308	131 394
88%	95%	947.9	55 141	186 879	131 738
90%	95%	1011.7	58 846	190 591	131 745
92%	96%	1086.0	63 172	194 429	131 257
92%	97%	1283.5	74 662	202 714	128 052
92%	98%	1607.3	93 497	212 238	118 741
92%	99%	2322.0	135 068	224 278	89 210

Table 2. Capacity, costs and benefits of down reserve under different confidence levels

Fuzzy confidence	Probability confidence	Reserve capacity/MW	Reserve cost/$	Reserve benefits/$
86%	742.6	42 890	21 049	21 841
88%	781.3	45 123	21 451	23 672
90%	824.1	47 596	21 861	25 735
92%	872.0	50 362	22 281	28 081
94%	926.3	53 493	22 712	30 781
96%	988.5	57 087	23 158	33 929
98%	1061.1	61 284	23 622	37 662

Table 2 shows the negative reserve capacity, reserve cost and reserve at different levels of fuzzy confidence. As can be seen from the figure, with the increase of confidence level, the reserve capacity required by the system increases gradually, and the corresponding reserve cost and reserve income increase. In order to further study the cost-benefit of negative reserve, this paper defines the net cost index of positive reserve as shown in the formula: $I_B = D_{\cos t} - B_{s2}$ (15)

Fifth in the table is the net income under the confidence level. It can be seen that with the increase of the confidence level, the net income index has been increasing. Therefore, different levels of fuzzy confidence should be set according to the system risk in the actual system.

6. Conclusion

The output of wind farm is uncertain and intermittent, which makes it more difficult to solve the unit commitment problem in power grid. The spinning reserve is an important method to solve such problem, and the decision-making of reserve is closely related to unit commitment.

In order to solve this problem, the output and load of wind farm are expressed by fuzzy parameters, and the related costs and benefits brought by spinning reserve to power system operation are analyzed through economic benefits. A mathematical model of unit commitment is established to optimize both generator output plan and spinning reserve plan, and particle swarm optimization method is proposed for the model solution. The feasibility and validity of the proposed model are verified by a 10-unit system with wind farms. The analysis shows that the model can reasonably consider the reserve decision-making in unit commitment to cope with large-scale wind power access.

7. References

[1] Qiu Wei and Zhang Jianhua J 2011 Model and solution for environmental economic dispatch considering large-scale wind power penetration *Proceedings of the CSEE*，vol 31pp879-193．

[2] Junfeng and Gaohu M 2014. China Wind Power Development Report *Environmental Science Press,*Beijing: China .

[3] Senjyu T,Shimabukuro K,Uezato K,J 2003 A fast technique for unit commitment problem by extended priority list *IEEE Trans on Power Systems*, vol 18 pp882-888.

[4] Ting T O and Rao M V C J 2003．A novel approach for unit commitment problem via an effective hybrid particle swarm optimization *IEEE Transactions on Power Systems*， vol 21 pp 411-418．

[5] Bouffard F and Galiana F D J 2008 Stochastic security for operations planning with significant wind power generation *IEEE Trans on Power Systems,*vol 23pp306-316.

[6] Liu Ningning M 2014. Studies on unit comment considering spinning reserve optimization *Jinan Shandong University*.

[7] YAO Yao, YU Ji-lai J 2011. Multi-objective hybrid optimal dispatch of power systems considering reserve risk due to wind power *Automation ofElectric Power Systems,*vol35pp118-124.

[8] Gouveia E M, Matos M A C 2004. Operational reserve of a power system with a large amount of wind power// *International Conference on Probabilistic Methods Applied to Power Systems. Iowa USA*,pp 717-722.

[9] Qu Chong,Wang Xiuli J 2014. Optimal Configuration of Spinning Reserve Based on Conditional Cost /Benefit Analysis *Automation of Electric Power Systems*,vol 38pp 62- 70.

[10] Zhang Guoquan,Wang Xiuli J 2000.Study on benefits and costs of spinning reserve capacity in power market *Automation of Electric Power Systems*, vol 24pp14-18.

[11] Doherty R, Malley M OJ 2005. A new approach to quantify reserve demand in systems with significant installed wind capacity. *IEEE Trans on Power Systems*, vol 20pp587-595.

[12] Gouveia E M, Matos M A C 2004. Operational reserve of a power system with a large amount of wind power *International Conference on Probabilistic Methods Applied to Power Systems. Iowa USA*pp 717-722.

[13] Doherty R, Malley M OC 2003. Quantifying reserve demands due to increasing wind power penetration *Power Tech Conference*..

[14] Morales J M, Conejo A J 2009. Economic valuation of reserves in power systems with high penetration of wind power *IEEE Trans on Power Systems,*vol 24pp900-910.

[15] Xue Zhiying, Zhou Ming J 2013. Survey on reserve decision of power systems with large scale wind power integration *Power System Protection and Control,* vol41pp148-155.

[16] Luo Chao， Yang Jun,Sun Yuanzhang,Lin Fang,Cui Mingjian J 2014.Dynamic economic dispatch of wind integrated power system considering optimal scheduling of reserve capacity． *Proceedings of the CSEE*，vol 34pp6109-9118．

[17] Wang Yanling, Xu Chuanlong J 2013. A Stochastic Programming Model for Spinning Reserve of Power Grid Containing Wind Farms Under Constraint of Time-Varying Reliability. *Power System Technology*, vol 37pp311-1316．

[18] Li Xia,Liu Junyong,Liu Youbo J 2013.Optimal distribution model for system reserve capacity with wind power connection regarding consistency performance of reserve dispatch. *Automation of Electric Power Systems*,vol37pp40-46.

[19] Zhao Jinquan,Tang Jie,J 2014.Day-ahead generation scheduling and spinning reserve decision-making model for power grid containing wind power.*Electric Power Automation Equipment*,vol 34pp21-27.

[20] Ruey-Hsun L，Liao JianhaoJ 2007．A fuzzy optimization approach for generation scheduling with wind and solar energy systems *IEEE Transactions on Power System*s,vol22pp1665-1674．

[21] Ai Xin，Liu XiaoJ 2011．A fuzzy chance constrained decision model for unit commitment of power grid containing large-scale wind farm *Power System Technology*，vol35pp202-207(in Chinese)．

[22] Xiong Hu,Xing Tieyuan,Chen Hongkun,J 2013.Research of fuzzy chance constrained unit commitment containing large-scale intermittent power *Proceedings of the CSEE,*vol 33pp36-44．

[23] Liu Baoding, Zhao Ruiqing, M 2003. Uncertain Planning and Application. *Beijing Tsinghua University Press.*

[24] Wang Jianxue,Wang Xifan,Bie Zhao hong J 2001. Reserve in the power market. *Automation of Electric Power Systems,* vol25pp7-12.

IOP Conf. Series: Earth and Environmental Science **431** (2020) 012065 doi:10.1088/1755-1315/431/1/012065

Analysis on the trading mode suitable for nuclear power in power market

Xuefei Zhang[1], Yi Xiong, Chuanyu Xiong, Xuejun Tang, Zhiwei Li

1 Master, State Grid Hubei Electric Power Co., Ltd. Economic Technology Research Institute Hubei China 430077
E-mail: luckjobgood@163.com

Abstract. The energy crisis in the 21st century has become the most imperative problem to be solved by human beings. Nuclear energy is a vital base-charge power supply, which has high security, clean function and high efficiency. With the gradual development of nuclear power, the power is participating in the direct trading of the electricity market step by step. However, the rules of direct trading in China is not relatively complete, which leads to the unreasonable decline of the economy of nuclear power units. And there are drawbacks in the adjustment of energy structure, which also has a negative impact on energy conservation and emission reduction. So the author analyzes the current national nuclear power policies and electricity price costs, and proposes the current problems faced by nuclear power in direct electricity market and provides the basic directions and ideas for solving measures to help nuclear power better participate in direct electricity trading.

1. Introduction

In 1993, first commercialized power grid in China began to operate, but the resource allocation and the economic development was unbalanced. [1] Specifically, hydropower, coal and electricity of China are relatively distributed in the western region, while the eastern region shows a shortage of resources. The eastern region is relatively more developed, while the western region is underdeveloped. [2] Up to now, the demand for the whole load is relatively uneven, which will directly affect the electricity price level of power grid region in China, but on the other hand, it provides a probability for better national resource allocation. [3] As a new type of energy, nuclear energy can relieve the energy crisis in China if the problems related to direct electricity trading can be solved.

2. Current policy and electricity price costs involved in national nuclear power

In order to further ensure the security of national energy, the entire energy structure will be adjusted to better carry out energy conservation and emission reduction, and the concept of “Lucid waters and lush mountains are invaluable assets.” will be realized, and the development of nuclear power will gradually mature. [4] The growth of the national economic development is gradually slowing down. The electricity prices of thermal power and coal power have been downgraded. The policy of the electricity market has been greatly affected by multiple factors, and the feed-in tariff and quantity of nuclear power are greatly affected. As a new type of clean energy, nuclear power itself has more advantages, and it has a pivotal position in the national security and energy strategy. It also has an excellent advantage in realizing energy conservation and emission reduction on electricity. Relevant departments in China have attached great importance to nuclear power. From the analysis of the documents, in the draft of "Energy Conservation and Low Carbon Electric Power Dispatching

Measures" issued by the state in 2016, the first power generation sequence is non-fossil energy generator sets, of which wind, solar and water energy and nuclear energy rank in the top four. [5]-[6] The basic principles of this draft are: safe and reliable, energy-saving and low-carbon, market allocation, and scientific supervision. In September of the same year, the National Development and Reform Commission and the Energy Bureau drafted a draft for nuclear power management. [7] This document directly clarified the strategic position of nuclear power development, coordinated the legal relationship and responsibility of nuclear power development, rights and obligations, and promoted the development of nuclear power in policy. In the following three years, although the Energy Bureau has always maintained a high degree of concern for the entire nuclear power, it does not make relevant policy guidance on the market-based feed-in tariff. [8] At present, the transaction price of nuclear power plants has caused great conflicts on the economic benefits of the entire nuclear power.

3. Analysis of power generation cost and pricing mechanism of feed-in tariff of nuclear power

The power generation cost of nuclear power is analyzed in details: investment and construction cost accounts for about 64%, including construction loan interest; fuel cost accounts for 21%; operation and maintenance cost accounts for 15%. [9] This generation cost of nuclear power is shown in Figure 1.

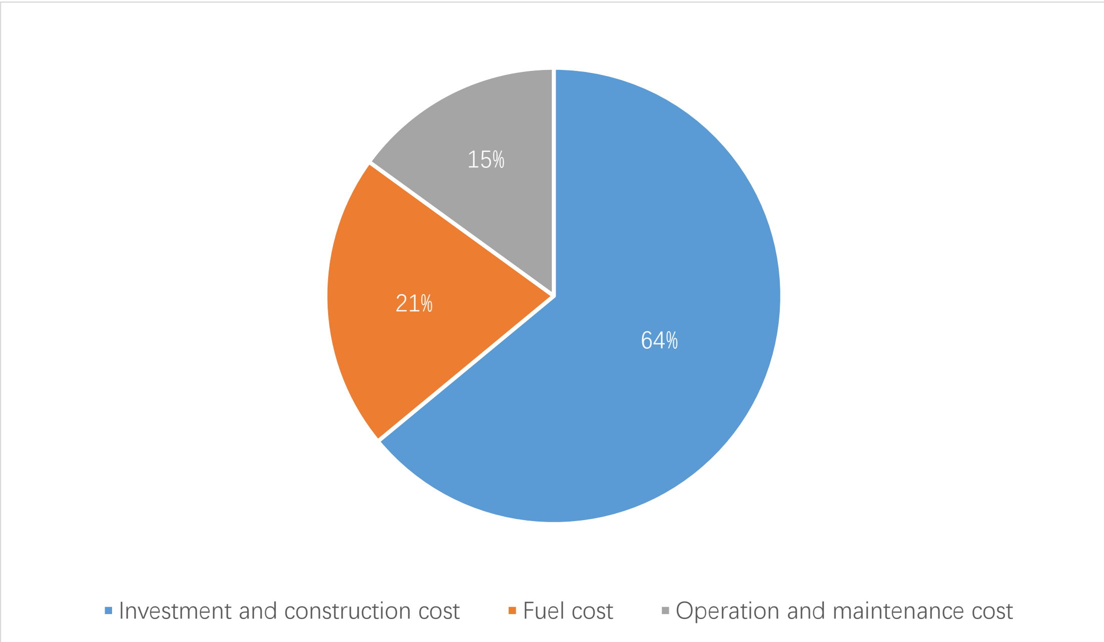

Figure 1 The power generation cost of nuclear power

Nuclear power technology itself is still in the stage of renewal and development, and the costs of different technology routes are quite different. With the particularity of costs of nuclear power, the cost of fuel disposal and decommissioning is mandatory, and the development of nuclear energy still needs to invest more energy. Among the fuel costs, nuclear fuel is about 1/3 of coal and 1/5 of natural gas, which is also one of the main factors for investors to invest in nuclear energy. [10] Another factor for investors to invest in nuclear energy is the relatively low cost of operation and maintenance. The cost of operation and maintenance, exclude the fuel costs, accounts for about 1% of the cost of power generation, which is easily neglected. Operation and maintenance costs are mostly fixed costs, and will not change significantly with the increase of power generation. But investment in nuclear energy is relatively high in spent fuel disposal and decommissioning. The decommissioning cost of nuclear power is generally included in the investment and construction cost, which means that after the operation period of nuclear power expires, the capital is needed to ensure the safety and reliability of nuclear reactor. This proportion is between 10% and 15% of the initial investment in nuclear power plants, which is currently 10% in China. [11] Spent fuel disposal costs are generally included in fuel costs, including the storage and management costs of radioactive waste during the nuclear fuel reaction stage, and the storage and management costs of spent nuclear fuel after use. At present, the levy standard is about 0.027 RMB/kWh in China.

Pricing mechanism of feed-in tariff for nuclear power units is analyzed. At first, the domestic policy was based on the operating period electricity price policy, but with the gradual development of nuclear energy technology and the rising cost of controlling nuclear energy investment, the pricing of feed-in tariff for nuclear power in China is gradually shifting to benchmark electricity price policy. There are tens of thousand electricity prices in operation period. The price is defined according to the mode of “one-case-one-discussion, one-plant-one-price”, that is, according to the construction cost of electricity prices.

Later, nuclear energy gradually developed. In order to better control the investment cost of nuclear energy, the relevant documents, issued by Development and Reform Commission, clarifies the implementation of benchmarking tariff policy for nuclear energy. It requires that the national electricity tariff for benchmarking is 0.43 RMB/kWh, and the cost of fuel lower than the benchmarking in nuclear power implements the electricity tariff for benchmarking in nuclear power; that higher than the region, or been undertaken the introduction of nuclear energy technology, independent innovation and the first demonstration project of localization of major special equipment can be suitable improved on the basis of the electricity tariff for benchmarking in nuclear power. The promulgation of this policy is of great help to stimulate the domestic nuclear power industry to reduce costs and actively introduce new types of equipment. After the reform of electricity market, it is expected that the pricing mechanism of domestic market will be relatively perfect in 2020, and the price regulation mechanism will be basically sound. [12] At present, the on-grid tariff of nuclear power plants for local power transactions is based on the protection of internal electricity, and the two parts of the protection of external electricity are realized.

4. Main problems and solutions of nuclear power in direct electricity transaction

4.1. Electricity scale should be combined with planning of energy development and requirements of supply-side reform.

The direct completion of transactions by large users is still in its infancy, limited by many factors such as resources and system, and the transactions can not be fully opened. Therefore, it is still necessary to reform the access mechanism of the main transaction entities, push nuclear power to power users and power generation enterprises to ensure the smooth completion of direct transactions. The scale of power construction and economic development of each city are different, and the access conditions for power generation enterprises and power enterprises are also different. Power generation enterprises and power users need not only to meet the national requirements of energy-saving and emission reduction, but also to comply with the relevant measures of local industrial policies. In The electric power development planning "in 13th Five-Year" (2016-2020), it is clearly pointed out that non-fossil energy consumption needs to be increased to 15% in 2020, and the installed power generation should be controlled around 770 million KW, accounting for 39%. At the end of 2017, the total installed thermal power units in China still accounted for about 60% of the total, so the current domestic energy structure adjustment is imperative and has a long way to go. Under such circumstances, the profit margin of high-emission power generation enterprises can be compressed by means of electricity market, which can reduce the enthusiasm of power generation, realize the adjustment of energy structure and better control the emission of carbon dioxide. Low-emission power generation enterprises, represented by nuclear power and water potential, can appropriately reduce the intensity of nuclear energy in direct electricity trading, realize electricity sales in the form of auxiliary services, and encourage the enthusiasm of power generation, so that the whole energy structure will be cleaner and lower carbon.

4.2. There is a lack of rationality in the unified pricing of nuclear power and thermal power.

The pricing mechanism mainly considers the management of transaction price, transmission and distribution price and auxiliary expenses, taxation, and the pricing mechanism of transaction price has a direct impact on the success or failure of direct electricity trading. The power generation costs of different power sources vary widely, and nuclear power and thermal power are particularly obvious. The fixed cost of the former is about 80% and the variable cost is about 20%. But the fixed cost of the latter is about 30%, and the remaining 70% can be recorded as variable cost. Therefore, if the nuclear power grid on-grid price and the coal-fired benchmark on-grid price are linked in a one-size-fits-all manner, there is a lack of rationality in direct power trading.

4.3. External cost factors and calculation basis of nuclear power unit

The external cost factor is mainly the incidental cost incurred during the production or consumption phase, but it has not paid the price for this. Environmental pollution cost is a typical representative. In the development of nuclear energy, waste treatment, spent fuel treatment, and nuclear equipment decommissioning are all calculated as power generation costs. With reference to the experience of Europe and the United States, the external cost of nuclear power is the lowest, and the external cost of coal-fired power is about 10 times than that of nuclear power.[13]-[14] When the EPA is currently managing coal, it is relatively inadequate in terms of environmental costs. The environmental value of clean energy is not fully incorporated into the price mechanism, which can easily distort the price mechanism and price distortion. There are drawbacks to the concept of energy conservation and emission reduction and the development of clean energy. External cost factors are not considered in the existing pricing mechanism.

The participation of direct electricity trading in nuclear energy is based on the unified pricing of local authorities, and there is no standardized calculation. However, in fact, taking a province with the highest proportion of nuclear power generation as an example, its theoretical value of nuclear power supportive absorption in 2016 is 7221 h, and its participation in direct electricity trading after landing is 1.847 billion kWh, which is far above policy that the actual power required by Provincial Party Committee is 7.3 billion kWh. [15] If the calculation of quantity of nuclear energy has better basis, and can better realize the overall transaction. In fact, the National Energy Administration has issued the document "Interim Method for Ensuring Nuclear Power Safety", which requires the priority generation rights plan to be determined by the multiple of the average hours of the previous year of the power generation equipment located at more than 6000 kW. [16] The multiple is planed based on the average utilization hours of the country in the previous three years. Such a model also has some drawbacks. It can integrate the average utilization hours of the whole country, and then make more flexible electricity consumption according to the actual needs of the enterprises and the background of the large market based on the local planning in the current year.

5. Conclusion

Nuclear power can be used in national defense and scientific research. It is also a vital power supply in China, and is a Chinese card in the construction of the whole area, and it is also a sign of the degree of industrialization and modernization in China. Based on the differences of R&D cost, input cost and pricing mode of nuclear energy and traditional power, local governments should fully integrate the cost and actual operation mode of quantity and feed-in tariff in direct trade about nuclear power, and formulate more reasonable and different principles from traditional fossil fuels under national policies.

6. References

[1] Mao L, Zhang S, Wei G. *Risks and Control Optimization Strategies for Network-Based Commissioning of Nuclear Power Plants in Large and Small Networks* [J]. Jilin Electric Power, 2017(1).

[2] Zhang M, Gao J, Liang Y. *Analysis of Operation Status of Large Nuclear Power Equipment under Failure of Power Grid* [J]. High Voltage Apparatus, 2018.

[3] Wei J. *Analysis and Treatment of the Problem of Poor Condensate Drainage in Air-conditioning of Nuclear Power Plants* [J]. Water Supply and Drainage, 2018.

[4] Yu W, Yao M. *Problems and Countermeasures of Condensate Water Treatment in 600mw Unit* [J]. Chemical Industry Management, 2018, No.488(17):145.
[5] Zhou Z. *Reactor Center of China Radio Nuclear Research Institute, China Radio Nuclear Group: Building Youth Civilization Number with "Five-One" Project* [J]. China Power Enterprise Management, 2017(15): 42-43.
[6] Zeng M. *Interpretation of the electric power development planning "in 13th Five-Year".* [J] China Power Enterprise Management 2017(1):14-16
[7] Jiang D. *Cause Analysis and Measures of Hose Burst in Nuclear Emergency Large-scale Emergency Diesel Units* [J]. Nuclear Science and Engineering, 2019(1).
[8] Yang A. *Analysis of Safety and Efficiency Development Path of Nuclear Power Industry: Based on Safety and Efficiency* [J]. China Nuclear Industry, 2017 (3).
[9] Qiao J. *Main Problems and Countermeasures of Metal Supervision in Power Plant Units* [J]. Science and Technology Innovation, 2017(17): 103-103.
[10] Liu T, Zhao J, Wu G. *Model and Method for Comprehensive Risk Assessment of Low Frequency Protection of Nuclear Power Connected to Power Grid* [J]. China Journal of Electrical Engineering, 2017(03): 38-47.
[11] Wen H. *Comparison and countermeasure study on external costs of nuclear power and coal-fired power.* [J] Chinese Journal of Nuclear Science and Engineering, 2005, 25(2):97-105.
[12] Zhang S, Li Q. *The Development and Scale of the Nuclear Power in China under the Restraint of Low Carbon.* [D] China Population Resources and Environment. 2015(06):49-54.
[13] Jing J, Luan H. *On the History of World Nuclear Development and the Road for China Nuclear Development.* [J] Northeast Electric Power Technology. 2008(2):48-52
[14] Ye P, Ma X, Zhu Y, Wang G, Zhang T, Sun F. *A Research Summary on Combined Peaking Load Strategies of Nuclear Power Plant.* [J] Northeast Electric Power Technology. 2014(9):55-59
[15] Zhi Y. *Research on Nuclear Power Dissolved Countermeasure.* [J] Energy of China.2017(7):20-24.
[16] Song Z, Shang W, Song W, Liu K, Lu Z, Zhang Z. *Development of Nuclear Power and Analysis on Peak Shaving.* [J] Northeast Electric Power Technology. 2015(5):40-44

IOP Conf. Series: Earth and Environmental Science **431** (2020) 012066 doi:10.1088/1755-1315/431/1/012066

Study on carbon emission reduction mechanism of thermal power plants in medium and long term trade

Xuefei Zhang[1], Yi Xiong, Chuanyu Xiong, Xuejun Tang, Zhiwei Li

1 Master, State Grid Hubei Electric Power Co., Ltd. Economic Technology Research Institute Hubei China 430077

E-mail: luckjobgood@163.com

Abstract. Electricity market is gradually tending to be more energy-saving and environmental-friendly. In the context of medium and long-term electricity trading mechanisms, it is important to implement energy-saving and emission reduction with more reasonable and effective mechanism to solve the shortcomings in the overall environment and achieve energy conservation. The author finds that the core idea of energy conservation and emission reduction mechanism abroad to internalize the external cost. After in-depth study, the author summarizes the problems in realizing energy conservation and emission reduction in the medium and long-term electricity trading mechanism in the current market. The core design ideas and main development models of the mechanism are analyzed. Finally, the author analyses the design of market mechanism under the mode of trading volume restriction and power transfer in power plants. In the whole process, the author makes an auxiliary analysis with actual cases for peer exchange.

1. Introduction

With the gradual development of human civilization, the continuous progress of society and the rapid development of economy, the coordination between human beings and the environment has gradually presented problems, and the contradictions have intensified in various environments. Over-emission of global carbon dioxide has a direct impact on climate [1]. Since the 21st century, the most important problem facing mankind is the energy crisis. Under such circumstances, how to achieve better energy conservation and emission reduction has become the focus of scholars. The document No. 9 issued by China Development Corporation in 2015 is to deepen the reform of the electricity constitution, to carry out a comprehensive reform of the electricity system in China [2]. At present, the development of domestic power and trading institutions have been completed, market-oriented transactions have been formed, and diversification of market transactions have been formed. Most domestic provinces and cities have realized the power system for large users to purchase electricity directly. The market has gradually developed certain trading rules, and the medium and long-term electricity trading mechanism has gradually become more diverse. [3]-[5] The medium and long-term transactions in various provinces and cities across the country are presented by annual and monthly transactions. [6] After the reform of the electricity constitution, the electricity commodity market has presented a posture of blooming flowers, the cost of electricity in multiple industries has decreased, and the society has gradually transformed into a more friendly and efficient posture.

2. Problems in realizing medium and long-term electricity trading mechanism for energy conservation and emission reduction in the current market

The most important part of electricity reform is to form a system of electricity price market and establish a more effective mechanism to optimize the whole market resources. [7] The lower the cost of generating units, the greater the competitiveness of the whole market, the more advantageous and more power generation share in the whole market transaction to enhance the operation efficiency of the electricity system. Power plants will choose lower cost coal consumption to complete power generation, so when market costs are relatively stable, the level coal consumption and cost show a positive correlation, that is to say, the lower the level of coal consumption is, the lower the cost is. [8] However, if the fixed cost of generating units increases and the level of coal consumption varies, the overall competitiveness may be reversed. After that, market competition and energy-saving and emission reduction will go against each other. First of all, low coal consumption units generally have larger capacity, higher parameters, shorter operation time, higher cost and interest, so the whole bidding stage takes longer. In addition, the retrofit of small capacity units can reduce the level of coal consumption, but it needs higher retrofit cost, and the market bidding will decline in a short time. The existence of this contradiction is more remarkable at this stage because of the influence of the current transaction form. In the future, market reform will gradually infiltrate, various mechanisms of the spot market will be established and perfected, and the variable price cost will be controlled relatively well, which can well avoid the risk of such problems. [9] Therefore, it is one of the core tasks to solve the problems of energy-saving and emission reduction in medium and long-term electricity trading and to improve the market bidding contradiction.

3. Core design and main development modes of energy conservation and emission reduction mechanisms

The basic design idea of energy-saving and emission reduction is internalization of external cost. Under this concept, in order to ensure that the market bidding is within a reasonable range, it is necessary to reduce the overall development cost, so that the whole market subject can develop steadily under different competition, and truly realize the macro-control of market resources. The main operating modes of exterior cost internalization include four kinds, which are the most recognized mechanisms in the world. They are carbon tax mode, green certificate trading mode, quota trading mode and carbon emissions trading mode. [10]-[11]

3.1. Carbon tax model

According to the company's carbon emissions, the company imposes tariffs, and reverse management enables enterprises to reduce costs through energy conservation and emission reduction. The carbon tax model is gradually evolved according to Pigou's theory. The core idea of this model is to manage the environmental problems by taxation, so that the external costs are internalized, and the individual emissions are monitored macroscopically to improve the overall social benefits. At present, five Nordic countries including the Netherlands, Finland and Denmark have fully implemented the carbon tax model. [12]-[14] This new tax does not require an organization and is easier to implement. However, there will be information asymmetry in the carbon tax model from the actual situation analysis, and the implementation of the tax rate needs to combine the enterprise cost and the social cost. In different regions, the marginal cost difference is large, there is lack of practicality on how to calculate such costs. On the other hand, enterprises whose taxes exceed the emission reduction rate will choose to pay taxes to reduce costs, and the monitoring of total emissions will lose its own value; the effect of low taxation on the management of enterprises is not obvious. Therefore, in the power industry, the demand for electricity is just needed, and the carbon tax management mode has some limitations on the role of enterprise emission reduction.

3.2. Green certificate trading model

Under the market, the completion of the transaction with the issuance of green certificates has enabled the development of the entire renewable energy source. [15] Theoretically, this model can quantify energy conservation and emission reduction. Currently, this model can be completed in two forms, that is, voluntarily purchasing certificates or mandatory quotas. However, the current domestic power market system is relatively imperfect, and there is still a lack of mechanisms to effectively transport renewable energy, so this trading model has not been carried out.

3.3. Quota trading model
Exhaust quotas or energy consumption quotas is implemented for enterprises and industries with certain standards. After enterprises exceed the rated quota, they need to accept the punishment of market supervision agencies or purchase quotas according to market transactions, so that the emissions and energy consumption of the entire province and city can be controlled within a certain range to achieve market management. [16]-[17] The entire quota is mainly distributed free of charge and distributed, and the quotas of different enterprises and industries are different. Free distribution can be assigned based on history and benchmarks. In historical distribution, enterprises are allocated in a fixed amount according to their historical emissions. The relative calculation is relatively simple and the supporting data is less, but the enterprises with poor development also need to bear high emissions and energy consumption, which will show problems on the quota. The benchmark allocation is based on the company's basic emissions, analyzing the average level of energy consumption, setting the minimum emissions and a reasonable performance management model, which will promote the energy-saving and emission reduction in the entire industry.

3.4. Carbon emissions trading model
This model essentially controls the entire market based on the total amount of carbon emissions. Under the carbon emission trading mechanism, enterprises with low emissions can sell shares to enterprises with excess emissions and obtain higher profits; enterprises with excess emissions need to pay high share fees, which promotes enterprises to increase energy conservation and emission reduction.[18] This model is relatively cheaper, it only needs to allocate the emission reduction targets and shares. However, the power industry is gradually developing, and the trend of big data is imperative. Under this model, it might be difficult to implement. [19]-[21]
The comparison and analysis of four kinds of trading mechanisms are shown in Table 1.

Table 1. Comparison and analysis of four kinds of trading mechanisms

Trading Mechanism	Advantages & Disadvantages
Carbon tax model	Reduce costs, and the monitoring of total emissions will lose its own value, the effect of low taxation on the management of enterprises is not obvious
Green certificate trading model	Low-cost, but relatively general at carbon reduction effect and promoting the development of nonaqueous renewable energy effect.
Quota trading model	Good at cost, carbon emission reduction effect, power industry installed structure and power generation structure optimization effect
Carbon emissions trading model	Relatively limited at the adjustment effect of power industry structure optimization at a certain cost.

4. Design of market mechanism under the limitation of trading volume and power transfer mode of power plants
The reform of electricity mechanism is advancing in an all-round way. The medium and long-term trading mechanism in months or years has gradually become the main body of domestic electricity transactions, and many provinces have been fully launched. If the goal of energy conservation and emission reduction is to be applied in the medium and long-term electricity trading mechanism, there are three principles to be followed: 1) to ensure that the emission of energy consumption can be controlled in the target; 2) to integrate closely with the market after linking up the current trading mechanism to avoid the significant changes in the market mechanism and the effect of the orderly conduct of the market; (3) higher execution, easier access to basic data and lower supporting investment. According to these requirements and background, a Capacity-and-Transfer (CAT) trading

mode can be selected for quota trading. C stands for capacity limitation; T refers to power plant power transfer. CAT takes the unit coal consumption as the quota object. According to the coal consumption and emission relationship table near the power plant, the comprehensive energy-saving side benefits and the emission reduction side benefits are realized. Integrating energy-saving and emission reduction into the current electricity constitution will have a significant role in promoting the construction of the entire electricity market. Market-oriented mechanism to achieve the allocation of power resources has a good role in promoting the research of renewable energy, and is conducive to the formation of a low-carbon energy structure in the whole market.

Under the medium-term and long-term bilateral trading mode, the basic electricity of power plant is allocated, and energy-saving and emission reduction is achieved according to the coal consumption level of the unit. The core factors include trading volume limitation of coal consumption level and power transfer in power plants. The level of coal consumption determines not only the amount of bilateral transactions to achieve the quota, but also the amount of electricity involved in bidding transactions for the whole annual cost of units. Under this mode, the contractual power transfer can be carried out again. Each power plant can transfer part or all of the electricity according to the situation. The seller can buy electricity and buyers can also conduct electricity sales transactions to achieve the role of energy saving and emission reduction. In this process, the core control point is that all contract transactions are completed under the concept of low carbon. CAT mechanism can promote the healthy development of the whole market according to the current situation of electricity market in China and the actual needs of the market and the timeliness and complexity of energy-saving and emission reduction. Therefore, the total emissions can be monitored and the competitiveness of the units with lower coal consumption is stronger, which is helpful for energy-saving and consumption reduction under the background of the whole medium-term and long-term power trading mechanism.

5. Conclusion

In summary, under the internalization mechanism of external costs, the author gradually develops the CAT mechanism, and carries out quota trading mechanism under the market mode of medium-term and long-term electricity trading, monitors the whole contract in the form of contract, realizes the optimal allocation of power resources, and the market scheme can closely link up all kinds of operation and adjustment. On the other hand, the current monitoring of power plants and market share can well encourage power plants to save energy and reduce consumption, develop new clean energy to obtain higher benefits. Moreover, it also can promote enterprises to think about how to better save energy and reduce emissions to reduce costs and to promote energy-saving and emission reduction policies in the medium-term and long-term electricity trading mechanism.

6. References

[1] Chen W, Wu Z, He J, et al. *Carbon emission control strategies for China: A comparative study with partial and general equilibrium versions of the China MARKAL model*[J]. Energy, 2007, 32(1):59-72.
[2] Yang Q, Cai H, Yan M. *Design and Application of Power Market Mechanism in Yunnan Based on Incentive Compatibility and Deep Game* [J]. Automation of Electric Power Systems, 2017(24): 33-40.
[3] Li Z, Sun R, Zhang J. *Design of Medium-term and Long-term Power Load Forecasting Algorithm Based on Improved BP Neural Network* [J]. Journal of Automation & Instrumentation, 2017(10).
[4] Wang J, Zhong H, Xia Q. *Design of Power Market Competition Mechanism Based on Value Fair Distribution* [J]. Automation of Electric Power Systems, 2019, 43(02): 16-27.
[5] Dong L, Gao C, Yu J. *FM Reserve Market Mechanism on Decomposition of Medium and Long-term Electricity Contracts* [J]. Automation of Electric Power Systems, 2018, v.42; No.636(14):67-72+80.
[6] Yang Q, Cai H, Yan M. *Design and Application of Power Market Mechanism in Yunnan Based on Incentive Compatibility and Deep Game* [J]. Yunnan Electric Power Technology, 2018, 46(2): 73-80.

[7] Cao Y, Ding T, Hou Y. *Design and Simulation of Long-term Transaction Mode in Electricity Market under the Background of Global Energy Internet* [J]. Global Energy Internet, 2018, V.1 (S1): 46-52.

[8] Chen G, Xie Z, Liu M. *Design and Application of Market-oriented Transaction Settlement Mechanism of Total Electricity Jiangxi in Province Based on Incentive Compatibility and Prospect Theory* [C]. China Electrical Engineering Society Power Market Professional Committee 2018 Annual Conference and National Electricity Trading Organization Alliance Forum.

[9] Jiang Z, Zhao T and Wang J. *Potential Impact of National Carbon Trading Market on Power Industry Based on Multi-Agent Model* [J]. Modern Power, 2017 (4).

[10] Chen W. *The costs of mitigating carbon emissions in China: findings from China MARKAL-MACRO modeling*[J]. Energy Policy, 2005, 33(7):885-896.

[11] Jiang K, Hu X, Zhuang X, etc. *China's Low-carbon Scenarios and Roadmap for 2050*[J]. Sino-global Energy, 2009.

[12] Ding W, Wang B, Xing Y. *Research on Multidimensional Electric Power Financial Market Mechanism: Based on the Practice of Foreign Mature Electric Power Financial Market* [C]. China Electrical Engineering Society Power Market Professional Committee 2018 Annual Conference and National Electricity Trading Organization Alliance Forum.

[13] Wang T, Wang Y. *Construction of Demand Side Response Mechanism under the Background of Power Market Reform* [J]. China Electric Power Enterprise Management, 2017 (13): 46-47.

[14] Xue X, Wu Q, Zhang J. *Discussion on Spot Market Models of Foreign Electricity and Spot Market Construction in China* [C]. China Electrical Engineering Society Power Market Professional Committee 2018 Annual Conference and National Electricity Trading Organization Alliance Forum.

[15] Tan Z, Liu W, Liu P. *Policy Effect of Tradable Green Certificate and Carbon Emission Trading on China's Electric Power Market*[J]. Technology Economics, 2014.

[16] Li X I, Yu C W. *Impacts of emission trading on Carbon, Electricity and Renewable Markets: A review*[J]. 2010:1-7.

[17] Baron R. *Policy Options for Low‐Carbon Power Generation in China: Designing an Emissions Trading System for China's Electricity Sector*[J]. Iea Energy Papers, 2012.

[18] Chen J. *Analysis of the International Carbon Emission Trading Market and China's Countermeasures*[J]. World Economic Research, 2015, 04(2):28-34.

[19] Zhang D, Liu P, Ma L, et al. *A multi-period optimization model for optimal planning of China's power sector with consideration of carbon mitigation—The optimal pathway under uncertain parametric conditions*[J]. Computers & Chemical Engineering, 2013, 50(31):196-206.

[20] Zhang D, Liu P, Ma L, et al. *A multi-period optimization model for planning of China's power sector with consideration of carbon dioxide mitigation—The importance of continuous and stable carbon mitigation policy*[J]. Energy Policy, 2013, 58:319-328.

[21] Guo Z, Cheng R, Xu Z, et al. *A multi-region load dispatch model for the long-term optimum planning of China's electricity sector*[J]. Applied Energy, 2017, 185:556-572.

IOP Conf. Series: Earth and Environmental Science **431** (2020) 012064 doi:10.1088/1755-1315/431/1/012064

Real-road energy consumption characteristics of electric passenger car in China: a case study in Shenzhen

Yi Ai[1], Jingyuan Li[2], Hanzhengnan Yu[2*] and Yu Liu[2]

1 Beijing Municipal Ecological Environment Bureau, Beijing, China
2 China Automotive Technology and Research Center Co., Ltd., Tianjin, China
E-mail: yuhanzhengnan@catarc.ac.cn

Abstract. As the increasing complains of the electric passenger car owners about the lower pure electric mileage under real-road driving condition than the regulation standard test result, the annual real-road energy consumption characteristics of 20 MPV electric passenger cars in Chinese city, Shenzhen, have been investigated to analyse the effect factors causing the energy consumption difference between these two results. Results showed that the annual variations of real-road energy consumption rate of each month were agreed with the variations of air conditioning using duration. The highest and lowest energy consumption rates were obtained in July and March, which increased the energy consumption rate of whole vehicle about 24% in the maximum extent. The difference of the energy consumption between real-road and regulation standard test was attributed to the effects of air conditioning using and driving condition (driving velocity and acceleration distribution), which have been qualified in this paper.

1. Introduction

To solve the two key issues of the environmental protection and energy conservation, electric vehicle is introduced into the transport sector due to its superior advantages of zero emission and high efficiency energy conversion characteristics. However, because of the lower energy density of the onboard battery of the electric vehicle compare to the gasoline or diesel fuel of the traditional ones, the short driving mileage seriously restricts its development [1-2]. In additions, the obvious decrease of the mileage with the use of air conditioning in summer and winter often caused the complaints of the electric vehicle owners. The energy consumption characteristics of the electric passenger car in every country's regulation standard are evaluated by the chassis dynamometer method implementing specific test cycle with no use of air conditioning. In current Chinese regulation standard (GB/T 18386-2017), NEDC is the chosen test cycle [3]. However, the real-road energy consumption characteristic is influenced by many parameters and can be divided into traffic condition (driving velocity and driving acceleration), road infrastructure (road grade or surface roughness), environmental parameters (temperature or wind speed), and driver's driving aggressiveness, which finally caused the gap between these two energy consumption results [4-6]. In this paper, the annual real-road energy consumption characteristics of 20 MPV electric passenger cars in Chinese city, Shenzhen, have been investigated and compared to the regulation standard test result. The effect factors on the energy consumption difference have been summarized and qualified.

2. Experiment vehicle and data acquisition

2.1. Vehicle specification

IOP Conf. Series: Earth and Environmental Science **431** (2020) 012064 doi:10.1088/1755-1315/431/1/012064

In this paper, the annual data of 20 MPV electric passenger cars in Shenzhen have been collected, which the specifications have been summarized in Table 1.

Table 1. Vehicle specification

Parameters	Value
Length*width*height(mm)	4560*1822*1630
Curb weight(kg)	2380
Motor maximum power(kW)	120
Motor maximum torque(N·m)	450
Motor type	DC motor
Battery capacity(kW·h)	82
Battery type	lithium iron phosphate

2.2. Data acquisition and preprocessing

Because of the excursion of the GPS's zero point and other data transmission errors, the acquisition data should be pre-processed, and the processing rules has been listed below.

The driving velocity below 0.5km/h was treated as stationary, and the points with driving velocity above 150km/h and the acceleration above 6m/s^2 or below -6m/s^2 had been removed, and the acceleration was calculated according to equation (1).

$$a_{i,i-1} = \frac{V_i - V_{i-1}}{t_i - t_{i-1}} * \frac{1000}{3600}\ , \mathrm{k} = 1,2,\cdots \mathrm{k} \tag{1}$$

The real-road energy consumption rate with the unit of kW·h/100km was calculated by equation (2). v is the vehicle driving velocity, which was collected by the GPS module of the data collection device. U and I were the output voltage and current of the onboard battery, which were obtained by the OBD module.

$$EC = \frac{100 \times (\int UI\, dt / 3600000)}{\int v dt / 3600} = 0.1 \times \frac{\Sigma(UI)}{\Sigma v} \tag{2}$$

The sampling frequency of the data collection device was fixed at 1Hz. The real-time data was uploaded to the server through the 4G net, thus enabling year-round 7*24 data acquisition from July, 2017 to June, 2018, and the annual average mileage of each electric passenger car was 31,000km.

3. Results and discussion

3.1. Annual variations of real-road energy consumption characteristics

The annual variations of the real-road energy consumption characteristics have been shown in Figure.1. Results showed that the annual average value of the energy consumption rate was 20.36 kW·h/100km, which was slightly higher than the regulation standard test value under NEDC (20.00 kW·h/100km). In additions, both the value of energy consumption rate and the error range showed a first decreasing then increasing variation trend. The highest value was obtained in July, which was 23.81 kW·h/100km, 19% higher than the regulation standard test value. And the lowest value was obtained in March, which was 19.15 kW·h/100km, 4% lower than the regulation standard test value. The differences between the real-road and regulation standard test could be attributed to the variations of using of air-conditioning and driving condition, which would be discussed in the below separately.

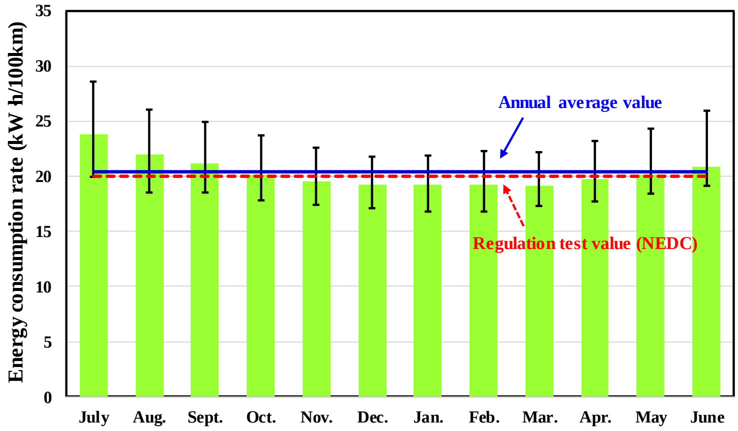

Figure 1. Annual variations of real-road energy consumption rate

3.2. Effect of air conditioning on real-road energy consumption characteristics

To investigated the effect of air conditioning on real-road energy consumption characteristics, the air conditioning using duration in each month should be counted firstly. According to the questionnaire's average result among the 20 drivers of the experimental passenger car in this study, the air conditioning was turned on when the environmental temperature was up to 28 ℃ or below to 12 ℃. The variations of the daily maximum and minimum environmental temperature have been presented to estimate the number of days using air conditioning in a round of year as shown in Figure.2.

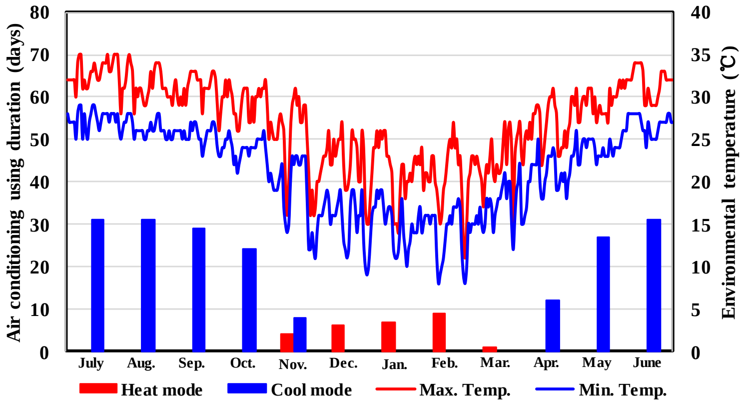

Figure 2. Variations of environmental temperature and air conditioning using duration

Results showed that the shortest air conditioning using duration was found in March, which was the same month of the lowest real-road energy consumption rate obtained. Comparing the highest energy consumption rate of July and the lowest value of March, it indicated that air conditioning using increased the energy consumption rate about 4.66 kW h/100km in the maximum extent, about 24% increase of the whole vehicle energy consumption.

3.3. Effect of driving condition on real-road energy consumption characteristics

To separate the effect of air conditioning on the real-road energy consumption characteristics, only the data of March,2018 has been analysed for investigating the effect of driving condition. The effect of the driving condition on energy consumption could be divided into the factors of driving velocity distribution and the driving acceleration distribution.

Figure.3 shows the driving velocity distributions of the real-road driving condition and the NEDC condition. It worth noting that the driving conditions with zero driving velocity (idling condition) have been dismissed. It could be found that the diving velocity distribution was concentrated in the low driving velocity range under real-road driving condition, and the largest proportion was the range of 10-20km/h. However, the diving velocity distribution was concentrated in medium velocity range under NEDC conditions, especially the range of 30-50km/h. This resulted the average driving velocity under NEDC condition (43.44km/h) was about 55% higher than the real-road driving condition (28.05km/h).

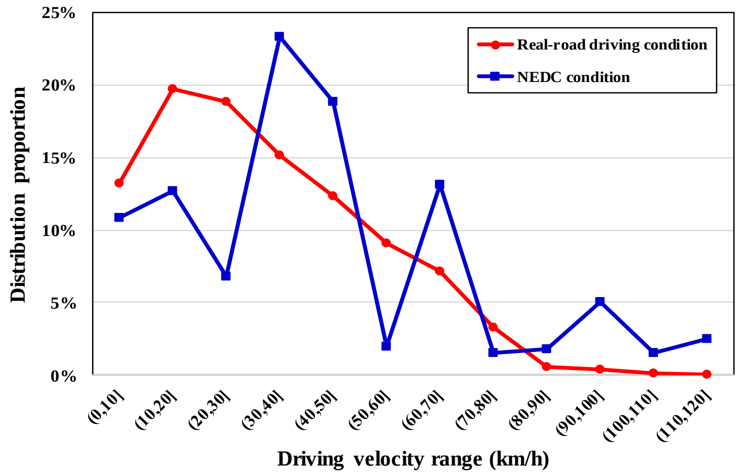

Figure 3. Driving velocity distribution under real-road driving and NEDC conditions

The varation of real-road energy consumption rate with the change of driving velocity is shown in Figure.4. Results showed that with the increase of the driving velocity, the real-road energy consumption rate first decreased then increased quadratically with the driving velocity extending, and the lowest value was obtained in the driving velocity range of 40-50km/h. The first decreasing trend of energy consumption was because of the movement of the motor’s operation points, from the low efficincy region to the high efficincy region. And the subsequent increasing trend was mainly attibuted to the increase of air resistance and rolling resistance.

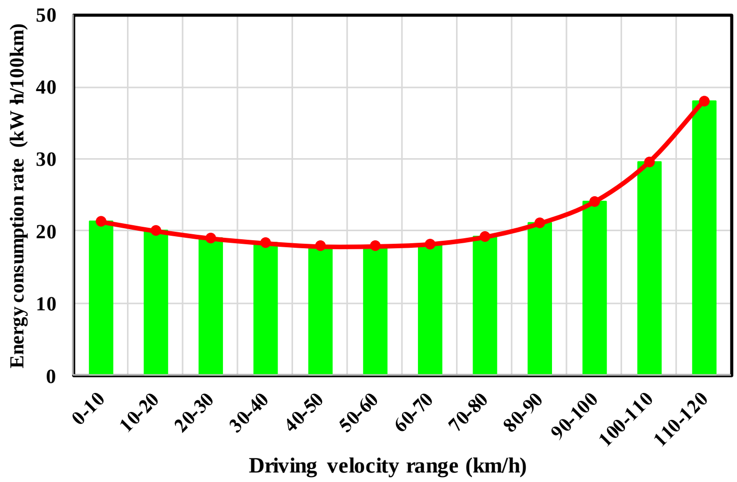

Figure 4. Variation of real-road energy consumption rate with the change of driving velocity

The energy consumption under NEDC condition was 19.81 kW h/100km which was calculated according to each driving velocity range proportion. This indicated that the effect of the driving velocity distribution caused a different energy consumption of 0.66 kW ћ/100km between real-road and regulation standard test.

The largest driving deceleration proportion and absolute negative acceleration value were beneficial to recover more braking energy resulting in a decrease in the energy consumption rate. The driving acceleration distributions of the real-road driving condition and the NEDC condition are shown in Figure.5. It worth noting that the driving conditions with zero acceleration (idling condition and constant velocity condition) have been dismissed, only the acceleration and deceleration conditions have been maintained.

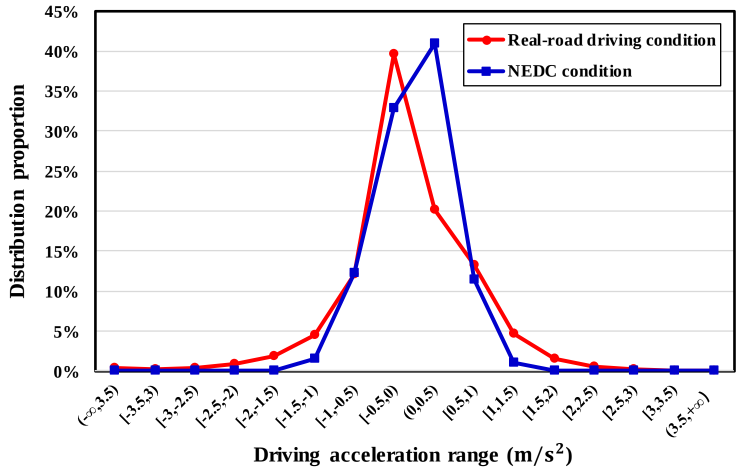

Figure 5. Driving acceleration distribution under real-road driving and NEDC conditions

Results showed that the driving acceleration distribution presented normal distribution, the largest proportion of the acceleration range was [-0.5,0) m/s^2 under the real-road driving condition, however, was the range (0,0.5) m/s^2 under the NEDC condition. The proportion of the deceleration condition was 59.67% under the real-road driving condition, which was higher than the NEDC condition (46.61%). The average negative acceleration was -0.77m/s^2 which the absolute value was higher than the NEDC condition (-0.74 m/s^2). This proved that the braking recovered energy under real-road driving condition was more than the NEDC condition, and indicated that the effect of the driving acceleration distribution caused a different energy consumption rate of 0.19 kW ћ/100km between real-road and regulation standard test.

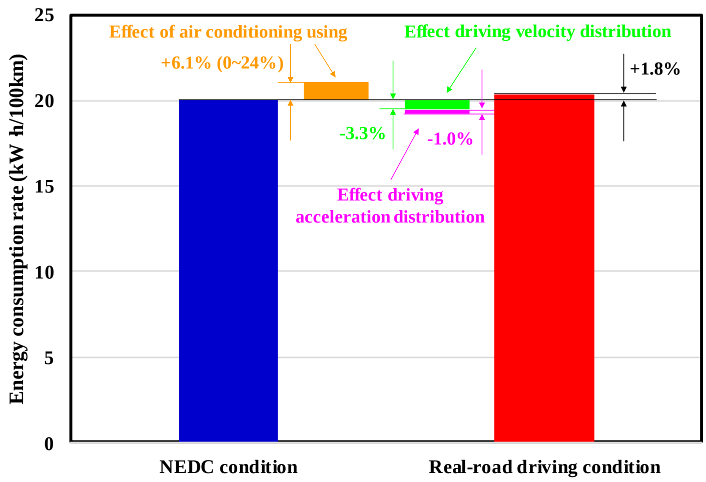

Figure 6. Contribution of each effect factor on energy consumption between real-road driving and NEDC conditions

To sum up, the difference of the energy consumption between real-road and regulation standard test could be attributed to the effects of air conditioning using, driving velocity distribution and driving acceleration distribution, and could be qualified as below, as seen in Figure.6. Results showed that the effect of air conditioning using contributed 0~24%, an average of 6.1% higher of real-road energy consumption, and the effects of driving velocity distribution and acceleration distribution contributed to -3.3% and -1.0%, respectively. Finally, the real-road energy consumption was 1.8% higher than the regulation standard test result.

4. Conclusion

In this paper, the real-road energy consumption characteristics of 20 MPV electric passenger cars in Shenzhen, China have been investigated. The conclusion can be reached as the following.

The annual average real-road energy consumption rate was 20.36 kW ħ/100km, which was slightly higher than the regulation standard test value under NEDC (20.00 kW ħ/100km), about 1.8%. The highest and lowest values were obtained in July and March respectively, which was agreed with the air conditioning using duration variation. Air conditioning using increased the energy consumption rate of whole vehicle about 24% in the maximum extent.

The effect factors including air conditioning using, driving velocity distribution and driving acceleration distribution which caused the energy consumption rate's difference between real-road and regulation standard test. Air conditioning using contributed an average of 6.1%, driving velocity distribution and acceleration distribution contributed to -3.3% and -1.0%, respectively.

5. References

[1] Roskilly A P, Palacin R and Yan J 2015 *J. Applied Energy* Novel technologies and strategies for clean transport systems *J. Applied Energy* **100(157)**: 563–6.

[2] Du J, Ouyang M and Chen J. 2017 Prospects for Chinese electric vehicle technologies in 2016–2020: Ambition and rationality *J Energy* **120**: 584-96.

[3] Electric vehicle-Energy consumption and range-Test procedures (GB/T 18386-2017) 2017 Standardization Administration of China.

[4] Yao E, Yang Z, Song Y and Zuo T 2013 Comparison of electric vehicle's energy consumption factors for different road types *J Discrete Dynamics in Nature and Society* **2013**.

[5] Yi Z and Bauer P H. 2015 Sensitivity analysis of environmental factors for electric vehicles energy consumption *C IEEE Vehicle Power and Propulsion Conference (VPPC)* **2015**: 1-6.

[6] Alvarez A D, Garcia F S, Naranjo J E, Anaya J J and Jimenez F 2014 Modeling the driving behavior of electric vehicles using smartphones and neural networks *J IEEE Intelligent Transportation Systems Magazine* **6(3)**: 44-53.

Acknowledgments

This study is supported by the National Key R&D Program of China (2018YFB0106404) and Research and Development of Chinese New Energy Automobile Products Test Driving Cycles (CATC).

Author Index